

**TWO-PHASE FLOW DYNAMICAL SIMULATIONS
AND MODELLING
BY
XIAOGANG YANG**

A thesis submitted to the
Faculty of Engineering
of the
University of Birmingham
for the degree of
Doctor of Philosophy.

Fluid and Surface Transport Team,
School of Chemical Engineering,
University of Birmingham,
Birmingham B15 2TT
England.

January 1996

UNIVERSITY OF
BIRMINGHAM

University of Birmingham Research Archive

e-theses repository

This unpublished thesis/dissertation is copyright of the author and/or third parties. The intellectual property rights of the author or third parties in respect of this work are as defined by The Copyright Designs and Patents Act 1988 or as modified by any successor legislation.

Any use made of information contained in this thesis/dissertation must be in accordance with that legislation and must be properly acknowledged. Further distribution or reproduction in any format is prohibited without the permission of the copyright holder.

19230524



v2471732

CAUTION: The ideas and methods described in this thesis include proprietary information whose copyright is jointly retained by FRED Ltd and University of Birmingham.

SYNOPSIS

Considerable progress in understanding and predicting two-phase flow phenomena has been advanced over the past 10 years or so using a combination of model development, computational techniques and well-designed experiments. However, there remain many modelling uncertainties mainly associated with inadequate physical prescriptions rather than with limitations of the numerical schemes. The present project addresses some of these questions, in particular in relation to dispersive transport by transient large eddies in free shear flows.

Recent literature on existing models is reviewed in chapter 1. There are several fundamentally different formulations couched in terms of macroscopic equations. The most obvious distinction between these approaches is in terms of their formulations as Eulerian-Eulerian, Eulerian-Lagrangian or Lagrangian-Lagrangian and we summarise the main advantages and disadvantages of these approaches.

In chapter 2 we address the behaviour of voidage profiles as reported by Serizawa *et al.* (1975a,b) and Wang *et al.* (1987) for vertical pipe flow, with notable near-wall voidage 'peaking' for upward flow and 'coring' on the centerline for downward flow. Using a simple transport model expressing the balance between lift force and wall attraction by transverse pressure gradient and an independent the bubble dispersion, the results showed how the lift force dominates the pressure gradient associated with the gradient of Reynolds averaged normal stresses.

Chapter 3 applies a Lagrangian-Lagrangian scheme first reported in Thomas *et al.* (1983) to survey the behaviour of bubble dispersion in two-dimensional turbulent free shear layer flows. Particular attention is paid to the trapping effect of large eddies and the evaluations in terms of bubble trajectories and Lagrangian statistical measures. Of the three dynamical parameters Π , Γ and γ , γ (mass density ratio) is irrelevant for bubbles, but Π plays a key role in attracting the bubbles into the large eddies and Γ in their retention and locations within the eddies. When $\Pi \rightarrow 0$ (negligible inertial attraction) the dispersion is nearly neutral and the use of the gradient diffusion model may well suffice. Following the approach of Sene *et al.* (1994), we estimate the dispersion coefficients through Lagrangian statistics, and compare

the values for the bubbles and for the fluid, showing their ratio is about 1.0 for a long term dispersion, and thus reinforcing the findings of Sene *et al.* (1994).

The dispersion calculations for particles in mixing layers (Chapter 4) indicate that the ratio of inertial to shear force (Π/Γ) represent a parameter scaling which plays a similar role to the Stokes number (e.g. Crowe *et al.* 1985), and that particle dispersion exceeds that of the fluid as reported by the other researchers (e.g. Crowe *et al.* 1993). Our simulations show that particles entrained into the large-scale structure are subsequently centrifuged to the outer edges of the eddies where they accumulate at, and preferentially migrate towards, the stagnant zone between adjoining large eddies. Supplemented by mass density ratio γ , Π and Γ comprise essential dimensionless groups characterizing discrete phase transport. The importance of transient pressure gradient in the external irrotational flows induced by travelling eddies is highlighted by comparing between the results of our discrete vortex simulation with a simple Gaussian stochastic model.

Chapter 5 applies the modelling approach to bubble dispersion in a plane free jet, using the simulation to show that inertial and shear-induced lift forces are responsible for bubble trapping by large eddies along the edges of the jet. For an upflowing jet, the calculations deliver bimodal voidage profiles consistent with expectations for the mixing layer studies, but are at odds with assumed Gaussian profiles adopted in previous studies of bubbly plumes and jets. An important genuine conclusion addressed in Chapter 6 is that discrete phase dispersion (particles and bubbles) is highly correlated with vorticity excursions.

In sum, we have addressed some important aspects of dispersive transport by transient large eddies in free shear flows. The implication is that dispersive transport is strongly influenced by vorticity transport. The need now is to formulate Eulerian statistical modelling that specifically incorporate this behaviour, thereby reducing the uncertainties of interphase pressure closure encountered with existing two-fluid couched in terms of momentum transport.

DEDICATION

To my wife, Xiaobing Huang, and our daughter, Jie Yang, my parents and my parents-in-law for their endless love, continual support and encouragement.

ACKNOWLEDGEMENTS

I would like to express my gratitude to my supervisor, Dr Neale Thomas, for his consistent help, encouragement, physical insight, creative influence and patient guidance in the preparation of this thesis, and support with FAST Team facilities, without which this project would not have been possible. Also, my thanks is go to the thesis' two referees, Dr M. W. Reeks of Nuclear Electric plc, Berkeley and Professor J. M. Gunn of School of Physics, University of Birmingham for their expert guidance.

I would like to thank the members of the FAST Team, past and present, for their assistance. In particular, Dr R. J. Onslow for many hours of pleasurable discussion. Also, thank you to Mr Duncan Webb for his very careful reading and revising the thesis draft in the preparation of this thesis.

Finally, I would especially like to thank my wife for her understanding and full support through duration of this project.

This work was sponsored by an ORS scholarship and the Freducational Foundation (FRED Ltd). The completion of this thesis was also supported by the Great Britain-China Educational Trust and the Gilchrist Educational Trust. Their sponsorship is gratefully acknowledged.

TABLE OF CONTENTS

LIST OF FIGURES	Page
Chapter 1	i
Chapter 2	iii
Chapter 3	iv
Chapter 4	vii
Chapter 5	x
Chapter 6	xi

NOMENCLATURE

Chapter 1	xiii
Chapter 2	xiii
Chapter 3	xiv
Chapter 4	xiv
Chapter 5	xiv
Chapter 6	xv
Chapter 7	xvi

CHAPTER 1: CURRENT STATUS OF TWO-PHASE FLOW DYNAMICAL SIMULATION AND MODELLING

SUMMARY	1-1
1 INTRODUCTION	1-2
2 CURRENT STATUS OF CFD SOFTWARE FOR TWO-PHASE FLOW	1-4
2.1 Basic Conservation Equations and Solution Procedure	1-4

2.2 Applications and Limitations	1-6
3 FORCES ACTING ON BUBBLES AND PARTICLES	1-6
3.1 Identification of Forces	1-7
3.1.1 Added mass and pressure gradient forces	1-7
3.1.2 Drag force	1-9
3.1.3 Lift force	1-11
3.1.4 Basset historic force	1-11
3.2 Generalised Force Law	1-12
3.3 Validation of the Equation of Motion	1-14
4 MATHEMATICAL MODELLING OF TWO-PHASE FLOW	1-15
4.1 Two-Fluid Model	1-15
4.1.1 Averaging methods	1-16
4.1.2 Averaged equation	1-17
4.2 Constitutive Equations	1-19
4.2.1 Pressure relations	1-19
4.2.2 Inertial force closure	1-20
4.3 Turbulence Closure	1-21
4.3.1 One-phase flow	1-21
4.3.2 Two-phase flow	1-25
4.3.3 Examples of application of turbulence closure models	1-28
4.4 Passive Scalar Transport By Turbulence	1-29
4.5 Bubble and Particle Dispersion in Free Shear Flows	1-33
5 OVERVIEW OF SIMULATION STRATEGIES	1-38
5.1 Eulerian Two-Fluid (Pseudo-Continua) Approaches	1-38
5.2 Eulerian-Lagrangian Approaches	1-39

5.3 Lagrangian-Lagrangian Approaches	1-40
6 RECAPITULATION AND IMPLICATIONS	1-42
REFERENCES	1-44
APPENDIX I	1-53
FIGURES	
 CHAPTER 2: PREDICTION OF VOID FRACTION PROFILES USING GRADIENT DIFFUSION MODELS	
SUMMARY	2-1
1 INTRODUCTION	2-2
2 TRANSPORT MODEL	2-7
2.1 Two-phase Mass Conservation and Force Balance	2-7
2.2 Closure Model	2-11
2.3 Boundary Conditions	2-13
3 NUMERICAL PROCEDURES	2-14
4 RESULTS AND DISCUSSION	2-15
4.1 Comparison With Experimental Data	2-16
4.2 The Effect of Lift Force and Radial Pressure Gradient	2-17
4.3 The Effect of Lift Coefficient C_L and Bubble Size	2-18
5 CONCLUSIONS	2-15
REFERENCES	2-21
FIGURES	
 CHAPTER 3: SIMULATION OF BUBBLE DISPERSION IN TURBULENT FREE SHEAR FLOWS	
SUMMARY	3-1

1 INTRODUCTION	3-2
2 MATHEMATICAL MODELLING	3-6
2.1 Modelling of Bubble and Particle Motion	3-6
2.2 Modelling of Turbulent Plane Mixing Layers	3-9
3 RESULTS	3-13
3.1 Demonstration of Examples With Rankine Vortex Flows	3-13
3.2 Validation of The Shear Layer Simulation	3-15
(a) Eddy structure and statistics	3-15
(b) Fluctuation velocity time records and spectra	3-17
3.3 Application to Bubble Transport and Dispersion	3-17
(a) Bubble dispersion in the vertical mixing layer	3-18
(b) Phase relationship between bubble introduction and large passage	3-22
3.4 Bubble Dispersion in Mixing Layer	3-18
(a) Bubbles released near the origin of mixing layer	3-18
(b) Bubble release across the approach flows	3-20
3.4 Measurements of Bubble Dispersion	3-23
4 DISCUSSION	3-25
4.1 Suitability of The Use of The Stokes Number For Bubble Transport in Shear Flows	3-25
4.2 The Effect of forces acting on bubbles in shear flows	3-26
4.3 Diffusion Model for Bubbles in Shear Flows	3-27
5 CONCLUSIONS	3-29
REFERENCES	3-31
FIGURES	3-36

CHAPTER 4: PARTICLE DISPERSION BY ORGANISED VORTEX STRUCTURES IN TURBULENT FREE SHEAR FLOWS

SUMMARY	4-1
1 INTRODUCTION	4-2
2 PARTICLE DYNAMICS	4-6
2.1 Equation of Particle Motion	4-6
2.2 Effect of Drag Force on Particle Dispersion	4-10
2.3 Particle Entrainment in a Time-Decayed Lamb-Oseen Vortex	4-11
3 NUMERICAL STUDIES	4-12
3.1 Particle Dispersion Patterns	4-13
(a) Effect of variations of Π/Γ on particle dispersion patterns	4-13
(b) Particle dispersion patterns under different release conditions	4-14
(c) Dispersion pattern difference between particles and bubbles	4-15
3.2 Eulerian and Lagrangian Measurements of Particle Dispersion	4-16
3.3 Distributions of Particle Velocity Field and Correlations	4-18
3.4 Effect of Pairing on Particle Dispersion	4-18
4 BROADER DISCUSSION	4-19
4.1 The Particle Dispersion in the Vicinity of the Stagnant Point	4-19
4.2 The Effect of Instantaneous Added Mass Force on Particle Dispersion	4-21
5 CONCLUSION	4-24

REFERENCES

4-26

FIGURES

CHAPTER 5: EFFECT OF EDDY STRUCTURE ON BUBBLE DISPERSION IN PLANE TURBULENT JETS

SUMMARY	5-1
1 INTRODUCTION	5-2
2 MODELLING FORMULATION	5-6
2.1 Discrete Vortex Model FOR a Plane Turbulent Jet	5-6
2.2 Bubble Motion	5-9
2.3 Bubble Trajectories in Two Separately Staggered Rankine Vortices	5-10
3 RESULTS AND DISCUSSION	5-11
3.1 The Plane Jet Flow Characterization	5-11
3.2 Bubble Dispersion	5-12
(a) Effect of large-scale structure of the jet on bubble dispersion	5-13
(b) Effect of lift force acting on bubbles on bubble dispersion	5-14
(c) Quantification of bubble dispersion in the plane jet	5-14
4 CONCLUSIONS	5-16
REFERENCES	5-17

FIGURES

CHAPTER 6: COUPLING OF FLUCTUATING VORTICITY AND VOIDAGE FLUXES

SUMMARY	6-1
1 INTRODUCTION	6-2
2 VOIDAGE-VORTICITY CORRELATION FOR DISPERSIVE	

TRANSPORT	6-4
3 CORRELATIONS BETWEEN BUBBLE OR PARTICLE NUMBER FLUX AND VORTICITY	6-6
4 DISCUSSION	6-8
4.1 Effect of Inertial Force on Bubble and Particle Crossing Trajectories	6-8
4.2 Implications For Practical Modelling of Voidage-Vorticity Transport Equation	6-9
5 CONCLUSIONS	6-11
REFERENCES	6-11
FIGURES	
CHAPTER 7: RECAPITULATION AND RECOMMENDATIONS	
1 TWO-PHASE FLOW NUMERICAL MODELLING	7-1
2 SPECIFIC REALISATIONS	7-3
2.1 Bubbly Pipe Flows	7-3
2.2 Bubbly Free Shear Flows	7-4
2.3 Particle Free Shear Flows	7-6
3 RECOMMENDATIONS FOR FUTURE WORK	7-6
REFERENCES	7-8

LIST OF FIGURES

Chapter 1

Figure 1. Examples of the blade drag force records and triggered flash photography of the bubble shedding events. Shaft speed: (a) 140 rpm, (b) 125 rpm. Gas flow rate: (a) 1.82 l/min, (b) 2.17 l/min. Taken from Pearse & Thomas (1990).

Figure 2. FRED "SPRAY" Nozzle: Air liquid spray. Mean drop size is about 100 μm . Spray speed is about 100 m/s. Spraying into still air. Taken from Thomas (1995).

Figure 3. A-Z applications of PHOENICS package to industrial problems.

Figure 4. Numerical predictions of a turbulent bubbly flow downstream of a sudden pipe expansion (bubble diameter $d_b=2$ mm, void fraction $\alpha_G\approx 0.1$). Taken from F'dhila & Simonin (1992).

Figure 5. A rigid body with volume V at $R(t)$ moving with velocity $v(t)$ through a non-uniform velocity field $u(x,t)$. Notice that at the particle $u_0=U(t)$, its rate of change, seen by the particle is dU/dt ; the fluid volume at time $t+\delta t$, which coincided with the body at time t , its acceleration is DU/Dt . Taken from Auton *et al.* (1988).

Figure 6. Estimate of the Basset force acting on a 707 μm bubble during entrainment, resolved into X, Y components in a Cartesian frame. Taken from Sridhar & Katz (1995).

Figure 7. Dependence of the trapping width on the vortex strength parameter for discrete with various specific gravities. Taken from Thomas *et al.* (1983).

Figure 8. Comparison between computed and experimental trapping width with different vortex strength for bubbles in water. Taken from Thomas *et al.* (1983).

Figure 9. Simulation of bubble trajectories in a horizontal mixing layer. 20 bubbles released with $\Pi=0.5, \Gamma=3.3$ (note: gravity acts upwards in the figure). Taken from Sene *et al.* (1994).

Figure 10. Calculation of the probability of bubbles escaping from a horizontal mixing layer ($\Delta, \Pi=0$; $\square, \Pi=0.05$; $\circ, \Pi=0.5$). Taken from Sene *et al.* (1994).

Figure 11. Computer simulation of bubble trajectories in a vertical mixing layer. Bubbles were released from the location close to the origin of the mixing layer. (a) $\Pi=0.5, \Gamma=10.0$; (b) $\Pi=0, \Gamma=10.0$. 200 bubbles. Taken from Yang & Thomas (1994).

Figure 12. Calculation of bubble number fluxes in a vertical downflowing mixing layer. $N_2(=40)$ bubbles released into the high speed stream in the region $0.0 < y < 0.135L$ (a) $\Pi=0, \Gamma=5.0$; (b) $\Pi=0.067, \Gamma=5.0$. $\Delta, x=0.2L$; $\circ, x=0.4L$; $\square, x=0.6L$; $\diamond, x=0.8L$). Taken from Sene *et al.* (1994).

Figure 13. Void fractions measured by trapping water between two quick closing valves. The same experiment was repeated several times. Taken from Banerjee & Chan (1980).

Figure 14. The response of a cylindrical hot-film probe to the passage of a bubble. Taken from Bruun (1995).

Figure 15. Turbulence measurement (two-dimensional) with X -probe. Turbulence intensity profiles have been significantly modified due to the presence of bubbles. Taken from Serizawa *et al.* (1974).

Figure 16. The properties of a two-phase jet flow at $x/D=20$. (a) normalized mean velocity and volume fraction profiles; (b) turbulence intensity profiles; (c) turbulence shear stress profiles. Taken from Elghobashi *et al.* (1984).

Figure 17. Decay of grid generated turbulence for bubbly flow ($U_L=0.6$ m/s). Taken from Lance & Bataille *et al.* (1991).

Figure 18. Experimental set-up of a spray evaporation in a co-flowing annular jet and a particle dispersion in a plane shear jet. Taken from the Proceedings of the Sixth Workshop on Two-Phase Flow Prediction (ed. by M. Sommerfeld 1992).

Figure 19. Particle dispersion in a plane mixing layer. Predicted axial particle mean velocity and axial velocity fluctuation profiles compared with the experimental data (Ishima 1993). (a) axial particle mean velocities; (b) axial particle velocity fluctuations. Taken from the Proceedings of the Sixth Workshop on Two-Phase Flow Prediction (ed. Sommerfeld 1992).

Figure 20. Particle dispersion in a plane mixing layer. Prediction results compared with the experimental data (Ishima 1993): (a) radial particle mean velocities; (b) radial velocity fluctuations; (c) normalized number densities. Taken from the Proceedings of the Sixth Workshop on Two-Phase Flow Prediction (ed. Sommerfeld 1992).

Figure 21. Prediction of two-phase turbulence and phase distribution in bubbly flow using a two-fluid model together with the modified $k-\varepsilon$ model. Taken from Lopez de Bertodano *et al.* (1994).

Figure 22. Comparisons of turbulence properties between numerical simulations and the experimental data. Taken from Lopez de Bertodano *et al.* (1994).

Figure 23. Void fraction profiles in a vertical downflowing mixing layer (Experimental data and simulation). Taken from Hunt *et al.* (1988).

Figure 24. Shadowgraph visualization of large-scale spanwise vortices in a plane mixing layer, taken at random times. Taken from Brown & Roshko (1974).

Figure 25. The smoke visualization of the large-scale vortex structures in a plane wake downstream of a bluff body. Taken from Crowe *et al.* (1993).

- Figure 26. Schematics of four successive phases (configurations C, D, E and F) of the pairing process. Taken from Hussain (1986).
- Figure 27. Dispersion pattern for 40 μm glass particles released in the fast stream of a plane mixing layer. $U_1=5$ m/s, $U_2=2$ m/s; (a) natural flow, (b) forced at first subharmonic of natural instability. Taken from Wen *et al.* (1992).
- Figure 28. Train of bubbly vortices in penetrating plunge-point flow. Depth of the jet about 2 cm; impact velocity about 2 m/s. Taken from Sene *et al.* (1994).
- Figure 29. Conceptual model for Stokes number effect on particle spreading in organized vortex structures. Taken from Crowe *et al.* (1993).
- Figure 30. Normalized particle distribution functions at various downstream locations of an axisymmetric jet as a function of Stokes number. Taken from Chung & Troutt (1988).
- Figure 31. Instantaneous particle dispersion patterns for tracers and particles with different Stokes numbers. Taken from Wen *et al.* (1992).
- Figure 32. Bubble trajectories computed near a line vortex. Notice that a narrow band of X starting points lead to bubble capture. Taken from Thomas *et al.* (1993)
- Figure 33. Sketch showing bubble trajectory inside a Rankine vortex with inertial and trapping forces, based on analysis of Auton's force law. Taken from Sene *et al.* (1994).
- Figure 34. Streamlines associated with the stream function ψ for (a) $k=0.50$; (b) $k=0.25$. The arrows indicate the direction of gravity. Note that the cateye shrinks as k decreases. Here constant k is a parameter that determines the distribution of vorticity. Taken from Tio *et al.* (1993).
- Figure 35. Closed particle orbits for $B=0.0$ and (a) $A=50.0$, $R_e^*/A=400.0$, $\epsilon=0.60$, $k=0.95$; (b) $A=50.0$, $R_e^*/A=400.0$, $\epsilon=0.62$, $k=0.85$; (c) $A=75.0$, $R_e^*/A=50.0$, $\epsilon=0.50$, $k=0.25$. The effect of the lift term is included in (c). Here A is the ratio of the response time of particle motion to the characteristic time of the fluid flow and B is a gravitational parameter. Taken from Tio *et al.* (1993)
- Figure 36. Vorticity contours with particle positions superimposed for $S_r=1.0$ at (a) $t=18.0$ and (b) $t=30.0$. Sharp spikes in the particle concentration profile indicated the particles' strong preferential residence along the stagnation streamline of the flow field. Taken from Martin & Meiburg (1994).
- Figure 37. Simulation of the flow around a flat plate using discrete vortex method. Particle dispersion pattern is influenced by coherent turbulent eddies. Taken from Chein & Chung (1988).
- Figure 38. Experimental bubble streakline visualisation photographs (cylinder radius: $R=0.015$ m) and numerically simulated bubble streaklines ($t=20$, $R=0.015$ m and the bubble

diameter $d=3$ mm. Taken from Bayly & Rielly (1994).

Figure 39. Control volume with two particle velocities. A stream of particles is assumed to be emitted from a vertical source. Two possible particle trajectories are shown which may traverse the same computational cell. Using exclusive Eulerian modelling approach would only predict one velocity direction. However, exclusive Lagrangian modelling approach can offer a correct configuration to this problem. Taken from Crowe (1982).

Figure 40. Simulation of the mixing layer: streakline plots of each discrete vortex for a unit time ($L/\Delta U$) with respect to the average velocity ($L\Delta U/\nu=1000$). Taken from Ashurst (1979).

Chapter 2

Figure 1. A bubble moving relative to a shear flow and the forces acting on the bubble.

Figure 2. The wall rolling eddies and the interaction between bubbles and the eddies (Rouhani 1976).

Figure 3. Effect of buoyancy force on the shear stress distribution in vertical bubbly pipe flow (Thomas 1984): (a) smaller buoyancy; (b) larger buoyancy.

Figure 4. Serizawa *et al.* (1986). Radial void fraction distribution in vertically upward flow.

Figure 5. Wang *et al.* (1987). Radial void fraction distribution in vertically downward flow.

Figure 6. Mean velocity and void fraction profiles in an upward bubbly flow in a pipe (Marié 1987).

Figure 7. Comparison of the predicted void fraction profile with Serizawa's data (1986): (a) with the pressure gradient; (b) without the pressure gradient.

Figure 8. Comparison of the calculated velocity profile with Serizawa's data (1986): (a) including the effect of the pressure gradient; (b) excluding the effect of radial pressure gradient.

Figure 9. Comparison of the calculated shear stress with Serizawa's data (1986): (a) including the effect of pressure gradient; (b) excluding the effect of pressure gradient.

Figure 10. Comparison with Wang's (1987) downflow experimental data: void fraction profile. (a) including the effect of pressure gradient; (b) without including the effect of pressure gradient.

Figure 11. Comparison of the calculated velocity profile with Wang's data (1987): (a) including the effect of radial pressure gradient; (b) excluding the effect of radial pressure gradient.

Figure 12. Comparison of the calculated shear stress profile with Wang's data (1987): (a)

including the effect of radial pressure gradient; (b) excluding the effect of radial pressure gradient.

Figure 13(a). Lift force and radial pressure gradient on the bubbles for circular pipe bubbly upflow.

Figure 13(b). Lift force and radial pressure gradient on the bubbles for circular pipe bubbly downflow.

Figure 14. Effect of variation of lift coefficient on phase distribution.

Figure 15. Comparison of the calculated velocity profile and void fraction profile with Serizawa's data (1986) when the effect of interaction between the wall and the bubbles is taken into account.

Figure 16. Effect of bubble size on the bubble-induced turbulence diffusivity.

Figure 17. Effect of bubble size on the predicted void fraction.

Chapter 3

Figure 1. Definition sketch for discrete vortex simulation of a two-stream planar turbulent mixing layer. Taken from Sene *et al.* (1994).

Figure 2. The effect of varying the mass ratios on bubble, droplet and particle trajectories. The terminal velocity is 0.2 m/s and initial velocity is set to equal to local velocity of the flow field for all three cases. For all three cases $\Pi_{Ran}=10.0$, $\Gamma_{Ran}=5.0$. Release locations are (0.0, 0.8R) inside the vortex and (0.0, 2.0R) outside the vortex. (a) $\gamma=0.0$ for bubbles; (b) $\gamma=0.9$ for droplet; (c) $\gamma=2.5$ for particles.

Figure 3. The effect of varying Π_{Ran} on bubble trajectories. The terminal velocity is 0.2 m/s and initial velocity is set to equal to local velocity of the flow field for all four cases. For all four cases $\Gamma_{Ran}=5.0$. Bubbles were released from (0.0, 0.8R) inside the vortex and (0.0, 1.5R) outside the vortex. (a) $\Pi_{Ran}=2.5$; (b) $\Pi_{Ran}=5.0$; (c) $\Pi_{Ran}=10.0$; (d) $\Pi_{Ran}=20.0$.

Figure 4a. The effect of varying Γ_{Ran} on bubble trajectories. The terminal velocity is 0.2 m/s and the initial velocity is set to equal local velocity of the flow field for all four cases. For all four cases $\Pi_{Ran}=10.0$. Bubbles were released from (0.0, 10.0R) of the vortex. (a) $\Gamma_{Ran}=2.5$; (b) $\Gamma_{Ran}=5.0$; (c) $\Gamma_{Ran}=10.0$; (d) $\Gamma_{Ran}=20.0$.

Figure 4b. The effect of varying Γ_{Ran} on bubble radius time series with $\Pi_{Ran}=10.0$ and $\gamma=0.0$.

Figure 5. Instantaneous discrete vortex patterns in a two-stream mixing layer: (a) $T=1.0L/\Delta U$ (b) $T=1.1L/\Delta U$; (c) $T=1.2L/\Delta U$; (d) $T=1.3L/\Delta U$.

Figure 6. Vorticity contours in the discrete vortex simulation at different times,

corresponding to figure 5. (a) $T=1.0L/\Delta U$ (b) $T=1.1L/\Delta U$; (c) $T=1.2L/\Delta U$; (d) $T=1.3L/\Delta U$.

Figure 7. Time-averaged mean velocity profiles from numerical simulations and the experimental results (Sene 1985).

Figure 8. Longitudinal turbulence intensities at different downstream cross-sections of the mixing layer.

Figure 9. Cross-stream turbulence intensities at different downstream cross-sections of the mixing layer.

Figure 10. Shear stress distributions at different downstream cross-sections of the mixing layer.

Figure 11. Spread rate at different locations of the mixing layer. The mixing layer width is defined as the distance between the points at which the velocity differs 10% from the stream value.

Figure 12. Fluctuation velocity time records for 2000 time steps, with three different random jitters, sampled at the centre of the mixing layer: (a) $\xi=0.0$; (b) $\xi=0.2U_m\Delta t$; (c) $\xi=0.4U_m\Delta t$.

Figure 13. Power spectra of axial velocity fluctuation u' , sampled at the centre of the mixing layer with $U_2/U_1=3.0$.

Figure 14. Computer simulations of bubble trajectories in a vertical, downflowing, two stream mixing layer. Bubbles (400 bubbles in total) were released every Δt at the location close to the origin of the mixing layer. (a) $\Pi=0.5$, $\Gamma=10.0$; (b) $\Pi=0.0$, $\Gamma=10.0$. (Note: Only 20 trajectory realisations were displayed.)

Figure 15. Computer simulations of bubble trajectories in a vertical, downflowing, two stream mixing layer. Bubbles (400 bubbles in total) were released every $10\Delta t$ at the location close to the origin of the mixing layer. (a) $\Pi=0.5$, $\Gamma=10.0$; (b) $\Pi=0.0$, $\Gamma=10.0$. (Note: Only 20 trajectory realisations were displayed.)

Figure 16. Bubble number fluxes in a vertical, downflowing, two stream mixing layer, calculated from the bubble trajectories shown in figure 14: (a) $\Pi=0.5$, $\Gamma=10.0$; (b) $\Pi=0.0$, $\Gamma=10.0$. Bubble were released every Δt . (Note: $N_T=400$. N_i is the bubble number sampled at i th sampling box in a downstream cross-section of the mixing layer and Y_0 is the axis of the mixing layer.)

Figure 17. Bubble number fluxes in a vertical, downflowing, two stream mixing layer, calculated from the bubble trajectories shown in figure 15: (a) $\Pi=0.5$, $\Gamma=10.0$; (b) $\Pi=0.0$, $\Gamma=10.0$. Bubble were released every $10\Delta t$. (Note: $N_T=400$. N_i is the bubble number sampled at i th sampling box in a downstream cross-section of the mixing layer and Y_0 is the axis of the mixing layer.)

Figure 18. Bubble concentration fluxes in a vertical, downflowing, two stream mixing layer, calculated from the bubble trajectories shown in figure 14: (a) $\Pi=0.5$, $\Gamma=10.0$; (b) $\Pi=0.0$, $\Gamma=10.0$. Bubble released every Δt . (Note: N_i and N_m are respectively the bubble number sampled at i th sampling box in a downstream cross-section of the mixing layer and the maximum bubble number sampled.)

Figure 19. Bubble concentration fluxes in a vertical, downflowing, two stream mixing layer, calculated from the bubble trajectories shown in figure 15: (a) $\Pi=0.5$, $\Gamma=10.0$; (b) $\Pi=0.0$, $\Gamma=10.0$. Bubble released every $10\Delta t$. (Note: N_i and N_m are respectively the bubble number sampled at i th sampling box in a downstream cross-section of the mixing layer and the maximum bubble number sampled.)

Figure 20. Time-averaged mean velocity profiles for bubbles at different locations of the mixing layer, based on 400 trajectory realisations. $\Pi=0.0$, $\Gamma=10.0$, $N_T=400$.

Figure 21. Time-averaged cross-stream velocity profiles for bubbles at different locations of the mixing layer, based on 400 trajectory realisations. $\Pi=0.0$, $\Gamma=10.0$, $N_T=400$.

Figure 22. Longitudinal velocity fluctuations for bubbles at different downstream locations of the mixing layer, based on 400 bubble trajectory realisations. $\Pi=0.0$, $\Gamma=10.0$, $N_T=400$.

Figure 23. Cross-stream velocity fluctuations for bubbles at different downstream locations of the mixing layer, based on 400 bubble trajectory realisations. $\Pi=0.0$, $\Gamma=10.0$, $N_T=400$.

Figure 24. Correlations of bubble velocity fluctuation at different downstream locations of the mixing layer, based on 400 bubble trajectory realisations. $\Pi=0.0$, $\Gamma=10.0$, $N_T=400$.

Figure 25. 10 bubble trajectories. Bubbles were released from both the high and low speed sides of a vertical, downflowing, two-stream mixing layer for $\Pi=0.0667$, $\Gamma=5.0$.

Figure 26. Computer simulations of bubble trajectories in a vertical, downflowing, two stream mixing layer. 400 bubbles were released from the high speed side of the mixing layer. (a) $\Pi=0.0$, $\Gamma=5.0$; (b) $\Pi=0.0667$, $\Gamma=5.0$. (Note: Only 20 trajectory realisations were displayed.)

Figure 27. Calculations of bubble number fluxes in a vertical, downflowing, two-stream mixing layer. $N_T(=400)$ bubbles were released into the high speed side ($0 < y < 0.15L$) of the mixing layer: (a) $\Pi=0.0$, $\Gamma=5.0$; (b) $\Pi=0.0667$, $\Gamma=5.0$. (Note: Only 20 trajectory realisations were displayed.)

Figure 28. Simulation of 20 bubble trajectories in a horizontal mixing layer. $\Pi=0.05$, $\Gamma=2.0$.

Figure 29. Calculations of the probability of bubble capture by the large eddies in a horizontal mixing layer: $\Pi=0.05$, $\Gamma=2.0$.

Figure 30. Ensemble-averaged time-of-transport measurement of bubble dispersion in a vertical, downflowing, two stream mixing layer.

Figure 31. Eulerian bubble dispersion measurements as a function of downstream distance in a vertical, downflowing, two stream mixing layer.

Figure 32. Ensemble-averaged Lagrangian prediction of bubble transverse dispersion in a vertical, downflowing, two stream mixing layer.

Figure 33. Bubble diffusivity and fluid diffusivity in a vertical, downflowing, two stream mixing layer.

Figure 34. Eddy Schmidt number of bubbles in a vertical, downflowing, two stream mixing layer.

Chapter 4

Figure 1. The effect of choice of drag law on particle and bubble trajectories within a Rankine vortex. For both cases particle was released from the same location at $(-r_0, 0)$. Here r_0 is a core radius for the Rankine vortex. r_0 is equal to 0.005 m and the angular velocity of the vortex is 200 s^{-1} . The density of bubble and the density of the fluid for case (a) and (b) are respectively 0.0 kg/m^3 and 1000.0 kg/m^3 . The density of particle and the density of the fluid for case (c) and (d) are respectively 2400.0 kg/m^3 and 1.25 kg/m^3 . (a) and (c): Linear drag law (i.e. $f=1$); (b) and (d): Non-linear drag law (i.e. $f=|\mathbf{v}-\mathbf{u}|/V_T$).

Figure 2. Particle and bubble radius time histories, using linear drag and non-linear drag law. The long term growth rate of particle and the long term decay rate of bubble are little affected by using different drag modifications.

Figure 3a. Particle trajectories within a turbulent Lamb-Oseen vortex and a Rankine vortex. For both cases particle was released from the same location at $(-r_0, 0)$. Here r_0 was an initial radius specified for the lamb-Oseen vortex and a core radius for the Rankine vortex. r_0 is equal to 0.005 m and the initial angular velocity of the vortex is 200 s^{-1} . The density of particle and the density of fluid are respectively 2400.0 kg/m^3 and 1.25 kg/m^3 . Trajectory 1 corresponds to the particle released in the Lamb-Oseen vortex. Trajectory 2 corresponds to the Particle released in the Rankine vortex.

Figure 3b. Particle radius time histories within a Lamb-Oseen vortex and a Rankine vortex. The initial radius is set to 0.005 m and the initial angular velocity is 200 s^{-1} . Particles were released at $(-r_0, 0)$.

Figure 4. Instantaneous particle dispersion patterns for fluid tracers and particles with different Π/Γ . (a) $\Pi/\Gamma=0.0$, $\gamma=1.0$; (b) $\Pi/\Gamma=0.002$, $\gamma=1920.0$; (c) $\Pi/\Gamma=0.032$, $\gamma=1920.0$; (d) $\Pi/\Gamma=0.155$, $\gamma=1920.0$. The corresponding Stokes numbers for (a), (b), (c) and (d) are 0, $O(0.1)$, $O(1.0)$, $O(10.0)$. The vorticity contours are displayed by red colour and blue dots represent fluid tracers or particles.

Figure 5a. Instantaneous vorticity contours and particle streaklines for $\Pi/\Gamma=0.032$ for particles released from the high speed of the mixing layer. A thin band of particles emerging

from the region between two successive large eddies and surrounds the lower perimeters. (Note: gravity acts from left to right here.)

Figure 5b. Instantaneous vorticity contours and particle streaklines for $\Pi/\Gamma=0.032$ for particles released from the low speed of the mixing layer. A thin band of particles emerging from the saddle point of two successive large eddies, surrounding the higher peripheries and a roll-over wave liked band surrounds the lower perimeters. (Note: gravity acts from left to right here.)

Figure 6a. Instantaneous vorticity contours and particle streaklines for $\Pi/\Gamma=0.05$ and $\gamma=1920.0$ at time $t=1.5625$. Particles are centrifuged from the large-scale vortex cores and surround the peripheries of the vortices, indicating an enhanced dispersion. (Note: gravity acts from left to right here.)

Figure 6b. Instantaneous vorticity contours and bubble streaklines for $\Pi/\Gamma=0.05$ and $\gamma=0.0$ at time $t=1.5625$. Bubbles are trapped by the large-scale vortex cores and obviously group in clusters, which is similar to the experimental observations (Thomas 1982). (Note: gravity acts from left to right here.)

Figure 7. Particle number flux distribution at various downstream locations of the mixing layer from numerical simulations with different values of Π/Γ .

Figure 8. Variations of particle mean square displacement, calculated from the particle number flux profiles shown in figure 7.

Figure 9. The ratio of dispersion as a function of Π/Γ (or the corresponding Stokes number S_s) for different downstream distance, calculated from the results as shown in figure 8.

Figure 10. Lagrangian measurements of particle dispersion in a vertical, downflowing mixing layer.

Figure 11. Particle dispersion coefficients versus time in a vertical, downflowing mixing layer, calculated from the data shown in figure 10.

Figure 12. Eddy turbulent Schmidt number of particles versus time in a vertical, downflowing mixing layer, calculated from the data shown in figure 11.

Figure 13. Time-averaged downstream mean velocity profiles of particles at various downstream locations of a vertical, downflowing mixing layer from numerical simulations ($\Pi/\Gamma=0.032$, $\gamma=1920.0$).

Figure 14. Time-averaged cross-stream velocities of particles at various downstream locations of a vertical, downflowing mixing layer from numerical simulations. ($\Pi/\Gamma=0.032$, $\gamma=1920.0$).

Figure 15. Longitudinal RMS velocities of particles at various downstream locations of a vertical, downflowing mixing layer from numerical simulations. η is defined as $\eta=y/x$.

($\Pi/\Gamma=0.032$, $\gamma=1920.0$).

Figure 16. Cross-stream velocity fluctuations of particles at various downstream locations of a vertical, downflowing mixing layer from numerical simulations. η is defined as $\eta=y/x$. ($\Pi/\Gamma=0.032$, $\gamma=1920.0$).

Figure 17. Shear stress of particles, $\overline{u_p'v_p'}$, at various downstream locations of a vertical, downflowing mixing layer from numerical simulations. ($\Pi/\Gamma=0.032$, $\gamma=1920.0$).

Figure 18. Joint probabilities of u and v fluctuations for fluid tracers and particles, sampled from the centre of the mixing layer. Total 1000 particles and 1000 fluid tracers were released from the location close to the origin of the mixing layer. (a) fluid tracers; (b) particles with $\Pi/\Gamma=0.032$.

Figure 19. Particle positions with vorticity contours superimposed for $\Pi/\Gamma=0.032$ at four different time instants for the coherent structures undergoing a pairing event. During the pairing, particle streaks between pairing vortices become depleted. An enhanced dispersion can be obviously observed.

Figure 20. Particle dispersion patterns (particle positions represented by blue spots and the pink lines indicate the streamlines.) in a series of Rankine vortices for different values of Π/Γ (Note: $\Pi=r_0^2\omega^2/2gr_0$ and $\Gamma=r_0\omega/V_T$ are defined here.). Particles were released from different radial positions at the same location at $-r_0$. Here r_0 is a core radius for the Rankine vortex and the coordinate origin is located at the stagnation point as shown in the figure. r_0 is equal to 0.005 m and the angular velocity of the vortex is 200 s^{-1} . The density of the particles and the density of the carrier fluid are respectively 2400.0 kg/m^3 and 1.25 kg/m^3 . (a) $\Pi/\Gamma=0.01$; (b) $\Pi/\Gamma=0.1$; (c) $\Pi/\Gamma=1.0$ and (d) the value of Π/Γ is the same as (c). A thick band of particle accumulation occurs.

Figure 21a. Particle trajectories with $\Pi/\Gamma=0.059$, computed by using a time-averaged modelling method (The mean flow properties were calculated by time-averaging the instantaneous flow field. 1000 time steps were chosen here). Particles were released from a location very close to the origin of the mixing layer. 1000 particles were released for this demonstration. For clarity, only 10 realisations amongst all particle trajectories are displayed. The density of particles is set to 2850.0 kg/m^3 and the density of carrier fluid is 1000.0 kg/m^3 . (Note: gravity acts from left to right here.)

Figure 21b. Particle trajectories with $\Pi/\Gamma=0.059$, computed by using a time-dependent modelling method (discrete vortex method). Particles were released from a location very close to the origin of the mixing layer. 1000 particles were released for this demonstration. For clarity, only 10 realisations amongst all particle trajectories are displayed. The density of particles is set to 2850.0 kg/m^3 and the density of carrier fluid is 1000.0 kg/m^3 . (Note: gravity acts from left to right here.)

Figure 22. Comparisons of particle number flux distributions at various downstream locations of a vertical, downflowing mixing layer, calculated by using the time-averaged

model and the time-dependent model.

Figure 23. Lagrangian measurements of particle dispersion in a vertical, downflowing mixing layer, calculated by using the time-averaged model and the time-dependent model.

Figure 24. Particle and fluid dispersion coefficients versus time in a vertical, downflowing mixing layer. (TD model: Time-dependent model; TA model: Time-averaged model).

Figure 25. Eddy turbulent Schmidt number of particles versus time in a vertical, downflowing mixing layer, calculated from the data shown in figure 24.

Chapter 5

Figure 1. Simply ideal flows induced by two infinite vortex sheets.

Figure 2. Sketch of discrete vortex simulation of a plane turbulent jet.

Figure 3. Coherent structure interaction in the near field of a plane jet; (a) top-hat velocity profile; (b) fully developed initial velocity profile. Two distinct modes of vortex formation can be clearly seen from the figure. Taken from Husain *et al.* (1987).

Figure 4. The trajectories of bubbles trapped by two allocated Rankine vortices. Bubbles were released from 2 radii below the first Rankine vortex. (a) Rankine vortices allocated horizontally; (b) Rankine vortices staggered.

Figure 5. The trajectories of bubbles trapped by two allocated Rankine vortices. The two vortices have been partially overlapped. Bubbles were released from 2 radii below the first Rankine vortex. (a) Rankine vortices allocated horizontally; (b) Rankine vortices staggered.

Figure 6. Plane jet development represented by two arrays of discrete vortex filaments. (a) $T=0.5$; (b) $T=1.0$; (c) $T=1.2$; (d) $T=1.4$; (e) $T=1.6$; (f) $T=1.8$; (g) $T=2.0$.

Figure 7. Instantaneous axial and transverse velocity time histories at $x/D=80$ on the centerline of the plane jet. The exit velocity: $U_0=0.3$ m/s. Carrier fluid: water.

Figure 8. Time-averaged mean axial velocity component and the experimental data fit (Bradbury 1965).

Figure 9. Time-averaged mean cross-stream velocity profiles and the experimental data fit (Bradbury 1965).

Figure 10. Longitudinal turbulence intensities at different downstream cross-sections and the experimental data fit (Bradbury 1965).

Figure 11. Cross-stream turbulence intensities calculated and the experimental data (Bradbury 1965).

Figure 12. Shear stress distribution calculated and the experimental data (Bradbury 1965).

Figure 13. Computer simulation of bubble trajectories in a upflowing turbulent plane jet. Bubbles were released from the centerline of the jet exit for the condition $\Pi=0.02$, $\Gamma=1.5$. Total 400 bubbles were released. For clarity only 20 bubble trajectories were displayed in the figure.

Figure 14. Computer simulation of bubble trajectories in a upflowing turbulent plane jet. Bubbles were released from the centerline of the jet exit for the condition $\Pi=0.05$, $\Gamma=2.5$. Total 400 bubbles were released. For clarity only 20 bubble trajectories were displayed in the figure.

Figure 15. Bubble number fluxes in a vertical, upflowing plane jet, calculated from the bubble trajectory statistics shown in figure 13. ($\Pi=0.02$, $\Gamma=1.5$, $N_0=400$.)

Figure 16. Bubble number fluxes in a vertical, upflowing plane jet, calculated from the bubble trajectory statistics shown in figure 14. ($\Pi=0.05$, $\Gamma=2.5$, $N_0=400$.)

Figure 17. Comparisons of two bubble trajectory calculations with and without inclusion of the effect of the lift force. ($\Pi=0.02$, $\Gamma=1.5$, $N_0=400$.)

Figure 18. Comparisons of bubble number fluxes in vertical, upflowing plane jets, with and without inclusion of lift force ($\Pi=0.02$, $\Gamma=1.5$, $N_0=400$). Case 1: Inclusion of the lift force; Case 2: Exclusion of the lift force.

Figure 19. Computer simulation of bubble and tagged fluid particle trajectories in a upflowing turbulent plane jet. Both bubbles and tagged fluid particles (total 400 for both) were released from the same location at the centerline of the jet exit for the condition $\Pi=0.02$, $\Gamma=1.5$.

Figure 20. Ensemble-averaged Lagrangian prediction of bubble transverse dispersion in vertical, upflowing plane jets. (Case 1: $\Pi=0.02$, $\Gamma=1.5$; Case 2: $\Pi=0.05$, $\Gamma=2.5$.)

Figure 21. The ratio between the dispersion functions (bubbles and tagged fluid particles) with time in a vertical, upflowing plane jet. Results were obtained from the least-square fitting for the data shown in figure 20.

Chapter 6

Figure 1. Instantaneous vorticity contours (red) and bubble streaklines (blue). Bubbles are trapped by the large-scale eddies and group in clusters. (a) $\Pi=0.5$, $\Gamma=10.0$ at time $t=1.5625$; (b) $\Pi=0.5$, $\Gamma=20.0$ at time $t=1.5625$.

Figure 2. Typical logarithmic correlation integral plots for particles from mixing layer simulations. (a) $S_i=0.01$; (b) $S_i=1.0$; (c) $S_i=10.0$. Taken from Tang *et al.* (1992). (Here S_i is the Stokes number, defined as $S_i=\rho_p d^2 \Delta U / 18 \mu \delta$.)

Figure 3. Instantaneous vorticity contours (red) and bubble locations (blue) at three different time instants with $\Pi=0.5$, $\Gamma=10.0$ and $\gamma=0.0$. (a) $T=2.525$; (b) $T=3.025$; (c) $T=3.525$.

Figure 4. Instantaneous vorticity contours (red) and bubble locations (blue) at $0.55L < x < 0.85L$ at $T=3.525$ with $\Pi=0.5$, $\Gamma=10.0$ and $\gamma=0.0$.

Figure 5. Instantaneous vorticity contours (red) and particle locations (blue) at three different time instants with $\Pi=0.5$, $\Gamma=10.0$ and $\gamma=1920.0$. (a) $T=2.525$; (b) $T=3.025$; (c) $T=3.525$.

Figure 6. Instantaneous vorticity contours (red) and particle locations (blue) at $0.55L < x < 0.85L$ at $T=3.525$ with $\Pi=0.5$, $\Gamma=10.0$ and $\gamma=1920.0$.

Figure 7. The contour plots of instantaneous vorticity, and bubble or particle number density at $0.55L < x < 0.85L$. (a) $\Pi=0.5$, $\Gamma=10.0$ and $\gamma=0.0$ at $T=1.425$; (b) $\Pi=0.5$, $\Gamma=10.0$ and $\gamma=1920.0$ at $T=0.725$.

Figure 8. A schematic layout of the bins for sampling the numbers of bubbles or particles and the numbers of point vortices.

Figure 9. Time-history records of local bubble number flux and local point vortex number flux under the conditions $\Pi=0.5$, $\Gamma=10.0$ and $\gamma=0$, sampled at $x=0.8L$ and $y=0.0147L$. Bubbles were released from the location close to the origin of the mixing layer. Sampling records were started when bubbles were fully engaged in the eddies in the computation domain.

Figure 10. Time-history records of local particle number flux and local point vortex number flux under the conditions $\Pi=0.5$, $\Gamma=10.0$ and $\gamma=1920$, sampled at $x=0.8L$ and $y=0.0147L$. Bubbles were released from the location close to the origin of the mixing layer. Sampling records were started when particles were fully engaged in the eddies in the computation domain.

Figure 11a. Cross-correlations between local bubble number flux $n_b(t)$ and local point vortex number flux $n_v(t)$ at different downstream cross-sections ($\eta=y/x$) of the mixing layer, with time delay $\tau=0$.

Figure 11b. Autocorrelations of local point vortex number flux $n_v(t)$ at different downstream cross-sections ($\eta=y/x$) of the mixing layer, with time delay $\tau=0$.

Figure 12. Cross-correlations between local particle number flux $n_p(t)$ and local point vortex number flux $n_v(t)$ at different downstream cross-sections ($\eta=y/x$) of the mixing layer, with time delay $\tau=0$.

Figure 13. Instantaneous vorticity contours, bubble streaklines and fluid particle streaklines at $t=2.575$. Both bubbles and fluid particles were released from the same locations with $\Pi=0.5$, $\Gamma=10.0$. Blue dots and green dots represent bubbles and fluid particles respectively.

Figure 14. Instantaneous vorticity contours, bubble streaklines and fluid particle streaklines at $t=2.575$. Both bubbles and fluid particles were released from the same locations with $\Pi=0.5$, $\Gamma=20.0$. Blue dots and green dots represent bubbles and fluid particles respectively.

Figure 15. Variation over time of cross-correlations between local bubble number flux /local point vortex number flux and local fluid particle number flux /local point vortex number flux under conditions $\Pi=0.5$, $\Gamma=10.0$ and $\gamma=0$, sampled at $x=0.8L$ and $y=0.0147L$. Bubbles and fluid particles were released from the location close to the origin of the mixing layer. Sampling records were started when bubbles and fluid particles were fully engaged in the eddies in the computation domain.

Figure 16. Variation over time of cross-correlations between local particle number flux /local point vortex number flux and local fluid particle number flux /local point vortex number flux under conditions $\Pi=0.5$, $\Gamma=10.0$ and $\gamma=1920$, sampled at $x=0.8L$ and $y=0.0147L$. Particles and fluid particles were released from the location close to the origin of the mixing layer. Sampling records were started when particles and fluid particles were fully engaged in the eddies in the computation domain.

NOMENCLATURE

Chapter 1

A^*	Bubble trapping width (-)
b	The mixing layer spread rate (-)
C	Concentration of bubbles or particles (-)
C_D	Drag coefficient (-)
C_L	The bubble lift coefficient (-)
C_T	Concentration of bubbles or particles inside the coherent structure (-)
C_m	The added mass coefficient (-)
C_0	Total particle concentration in mesh (-)
C_μ	The empirical constant
C_{ϕ^5}	The empirical constant in $k-\varepsilon$ model
$C_{1\varepsilon}$	The empirical constant in $k-\varepsilon$ model
$C_{2\varepsilon}$	The empirical constant in $k-\varepsilon$ model
$C_{3\varepsilon}$	The empirical constant in $k-\varepsilon$ model
C^*	Vortex strength parameter (-)
D_{by}	Bubble diffusivity (m^2/s)
D_{fy}	Fluid particle diffusivity (m^2/s)
D_{pi}	Particle diffusion coefficient (m^2/s)
D_ϕ	Particle dispersion coefficient
d	Bubble diameter (mm)
d_p	Particle diameter (mm)
F_B	Basset force (N)
F_D	Drag force (N)

F_I	Inertial force (N)
F_L	Lift force (N)
f	Drag coefficient function (-)
g	Gravitational acceleration (m/s ²)
I	Unit matrix
k	Turbulence kinetic energy
L	The length of the simulation domain (m)
l_i	Integral length scale
l_m	The mixing-length
M_m	The interfacial force per unit interfacial area.
M_k^d	Interfacial force (N)
m_f	The mass of the fluid displaced by the particle
m_p	The mass of the particle
n_k	The unit normal
p	The pressure (N/m ²)
p_k	The pressure of phase k (N/m ²)
$p_{k,i}$	The interfacial pressure on interface i (N/m ²)
R	The Rankine vortex core radius (m)
Re	Reynolds number (-)
R_f	Richardson number (-)
S_c	Eddy Schmidt number (-)
S_i	The source term
S_t	Stokes number, $S_t = \tau_p / \tau_f$ (-)
T	Time (s)
T_k	The stress tensor
t	Time (s)
U	Fluid velocity (m/s)
U_∞	Oncoming velocity of Stuart vortex (m/s)
u	The liquid velocity of the liquid (m/s)
u_i	Interface velocity (m/s)
u'	The RMS velocity, u component (m/s)
V	The volume of a bubble
V_T	The terminal slip velocity of the discrete phase (m/s)
v	The velocity of the bubble or particle (m/s)
v_b	The Lagrangian velocity of the particles (m/s)
v'	The RMS velocity, v component (m/s)
w	The bubble slip velocity, $w = v - u$ (m/s)
X	Downstream location of the mixing layer (m)
X_i	The mean squared displacement of particles (m)
X_k	The phase function
X_0	The x coordinate of origin of the mixing layer (m)
Y	The y coordinate of origin of the mixing layer (m)
Y_0	The y coordinate of origin of the mixing layer (m)
y	The distance measured from the origin of the coordinate (m)
α_k	Locally averaged volume fraction
α_L	Disperse phase volume fraction

α_p	Carrier fluid volume fraction
Γ	Trapping parameter (-)
Γ_i	The exchange coefficient of ϕ in phase i (-)
γ	Mass ratio, $\gamma=\rho_b/\rho_f$ (-)
γ_i	The volume fraction of phase i
δ	Transverse width of the mixing layer or the eddy size (m)
δ_b	The nominal thickness of the boundary layer on the end of both sides of the splitter plate (m)
$\Delta\rho$	Density difference, $\Delta\rho=\rho_b-\rho_f$ (kg/m ³)
ΔU	Velocity difference, $\Delta U=U_2-U_1$ (m/s)
μ	Dynamical viscosity
ν	Kinematic viscosity
ν_t	Turbulence viscosity
Π	The ratio of inertia to buoyancy (-)
ρ_b	The gas density (kg/m ³)
ρ_f	The fluid density (kg/m ³)
τ	Time (s)
τL	Total shear stress (N/m ²)
τ_b	The shear stress due to the bubbles (N/m ²)
τ_t	The shear stress due to the shear turbulence (N/m ²)
τ_f	Eddy time scale, $\tau_f=\delta/\Delta U$ (s)
τ_p	Aerodynamic response time of the particle, $\tau_p=\rho_p d^2/18\mu$ (s)
Φ	The local average value of the scalar quantity
ϕ_i	Any conserved property of phase i
σ	The cut-off point vortex core radius (m)
σ_k	Eddy Schmidt number
σ_ϕ	
σ_ε	Empirical constant in K - ε model
σ_τ	
Ω	The vorticity
ε	Turbulence dissipation rate

Chapter 2

B	Richardson number, $B=gR/u_\omega^2$ (-)
b	The empirical constant (-)
C_D	Drag coefficient (-)
C_L	The bubble lift coefficient (-)
C_{w1}	The empirical constant (m/s)
C_{w2}	The empirical constant (m/s)
C_μ	The empirical constant
D	Pipe diameter (m)
d_B	The average bubble diameter (mm)
e_r	The unit vector in axial direction
e_x	The unit vector in radial direction
F_D	Drag force (N)
F_W	Wall force (N)

g	Gravitational acceleration (m/s^2)
j_G	The gas flow rate (m/s)
j_L	The liquid flow rate (m/s)
K	The turbulent kinetic energy
k	The subscript
k_b	The empirical constant (-)
L	The length of the pipe (m)
Q_L	Liquid volumetric flow rate (m^3/s)
p	Pressure (N/m^2)
p^*	Non-dimensional pressure (-)
R	The radius of the pipe (m)
r	The radius (m)
r^*	Non-dimensional radius (-)
r_b	The radius of the bubble (mm)
t	Time (s)
u_b	Bubble velocity (m/s)
u_k	The corresponding velocity for phase k (m/s)
u_L	Liquid velocity (m/s)
u'_L	Liquid fluctuation velocity (m/s)
u_τ	The shear stress at $y^+=40$ (N/m^2)
V_r	The bubble lateral migration velocity (m/s)
V_s	The slip velocity vector (m/s)
V_T	The bubble rise velocity in still water (m/s)
V_x	The axial component of the slip velocity vector (m/s)
v'_b	The transverse turbulence fluctuation velocity (m/s)
v'_L	The transverse turbulence fluctuation velocity due to the bubble perturbation (m/s)
y	Distance measured from the wall (m)
y^+	Non-dimensional distance measured from the wall (-)
y_0	The distance measured from the wall (m)
α	Bubble void fraction (-)
α_{cal}	Averaged bubble void fraction (-)
α_b	The volume fraction for bubbles (-)
α_k	The volume fraction of phase k (-)
α_L	The volume fraction for liquid (-)
α_m	The average void fraction over the cross-section of the pipe (-)
ϵ_b	Bubble dispersion coefficient (-)
κ	The empirical constant (-)
ν_L	The kinematic viscosity of the liquid (m^2/s^2)
ν_L^t	The turbulence viscosity (m^2/s^2)
ν_B^t	The pseudo-turbulence viscosity due to the bubbles (m^2/s^2)
ρ_G	The gas density (kg/m^3)
ρ_L	The liquid density (kg/m^3)
$\Delta\rho$	Density difference, $\Delta\rho=\rho_G-\rho_L$ (kg/m^3)
σ_K	Turbulence Schmidt number (-)
σ_T	Effective inverse Prantl-Schmidt number (-)
τ^+	Non-dimensional shear stress (-)

τ_w	The shear stress on the wall (N/m ²)
ϕ_k	The scale variable of interest for phase k (-)

Chapter 3

b	The mixing layer spread rate (-)
C	Concentration of bubbles or particles (-)
C_D	Drag coefficient (-)
C_L	The bubble lift coefficient (-)
C_m	The added mass coefficient (-)
C_T	Concentration of bubbles or particles inside the coherent structure (-)
C_0	Total particle concentration in mesh (-)
D_{by}	Bubble diffusivity (m ² /s)
D_{fy}	Fluid particle diffusivity (m ² /s)
d	Particle diameter (mm)
f	Drag coefficient function (-)
g	Gravitational acceleration (m/s ²)
g_x	The x component of gravitational acceleration (m/s ²)
g_y	The y component of gravitational acceleration (m/s ²)
L	The length of the simulation domain (m)
N	The average number of the point vortices in the simulation domain (-)
N_0	Total number of bubbles released (-)
R	The Rankine vortex core radius (m)
R_L	The Lagrangian auto-correlation coefficient (-)
R_n	The distance between n th point vortex and j th point vortex (m)
r	The distance between n th point vortex and j th point vortex (m)
S_t	Stokes number, $S_t = \tau_p / \tau_f$ (-)
T	Time (s)
t	Time step (s)
U_b	Bubble velocity (m/s)
U_{by}	The radial convergence velocity of bubbles (m/s)
U_m	The mean convective velocity in main flow direction, $U_m = 1/2(U_1 + U_2)$ (m/s)
U_n	The velocity component in x direction of n th point vortex (m/s)
U_1	The low speed side velocity of the mixing layer (m/s)
U_2	The high speed side velocity of the mixing layer (m/s)
u	The liquid velocity of the liquid (m/s)
u_θ	The induced velocity at n th point vortex by j th point vortex (m/s)
u'	The RMS velocity, u component (m/s)
V_m	The mean cross-stream convective velocity (m/s)
V_n	The velocity component in y direction of n th point vortex (m/s)
V_T	The terminal slip velocity of the discrete phase (m/s)
v	The velocity of the bubble (m/s)
v_b	The Lagrangian velocity of the particles (m/s)
v_x	The x component of the bubble velocity (m/s)
v_y	The y component of the bubble velocity (m/s)
v'	The RMS velocity, v component (m/s)

w	The bubble slip velocity, $w=v-u$ (m/s)
X	Downstream location of the mixing layer (m)
X_n	n th point vortex coordinate in x direction (m)
X_0	The x coordinate of origin of the mixing layer (m)
Y	The y coordinate of origin of the mixing layer (m)
Y_n	n th point vortex coordinate in y direction (m)
Y_0	The y coordinate of origin of the mixing layer (m)
y	The displacement of a fluid particle (m)
Γ	Retention parameter (-)
Γ_{Ran}	Trapping parameter for the Rankine vortex (-)
γ	Mass ratio, $\gamma=\rho_b/\rho_f$ (-)
δ	Transverse width of the mixing layer or the eddy size (m)
δ_b	The nominal thickness of the boundary layer on the end of both sides of the splitter plate (m)
η_{off}	Offsetting (-)
μ	Fluid dynamical viscosity (kg/m s)
ν	Kinematic viscosity (m ² /s)
ρ_b	The gas density (kg/m ³)
ρ_f	The liquid density (kg/m ³)
ρ_p	The particle density (kg/m ³)
$\Delta\rho$	Density difference, $\Delta\rho=\rho_b-\rho_f$ (kg/m ³)
ΔU	Velocity difference, $\Delta U=U_2-U_1$ (m/s)
Δt	Time step (s)
$\Delta\Gamma$	The vorticity strength of point vortex (m ² /s)
ζ'	The vector jitter, $\zeta'=\varepsilon U_m \Delta t$ (m)
ζ_x	The x component of the vector jitter (m)
ζ_y	The y component of the vector jitter (m)
τ	Time delay (s)
τ_f	Eddy time scale, $\tau_f=\delta/\Delta U$ (s)
τ_p	Aerodynamic response time of the particle, $\tau_p=\rho_p d^2/18\mu$ (s)
Π	The ratio of inertia to buoyancy (-)
Π_{Ran}	The ratio of inertia to buoyancy for the Rankine vortex (-)
σ	The cut-off point vortex core radius (m)
ω	The angular velocity (1/s)
ε	Coefficient (-)

Chapter 4

C_L	The bubble lift coefficient (-)
C_m	The added mass coefficient (-)
C_D	Drag coefficient (-)
D_p	The particle dispersion coefficient (m ² /s)
d_p	The particle radius (m)
f	Drag coefficient function (-)
g	Gravitational acceleration (m/s ²)

k	The turbulent kinetic energy (m^2/s^2)
L	The length of the simulation domain (m)
m_f	The mass of the fluid displaced by the particle (kg)
m_p	The mass of the particle (kg)
N	The average number of the point vortices in the simulation domain (-)
N_0	Total number of particles passing through mesh (-)
R	The Rankine vortex core radius (m)
R_{ep}	The particle Reynolds number, defined as $R_{ep}=d_p \mathbf{v}-\mathbf{u} /\nu$
r	The distance measured from the Rankine vortex centre (m)
r_0	The radius of the Rankine vortex (m)
S_t	Stokes number, $S_t=\tau_p/\tau_f$ (-)
T	Time (s)
t	Time (s)
U_m	The mean convective velocity in main flow direction, $U_m=1/2(U_1+U_2)$ (m/s)
U_1	The low speed side velocity of the mixing layer (m/s)
U_2	The high speed side velocity of the mixing layer (m/s)
\mathbf{u}	The liquid velocity of the liquid (m/s)
u'	The RMS velocity, u component (m/s)
V_m	The mean cross-stream convective velocity (m/s)
V_T	The terminal slip velocity of the discrete phase (m/s)
\mathbf{v}	The velocity of the particle (m/s)
v_θ	The tangential velocity (m/s)
v'	The RMS velocity, v component (m/s)
\mathbf{w}	The bubble slip velocity, $\mathbf{w}=\mathbf{v}-\mathbf{u}$ (m/s)
x	Downstream location of the mixing layer (m)
x_k	k th Rankine vortex coordinate in x direction (m)
x_0	The x coordinate of origin of the mixing layer (m)
y	The y coordinate of origin of the mixing layer (m)
y_f	The displacement of a fluid particle (m)
y_k	k th Rankine vortex coordinate in y direction (m)
y_0	The y coordinate of origin of the mixing layer (m)
y_p	The displacement of a particle (m)
Γ	Retention parameter (-)
Γ_0	The circulation around the vortex (m^2/s)
γ	Mass ratio, $\gamma=\rho_p/\rho_f$ (-)
$\Delta\rho$	Density difference, $\Delta\rho=\rho_b-\rho_f$ (kg/m^3)
ΔU	Velocity difference, $\Delta U=U_2-U_1$ (m/s)
Δt	Time step (s)
$\Delta\Gamma$	The vorticity strength of point vortex (m^2/s)
δ	Transverse width of the mixing layer or the eddy size (m)
ζ_x	The x component of the vector jitter (m)
ζ_y	The y component of the vector jitter (m)
ζ'	The vector jitter, $\zeta'=\varepsilon U_m \Delta t$ (m)
λ	The distance between two adjoining Rankine vortices (m)
μ	Dynamic viscosity of the fluid (kg/ms^2)
ν	Kinematic viscosity of the fluid (m^2/s^2)

ξ_u	The x component of a Gaussian jitter (-)
ξ_v	The y component of a Gaussian jitter (-)
τ	Time delay (s)
τ_f	Eddy time scale, $\tau_f = \delta / \Delta U$ (s)
τ_p	Aerodynamic response time of the particle, $\tau_p = \rho_p d^2 / 18\mu$ (s)
Π	The ratio of inertia to buoyancy (-)
ρ_p	The particle density (kg/m^3)
ρ_f	The liquid density (kg/m^3)
ω	The angular velocity (1/s)

Chapter 5

b_u	The mixing layer spread rate (-)
C_L	The bubble lift coefficient (-)
C_m	The added mass coefficient or empirical constant (-)
D	The jet exit width (m)
D_y^2	Lateral dispersion function (m^2)
D_{fy}^2	Lateral fluid particle dispersion function (m^2)
f	Drag coefficient function (-)
g	Gravitational acceleration (m/s^2)
L	The length of the simulation domain (m)
N	The average number of the point vortices in the simulation domain or the total number of particles in the flow at time T (-)
N_0	Total number of particles passing through mesh (-)
R	The Rankine vortex core radius (m)
R_n	The distance between n th point vortex and j th point vortex (m)
r	The distance between n th point vortex and j th point vortex (m)
T	Time (s)
t	Time step (s)
U_b	Bubble velocity (m/s)
U_m	The mean convective velocity in main flow direction, $U_m = 1/2(U_1 + U_2)$ (m/s)
U_n	The velocity component in x direction of n th point vortex (m/s)
U_0	The jet exit velocity (m/s)
U_1	The low speed side velocity of the mixing layer (m/s)
U_2	The high speed side velocity of the mixing layer (m/s)
u	The liquid velocity of the liquid (m/s)
u_θ	The induced velocity at n th point vortex by j th point vortex (m/s)
u'	The RMS velocity, u component (m/s)
V_m	The mean cross-stream convective velocity (m/s)
V_n	The velocity component in y direction of n th point vortex (m/s)
V_T	The terminal slip velocity of the discrete phase (m/s)
v	The velocity of the bubble (m/s)
v'	The RMS velocity, v component (m/s)
w	The bubble slip velocity, $w = v - u$ (m/s)
X_n	n th point vortex coordinate in x direction (m)

X_0	The x coordinate of origin of the plane jet (m)
X	Downstream location of the plane jet (m)
Y_i	The lateral location of the i th particle at time T (m)
Y_m	The mean value of particle lateral displacement position at time T (m)
Y_n	n th point vortex coordinate in y direction (m)
Y_0	The y coordinate of origin of the plane jet (m)
Y	The y coordinate of origin of the plane jet (m)
β	The empirical constant
Γ	Retention parameter, $\Gamma=\Delta U/V_T$ (-)
γ	Mass ratio, $\gamma=\rho_b/\rho_f$ or the ratios of particle dispersion and tagged fluid particle dispersion (-)
$\Delta\rho$	Density difference, $\Delta\rho=\rho_b-\rho_f$ (kg/m ³)
ΔU	Velocity difference, $\Delta U=U_2-U_1$ (m/s)
Δt	Time step (s)
$\Delta\Gamma$	The vorticity strength of point vortex (m ² /s)
ν	Fluid kinematic viscosity (m ² /s)
Π	The ratio of inertia to buoyancy (-)
ρ_b	The gas density (kg/m ³)
ρ_f	The liquid density (kg/m ³)
σ	The cut-off point vortex core radius (m)
ω	Rankine vortex strength (1/s)

Chapter 6

c	local concentration
C_T	Local bubble concentration
D_{cor}	Correlation dimension
f	frequency (Hz)
K_{pr}	Diffusion coefficient
L	Length of computational domain (m)
l	Spacing parameter
M	The number of sampling stations
N	The number of sampling bins in a particular station
$n_{bi,j}$	The number of bubbles received by the bin around $y_{i,j}$
$n_{pi,j}$	The number of particles received by the bin around $y_{i,j}$
$n_{vi,j}$	The number of point vortices received by the bin around $y_{i,j}$
p_i	The probability that the spacing between two particles is less than l
N_T	Total number of sampling time steps
S_h	Strouhl number, defined as $S_h=Fl/\Delta U$
S_t	Stokes number (-)
t	Time (s)
U_m	Mean convection velocity (m/s)
U_{pr}	Bubble converge velocity (m/s)
u	Local velocity of fluid (m/s)
u_{dj}	The particle or bubble drift velocity in j direction (m/s)
u_j	Local velocity of fluid (m/s)

V_T	Terminal speed of particle or bubble (m/s)
x	Downstream distance (m)
α_p	Local particle volume fraction
Γ	Retention parameter (-)
γ	Mass ratio (-)
Δt	Time step (s)
ΔU	Velocity difference across shear layer (m/s)
δ	Shear layer width (m)
ξ	The fluctuation attenuation
Π	The ratio of inertia to buoyancy (-)
τ	Time delay (s)
Ω	Time-averaged vorticity
ω	Vorticity
ω'	Vorticity fluctuation

Chapter 7

Γ	Retention parameter (-)
γ	Mass ratio (-)
Π	The ratio of inertia to buoyancy (-)

CHAPTER 1: CURRENT STATUS OF TWO-PHASE FLOW DYNAMICAL SIMULATION AND MODELLING

SUMMARY

Accurate prediction of two-phase flow is of importance in many industrial applications, including process needs in chemical engineering. Recently, considerable progress in understanding and predicting two-phase flow phenomena has been made using a combination of rigorous model development, advanced computational techniques and supporting experiments. In particular, numerical methods of prediction for two-phase flow as a versatile and functional tool have received increasing attention. This chapter reviews the current status of such developments in simulation and modelling, with the emphasis on discrete phase transport dynamics in free shear flows, but also extending more widely to established computational schemes. As a first cut distinction, all such methods can be described as Eulerian, Lagrangian or mixed Eulerian-Lagrangian approaches, each with certain advantages and disadvantages. Numerical modelling limitations mainly arise from inadequate physical prescriptions rather than the limitations of the numerical methods adopted. Virtually, all practical methods employed for engineering calculations are based on either integral approaches or time-averaged turbulence models, both of these exclude the flow structures which may often be largely responsible for the discrete phase transport. Whilst exclusively Lagrangian approaches can incorporate important eddy structural effects on the discrete phase transport, they still rely on independent formulation of a Lagrangian force law. The status of such formulation remains uncertain for other than a few asymptotic idealisations and such developments are summarised here. We also briefly describe current status of CFD codes for two-phase flow.

1 INTRODUCTION

Two-phase flows are almost universally encountered in nature and in a large variety of industrial settings such as chemical, metallurgical, nuclear, plastics, pharmaceutical and food processing. Consequently, their study forms an important area in chemical engineering research. Even a small improvement in the design of two-phase and multiphase system may lead to significant savings in industrial processes. In two-phase flows, the flow structure may be significantly modified by the presence of a discrete phase in the carrier fluid. One obvious example would be the performance of mechanically agitated reactors and mixing tanks where the presence of bubbles behind the impeller blades causes a pronounced change in the trailing vortex structure and striking intermittency in shaft power draw (e.g. Pearse & Thomas 1990), as shown in figure 1. A second example is seen in nozzle sprays for which the nozzle was deliberately designed to introduce and exploit the effect of large eddies on the spray behaviour, as shown in figure 2 (FRED SMART project, Thomas 1995). Unfortunately, present knowledge of the detailed structural interaction in such flows is still very limited. Indeed, it would not be exaggerating to say that such inadequacies in understanding and characterisation represent a limiting factor in the improved design of many industrial processes.

Although considerable progresses in simulation and modelling has been achieved over past decades, there remain many problems that need to be solved. Difficulties mainly arise from variabilities in phase distribution patterns from flow-to-flow, which must usually be specified empirically (Ishii 1975). Indeed, it is not misleading to suggest that modelling difficulties mainly arise from inadequate physical formulation rather than in the numerical approaches

available. The project reported here aims to strengthen the understanding of the models and numerical approaches, particularly in two-phase free shear flows. Emphasis will be placed on linking current advances in theoretical modelling with improved numerical approaches for engineering applications.

Literature produced over the last two decades as reviewed here represents a special focus within the context of our interests described in the summary. Extensive accounts of the detailed aspects of two-fluid models can be found in Drew (1983), on modelling disperse two-phase flows in Hunt *et al.* (1994), and for particle dispersion in free shear flows in Crowe *et al.* (1993). Particular attention has recently been drawn to the fundamental role played by eddy structure in shear flows and how these features can largely determine the discrete phase transport dynamics (e.g. Sene *et al.* 1994; Crowe *et al.* 1993). Such advances hold the key to improve physical insight which in turn will be a prerequisite for improved industrial and environmental practices.

As in our initial indication of the aspects addressed here, section 2 outlines numerical codes for two-phase flow prediction and outline their current status. As our main interest lies with discrete phase transport dynamics in free shear flows, section 3 concentrates on Lagrangian formulations currently available for such discrete phase trajectory calculations. Section 4 reviews the main elements of the general mathematical modelling adopted. Section 5 outlines current numerical prediction methods, including physical modelling techniques and their limitations, and we end with recapitulation and implications in section 6.

2 CURRENT STATUS OF CFD SOFTWARE FOR TWO-PHASE FLOW

CFD codes are now used and developed widely in the analysis of a broad range of two-phase flow problems. Examples of such codes include commercially available packages, **PHOENICS, FLUENT, FLOW3D, FIDAP**, etc, with academic codes, e.g. **Mélodif, ESTET-ASTRID**. The vast majority of work pursued by these codes is for single phase flow, i.e. the transport of all the fluid species can be represented by a single velocity field. However, they do deal with two-phase flow situations. If separate phases are present, then they are usually treated in one of the following ways in these codes.

- If the second phase is dilute it may offer be adequately modelled as a concentration of the host phase (Crowe 1982), provided that special source terms are added to reflect the difference in density.
- For some problems, notably gas injection into a liquid bath, the system can be adequately represented with a drift velocity added to the vertical component of the velocity for the gaseous concentration.
- In some dilute flow cases, particles can be tracked through the host fluid flow field as described by Crowe (1982). This mixed Eulerian-Lagrangian approach, however, assumes that the fluid field is not affected by the presence of particles, i.e. excluding two-way coupling effects.

2.1 Basic Conservation Equations and Solution Procedure

The general and widely used equations representing the conservation for two-phase flows, employed in most of CFD codes, assumes the following general form:

$$\frac{\partial}{\partial t}(\gamma_i \rho_i \phi_i) + \nabla \cdot (\gamma_i \rho_i \mathbf{u} \phi_i - \gamma_i \Gamma_i \nabla \phi_i) = \gamma_i S_i \quad (1)$$

where γ_i is the volume fraction of phase i , ρ_i is the density of phase i , Γ_i and S_i are respectively the exchange coefficient of the ϕ in phase i and the source term, and ϕ_i denotes any conserved property of phase i . When time-averaged values of the various quantities are to be solved, as is commonly the case when two-phase turbulent flows are to be simulated, special expressions may have to be introduced for Γ and S , accounting for the correlations between velocity, density, ϕ and other quantities of the flow concerned. Normally, many equations of the above type have to be solved simultaneously in the calculations because links exist among them in many ways. It is obvious that by setting ϕ_i to unity equation (1) reduces to the continuity equation, and by setting γ_i to unity equation (1) is solved for single-phase flow. In numerical processes, some auxiliary equations may also be required for the closure of the problem, e.g. density, diffusion coefficients, etc.

In most two-phase flow Eulerian codes, the governing equations are discretised using a finite volume, finite difference or finite element approach. Integration of the governing equations over the finite volume of a computational cell (note: a staggered grid technique (Patankar 1980) still prevails!) and over a finite time results in a set of algebraic equations (e.g. Patankar 1980). The resulting volume, area and time averages are approximated by the use of different interpolation assumptions, i.e. differencing schemes (e.g. Upwind Difference Scheme; UDS, Hybrid Difference Scheme; HDS, Central Difference Scheme; CDS, and QUICK, etc.) which have involved much development. The non-linear nature of the algebraic equations necessitates the employment of iterative procedures in which the coefficients appearing in the algebraic equations are updated in the light of new estimates

of the variables and solved until convergence is achieved.

2.2 Applications and Limitations

The commercial codes as listed above have now been applied to nearly all flow situations which can be found in the literature. For example, an A-Z of applications for **PHOENICS** is shown in figure 3. Although a lot of successes have been declared in using these codes, none can reliably predict the transient behaviour of large eddy structures since they all employ Eulerian turbulence closure modelling. As reviewed later, such an Eulerian approach excludes the transient structure of large eddies. This shortcoming can be seen clearly in predictions of two-phase bubbly flow over a sudden expansion (Bel F'dhila 1992) using the code **Mélodif**, as shown in figure 4. The void fraction profiles predicted are in poor agreement with their experimental data. Obviously, the strong interaction between bubbles and the vortex structure behind the back step influences the void fraction distributions. However, double Eulerian approaches as used in **Mélodif** cannot reasonably capture this interaction due to the transient pressure and velocity field.

3 FORCES ACTING ON BUBBLES AND PARTICLES

In the determination of the bubble and particle transport, or the dynamics of a dilute two-phase flow system, one of the important issues to be addressed is how an individual, isolated bubble or particle moves in response to the ambient flow conditions; so that bubble or particle motion can be properly described. A wide range of theoretical studies into particle dynamics have been documented. The studies on particle dynamics have started from those considering simple rectilinear motion in a still fluid (e.g. Basset 1888) to those involving

more complex numerical simulation models concerning particle dispersion in turbulence (e.g. Elgobashi 1991, Squires & Eaton 1994). A key factor in all of these studies is the formulation of an equation of motion for the particle. Unfortunately, present calculations are all possible only when a number of limiting assumptions have been imposed. We review current proposed equations of motion before considering calculation methods in conjunction with addressing the calculation of the carrier fluid flow field.

3.1 Identification of Forces

The force on an isolated bubble or particle depends on its size, shape, density and velocity, and on the density, viscosity and velocity of the surrounding transport fluid. Some of these factors further depend on the physical properties of the fluid, such as the surface tension, the presence of surfactant, and even any non-Newtonian properties. The identification of the forces acting on a bubble or particle is therefore ambiguous, and the approach adopted recently has been limited to certain cases - for example, assuming particles to be spherical and immersed in inviscid weak shear flows (e.g. Thomas *et al.* 1983; Auton *et al.* 1988) or particles in low Reynolds number flows (Maxey and Riley 1983, Maxey 1993). However, once the expressions for different force contributions for the limiting cases have been obtained, the forces acting on particles are modelled using a combination of interpolation and superposition based on fluid mechanics principles. It is now broadly accepted that the contributions towards the forces on the particles can be identified as follows.

3.1.1 Added mass and pressure gradient forces

For spherical bubbles and particles in inviscid irrotational flows, the sum of the added mass and pressure gradient forces can be expressed (Auton *et al.* 1988)

$$F_I = \rho_f V \left(\frac{Du}{Dt} \Big|_{x_p} + C_m \frac{Du}{Dt} \Big|_{x_p} - C_m \frac{dv}{dt} \right) \quad (2)$$

where Du/Dt is the acceleration of the ambient flow at X_p and C_M is the added mass coefficient. V is the bubble or particle volume. But for a particle moving in an unsteady, non-uniform flow, Maxey and Riley (1983) suggested:

$$F_I = \rho_f V \left(\frac{Du}{Dt} \Big|_{x_p} + C_m \frac{du}{dt} \Big|_{x_p} - C_m \frac{dv}{dt} \right) \quad (3)$$

Formulation of the added mass force (like equation (2)) has been contentious for some considerable time, with a consensus agreement only recently attained (Thomas 1994). The mistakes in modelling this force in earlier work have been reviewed by Thomas *et al.* (1983).

(a) Convective operator The key point is that the advective contribution $(v-u) \cdot \nabla u$ was omitted from the original formulations (e.g. Corrsin & Lumley 1956). These mistakes can be clearly identified with reference to figure 5 (Auton *et al.* 1988). Other approaches such as the use of constitutive equation of motion (Drew & Lahey 1979; Hinze 1963) also failed to obtain this term. However, Drew & Lahey (1990) have revised their analysis and obtained the same conclusion as Auton *et al.* (1988). Maxey and Riley (1983) argued that there is no distinction between their form given by them and the form given by Auton at low Reynolds number. However, Maxey himself (1993) has recently indicated that the form given by Auton is probably correct under a wide range of conditions. Although the formulation of Maxey and Riley (1983) has been widely applied to the predictions of particle trajectories, recent numerical simulations (e.g. Ruetsch & Meiburg 1993; Maxey *et al.* 1994) have employed the same form of the added mass force given by Auton *et al.* (1988) and Thomas *et al.* (1983) instead of the original of Maxey & Riley (1983) (equation (3)).

(b) Added mass coefficient The added mass coefficient C_M has been calculated classically for inviscid flows and is found to be 0.5 for a sphere (Milne-Thomson 1968). This is identical to that in Auton *et al.*'s (1988) and Maxey and Riley's (1983) equations. Experiments (e.g. Hamilton & Lindell 1971) for spheres accelerating in water with the Reynolds number from 3.3×10^3 to 3.5×10^4 do support this conclusion. Recent studies by Rivero *et al.* (1991) and Chang (1992), using the time-dependent Navier-Stokes equations for a stationary solid sphere, or a stationary spherical inviscid bubble, have revealed that the added mass coefficient $C_M=0.5$ was constant under a very wide range of conditions (even for oscillatory flow). Furthermore, their striking results demonstrated that neither the history of the flow nor the type of wake affected the added mass coefficient and the form given by Auton for the evaluation of the added mass force is correct.

3.1.2 Drag force

Since bubbles or particles are immersed in moving liquid, they experience a drag force. It has been customary to determine the drag force according to a drag coefficient. For solid particles the steady state drag coefficient is normally taken from an empirical relation approximating to the standard curve such as proposed by Clift *et al.* (1978). For particle Reynolds number less than 1000, Clift *et al.* suggested the use of the following relation:

$$C_D = \frac{24}{R_e} f \quad (4)$$

where f is the modified factor which reflects deviation of true drag to Stokes drag:

$$f = 1 + 0.15 R_e^{2/3} \quad (5)$$

and R_e is the particle Reynolds number based on the slip velocity, defined as $R_e = d_p |\mathbf{v} - \mathbf{u}| / \nu$.

The numerical results obtained for the rigid sphere have confirmed that the empirical drag law (4) gives an estimation with error less than 6% for Re up to 300 (Magnaudet *et al.* 1995). The drag on a bubble, however, depends on the purity of the carrier fluid. The bubble drag force, as suggested by Thomas *et al.* (1983), may be more conveniently expressed as

$$\mathbf{F}_D = -\frac{\mathbf{v}-\mathbf{u}}{V_T} g \rho_f f\left(\frac{|\mathbf{v}-\mathbf{u}|}{V_T}\right) \quad (6)$$

where g is gravitational acceleration and V_T the terminal rise velocity in stationary liquid. The factor f is employed to accommodate surface tension non-uniformities arising from accumulation of contaminants on the bubble. For a bubble in a non-contaminated fluid where surface tension is uniform around the bubble's surface, a narrow wake is found and the drag force would be proportional to relative vorticity, thus f is equal to 1. For an impure system, e.g. tap water, surface tension varies due to contaminant accumulation, resulting in premature separation of the boundary layers and the formation of a broad fluctuating wake, much as in the flow around a solid body. The drag force is mainly caused by form drag so f would favour the form $f(|\mathbf{v}-\mathbf{u}|/V_T) = |\mathbf{v}-\mathbf{u}|/V_T$.

The effect of turbulence on the drag coefficient, such as caused by mean shear and particle or bubble wakes, is not covered yet, although it has been realised to have a significant effect on the drag (Thomas *et al.* 1983). Unfortunately, we are still not in position to consider this effect. We should note here that the above correlations are all based on the assumptions that the particle or bubble is in rectilinear motion and the effect of any curvature in the particle or bubble motion on the drag force has been excluded.

3.1.3 Lift force

The lift force experienced by a particle in weakly shearing flow is shear-vorticity induced due to velocity gradients in the flow field and can be evaluated by

$$F_L = \rho_f V C_L (\mathbf{v} - \mathbf{u}) \times \boldsymbol{\Omega} \quad (7)$$

where $\boldsymbol{\Omega}$ is the vorticity around the bubble. Auton (1987) showed by theory and numerical computation that the lift coefficient for a sphere in an inviscid weakly shear flow is $C_L=0.5$. Drew and Lahey (1987) also derived a similar results by different (less rigorous) arguments. However, numerical simulations for bubbly upward and downward flows (Lopez de Bertodano *et al.* 1990, Yang and Thomas 1992) have shown that the lift coefficient C_L can vary from 0.5 to 0.01 (highly viscous flows). In fact, this coefficient is strongly affected by local flow conditions.

Other lift forces have been considered by various researchers, e.g. the lift due to viscous shear (Saffman 1965, McLaughlin 1991) for very low Re particles and a Magnus lift associated with the self-spin of the particles especially when particle-wall collisions are being addressed (Sommerfeld 1990).

3.1.4 Basset historic force

This force arises from the response of a particle to a change in direction or speed of the flow and can be written as

$$F_B = \frac{3}{2} \pi d_p^2 \mu \int_0^t \frac{d(\mathbf{v} - \mathbf{u})/d\tau}{\sqrt{\pi \nu (t - \tau)}} d\tau \quad (8)$$

where d_p is the particle diameter and μ is the fluid dynamic viscosity. This term is often

neglected when calculating particle trajectories due to the expensive numerical effort required to solve it, as indicated by Maxey (1990). This force has been recently reinvestigated, for example, by Mei *et al.* (1991). They showed that the kernel $(t-\tau)^{-1/2}$ in the Basset term is correct only for short times, and decays much faster for long times because the kernel behaves like $(t-\tau)^{-2}$. This would suggest that at longer times the kernel within the Basset history integral should be modified, and that it decays faster than usually expected.

The analysis of Rivero *et al.* (1991) revealed that in the case of a bubble this force was always found to be negligible in comparison with the other forces, as was also verified by Sridhar & Katz (1995) (see figure 6). This force was neglected in Auton's force law for many applications, such as in Thomas *et al.* (1983), Sene *et al.* (1994), Yang & Thomas (1994) and Onslow *et al.* (1993).

3.2 Generalised Force Law

By analysing inviscid flow around a sphere in a rotational straining flow, Thomas *et al.* (1983) and Auton *et al.* (1988) concluded that the interfacial force on a sphere in the condition that local homogeneity in flow velocity gradients is assumed; i.e. $|\Omega|a \ll |\mathbf{v}-\mathbf{u}|$, can be expressed by the sum of the added mass force and the lift force summarised in the previous section. Thomas *et al.* (1983) further suggested that the viscous drag could simply be added to the inviscid force so that the resultant forces experienced by the particle can be expressed to be a linear combination of all forces reviewed in the previous section. The composite force law can be written

$$\left(\frac{\rho_b}{\rho_f} + C_m\right) \frac{d\mathbf{v}}{dt} = (1 + C_m) \frac{D\mathbf{u}}{Dt} - g \frac{\mathbf{w}}{V_T} f\left(\frac{|\mathbf{w}|}{V_T}\right) - \left(\frac{\rho_b}{\rho_f} - 1\right) \mathbf{g} - C_L \mathbf{w} \times (\nabla \times \mathbf{u}) \quad (9)$$

A similar approach was also employed by Maxey and Riley (1983) in their derivation for a small spherical particle at low Reynolds number.

$$m_p \frac{dv}{dt} = (m_p - m_f)g + m_f \frac{Du}{Dt} + \frac{1}{2} m_f \left(\frac{Du}{Dt} - \frac{dv}{dt} \right) + 3\pi d_p \mu w + \frac{3}{2} \pi d_p^2 \mu \int_0^t \frac{dw/d\tau}{\sqrt{\pi \nu (t-\tau)}} d\tau \quad (10)$$

where m_p and m_f are the mass of the particle and the mass of the fluid displaced by the particle. As we can see from equations (9) and (10), as well as the discussion in the previous section, the important differences in determining the motion of isolated particles in dilute systems using the force laws are the appropriate forms of the added-mass term and vorticity induced lift term. Auton *et al.* (1988) and Thomas *et al.* (1983) have shown that, at least for inviscid flows involving bubbles, the added mass term is $[dv/dt - Du/Dt]$ instead of the form $[dv/dt - du/dt]$, given by Maxey and Riley (1983). At the level of approximation for low Reynolds number, it is difficult to distinguish differences between two, as indicated by Maxey (1993). However, the difference will become more obvious with the increase of the particle or bubble Reynolds number R_e . Recent numerical simulations by Rivero *et al.* (1991) have supported that the added mass form of Auton (1987) and Thomas *et al.* (1983) is validated even for small to moderate Reynolds numbers. This indicates that the added mass suggested by Auton *et al.* (1988) and Thomas *et al.* (1983) is probably the only correct form for a wide range of conditions.

Whilst Auton's force law is undoubtedly correct asymptotically in the limits as prescribed, it should be noted here that there are two forces which may be of practical significance and are not included in its formulation. The first is the Basset force accrued from the unsteady viscous flow around the particle, which is certainly important at low Reynolds number. For bubbles, this term is usually neglected as discussed in the previous section. We therefore

neglect this term throughout our simulations. The second is the Magnus force with regard to particle self-spin, especially when particle-wall collisions are being concerned, as reviewed above. Other factors like non-sphericity, particle-particle interaction and liquid turbulence generated by mean shear or particle wakes may be important. However, the studies of these aspects are still limited. For these reasons we are confident that Auton's force law can be applied to most dispersed phase transport simulations in two-phase flows.

3.3 Validation of the Equation of Motion

Although the validity of Auton's equation (9) has not been justified directly, such as in a single particle trajectory in comparison with the experimental observations, indirect verification through experiments and numerical simulations can be found in the literature. Thomas *et al.* (1983) used the force law to compute freely rising bubble trajectories in the vicinity of a horizontal line vortex regarded as a far field representation of a Rankine vortex with viscous core, as shown in figure 31. They also presented the experimental results for a bubble rising from below a spinning rod in terms of a non-dimensional trapping width A^* as function of non-dimensional vortex strength C^* , as shown in figure 7 which shows how this trapping width A^* varied with vortex strength parameter C^* for bubbles and oil droplets. The comparison between experimental results and their numerical predictions is shown in figure 8, demonstrating a qualitative agreement. As a refinement of this idealised model, Sene *et al.* (1994) investigated the motion of bubbles attracted into a horizontal Rankine vortex, and showed how their trajectories within the viscous core converge to a focus with horizontal offset about 0.3 times the ratio of slip-speed over vortex strength. This location yields vertical and horizontal equilibrium respectively between the buoyancy and the drag forces and between the inertia and lift forces. Again, they employed the generalised force

law (9) for the analysis. Further extending the calculations as a model of bubbles travelling within the organised large structure of a turbulent free shear flow such as the mixing layer, the discrete vortex method was used to mimic the evolving large eddies. Bubble escape from a horizontal shear layer and the effect of eddy pairing on bubble escape were investigated as shown in figures 9 and 10. Bubble capture deduced from the idealised calculations was broadly reproduced as a probabilistic measure recovered from the numerical simulations and further reinforced by an experimental study on a bubbly downflowing shear layer (Sene *et al.* 1994; Yang & Thomas 1994), which can be seen clearly in figures 11 and 12.

It is again noted here that all the equations of motion considered have adopted the assumption that the particles or bubbles are non-deformable and spherical. For most particles of interest and small bubbles, say $d < 1$ mm, this assumption may suffice. However, large bubbles are easily deformed, and change shape due to surfactant etc. Accordingly, both added mass and drag coefficients are affected. To accommodate the effect of shape, Maxey (1990) has suggested the use of the equation of motion together with a complement of the equation of torque for trajectory prediction.

4 MATHEMATICAL MODELLING OF TWO-PHASE FLOW

4.1 Two-Fluid Model

Two-phase flows consist of dynamically interacting phases that are dispersed randomly in space and time. Although phase conservation equations for mass, momentum, and energy can in principle be written down, along with their interfacial conservation relations, they are most usually far too complicated to allow detailed solutions (Drew 1983). In fact, in uses

with simplified idealisations of the initial and boundary conditions in engineering applications, it usually suffices to consider only locally averaged quantities, as is done in the so-called 'two-fluid model' considered in outline below.

4.1.1 Averaging methods

One approach which at first might appear related is to impose a low pass filter that eliminates high frequency content from local instant fluctuations of variables. However, the statistical properties of these fluctuations and the collective contribution of interfaces which affect the macroscopic processes are taken into account in the formulation through various constitutive relations or closure laws. Averaging operators in the derivation of the two-fluid model have been addressed, for example, Ishii (1975), Nigmatulin (1979), Drew (1983) and Soo (1990). The commonly used averaging procedures (Drew 1983) are: (1) volume or area averaging, with no averaging in time; (2) time averaging, with no averaging in space; (3) ensemble averaging, with no averaging in space; (4) ensemble/space averaging or time/space averaging. Different averaging operators are illustrated in appendix I. This averaging should result in flow parameters that are continuous and posing continuously first derivatives, irrespective of the procedure adopted. In other words, the procedure must separate the essential elements of the signal from what is essentially noise, and result in averaged variables that are measurable with practical instrumentation. However, difficulties may arise from inappropriate averaging. For example, the time derivative of a point void fraction measurement becomes discontinuous because at any instant the gas phase is either present or not present. Therefore, double averages, time/space or ensemble/space, are usually adopted (e.g. Nigmatulin 1979; Banerjee & Chan 1980; Soo 1990). An obvious benefit of double averages is illustrated in figure 13 (Banerjee & Chan 1980) where the results for the

volume averaged void fraction and the ensemble average over the volume averaged measurements are respectively shown. It is evident that after only a few experiments the ensemble average converges onto the true average.

Choice of averaging procedure is strongly influenced by the available experimental methods. Most experimental measurements in two-phase flows involve some degree of spatial averaging because of the finite sensing volume, but they can usually deliver adequate time response (with careful design). While space/time averages are the simplest to obtain in experiments (e.g. the use of pitot tube or hot wire anemometry), difficulties may arise in distinguishing the signal from noise in rapid transients. Such an example can be seen in figure 14, where the transient signal due to the presence of the bubble must be identified properly. In general, time/space or ensemble/space averaging can achieve the necessary properties since their averaging operators are commutative.

4.1.2 Averaged conservation equations

Several derivations of the two-fluid models based on different averaging procedures have appeared in the literature. The equations cited most frequently are those presented by Drew (1983) and Ishii (1975). Other derivations include those by Soo (1990), Nigmatulin (1979), Banerjee & Chan (1980) and, more recently, Stewart & Crowe (1993). For any phase k , the equations of mass and momentum conservation can be written respectively (e.g. Truesdell & Toupin 1960):

$$\frac{\partial \rho_k}{\partial t} + \nabla \cdot (\rho_k \mathbf{u}_k) = 0 \quad (11)$$

$$\frac{\partial \rho_k \mathbf{u}_k}{\partial t} + \nabla \cdot (\rho_k \mathbf{u}_k \mathbf{u}_k) = \nabla \cdot \mathbf{T}_k + \rho_k \mathbf{f} \quad (12)$$

where ρ_k denotes the density, \mathbf{u}_k the velocity, \mathbf{T}_k the stress tensor, and \mathbf{f} the body force density. The mass and momentum balance equations for two-phase interfaces, also known as interfacial jump conditions, were given by Ishii (1975), Kataoka *et al.* (1986):

$$\sum_{k=1}^2 \rho_k (\mathbf{u}_k - \mathbf{u}_i) \cdot \mathbf{n}_k = 0 \quad (13)$$

$$\sum_{k=1}^2 [\rho_k \mathbf{u}_k (\mathbf{u}_k - \mathbf{u}_i) \cdot \mathbf{n}_k + \mathbf{T}_k \cdot \mathbf{n}_k] = \mathbf{M}_m \quad (14)$$

where \mathbf{u}_i is interface velocity. \mathbf{n}_k is the unit normal and \mathbf{M}_m is the interfacial force per unit interfacial area. Multiplication to the phase conservation equations (1) and (2) together with the jump conditions (3) and (4) by the phase function X_k , defined by

$$X_k(\mathbf{x}, t) = \begin{cases} 1 & \text{if } \mathbf{x} \text{ in phase } k \text{ at time } t \\ 0 & \text{otherwise.} \end{cases} \quad (15)$$

and an application of the averaging theorems leads to a set of local volume-averaged conservation equations for two-phase flows that can be written as:

$$\frac{\partial \alpha_k \bar{\rho}_k}{\partial t} + \nabla \cdot \alpha_k \bar{\rho}_k \hat{\mathbf{u}}_k = \Gamma_k \quad (16)$$

$$\frac{\partial \alpha_k \bar{\rho}_k \hat{\mathbf{u}}_k}{\partial t} + \nabla \cdot \alpha_k \bar{\rho}_k \hat{\mathbf{u}}_k \hat{\mathbf{u}}_k = -\alpha_k \nabla \bar{p}_k + \nabla \cdot \alpha_k (\bar{\boldsymbol{\tau}}_k + \bar{\boldsymbol{\sigma}}_k) + \Gamma_k \mathbf{u}_{k,i} + (p_{k,i} - \bar{p}_k) \nabla \alpha_k + \mathbf{M}_k^d \quad (17)$$

Here two types of averaged variables have been used, namely the phasic and the mass-weighted average. They are respectively defined as $\bar{\phi} = \langle X_k \phi \rangle / \alpha_k$ and as $\bar{\psi} = \langle X_k \rho_k \psi \rangle / \alpha_k \bar{\rho}_k$.

$\langle \rangle$ denotes an averaging process. Obviously, $\alpha_k = \langle X_k \rangle$. The jump conditions, (3) and (4), are then written as

$$\sum_{k=1}^2 \Gamma_k = 0 \quad (18)$$

$$\sum_{k=1}^2 [\Gamma_k \mathbf{u}_{k,i} + p_{k,i} \nabla \alpha_k + \mathbf{M}_k^d] = \mathbf{M}_m \quad (19)$$

The term \mathbf{M}_m is the contribution to the total force on the two-phase mixture due to the interface, and is especially due to surface tension. For tractability here, we assume incompressible fluid and no interfacial phase change so that $\bar{\rho}_k = \text{constant}$ and $\Gamma_k = 0$.

Other types of averaged equations can be derived and do not change the form of the equations. In particular, local-volume averaging (e.g. Banerjee & Chan 1980; Soo 1990) can be done first, followed by time averaging. It should be noted that whatever averaging is taken, important characteristics of the flow field are lost in the process of averaging, and this subsequently requires supplementary consideration of appropriate closure models.

4.2 Constitutive Equations

In the absence of an interfacial mass transfer term, the main difficulties in any two-fluid model arise from the closure of those terms such as the stresses $(\tilde{\boldsymbol{\tau}}_k + \tilde{\boldsymbol{\sigma}}_k)$, the pressure differences $p_k - p_{k,i}$, and interfacial force \mathbf{M}_k^d . This requires constitutive equations for these terms. The closure for $(\tilde{\boldsymbol{\tau}}_k + \tilde{\boldsymbol{\sigma}}_k)$ is discussed in section 4.3.

4.2.1 Pressure relations

The simplest assumption for the pressure differences is to assume that there are none! That is, assume $p_k = p_{k,i}$ for $k=1,2$. For the case where the speed of sound in each phase is large compared with the velocities of interest, there is an instantaneous microscopic pressure equilibration. In applications that are not concerned with acoustic effects or bubble expansion/contraction, this assumption can be considered to be adequate (e.g. Drew 1983).

In situations where surface tension is important and no contact occurs between the bubbles, proper averaging of the jump condition gives $p_{1,i} - p_{2,i} = \sigma \kappa$. Here κ is the exact curvature of the interface. When contact between the particles is taken into account, the situation becomes complicated since contact may cause the average pressure at the interface in one phase to be higher than at the other (e.g. Drew 1983). However, under normal circumstances, the contact areas are usually a small fraction of the total interfacial area, and the approximation $p_{1,i} \approx p_{2,i} = p_i$ is adopted (Drew 1983).

4.2.2 Interfacial force closure

The interfacial momentum transfer M_k^d contains the forces on both phases due to viscous drag, wake and boundary layer formation plus added mass effects due to (pressure gradient) acceleration and lift due to vorticity. The closure models for these forces are key issues in two-fluid models. In the case of low disperse phase fraction, the interaction between the particles is usually assumed to be slight. The momentum interfacial transfer terms in the basic equations (17) can be derived by averaging the local balance of forces acting on an isolated particle or bubble (e.g. Maxey & Riley 1983; Thomas *et al.* 1983). If the surface tension is neglected, then the interfacial jump condition reduces to $M_G = -M_L$ (e.g. two phases are gas and liquid). Here subscript G and L denote respectively gas phase and liquid phase. Thus we only need to find constitutive relations for M_L . It has now been generally accepted that the essential contributions to the interfacial transfer terms derive from the added mass force, drag force, lift force and the averaged interfacial pressure term (e.g. Drew and Lahey 1982) are customarily expressed as

$$M_L^d = M_L^D + M_L^{vm} + M_L^L + M_L^P \quad (20)$$

Of all these, the drag force has been most heavily investigated and is usually written as:

$$M_L^D = \frac{3}{4} C_D \frac{\rho_L}{d_p} \alpha_G |\mathbf{u}_G - \mathbf{u}_L| (\mathbf{u}_G - \mathbf{u}_L) \quad (21)$$

The added mass force is expressed as:

$$M_L^{vm} = C_m \alpha_G \rho_L \left(\frac{d\mathbf{u}_G}{dt} - \frac{D\mathbf{u}_L}{Dt} \right) \quad (22)$$

The lift force, as suggested by Auton (1988) and Thomas et al. (1983), can be written as

$$M_L^L = C_L \alpha_G \rho_L (\mathbf{u}_G - \mathbf{u}_L) \times \nabla \times \mathbf{u}_L \quad (23)$$

Both the turbulence and the relative velocity affect the instantaneous pressure at the interface and can be expressed as:

$$M_L^P = -p_{Li} \nabla \alpha_L \quad (24)$$

The above model technique has been used for the derivation of an Eulerian formulation for particle and bubble dispersion in turbulent two-phase flows (e.g. Simonin & Viollet 1987), and used heavily for the prediction of void fraction distribution in bubbly pipe flows (e.g. Drew & Lahey 1982; Lopez de Bertodano *et al.* 1990; Lopez de Bertodano *et al.* 1994).

4.3 Turbulence Closure

Neglecting viscous stresses, the stress tensor for phase k can be written as

$$\tilde{\boldsymbol{\tau}}_k + \tilde{\boldsymbol{\sigma}}_k = -\tilde{p}_k \mathbf{I} - \rho_k \overline{\mathbf{u}_k' \mathbf{u}_k'} \quad (25)$$

The second term of equation (25) is the Reynolds stress tensor. The key issue of closure for stress ($\tilde{\boldsymbol{\tau}}_k + \tilde{\boldsymbol{\sigma}}_k$) is concerned with this tensor (Drew 1983), analogous to the central problem for single-phase turbulent momentum transport (Rodi 1984; Lopez de Bertodano *et al.* 1994).

4.3.1 One-phase flow

Turbulence closure models and their applications for single phase flow have received enormous coverage in the literature (Launder & Spalding 1974; Launder *et al.* 1975; Rodi

1984; Makataos 1986 among others). Boussineq's (1877) eddy-viscosity concept for modelling the turbulence stress $-\rho\overline{u_i u_j}$ is still widely used. In analogy to the viscous stresses in laminar flows, the turbulent stresses are assumed to be proportional to the mean-velocity gradients and this concept can be generally expressed as

$$-\overline{u_i u_j} = \nu_t \left(\frac{\partial U_i}{\partial x_j} + \frac{\partial U_j}{\partial x_i} \right) - \frac{2}{3} k \delta_{ij} \quad (26)$$

where ν_t is the turbulent or eddy viscosity and k denotes the turbulence kinetic energy. The eddy viscosity ν_t is proportional to a velocity scale and a length scale L characterising the turbulent motion. However, turbulence models were developed which do not make use of the eddy viscosity concept, but employ different transport equations for modelling the turbulent stresses. These models are often classified as zero equation, one equation, two equations and more advanced models, such as the Reynolds stress model etc. according to whether or not the models adopt the eddy viscosity concept (Rodi 1984). The simplest models for determining the distribution of ν_t over the flow field relate ν_t directly to the mean-velocity distribution (e.g. the local gradient). These models implicitly assume that the turbulence is dissipated where it is generated, that is, local equilibrium. One typical example of such models is Prandtl's mixing-length model which relates the eddy viscosity to the local mean-velocity gradient and involves an unknown parameter - the mixing length l_m , and is expressed as (assuming the a proportionality constant of unity)

$$\nu_t = l_m^2 \left| \frac{\partial U}{\partial y} \right| \quad (27)$$

The mixing-length hypothesis has been, and still is applied with great success for some relatively simple flows, because l_m can be specified by simple empirical formulae in many situations, for example, free shear layers (Rodi 1984, Markatos 1986). However, when turbulence history effects are significant, such models neglecting turbulence transport are

inadequate. One obvious example is grid turbulence. The turbulence generated by the wakes directly behind the grid is transported downstream by the mean motion, but the mixing length model would yield zero turbulence since ν_t is calculated to be zero.

One-equation models were developed which attempt to account for the transport of turbulent quantities by solving a different transport equation. The model using the eddy-viscosity concept was introduced by Kolmogorov and Prandtl independently and derived exactly from the Navier-Stokes equations (Rodi 1984). The formulation of this kinetic energy transport equation is

$$\frac{\partial k}{\partial t} + U_i \frac{\partial k}{\partial x_i} = - \frac{\partial}{\partial x_i} \left[\overline{u_i \left(\frac{u_j u_j}{2} + \frac{p}{\rho} \right)} \right] - \overline{u_i u_j} \frac{\partial U_i}{\partial x_j} - \beta g_i \overline{u_i \varphi} - \nu \frac{\partial u_i}{\partial x_j} \frac{\partial u_i}{\partial x_j} \quad (28)$$

where the first term LHS is the time rate of change and the second term LHS is the convective transport. The first term RHS is the diffusive transport, the second term RHS is the production of kinetic energy by shear, the third term RHS is the buoyant production of k and the last term RHS is the viscous dissipation ε of turbulent kinetic energy. This equation is of little use as it stands due to the new correlations of fluctuating quantities in the diffusion and dissipation terms. These are cleared up using model assumptions for diffusion flux of k and the dissipation ε , expressed as

$$\overline{u_i \left(\frac{u_j u_j}{2} + \frac{p}{\rho} \right)} = \frac{\nu_t}{\sigma_k} \frac{\partial k}{\partial x_i}, \quad \varepsilon = C_D \frac{k^{3/2}}{L} \quad (29)$$

where σ_k is eddy Schmidt number and C_D is empirical constant. It should be note that this form of the k equation is for high Reynolds number flows and is not applicable to the viscous sublayer near walls. When the rate of change, diffusive and convective terms of the equation are negligible, production and dissipation are equal and a local equilibrium of k is

obtained, and a mixing length model can be retrieved.

The length scale L characterising the size of the large, energy-containing eddies is subject to transport processes in a similar manner to the kinetic energy k . The difficulties in finding widely valid formulae for prescribing or calculating L result in the use of such a length scale transport equation. The models using both the k equation and the length equation are two-equation models. Among two-equation models, the k - ε model is widely used and it is written as

$$v_t = c_\mu \frac{k^2}{\varepsilon}, \quad \Gamma = \frac{v_t}{\sigma_t} \quad (30)$$

$$\frac{\partial k}{\partial t} + U_i \frac{\partial k}{\partial x_i} = \frac{\partial}{\partial x_i} \left(\frac{v_t}{\sigma_k} \frac{\partial k}{\partial x_i} \right) + v_t \left(\frac{\partial U_i}{\partial x_j} + \frac{\partial U_j}{\partial x_i} \right) \frac{\partial U_i}{\partial x_j} + \beta g_i \frac{v_t}{\sigma_t} \frac{\partial \varphi}{\partial x_i} - \varepsilon \quad (31)$$

$$\frac{\partial \varepsilon}{\partial t} + U_i \frac{\partial \varepsilon}{\partial x_i} = \frac{\partial}{\partial x_i} \left(\frac{v_t}{\sigma_\varepsilon} \frac{\partial \varepsilon}{\partial x_i} \right) + c_{1\varepsilon} \frac{\varepsilon}{k} (P + G) (1 + C_{3\varepsilon} R_f) - c_{2\varepsilon} \frac{\varepsilon^2}{k} \quad (32)$$

The ε -equation (32) contains the empirical constants σ_ε , $c_{1\varepsilon}$, and $c_{2\varepsilon}$ and in buoyant situations also $c_{3\varepsilon}$. The buoyancy correction involves the flux Richardson number R_f . The k - ε model has been applied successfully to many flow situations, as summarised by Rodi (1984) and Markatos (1986). However, the k - ε model either neglects the transport of the individual turbulence stresses or accounts for them in rather approximative manner since it still adopts the eddy-viscosity concept. Although more advanced turbulence models such as Reynolds stress equation (Launder 1975) can theoretically handle the problem mentioned above, they still introduce more or less artefact model assumptions and they are very difficult to be verified through the experiments.

Large-eddy simulation (LES) involves the integration of the NS equations in time using an

appropriate finite difference or spectral representation, and therefore free from the closure difficulty. The technique of full simulation is very expensive on computer time. Once turbulence is fully developed, the range of eddy size is too great to be represented on any computer now available. The remedy is to represent the large eddies only and to account for their interaction with the small or subgrid eddies by means of a subgrid model. However, this reintroduces 'closure', but is more realistic and universal than the transport closure models.

4.3.2 Two-phase flow

In two-phase flows, the flow structure is modified by the presence of a dispersed phase (figure 15), and direct application of one-phase flow turbulence closure models to two-phase flow would not give satisfactory results. In calculation, it requires adaption of the one-phase turbulence models, as reported, for example, by Elghobashi & Abou-Arab (1983), Besnard & Harlow (1988), Kataoka & Serizawa (1989) among others. The approach for modelling turbulence usually follows one-phase eddy viscosity formulation (e.g. Elghobashi & Abou-Arab 1983; Elghobashi *et al.* 1984; Mostafa & Mongia 1987; Rizk & Elghobashi 1989; Simonin 1991 among many others) according to which

$$\overline{\rho_k u_{k,j} u_{k,i}} = -\rho_k \nu_k' \left[\frac{\partial U_{k,i}}{\partial x_j} + \frac{\partial U_{k,j}}{\partial x_i} \right] + \frac{2}{3} \left[\frac{1}{2} \overline{\rho_k u_m u_m} + \rho_k \nu_k' \frac{\partial U_{k,m}}{\partial x_m} \right] \quad (33)$$

Here the turbulent viscosity ν_k' is written as the product of the turbulent kinetic energy and a characteristic time scale (e.g. Viollet & Simonin 1994), an approach that is almost universally used to model one-phase turbulence. Here it is extended to model the dispersed phase turbulence as well. However, the fluctuation of the dispersed phase is highly anisotropic, and a more sophisticated treatment of the Reynolds stresses of the dispersed phase may be necessary, as indicated by Simonin (1991). Then the transport equations

allowing computation of the turbulent kinetic energy K and the dissipation rate ε are modelled as one-phase turbulence (Launder & Spalding 1974), with an additional source term, as reported by Elghobashi & Abou-Arab (1983). They developed a two-equation two-phase k - ε model in which the averaged momentum equations were closed by modelling the turbulent correlations to third order, and claimed to have eliminated the need to simulate in an *ad hoc* manner the effects of dispersed phase on turbulence structure. The 38 terms in their equation set for the turbulent kinetic energy and the 67 terms for the turbulent kinetic energy dissipation rate were each modelled independently and all above third order terms were ignored. They adopted the same set of coefficients as for k - ε in single phase flows. Another three new coefficients ($C_{\varepsilon 3}$, $C_{\phi 5}$, σ_{ϕ}) were optimized by Elghobashi *et al.* (1984), who used the model to "predict" the behaviour of a turbulent axisymmetric gas jet conveying solid particles of uniform size. They found good agreement with the experimental data, as shown in figure 16.

Besnard & Harlow (1988) described a two-fluid-field turbulent flow model designed to assess mixing quality between the phases. They addressed solid particle dispersion in incompressible flow for the case where the volume fraction of the dispersed phase was small enough to reasonably assume no interaction between the particles, i.e. such that the turbulence scale was much larger than both the dispersed phase particle size and the inter-particle distance. They introduced a coupling function between the two fields, K , such that

$$K = C_D \alpha_p \alpha_L \rho_L |U_L - U_p| = \alpha_p \alpha_L C \quad (34)$$

The coupling coefficient C was assigned according to how high Reynolds numbers were associated with particle drag. However, no comparison with experimental data was conducted. Also, the real fluid-particle interactions due to the shear-induced lift and added

mass terms have been excluded in the model derivation.

For two-phase bubbly flows, Kataoka & Serizawa (1989) derived the conservation equations for turbulent energy and turbulent dissipation based on the local instant and averaged formulations. The interfacial transport terms appeared in the equations, but the closure modelling for these terms was not reported. They adopted eddy viscosity, μ_t , as turbulence closure, noting that in two-phase flows there are two mixing lengths, one related to the size of the eddy, and the other related to the size of the discrete phase. Both length scales were considered to be strongly related to turbulent energy and dissipation rate, but they cautioned against simply using the same turbulent viscosity as for one-phase flow. For low void fraction dilute bubbly flow, the experimental data of Lance and Bataille (1991) (see figure 17) shows that the linear superposition of grid generated shear-induced (SI) turbulence and bubble-induced (BI) turbulence is appropriate:

$$k_t = k_{SI} + k_{BI} \quad (35)$$

Theofanous (1982) made the same observation for turbulence on the centerline of a vertical pipe, for up to 10% void fraction. The bubble-induced turbulence is primarily composed of the irrotational motion (i.e., pseudo-turbulence due to liquid displacement by the bubbles) and some rotational contribution due to the bubble wakes. As with the turbulent kinetic energy, the Reynolds stresses tensor for carrier fluid is assumed to be linearly superposable where written as (Sato *et al.* 1981):

$$\tau_L = \tau_t + \tau_b \quad (36)$$

where τ_L is total shear stress in the flow, τ_t is the shear stress due to the shear turbulence of the carrier fluid and τ_b the shear stress due to the bubble perturbation. This simple model, though naive, has been adopted in many calculations (e.g. Lopez de Bertodano *et al.* 1994;

Yang & Thomas 1992).

4.3.3 Examples of application of turbulence closure models

Applications of the two-fluid model together with the turbulence closure models mentioned have been widely used to solve various problems. As examples, we mention standard benchmark comparisons between numerical predictions and velocimetry measurements in two-phase turbulent jets and in plane mixing layers (figure 18), the proceedings of the Erlangen workshops (ed. by M. Sommerfeld 1990, 1992). For particle dispersion in a plane mixing layer, figures 19 and 20 show similar comparisons reported by Ishima *et al.* (1993). As an example for bubbly flows, the predicted velocities, void fraction profiles and turbulence properties are compared with measurements in circular pipe upward or downward bubbly flow (Serizawa *et al.* 1975; Wang *et al.* 1987), and in a triangular duct using a two-fluid model together with a modified $K-\varepsilon$ model (Lopez de Bertodano *et al.* 1994) (figure 18). In their $k-\varepsilon$ model, Lopez de Bertodano *et al.* (1994) assumed that shear turbulence and bubble turbulence may be linearly superposed. The model was assigned to match the decay of homogeneous two-phase turbulence (Lance & Bataille 1991) and pipe data (Serizawa *et al.* 1975). Their simulation results using the model were shown to agree with data trends, as can be seen in figure 21, even to the extent of reproducing turbulence suppression measured in high Reynolds number bubbly air/water flows in pipes. However, because these modelling approaches are usually based on *ad hoc* modification of single-phase turbulent kinetic energy equations, or on the local instant formulation of two-phase flow and its averaging, the use of a two-fluid model, together with the turbulence closure equations, is often unsatisfactory to predict the physical behaviour of two-phase flows, especially for turbulence properties (e.g. Lopez de Bertodano 1994) seen in figure 22. Indeed, most often

the turbulence closure models for single phase flow are still adopted with either no or only minimal modifications, for example, by modifying the parameter C_μ and the effective Prandtl number σ_k (e.g. Lahey 1989). In applications to two-phase flow, the effect of two-way coupling, via dynamical feedback for the dispersed phase on turbulence structure has recently been considered (e.g. Viollet & Simonin 1994).

4.4 Passive Scalar Transport By Turbulence

By analogy with turbulent transport of momentum, scalar transport (viz. temperature, mass, concentration) is represented in terms of a (simple gradient transport) coefficient as follows:

$$\overline{u_i \phi} = -D_\phi \frac{\partial \Phi}{\partial x_i} \quad (37)$$

where Φ is the local average value of the scalar quantity, ϕ is its turbulent fluctuation and D_ϕ denotes turbulent diffusivity. It is generally accepted that homogeneous turbulent transport can be indeed modelled as gradient (Fickian) transport, providing the diffusion time is large compared with an integral time scale of the turbulence (Hinze 1975; Hunt 1985). There seems to be less unanimity as regards inhomogeneous turbulence. Indeed, Corrsin (1974) indicated that generalisation to a diffusivity tensor, as commonly advocated, does not necessarily represent a suitable generalisation. A number of authors, most recently Sreenivasan *et al.* (1981), presented detailed comparisons of various transport models, in which the gradient term was extended to represent turbulent convection not accounted by the mean Eulerian transport velocity (Lumley 1975). Other extensions (e.g. Kronenburg 1977) proposed an expression in which an extra term proportional to spatial change of the mean concentration was introduced with the gradient and turbulent convection terms, hereby accounting for observed negative diffusivity in inhomogeneous flows. Thus, the turbulent

flux of any scalar can be written as follows:

$$-\overline{u_i \phi} = D_\phi \frac{\partial \Phi}{\partial x_i} + l_i \frac{\partial}{\partial x_i} \left(D_\phi \frac{\partial \Gamma}{\partial x_j} \right) \quad (38)$$

where l_i is integral length scale. However, evaluations by Sreenivasan *et al.* (1981) indicated that the simple gradient transport model is often perfectly adequate, with a constant diffusivity assigned for homogeneous flows, although they also concluded that it cannot handle inhomogeneous flows, sometimes even being qualitatively in error. Indeed, few available generalisations of the gradient diffusion model have had reliable success in evaluating the turbulent transport in inhomogeneous flows.

The assumptions of gradient diffusion models are clearly invalid for two-phase flows in which the dispersed transport is dominated by body forces-induced by coherent structures, for example. On the other hand, it seems that they may be adequate for concentration distributions in free shear layers (e.g. Goldschmidt & Eskinazi 1966; Sene *et al.* 1994), at least so long as a suitable dispersion coefficient can be assigned. Indeed, this is always the main difficulty in using such models, not surprising seeing as the body forces is expressed by a discrete phase scale on the mass density whose ratio ρ_p/ρ_f ranges from 10^3 to 10^{-3} . In reality, then, the response of a particle to the carrier flow is controlled by not only fine structure within the flow but also external forces and any significant surface force. Whilst particle diffusion is necessarily different from passive scalar diffusion, the correlation $\overline{u_i \phi}$ still has its meaning as flux even for the transport of discrete particles, so long as the time averaging is done such that the scalar phase can be statistically assigned as it would be for a continuum (Batchelor 1966). Attempts at generalized formulation for the turbulent viscosity, ν_t , have not really succeeded in removing uncertainty as to the effective dispersion

coefficient, ε_T , parameterised in terms of the flow field (e.g. Elghobashi & Abou-Arab 1983). In two phase flows, ε_T is approximated by analogy with the turbulent kinematic viscosity, ν_t , the latter expressed via turbulence closure modelling, in terms of typical turbulence length and velocity scales. The turbulent scalar flux coefficient is then usually assigned via the ratio $\nu_t/\varepsilon_T=S_c$, where S_c is an empirical turbulent Schmidt number (e.g. Launder & Spalding 1972). Engineering approximations usually state that $S_c=1$. Whilst this assumption is strictly inconsistent with the measurements and analysis of two-phase flow with discrete phase slip (e.g. Chao 1964; Yuu *et al.* 1978; Peskin 1971), there are often situations where it may suffice to assign a fixed eddy Schmidt number, as demonstrated by Sene (1985) for bubbles in high speed shear layers. Indeed, Reeks (1981) pointed out that in the absence of a general transport equation it is reasonable to assume on the basis of experimental evidence, for both passive scalar and heavy particle motion in such turbulence, that a Fickian law is a suitable approximation irrespective of particle inertia, in which case the particle dispersion coefficient D_p uniquely determines the temporal evolution of the particle concentration. He showed that the long term particle dispersion coefficient exceeds that of the fluid (Reeks 1977), a result differing significantly from the classical work by Tchen (1947), and also Peskin (1971) where the long term particle dispersion coefficient was either the same or less than that of the fluid. The reason underlying this trend derives from the fact that the particle dispersion is proportional to the product of the RMS particle velocity fluctuations and the particle Lagrangian integral time scale. Although the particle fluctuation velocity of the heavier particle is reduced, the Lagrangian time scale is increased in greater proportion, thereby giving rise to an increased diffusion. The simultaneous effects of finite particle inertia and crossing trajectory effect due to slip have been estimated by Lumley (1978), Nir & Pismen (1979) and Wells & Stocks (1983), all of whom found that

the inertia has only slight effect on D_ϕ although crossing trajectory reduces D_ϕ by a large direction invariant factor:

$$D_{px} = D_f \left(1 + \frac{4V_T^2}{9u'^2}\right)^{-1} \quad (39)$$

$$D_{py} = D_f \left(1 + \frac{16V_T^2}{9u'^2}\right)^{-1} \quad (40)$$

where V_T is the particle slip velocity and u' is isotropic velocity scale.. For bubble dispersion in a free shear layer, Sene *et al.* (1994) indicated that an effective Schmidt number of about unity, significantly larger than for passive scalar transport (i.e. indicating bubble confinement within the shear layer), adequately reproduces experimental measured spread rate behaviour of the bubble layer, as seen in the results of Sene (1985); see figure 23.

In sum then, all these works concentrated on finding a suitable dispersion coefficient so as to close equation (10), a model of the dispersion. In reality, however, the dispersion coefficient is a function of the elapsed time t (i.e. $D_\phi = f(t)$), and is not simply a function of the local flow properties - a convenient assumption, but one which is often incorrect according to Hunt (1985) who recalled the origins of this in G. I. Taylor's (1921) theory of diffusion by continuum motions, also as recounted in Snyder and Lumley (1971). Taylor (1921) showed that for a stationary process in a homogeneous turbulence, the long-time particle diffusion coefficient may be expressed as

$$D_{pi}(t) = \frac{1}{2} \frac{d}{dt} \overline{X_i^2(t)} \quad (41)$$

where $\overline{X_i^2}$ is the mean squared displacement of the particles. In order to model D_ϕ , the prerequisite is to properly find the growth of $\overline{X_i^2}$ (Hunt 1985).

4.5 Bubble and Particle Dispersion in Free Shear Flows

It has long been recognised that free shear flows are often best characterized in terms of large-scale coherent structures, as first reported in detail by Brown and Roshko (1974) in their experimental study of mixing layers. Their pictures (see figure 24) showed that a turbulent mixing layer can often consist of a succession of quasi-two dimensional large eddies (coherent structures), connected by braids of turbulent fluid that contain small scale, three dimensional turbulence. Subsequent experimental studies by Hussain (1983) and Tang *et al.* (1992) confirmed these braid pattern behaviour, including in other types of turbulent shear flows, such as jets and wakes, as shown in figure 25 (Crowe *et al.* 1993). On the other hand, it must be admitted that the prevalence of these features has not been universally accepted - viz. (Pui & Gartshore 1979). Nevertheless, there is now sufficient evidence to believe that such large eddy structure is frequently formed, such as described in many early works (e.g. Townsend 1976) and more recently reassured by Hussain (1986). Their origins reside in Kelvin-Helmoltz (KH) instability associated with strong shear between parallel flows at different velocities. As reported in Brown and Roshko (1974), the KH waves grow and roll up to produce vortices which are convected downstream and pair to yield larger eddies. This process is shown in figure 26. This pairing and growth mechanism is responsible for property transfer in turbulent free shear flows.

When such large scale vortex features are present, the motions of particles and bubbles can be largely dictated by the local and unsteady flows, and the pressure gradients that they induce as seen in experiments on particle dispersion in a mixing layer (Wen *et al.* 1992) and observations of the motions of bubbles in air-entraining flows (Thomas *et al.* 1983). Figures 27 and 28 clearly demonstrate this essential point, and provide specific evidence that the

particle and bubble transport should not be simply represented as Fickian diffusion. Although the small-scale, local turbulence may produce a local diffusion (Sene *et al.* 1994), the primary dispersion is dominated by the large-scale turbulent vortex structures.

A conceptual model (figure 29) for particle dispersion in large-scale structures which describes the entrapment of particles by rotational fluid motion, and their subsequent centrifugation was proposed by Crowe *et al.* (1985), following the earlier ideas on bubble entrainment as reported in Thomas *et al.* (1983), and later summarised and extended in Hunt *et al.* (1988). Crowe's *et al.* model describes how small particles essentially travel with the flow, and thus disperse with the fluid, whilst larger particles are entrapped by the eddies and subsequently centrifuged so as to attain a larger long term dispersion than the fluid. Bigger particles still do not significantly respond to these fluctuating flows associated with the shear layer eddies and their trajectories are hardly affected. In contrast, bubbles are monotonically entrapped by the large eddies and travel in clusters inside the these large eddies. To quantify these interaction scales for particles, Crowe *et al.* (1985) adopted the Stokes number, defined as $S_i = \tau_p / \tau_f = \rho_p d^2 \Delta U / 18 \mu \delta$. Here τ_p and τ_f are respectively the particle aerodynamic response time and the measure of the Lagrangian time scale of vortex structures. For bubbles, there are two key dimensionless groups which represent, respectively, the ratio of inertial to buoyancy forces $\Pi = \Delta U^2 / g \delta$ and a trapping parameter $\Gamma = \Delta U / V_T$, as suggested in Thomas *et al.* (1983) and further evaluated in Hunt *et al.* (1988); Sene *et al.* (1994). Evaluation of particle dispersion within this framework has been reported by Crowe *et al.* (1985), Chung & Troutt (1988), Wen *et al.* 1992; Lazaro & Lasheras (1989) and Martin & Meiburg (1994), these studies showing the tendency of particles to achieve a maximum spread for a Stokes number of the order of unity as seen in figure 30 and figure 31 for particle dispersion in an

axisymmetric jet and in a mixing layer respectively.

The majority of numerical models for particle dispersion in large scale structures have been based on the use of the discrete vortex method (Crowe *et al.* 1993). As we will address in the next section, the discrete vortex method can characterise rather well the mean flow and turbulent stress profiles in free shear flows. Chein and Chung (1988) used a vortex pair to represent the starting flow of a jet in conjunction with a force law for particle motion to retrieve the particle trajectories in this unsteady, rotational flow. They showed that solid particles disperse more than fluid elements for Stokes number of the order of unity. They used essentially the same approach to calculate particle trajectories in a developing shear layer, and again obtained similar conclusions. They also observed how particles tend to accumulate around the edges of the vortices, as seen in visualisation experiments (e.g. Wen *et al.* 1992)(recall figure 27). Chung and Troutt (1988) also demonstrate that axisymmetric jet flow follows similar trends and they showed how detailed understanding of the dynamics of particle dispersion can be gained by tracking the motions of individual particles prior to statistical averaging. Thomas *et al.* (1983) earlier applied a generalised force law to Lagrangian tracking of bubbles in simulation of planar mixing layers and in Rankine vortices (figure 32, taken from Thomas *et al.* 1983). More elegant analytical work has been reported in Sene *et al.* (1994), describing trajectories of individual bubble within the vortex, showing how they converge to a stable equilibrium, but in reality are distributed around this point by fine-scale turbulence (figure 33). The same route was also followed by Ganán-Calvo and Lasheras (1991) and Tio *et al.* (1993), who utilised generalised methods of nonlinear dynamical systems analysis in studying the behaviour of particles in a row of Stuart vortices (see figure 34), defined by

$$\psi = \frac{\lambda U_{\infty}}{2\pi} \ln \left[\cosh \left(\frac{2\pi y}{\lambda} \right) - k \cos \left(\frac{2\pi x}{\lambda} \right) \right] \quad (42)$$

where ψ is the stream function, λ is the distance between two contiguous vortices and U_{∞} is the free-stream velocity. The constant k is a parameter that determines the distribution of vorticity. They observed that if gravity force is of moderate importance, the particle can be suspended above the mixing layer and the particle trajectories can be periodic, quasiperiodic, or even chaotic. If gravity is stronger, the particles sediment (figure 35). A more detailed understanding of the important mechanisms of particle dispersion in free shear flows was given by Martin and Meiburg (1994) and by Raju and Meiburg (1995), who found that the braid region between the adjoining vortices tends to accumulate particles, as shown in figure 36. A excellent review on these aspects can be found in Eaton & Fessler (1994).

Numerical simulation of the dispersion of particles and bubbles in the vortex wake of bluff bodies has received far less attention, not least because of the difficulty in representing the unsteady instantaneous vortex shedding patterns in the near wake region. Laitone (1981) used a discrete vortex method to modelling the wake patterns of particles behind a circular cylinder. Whilst the particles were shown to generally interact with the large eddies and to be later centrifuged from them, he failed to correlate the findings in terms of a control parameter like the Stokes number. Chein and Chung (1988) also employed a discrete vortex method to simulate particle impact on a normal plate and an inclined plate. They found that particles with Stokes number less than 0.5 are captured in the vortex structure behind the plate, but for larger particles, the trajectories were not particularly influenced by the large eddies; see figure 37. These simulations are limited in that only the drag terms in the equation of motion used to calculate particle trajectories were considered. These simulations highlight the effect of a vortex or disturbance on the particle dispersion to be qualified by

the Stokes number, S_t (Crowe *et al.* 1985). However, for particles with the same order of density as the carrier fluid (Onslow *et al.* 1993), the use of the Stokes number is inadequate to describe the particle dispersion since the effect of the added mass force on the particle motion increases considerably. In that case, it would be appropriate to use a relaxation parameter Π , the ratio of inertial to buoyancy forces, and a trapping parameter Γ , as will be demonstrated throughout this thesis.

The discrete vortex method was first applied to bubbly flow by Thomas *et al.* (1983) to simulate bubble entrapment by the large eddies, and further refined by Sene *et al.* (1994) and Yang & Thomas (1994). This work, which uses a general Lagrangian force law (recall section 3), is summarised by Hunt *et al.* (1988), Hunt *et al.* (1993) and Thomas (1994). The simulations showed vortices trapped by large eddies and remaining trapped downstream. They demonstrated that inertial forces inside the vortices can be considerably larger than the bubble buoyancy force, so that a time-averaged model would give incorrect results, as these transient forces would be averaged out. Therefore, they concluded that these dynamical forces play a crucial role in controlling bubble dispersion in such flows. Bayly and Rielly (1994) also used a discrete vortex method to simulate cylinder wake flow and they calculated the bubble trajectories using the generalised force law reported in Thomas *et al.* (1983) and Auton *et al.* (1988). The computed bubble streaklines were qualitatively consistent with experimental observations (figure 38). Indeed, despite the outcome of conceiving vortex structures in their simulated flow field, to secure a smooth convective derivative $D\mathbf{u}/Dt$ (needed to evaluate the added mass force term) they introduced a vortex "blob" with cut-off radius of $0.2R$ (R denotes radius of the cylinder in simulation). We regard this device as an unacceptably crude idealisation.

5 OVERVIEW OF SIMULATION STRATEGIES

Numerical methods for two-phase shear flows can be categorised into two general groups, time-averaged models and time-dependent (including direct numerical simulation; DNS) models. There are also two ways of calculating the dispersed phase variables: Lagrangian tracking or Eulerian two-fluid methods.

5.1 Eulerian Two-Fluid (Pseudo-Continua) Approaches

The modelling approach here regards not only the carrier fluid but also the dispersed phase as statistical continua. As there are two 'fluids' present, the definition of a volume concentration of each phase, the so-called void fraction, is necessary and it is not possible to resolve every point in time or space, but is rather necessary to average over a specific time and space. This modelling technique have been extensively used in two-phase flow prediction. Cook & Harlow (1986) studied vortex shedding behind a rectangular cylinder in bubbly two-phase flow by using this approach. The time-dependent Navier-Stokes equation for each phase is solved. The equations for the two phases are coupled by a local pressure gradient, added mass and momentum exchange terms. Their predictions of vortex trapping of bubbles are consistent with the experimental observations (Hulin *et al.* 1982). Viollet and Simonin (1994) also reviewed their work on closure for the Eulerian modelling of two-phase flows. They modeled the disperse phase turbulence using eddy viscosity and extension of the Tchen's (1947) theory accounting for crossing trajectory effect, and have validated the closure model using large-eddy simulation and comparing numerical predictions with laser doppler velocimeter measurements in two phase turbulent jets and with the measurements of a turbulent bubbly flow downstream a sudden expansion (F'dhila 1992). However, this

approach has distinct shortcomings. Because it smears the discrete phase over the control volume or computational cell, the real flow picture of the discrete phase cannot be addressed correctly. Figure 39 shows such an example. This shortcoming becomes serious when it is applied to simulation of two-phase transport in free shear flows since the discrete phase transport is very sensitive to the local flow features. To achieve high resolution, a finer grid is required, and this is prohibited at present by available computer speed.

5.2 Eulerian-Lagrangian Approaches

A more promising approach is the mixed Eulerian-Lagrangian modelling technique. Most of these models involve the calculation of the continuous phase time-averaged flow field using a grid based method, such as a finite volume or a finite element technique. The earliest models (Crowe 1982) assumed that the velocities of the dispersed phase were coincident with the flow field velocity. Later approaches (e.g. Berlemont *et al.* 1990) calculated discrete trajectories by integrating their equation of motion in a Lagrangian manner. These methods have been reviewed in detail by Faeth (1987). Most of such models were deficient for quantitative prediction of the structure of dispersed phase flows, but an improved approach - the 'stochastic separate flow' approach - allows for particle turbulent eddy interaction and has shown more promising results when used in conjunction with the modified equation of motion for modelling bubbly jets (Sun & Faeth 1986). This Monte-Carlo type method allows the particles to interact with eddies which have statistically independent properties, but are uniform within each eddy and change in a random manner from eddy to eddy. Eddy properties are usually obtained from a time-averaged continuous phase model, for which k - ϵ formulation is widely adopted. The coupling between dispersed and continuous phases can be included as a source term in momentum equations (Crowe 1982). The main deficit of

time-averaged models is that they still cannot properly address instantaneous features of the large eddy structures in free shear flows, since the transient flow features have been averaged out. This lost transient information is still not compensated for by introducing a random diffusion process.

5.3 Lagrangian-Lagrangian Approaches

In Lagrangian modelling approaches, both the flow field and the dispersed phase transport are calculated using time-dependent models. The key feature of this approach is that it addresses a physical description of the dispersed phase transport in free shear flows subject to the use of a correct force law for the particles or bubbles. To model the dispersive transport, a large number of particles/droplets/bubbles are introduced into the flow field from specific source points and their individual trajectories are then numerically tracked by the integration of the generalised force law. The statistical information on the dispersion characteristics may be drawn from the trajectory realisations and their instantaneous velocities. Lagrangian-Lagrangian approaches for predicting dispersive transport and their applications were usually limited by the following conditions: (1) The flow field is two-dimensional and dominated by large-scale vortex structure as mentioned before; (2) The dispersed phase is composed of monodispersed, spherical particles/droplets/bubbles with uniform density; (3) The dispersive transport is assumed to be controlled exclusively by the large structures rather by small-scale turbulence and (4) The two-phase flow is considered to be 'dilute' so any particle-particle or particle-fluid interaction is precluded based on low particle concentration assumptions (Hunt *et al.* 1988).

To model time-dependent flow field of free shear flows, the most widely used method for

simulating the flow field is the discrete vortex method, as reviewed by Leonard (1980) and more recently by Sarpkaya (1989). This method simulates the shear flow field using an array of point vortices which move under their own influence, and has been successfully applied to various shear flows such as plane mixing layers (Ashurst 1979; Inoue 1985); flow around a cylinder (Sarpkaya & Schoaff 1979; Stansby & Slaouti 1993). The important feature of this method is that it mimics the evolving eddy structures of free shear layers, which can be seen from the example shown in figure 40. Most studies of dispersive transport in free shear flows using this method were focused on particle-laden shear flows, as reviewed in previous sections. This is perhaps due to due to a simplification in which only the drag force becomes dominant in comparison with the other forces for small particles in gas flows. The disadvantage of this method is that it is difficult to apply to those flow fields with complicated geometry, and indeed its applications are still confined to simple shear flows.

Another very promising method for modelling time-dependent flow field is the spectral method. Spectral methods have been a standard tool for linear separable differential equations. Their applications to strongly nonlinear Navier-Stokes equation have been assisted by the development of the Fast Fourier Transform (FFT) in the early 1970s. Since that time, spectral methods have undergone further refinement and show promise for modelling turbulent flows, as reviewed by Zang and Hussaini (1985). The spectral method has found limited use in modelling particle dispersion in large-scale turbulent structures. Gore *et al.* (1989) used the pseudo-spectral method developed by Riley and Metcalfe (1980) to generate a flow field of vortex pairing and predict particle dispersion in such flow field. Squires and Eaton (1990) also applied the pseudo-spectral method to predict the effects of particles on turbulence in homogeneous turbulence. Even though spectral methods are especially useful

to include three dimensional effects, their use imposes a heavy computation demand.

Other methods to calculate time-dependent flow fields, such as using finite difference methods (e.g. Elgobashi 1991, Eaton 1994) have been also used. These studies have allowed direct numerical simulations of microscopic turbulence to be modelled and the discrete phase dispersion within three dimensional flow fields studied. Elgobashi (1991) suggested that these studies could lead to the development of closure models for particle-laden flows which could then be used in time-averaged models for more complex geometries. There remains much work to be done to reach this goal.

6 RECAPITULATION AND IMPLICATIONS

We began this chapter with an outline discussion on the modelling and numerical simulation technique adopted in two-phase flows, as well as a broader perspective of their options and limitations. The most crucial conclusion to be drawn from this review is that numerical models employed for two-phase flows at present have many serious limitations. Numerical prediction of particle and bubbly two-phase flows using two-fluid closure models with an Eulerian approach for both phases is strongly affected by the closure assumptions. Such a prediction using an Eulerian approach to model the fluid flow and a Lagrangian approach for the discrete phase transport is influenced by both the flow closure modelling and the assumption of effective Lagrangian scales. Full adoption of Lagrangian approach (for example, the discrete vortex method for modelling the flow field and the Lagrangian for particle and bubble tracking) for both phases is also restricted by some *ad hoc* assumptions. The best choice is to select a particular approach according to the problem under study.

Related developments in numerical modelling for two-phase flows have also been discussed, especially concerning the large scale structures responsible for the particle and bubble dispersion in turbulent free shear flows. The broad distinction is between fundamental diagnostics and applicable guidelines. The former modelling approach is manifested by using doubly Lagrangian formulations which can adequately capture eddy structural features and events, and their transient influence on the discrete phase transport. The latter typically involves using Eulerian modelling for both the Reynolds averaged flow and transport equations, thus excluding both the structure features and the statistical coupling between transient voidage and vorticity. Mixed Lagrangian-Eulerian modelling based on the Eulerian averaged equations for mean flow superimposed with a pseudo-Lagrangian fluctuations, usually rendered by Gaussian jitter, and Lagrangian calculations for the discrete phase also fails because the features of the coherence of shear-turbulent eddies still are not captured. Hence, the adoption of fully Lagrangian approaches is the key step to capturing essentials of particle-turbulence interactions in such a flow.

Current status of the development of CFD software is also reviewed. Most adopts an Eulerian approach with the turbulence closure models. Even though they can supply a diagnosis to engineering applications, they are not helpful in the understanding of physical phenomena involved with two-phase flows. The numerical modelling of two-phase flows remains as a significant challenge to the CFD community.

It is clear from the foregoing review that the accurate prediction of two phase flow relies on adequate representations of flow phenomena, and on the suitable numerical modelling of the physical processes. Our concern here is with the second aspect, in particular

concentrating on the numerical simulation of the dispersed phase transport in turbulent free shear flows. Chapter 2 will address one of the fundamental aspects in two-phase flow - void fraction distribution in bubbly upward and downward flows. From chapter 3 to chapter 6, the dispersed phase transport dynamics and the central role played by large scale vortex structures in free shear flows are investigated extensively. Chapter 7 contains our main conclusions derived from further understanding of the dispersed phase transport dynamics in shear flows and recommendations for advancing the understanding on this aspect.

REFERENCES

- Auton, T. R. 1987 The lift force on a spherical body in a rotational flow *J. Fluid Mech.* **183**, 199-213.
- Auton, T. R., Hunt, J. C. R. & Prud'homme, M. 1988 The force exerted on a body in inviscid unsteady nonuniform rotational flow. *J. Fluid Mech.* **197**, 241.
- Ashurst, , W. T. 1979 Numerical simulation of turbulent mixing layers via vortex dynamics. *Turbulent Shear Flows I.*, (Eds. F. Durst *et al.*), Springer, 402-413.
- Banerjee, S. & Chan, A. M. C. 1980 Separated flow models-I: Analysis of the averaged and local instantaneous formulations. *Int J. Multiphase Flow* **6**, 1-24.
- Basset, A. B. 1888 A treatise on hydrodynamics. Vol 2, Deighton Bell, Cambridge.
- Batchelor, G. K. 1966 The motion of small particles in turbulent flow, *Proc of the 2nd Australasian Conf on Hydraulics and Fluid Mechanics*, Univ. of Auckland, N.Z.
- Bayly, A. E. & Rielly, C. D. 1994 Bubble dynamics in two-phase flows around cylinders. *Cavitation and Multiphase Flow FED-Vol.* **194**, 29-33.
- Berlemont, A., Desjonqueres, P. & Gouesbet, G. 1990 Particle lagrangian simulation in turbulent flows. *Int. J. Multiphase Flow* **16**, 19-34.
- Besnard, D. C. & Harlow, F. H. 1988 Turbulence in multiphase flow. *Int. J. Multiphase Flow* **14**, 679-699.
- Brown, G. L. & Roshko, A. 1974 On the density effects and large structure in turbulent mixing layers. *J. Fluid Mech.* **64**, 775-816.

- Brunn, H. H. 1995 *Hot-Wire Anemometry: Principles and Signal Analysis*. Oxford University Press.
- Chao, B. T. 1964 Turbulent transport behaviour of a small particles in dilute suspension. *Österreichisches Ingenieur Archiv* **18**, 7-21.
- Chang, E. J. 1992 Accelerated motion of rigid spheres in unsteady flows at low to moderate Reynolds numbers. PhD Thesis, Brown University.
- Chein, R. & Chung, J. N. 1988 Particle dynamics in a gas-particle flow over normal and inclined plates. *Chemical Engng. Science* **43**, 1621-1636.
- Chung, J. N. & Troutt, T. R. 1988 Simulation of particle dispersion in an axisymmetric jet. *J. Fluid Mech.* **186**, 199-222.
- Clift, R., Grace, J. R. & Weber, M. E. 1978 *Bubbles, Drops and Particles*. Academic Press.
- Cook, T. L. & Harlow, F. H. 1986 Vortices in bubbly two-phase flow. *Int. J. Multiphase Flow* **12**, 35-61.
- Corrsin, S. & Lumley, J. L. 1956 On the equation of motion for a particle in turbulent fluid. *Appl. Sci. Res.* **A6**, 114-116.
- Corrsin, S. 1974 Limitations of gradient transport models in random walks and in turbulence. in *Advances in Geophysics*, Vol. **18A** (eds. H. E. Landesberg & J. Van Mieghem), New York: Academic Press, 25-60.
- Crowe, C. T. 1982 Review - Numerical models for dilute gas-particles flows. *J. Fluids Engng.* **104**, 297-303.
- Crowe, C. T., Gore, R. A. & Troutt, T. R. 1985 Particle dispersion by coherent structures in free shear flows. *Particle Science and Tech.* **3**, 149.
- Crowe, C. T., Chung, J. N. & Troutt, T. R. 1993 Particle dispersion by organized turbulent structures. In *Particulate Two-Phase Flows* (Edited by Roco, M. C.), Butterworth-Heinemann, New York.
- Drew, D. A. & Lahey Jr, R. T. 1979 Application of general constitutive principles to the derivation of multidimensional two-phase flow equation. *Int. J. Multiphase Flow* **5**, 234-264.
- Drew, D. A. & Lahey, R. T. 1982 Phase-distribution mechanisms in turbulent low-quality two-phase flow in a circular pipe. *J. Fluid Mech.* **117**, 91-106.
- Drew, D. A. 1983 Mathematical modelling of two-phase flow. *Ann. Rev. Fluid Mech.* **15**, 261-291.

- Drew, D. A. & Lahey Jr, R. T. 1987 The virtual mass and lift force on a sphere in rotating and straining inviscid flow. *Int. J. Multiphase Flow* **13**, 113-121.
- Drew, D. A. & Lahey, R. T. Jr 1990 Some supplemental analysis concerning the virtual mass and lift force on a sphere in a rotating and straining flow. *Int. J. Multiphase Flow* **16**, 1127-1130.
- Eaton, J. K. 1994 Experiments and simulations on turbulence modification by dispersed particles. *Appl. Mech. Rev.* **47**(6), s44-s48.
- Eaton, J. K. & Fessler, J. R. 1994 Preferential concentration of particles by turbulence. *Int. J. Multiphase Flow* **20**, 169-204.
- Elghobashi, S. E. & Abou-arab, T. W. 1983 A two-equation turbulence model for two-phase flows. *Phys. Fluids* **26**(4), 931-938.
- Elghobashi, S., Abou-arab, T., Rizk, M. & Mostafa, A. 1984 Prediction of the particle-laden jet with a two-equation turbulence model. *Int. J. Multiphase Flow* **10**, 697-710.
- Elghobashi, S. 1991 *Appl. Sci. Res.* **48**, 301-314.
- Faeth, G. M. 1987 Mixing, transport and combustion in sprays. *Prog. Energy Comb. Sci.* **13**, 293-346.
- F'dhila, R. B. & Simonin, O. 1992 Eulerian prediction of a turbulent bubbly flow downstream of a sudden pipe expansion. *Proc of 6th International Workshop on Two-phase Flow Prediction*, (ed. M.Sommerfeld) Erlangen, 264-273.
- Ganán-Calvo, A. M. & Lasheras, J. C. 1991 The dynamics and mixing of small spherical particles in a plane, free shear layer. *Phys. Fluids A* **3**, 1207-1217.
- Goldschmidt, V. W. & Eskinazi, S. 1966 Two phase turbulent flow in a plane jet. *J. Appl. Mech.* **33**, 735.
- Gore, R. A., Crowe, C. T., Kamalu, N., Troutt, T. R. & Riley, J. J. 1989 Particle dispersion by large scale vortex structures. *Particle Sci. and Tech.* **7**, 201-207.
- Hamilton, W. S. & Lindell, J. E. 1971 *J. Hydr. Div.-ASCE* **97**, 805-817.
- Hinze, J. O. 1963 Momentum and energy balance equations for a flowing homogeneous suspension with slip between the two phases. *Appl. Sci. Res.* **A11**, 33.
- Hinze, J. O. 1975 *Turbulence*, McGraw-Hill, N.Y.
- Hulin, J. P., Fierfort, C. & Coudol, R. 1982 Experimental study of vortex emission behind bluff obstacles in a gas liquid vertical two-phase flow. *Int. J. Multiphase Flow* **6**, 475-490.

- Hunt, J. C. R. 1985 Turbulent diffusion from sources in complex flows. *Ann. Rev. Fluid Mech.* **17**, 447-485.
- Hunt, J. C. R., Auton, T. R., sene, K., Thomas, N. H. & Kowe, R. 1988 Bubble motions in large eddies and turbulent flows. In *Transient Phenomena in Multiphase Flow* (ed. N. H. Afgan), Hemisphere.
- Hunt, J. C. R., Perkins, R. J., Lunde, K. & Thomas, N. H. 1993 Modelling bubbly flows. *Bubble Dynamics and Interface Phenomena* (eds. J. R. Blake & N. H. Thomas) (1994), 257-268, Kluwer Academic Publishers.
- Hunt, J. C. R., Perkins, R. J. & Fung, J. C. H. 1994 Problems in modeling disperse two-phase flows. *Appl. Mech. Rev.* **47**(6), s49-s60.
- Hussain, A. K. M. F. 1983 Coherent structures - reality and myth. *Phys. Fluids* **26**, 2816-2850.
- Hussain, A. K. M. F. 1986 Coherent structures and turbulence. *J. Fluid Mech.* **173**, 303-356.
- Inoue, O. 1985 Vortex simulation of a turbulent mixing layer. *AIAA J.* **23**, 367-373.
- Ishii, M. 1975 *Thermo-fluid Dynamic Theory of Two-Phase Flow*. Paris: Eyrolles.
- Ishima, T., Hishida, K. & Maeda, M. 1993 Effect of particle residence time on particle dispersion in a plane mixing layer. *J. Fluids Engng.* **115**, 751-759.
- Kataoka, I., Ishii, M. & Serizawa, A. 1986 Local formulation and measurements of interfacial area concentration in two-phase flow. *Int. J. Multiphase Flow* **12**, 505-529.
- Kataoka, I. & Serizawa, A. 1989 Basic equations of turbulence in gas-liquid two-phase flow. *Int. J. Multiphase Flow* **15**, 843-855.
- Kronenburg, C. 1977 On the extension of Gradient-type transport to turbulent diffusion in inhomogeneous flows. *Applied Science Research* **33**, 163-175.
- Lahey, R. T., Jr. 1989 Turbulence and phase distribution phenomena in two-phase flow. *Invited lecture, ICHMT International Seminar on Transient Phenomena in Multiphase Flow*, Dubrovnik, Yugoslavia, 139-177.
- Laitone, J. A. 1981 A numerical simulation for gas-particle flow at high Reynolds numbers. *J. Appl. Mech.* **48**, 465-471.
- Lance, M. & Bataille, J. 1991 Turbulence in the liquid phase of a uniform bubbly air-water flow. *J. Fluid Mech.* **222**, 95-118.
- Launder, B. E. & Spalding, D. B. 1972 *Mathematical Models of Turbulence*, Academic Press, London.

- Launder, B. E. & Spalding, D. B. 1974 The numerical computation of turbulent flow, *Comp. Meth. in Appl. Mech. and Eng.* **3**, 269.
- Launder, B. E., Reece, G. J. & Rodi, W. 1975 Progress in the development of a Reynolds-stress turbulence closure. *J. Fluid Mech.* **68**, 537-566.
- Lazaro, B. J. & Lasheras 1989 Particle dispersion in a turbulent, plane shear layer *Phys. Fluids* **A1(6)**, 1035-1044.
- Leonard, A. 1980 Review of vortex dynamics for flow simulation. *J. Comput. Phys.* **37**, 289.
- Lopez de Bertodano, M., Lee, S-J., Lahey Jr. R. T. & Drew, D. A. 1990 The prediction of two-phase turbulence end phase distribution phenomena using a Reynolds stress model. *J. Fluids Engng.* **112**, 107-113.
- Lopez De Bertodano, M., Lahey Jr, R. T. & Jones, O. C. 1994 Development of $K-\epsilon$ model bubbly two-phase flow. *J. Fluids Engng.* **116**, 128-134.
- Lumley, J. L. 1975 Modeling turbulent flux of passive scalar quantities in inhomogeneous flows. *Phys. Fluids* **18(6)**, 619-621.
- Lumley, J. L. 1978 Two-phase and non-Newtonian flows. In *Topics in Applied Physics, Vol 12*, (ed. P. Bradshaw), New York: Springer-Verlag, 289-324.
- Magnaudet, J., Rivero, M. & Fabre, J. 1995 Accelerated flows past a rigid sphere or a spherical bubble. Part 1. Steady straining flow. *J. Fluid Mech.* **284**, 97-135.
- Makataos, N. C. 1986 The mathematical modelling of turbulent flows. *Appl. Math. Modelling* **10**, 190-220.
- Martin, J. E. & Meiburg, E. 1994 The accumulation and dispersion of heavy particles in forced two-dimensional mixing layers. I. The fundamental and subharmonic cases. *Phys. Fluids* **6 (3)**, 1116-1132.
- Maxey, M. R. & Riley, J. J. 1983 Equation of motion for a small-rigid sphere in a nonuniform flow. *Phys. Fluids* **26**, 883-889.
- Maxey, M. R. 1990 On the advection of spherical and non-spherical particles in a non-uniform flow. *Phil. Trans. R. Soc. Lond. A* **333**, 289-307.
- Maxey, M. R. 1993 The equation of motion for a small rigid sphere in a nonuniform or unsteady flow. in *the Gas-Solid Flows*, FED-Vol. **166**, ASME 93, 57-62.
- Maxey, M. R., Chang, E. J. & Wang, L-P. 1994 Simulation of interactions between microbubbles and turbulent flows. *Appl. Mech. Rev.* **47(6)**, s70-s74.
- McLaughlin, J. B. 1991 Inertial migration of small sphere in linear shear flows. *J. Fluid*

- Mech.* **224**, 262-274.
- Mei, R., Lawrence, C. J. & Adrain, R. J. 1991 Unsteady drag on a sphere at finite Reynolds number with small fluctuations in the free-stream velocity. *J. Fluid Mech.* **233**, 613-631.
- Milne-Thomson, L. M. 1968 *Theoretical Hydrodynamics*, 5th ed. The MacMillan Co., New York.
- Mostafa, A. A. & Mongia, H. C. 1987 On the modelling of turbulent evaporating sprays: Eulerian versus Lagrangian approach. *J. Heat Mass Transfer* **30**, 2583-2593.
- Nigmatulin, R. I. 1979 Spatial averaging in the mechanics of heterogeneous and dispersed systems. *Int. J. Multiphase Flow* **5**, 353-385.
- Nir, A. & Pismen, L. M. 1979 The effect of a steady drift on the dispersion of a particle in turbulent fluid. *J. Fluid Mech.* **94**, 364-381.
- Onslow, R. J., Thomas, N. H. & Whitehouse, R. J. S. 1993 Vorticity and sandwaves: the dynamics of ripples and dunes. In *Turbulence Perspective on Flow and Transport* (ed. N. J. Clifford), Wiley.
- Patankar, S. V. 1980 *Numerical Heat Transfer and Fluid Flow*, Hemisphere Publishing Corporation, New York.
- Pearse, B. A. & Thomas, N. H. 1990 Structure and force transients of bubble shedding from rotating stirrers. *Trans IChemE, Part A*, **68**, 57-62.
- Peskin, R. L. 1971 Stochastic application to turbulent diffusion. In *Int. Symp. on Stochastic Hydraulics* (Ed. C. L. Chiu) University of Pittsburg: Pittsburg, Pa, 251-267.
- Picart, A., Berlemont, A. & Gouesbet, G. 1986 Modelling and predicting turbulence fields and the dispersion of discrete particles transported by turbulent flows. *Int. J. Multiphase Flow* **12**, 237-261.
- Pui, N. K. & Gartshore, I. S. 1979 Measurements of the growth rate and structure in plane turbulent mixing layers. *J. Fluid Mech.* **91**, 111-130.
- Raju, N. & Meiburg, E. 1995 The accumulation and dispersion of heavy particles in forced two-dimensional mixing layers. Part 2: The effect of gravity. *Phys. Fluids* **7**(6), 1241-1264.
- Reeks, M. W. 1977 On the dispersion of small particles in homogeneous turbulence. *J. Fluid Mech.* **83**, 529-546.
- Reeks, M. W. 1981 The Transport of discrete particles in turbulent shear flows. *Paper*

C71/82 Conference on gas-borne particles, Inst. of Mech. Engr., Oxford-England, 87-92.

- Riley, J. J. & Metcalfe, R. W. 1980 Direct numerical simulation of a perturbed, turbulent mixing layer. *AIAA paper No. 80-0274*.
- Rivero, M., Magnaudet, J. & Fabre, J. 1991 New results on the forces exerted on a spherical body by an accelerated flow. *C.R.Acad. Sci. Paris Serie II* **312**, 1499-1506.
- Rizk, M. A. & Elghobashi, S. E. 1989 A two-equation turbulence model for dispersed dilute confined two-phase flows. *Int. J. Multiphase Flow* **15**, 119-133.
- Rodi, W. 1984 *Turbulence Models and Their Application in Hydraulics*. IAHR state-of-the-art paper presented by the section on Fundamentals of Division II: Experimental and Mathematical Fluid Dynamics.
- Ruetsch, G. R. & Meiburg, E. 1993 On the motion of small spherical bubbles in two-dimensional vortical flows. *Phys. Fluids A* **5**, 2326-2341.
- Saffman, P. G. 1965 The lift on a small sphere in a slow shear flow. *J. Fluid Mech.* **22**, 385.
- Sarpkaya, T. & Schoaff, R. L. 1979 Inviscid model of two-dimensional vortex shedding by a circular cylinder. *AIAA J.* **17**, 1193-1200.
- Sarpkaya, T. 1989 Computational methods with vortices - The 1988 Freeman Scholar Lecture. *J. Fluids Engineering.* **111**, 5-52.
- Sato, Y., Sadatomi, M. & Sekoguchi, K. 1981 Momentum and heat transfer in two-phase bubbly flow I. *Int. J. Multiphase Flow* **7**, 167-177.
- Sene, K. J. 1985 Aspects of bubbly two-phase flow. PhD thesis, University of Cambridge.
- Sene, K. J., Hunt, J. C. R. & Thomas, N. H. 1994 The role coherent structures in bubble transport by turbulent shear flows. *J. Fluid Mech.* **259**, 219-240.
- Serizawa, A., Kataoka, I. & Michiyoshi, I. 1975 Turbulence structure of air-water bubbly flow II. Local properties. *Int. J. Multiphase Flow* **2**, 235-246.
- Simonin, O. & Viollet, P. L. 1987 Numerical modeling of devolatilization in pulverised coal injection inside a hot coflowing air flow. *Proc USA-France Workshop on Turbulent Reactive Flows, Rouen, Lectures Notes in Engineering*, **40**, 824-846, Springer-Verlag.
- Simonin, O. 1991 Second moment prediction of dispersed phase turbulence in particle-laden flows. *Proc 8th Int Symp on Turbulent Shear Flows*, Munich.
- Simonin, O. & Viollet, P. L. 1992 Modelling of turbulent two-phase jets loaded with discrete particles. *Proc of 6th Int Workshops on Two-phase Flow Predictions*, (ed.

M. Sommerfeld) Erlangen.

- Snyder, W. H. & Lumley, J. L. 1971 Some measurements of particle velocity autocorrelation function in a turbulent flow. *J. Fluid Mech.* **48**, 41-71.
- Sommerfeld, M. 1990 Numerical simulation of the particle dispersion in turbulent flow: The importance of particle lift forces and particle/wall collision models. *Numerical Methods for Multiphase Flows* ASME FED-Vol. **91**, 11-18.
- Soo, S. L. 1990 Basic equations of multiphase systems. *Multiphase Fluid Dynamics*, Science Press and Gower Technical. Beijing. 303-355.
- Squires, K. D. & Eaton, J. K. 1990 Particle response and turbulence modification in isotropic turbulence. *Phys. Fluids A*. **2**(7), 1191-1203.
- Squires, K. D. & Eaton, J. K. 1994 Effect of selective modification of turbulence on two-equation models for particle-laden turbulent flows. *J. Fluids Engng.* **116**.
- Sreenivasan, K. R., Tavoularis, S. & Corrsin, S. 1981 Turbulent transport in passively heated homogeneous flows, *Proc 3rd Symp Turbulent Shear Flows*, Univ. of Calif.-Davis.
- Sridhar, G. & Katz, J. 1995 Drag and lift forces on microscopic bubbles entrained by a vortex. *Phys. Fluids* **7**(2), 389-399.
- Stansby, P. K. & Slaouti, A. 1993 Simulation of vortex shedding including blockage by the random-vortex and other methods. *Int. J. Numerical Methods in Fluids* **17**, 1003-1013.
- Stewart, C. W. & Crowe, C. T. 1993 Bubble dispersion in free shear flows. *Int. J. Multiphase Flow*. **19**, 501-507.
- Sun, T-Y. & Faeth, G. M. 1986 Structure turbulent bubbly jets - II. phase property profiles. *Int. J. Multiphase Flow* **12**, 115-126.
- Tang, L., Wen, F., Yang, Y., Crowe, C. T., Chung, J. N. & Troutt, T. R. 1992 Self-organized particle dispersion mechanisms in free shear flows. *Phys. Fluids*, 2244-2251.
- Taylor, G. I. 1921 Diffusion by continuous movements. *Proc. R. Soc. Lond. A* **20**, 196-211.
- Tchen, C. M. 1947 Mean value and correlation problems connected with the motion of small particles suspended in a turbulent fluid. PhD dissertation, Technische Hogeschool Delft.
- Thomas, N. H., Auton, T. R., Sene, K. & Hunt, J. C. R. 1983 Entrainment and transport of bubbles by transient large eddies in multiphase turbulent shear flows. In *Proc. Intl*



Conf. on Physical Modelling of Multiphase Flows, Coventry, UK. BHRA.

- Thomas, N. H. 1994 Plunging flow aeration: some fundamental and functional factors. *Aeration Technology* ASME FED-Vol.184.
- Thomas, N. H. 1995 Private communications.
- Tio, K., Linan, A., Lasheras, J. C. & Ganan-Calvo, A. M. 1993 On the dynamics of buoyant and heavy particles in a periodic Stuart vortex flow. *J. Fluid Mech.* **254**, 671-699.
- Townsend, A. A. 1976 *The Structure of Turbulent Shear Flow*. Cambridge University Press.
- Truesdell, C. & Toupin, R. 1960 The classical field theories. In *Encyclopedia of Physics*, Vol. III/1, 226-793. Berlin, Göttingen, Heidelberg: Springer.
- Viollet, P. L. & Simonin, O. 1994 Modelling dispersed two-phase flows: Closure, validation and software development. *Appl. Mech. Rev.* **47**(6), s80-s84.
- Wang, S. K., Lee, S. J., Jones, O. C., Jr., & Lahey, R. T., Jr. 1987 3-D turbulence structure and phase distribution measurements in bubbly two-phase flows. *Int. J. Multiphase Flow* **13**, 327-343.
- Wells, M. R. & Stock, D. E. 1983 The effects of crossing trajectories on the dispersion of particles in a turbulent flow. *J. Fluid Mech.* **136**, 31-62.
- Wen, F., Kamalu, N., Chung, J. N., Crowe, C. T. & Troutt, T. R. 1992 Particle dispersion by vortex structures in plane mixing layers. *J. Fluids Engng.* **114**, 657-666.
- Yang, X. & Thomas, N. H. 1992 Void fraction profiles in two-phase bubbly upward and downward flow. *Proc of 6th International Workshop on Two-phase Flow Prediction*, Erlangen, 264-273.
- Yang, X. & Thomas, N. H. 1994 Simulation of particle and bubble dispersion in turbulent free shear flows. *Numerical Methods for Multiphase Flow*, ASME FED-Vol. **85**, 259-268.
- Yuu, S., Yasukoucki, N. & Tomosada, J. 1978 Particle turbulent diffusion in a dust-laden round jet. *AIChE J.* **24**(3), 508.
- Zang, T. A. & Hussiaini, M. Y. 1985 Recent applications of spectral methods in fluid dynamics. *Lect. Appl. Math.* **22**, 379-409.

APPENDIX I

Let $\langle \rangle$ denote an averaging process so that if $f(\mathbf{x},t)$ is an exact microscopic field, $\langle f \rangle(\mathbf{x},t)$ is then the corresponding averaged field. The averaging requires that the average should be smooth in the sense that no details appear in the averaged variables. The most commonly used averages in two-phase flows are as follows:

(1) Time average:

$$\langle f \rangle = \frac{1}{T} \int_{t-T}^t f(\mathbf{x},t') dt' \quad (\text{A1})$$

where T is an averaging time scale.

(2) Spatial average:

$$\langle f \rangle(\mathbf{x},t) = \frac{1}{L^3} \int_{x_1 - \frac{1}{2}L}^{x_1 + \frac{1}{2}L} \int_{x_2 - \frac{1}{2}L}^{x_2 + \frac{1}{2}L} \int_{x_3 - \frac{1}{2}L}^{x_3 + \frac{1}{2}L} f(\mathbf{x}',t) dx'_3 dx'_2 dx'_1 \quad (\text{A2})$$

where L is an averaging length scale over the space. Also a weighted space average:

$$\langle f \rangle(\mathbf{x},t) = \int \int \int_{R^3} g(\mathbf{x} - \mathbf{x}') f(\mathbf{x}',t) d\mathbf{x}' \quad (\text{A3})$$

where $\int \int \int_{R^3} g(\mathbf{s}) d\mathbf{s} = 1$; also various combinations of averages and/or specific types of weighting.

(3) Ensemble average:

$$\langle f \rangle(\mathbf{x},t) = \frac{1}{N} \sum_{n=1}^N f_n(\mathbf{x},t) \quad (\text{A4})$$

where $f_n(\mathbf{x},t)$ denotes a realisation of the quantity f over a set of possible equivalent realisations Ω .

In averaging, the averaging process is usually assumed to satisfy

$$\langle f+g \rangle = \langle f \rangle + \langle g \rangle \quad (\text{A5})$$

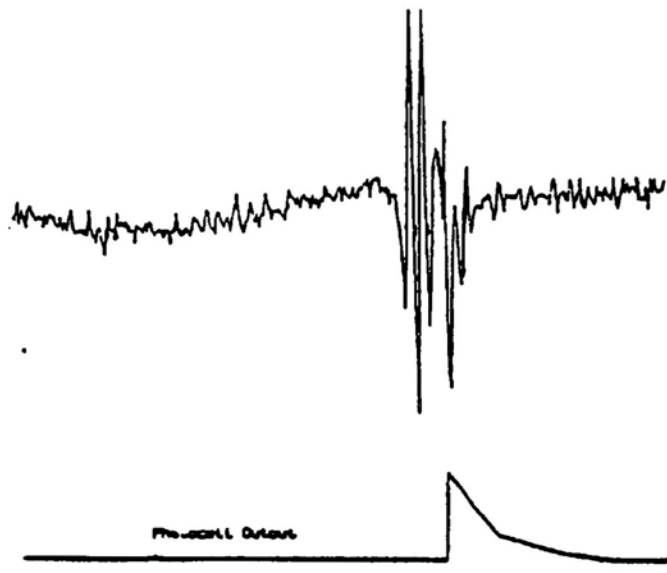
$$\langle \langle f \rangle g \rangle = \langle f \rangle \langle g \rangle \quad (\text{A6})$$

$$\langle c \rangle = c \quad (\text{A7})$$

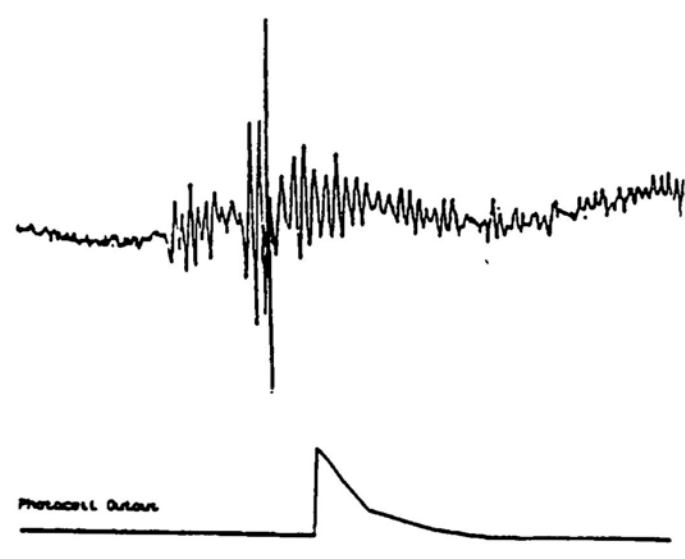
$$\left\langle \frac{\partial f}{\partial t} \right\rangle = \frac{\partial}{\partial t} \langle f \rangle \quad (\text{A8})$$

$$\left\langle \frac{\partial f}{\partial x_i} \right\rangle = \frac{\partial}{\partial x_i} \langle f \rangle \quad (\text{A9})$$

Relations (5), (6) and (7) are called Reynolds' rules. Relation (8) is referred to as Leibnitz's rule, and relation (9) is called Gauss' rule. Relations (8) and (9) are mainly applied in volume averaging.



(a)



(b)

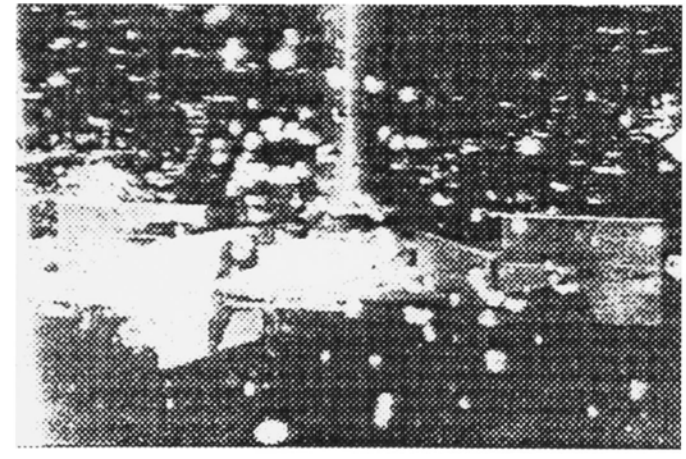
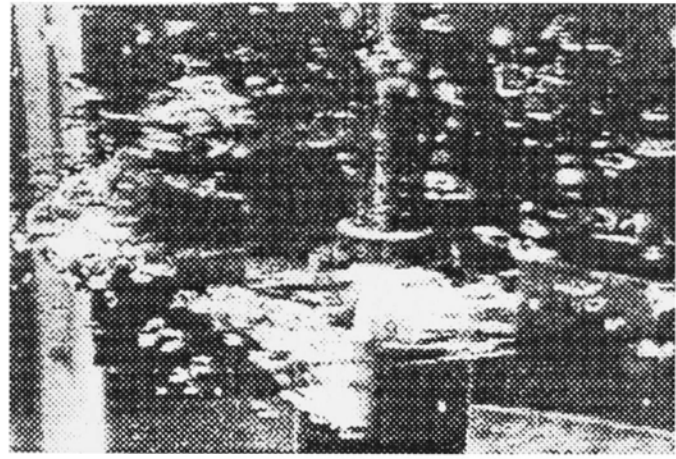


Figure 1. Examples of the blade drag force records and triggered flash photography of the bubble shedding events. Shaft speed: (a) 140 rpm, (b) 125 rpm. Gas flow rate: (a) 1.82 l/min, (b) 2.17 l/min. Taken from Pearse & Thomas (1990).

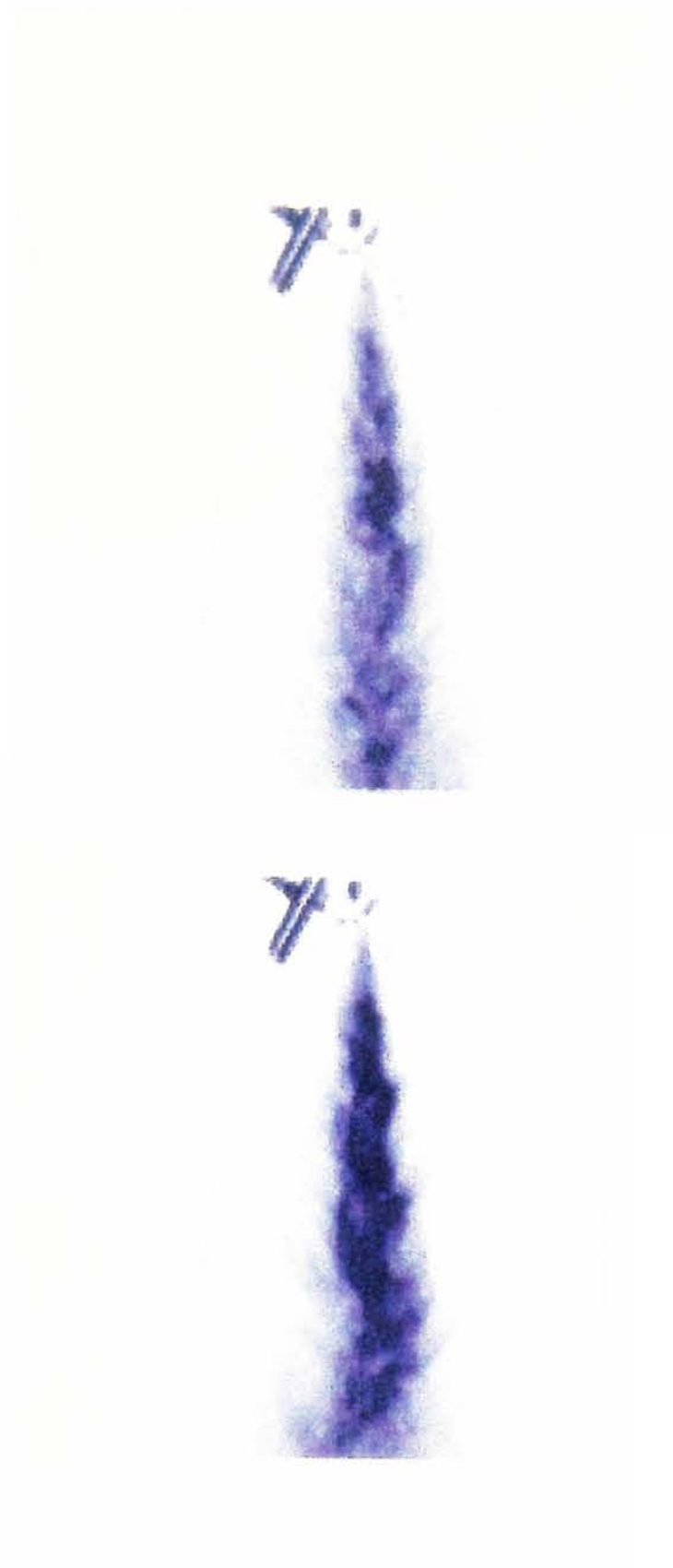
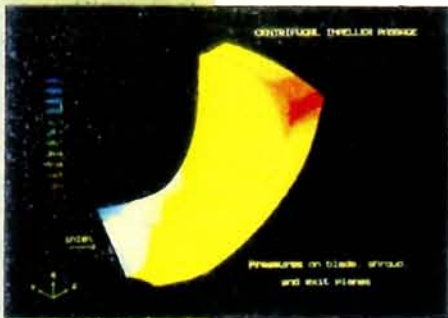


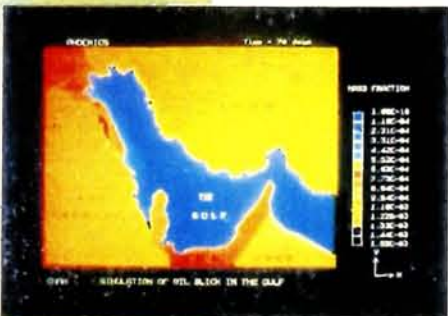
Figure 2. FRED "SPRAY" Nozzle: Air liquid spray. Mean drop size is about $100\ \mu\text{m}$. Spray speed is about $100\ \text{m/s}$. Spraying into still air. Taken from Thomas (1995).

PHOENICS: CFD from A to Z

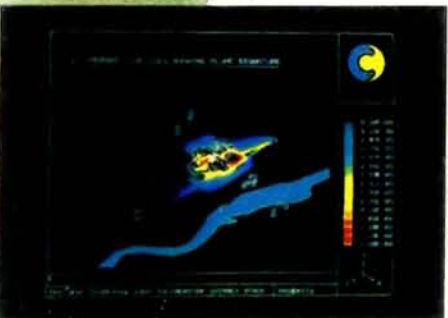
I



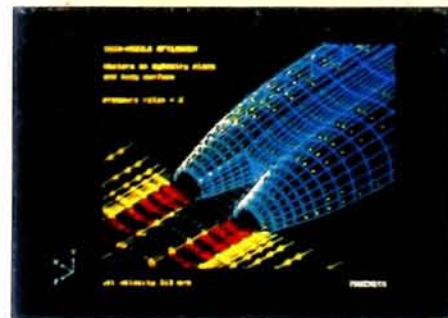
O



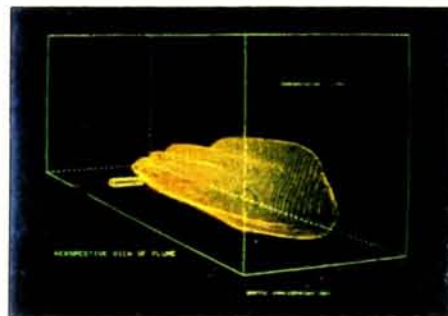
U



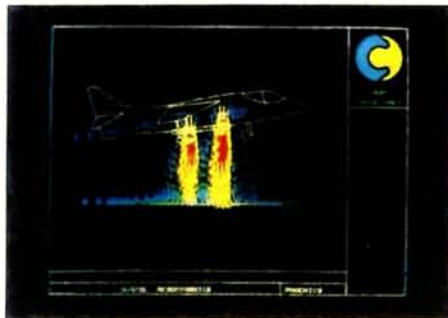
J



P



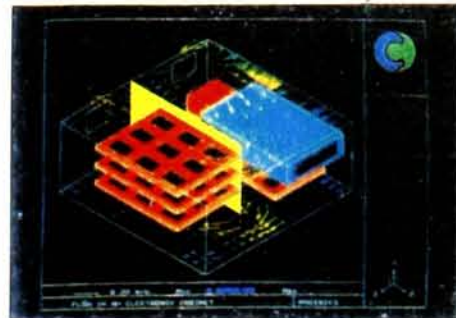
V



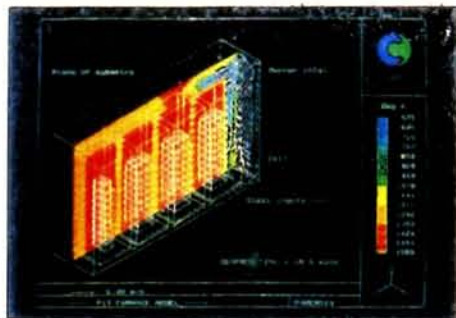
A



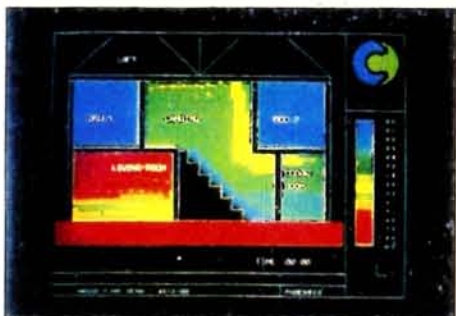
E



K



Q



W

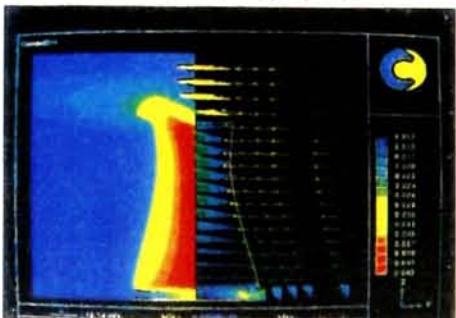
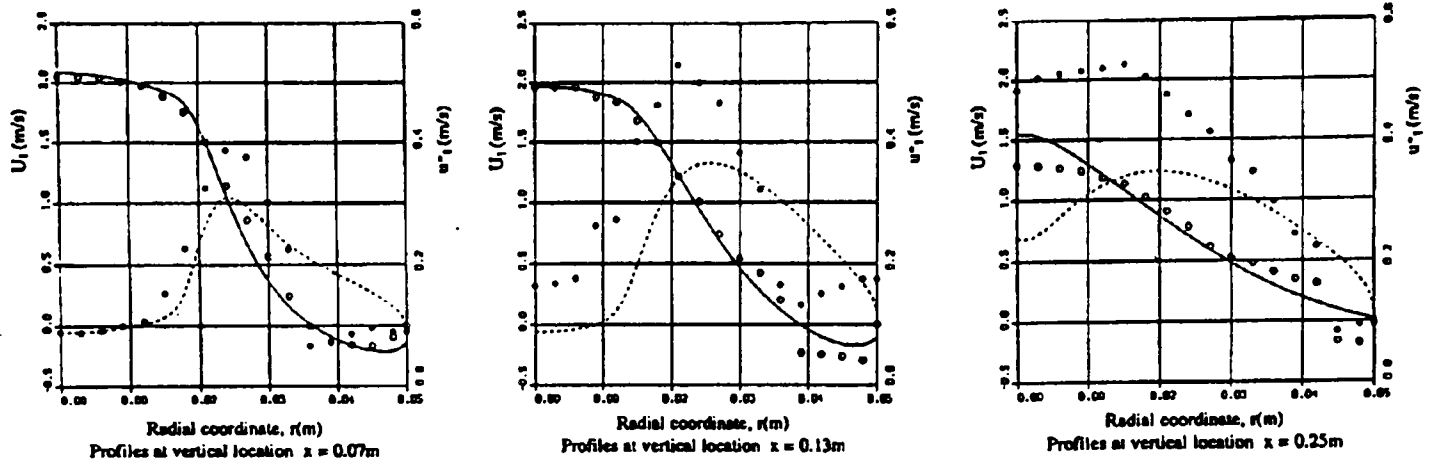
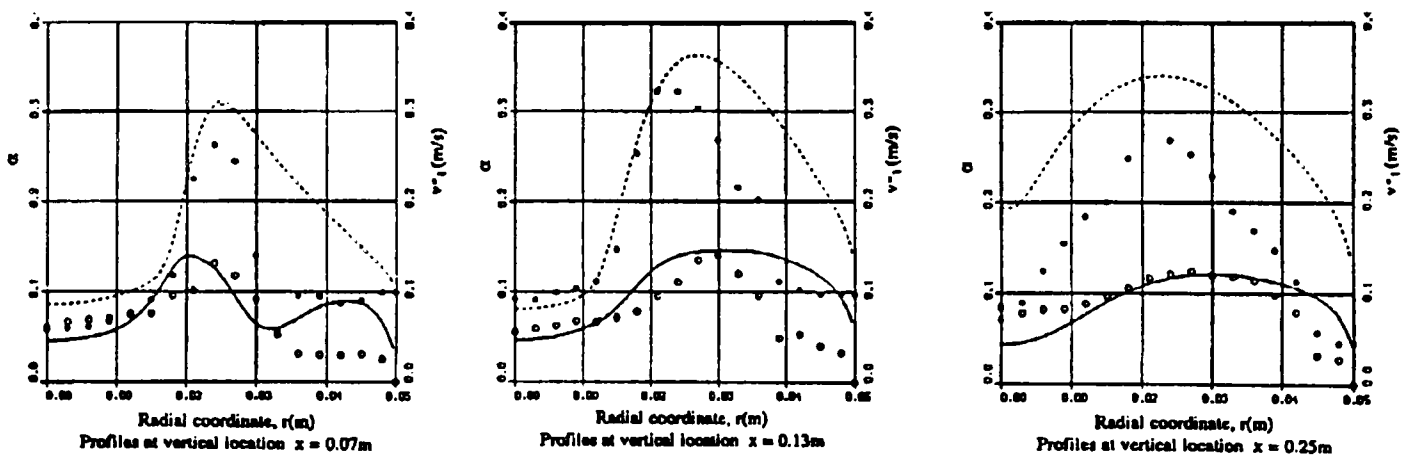


Figure 3. For caption see facing page.



— axial mean liquid velocity, ... axial r.m.s. liquid velocity, \circ and \bullet experimental data



— local void fraction, ... radial r.m.s. liquid velocity, \circ and \bullet experimental data

Figure 4. Numerical predictions of a turbulent bubbly flow downstream of a sudden pipe expansion (bubble diameter $d_B=2$ mm, void fraction $\alpha_G \approx 0.1$). Taken from F'dhila & Simonin (1992).

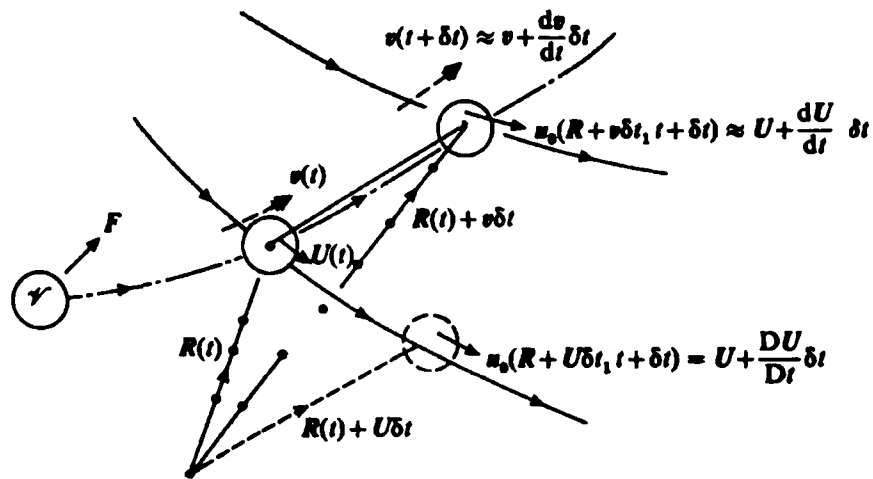


Figure 5. A rigid body with volume V at $R(t)$ moving with velocity $\mathbf{v}(t)$ through a non-uniform velocity field $\mathbf{u}(\mathbf{x},t)$. Notice that at the particle $\mathbf{u}_0=U(t)$, its rate of change, seen by the particle is dU/dt ; the fluid volume at time $t+\delta t$, which coincided with the body at time t , its acceleration is DU/Dt . Taken from Auton *et al.* (1988)

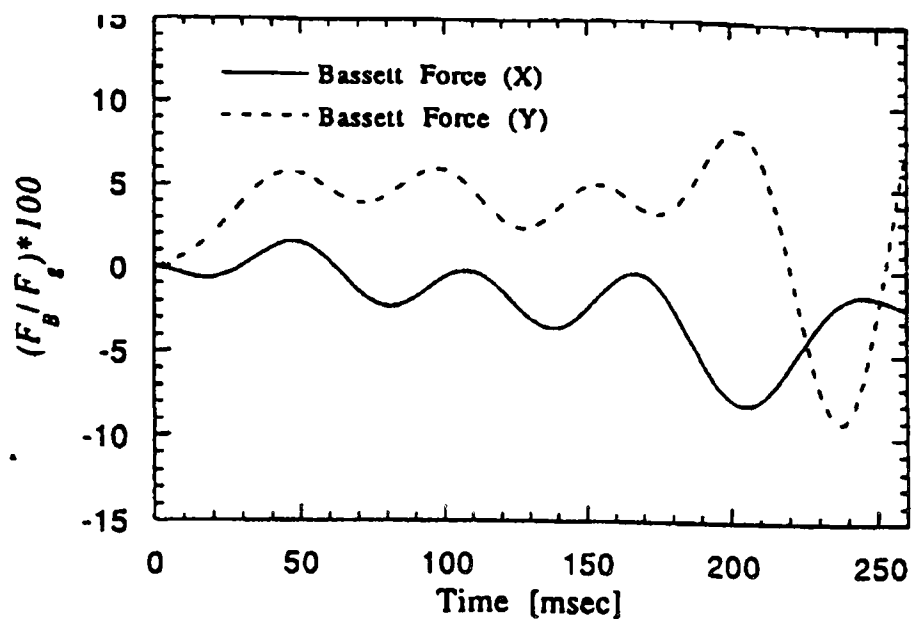


Figure 6. Estimate of the Basset force acting on a $707 \mu\text{m}$ bubble during entrainment, resolved into X, Y components in a Cartesian frame. Taken from Sridhar & Katz (1995).

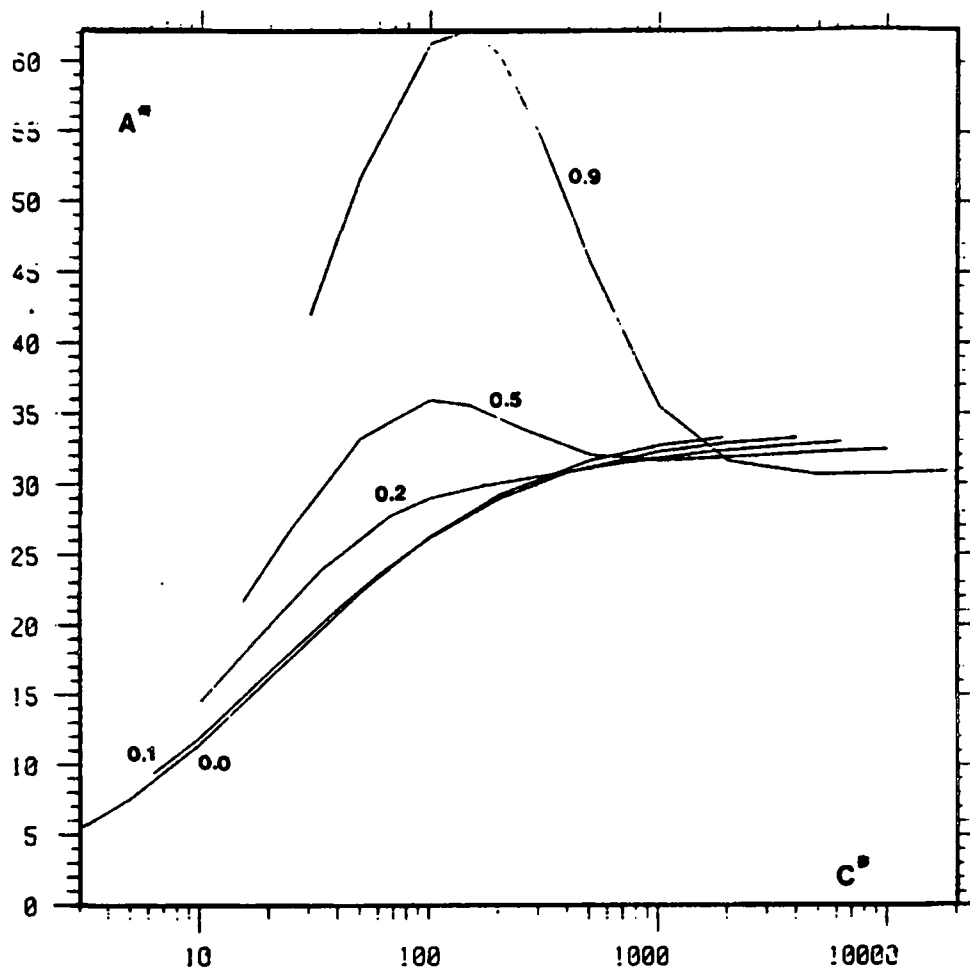


Figure 7. Dependence of the trapping width on the vortex strength parameter for discreta with various specific gravities. Taken from Thomas *et al.* (1983)

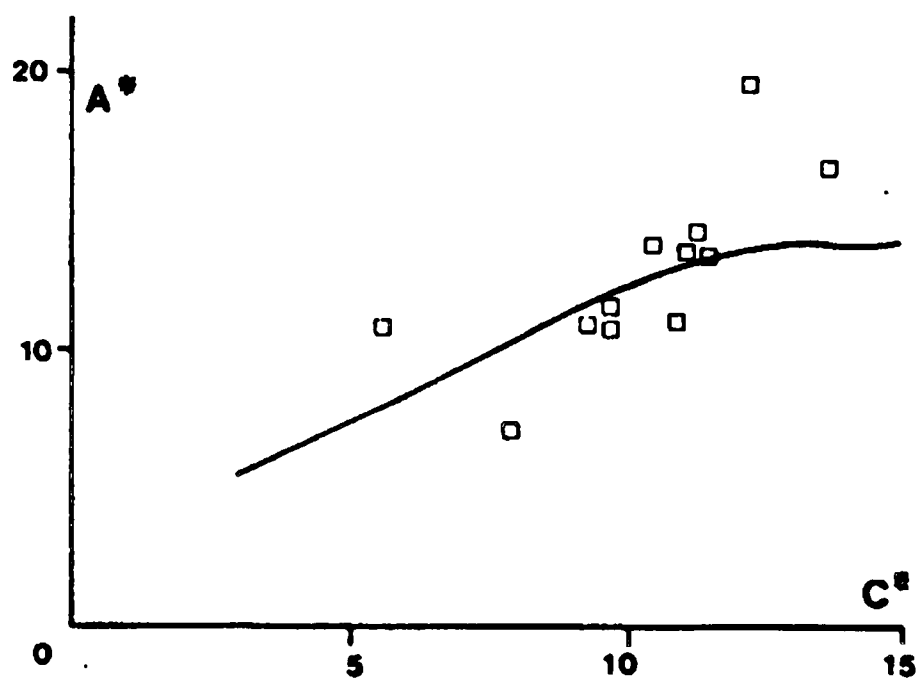


Figure 8. Comparison between computed and experimental trapping width with different vortex strength for bubbles in water. Taken from Thomas *et al.* (1983).

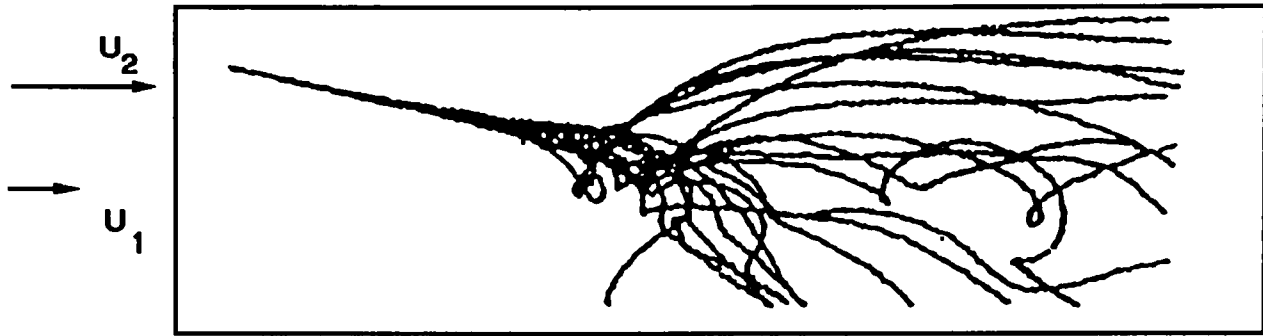


Figure 9. Simulation of bubble trajectories in a horizontal mixing layer. 20 bubbles released with $\Pi=0.5$, $\Gamma=3.3$ (note: gravity acts upwards in the figure). Taken from Sene *et al.* (1994)

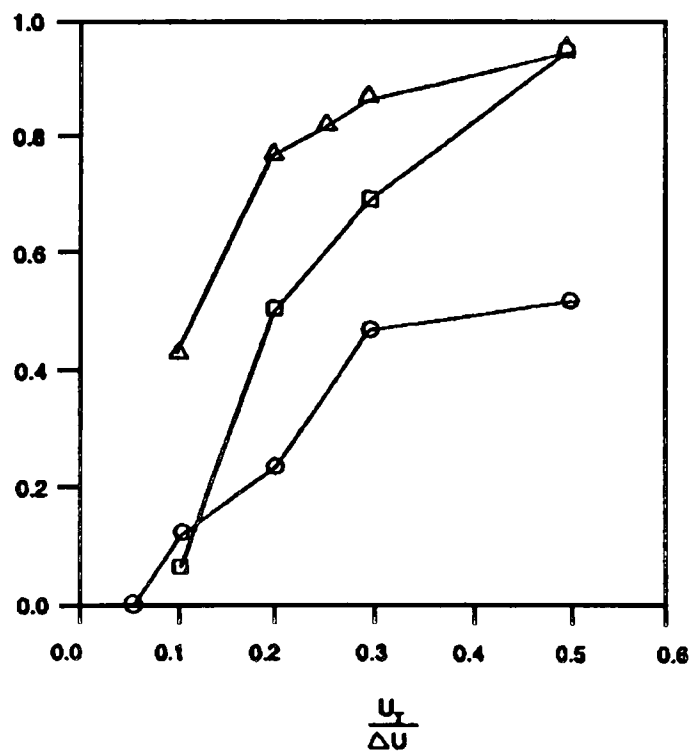
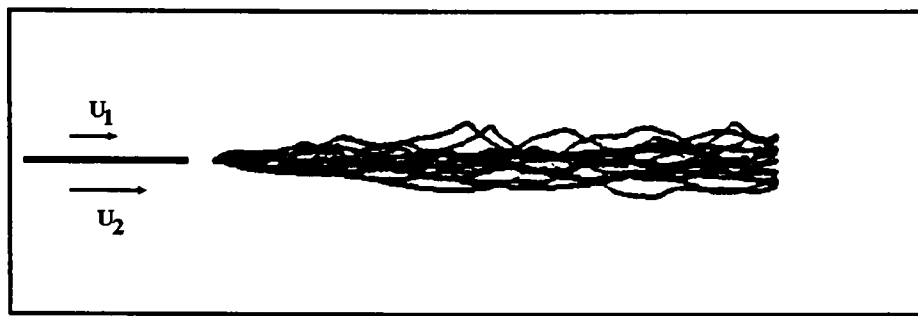
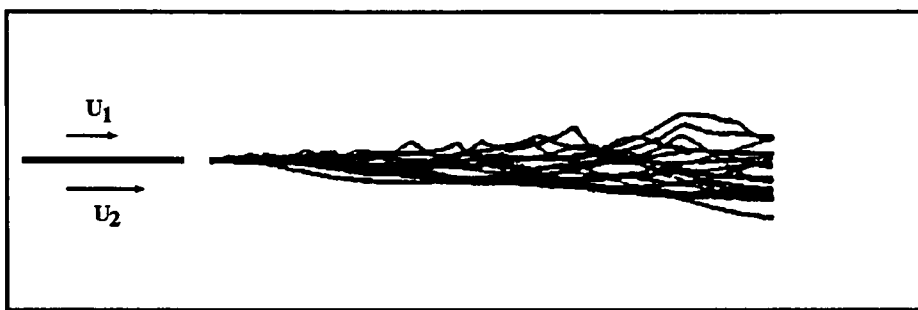


Figure 10. Calculation of the probability of bubbles escaping from a horizontal mixing layer (Δ , $\Pi=0$; \square , $\Pi=0.05$; \circ , $\Pi=0.5$). Taken from Sene *et al.* (1994).



(a)



(b)

Figure 11. Computer simulation of bubble trajectories in a vertical mixing layer. Bubbles were released from the location close to the origin of the mixing layer. (a) $\Pi=0.5$, $\Gamma=10.0$; (b) $\Pi=0$, $\Gamma=10.0$. 200 bubbles. Taken from Yang & Thomas (1994).

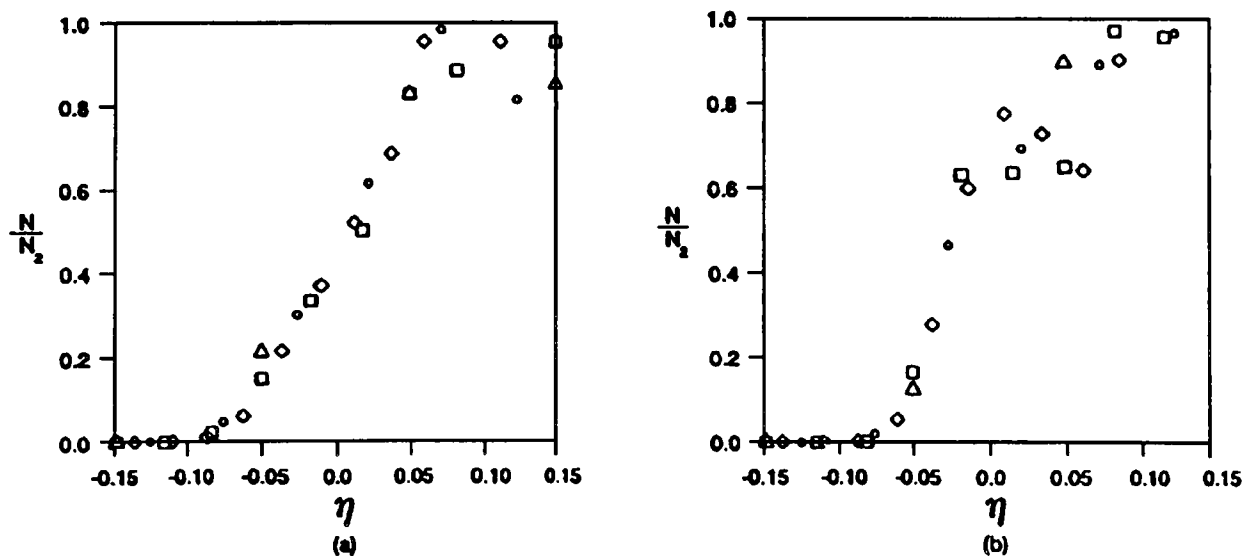


Figure 12. Calculation of bubble number fluxes in a vertical downflowing mixing layer. $N_2(=40)$ bubbles released into the high speed stream in the region $0.0 < y < 0.135L$. (a) $\Pi=0$, $\Gamma=5.0$; (b) $\Pi=0.067$, $\Gamma=5.0$. Δ , $x=0.2L$; \circ , $x=0.4L$; \square , $x=0.6L$; \diamond , $x=0.8L$). Taken from Sene *et al.* (1994).

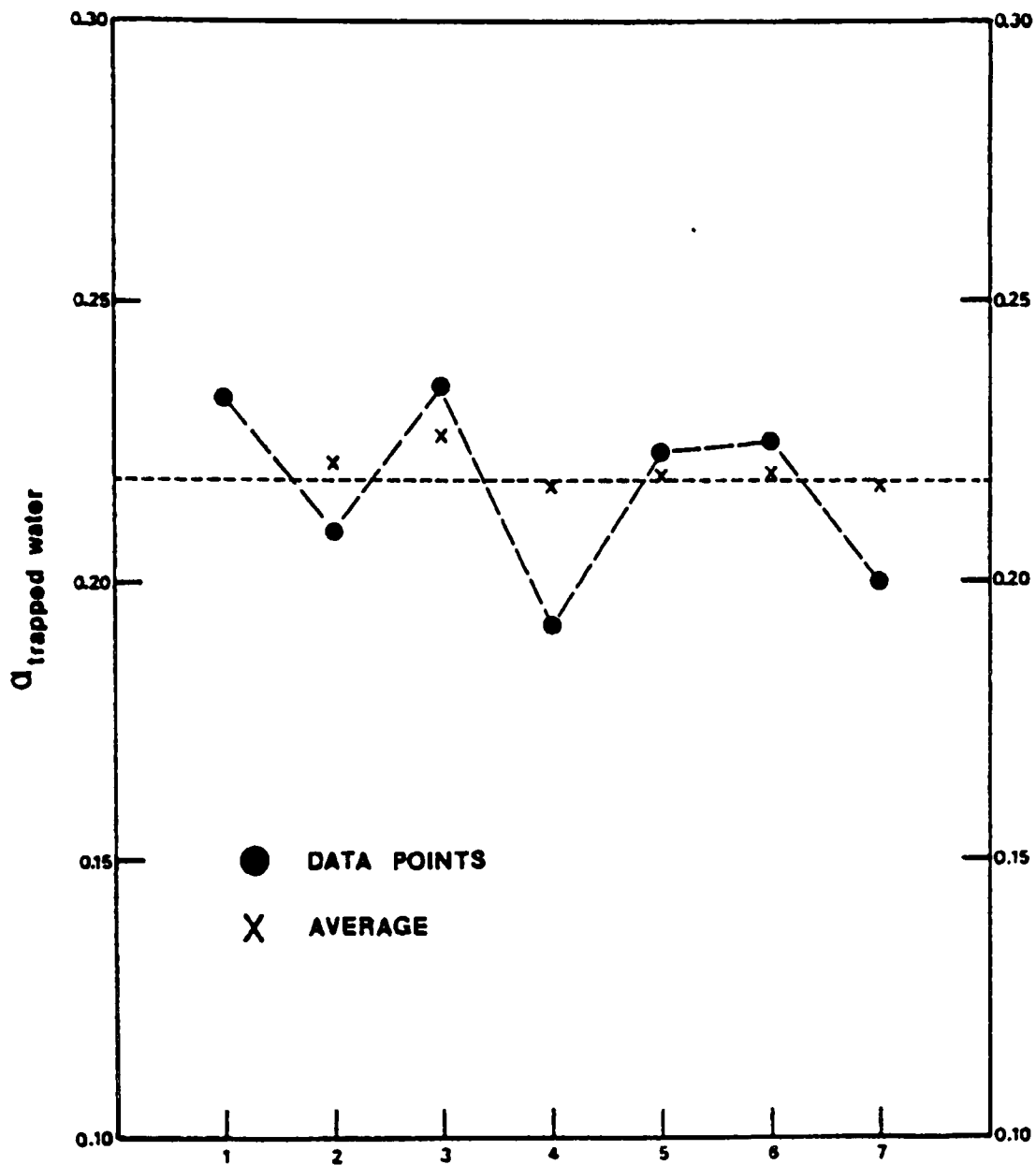


Figure 13. Void fractions measured by trapping water between two quick closing valves. The same experiment was repeated several times. Taken from Banerjee & Chan (1980).

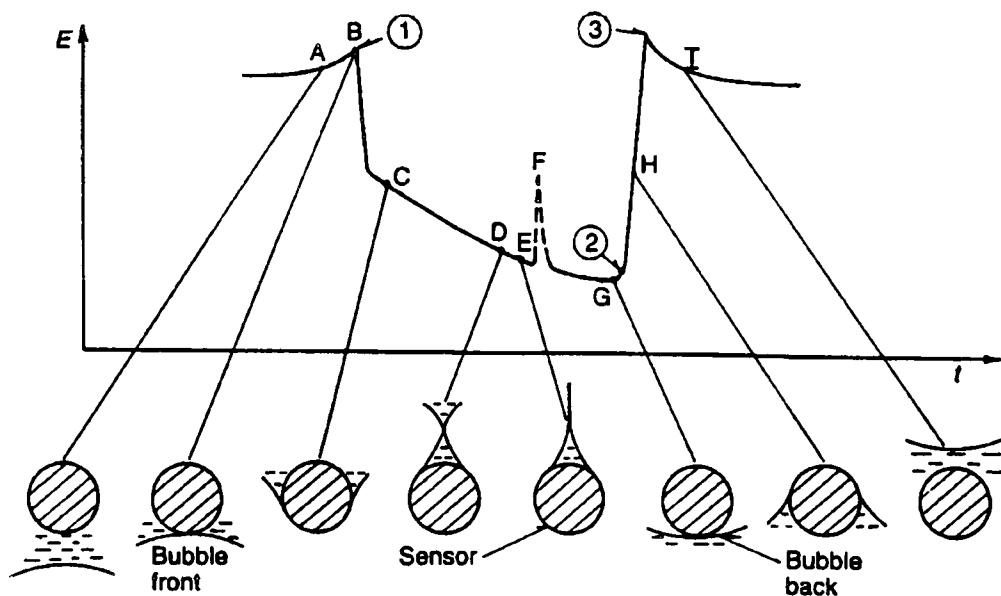


Figure 14. The response of a cylindrical hot-film probe to the passage of a bubble. Taken from Bruun (1995).

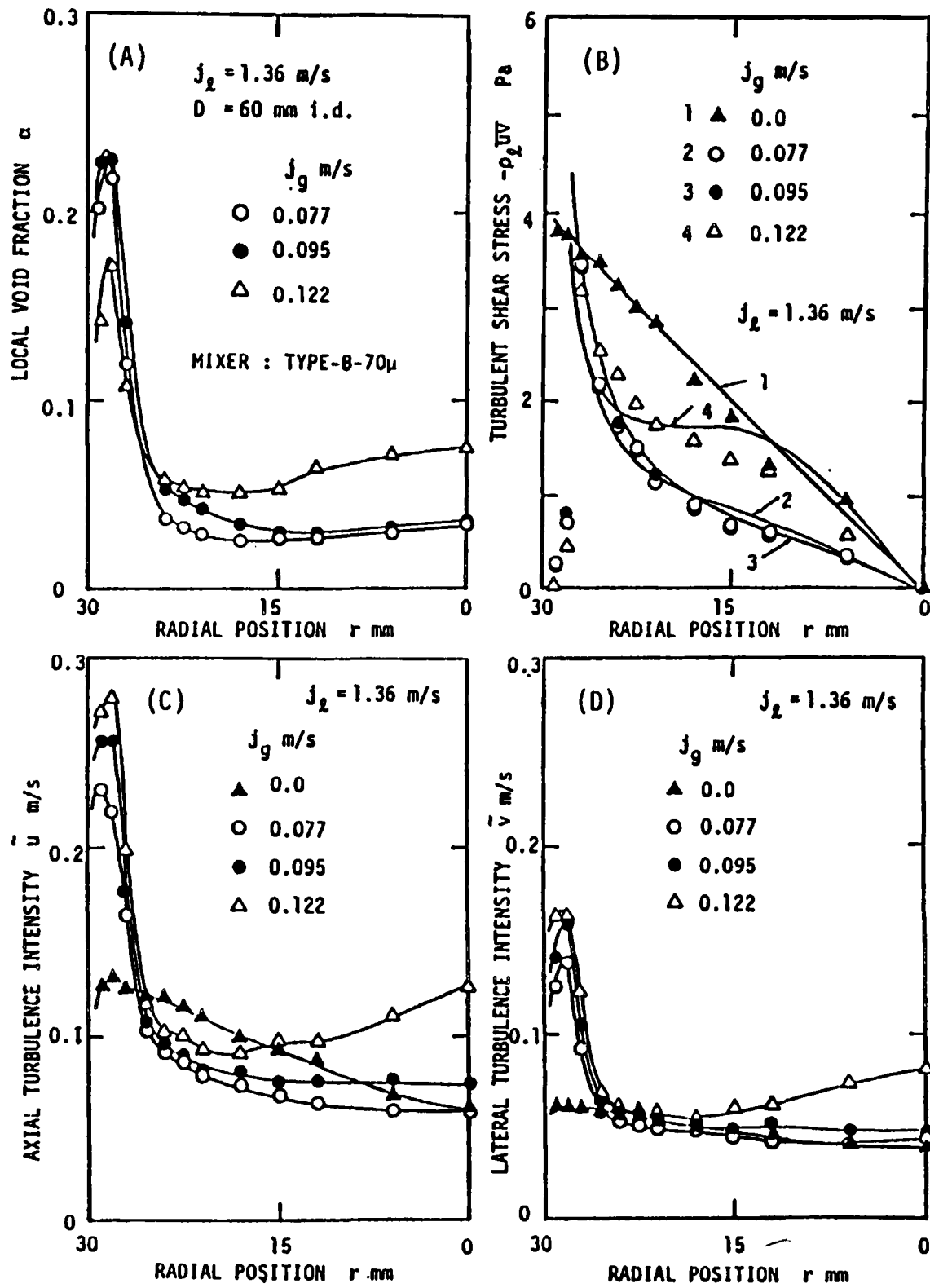
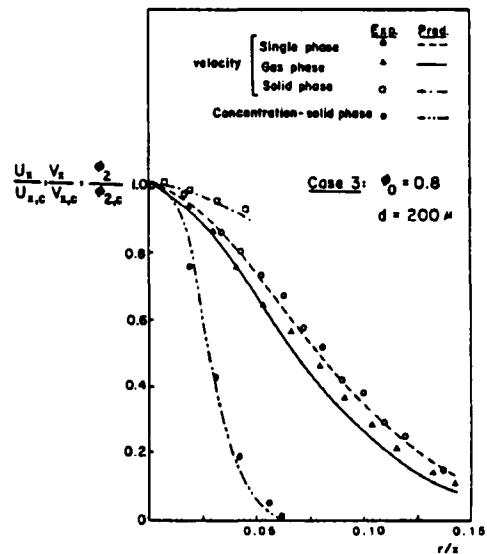
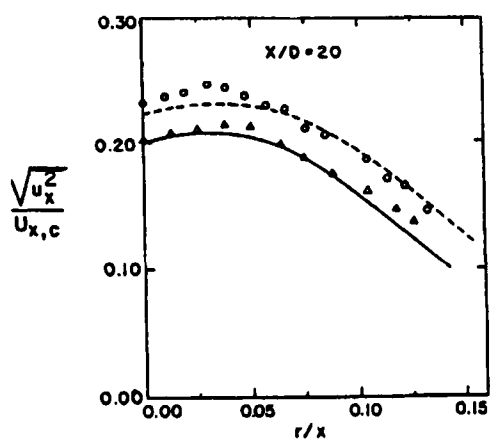


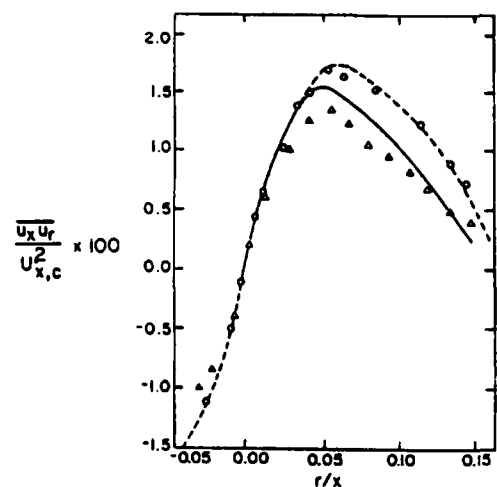
Figure 15. Turbulence measurement (two-dimensional) with X-probe. Turbulence intensity profiles have been significantly modified due to the presence of bubbles. Taken from Serizawa *et al.* (1974).



(a)



(b)



(c)

Figure 16. The properties of a two-phase jet flow at $x/D=20$. (a) normalized mean velocity and volume fraction profiles; (b) turbulence intensity profiles; (c) turbulence shear stress profiles. Taken from Elghobashi *et al.* (1984).

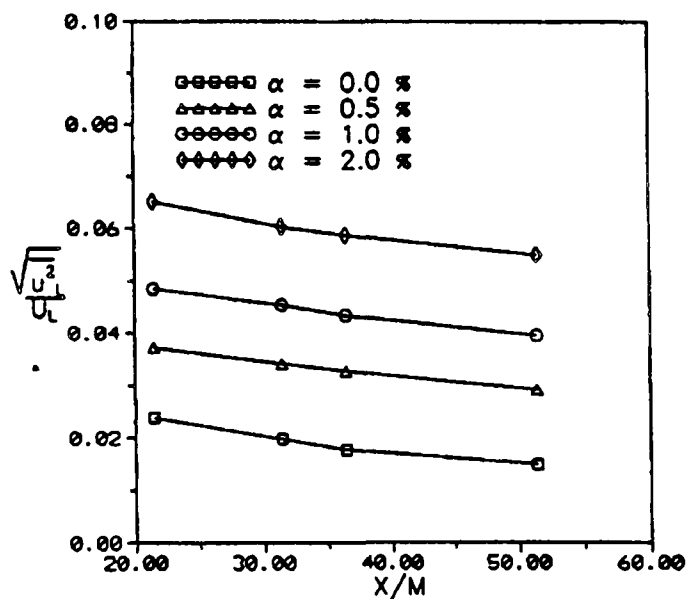
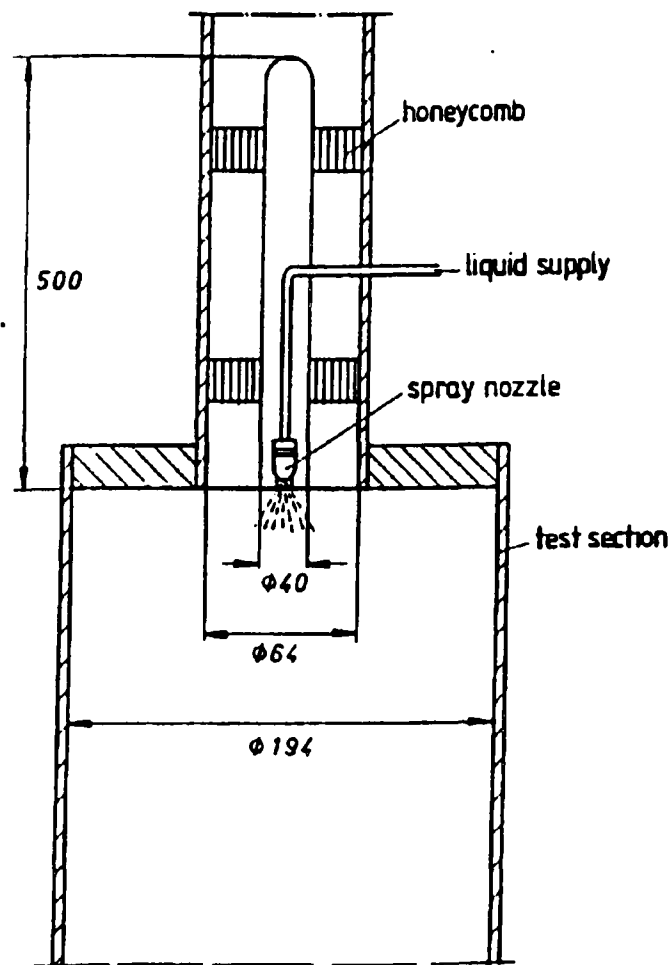
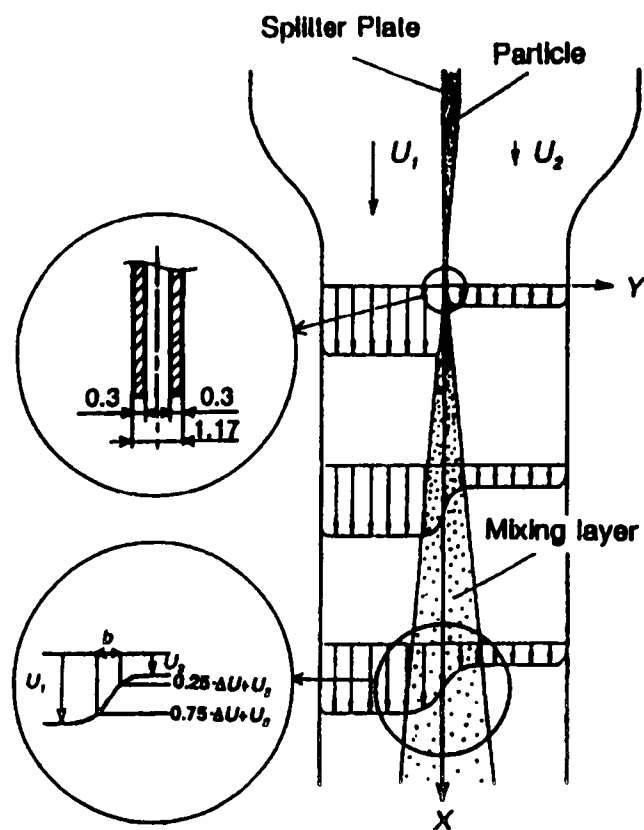


Figure 17. Decay of grid generated turbulence for bubbly flow ($U_L=0.6$ m/s). Taken from Lance & Bataille *et al.* (1991).



(a) Spray evaporation in a co-flowing annular jet



(b) Particle dispersion in a plane shear jet

Figure 18. Experimental set-up of a spray evaporation in a co-flowing annular jet and a particle dispersion in a plane shear jet. Taken from the Proceedings of the Sixth Workshop on Two-Phase Flow Prediction (ed. by M. Sommerfeld 1992).

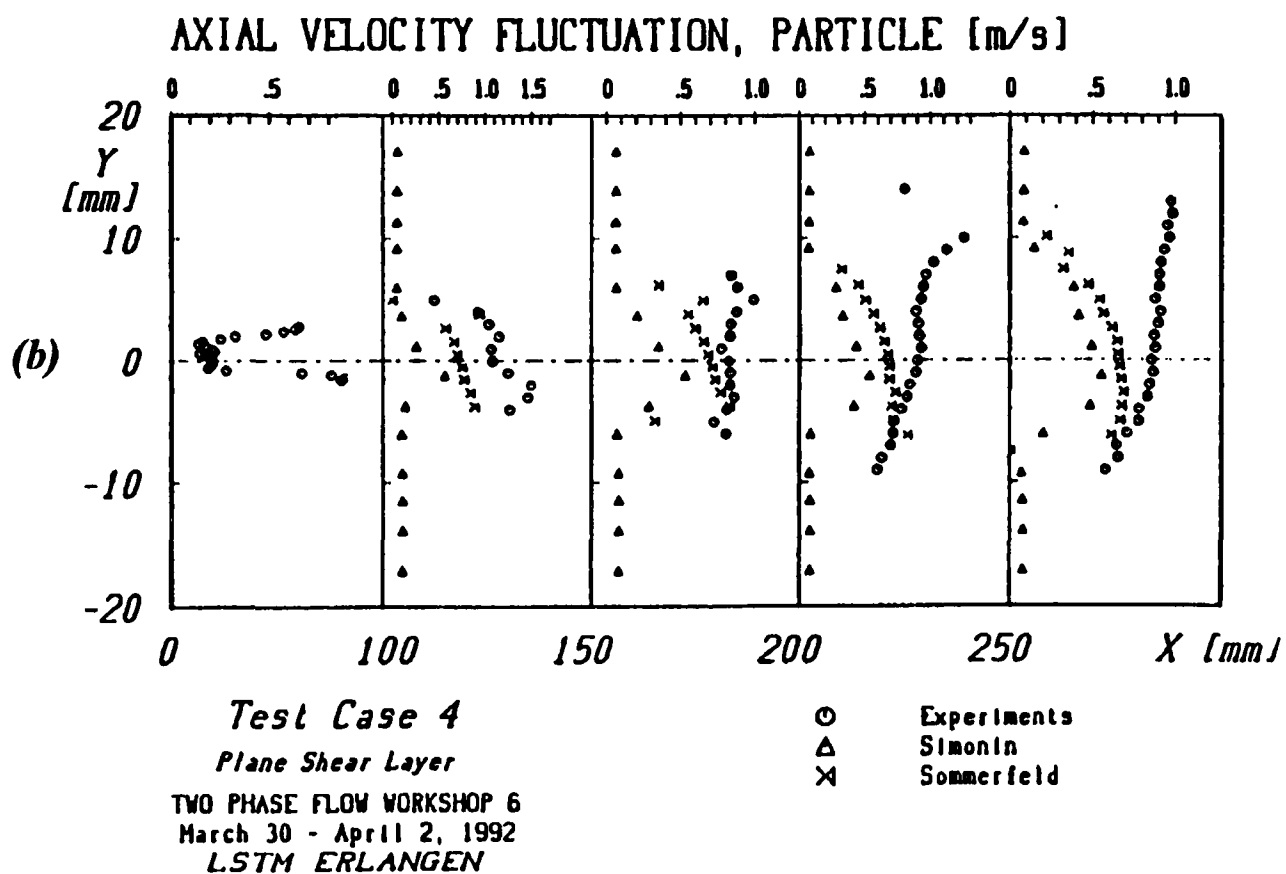
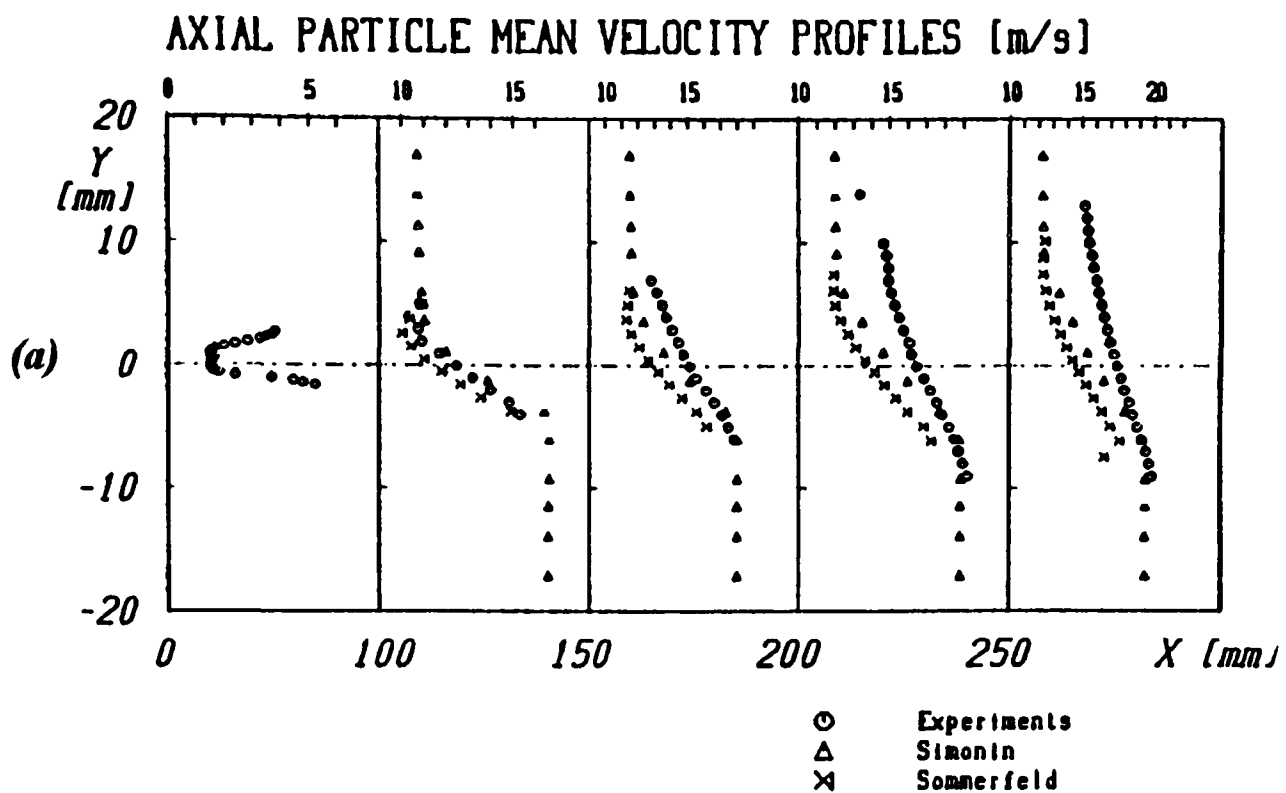


Figure 19. Particle dispersion in a plane mixing layer. Predicted axial particle mean velocity and axial velocity fluctuation profiles compared with the experimental data (Ishima 1993). (a) axial particle mean velocities; (b) axial particle velocity fluctuations. Taken from the Proceedings of the Sixth Workshop on Two-Phase Flow Prediction (ed. M. Sommerfeld 1992).

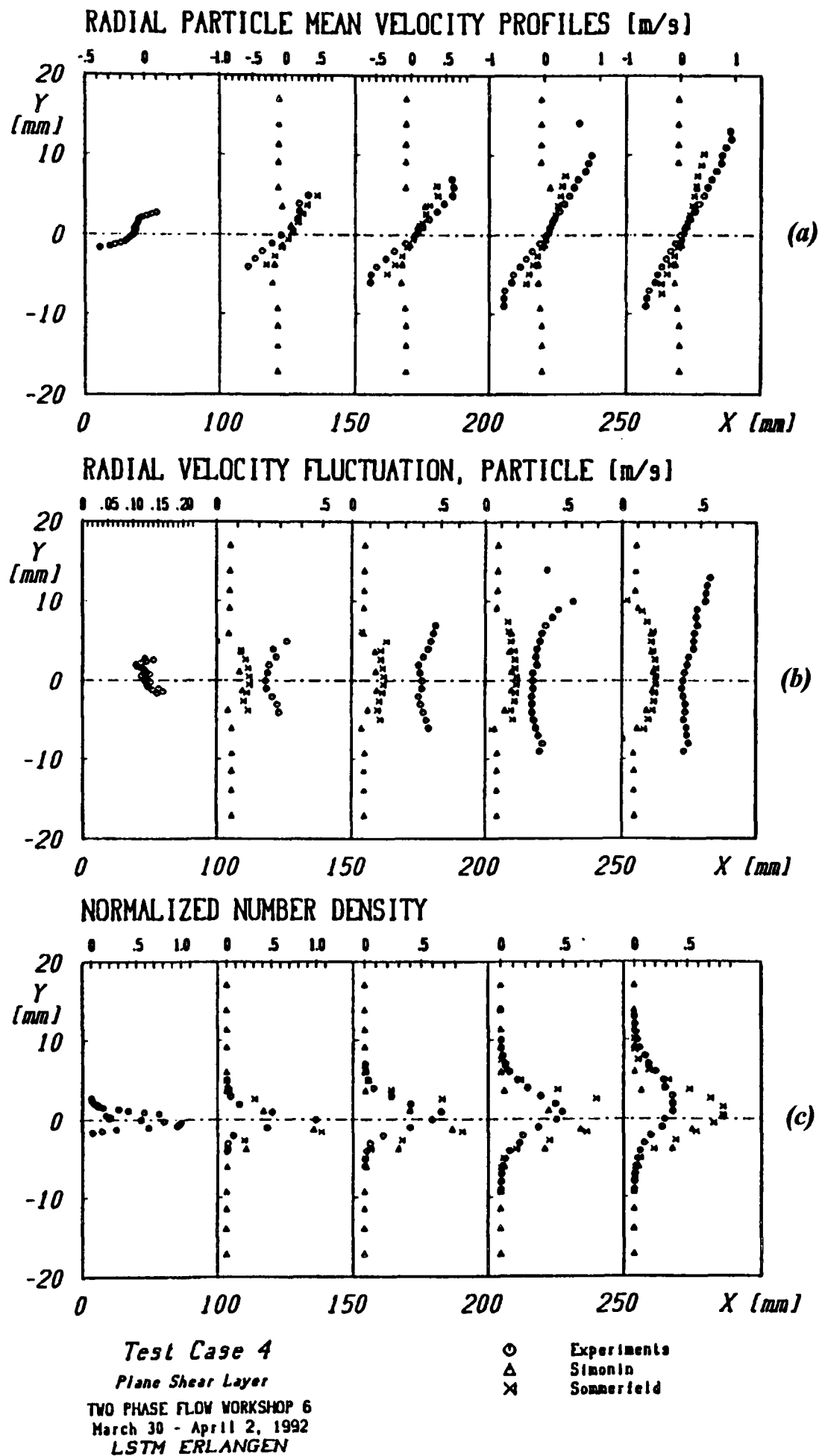
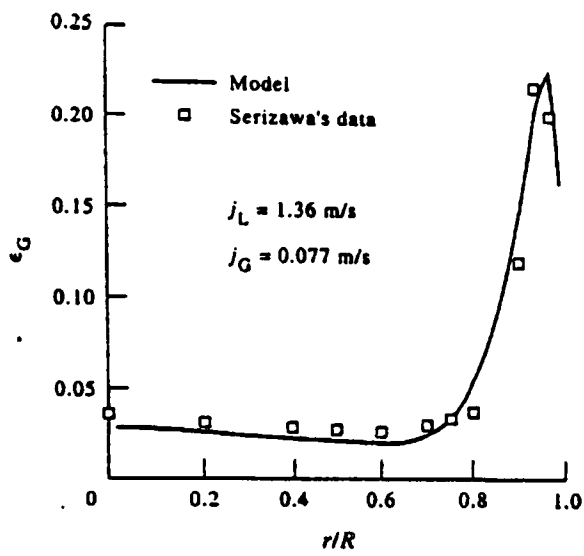
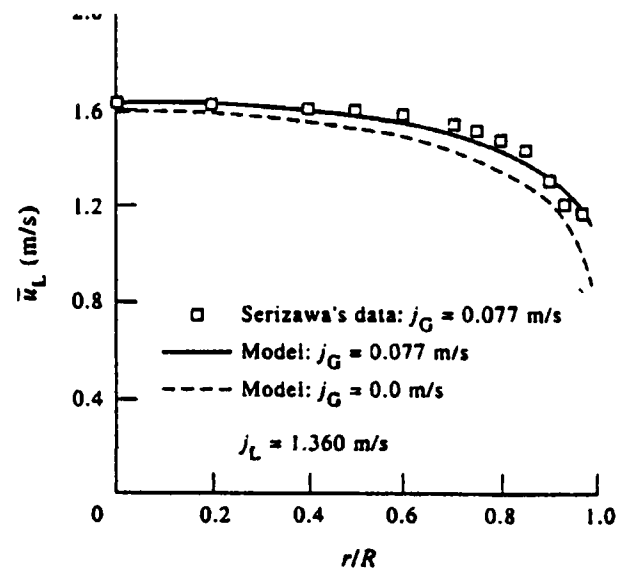


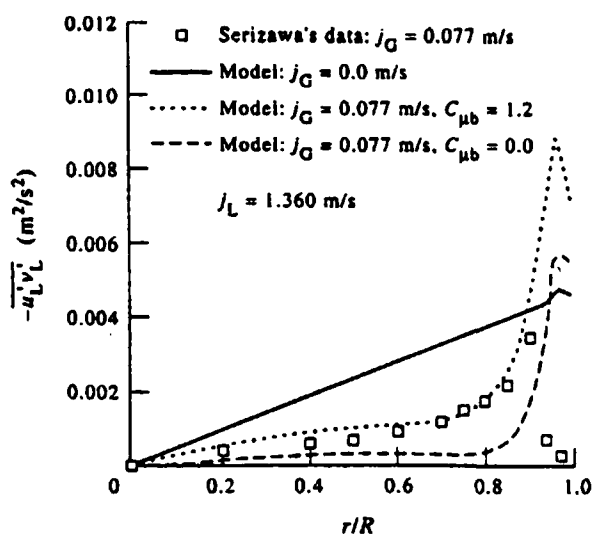
Figure 20. Particle dispersion in a plane mixing layer. Prediction results compared with the experimental data (Ishima 1993): (a) radial particle mean velocities; (b) radial velocity fluctuations; (c) normalized number densities. Taken from the Proceedings of the Sixth Workshop on Two-Phase Flow Prediction (ed. by M. Sommerfeld 1992).



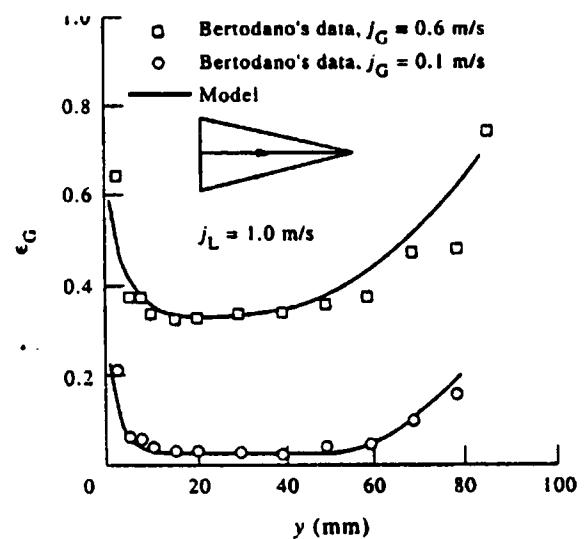
(a) Comparison with Serizawa's data: void fraction.



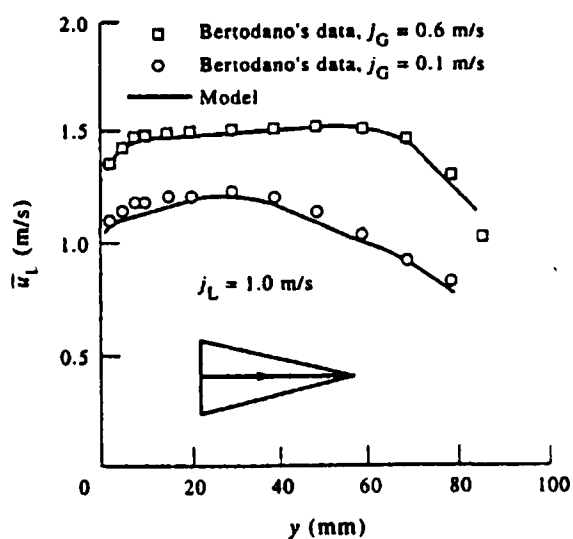
(b) Comparison with Serizawa's data: average axial velocity.



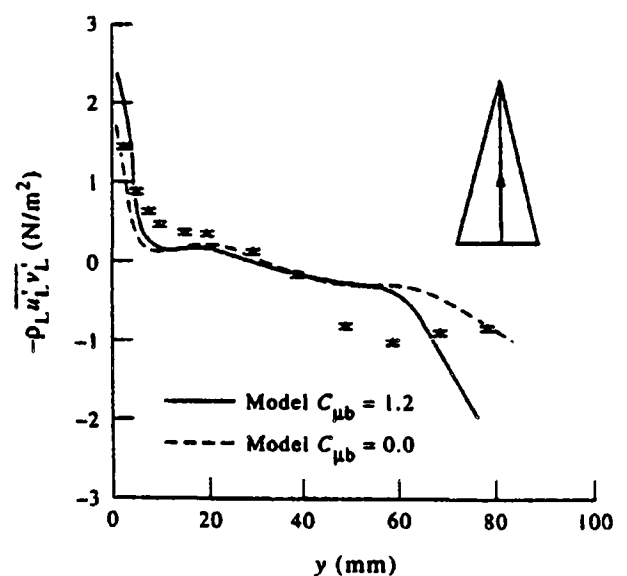
(c) Comparison with Serizawa's data: shear stress



(d) Comparison with Lopez de Bertodano's data: void fraction (triangular duct).

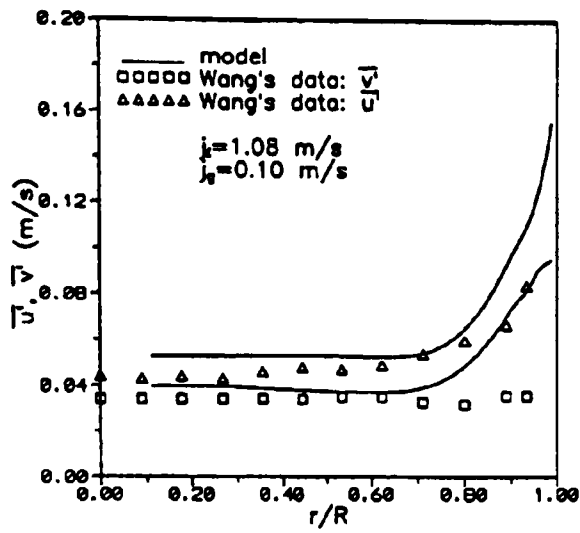


(e) Comparison with Lopez de Bertodano's data: average axial velocity (triangular duct).

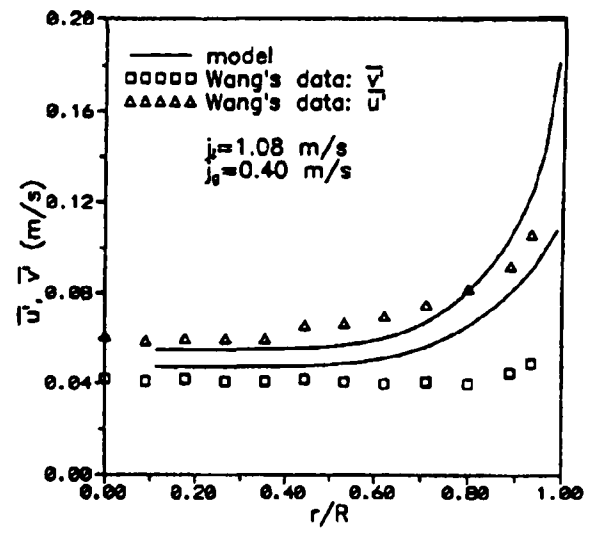


(f) Comparison with Lopez de Bertodano's data: shear stress (triangular duct).

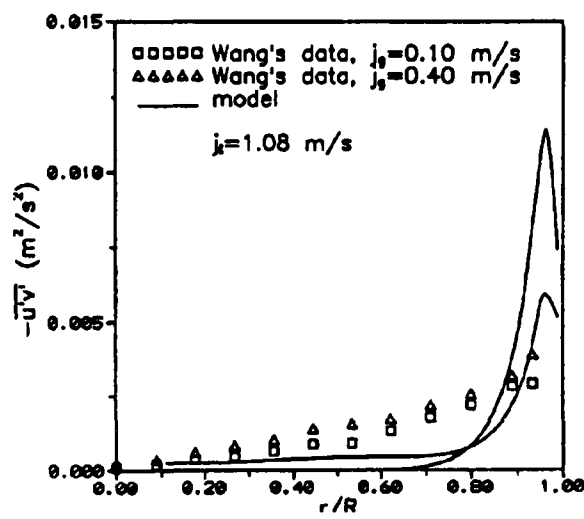
Figure 21. Prediction of two-phase turbulence and phase distribution in bubbly flow using a two-fluid model together with the modified $k-\epsilon$ model. Taken from Lopez de Bertodano *et al.* (1994).



(a) Comparison with Wang's (1987) data: velocity fluctuations ($j_f=1.08$ m/s, $j_g=0.10$ m/s)



(b) Comparison with Wang's (1987) data: velocity fluctuations ($j_f=1.08$ m/s, $j_g=0.40$ m/s)



(c) Comparison with Wang's (1987) data: shear stress

Figure 22. Comparisons of turbulence properties between numerical simulations and the experimental data. Taken from Lopez de Bertodano *et al.* (1994).

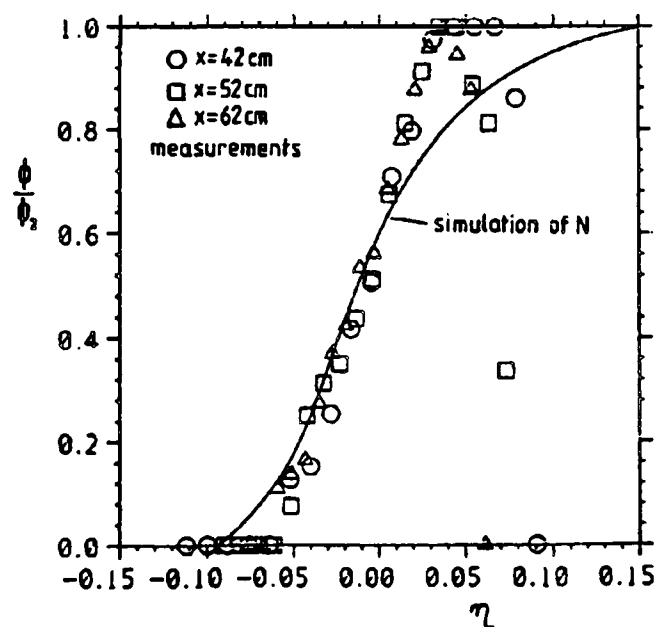


Figure 23. Void fraction profiles in a vertical downflowing mixing layer (Experimental data and simulation). Taken from Hunt *et al.* (1988).

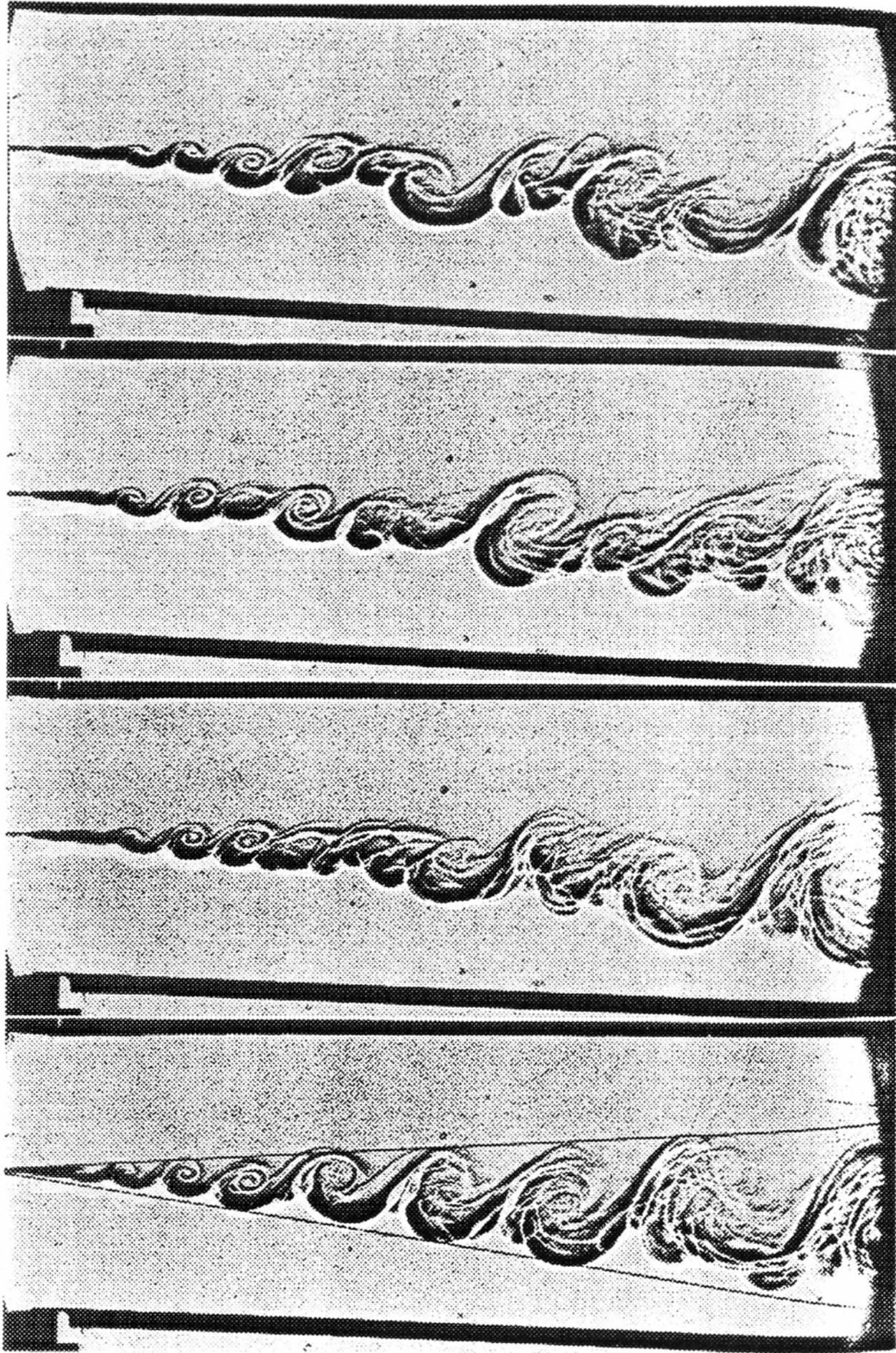


Figure 24. Shadowgraph visualization of large-scale spanwise vortices in a plane mixing layer, taken at random times. Taken from Brown & Roshko (1974).

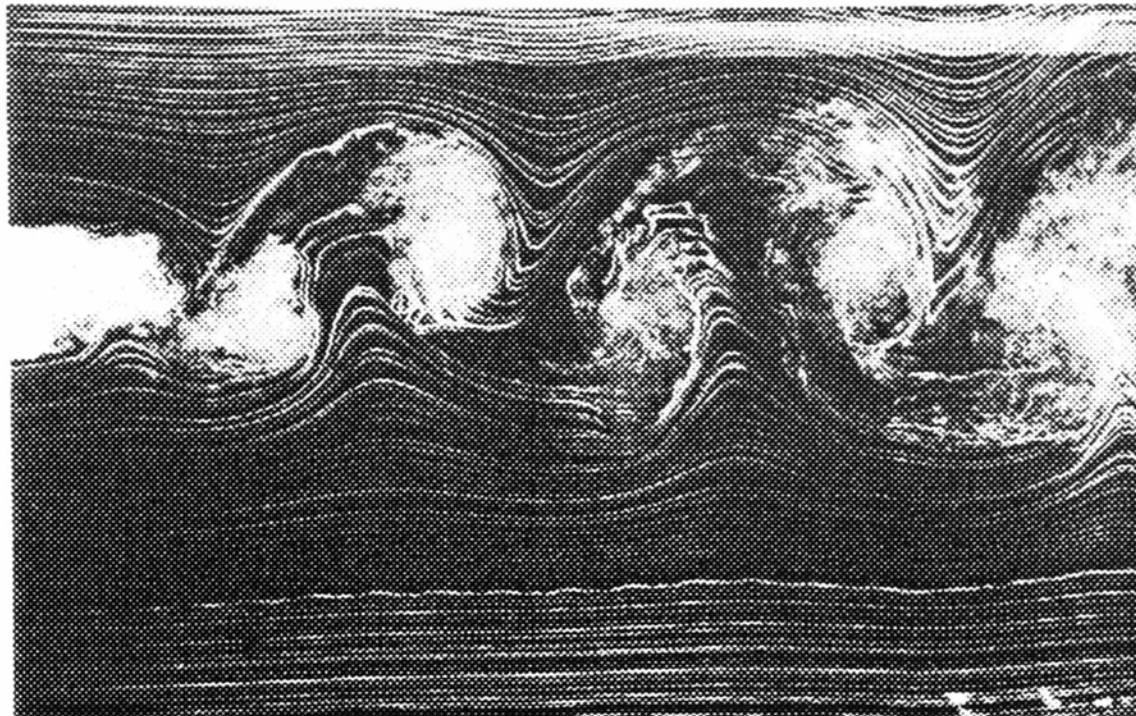


Figure 25. The smoke visualization of the large-scale vortex structures in a plane wake downstream of a bluff body. Taken from Crowe *et al.* (1993).

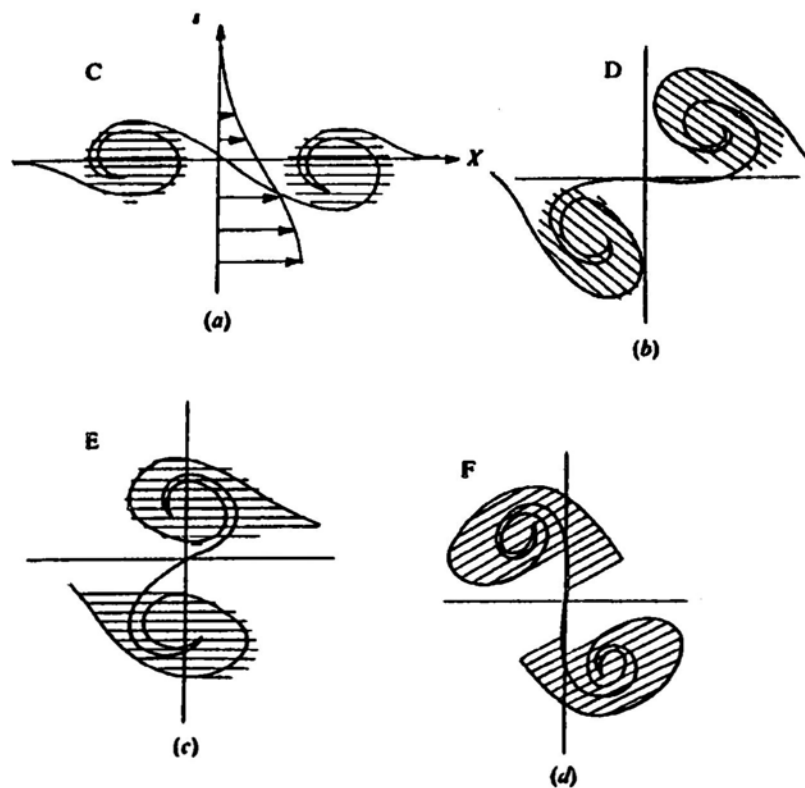


Figure 26. Schematics of four successive phases (configurations C, D, E and F) of the pairing process. Taken from Hussain (1986).

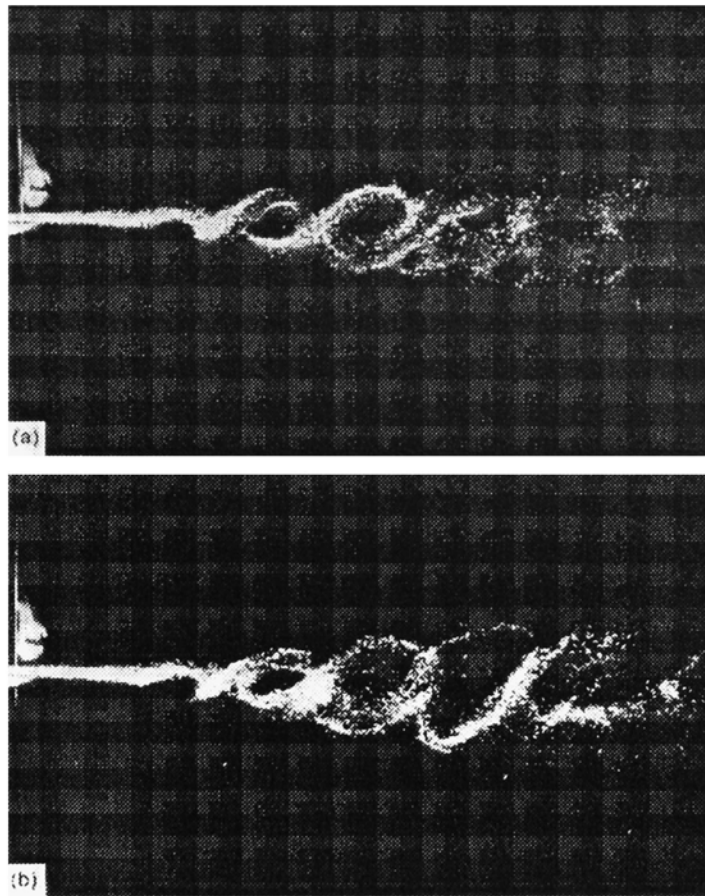


Figure 27. Dispersion pattern for $40\ \mu\text{m}$ glass particles released in the fast stream of a plane mixing layer. $U_1=5\ \text{m/s}$, $U_2=2\ \text{m/s}$; (a) natural flow, (b) forced at first subharmonic of natural instability. Taken from Wen *et al.* (1992).

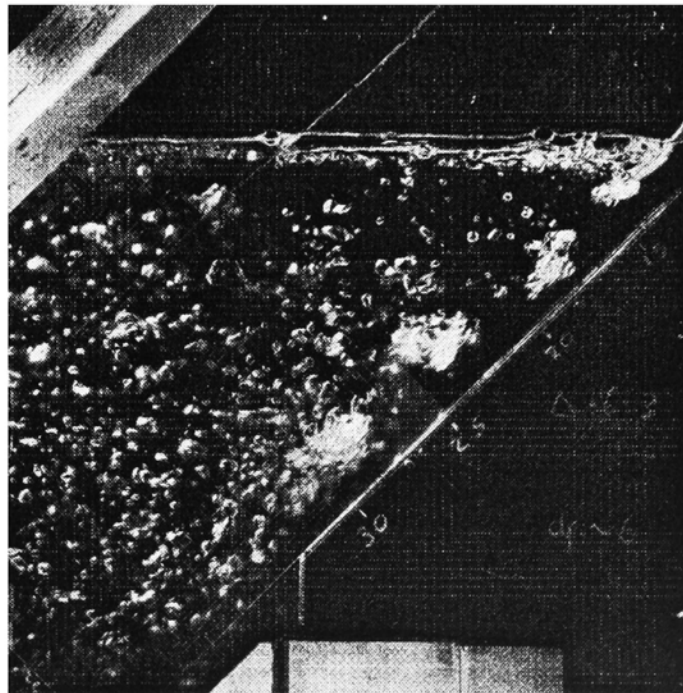


Figure 28. Train of bubbly vortices in penetrating plunge-point flow. Depth of the jet about 2 cm; impact velocity about 2 m/s. Taken from Sene *et al.* (1994).

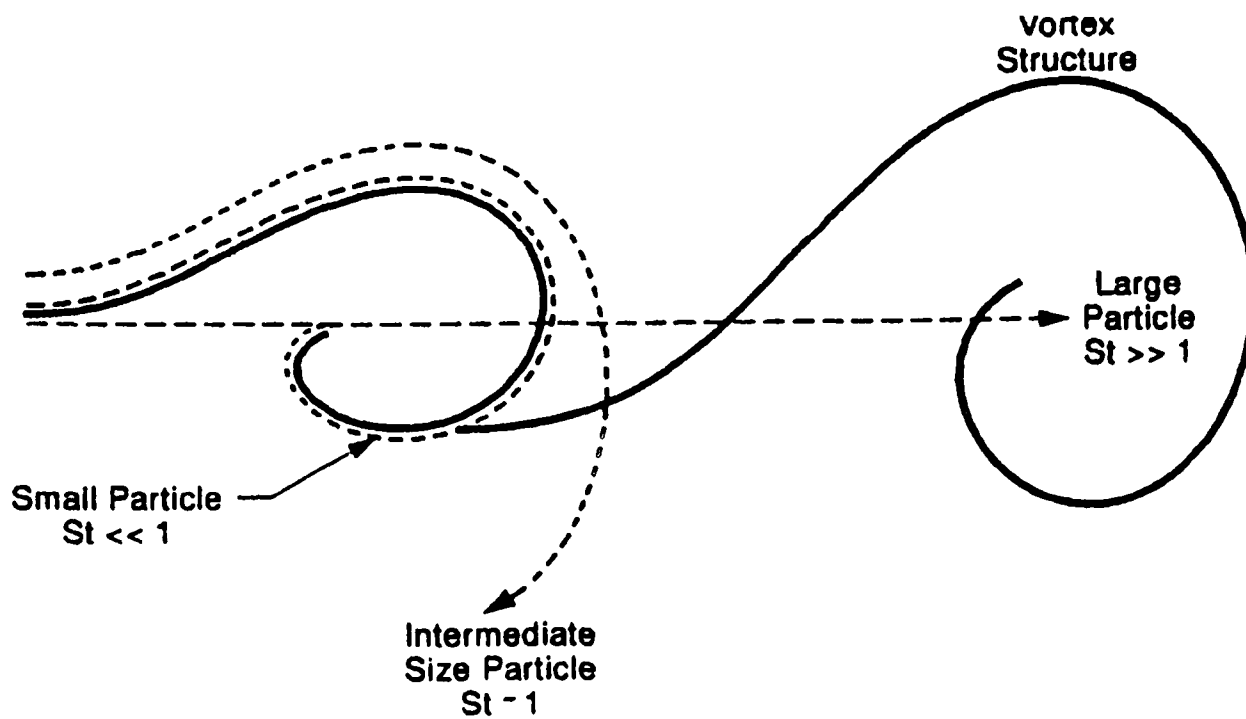


Figure 29. Conceptual model for Stokes number effect on particle spreading in organized vortex structures. Taken from Crowe *et al.* (1993)

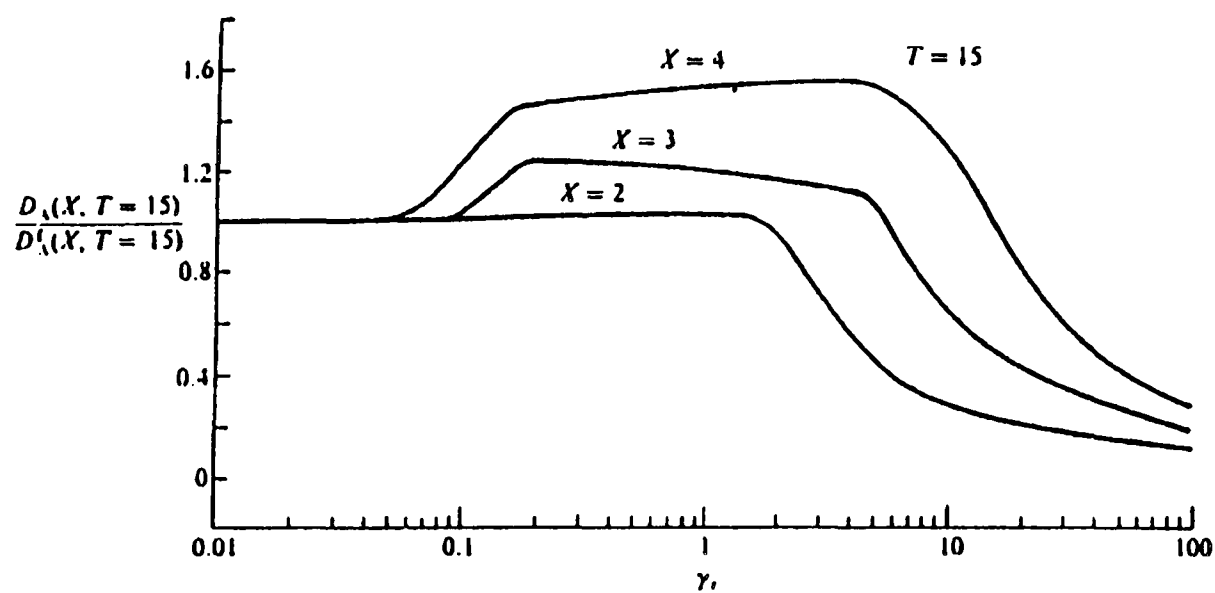


Figure 30. Normalized particle distribution functions at various downstream locations of an axisymmetric jet as a function of Stokes number. Taken from Chung & Troutt (1988).

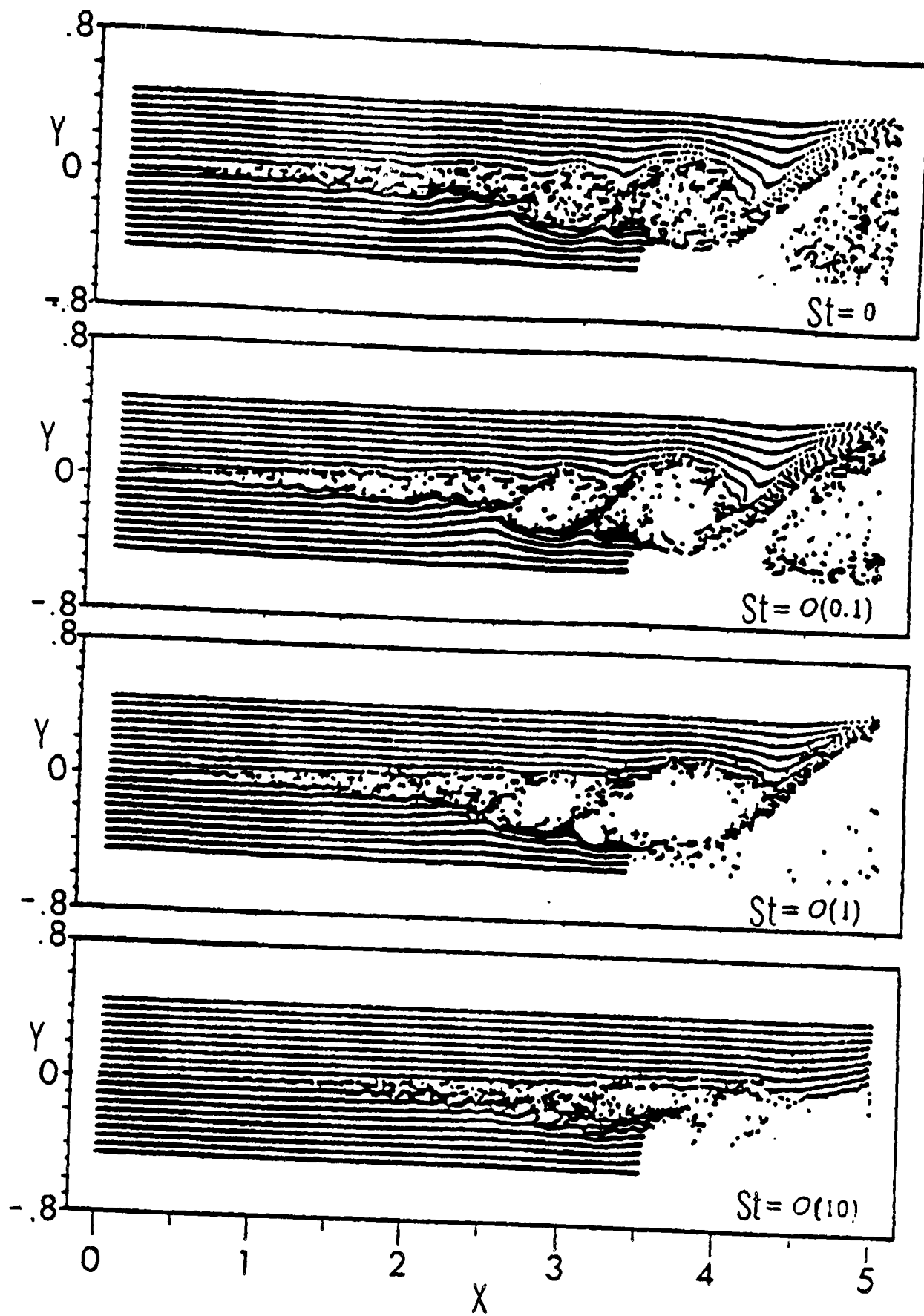


Figure 31. Instantaneous particle dispersion patterns for tracers and particles with different Stokes numbers. Taken from Ashurst (1979).

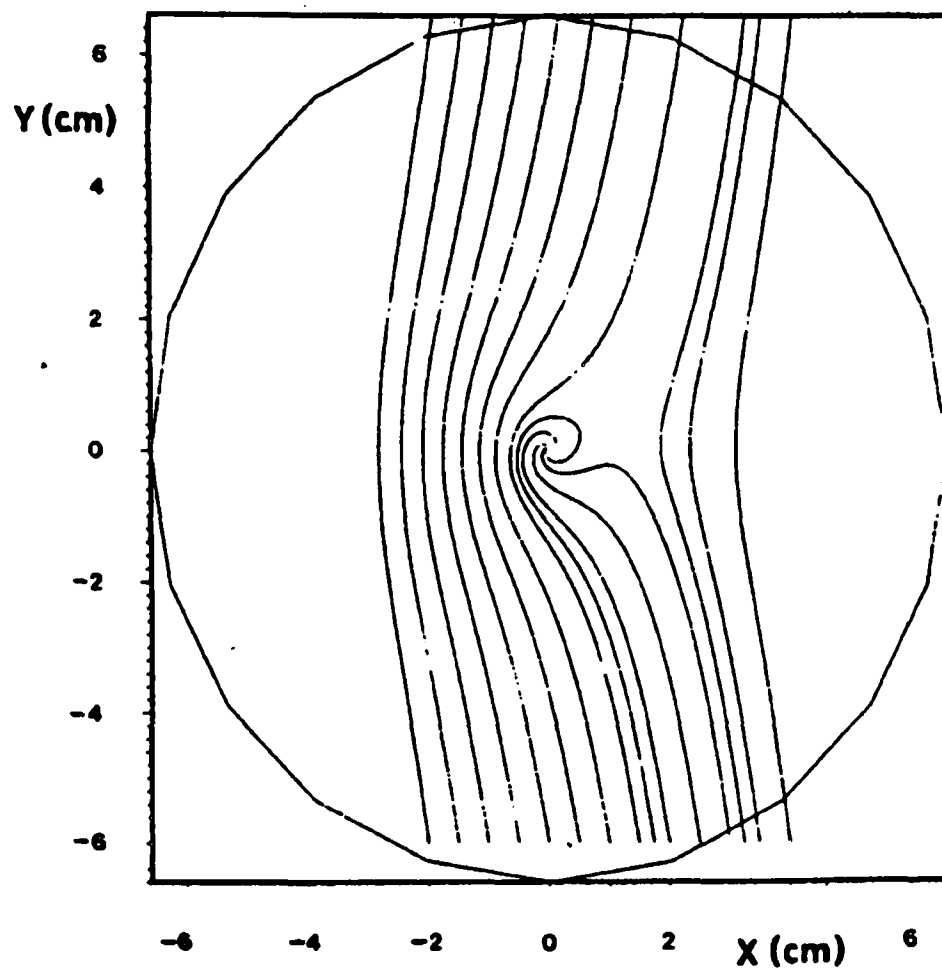


Figure 32. Bubble trajectories computed near a line vortex. Notice that a narrow band of X starting points lead to bubble capture. Taken from Thomas *et al.* (1983)

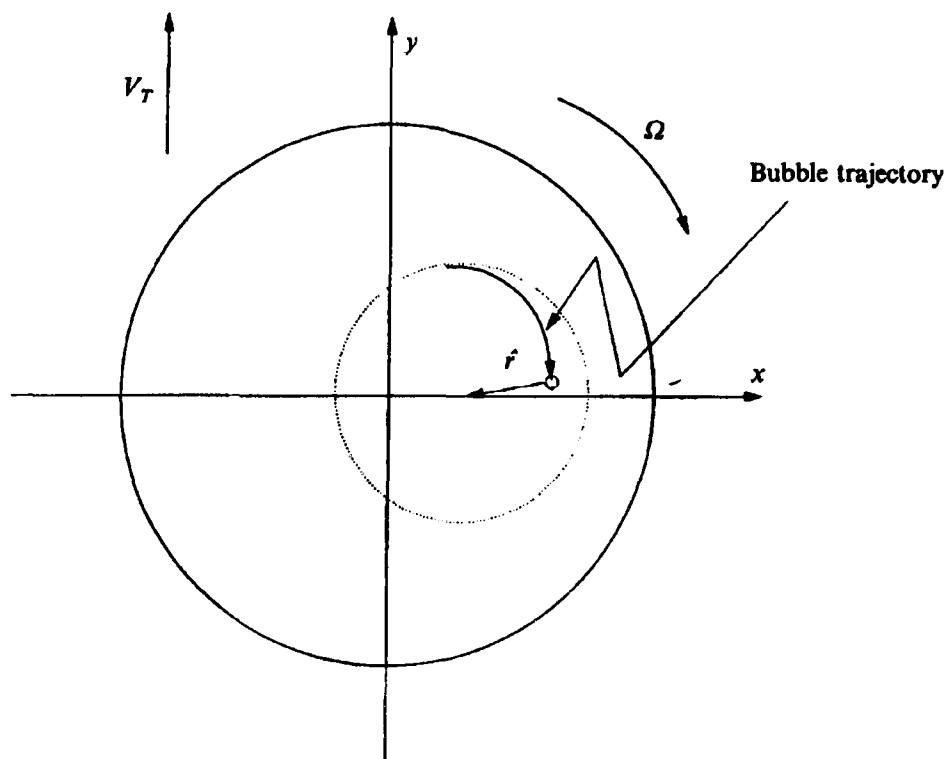


Figure 33. Sketch showing bubble trajectory inside a Rankine vortex with inertial and trapping forces, based on analysis of Auton's force law. Taken from Sene *et al.* (1994).

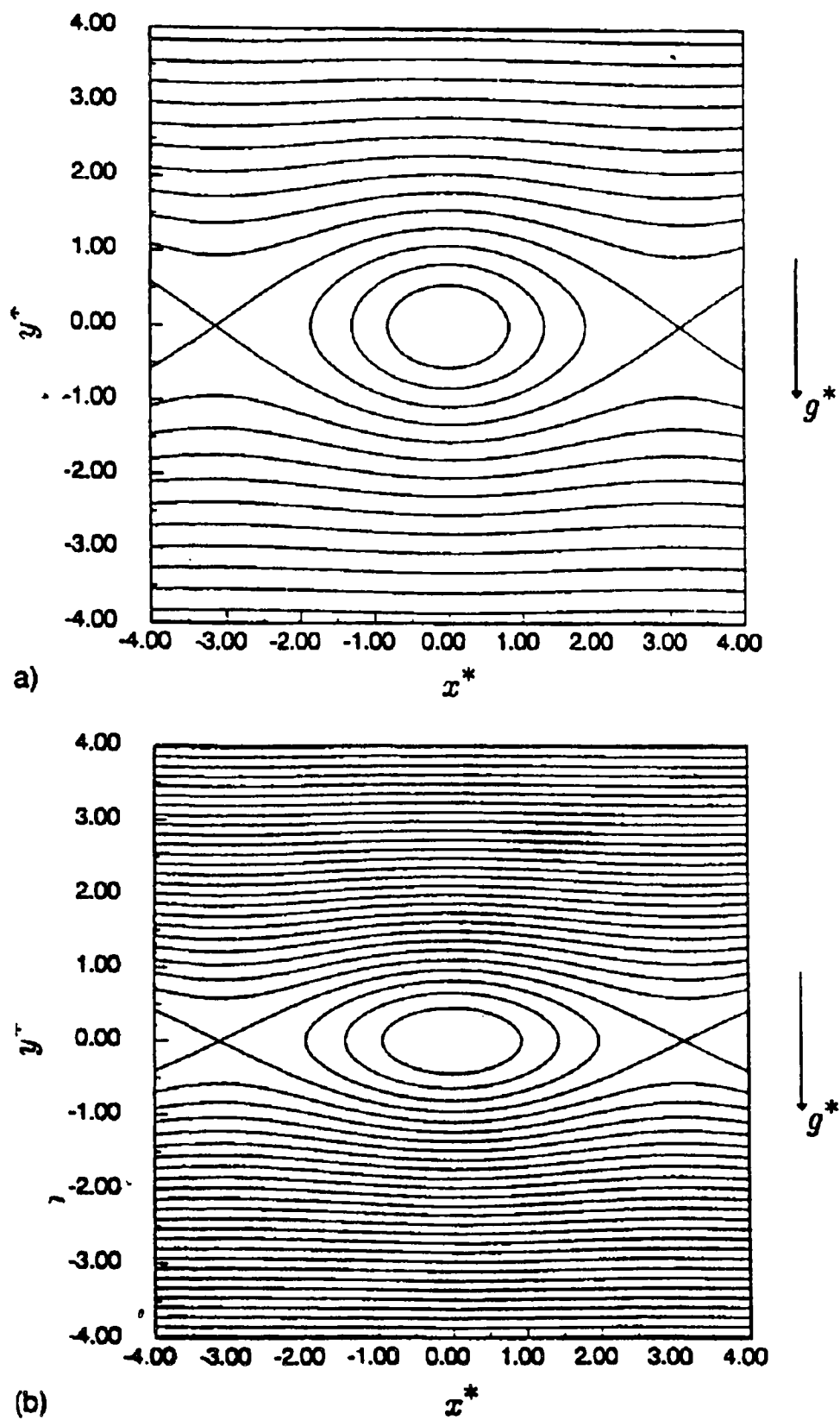
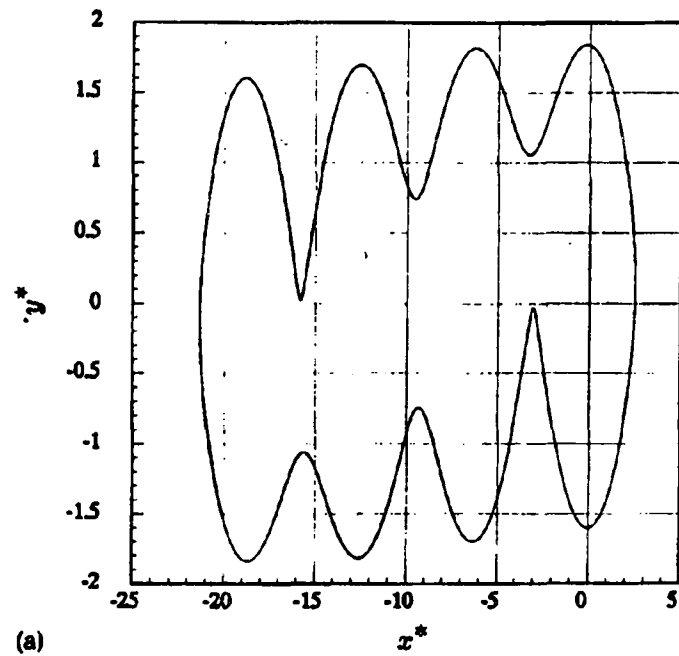
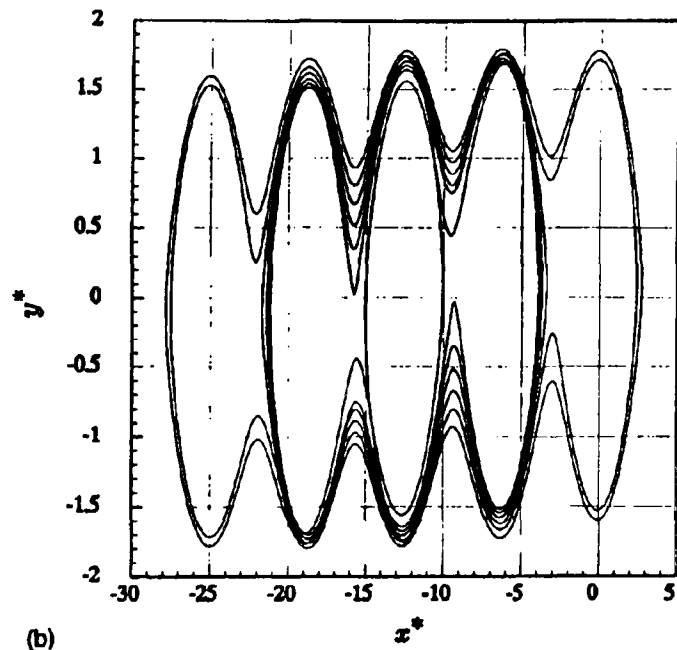


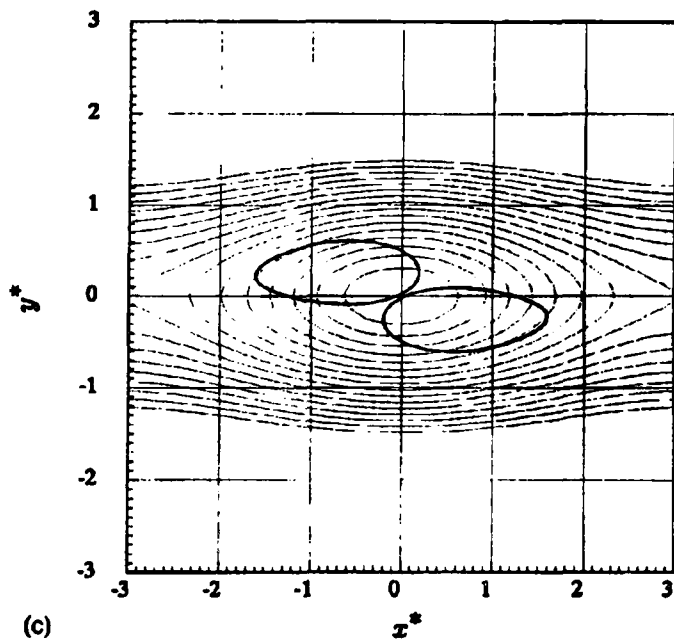
Figure 34. Streamlines associated with the stream function ψ for (a) $k=0.50$; (b) $k=0.25$. The arrows indicate the direction of gravity. Note that the cateye shrinks as k decreases. Here constant k is a parameter that determines the distribution of vorticity. Taken from Tio *et al.* (1993).



(a)



(b)



(c)

Figure 35. Closed particle orbits for $B=0.0$ and (a) $A=50.0$, $R_{ep}^*/A=400.0$, $\epsilon=0.60$, $k=0.95$; (b) $A=50.0$, $R_{ep}^*/A=400.0$, $\epsilon=0.62$, $k=0.85$; (c) $A=75.0$, $R_{ep}^*/A=50.0$, $\epsilon=0.50$, and $k=0.25$. The effect of the lift term is included in (c). Here A is the ratio of the response time of particle motion to the characteristic time of the fluid flow and B is a gravitational parameter. Taken from Tio *et al.* (1993).

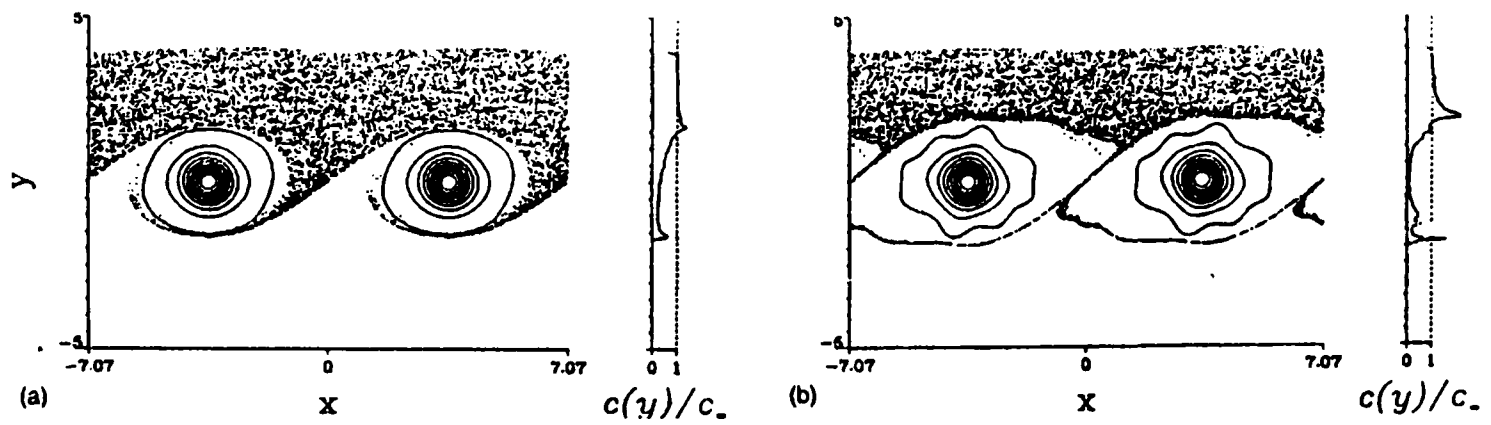


Figure 36. Vorticity contours with particle positions superimposed for $St=1.0$ at (a) $t=18.0$ and (b) $t=30.0$. Sharp spikes in the particle concentration profile indicated the particles' strong preferential residence along the stagnation streamline of the flow field. Taken from Martin & Meiburg (1994).

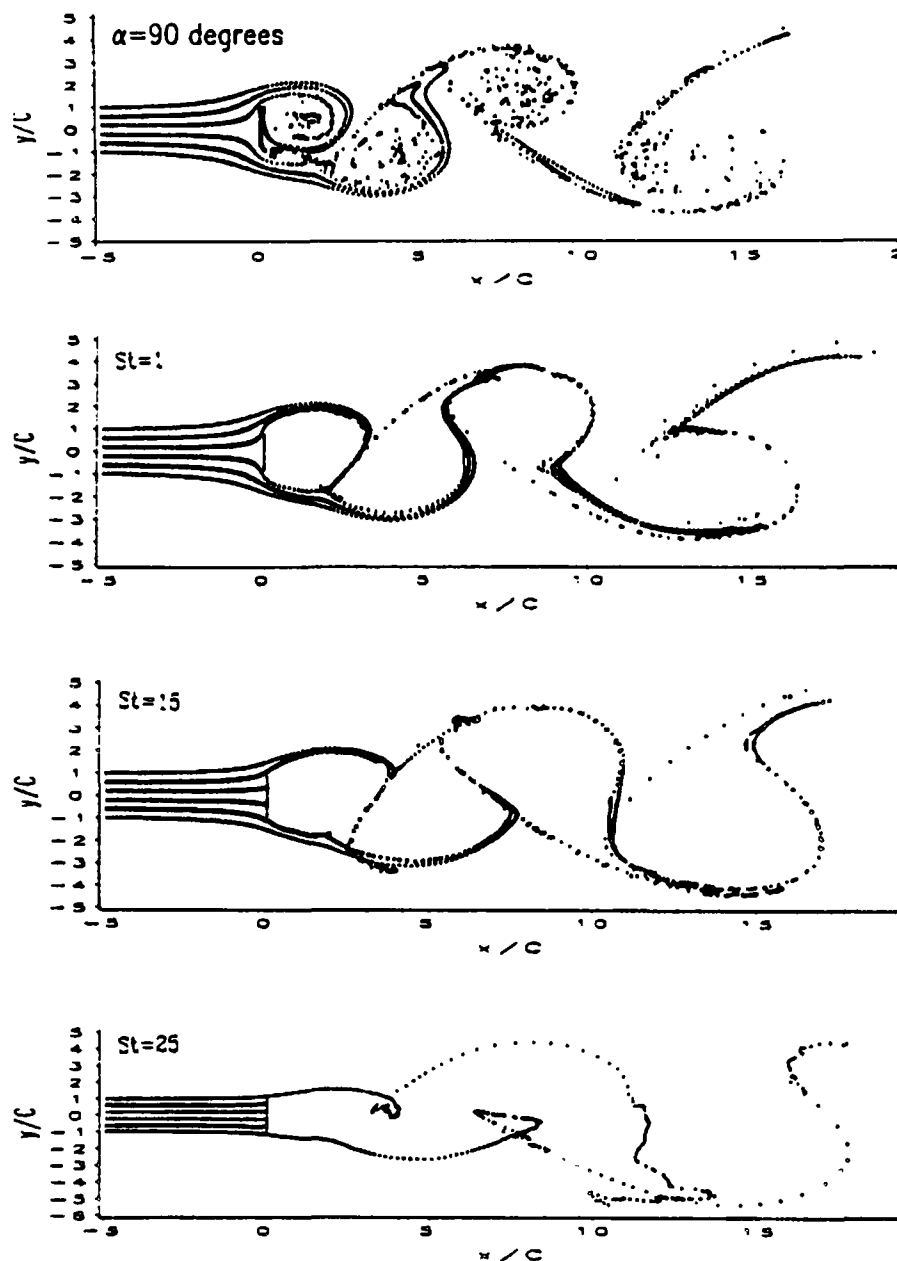


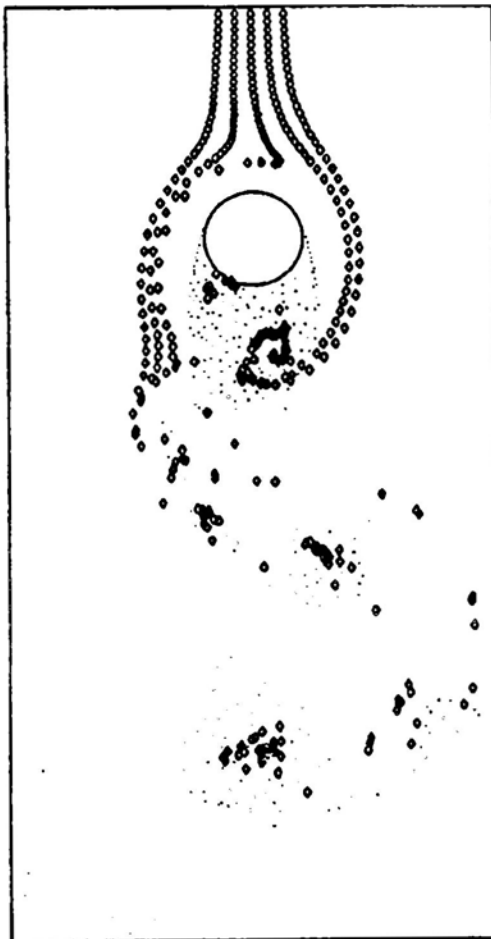
Figure 37. Simulation of the flow around a flat plate using discrete vortex method. Particle dispersion pattern is influenced by coherent turbulent eddies. Taken from Chein & Chung (1988).



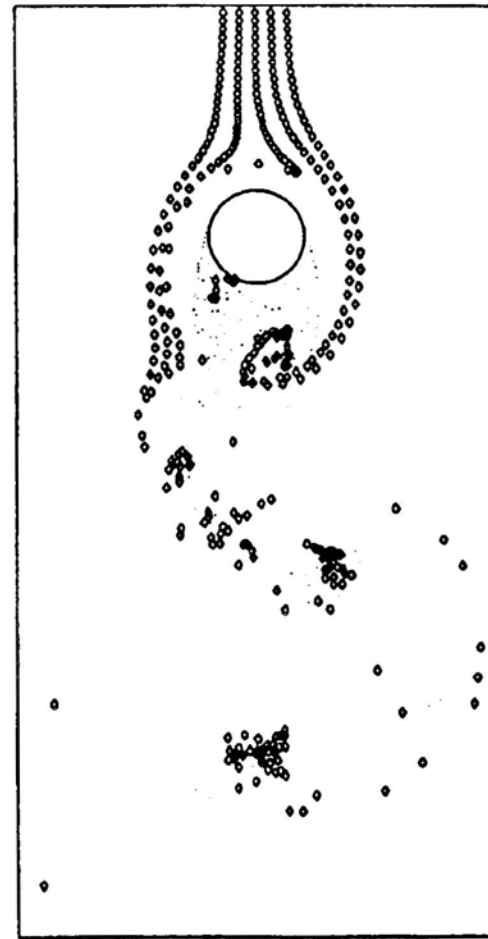
a) $U = 1.4$ m/s



b) $U = 2.2$ m/s



a) downflow $U = 1.4$ m/s



b) downflow $U = 3.0$ m/s

Figure 38. Experimental bubble streakline visualisation photographs (cylinder radius: $R=0.015$ m) and numerically simulated bubble streaklines ($t=20$, $R=0.015$ m, $d_B=3$ mm). Taken from Bayly & Rielly (1994).

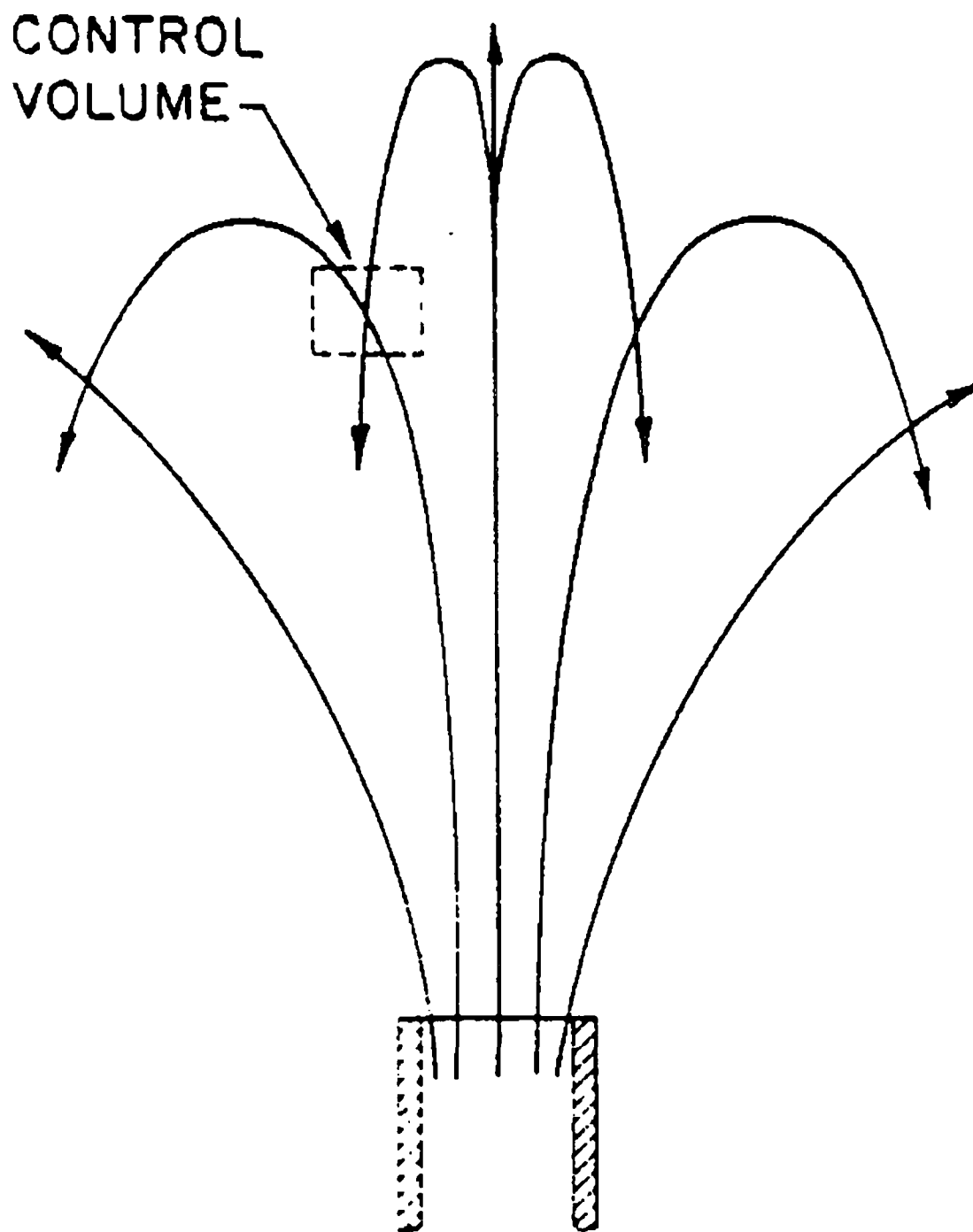


Figure 39. Control volume with two particle velocities. A stream of particles is assumed to be emitted from a vertical source. Two possible particle trajectories are shown which may traverse the same computational cell. Using exclusive Eulerian modelling approach would only predict one velocity direction. However, exclusive Lagrangian modelling approach can offer a correct configuration to this problem. Taken from Crowe (1982).

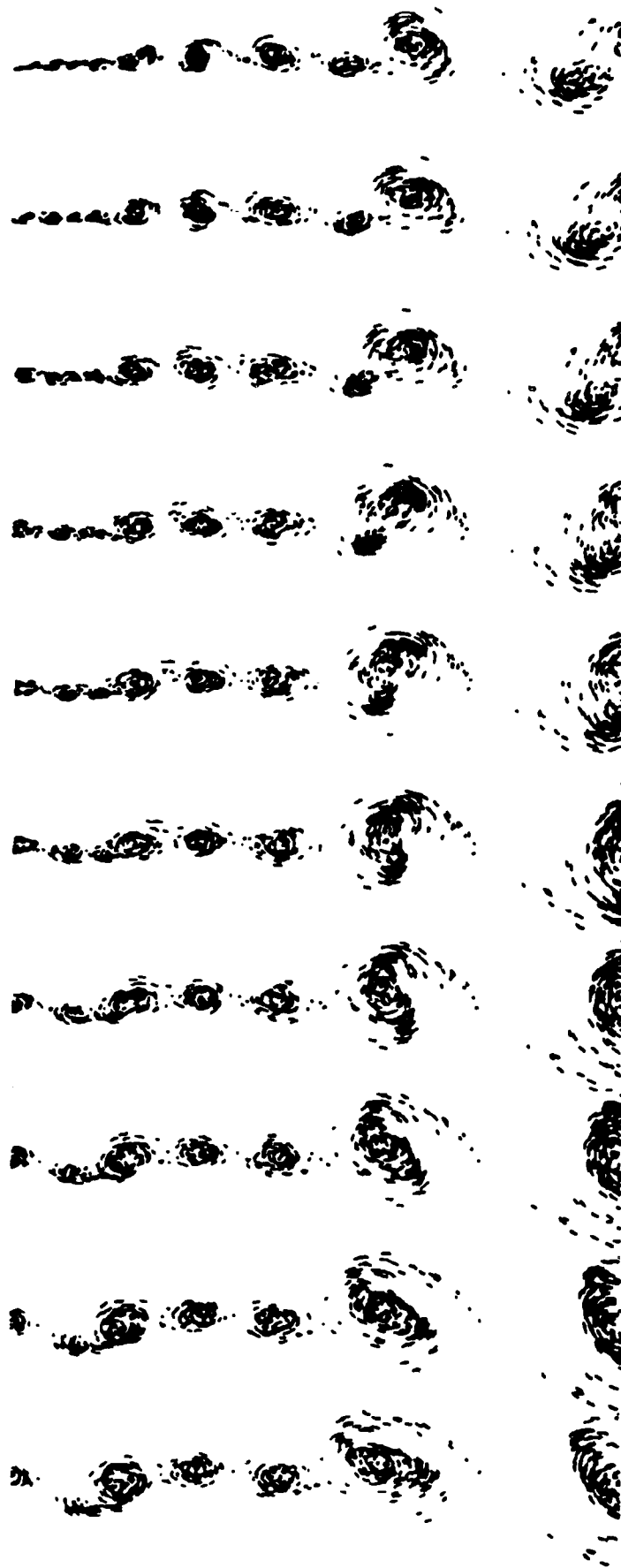


Figure 40. Simulation of the mixing layer: streakline plots of each discrete vortex for a unit time ($L/\Delta U$) with respect to the average velocity ($L\Delta U/\nu=1000$). Taken from Ashurst (1979).

CHAPTER 2: PREDICTION OF VOID FRACTION PROFILES USING GRADIENT DIFFUSION MODELS

SUMMARY

Adopting a similar approach to Beyerlein *et al.* (1985), void fraction distributions in turbulent two-phase bubbly air/water upflows and downflows in a vertical pipe were analyzed using a simple transport model which was based on the assumptions that the lateral shear-induced lift force acting on bubbles (Thomas *et al.* 1983) is balanced by bubble dispersion, and that bubbles in the flow are conserved i.e. no bubble breakup or coalescence occurs. The model shows the importance of considering the lateral lift force experienced by bubbles as they move relative to the liquid phase in a non-uniform velocity field. This force causes the bubbles to accumulate near the wall forming a high concentration for upward flow, while the concentration increases toward the centre of the pipe for downward flow. The eddy diffusivity, as widely used in calculation of single-phase flow, can be extended to include the effect of pseudo-turbulence (Lance & Bataille 1991) due to bubbles, and thus can be linked with the bubble dispersion coefficient. It is also demonstrated that the transverse or radial pressure gradient induced by the Reynolds stress exerts a lateral force on the bubbles, and thus affects their distribution in the flow. A comparison of the model predictions with experimental data from Serizawa *et al.* (1975) for upflows and Wang *et al.* (1987) for both upflows and downflows shows that our model predicts void fraction peaking near the wall for upflows and coring at the centre-line for downflows. Compared with similar investigations (e.g. Drew & Lahey 1982; Lopez de Bertodano *et al.* 1990) of the same problem, our model approach appears to be simpler and more suitable for engineering calculations.

1 INTRODUCTION

One of the most important, and yet still poorly understood aspects of two-phase bubbly flow is the lateral phase distribution mechanism which is represented by void fraction profiles. Such examples can be found in two-phase flows in vertical ducts and channels. Since void fraction distribution plays an important role in affecting the flow structure of two-phase bubbly flow, a great deal of research effort has gone into this topic over the past twenty years. Unfortunately, little definitive progress has been achieved because of the complexity of two-phase bubbly flow. However, there does seem to be an overall consensus that void fraction peaking near the wall occurs in concurrent upflows and concentration on the axis occurs in concurrent downflows (e.g. Kobayashi *et al.* 1970; Serizawa *et al.* 1975; Wang *et al.* 1987; Žun 1987). The physical mechanism behind these processes is still not entirely clear even though there have been many explanations offered to account for this phenomenon. Contributory physical features were recently summarised by Žun (1987) as follows:

- (1) Magnus and Bernoulli forces acting on the bubbles, viewed as spinning spheres
(e.g. Zuber 1960);
- (2) Reynolds mean radial pressure gradient due to transverse velocity fluctuations in the liquid (e.g. Subbotin *et al.* 1971);
- (3) transverse lift forces, and lateral motion due to spiralling of the bubbles
(e.g. Žun 1980, see figure 1);
- (4) interaction between bubbles and the structure of the turbulent boundary layer
(e.g. Rouhani 1976, see figure 2), so referred to as the wall-vortex interaction and attributed to rolling vortices near the wall;
- (5) bubble diffusion (e.g. Hinata 1980);

- (6) turbulent structure of bulk liquid leading to void peaking occurring in the region of largest turbulent kinetic energy (e.g. Drew and Lahey 1982);
- (7) the finite size of the bubbles confining their domain of movement (e.g. Serizawa *et al.* 1975).

In addition, recent study on bubbly boundary layers at Lyon (Moursali *et al.* 1995) has revealed that the bubble lateral migration and the significant deceleration of the bubbles near the wall surface are two main mechanisms responsible for the void peaking phenomenon. Among all the explanations mentioned above, it is now broadly held that (2) and (3) are the dominant forces determining the phase distribution both in the pipe (Lopez de Bertodano *et al.* 1990) and in the free shear flows (Thomas *et al.* 1983). Earlier studies and interpretations indicate the following main contributions.

The lateral void fraction distribution for two-phase bubbly flow was first analyzed by Bankoff (1960), assuming both the velocity distribution and the void fraction concentration follow a power law distribution. This, of course, precludes any description of wall peaking. Levy (1963) extended the mixing length theory used widely in single-phase turbulent flow to two-phase flows and, like Bankoff, found that void fraction peaks on the centre-line of the pipe. Kobayashi *et al.* (1970) experimentally observed "void peaking" near the wall for two-phase upward flow and proposed an empirical formula to describe the void fraction distribution of two-phase bubbly and slug flows. However, this approach offered no insight into the physical phenomena involved in lateral bubble transport. Moujaes and Dougall (1985) deduced the radial void fraction profiles and velocity distribution from a two-fluid model of the momentum equations based on several key assumptions, but their model failed to capture wall peaking of voidage.

As is well known, there is a Reynolds mean radial pressure gradient induced by the shear turbulence gradient across a turbulent pipe flow. In contrast, for laminar flows this radial gradient is zero. The transverse turbulent pressure gradient must exert a lateral force on bubble motion due to its relatively low axial inertia response. However, in order to properly evaluate the lateral pressure gradient, the turbulence structure needs to be described appropriately, ideally extending to the interaction between turbulence and the bubbles. Various turbulence transport models developed for single-phase flow have been modified to apply to bubbly flow (e.g. Kataoka & Serizawa 1989). Drew & Lahey (1982) introduced a two-fluid model in conjunction with a mixing length model to represent the turbulence structure. Their results qualitatively reproduced void peaking near the wall for upflows and 'coring' on the centerline for downflows. Indeed, it was shown that shear turbulence could be the dominant mechanism for lateral phase distribution. However, in order to obtain void fraction profiles matching those from experimental data, the turbulent kinetic energy distribution of the liquid phase and its anisotropic structure had to be prescribed *a priori*. Lee *et al.* (1989) adapted the one-phase k - ϵ model for bubbly flow with some modifications, being able to capture the phenomena of voidage peaking. Lopez de Bertodano *et al.* (1990) extended Lee's *et al.* work to use the Reynolds stress model (they called it the τ - ϵ model) for the effect of anisotropy. Lopez de Bertodano *et al.* (1994a) further extended their work to prediction of the phase distribution for bubbly flow in vertical ducts using a k - ϵ model with two time constants. A simple lateral transport model, using a similar approach to Beyerlein's *et al.* (1985), was also presented by Yang and Thomas (1992) for the problem with one equation closure. While most of the recent approaches partially reproduce experimental findings, none do so adequately. This indicates that certain physical mechanisms contributing to phase distribution in the pipe are still not well understood and

therefore need more exploration.

The effect of the bubbles on the turbulence structure is often significant, and a strong interaction has been experimentally observed. For example, Serizawa *et al.* (1975) and Wang *et al.* (1987) have shown that when the bubble void fraction is higher the turbulence near the centre of the pipe may be suppressed, and the intensities can be lower than those for single-phase flow. On the other hand, for lower void fraction Lance & Bataille (1991) have demonstrated that two-phase bubbly grid-generated turbulence can be linearly superimposed (i.e. as liquid grid turbulence and as bubble-induced turbulence), indicating a weak coupling between the two contributions. A similar argument was made earlier by Theofanous & Sullivan (1982) in interpreting their measurements along the centerline of a pipe at low flow rate. The same principle has been incorporated in calculation methods for bubbly flow. For example, Sato *et al.* (1981) proposed that the turbulence in the liquid phase can be decomposed into two parts, one due to the mean shear turbulence and the other due to the pseudo-turbulence caused by bubble disturbance. He thus expressed the eddy diffusivity as a simple linear combination of the diffusivity due to single-phase turbulence and that due to bubbles. Even though this naive prescription lacks a firm physical basis, the assumption has been widely adopted for modelling due to its simplicity (e.g. Lopez de Bertodano *et al.* 1994b).

The effect of the buoyancy force caused by the presence of bubbles on the shear stress distribution in the pipe was highlighted by Thomas (1984) using a very simple conceptual analysis (figure 3), adapted for modelling thermal convection with significant buoyancy forces confined to the wall region. For upflows the effect of buoyancy force is to locally

decrease the shear stress. In contrast, for downflows the buoyancy force augments the local shear stress. It should be noted that when buoyancy is large enough the shear stress may even be negative for bubbly upflow, and such a major reduction in the forced convection may result in a heat transfer crisis (e.g. Hall & Jackson 1969).

Experimental measurements of void fraction and turbulence structure in pipes have been made by numerous investigators, notably Serizawa *et al.* (1975); Wang *et al.* (1987) and Liu (1993), whose data is more complete than most others. For bubbly upflows, they all found void peaking near the wall, as shown in figure 4. Whereas, for downflows, Wang *et al.* (1987) found the opposite trend, as shown in figure 5. Liu (1993) investigated the effect of bubble size on void fraction distribution in a vertical pipe and found the void fraction distribution to be very sensitive to bubble size. When the bubble size increases to some limiting value, the void profile can change from void peaking near the wall to void accumulating in the centre. Most recent experimental investigations on vertical bubbly flow have extended to flow through sudden area expansions (e.g. Bel Fdhila *et al.* 1992). They found a voidage amplification within the reattaching free shear layer, as expected from the theoretical work by Thomas *et al.* (1983); see also Sene *et al.* (1994).

It should be noted here that different contributions to the lateral force experienced by the bubbles (e.g. from the lift force due to local shear and from pressure gradient due to Reynolds stress variations) have been itemised only in recent years. The lift force (Auton *et al.* 1987) drives bubbles towards the wall in upflows and away from it in downflows. The pressure force always acts so as to attract bubbles towards the wall because the local static pressure is lowest near the wall due to non-uniformity of the radial component eddy stress.

Even though their magnitudes are comparable, documented experimental findings indicate the effect of the lift force is dominant. According to this argument, Beyerlein *et al.* (1985) proposed a lateral transport model which can also be derived from the general force law (Thomas *et al.* 1983; see appendix I). Recent work by Kowe (cited by Hunt *et al.* 1994) on bubble motion in turbulent pipe flow addressed the different effects on bubble motion by calculating the trajectories of bubbles in an inclined channel flow. The flow field was generated using kinematic simulation from a sum of random Fourier modes. The simulation results showed the important finding that bubbles only begin to move towards the wall for $V_T/u' > 1$ for upflows, and are driven towards the centre of the channel for $V_T/u' > 1$ for downwards flows. Here V_T is the terminal velocity of bubble in still water and u' is the turbulent fluctuation velocity in the flow.

In our present study, a relatively simple lateral bubble transport model is described, following the work of Beyerlein's *et al.* (1985), and further developing the approach reported in Yang & Thomas (1992). This model is used to predict void fraction profiles in two-phase bubbly upward and downward flows. Comparisons of the predictions with experimental data (Serizawa *et al.* 1975, Wang *et al.* 1987) are given, and show that the lift force acting on bubbles plays a key role in determining the void fraction profiles in two-phase bubbly flow. We begin with presentation of a simple transport model, closure model and boundary conditions in section 2. Section 3 briefly describes numerical procedures for solving the model equations. Section 4 presents results and discussions. Our simulations are summarised and conclusions drawn in section 5.

2 TRANSPORT MODEL

2.1 Two-phase Mass Conservation and Force Balance

The Eulerian conservation equations for each phase may be averaged using different averaging methods (e.g. time averaging, volume averaging, ensemble averaging etc.) (e.g. Drew 1983). Such averaged equations are now widely referred to as the two-fluid model (e.g. Drew 1983). For air/water flow, if the bubbles in the flow are conserved (i.e. no breakup and coalescence) then the local mass conservation for each phase can be expressed as

$$\frac{\partial \phi_k}{\partial t} + \nabla \cdot (\phi_k \mathbf{u}_k) = 0 \quad (1)$$

where the subscript k represents the liquid or gas phase, ϕ_k is the scalar variable of interest for phase k and \mathbf{u}_k is the corresponding velocity. If we replace ϕ_k with the volume fraction of phase k , α_k , then time-averaging for equation (1) gives:

$$\frac{\partial \alpha_k}{\partial t} + \nabla \cdot (\alpha_k \mathbf{u}_k) + \nabla \cdot (\overline{\alpha'_k \mathbf{u}'_k}) = 0 \quad (2)$$

Here an overbar, usually used to represent a time-average, is dropped for convenience. We now focus on the gas phase. For convenience, the subscript k is now replaced by b for bubble and L for liquid. Also, α stands for the bubble void fraction and the time-average symbol overbar for α is dropped, so $\alpha \equiv \alpha_b = 1 - \alpha_L$. By analogy with single phase turbulence transport, we suppose a simple gradient diffusion approximation for bubbles, which implies:

$$\overline{\mathbf{u}'_b \alpha'} = -\varepsilon_b \nabla \alpha \quad (3)$$

where ε_b is the bubble dispersion coefficient. Substitution of (3) into (2) yields the simple advective-diffusive dispersion model found in all Reynolds averaged formulations (e.g.

Tennekes & Lumley 1972)

$$\frac{\partial \alpha}{\partial t} + \nabla \cdot (\alpha \mathbf{u}_b) = \nabla \cdot (\varepsilon_b \nabla \alpha) \quad (4)$$

For fully developed bubbly pipe flow the time-averaged transverse velocity component of the liquid is zero and we also suffice steady flow when equation (4) simplifies to read

$$\varepsilon_b \frac{\partial \alpha}{\partial r} = \alpha V_r \quad (5)$$

where V_r is bubble lateral migration velocity or lateral drift velocity. It should be noted that the assumption $\mathbf{u}_b = \mathbf{u}_L + \mathbf{V}_s$ has been applied. Here \mathbf{V}_s is the slip velocity vector and is defined as $\mathbf{V}_s = V_x \mathbf{e}_x + V_r \mathbf{e}_r$. \mathbf{e}_x and \mathbf{e}_r are the unit vectors in axial and radial directions respectively.

Equation (5) equates the lateral voidage slip migration flux to balance bubble turbulent dispersive flux. In order to obtain the void fraction profile, the radial migration velocity and the bubble dispersion coefficient are required. The bubble dispersion coefficient is here postulated as proportional to the eddy shear diffusivity, with an effective inverse Prantl-Schmidt number, σ_T . The bubble radial migration velocity, V_r , can be obtained directly from basic ideas reported in Thomas *et al.* (1983). Here, it is given by an equilibrium between the resolved component of drag opposing both the lift force and the radial pressure gradient force due to Reynolds stress gradient; see appendix I. When the Reynolds stress gradient in this balance is neglected, it reads

$$V_r = \frac{\rho_L C_L V_T |V_T| \frac{\partial \bar{u}_L}{\partial r}}{g |\Delta \rho|} \quad (6a)$$

Here the drag force F_D is expressed in terms of the observed value of the rise velocity V_T rather than the unknown drag coefficient C_D and the bubble radius (Thomas *et al.* 1983).

When the effect of Reynolds stress gradient is included, we have

$$V_r = \frac{\rho_L C_L V_T |V_T| \frac{\partial \bar{u}_L}{\partial r} - V_T \frac{\partial p}{\partial r}}{g |\Delta \rho|} \quad (6b)$$

where C_L is the bubble lift coefficient and V_T is the bubble rise velocity in still water. ρ_L is the liquid density and g the acceleration due to gravity. $\Delta \rho = \rho_G - \rho_L$. The value of C_L may vary from 0.5 in inviscid weak shear flow (Auton 1987) to 0.01 in highly viscous shear flow (Wang *et al.* 1987). When a bubble comes in close proximity to a wall the normal drainage of the fluid around the bubble changes significantly. The no-slip condition at the wall reduces the drainage rate between the bubble and the wall and in turn increases the drainage rate on the other side of the bubble. The assumption used to derive the vorticity lift force experienced by the bubble is then inappropriate. In other words, the lift coefficient should be a function of local flow properties. It is expected that the value of C_L should be quite different from that for inviscid weakly sheared flow. We will discuss this point in the next section. In this study we used values from 0.05-0.15, in line with the fitting from the experimental study by Wang *et al.* (1987).

Determination of the bubble lateral drift velocity from (6a) or (6b) requires knowledge of the liquid mean shear and the radial pressure gradient. The liquid mean shear can be related to the shear stress using the mean momentum equation, here with an eddy viscosity model. When the effect of bubble buoyancy on the shear stress is taken into account, the shear stress distribution in the flow follows (Thomas 1984; Drew & Lahey 1982)

$$\tau^* = \left(1 \mp \frac{B}{2} \overline{\alpha}_m\right) r^* \pm \frac{B}{r^*} \int_0^{r^*} \alpha r^* dr^* \quad (7)$$

where overbar $\overline{\alpha}_m$ stands for the average void fraction over the cross-section of the pipe, B is a bulk Richardson number, $B=gR/u_\tau^2$ and the '*' denotes nondimensional radius scaled on pipe radius R . With eddy viscosity closure, we have also that

$$\tau^* = \frac{(1-\alpha)(\nu_L + \nu_L^t + \nu_B^t)}{Ru_\tau} \frac{\partial u_L^+}{\partial y^*} \quad (8)$$

where ν_L is the kinematic viscosity of the liquid, ν_L^t is the turbulence viscosity and ν_B^t the pseudo-turbulence viscosity due to the bubbles. We recognise that this formula represents a pragmatic simplification of the complex reality, in particular it ignores coupling effects.

After rearrangement, the resulting expression for the void fraction profile can be written

$$\frac{1}{\alpha} \frac{\partial \alpha}{\partial r^*} = \frac{\frac{C_L R V_T |V_T| u_\tau^2}{g \nu_L^2} \left\{ \left(1 \mp \frac{B}{2} \overline{\alpha}_m\right) r^* \pm \frac{B}{r^*} \int_0^{r^*} \alpha r^* dr^* \right\}}{\sigma_T (1-\alpha)^2 \left[\left(\frac{\nu_L^t}{\nu_L} + \frac{\nu_B^t}{\nu_L}\right) + \left(\frac{\nu_L^t}{\nu_L} + \frac{\nu_B^t}{\nu_L}\right)^2 \right]} \quad (9a)$$

without inclusion of the influence of the radial pressure gradient and

$$\frac{1}{\alpha} \frac{\partial \alpha}{\partial r^*} = \frac{\frac{C_L R V_T |V_T| u_\tau^2}{g v_L^2} \left\{ \left(1 \mp \frac{B}{2} \alpha_m \right) r^* \pm \frac{B}{r^*} \int_0^{r^*} \alpha r^* dr^* \right\} + \frac{V_T u_\tau^2}{g v_L} \frac{\partial p^*}{\partial r^*}}{\sigma_T (1-\alpha)^2 \left[\left(\frac{v_L^t}{v_L} + \frac{v_B^t}{v_L} \right) + \left(\frac{v_L^t}{v_L} + \frac{v_B^t}{v_L} \right)^2 \right]} \quad (9b)$$

with inclusion of the influence of the radial pressure gradient.

In order to find the void fraction profiles, the radial pressure gradient due to the shear turbulence is required and this needs a closure with the radial component turbulence stress. Present knowledge of the turbulence structure in bubbly flows is not so well established and most studies still adopt the modelling used for single-phase flow. For this reason we employ a simple one-equation model to close this fluctuation term, outlined as follows..

2.2 Closure Model

Supposing the difference between the radial component of Reynolds stress and the tangential component is negligible, the radial pressure gradient ($\partial p / \partial r$) due to the shear turbulence and the presence of the bubbles, following some assumptions and simplifications (see appendix II) can then be written

$$\frac{\partial p}{\partial r} = \frac{d}{dr} [(1-\alpha) \rho_L (\overline{v_L'^2} + \overline{v_b'^2})] \quad (10)$$

where $\overline{v_L'^2}$ is the transverse turbulence fluctuation intensity and $\overline{v_b'^2}$ is the turbulence due to the bubble perturbations. Consistent with the approximations of a simple one-point closure, we suppose a turbulence kinetic energy closure for the radial fluctuation velocity. The bubble-induced turbulence is described by a potential theory according to Lance and

Bataille (1991):

$$\overline{v_b'^2} = \frac{3}{20} \alpha V_T^2 \quad (11)$$

and they showed that this formulation is a reasonably good approximation for practical use.

Hence, equation (10) can be expressed as

$$\frac{\partial p}{\partial r} = \frac{d}{dr} \left[(1-\alpha) \rho_L \left(\frac{2}{3} K + \frac{3}{20} \alpha V_T^2 \right) \right] \quad (12)$$

where K is the turbulent kinetic energy. The turbulent kinetic energy K in turn is recovered from the well-known model equation, here using a specified dissipation length scale under the appropriate boundary conditions $\varepsilon = C_\mu K^2 / (\nu_L' + \nu_B')$. For fully developed bubbly pipe flow and neglecting buoyancy production by bubbles, the turbulent kinetic energy equation reduces to the following form:

$$0 = \frac{1}{r} \frac{\partial}{\partial r} \left[r \rho_L (1-\alpha) \left(\nu_L' + \frac{\nu_L' + \nu_B'}{\sigma_K} \right) \frac{\partial K}{\partial r} \right] + \rho_L (1-\alpha) \left[(\nu_L' + \nu_B') \left(\frac{\partial \overline{u_L}}{\partial r} \right)^2 - \frac{C_\mu K^2}{(\nu_L' + \nu_B')} \right] \quad (13)$$

where $\sigma_K = 1.0$ and $C_\mu = 0.09$ were employed (e.g. Rodi 1984). The form of equation (13) has also been adopted by other workers (e.g. Lahey 1987). It should be noted here that the turbulent eddy viscosity includes contributions from both the shear turbulence and from the pseudo-turbulence due to bubbles. As has been mentioned, the key assumption made to model the two-phase bubbly flow turbulence in the liquid phase is that there exists weak coupling between the shear-induced turbulence and the bubble-induced turbulence; here the assumed superposition at leading order as an additive combination from the shear turbulence without bubble perturbation, ν_L' , and the pseudo-turbulence due to bubbles, ν_B' , the latter being proportional to local void fraction α (Sato *et al.* 1981). ν_L' is assumed to follow the classical law based on the wall scaling (e.g. Tennekes & Lumley 1972):

$$v_L^t = \kappa u_\tau y \quad (14)$$

where $\kappa=0.4$, u_τ is the shear stress at $y^+=40$ (i.e. fully turbulent layer) and y is the distance measured from the wall. Because bubble Reynolds numbers are often large (typically bubbles ranging from 2 to 5 mm in diameter) about the order of 10^3 (Thomas *et al.* 1983), ν_B' is expressed as

$$v_B^t = 0.5k_b \alpha \overline{d_B} V_T \quad (15)$$

where d_B is the average bubble diameter and k_b is an empirical constant, about 1.2 according to Sato *et al.* (1981). It should be noted that the empirical constant k_b is not only a function of bubble Reynolds number, but also of the potential fluctuations associated with bubble jitter (Lance & Bataille 1991) because bubble diffusivity is in fact determined by the bubble shedding wake. This influence remains to be evaluated in future work.

2.3 Boundary Conditions

The liquid phase profile across the pipe needed to be prescribed, and strictly this requires that the no-slip condition at the wall is satisfied. However, it is impractical to impose the no-slip condition numerically because the necessary mesh size to resolve the flows in the buffer and viscous zones will be very fine, and this would impose a serious restriction on computer capacity. Fortunately, we do not need to do this since we can follow the well-established procedure of substituting the no-slip condition with a specification of the velocity within the logarithmic layer adjoining the wall. For low wall-layer voidage, it seems the law of the wall is still valid for bubbly flows, but the slope is slightly shifted as demonstrated by Marié (1987); see figure 6. The data presented by Lopez de Bertodano *et al.* (1994b) also confirmed this point. Nevertheless, for simplicity, in this study we adopt the single phase

logarithmic law as the asymptotic boundary condition, namely (Launder & Spalding 1974):

$$\frac{\bar{u}_L}{u_\tau} = \frac{1}{\kappa} \ln y^+ + b \quad (16)$$

where

$$u_\tau = \sqrt{\frac{\tau_w}{\rho_L}} ; \quad y^+ = \frac{y u_\tau}{\nu_L} \quad (17)$$

$\kappa=0.4$ and $b=5.0$. τ_w denotes the shear stress on the wall and can be recovered from relation (8). Boundary conditions for the turbulent kinetic energy, based on the same argument as above, are given by Launder *et al.* (1975):

$$\overline{u'_L u'_L} = \begin{pmatrix} 5.1 & 0 & 1.0 \\ 0 & 2.3 & 0 \\ 1.0 & 0 & 1.0 \end{pmatrix} u_\tau^2 \quad (18)$$

Thus the kinetic energy near wall can be derived from this equation:

$$K = 4.2 u_\tau^2 \quad \text{at } y^+ = 40 \quad (19)$$

The symmetry conditions at centerline impose:

$$\frac{\partial K}{\partial r} = 0 \quad \text{at } r = 0 \quad (20)$$

Equations (9), (11) and (13) with the boundary conditions specified here provide a set of lateral bubble transport equations describing the bubble void fraction distribution in fully developed bubbly flow in a pipe. Hence, it should be reasonably straightforward to integrate these equations for prediction of the bubble distribution.

3 NUMERICAL PROCEDURES

For a prescribed pipe diameter D , liquid volumetric flow rate Q_L and the averaged void fraction α , the step-by-step calculation procedures are as follows:

- (1) Assign D , Q_L and the given average α_m .
- (2) Evaluate the initial τ_w by use of the law of the wall (Schlichting 1979).
- (3) Determine the corresponding ν_L' and ν_B' according to the relations (14) and (15).
- (4) Calculate the void fraction profile from (9a) or (9b), using a forward finite-difference method under the boundary conditions specified and assigning an initial value of α on the centerline. When the effect of the radial pressure gradient is taken into account, i.e. equation (9b) is solved, an internal iteration loop is adopted to calculate the turbulent kinetic energy distribution across the cross-section of the pipe so as to obtain the radial pressure gradient.
- (5) Obtain the averaged void fraction value and compare the averaged α_{cal} with the prescribed α_m .
- (6) Repeat the foregoing process (steps 3-5) until the specified boundary condition is satisfied and a consistent void fraction profile is obtained.
- (7) Calculate the liquid velocity distribution u_L from (8) under the obtained void fraction profile and ensure that continuity is satisfied, otherwise modify the shear stress τ_w and return to step 3.
- (8) Repeat the foregoing steps 3-7 until convergence and consistent void fraction and velocity distribution are achieved.

Mesh convergence tests were carried out in preliminary calculations. We repeated calculations with reduced mesh size and found that with the arrangement of more than 50 radial nodes the calculations are less affected by the node number. We thus chose 50 radial mesh nodes throughout our calculations.

4 RESULTS AND DISCUSSION

We evaluate our results against the experimental findings of Serizawa *et al.* (1986) and Wang *et al.* (1987), regarded not only by us as confirming more complete data set but having been acknowledged as the reference database by other workers (e.g. Drew & Lahey 1982; Lopez de Bertodano *et al.* 1990). In particular, we use Serizawa's data for upflows and Wang's data for downflows, as follows.

4.1 Comparison With Experimental Data

Figures 7 to 9 show comparisons of the void fraction profiles, velocities and shear stresses obtained from our present model with the reported experimental data (Serizawa *et al.* 1986) for upflow. The experimental conditions are that the liquid flow rate $j_L=1.36$ m/s and the gas flow rate $j_G=0.077$ m/s. The pipe diameter was 60 cm and the ratio between the length and diameter was $L/D=43$, so it should have achieved the fully-developed condition. We should caution that bubbly flow development length can even be over 100 times of pipe diameters. The predictions with assigned $C_L=0.10$ correspond to the cases when the radial pressure gradient is either neglected or is taken into account. It can be seen from the comparisons that with the exception of figure 9 the predictions broadly follow the trends of the experimental data. It can also be seen from these figures that for two-phase flow the velocity profile appears to be flatter than for single-phase flow and the shear stress profile is quite different from that in single phase flow, probably due to the buoyancy nonuniformities incorporated in our calculations. It is interesting to note that no obvious improvement on the predicted void fraction profiles is achieved when the radial pressure gradient is taken into account. However, as cautioned above, this is essentially due to the unreasonable K description used here - a shortcoming which must be eliminated in future work.

The same value of C_L was adopted in the comparisons (figures 10 to 12) with Wang's *et al.* (1987) data for downwards flow with $j_L=1.08$ m/s and $j_G=0.1$ m/s. In this case, the pipe diameter was 50 mm. and $L/D=40$. Again, the broad agreement between the void fraction profiles and velocity profiles as compared with the experimental data are encouraging. However, it can be seen from figure 12 that the shear stress distribution does not display the expected trend as it does for upflow.

The calculations indicate that our model incorporates at least some of the important physical phenomena, to the extent that it discriminates the different behaviours found in upflow and downflow. However, one significant discrepancy is that the peaking of void fraction away from the wall, as found in the experiments, is not predicted properly. We attribute this failure to the limitations of our simple bubble force law in the vicinity of the wall - in particular, that real bubbles are not spherical nor are they of single size. Asymmetric bubble wake patterns when the bubbles move near the wall are likely to radically alter the lateral forces experienced by the bubbles, as noted in the previous sections. Antal *et al.* (1991) used a 'wall force' to account for this effect in laminar bubbly flow, but for turbulent bubbly flow the effect should be different.

4.2 The effect of Lift Force and Radial Pressure Gradient

It is clearly demonstrated from figures 9 and 12 that inclusion of the radial pressure gradient does not affect the results very much, although we again caution about the shortcomings of the present prescriptions for K . Apart from this reservation, the void fraction profiles mainly depend on the bubble radial migration velocity and bubble dispersion coefficient. In the core region, the lift force acting on bubbles is relatively small (due to weak shear) and bubble

dispersion dominates due to turbulence diffusion. Hence, the void fraction profile appears quite flat. In contrast, in the region near the wall the strong velocity shear gives rise to a larger vorticity lift force, whereas shear dispersion is smaller; being proportional to distance from the wall according to our model. This results in the accumulation of bubbles near the wall for upward flow. Thus, it appears that the voidage pattern in two-phase bubbly upward flow can be divided into two zones, viz. a zone where the lateral lift force dominates and a zone where the bubble dispersion is dominant, as can be seen from figure 13(a). For downward flow, the effect of lift force is to drive bubbles towards the pipe centre; opposing to the effect of the radial pressure gradient. In the region near the wall, the effect of lift force is larger than that of the radial pressure gradient and this promotes bubbles to move away from the wall as seen in figure 13(b). Again we caution that the pressure gradient force is underestimated in present calculations because of inappropriate use of the K equation to recover the radial velocity fluctuations. In the core region, the competing effects are nearly equal and this results in a flat void fraction profile. In sum then, though the effect of lift force is important, the radial pressure gradient also has a significant/comparable influence on the voidage profiles.

4.3 Effects of Lift Coefficient C_L and Bubble Size

Because the lift force plays an important role in determining the void fraction profiles, it is important to assess the significance of assigning different values to the lift coefficient. A sensitivity study for the value of the lift coefficient is shown in figure 14. The values were varied from 0.05 to 0.12. As expected, the larger the lift coefficient the higher the peak void fraction found close to the wall. This result is similar to those obtained by Antal *et al.* (1991) for laminar bubbly flow. However, recent experiments performed at the Ecole

Centrale de Lyon by Lance & Naciri (1991) for single bubbles in the shear flow indicated that the lift coefficient $C_L \cong 1/4$ for a wide range of sizes, from 0.5 mm to 8 mm. It is interesting to note two points here:

- (1) the lift coefficient adopted for the present calculations is far smaller than that for inviscid weak shear flow; $C_L=0.5$ (Auton 1987; Thomas *et al.* 1983),
- (2) the void peaking actually occurs at a small distance away from the wall and this behaviour is not reproduced by our model.

We have already cautioned that the relative flow field around a bubble in the vicinity of the wall is distorted, and that the bubbles experience also a strong shear. The shear-lift terms in the general force law should be modified, because the assumptions used to derive the general force law presume that bubbles only experience weak shear. On the other hand, the modification of the bubble wake is also affected by the locally distorted velocity field, which may cause a serious reduction of circulation around the bubble resulting in a smaller lift coefficient than expected, or even a reversal of the acting direction of the lift force. The latter case has been supposed to exist as a lubrication-like lift force (Antal *et al.* 1991) which pushes the bubbles away from the wall. Hence, we should consider incorporating variations in the lift coefficient if we can capture the effects mentioned above. However, present lack of knowledge about the lift coefficient for a bubble in strong shear flow prevents a systematic study. As a first approximation we can incorporate the correction of a wall force (Antal *et al.* 1991), which is written as

$$F_w = \frac{\alpha \rho_L V_T^2}{r_b} \left[C_{w1} + C_{w2} \left(\frac{r_b}{y_0} \right) \right] \quad (21)$$

where $C_{w1} = -0.104 - 0.06V_T$ and $C_{w2} = 0.147$. r_b is the radius of the bubble and y_0 is the distance

measured from the wall. Figure 15 shows the predictions for bubbly upflow including the wall force, and the predictions have indeed been improved. We caution that the mechanism of the interaction between the bubbles and the wall remains essentially unsolved, and needs further investigation.

The effect of bubble size on the void fraction was addressed by Serizawa & Kataoka (1987) and Liu (1993). They found that the void fraction distribution is very sensitive to bubble size. For example, Liu found that when the bubble diameter is about 5-6 mm, the void fraction profile will be transfigured. In our model, the effect of bubble size is explicitly assessed through the bubble-induced turbulence diffusivity. However, it can be seen from equation (8) that the bubble-induced turbulence diffusivity only depends on the local void fraction for a given bubble size, since we have applied the assumption that the local slip velocity is equal to the bubble rise velocity in still liquid. We note that the bubble rise velocity is nearly constant for a wide range of bubble sizes; say 2-8 mm in equivalent diameter (Clift *et al.* 1978). Figure 16 shows the effect of different bubble sizes on the bubble-induced turbulence diffusivity. Figure 17 shows how increasing bubble size causes the void fraction to reduce in the near wall region.

5 CONCLUSIONS

Near-wall voidage 'peaking' for upward flow and centerline 'coring' for downward bubbly flow have been reproduced using a simple transport model based on the assumption that the lift force and the transverse pressure gradient force acting on bubbles are balanced by the bubble dispersion. The model was easily applied to demonstrate the phenomena of void peaking and coring in bubbly flow. The prediction indicates how the lift force competes with

the pressure gradient term due to the turbulent normal stresses in the determination of lateral bubble transport. However, the latter has been substantially underestimated here due to inadequate formulation of the K equation which cannot really recover the radial velocity fluctuations.

For upflows, the lift force is directed toward the wall and so is the radial pressure gradient due to the Reynolds stresses. The effect is to cause bubbles to accumulate near the wall, so that voidage peaking near the wall is observed. For downward flows, the lift force is directed toward the centre of the pipe while the pressure gradient is still directed to the wall. However, the effect of lift force is larger than that of the pressure gradient. As a result of these two forces' interaction, the void fraction distribution appears flatter and no voidage peaking near the wall is predicted.

The profile of void fraction was also found to be affected by the bubble-induced turbulence, as a bubble size effect in the assigned bubble diffusivity. This bubble-induced turbulence promotes the diffusion of bubbles so as to decrease the voidage peaking.

The calculations suggest that the eddy diffusivity used for single-phase flows can be extended to include bubble dispersion by introducing an empirical constant similar to the turbulence Prantl-Schmidt number, with value of about 1.0, as employed by Lopez de Bertodano *et al.* (1994a) for their developing a K - ϵ model for bubbly two-phase flow, and by Sene *et al.* (1994) to reproduce the spread rate behaviour of a bubbly shear layer. This argument will be further discussed in more detail in the following chapter. The deduction can then be extended to include the effect of pseudo-turbulence due to bubble perturbation

in the flow.

REFERENCES

- Auton, T. R. 1987 The lift force on a spherical body in a rotational flow. *J. Fluid Mech.* **183**, 199.
- Antal, S. P., Lahey, R. T. and Flaherty, J. E. 1991 Analysis of phase distribution in fully developed laminar bubbly two-phase flow. *Int. J. Multiphase Flow.* **17**, 635-652.
- Bankoff, S. G. 1960 A variable density single-fluid model for two-phase flow with particular reference to steam-water flow. *Trans. ASME, Series C* **82**, 265-272.
- Bel Fdhila, R., Masbernat, L. & Suzanne, C. 1992 Two-phase bubbly flow measurements in a vertical sudden expansion. *Proceedings of the Sixth International Workshop on Two-Phase Flow*, 335-347.
- Beyerlein, S. W., Cossmann, R. K. & Richter, H. J. 1985 Prediction of bubble concentration profiles in vertical turbulent two-phase flow. *Int. J. Multiphase Flow* **11**, 629-641.
- Clift, R., Grace, J. R. & Weber, M. E. 1978 *Bubbles, Drops, and Particles*. Academic Press, New York.
- Drew, D. & Lahey, R. T. Jr 1982 Phase distribution mechanisms in turbulent low-quality two-phase flow in a circular pipe. *J. Fluid Mech.* **117**, 91-106.
- Drew, D. 1983 Mathematical modeling of two-phase flow. *Ann. Rev. Fluid Mech.* **15**, 261-291.
- Hall, W. B. & Jackson, J. D. 1969 Laminarisation of a turbulent pipe flow by buoyancy forces. *ASME Paper* 69-HT-55.
- Hinata, S. 1980 A method of estimation for the distribution of void fraction in bubbly flow. *17th National Heat Transfer Symp of Japan*, B204 Kanazawa.
- Hunt, J. C. R., Perkins, R. J. & Fung, J. C. H. 1994 Problems in modelling disperse two-phase flows. *Applied Mech. Rev.* **47**(2), s49-s60.
- Kataoka, I. & Serizawa, A. 1989 Basic equations of turbulence in gas-liquid two-phase flow. *Int. J. Multiphase Flow* **15**, 113-121.
- Kobayashi, K., Iida, Y. & Kanegae, N. 1970 Distribution of local void fraction of air-water two-phase flow in a vertical channel. *Bull. JSME* **13**, 1005-1012.
- Lahey, R. T. Jr. 1987 Turbulence and phase distribution phenomena in two-phase flow.

ICHMT International Seminar on Transient Phenomena in Multiphase Flow,
Dubrovnik, Yugoslavia, May 24-30.

- Lance, M. & Bataille, J. 1991 Turbulence in the liquid phase of a uniform bubbly air-water flow. *J. Fluid Mech.* **222**, 95-118.
- Lance, M. & Naciri, A. 1991 Lift and added mass coefficient for a single bubble. *First European Fluid Mechanics Conference*, September 1991, Cambridge, U.K.
- Lauder, B. E. & Spalding, D. B. 1974 The numerical computation of turbulent flows. *Comput. Meth. Appl. Mech. Engng* **3**, 269-289.
- Lauder, B. E., Reece, G. J. & Rodi, W. 1975 Progress in the development of a Reynolds stress turbulence closure. *J. Fluid Mech.* **68**, 537-566.
- Lee, S. J., Lahey, R. T. Jr & Jones, O. C. 1989 The prediction of two-phase turbulence and phase distribution phenomena using a $K-\epsilon$ model. *Jap. J. Multiphase Flow* **3**, 335-368.
- Levy, S. 1963 Prediction of two-phase pressure drop and density distribution from mixing length theory. *Trans. ASME, Series C* **85**, 137-152.
- Liu, T. J. 1993 Bubble size and entrance length effects on void development in a vertical channel. *Int. J. Multiphase Flow* **19**, 99-113.
- Lopez de Bertodana, M., Lee, S. J., Lahey, R. T. Jr & Drew, D. A. 1990 The prediction of two-phase turbulence and phase distribution using a Reynolds stress model. *J. Fluids Engng* **112**, 107-113.
- Lopez de Bertodano, M., Lahey, R. T. Jr & Jones, O. C. 1994a Development of a $k-\epsilon$ Model for bubbly two-phase flow. *J. Fluids Engng* **116**, 128-134.
- Lopez de Bertodano, M., Lahey, R. T. Jr & Jones, O. C. 1994b Phase distribution in bubbly two-phase flow in vertical ducts. *Int. J. Multiphase Flow* **20**, 805-818.
- Marié, J. L. 1987 Modelling of the skin friction and heat transfer in turbulent two-component bubbly flow in pipes. *Int. J. Multiphase Flow* **113**, 309-325.
- Moujaes, S. & Dougall, R. S. 1985 Two-phase upflow in rectangular channels. *Int. J. Multiphase Flow* **11**, 503-513.
- Moursali, E., Marié, J. L. & Bataille, J. 1995 An upward turbulent bubbly boundary layer along a vertical flat plate. *Int. J. Multiphase Flow* **21**, 107-117.
- Rodi, W. 1984 *Turbulence Models and Their Applications in Hydraulics*. IAHR Monograph.
- Rouhani, Z. 1976 Effect of wall friction and vortex generation on radial void distribution,

- the wall-vortex effect. *Int. J. Multiphase Flow* **3**, 30-50.
- Sato, Y., Sadatomi, M. & Sekoguchi, K. 1981 Momentum and heat transfer in two-phase bubbly flow - I. *Int. J. Multiphase Flow* **7**, 167-190.
- Schlichting, H. 1979 *Boundary layer theory*. McGraw-Hill, New York.
- Sene, K. J., Hunt, J. C. R. & Thomas, N. H. 1994 The role of coherent structures in bubble transport by turbulent shear flows. *J. Fluid Mech.* **259**, 219-240.
- Serizawa, A., Kataoka, I. & Michiyoshi, I. 1975 Turbulence structure of air-water bubbly flow. *Int. J. Multiphase Flow* **2**, 221-259.
- Serizawa, A. & Kataoka, I. 1987 Phase distribution in two-phase flow. In *Proc. Transient Phenomena in Multiphase Flow - ICHMT Int. Semin.*, Dubrovnik, Croatia, 179-224.
- Serizawa, A., Kataoka, I. & Michiyoshi, I. 1986 Phase distribution in bubbly flow. *Proceedings of the Second International Workshop on Two-Phase Flow Fundamentals*, Data Set No. 24.
- Subbotin, V. I., Ibragimov, M. Kh., Bobkov, V. P. & Tychinskii, N. A. 1971 Turbulent channel flow characteristics of gas-water mixtures. *Soviet Physics - Doklady* **16**(3), 192-194.
- Tennekes, H. & Lumley, J. L. 1972 *A First Course in Turbulence*. MIT Press, Cambridge, Massachusetts.
- Theofanous, T. G. & Sullivan, J. 1982 Turbulence in two-phase dispersed flows. *J. Fluid Mech.* **116**, 343-362.
- Thomas, N. H., Auton, R. T., Sene, K. & Hunt, J. C. R. 1983 Entrapment and transport of bubbles by transient large eddies in multiphase turbulent shear flows. *Proceedings of Int. Conf. on the Physical Modelling of Multiphase Flow*, Coventry, U.K., Paper E1.
- Thomas, N. H. 1984 Chemical Engineering Final Examination. University of Birmingham.
- Wang, S. K., Lee, S. J., Jones, O. C. & Lahey, R. T. 1987 3-D turbulence structure and phase distribution measurements in bubbly two-phase flows. *Int. J. Multiphase Flow* **13**, 327-343.
- Yang, X. & Thomas, N. H. 1992 Void fraction profiles in two-phase bubbly upward and downward flow. *Proceedings of the Sixth International Workshop on Two-Phase Flow*, 274-281.
- Zuber, N. 1960 On the variable density single fluid model for two-phase flow. *Trans. ASME*

J. Heat Transfer **82**, 255-258.

Zün, I. 1980 The transverse migration of bubbles influenced by wall in a vertical bubbly flow. *Int. J. Multiphase Flow* **6**, 583-588.

Žun, I. 1987 Transition from wall void peaking to core void peaking in turbulent bubbly flow. *ICHMT International Seminar on Transient Phenomena in Multiphase Flow*, Dubrovnik, Yugoslavia.

APPENDIX I

Derivation of the Bubble Transverse Migration Velocity

In this section we summarize the equation derived in the preceding sections for a bubble transverse migration velocity.

Thomas *et al.* (1983) suggested that a viscous drag F_D can be simply added to the inviscid force experienced by bubble, so that the total interfacial force acting on a spherical bubble may be expressed as

$$\mathbf{F}_i = \mathbf{F}_L + \mathbf{F}_D \quad (\text{I.1})$$

where F_i can be written

$$\mathbf{F}_i = \rho_L V_b \left\{ (1 + C_m) \frac{D\mathbf{u}_L}{Dt} - C_m \frac{d\mathbf{v}}{dt} - \mathbf{g} - [C_L (\mathbf{v} - \mathbf{u}_L) \times \boldsymbol{\omega}] \right\} \quad (\text{I.2})$$

Here \mathbf{u}_L and $\boldsymbol{\omega}$ are the liquid velocity and vorticity ($\boldsymbol{\omega} = \nabla \times \mathbf{u}_L$) in the absence of the bubble, $D\mathbf{u}_L/Dt$ is the liquid acceleration at the location of the bubble and \mathbf{v} is the bubble velocity. ρ_L is the liquid density, V_b is the volume of the bubble, \mathbf{g} is the acceleration due to gravity, C_L is the bubble lift coefficient and C_m denotes the bubble added mass coefficient. F_D can be conveniently defined in terms of V_T the terminal rise velocity of the bubble in still liquid:

$$\mathbf{F}_D = -\rho_L V_b \frac{|\Delta\rho|}{\rho_L} \mathbf{g} \frac{(\mathbf{v} - \mathbf{u}_L)}{V_T} f\left(\frac{\mathbf{v} - \mathbf{u}_L}{V_T}\right) \quad (\text{I.3})$$

where $\Delta\rho = \rho_G - \rho_L$. For a spherical bubble the deformation of the bubble in a pure liquid is neglected so $f=1$. For a high Reynolds number bubble in dirty liquid, $f = |\mathbf{v} - \mathbf{u}_L|/V_T$ because the drag coefficient of the bubble is approximately constant.

Once the interfacial force \mathbf{F}_i is determined, the motion of the bubble is related to \mathbf{F}_i by the force law and can be expressed as

$$\begin{aligned} \left(\frac{\rho_G}{\rho_L} + C_m\right) \left(\frac{\partial \mathbf{v}}{\partial t} + \mathbf{v} \cdot \nabla \mathbf{v}\right) = (1 + C_m) \frac{D\mathbf{u}}{Dt} - g \frac{|\Delta\rho|}{\rho_L} \frac{(\mathbf{v} - \mathbf{u}_L)}{V_T} f\left(\frac{|\mathbf{v} - \mathbf{u}_L|}{V_T}\right) \\ + \left(\frac{\rho_b}{\rho_L} - 1\right) \mathbf{g} - C_L (\mathbf{v} - \mathbf{u}_L) \times (\nabla \times \mathbf{u}_L) \end{aligned} \quad (\text{I.4})$$

The radial component of equation (4) is

$$\begin{aligned} \left(\frac{\rho_G}{\rho_L} + C_m\right) \left(\frac{\partial v_r}{\partial t} + v_x \frac{\partial v_r}{\partial x} + v_r \frac{1}{r} \frac{\partial r v_r}{\partial r}\right) = (1 + C_m) \left(\frac{\partial u_r}{\partial t} + u_L \frac{\partial u_r}{\partial x} + u_r \frac{1}{r} \frac{\partial u_r}{\partial r}\right) \\ - g \frac{|\Delta\rho|}{\rho_L} \frac{(v_r - u_r)}{V_T} f\left(\frac{|v_r - u_r|}{V_T}\right) - C_L (v_x - u_L) \frac{\partial u_L}{\partial r} \end{aligned} \quad (\text{I.5})$$

If two-phase bubbly flow in the pipe is assumed to be fully developed, then the time derivative and convective terms about the liquid are zero. We notice that the radial bubble velocity can be approximated by $v_r = u_r + V_r$. Here V_r is the bubble transverse migration velocity or radial slip velocity. v_r and u_r are respectively the bubble and liquid radial velocity components. The following result is obtained:

$$\frac{V_r}{r} \frac{\partial r V_r}{\partial r} = - \frac{|\Delta\rho|}{\rho_L} g \frac{v_r - u_r}{V_T} f\left(\frac{|v_r - u_r|}{V_T}\right) - C_L (v_x - u_L) \frac{\partial u_L}{\partial r} \quad (\text{I.6})$$

We note here that the effect of time-averaging of the first term of equation (6) is the bubble-induced turbulence and generates a radial pressure gradient. On condition that this term is ignored, equation (6) can be simplified as

$$C_L (v_x - u_L) \frac{\partial u_L}{\partial r} = - \frac{|\Delta\rho|}{\rho_L} g \frac{v_r - u_r}{V_T} f\left(\frac{|v_r - u_r|}{V_T}\right) \quad (\text{I.7})$$

In many situations, it is reasonably assumed that the bubble relative velocity in main flow is equal to the bubble terminal rise velocity, i.e. $(v_x - u_L) = V_T$. Thence equation (7) can be further simplified and gives the estimation of the bubble transverse migration velocity:

$$V_r = \frac{-\rho_L C_L V_T^2 \frac{\partial u_L}{\partial r}}{g |\Delta \rho|} \quad (\text{I.8})$$

for the bubble in a pure liquid and

$$V_r = \sqrt{\frac{-\rho_L C_L V_T^3 \frac{\partial u_L}{\partial r}}{g |\Delta \rho|}} \quad (\text{I.9})$$

for the bubble in dirty liquid.

It should be noted here that all the above equations are derived in a Lagrangian frame. However, for fully developed bubbly flow the Eulerian two-fluid model gives the same result when the equations for gas phase are considered.

APPENDIX II

Derivation of the Radial Pressure Distribution

The general form of the momentum equation of the two-fluid model for air-water flow can be written as

$$\frac{\partial(\alpha_k \rho_k \mathbf{u}_k)}{\partial t} + \nabla \cdot (\alpha_k \rho_k \mathbf{u}_k \mathbf{u}_k) = -\alpha_k \nabla p_k + \nabla \cdot [\alpha_k (\boldsymbol{\sigma}_k + \boldsymbol{\sigma}_k^T)] + (p_{ki} - p_k) \nabla \alpha_k + \alpha_k \rho_k \mathbf{g} + \mathbf{M}_{ki} - \boldsymbol{\sigma}_{ki} \cdot \nabla \alpha_k \quad (\text{II.1})$$

Here the subscript k denotes phase k ($k=b$ for the gas phase; $k=L$ for the liquid phase) and the subscript i stands for the value at the interface between the two phases. The spatial/time averaged density, pressure, volume fraction, viscous shear and bubble-induced turbulence are represented by ρ_k , \mathbf{u}_k , p_k , α_k , $\boldsymbol{\sigma}_k$ and $\boldsymbol{\sigma}_k^T$, respectively. The spatial/time averaged interfacial momentum exchange, velocity, shear and pressure are denoted by \mathbf{M}_{ki} , \mathbf{u}_{ki} , $\boldsymbol{\sigma}_{ki}$ and p_{ki} , respectively.

For fully developed bubbly flow in a pipe the time derivative and convective derivative in the main flow direction are zero. The convective terms in the radial direction are assumed to be negligible because they are the terms of high order compared with those in right side of equation (II.1). Thus the momentum equation reduces to:

$$-\alpha_k \nabla p_k + \nabla \cdot [\alpha_k (\boldsymbol{\sigma}_k + \boldsymbol{\sigma}_k^T)] + (p_{ki} - p_k) \nabla \alpha_k + \alpha_k \rho_k \mathbf{g} + \mathbf{M}_{ki} - \boldsymbol{\sigma}_{ki} \cdot \nabla \alpha_k = 0 \quad (\text{II.2})$$

Further simplifications can be made. For example, the total shear and the $(p_{bi} - p_b)$ terms can be neglected due to the relatively small viscosity and density of the gas phase in contrast to the liquid phase. Introduction of these assumptions and adoption of the definition $\alpha \equiv \alpha_b = 1 - \alpha_L$ yields:

$$0 = -\alpha \nabla p_b + \alpha \rho_b \mathbf{g} + \mathbf{M}_{bi} \quad (\text{II.3})$$

and

$$0 = -(1-\alpha)\nabla p_L + \nabla \cdot [(1-\alpha)(\boldsymbol{\sigma}_L + \boldsymbol{\sigma}_L^T)] + (p_{Li} - p_L)\nabla(1-\alpha) + (1-\alpha)\rho_L \mathbf{g} + \mathbf{M}_{Li} - \boldsymbol{\sigma}_{Li} \cdot \nabla(1-\alpha) \quad (\text{II.4})$$

The interfacial force terms such as the lift force and the drag force can be eliminated by adding (II.3) and (II.4) and this gives:

$$\alpha \nabla p_b + (1-\alpha)\nabla p_L = \nabla \cdot [(1-\alpha)(\boldsymbol{\sigma}_L + \boldsymbol{\sigma}_L^T)] + (p_{Li} - p_L)\nabla(1-\alpha) - \boldsymbol{\sigma}_{Li} \cdot \nabla(1-\alpha) + \alpha \rho_b \mathbf{g} + (1-\alpha)\rho_L \mathbf{g} \quad (\text{II.5})$$

The radial component of equation (II.5) reads

$$\frac{\partial p_L}{\partial r} + \alpha \left(\frac{\partial p_b}{\partial r} - \frac{\partial p_L}{\partial r} \right) = \frac{\partial}{\partial r} [(1-\alpha)(\sigma_{Lr} + \sigma_{Lr}^T)] - (p_{Li} - p_L) \frac{\partial \alpha}{\partial r} + \sigma_{Li,r} \frac{\partial \alpha}{\partial r} \quad (\text{II.6})$$

It is convenient to assume that $p_b = p_L = p$. The interfacial momentum jump condition for spherical bubbles can be written as

$$p_G - p_L = \frac{2\sigma}{R_b} + (p_{Li} - p_L) + \sigma_{Li,r}^T \quad (\text{II.7})$$

Here R_b is the radius of the bubble and σ is the surface tension. If we neglect the effects of surface tension and substitute (II.7) into (II.6), then we have

$$\frac{\partial p}{\partial r} = \frac{\partial}{\partial r} [(1-\alpha)(\sigma_{Lr} + \sigma_{Lr}^T)] \quad (\text{II.8})$$

Here the turbulence stress in radial direction is defined by

$$\sigma_{Lr} = -\rho_L \overline{v^2}$$

and the part for bubble-induced turbulence can be approximated (Lance & Bataille 1991)

$$\sigma_{Lr}^T = \frac{3}{20} \alpha V_T^2$$

We note from equation (II.8) that in regions where the radial turbulent fluctuations are large, the local static pressure, $p(r)$, is low.

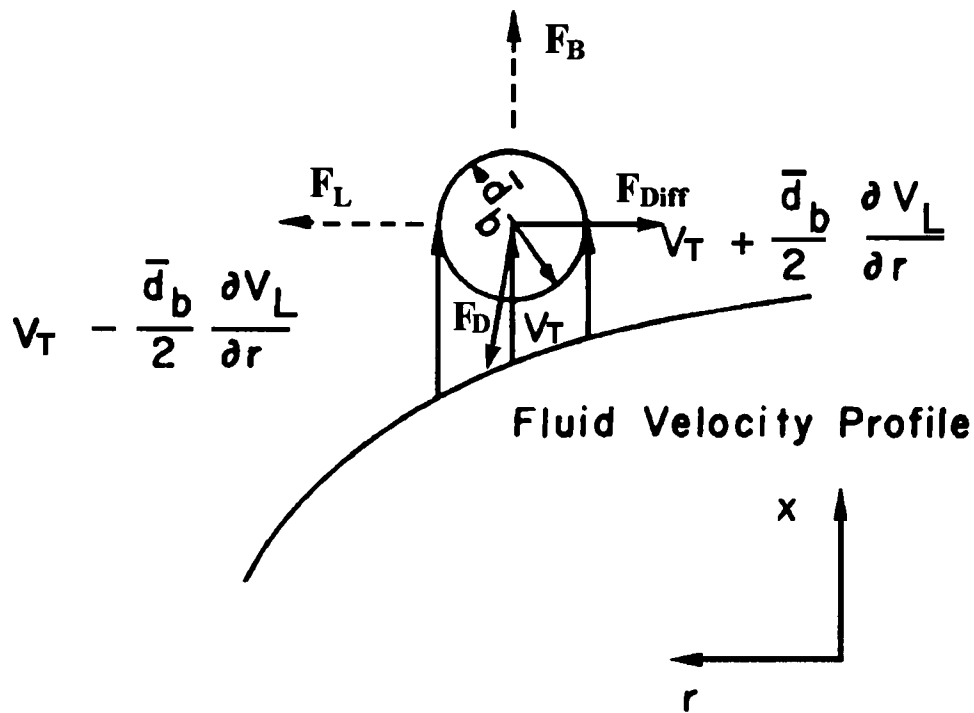


Figure 1. A bubble moving relative to a shear flow and the forces acting on the bubble.

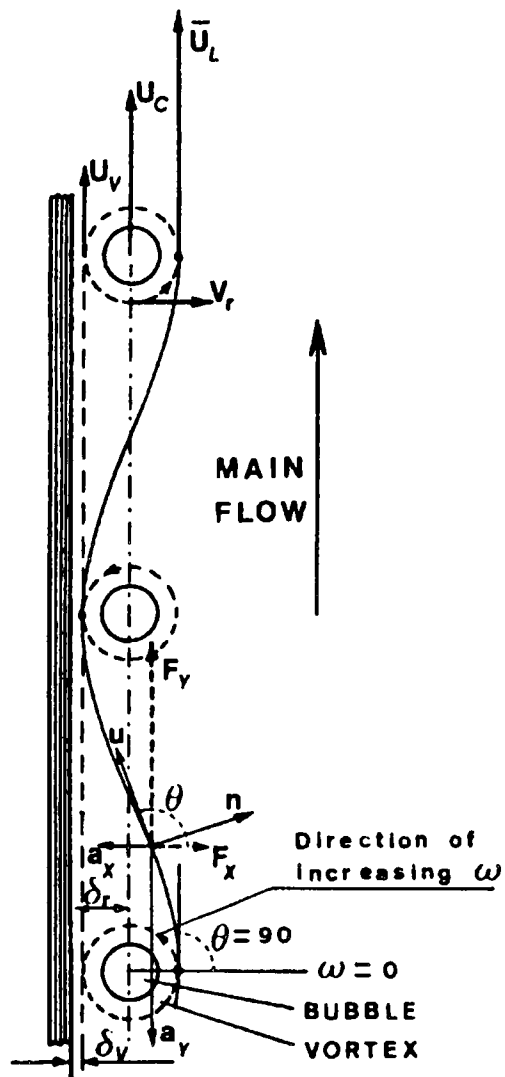


Figure 2. The wall rolling eddies and the interaction between bubbles and the eddies (Rouhani 1976).

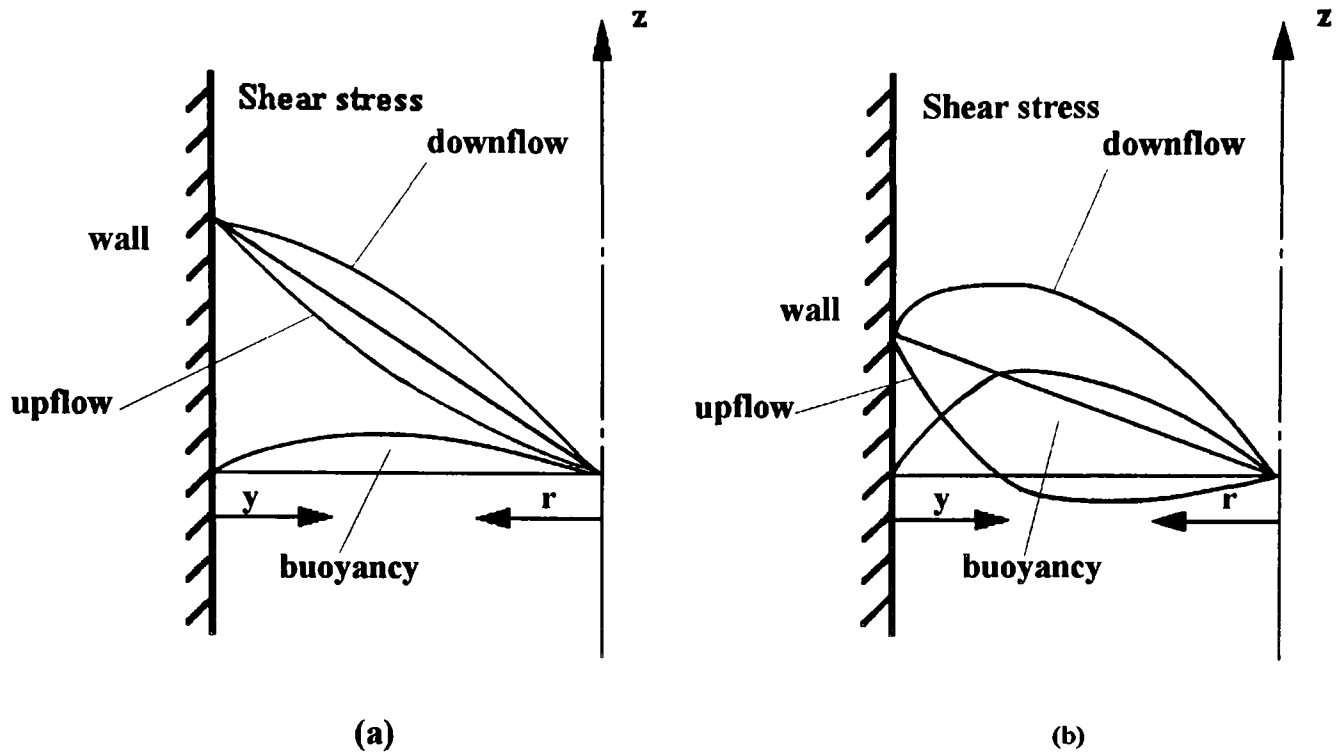


Figure 3. Effect of buoyancy force on the shear stress distribution in vertical bubbly pipe flow (Thomas 1984): (a) smaller buoyancy; (b) larger buoyancy.

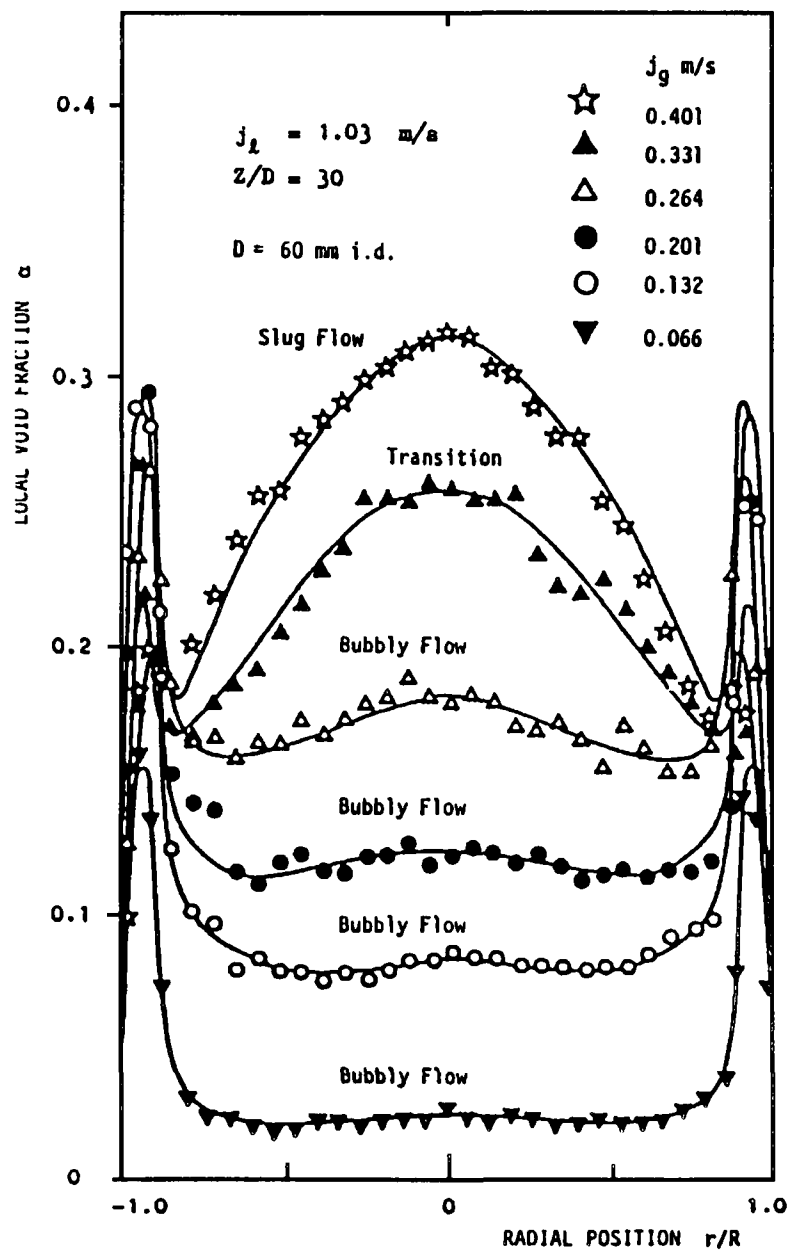


Figure 4. Serizawa *et al.* (1986). Radial void fraction distribution in vertically upward flow.

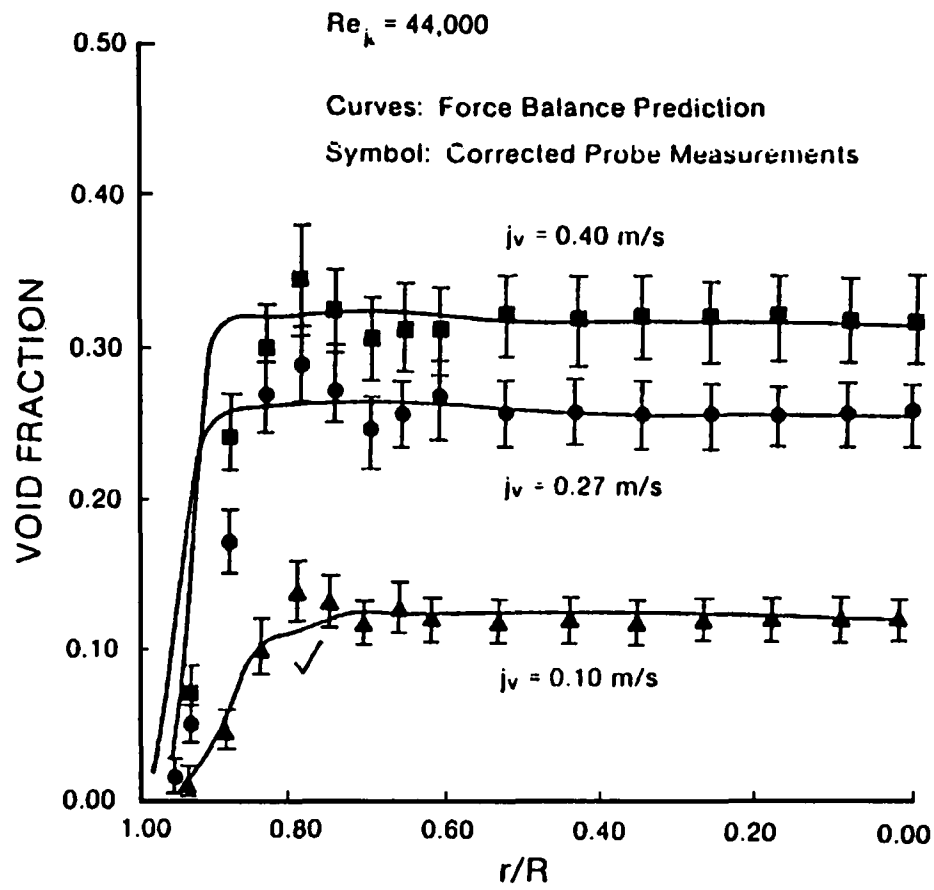


Figure 5. Wang *et al.* (1987). Radial void fraction distribution in vertically downward flow.

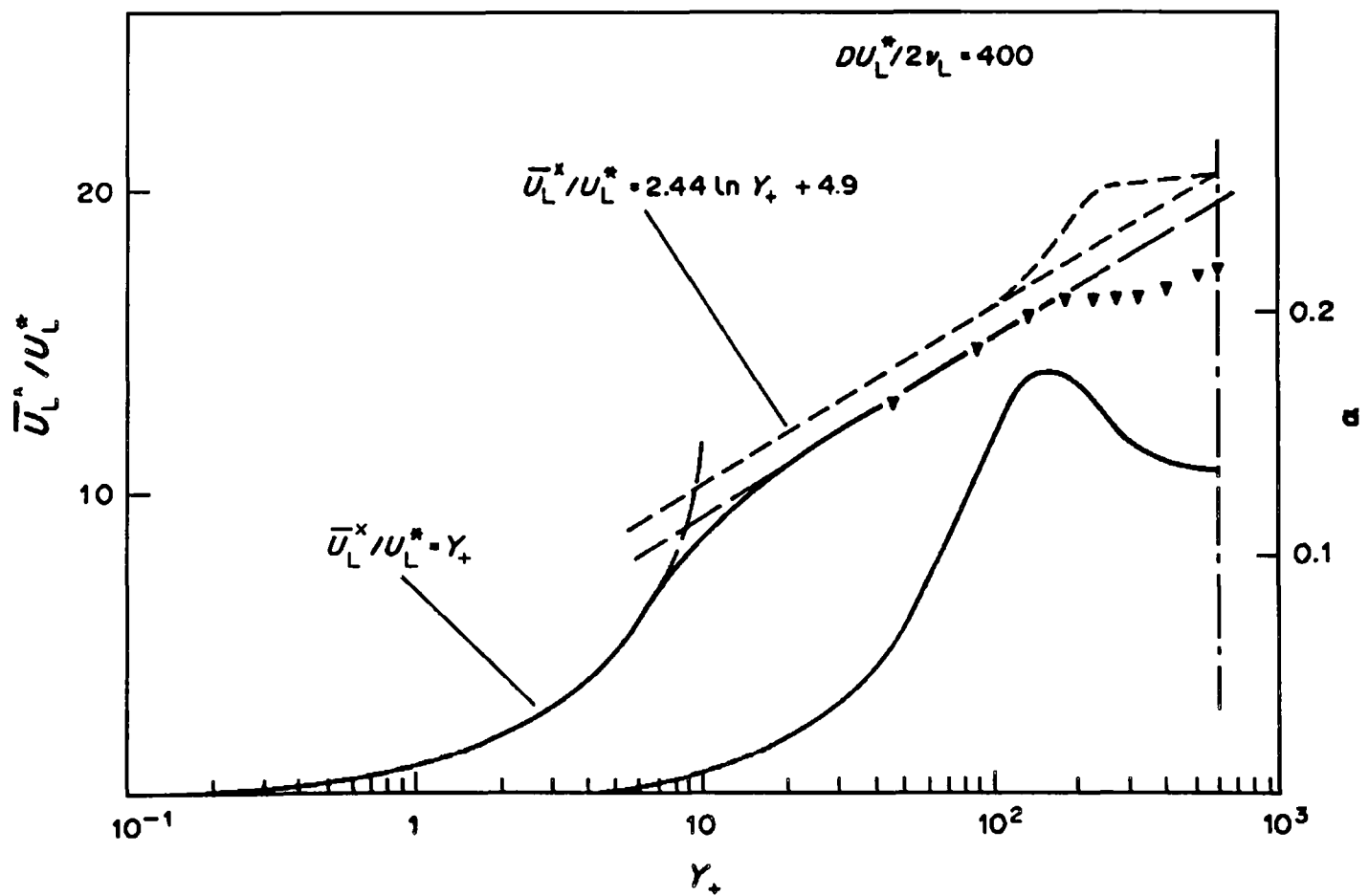


Figure 6. Mean velocity and void fraction profiles in an upward bubbly flow in a pipe (Marié 1987).

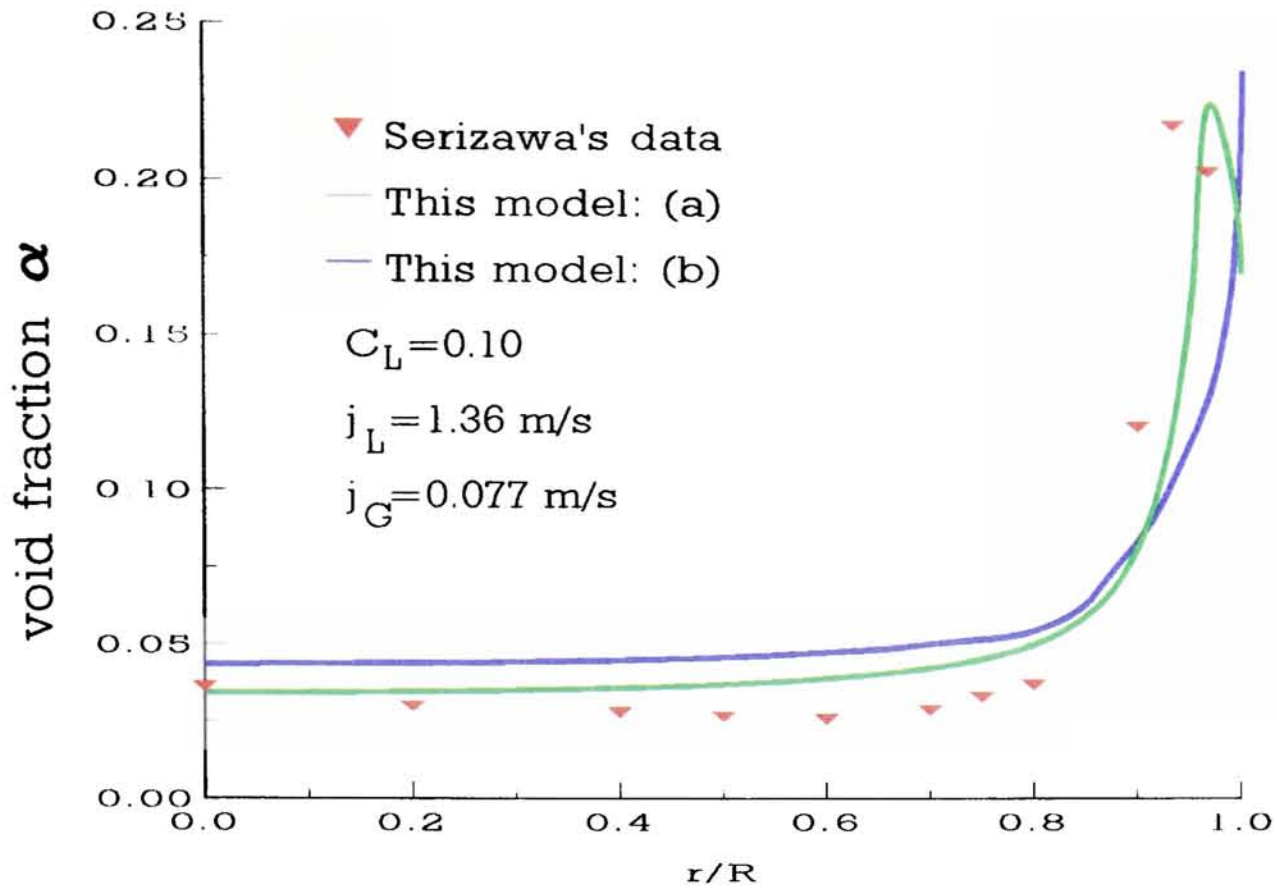


Figure 7. Comparison of the predicted void fraction profile with Serizawa's data (1986): (a) with the pressure gradient; (b) without the pressure gradient.

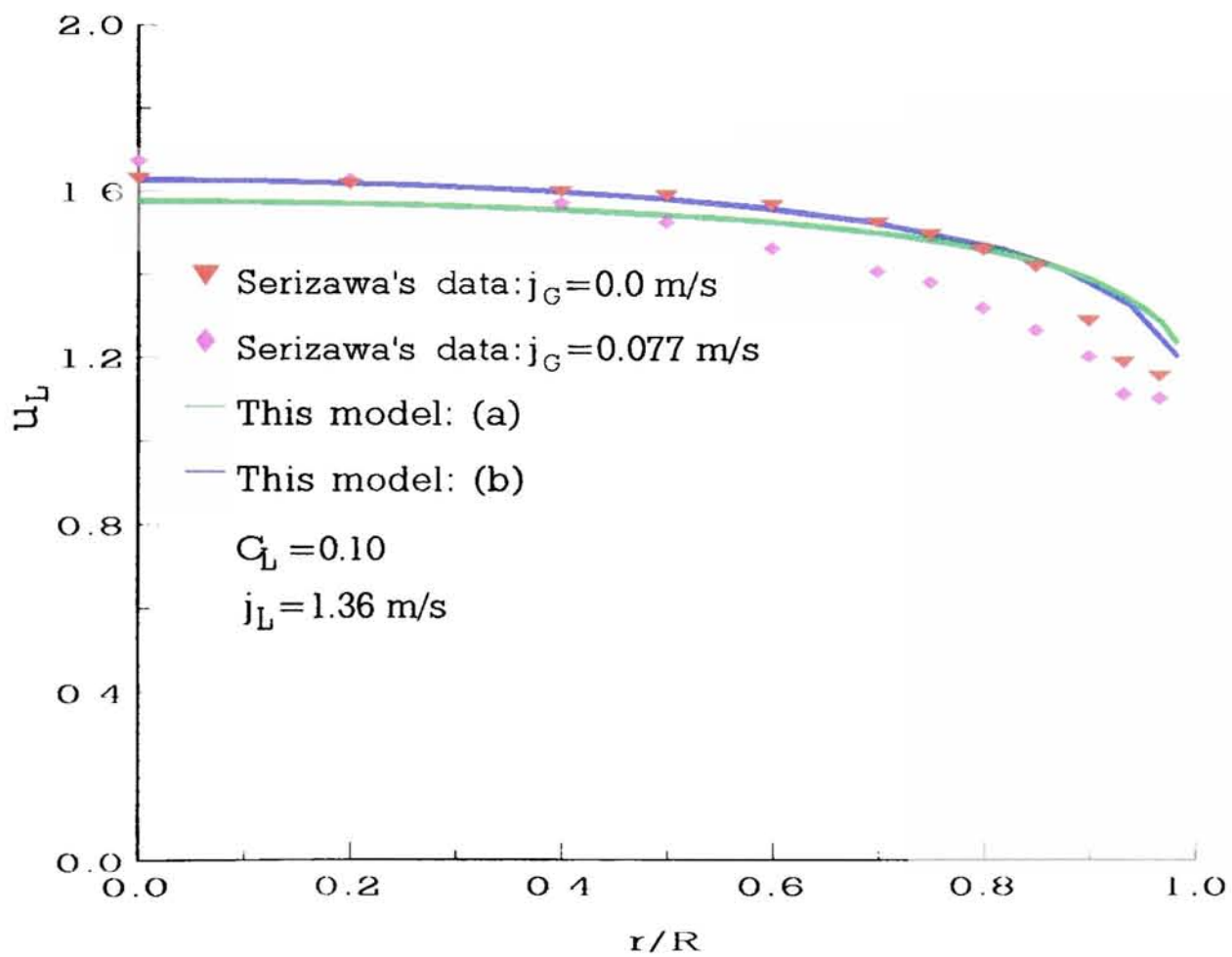


Figure 8. Comparison of the calculated velocity profile with Serizawa's data (1986): (a) including the effect of pressure gradient; (b) excluding the effect of radial pressure gradient.

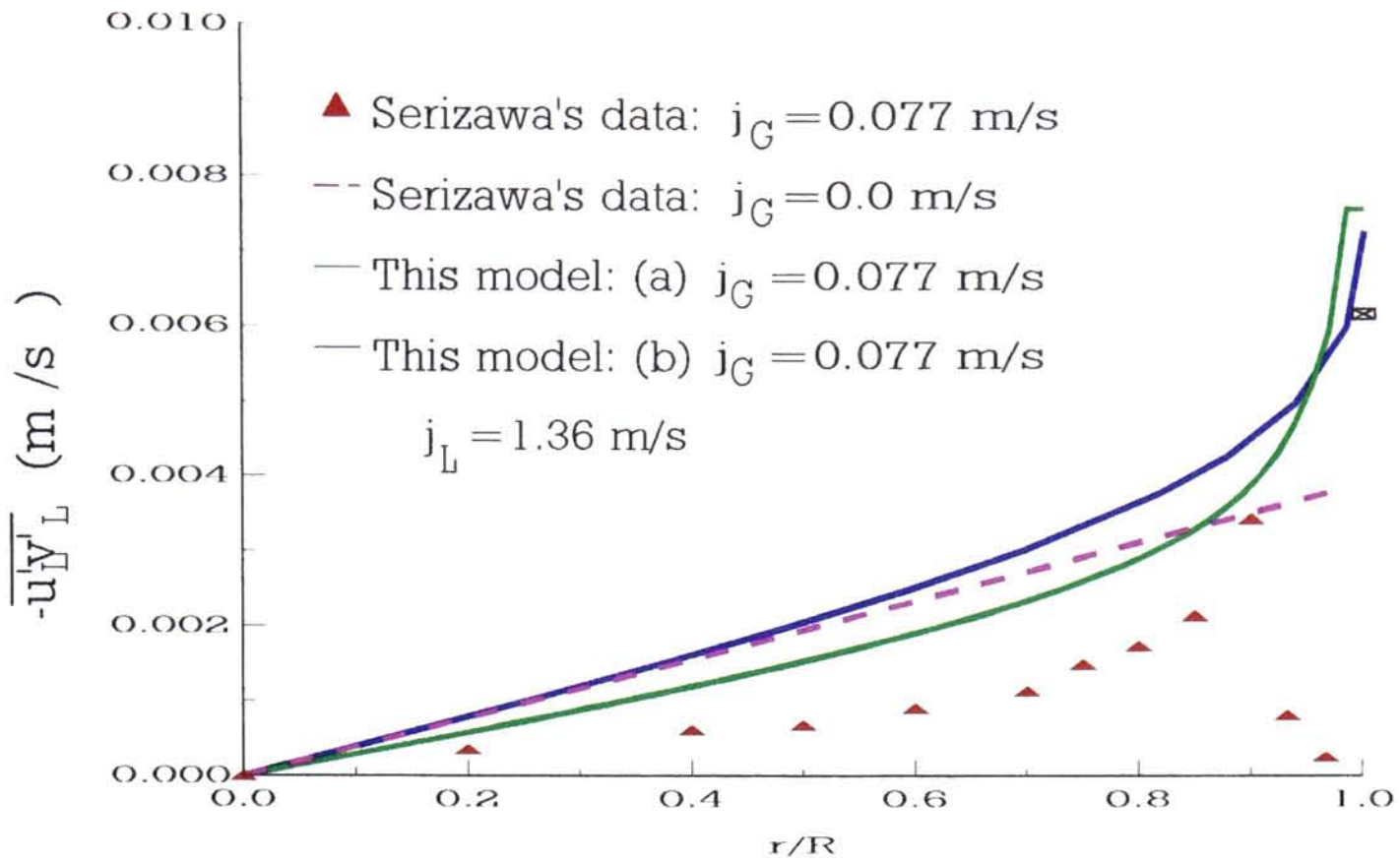


Figure 9. Comparison of the calculated shear stress with Serizawa's data (1986): (a) including the pressure gradient; (b) excluding the pressure gradient.

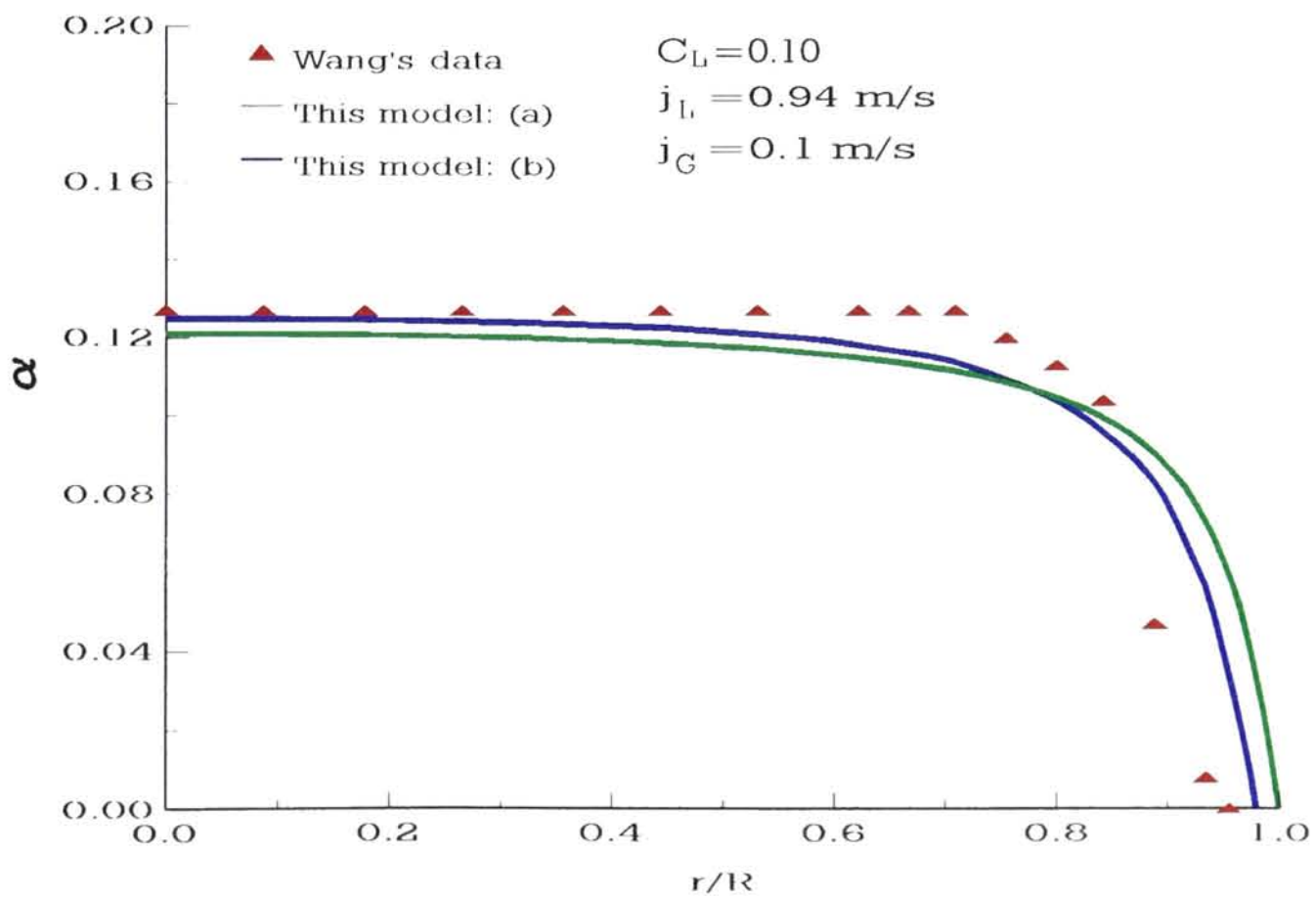


Figure 10. Comparison of Wang's (1987) downflow experimental data: void fraction profile. (a) including the effect of radial pressure gradient; (b) excluding the effect of radial pressure gradient.

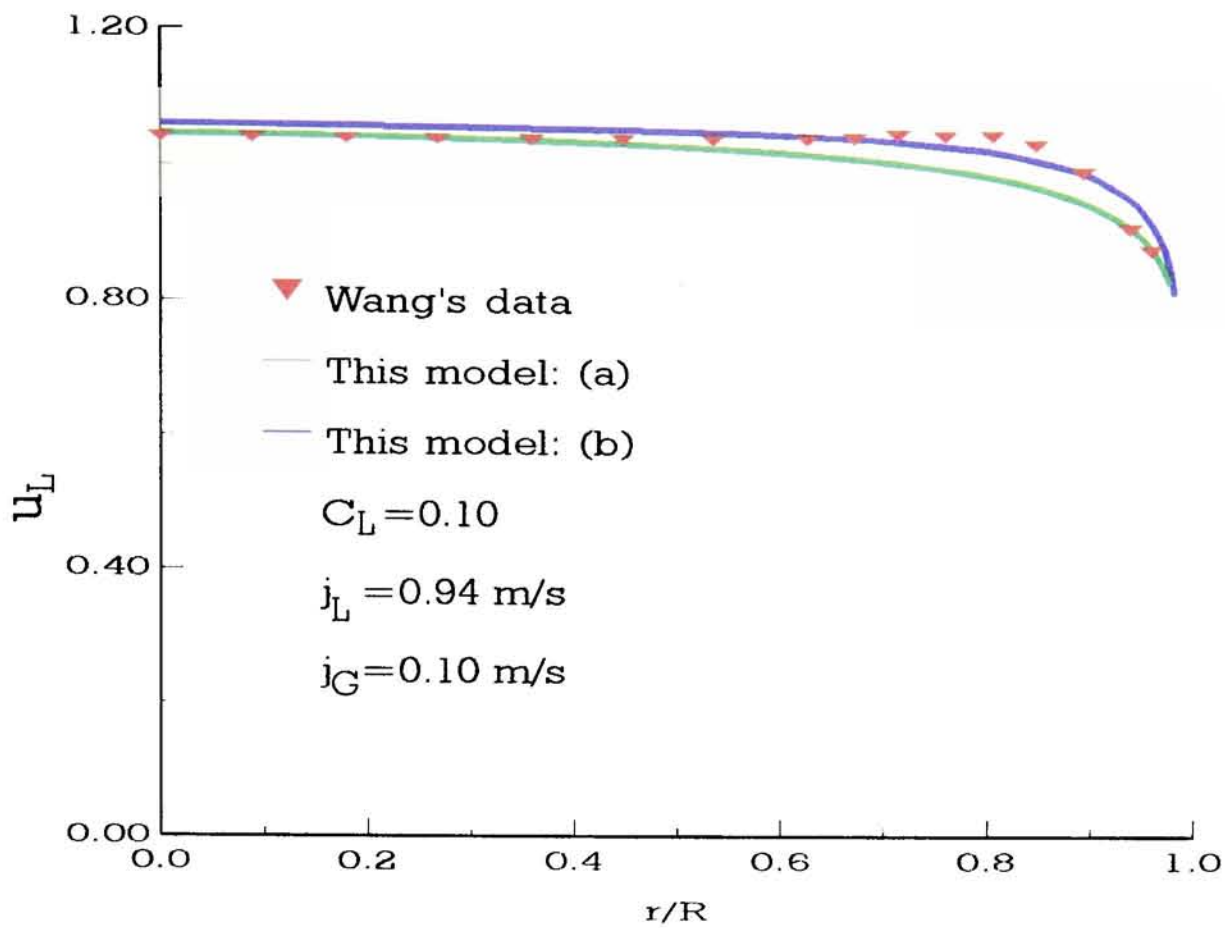


Figure 11. Comparison of the calculated velocity profile with Wang's data (1987): (a) including the effect of the radial pressure gradient; (b) excluding the effect of the radial pressure gradient.

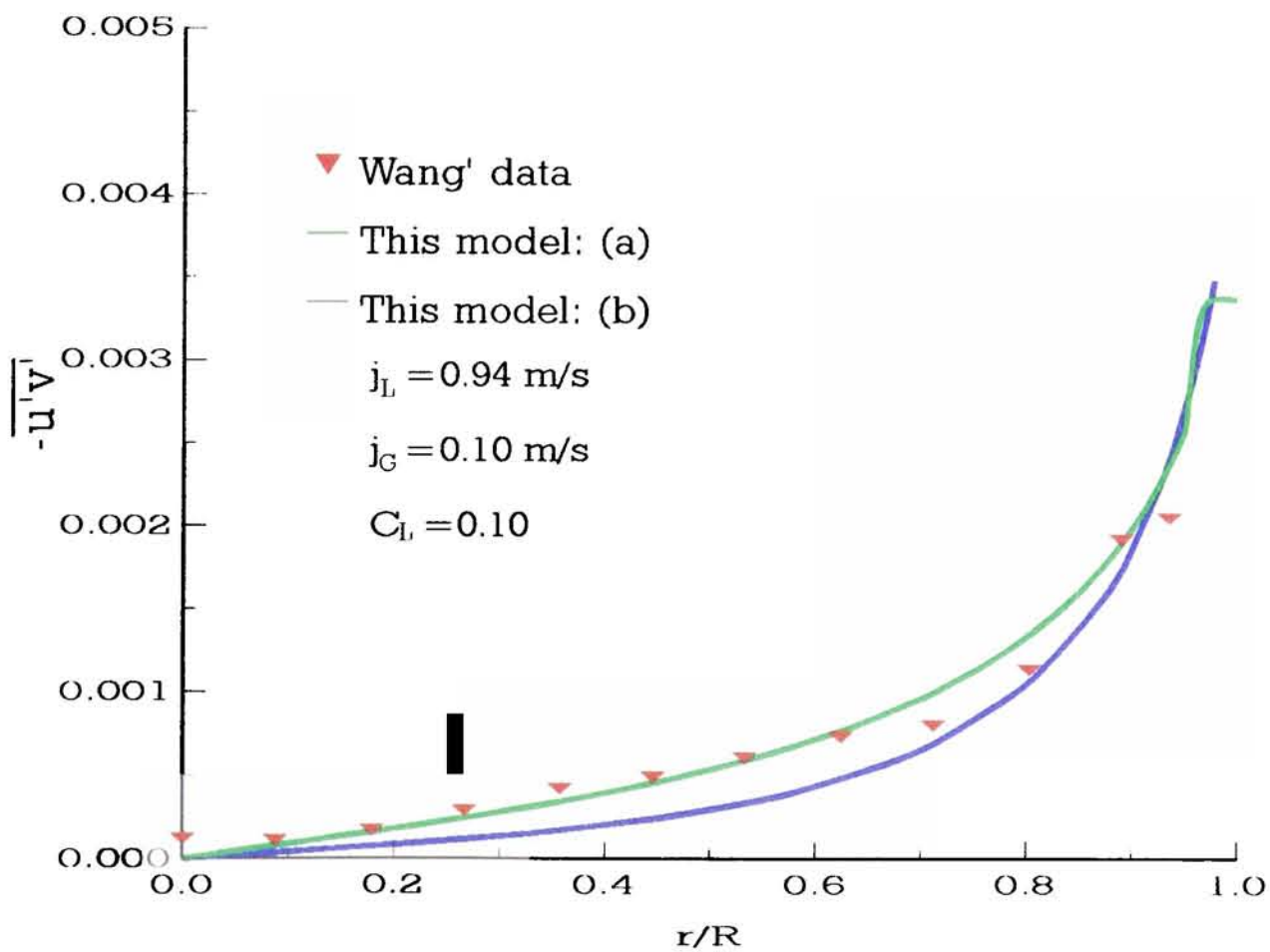


Figure 12. Comparison of the calculated shear stress profile with Wang's data (1987): (a) including the effect of radial pressure gradient; (b) excluding the effect of radial pressure gradient.

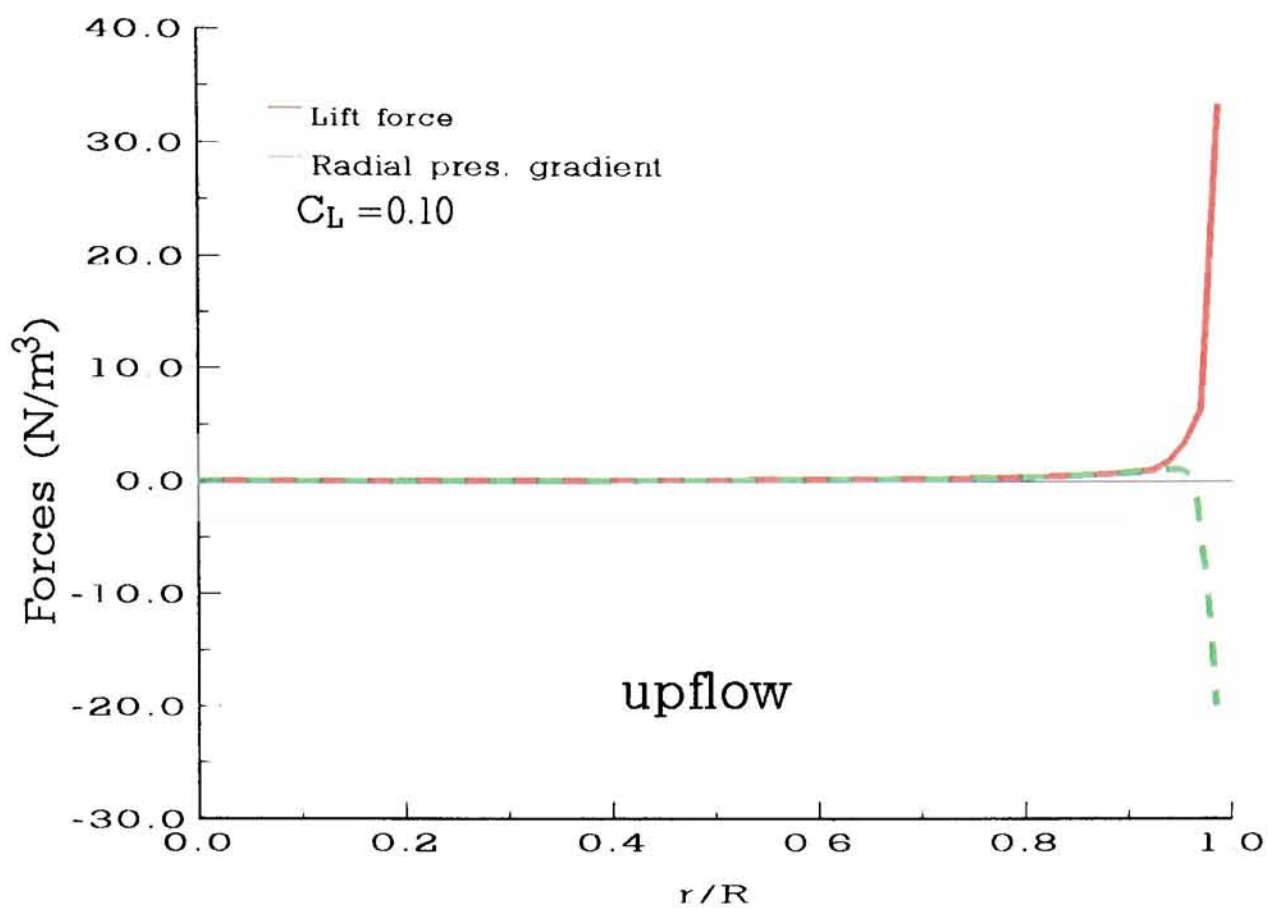


Figure 13(a). Lift force and radial pressure gradient on the bubbles for circular pipe bubbly upflow.

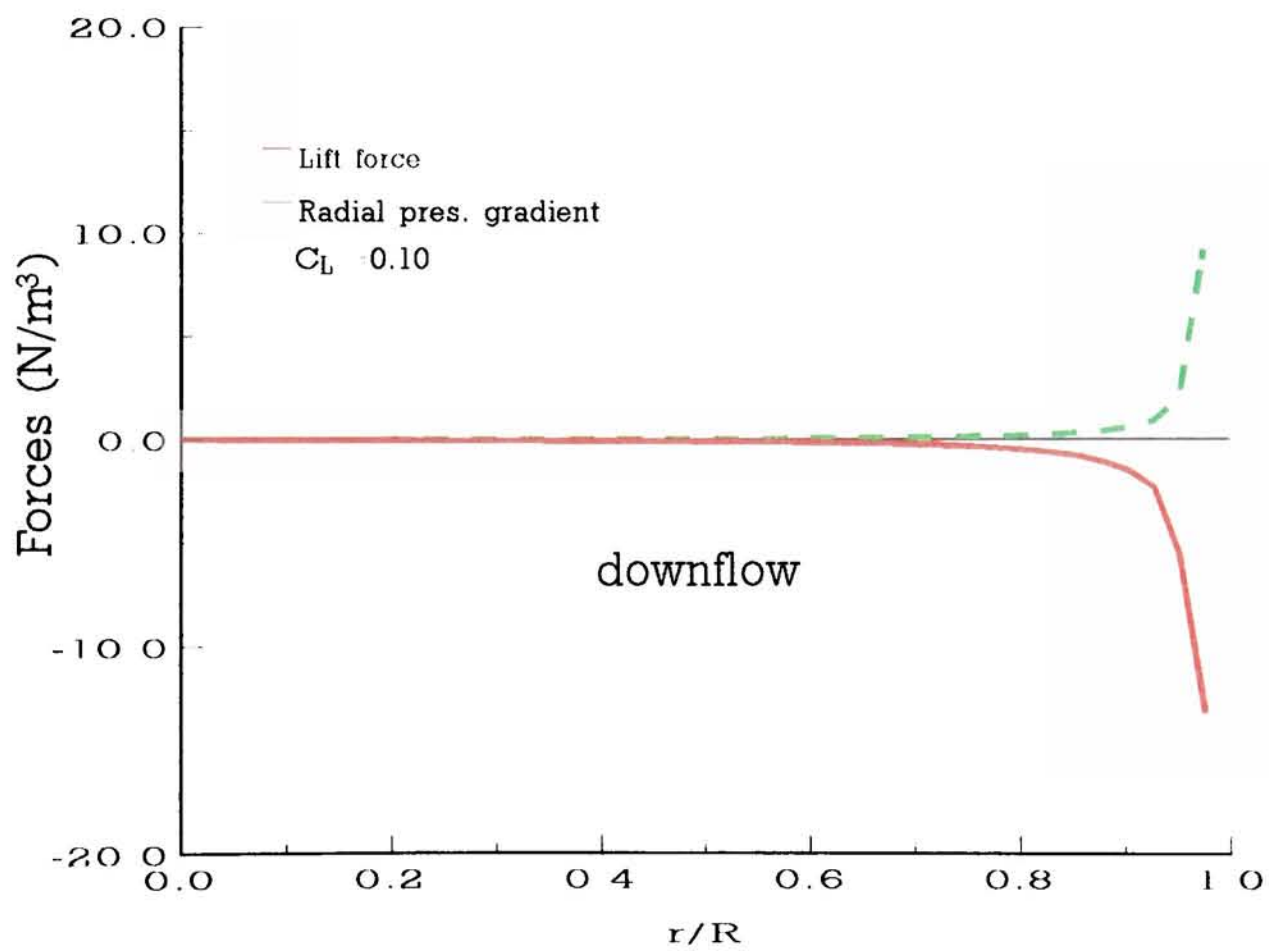


Figure 13(b). Lift force and radial pressure gradient on the bubbles for circular pipe bubbly downflow.

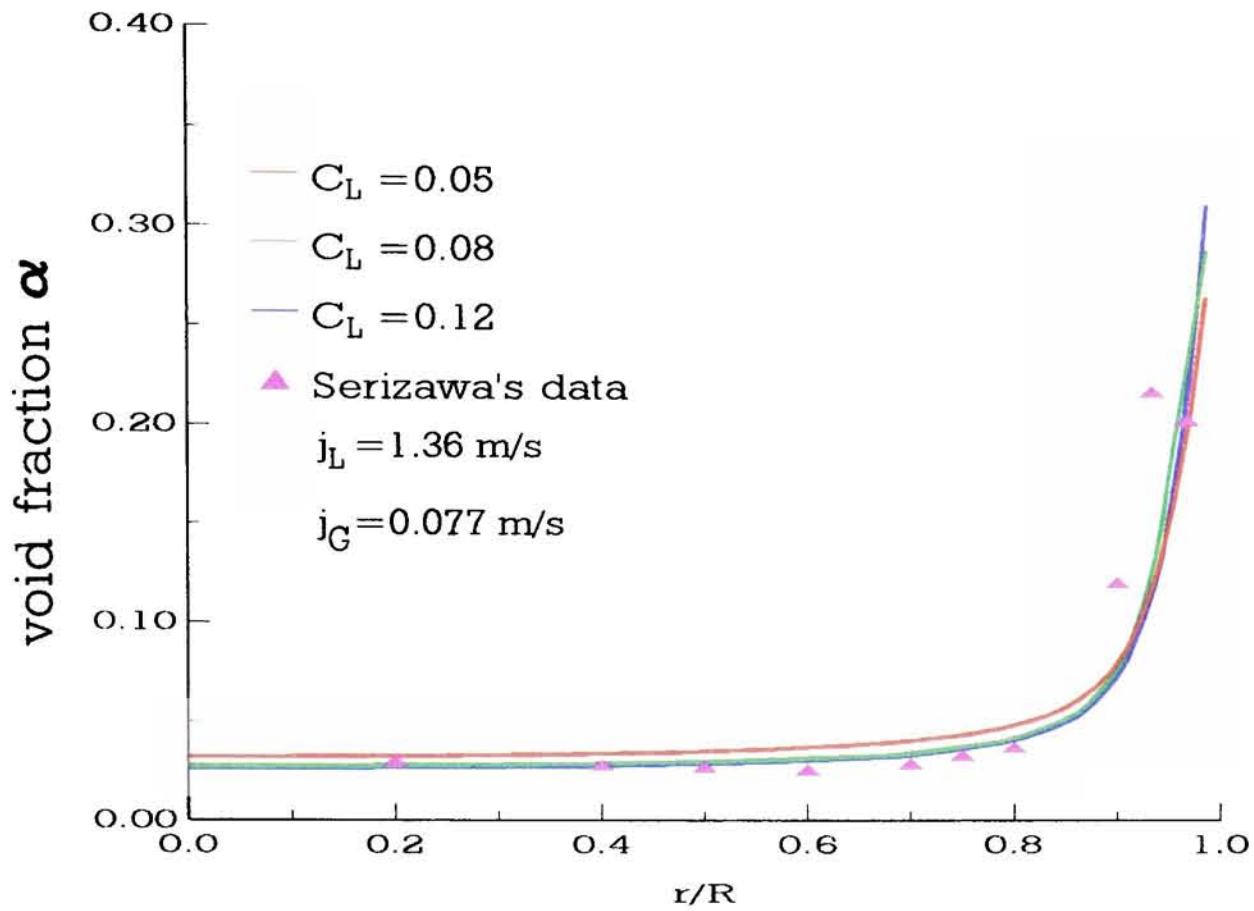


Figure 14. Effect of variation of lift coefficient on phase distribution.

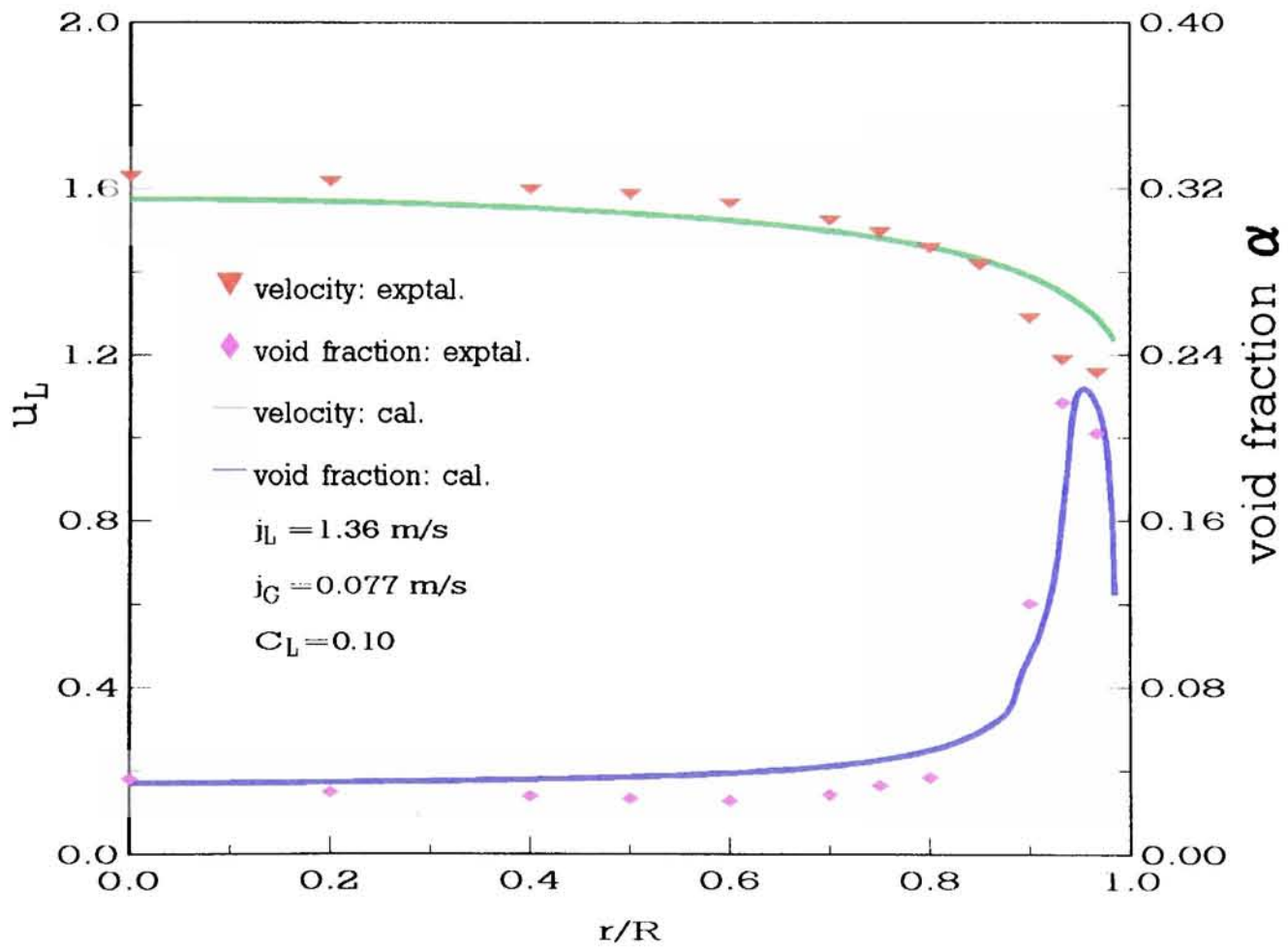


Figure 15. Comparison of the calculated velocity profile and void fraction profile with Serizawa's data (1986) when the effect of interaction between the wall and the bubbles is taken into account.

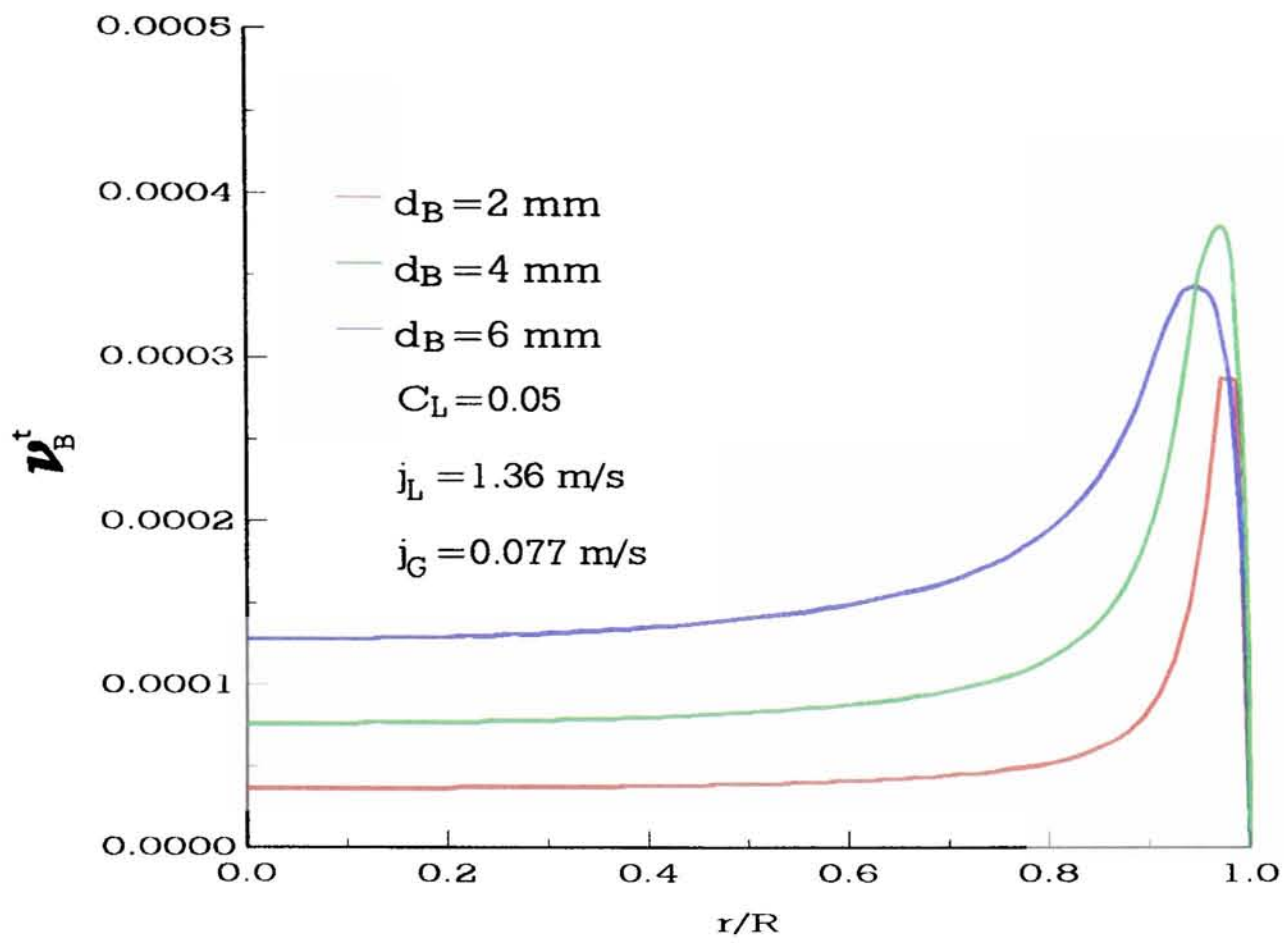


Figure 16. Effect of bubble size on the bubble-induced turbulence diffusivity.

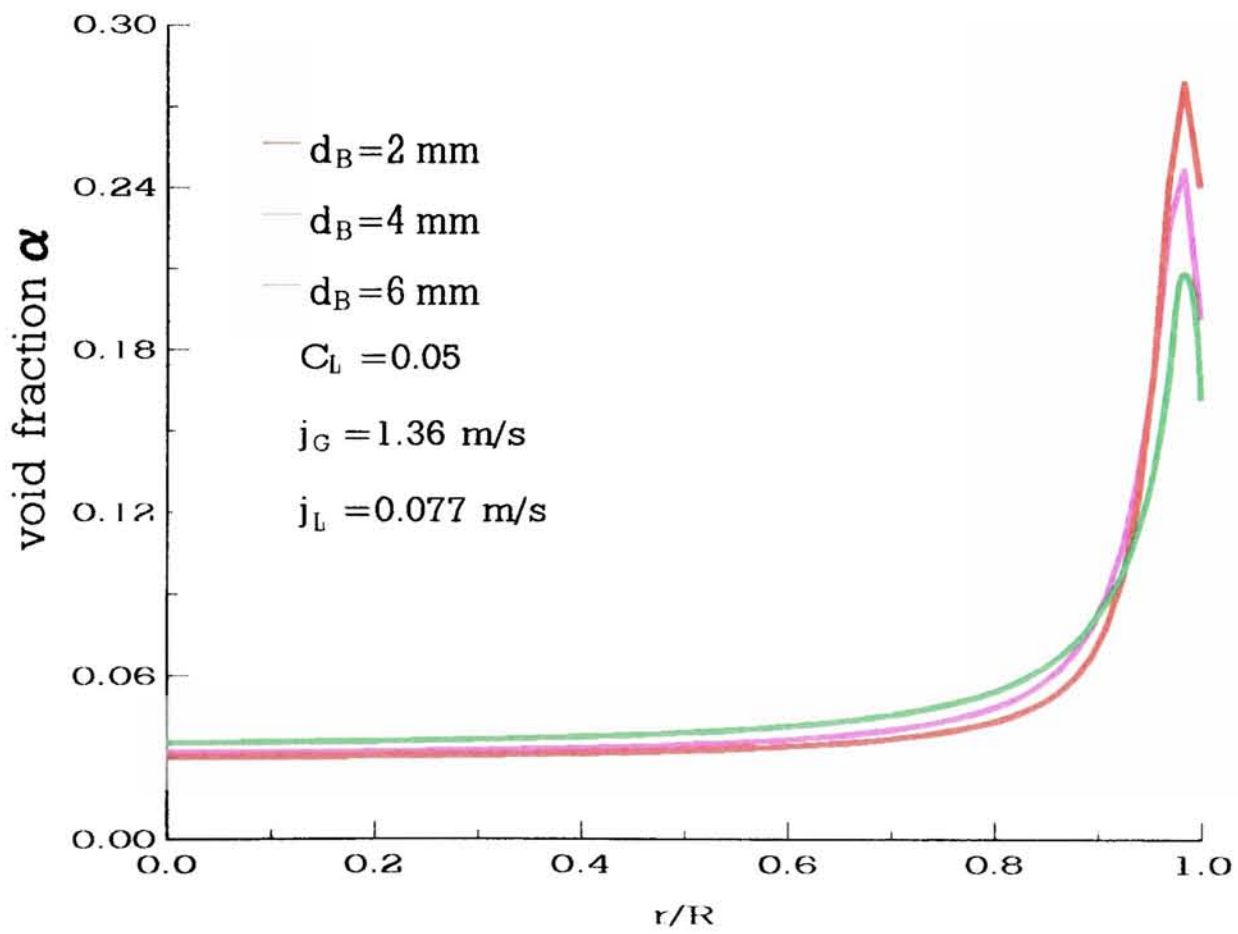


Figure 17. Effect of bubble size on the predicted void fraction.

CHAPTER 3: SIMULATION OF DISPERSIVE TRANSPORT IN TURBULENT TWO-PHASE FREE SHEAR FLOWS.

SUMMARY

The dispersion of small, spherical non-interacting particles and bubbles (i.e. the discrete phase) in two-dimensional turbulent free shear flows is investigated. After a brief preamble concerning the general equation for motion of bubbles and particles, we introduce and discuss the roles played by two key scaling parameters, the ratio of inertia to buoyancy ($\Pi = \Delta U^2 / g\delta$) and a retention parameter ($\Gamma = \Delta U / V_T$), following and extending the ideas reported in Sene *et al.* (1994). Here ΔU is the velocity difference across the eddy or the shear layer, δ is transverse width of the mixing layer or the eddy size and V_T is the terminal slip speed of the discrete phase. We also introduce the mass ratio parameter, $\gamma = \rho_b / \rho_f$ which was previously used by Thomas *et al.* (1983) and Hunt *et al.* (1993) to incorporate the influence of particle mass as an extension of earlier work concerned with bubbles. We demonstrate that these three parameters, together with the assigned added mass coefficient, define a non-dimensional group to describe the motion of bubbles and particles (and non-deformable droplets) in preference to the Stokes number (Crowe *et al.* 1985) for particles and Froude number for bubbles (Stewart & Crowe 1993).

Following and further extending the methods reported in Sene *et al.* (1994), the discrete vortex model is described and used to simulate large eddy emergence and evolution in turbulent free shear flows and the eddy dispersion of bubbles and particles in such flows is investigated as a doubly Lagrangian calculation through statistical analysis of the bubble and particle trajectories. For the special case of bubbly vertical mixing layers we compute

the turbulent Schmidt number characterising lateral dispersion and show that it takes values of about unity when the inertia forces are weak ($\Pi \rightarrow 0$), but is larger when the inertia forces increase. Our results throughout highlight the importance of incorporating all three non-dimensional parameters rather than merely the one-parameter formulations offered in some earlier works - viz. the Stokes number and Froude number representatives noted above. In general, all three parameters are needed to properly represent the behaviour of physical mechanisms relating to captured accumulation of bubbles towards a vortex centre, as opposed to ultimate centrifuged expulsion of particles outwards from a vortex. The predictions are shown to agree reasonably with the limited experimental data (Sene 1985) on bubble fluxes in downflowing free shear layer flows.

1 INTRODUCTION

The dispersion of particles, drops and bubbles by turbulent shear flows is a crucial consideration in many technological processes. Typical examples arise in liquid fuel injection for combustion and aeration sparging for biochemical processing. The performance of these processes and many others is often largely determined by the quality of the resulting dispersion. Obviously, both experimental and numerical studies of bubble and particle dispersion in organised, large turbulent structures are very important to the understanding of the physical mechanisms involved, as well as in supporting the improved design of many industrial processes. Most numerical predictive schemes for discrete phase dispersion by turbulent shear flows have been directed towards particle and droplet dispersion in gases, usually based on engineering calculation methods for Reynolds time-averaged properties of the turbulence. According to these methods, fluctuation particle transport is then introduced

as a Gaussian perturbation on the base field (Gosman & Ioannides 1981; Faeth 1987; Shuen *et al.* 1983). More recently, such approaches have to some extent sought to incorporate two-way coupling of the inertia forces (Durst *et al.* 1984; Berlemont *et al.* 1991). Virtually all such methods utilise variations on the two-equation k - ε model (Launder & Spalding 1974) within a statistical averaged framework representing eddy transport as diffusive fluxes of the exchanges. Variations on this theme include (Berlemont *et al.* 1990; Shuen *et al.* 1983, 1985) mixed Eulerian-Lagrangian treatment, the latter to compute individual trajectories of the discrete phase, realised via a supposed Gaussian fluctuation on the base flow or by introducing a Lagrangian correlation matrix to account for fluctuation processes. Alternatively, some predictions adopt an Eulerian approach for both phases, in which the disperse phase is treated as a pseudo-continuum, for example, the methods reported by Durst *et al.* (1984), Elghobashi *et al.* (1984), Picart *et al.* (1986) amongst many others, with perhaps the more sophisticated "two-fluid" closure models being advocated by Simonin (1991).

Whichever of these approximate approaches is employed, it is widely recognised that the predictions of particle dispersion are subject to considerable uncertainty (Hunt *et al.* 1993). The two-fluid doubly Eulerian closure models are very sensitive to closure assumptions on phase interactions; whilst turbulence models for two-phase flows are still poorly consolidated. At the same time, the mixed Eulerian-Lagrangian approach usually ignores feedback coupling and is also sensitive to modelling assumptions on the Lagrangian integral timescale experienced by the discrete phase; viz crossing trajectory effect (Nir & Pisman 1979; Wells & Stock 1983). Many authors (e.g. Crowe *et al.* 1985) have used the Stokes number as time scale ratio $S_t = \tau_p / \tau_f$ for particle-eddy interaction, here with τ_p as aerodynamic

response time, defined as $\tau_p = \rho_p d^2 / 18\mu$ and τ_f the eddy time scale, defined by $\tau_f = \delta / \Delta U$.

Whilst turbulence modelling of fluid continua remains contentious and essentially unresolved (Hunt *et al.* 1993), independent formulation of the Lagrangian force law for discrete phase elements remains uncertain except for a few idealizations (Hunt *et al.* 1993). Indeed most of the earliest studies of discrete phase trajectories in unsteady, non-uniform flow were restricted to small, solid particles in a Stokes regime. The Basset-Boussinesq-Oseen (BBO) equation (e.g. Hinze 1975) originally derived for a sphere moving under gravity has recently been modified and extended by many authors (e.g. Maxey & Riley 1983) to accommodate representation of motion in turbulent flows. However, all of these "more complete" models require that the Reynolds number of a particle based on slip velocity is less than one or so. Studies of the motions of larger particles and bubbles are still limited (e.g. Thomas *et al.* 1983; Sene *et al.* 1994; Onslow & Thomas 1994), often either relying on *ad hoc* extrapolations from low Reynolds number theory or on simplifications such as retaining only the drag force (Clift *et al.* 1978). However, more recent studies utilising the general force law have shown that it can plausibly be applied to a wide range of Reynolds numbers and is now supported by results from a variety of numerical simulations (Sene *et al.* 1994; Yang & Thomas 1994; Rivero *et al.* 1991) and their comparison with experimental results.

Of special interest to us here is the effect that organised eddy structures in turbulent shear flows have on the transport and dispersion of bubbles and particles. For example, entrapment of bubbles by large eddies in turbulent free shear flows was reported in Thomas *et al.* (1983) and later analysed in more detail by Hunt *et al.* (1988) using a Lagrangian force law for the discrete phase motions. Such simulations have clearly demonstrated that added mass, lift and buoyancy forces all make important contributions to the bubble motion, especially in the

vicinity of large eddies which can scavenge the bubbles and entrap them. The resulting Lagrangian trajectories and Eulerian fluxes then depend not only on the ratio of the buoyancy and drag force to the inertial force but also on the ratio of slip to shear velocity. Particle dispersion by large eddies in turbulent free shear flows has been substantially investigated by Crowe *et al.* (1988, 1993) using the same methods. Most of these studies employ discrete vortex modelling (DVM) to represent the flow field, in which the shear layer development is represented by point vortices (e.g. Leonard 1980; Inoue 1985). DVM has the important advantage that the main features of turbulence structure are reproduced and the transient vorticity distribution looks very similar to real measurements (e.g. Wygnanski & Weisbrot 1988), including evolutionary features such as growth and pairing of coherent eddies. Other application of Lagrangian-Lagrangian discrete vortex modelling approaches for the lateral or radial dispersion of solid particles in turbulent free shear flows have been reported by Chein & Chung (1988), Wen *et al.* (1992) for a spatially evolving plane mixing layer, Chung & Trout (1988) for an axisymmetric jet, Laitone (1981) for gas-particle flow over a cylinder and Chein and Chung (1988) for gas-particle flow over normal and inclined plates. Ruetsch and Meiburg (1993) also used discrete vortex methods to investigate bubble motion in a temporally evolving shear layer.

It should be noted that direct numerical simulation (DNS) has also been used to investigate particle dispersion in turbulence (e.g. Squires & Eaton 1991) and microbubble transport in turbulence (Maxey *et al.* 1994). One other very promising numerical methods is the spectral method for calculating particle trajectories in turbulent flow, as reported in the literature (e.g. Squires & Eaton 1990).

In the present study, we investigate the dispersion of the discrete phase, but with the emphasis on bubble dispersion in turbulent plane mixing layers which are dominated by large-scale eddies, following and extending the methods described in Sene *et al.* (1994). The bubble trajectories are traced according to the force law and their behaviour is subsequently characterised in terms of time averaged statistics, most notably for mean and fluctuation velocities as well as dispersion in terms of turbulent Schmidt number. In the following sections we outline the main aspects of the mathematical model, discuss the adequacy of three parameters, Π , Γ and γ , to describe the motion of the bubbles and particles in large eddy structures, present our findings for the free shear simulations and conclude with a brief indication of remaining needs.

2 MATHEMATICAL MODELLING

2.1 Modelling of Bubble and Particle Motion

As reviewed in Chapter 1, the force law (e.g. Auton *et al.* 1987), as discussed by Thomas *et al.* (1983) with regard to omissions and misconceptions in previous formulations, provides an asymptotically correct description of the motions of vanishingly small spherical bubbles in weakly unsteady and weakly nonuniform inviscid flows, in which the vorticity-induced lift force is incorporated and the added mass force is expressed correctly for the limit of rarely void fraction. We follow the analysis given in Thomas *et al.* (1983) as extended and enhanced in Sene *et al.* (1994), adopting their model in our simulations.

As emphasized in these papers, the resulting equation of motion is strictly confined to situations for which:

- (1) All the bubbles or particles are spherical and small compared with the eddy sizes;
- (2) Slip-speed Reynolds number of the bubble or particle is large;
- (3) Interactions between bubbles or particles are neglected;
- (4) The vorticity shed by the bubble or the particle does not affect its motion.

In these circumstances, the motion of the bubbles or particles is given by (Auton 1987)

$$\left(\frac{\rho_b}{\rho_f} + C_m\right) \frac{d\mathbf{v}}{dt} = (1 + C_m) \frac{D\mathbf{u}}{Dt} - \mathbf{g} \frac{|\Delta\rho|}{\rho_f} \frac{\mathbf{w}}{V_T} f\left(\frac{|\mathbf{w}|}{V_T}\right) + \left(\frac{\rho_b}{\rho_f} - 1\right) \mathbf{g} - C_L \mathbf{w} \times (\nabla \times \mathbf{u}) \quad (1)$$

where \mathbf{v} is the velocity of the bubble, \mathbf{u} is the velocity of the liquid and $\mathbf{w} = \mathbf{v} - \mathbf{u}$ is the relative bubble velocity, V_T is the rise velocity of bubbles in still water, C_m ($=1/2$) is the added mass coefficient (Magnaudet *et al.* 1995) and C_L ($=1/2$) is the lift coefficient of the bubble (Auton *et al.* 1988) under the conditions we have defined. We note that the Basset force has been excluded here, following the work of Sridhar and Katz (1995). The drag coefficient function or factor $f(|\mathbf{w}|/V_T)$ approximately accommodates the distinction between clean and dirty water, as reviewed in chapter 1. For clean water (narrow wake)

$$f\left(\frac{|\mathbf{w}|}{V_T}\right) = 1 \quad (2)$$

whereas for dirty water (broad wake)

$$f\left(\frac{|\mathbf{w}|}{V_T}\right) = \frac{|\mathbf{w}|}{V_T} \quad (3)$$

We caution here that the effect of the drag coefficient C_D has been approximated by introducing the drag coefficient function since V_T is better known than the drag coefficient (Kowe *et al.* 1988). Finally, for the rise velocity V_T , we adopt the value $V_T = 0.2$ m/s as representative of a wide range of experimental data (e.g. Clift *et al.* 1978) and, like Sene *et*

al. (1994), use it throughout our calculations.

As also discussed in Sene *et al.* (1994), the terms on the right hand of equation (1) represent the contributions to bubble acceleration arising respectively from flow inertia forces, from pressure gradient and from added mass, also from the drag force, the buoyancy force and the lift force due to local shear. Derivation of the inertia and lift terms assumes that the bubble experiences only weak shear and inhomogeneity (Auton 1987; Thomas *et al.* 1983), here meaning equation (1) is applicable to shear layers whose thickness is substantially larger than the bubble size. Again, following Thomas *et al.* (1983), we nondimensionalize equation (1) with scales representing key physical measures for the plane free shear layer (Schlichting 1968), namely ΔU as the vortex/eddy shear velocity field, and δ as the length scale representative of the large eddy series and the vorticity thickness for the mixing layer:

$$(\gamma + C_m) \frac{d\bar{v}}{d\bar{t}} = (1 + C_m) \frac{D\bar{u}}{D\bar{t}} - |\gamma - 1| \frac{\Gamma \bar{w}}{\Pi} f\left(\frac{|\bar{w}|}{\Gamma}\right) + (\gamma - 1) \frac{\mathbf{g}}{g\Pi} - C_L \bar{w} \times (\nabla \times \bar{u}) \quad (4)$$

where $v = v/\Delta U$, $\bar{u} = u/\Delta U$ and $\bar{t} = t\Delta U/\delta$. Here we have introduced the non-dimensional parameters, $\Gamma = V_\gamma/\Delta U$ and $\Pi = \Delta U^2/g\delta$ (Hunt *et al.* 1993), also $\gamma = \rho_p/\rho_f$ as a density ratio parameter which ultimately demonstrates the different trajectories followed by bubbles and particles. Values of γ ranging from 0 (bubbles in liquid) to ∞ (particles in gas) are of interest to us here. In passing, for $\gamma=1$ the pressure gradient has the same effect on the particle as on a fluid element, so their trajectories coincide in this special case. For heavy particles ($\gamma \rightarrow \infty$), the pressure gradient has no effect on the motion. However, for bubbles ($\gamma=0$) the bubble responds to the pressure forces three times as rapidly as the fluid elements. We shall see that this distinction is crucial to adequate description of the long term

centrifugal expulsion of particles from vortices and retention of bubbles within the vortices.

The parameter Γ measures the retention effect of the shear vortex field as a ratio with the slip speed. We note that Γ effectively plays the role of a Stokes number because it implicitly represents the relative importance of inertial to viscous effects, the former here relating specifically to rotational/shear motion rather than translational velocity as is more usual. Parameter Π represents the ratio of inertial to buoyancy forces, and is physically equivalent to a Froude number based on the rotational/shear velocity. In next chapter, we will show how the combination between Π and Γ is an equivalent Stokes number. For particles, the drag force dominates when this parameter is large as happens in most gas flows. It is for this reason that the Stokes number is adopted and recommended for gas-particle shear flows (e.g. Stewart & Crowe 1993). For bubbles, the buoyancy force and drag force play comparable roles, and both Γ and Π contribute to the description of their motions in shear flows. We are now clear how both the bubble and the particle motion in shear flows can be described solely by the united non-dimensional parameter groups Π , Γ and γ . In simulation, the incorporation of different force contributions can be identified (e.g. Sene *et al.* 1994). We can neglect the lift force when $\Delta U/V_T \ll 1$ and both lift forces and inertial forces when $\Delta U^2/\delta \ll g$ or $\Pi \ll 1$. However, we should not neglect both lift and inertial forces in the simulation when $\Pi \sim 1$, which corresponds most conditions of laboratory experiments (e.g. Sene 1985).

2.2 Modelling of Turbulent Plane Mixing Layers

Following Sene *et al.* (1994), the discrete vortex method (e.g. Leonard 1980) is adopted because it takes only a short time to establish the mixing layer structure and is thus suitable

for use on a microcomputer (here as a 386 or 486 DOS PC, typically runtimes are about 5 minutes). As shown in figure 1, the mixing layer simulation comprises two fields associated with bound vorticity and free vorticity. The bound vorticity is sustained by upstream boundary layer flows over the splitter plate and this is represented by a semi-infinite vortex sheet of strength $\Delta U = U_2 - U_1$ per unit length (see figure 1). Before outlining the modelling procedures, we mention also that the shed vorticity exiting downstream is represented by a second semi-infinite sheet. To establish the simulation this downstream sheet is initially located downstream from $X=0$ (i.e. contiguous with the end of the splitter plate) and is then moved downstream at velocity $U_m = \frac{1}{2}(U_1 + U_2)$ to its final location at $X=L$, where L is the length of the simulation domain. Whilst this approximation fails to meet the normal component boundary conditions on the splitter plate, Leonard (1980) showed that the procedure adequately conserves total circulation in the simulation domain. Our numerical experiments have confirmed that the perturbations are acceptably small.

Focusing now on the computational domain, we begin by noting that all vorticity is approximated as a series of point vortices shed from the splitter plate at discrete time steps. Thus, at each time step one point vortex leaves $X=0$ with strength corresponding to that of the shed sheet: namely,

$$\frac{\Delta \Gamma}{\Delta t} = \int_0^{\delta_b} U_2 \left(\frac{\partial U_2}{\partial y} \right) dy - \int_0^{\delta_b} U_1 \left(\frac{\partial U_1}{\partial y} \right) dy = \frac{1}{2} (U_2 - U_1) (U_2 + U_1) \quad (5)$$

where δ_b denotes the nominal thickness of the boundary layer developed on the end of both sides of the splitter plate. Point vortices inside the computational domain move under the influence of the convection velocity field U_m , receiving contributions from the bound

vorticity on the plate and from the downstream vortex sheet, as well as from all the elemental velocities with the vortices of the domain. Thus the velocity of the n th vortex is then given by (Leonard 1980)

$$U_n = U_m + \frac{\Delta U}{2\pi} \left[\tan^{-1} \left(\frac{Y_n}{X_n} \right) - \tan^{-1} \left(\frac{Y_n}{X_n - L} \right) \right] + \sum_{\substack{j=1 \\ j \neq n}}^N \frac{\Delta \Gamma}{2\pi R_n^2} (X_n - X_j) \quad (6)$$

$$V_n = V_m + \frac{\Delta U}{2\pi} \ln \frac{\sqrt{(X_n^2 + Y_n^2)}}{\sqrt{((X_n - L)^2 + Y_n^2)}} - \sum_{\substack{j=1 \\ j \neq n}}^N \frac{\Delta \Gamma}{2\pi R_n^2} (X_n - X_j) \quad (7)$$

Here $R_n^2 = (X_n - X_j)^2 + (Y_n - Y_j)^2$ and N is the total number of point vortices. The first term on the right hand side of these equations is simply the mean convective velocity U_m , the second term comes from bound sheets and the third term represents the influence from all point vortices within the internal region of the domain. Motions of the vortices are then described by the kinematic relations

$$\frac{dX_n}{dt} = U_n, \quad \frac{dY_n}{dt} = V_n \quad (8)$$

in our case discretised as a first-order Euler approximation

$$X_n^{j+1} = X_n^j + U_n(X_n^j, Y_n^j) \Delta t, \quad Y_n^{j+1} = Y_n^j + V_n(X_n^j, Y_n^j) \Delta t \quad (9)$$

Sene *et al.* (1994) have shown that the first-order Euler scheme can provide a reasonable comparison with experimental results. Again, we emphasize our purpose here is not to investigate or improve the quality of the DVM simulation but rather to adopt it as an adequate platform for trajectory calculations of discrete phases in free shear flow with large

structure.

It is now known that two-dimensional discrete vortex methods usually overpredict the turbulence intensities (e.g. Sene *et al.* 1994). The overprediction of turbulence intensities by the discrete vortex model arises from its lack of energy transfer into the third component, in reality associated with transverse instabilities of two-dimensional structure. In nearly all two-dimensional discrete vortex simulations, artificial diffusion is introduced to compensate this deficit. This diffusion is included either as Gaussian random jitter or as a time-expanding viscous core. In order to assess the effect of this diffusion on the simulation, we introduce a Gaussian random jitter on the motion of each vortex, superposing it on scheme (9):

$$X_n^{j+1} = X_n^j + U_n(X_n^j, Y_n^j) \Delta t + \zeta_x, \quad Y_n^{j+1} = Y_n^j + V_n(X_n^j, Y_n^j) \Delta t + \zeta_y \quad (10)$$

where ζ_x and ζ_y are respectively the components of the vector jitter in x and y direction, with standard deviation expressed here as a fraction of the average distance moved by each vortex in each time step - that is $\zeta' = \varepsilon U_m \Delta t$. The results of the effect of the coefficient ε on fluctuation velocities will be presented later.

Sufficient vortices must be introduced to provide an adequate representation in term of structure (see figure 5) and statistics as Reynolds averaged values compared with established experimental results (shown later). Typically a few hundred are employed in our calculations although some works (e.g. Ashurst 1979) have used many thousands. The practical limit is set by computational speed, even when an approximate algorithm (Spalart & Leonard 1981)

- in which the long distance interactions among the point vortices are calculated from group to group instead of vortex to vortex - is used. Except for reproducing the correct vorticity influx to the mixing layer, selection of the time step increment is required by meeting a stability restriction of trajectory calculation according to the force law. Accordingly, we find that $\Delta t=L/NU_m$ can match this with sufficient point vortices. Here N is the average number of the point vortices in the simulation domain, and we also adopted Chorin's (1973) device to ensure that the induced velocities remain bounded when vortices approach each other, by imposing a finite core size on each vortex element, namely:

$$u_{\theta} = \begin{cases} \frac{1}{2\pi r} \Delta\Gamma & (r \geq \sigma) \\ \frac{r}{2\pi\sigma^2} \Delta\Gamma & (r < \sigma) \end{cases} \quad (11)$$

with $\sigma=2.24\sqrt{\nu t}$ representing viscous core expansion (ν is kinematic viscosity, t is the time elapsed since the vortex is introduced into the calculation domain) (e.g. Sarpkaya 1989). Again, following Sene *et al.* (1994), we say that our purpose here is not predictive modelling of the base flow, but rather the prediction of bubble trajectories in that flow.

3 RESULTS

3.1 Demonstration Examples With Rankine Vortex Flows

In this section we present the results of disperse phase motion in a steady, isolated solid-body vortex, i.e. Rankine vortex, not only because the equation of motion simplifies in such flows but also because inductional large eddies in a turbulent mixing layer can be represented as such structures, at least as a first approximation (Sene *et al.* 1994). This simple model has been developed by Sene *et al.* (1994) in detail as an aid to understanding

qualitatively how inertial and turbulent dispersive forces affect the distribution of bubbles in mixing-layer vortices. The demonstration presented here is to provide some insight into the differences of response to large eddies between disperse phases.

For the case of a Rankine vortex whose axis is horizontal we use $T=1/\omega$, $L=R$ as the time and length scales (so $U=\omega R$ as velocity scale), with R the core radius and ω the angular velocity. The motion equation for the discrete phases can then be written down directly for this defined velocity field according to equation (4):

$$\frac{d\bar{v}_x}{d\bar{t}} = -\frac{(1+C_m)\bar{x}}{(\gamma+C_m)} - \frac{|\gamma-1|}{\gamma+C_m} \frac{\Gamma_{Ran}(\bar{v}_x-\bar{y})}{\Pi_{Ran}} f\left(\frac{|\bar{v}-\bar{R}|}{\Gamma_{Ran}}\right) + \frac{(\gamma-1)}{(\gamma+C_m)} \frac{\mathbf{g}_x}{g\Pi_{Ran}} - \frac{C_L}{(\gamma+C_m)}(\bar{v}_y-\bar{x}) \quad (12)$$

$$\frac{d\bar{v}_y}{d\bar{t}} = -\frac{(1+C_m)\bar{y}}{(\gamma+C_m)} - \frac{|\gamma-1|}{\gamma+C_m} \frac{\Gamma_{Ran}(\bar{v}_y-\bar{x})}{\Pi_{Ran}} f\left(\frac{|\bar{v}-\bar{R}|}{\Gamma_{Ran}}\right) + \frac{(\gamma-1)}{(\gamma+C_m)} \frac{\mathbf{g}_y}{g\Pi_{Ran}} + \frac{C_L}{(\gamma+C_m)}(\bar{v}_x+\bar{y}) \quad (13)$$

For this idealisation, then $\Gamma_{Ran}=R\omega/V_T$, $\Pi_{Ran}=R\omega^2/g$. As typical values for bubbles, drops and particles we consigned $\gamma=0, 0.9, 2.5$ and computed their trajectories for initial conditions corresponding to release either from within or outside the Rankine vortex, as shown in figure 2 for $\Pi_{Ran}=10$ and $\Gamma_{Ran}=5$. Here the local fluid velocity is used as an initial condition, i.e. zero slip condition at $t=0$. We note that since the same force law is employed, the differences between these trajectories arise only from the different fractional contributions from each of the forces as γ is changed. The coefficients respectively on the inertia, drag, buoyancy and lift forces successively take values of 3, 2, 2, 1 for bubbles, 1.071, 0.071, 0.071, 0.357 for drops and 0.5, 0.5, 0.5, 0.167 for particles. It can be seen from figure 2 that the trajectories for the bubble, droplet and particle are obviously different.

Figure 3 shows how the bubble trajectories depend on Π_{Ran} , for a fixed value of $\Gamma_{Ran}=10.0$. At smaller Π_{Ran} , the drag forces dominate, act to and inhibit the radial motion, so that the trajectories take longer to settle to equilibrium. As Π_{Ran} increases, the radial velocity component becomes larger and the bubbles move more quickly towards the equilibrium point. However, when Π_{Ran} further increases, the bubbles once again approaches the equilibrium point slowly. This reflects the effect of variation of Π_{Ran} on the forces experienced by the bubbles. When Π_{Ran} increases, in general, the effect of drag force on the bubble radial motion decreases so that the effect of the pressure gradient becomes more eminent and the bubble moves more quickly towards equilibrium point. Nevertheless, when Π_{Ran} exceeds some value, the local slip of the bubble increases again, resulting in the drag force experienced by the bubble to increase. This effect will inhibit the bubble radial motion towards its equilibrium point.

We now turn to the effect of Γ_{Ran} . We can condense this information both by plotting the trajectories and by plotting the time series of radial distance from the vortex centre, as shown in figures 4a and 4b. Here, for a given value of Π_{Ran} , bubbles were released from the edge of the vortex core. We note that for a given Π_{Ran} the effect of Γ_{Ran} on the bubble motion is to change the drag force term. It can be seen clearly from the curves in figure 4b that when Γ_{Ran} exceeds some value, the bubble again takes more time to settle to equilibrium. Using these two methods of presentation, namely trajectories and time series of radial distances, we have demonstrated the different roles of γ , Π and Γ on bubbles.

3.2 Validation of the Shear Layer Simulation

Several important aspects of the simulation were assessed for quality in reproducing the

basic flow structure and statistics; namely evolution, pairing and clustering events; mean velocity and turbulence intensity profiles; single-point power spectra, including survey of effect of modelling parameters like random jitter.

(a) Eddy structure and statistics

A two-stream mixing layer with velocity ratio $U_2/U_1=3$ was adopted, as in Sene *et al.* (1994), because it accords with the conditions of Sene's (1985) experimental study. Two random jitter magnitudes were tested, namely $\zeta^2=0.2U_m\Delta t$ and $\zeta^2=0.4U_m\Delta t$, and the effects were assessed as follows.

As demonstration of how persuasively the macro-structures and events are reproduced, figure 5 demonstrates how the vortices cluster into groups that closely resemble the coherent structures observed in experimental studies (Roshko 1976) and figure 6 displays the corresponding vorticity contours. Even the vortex pairing process (Winant and Browand, 1974) is well reproduced insofar as adjoining clusters interact by rotating around each other, then gradually merging as an enlarged single eddy.

As basic validation of our simulation, like Sene *et al.* (1994), we present time-averaged mean velocity profiles, turbulent intensity profiles and shear stress profiles in figures 7 to 10 and found that they are in reasonable agreement with experimental measurements (e.g. Pui & Gastshore 1979). Pui and Gastshore show that peak values of the r.m.s. u' and v' components are about 0.18 and 0.14 of the shear velocity ΔU , and the peak value of the Reynolds shear stress $u'v'$ is about $0.013\Delta U^2$. As can be seen in figures 7 to 10, the mean velocity profiles rapidly establish self-preserving character and the turbulence intensities are

reproduced by the calculations, except for the normal component r.m.s. fluctuations (figure 9) which Sene *et al.* also found problematical in their simulations. As noted in Sene *et al.* (1994), this shortcoming may be associated with the modelling limitations of a two-dimensional simulation or with numerical simplifications relating to representation of those point vortices out of the computational domain by a half infinite vortex sheet, or most probably both. The same inadequacy has been previously documented by Inoue (1985) and Sarpkaya (1989), and we do not regard it as a significant limitation for our purpose here. The thickness of the mixing layer with $\Delta U/U_i=2.0$, defined as the distance between the points at which the velocity differs by 0.5% from the stream value, is about $0.12X$ calculated from our simulations, as shown in figure 11. This result agrees well with the expectation of Townsend (1976).

(b) Fluctuation velocity time records and spectra

Figure 12 shows the records of time-dependent u fluctuation velocity field for three different values of prescribed random jitter ($\zeta'=0, 0.2U_m\Delta t, 0.4U_m\Delta t$) and figure 13 shows the power spectra of axial component velocity fluctuation sampled at the centre of the mixing layer with $X=0.5L$ for each of the three prescribed levels of random jitter. It can be seen that adjusting the random jitter only slightly affects the mid range frequency behaviour which is apparently dominated by the fine-scale diffusion effect due to introduction of a random jitter to each point vortex. However, the high frequency range is clearly very nonsensitive to the value of the random jitter. This indicates that the function of alteration of random jitter is similar to the use of a different core cut-off scheme which is employed for elimination of infinite velocity when two point vortices approach each other, but they do not change significantly flow features such as turbulence intensities. This finding is consistent

with Inoue's (1985) suggestion that the effect of core radius on the flow features is slight.

3.3 Application to Bubble Transport and Dispersion

The effect of different bubble release conditions on the bubble distribution in a vertical downflowing mixing layer is evaluated and the effect of different time delay of bubble release on the capture of bubbles across a horizontal mixing layer and the interactions between bubbles and large eddies is then presented. We should recall Sene's *et al.* (1994) suggestion that inertial forces cause the bubbles to offset toward the high speed side of the mixing layer in downflow. As a simplification for initiating all the calculations, we use the reduced equations

$$\mathbf{v} = \mathbf{u} + \mathbf{U}_T, \quad (14)$$

i.e. neglecting the influence of inertial and lift forces. Here \mathbf{U}_T is the slip velocity vector. However, subsequent bubble motion is computed using the full force law, i.e. employing equation (4).

(a) Bubble Dispersions in the Vertical Mixing Layer

The distributions of bubbles in realisations of established vertical mixing layers were calculated for various bubble release points including at the origin of the mixing layer and from transverse locations outside the mixing layer. Vertical orientation eliminates cross-stream buoyant drift and escape, and is appropriate for comparisons with Sene's (1985) experiments and with the gradient diffusion model outlined to assess the usefulness of traditional calculation methods and what we also further addresses here including in terms of Lagrangian measures of the dispersion coefficient. We begin with an account of the

trajectory pattern record for the statistics.

Bubbles released near the origin of mixing layer

Bubbles were released from the position very close to the end of the splitter plate at different times to assess the effect of coherent eddy phasing on the bubble dispersion. Two cases were investigated as follows: release every Δt for total 400 bubbles; and release every $10\Delta t$ for 400 bubbles. Selection of different bubble release intervals is to access the effect of large eddy passage in the mixing layer on bubble dispersion.

Typical bubble trajectories for the two cases $\Pi=0.5$, $\Gamma=10$ and $\Pi=0$, $\Gamma=10$ are shown in figures 14-15. In both cases, the bubble transport was confined within the edges of the mixing layer, but we note a decreased confinement when $\Pi=0$. Further inspection of figures 14 and 15 reveals that bubble trajectories are more skewed to the high speed side when $\Pi=0.5$, due to the influence of inertial and lift forces, whilst the influence of both forces is negligible when $\Pi=0$, as discussed in section 2. This behaviour is emphasised in the comparison of trajectories for the two cases as seen in figures 14a-15a. Asymmetric equilibrium of bubbles within vortices and confinement of the bubble concentration profiles within mixing layer flow was addressed in Sene *et al.* (1994), who showed the profile offset could be estimated as $\eta_{off} \sim bV_\gamma/\Delta U$, where b is the mixing layer spread rate (0.12 here) and η_{off} is the offset from the axis of the mixing layer. It can be seen from the bubble number flux profiles (figures 16 and 17) that this location estimation (roughly 0.02) agrees well with our simulation results.

Since the mean velocity profiles are self-preserving in the fully developed region of the

mixing layer, it is interesting to investigate whether the bubble flux profiles exhibit the same performance. Bubble flux profiles for the cases $\Pi=0.5$ and $\Pi=0$, drawn by the use of the mixing layer similarity coordinate $(Y-Y_0)/(X-X_0)$, appear in figures 18 and 19, at streamwise stations $X=0.2L$, $0.4L$, $0.6L$ and $0.8L$. They are approximately self-preserving but are skewed towards high speed side of the mixing layer when bubbles are fully engaged in the mixing layer. However, a violation of self-preserving in the concentration flux profiles for station $X=0.2L$ is observed. This is probably attributed to the bubbles still not being fully engaged by the coherent eddies.

The bubble mean velocity and fluctuation correlations are displayed in figures 20-24 for the case $\Pi=0$. A significant situation is observed for the time-averaged cross-stream bubble velocity from figure 21. This reveals that resemblances exist between the flow and bubble cross-stream velocity. The cross-stream velocities of the fluid particles tend to be negative on high speed side of the flow and positive on low speed side, as expected. The cross-stream bubble velocities exhibit a similar trend, indicating that bubbles are being trapped towards the centre of the mixing layer. The time averaged results strongly support the experimental observations (Thomas 1982) and the physical model of bubble trapping in shear flows (Sene *et al.* 1994). Whilst the other quantities are of crucial importance for assessing the implications of our findings for Eulerian closure models, we are not yet in a position to comment on their physical significance. This aspect remains for future work.

Comparison with the predictions using the gradient diffusion model

As passive transport in free shear flows can be well described using the gradient diffusion model method (Hinze 1975), we may expect that the use of the gradient diffusion model for

bubble transport can give reasonable estimations. To do this we compare the results obtained using the gradient diffusion model with our Lagrangian simulation results, as shown in figure 18. We caution this comparison is only qualitative because the ordinate used here for the gradient diffusion model is number density (concentration) rather than number flux as used for the simulation results. However, the profiles can be related directly if the slip speed is small ($V_T \ll U_m$), as was noted by Sene (1985). It can be seen from figure 18 that the bubble number flux profiles obtained are consistent with the bubble number concentration profile predicted by employing the gradient diffusion model method in which the Schmidt number of unity is assigned. As noted previously by Sene (1985), the eddy Schmidt number for bubble transport is roughly unity or so, corresponding to confinement within the vorticity field of the large eddy motions. We note that passive scalars display eddy Schmidt numbers significantly less than unity (0.7 or so), corresponding to significant 'edge-diffusion' outside the vortical core zone.

Bubble release across the approach flows

Because we expect that individual realisations are highly dependent on the phase relationship between bubble release and the passage of large eddies, it is useful to examine bubble trajectories for different release situations. We choose bubbles released from both the low speed and the high speed side of the mixing layer. Figure 25 shows sample trajectories of 10 such bubbles introduced at the same time. It is clear that bubbles introduced from the low speed side are more sensitive to the inertia force than bubbles introduced from the high speed side. To firm up this picture with properly converged statistics 400 bubbles were released from the high speed side with random initial positions in the range $0.0 < y_0 < 0.15L$. Bubbles released beyond the positions $y_0 > 0.15L$ are hardly to interact with the eddies of the

mixing layer since the effect of inertia is larger than that of pressure gradient. In the calculation, values of $\Pi=0.0667$ and $\Gamma=5$ were chosen to allow direct comparison with Sene's (1985) experimental results for voidage profiles of bubbly flow entering on the high speed side.

The bubble trajectories as calculated by the simulation for this condition appear in figure 26. Bubble number flux profiles obtained from the statistics are shown in figure 27. We note that they are broadly similar to the mean velocity profiles (figure 7), here reproducing the findings reported by Sene *et al.* (1994). Because this self-preservation behaviour exists for passive transport, the spread of bubbles in the mixing layer can be reproduced by using the gradient diffusion model but with an effective Schmidt number of roughly about unity adopted. Further validation of this finding can be achieved by the use of Lagrangian measurements of bubble dispersion, which is given in section 3.4.

(b) Phase relationship between bubble introduction and large eddy passage

The escape of bubbles across a horizontal shear layer (i.e. between the large eddies) was investigated by Sene *et al.* (1994). They found the probability of bubble escape depends on both Π and Γ . High values of Π encourages capture due to inertial attraction and high Γ discourages escape by vorticity lift. Since the passage of large eddies is intermittent, we expect bubble capture or escape to depend strongly on the phase relationship between large eddy passage and bubble encounter with the shear layer. Following Sene *et al.* (1994), the bubbles were introduced into the flow at coordinate $(0.05L, y_0)$ with variations in time interval between each bubble introduction. The value of y_0 was determined in such a way that the bubbles would travel through the point $(0.5L, 0)$ in the absence of the mixing layer

because this allows bubbles to experience similar shear histories while travelling in the mixing layer.

Figure 28 shows the bubble trajectories when $\Pi=0.05$ and $\Gamma=2.0$ with a time interval $90\Delta t$, corresponding to the highest capture probability, a ratio calculated by counting the trajectories confined within the mixing layer. The dependence of bubble capture probability on bubble introduction time interval is depicted on figure 29. These results reveal phase relationship between bubble release and the passage of large eddies in shear layers. A further implication of the results is that a maximum capture rate of bubbles in the mixing layer can be acquired through control of time interval between bubble introduction.

3.4 Measurements of Bubble Dispersion

Most measurements of shear layer dispersion presented in the literature are of the Eulerian type, i.e. the data is obtained solely in the spatial domain, as we have presented in the previous section. Measurements such as these may not be ideal for the development of the diffusion models. Lagrangian statistics are fundamentally more relevant in developing the diffusion models. In this section we present Lagrangian statistical measurements of bubble dispersion and the determination of bubble diffusivity in such shear flows. Bubble diffusivity is evaluated for discussion of the ability of the bubbles to be trapped or dispersed by the large eddy.

The turbulent eddy diffusivity was introduced by Taylor (1921) through extending the concept of molecular diffusion for isotropic turbulent flow. It was confirmed after Taylor's great study that the theory may be applied to discrete particles in inhomogeneous turbulence

such as in the mixing layer when non-homogeneity is taken into consideration (Batchelor 1957). According to Taylor's diffusion theory, the mean square displacement $y^2(t)$ of a fluid particle (here as tagged fluid tracer) is given by

$$\overline{y^2(t)} = 2\overline{v_b^2(t)} \int_0^t \int_0^{t'} R_L(\tau) d\tau dt' \quad (15)$$

where $v_b(t)$ is the Lagrangian velocity and $R_L(\tau)$ is the Lagrangian auto-correlation coefficient, defined by

$$R_L(\tau) = \frac{\overline{v_b(t)v_b(t+\tau)}}{\overline{v_b^2(t)}} \quad (16)$$

Two important special cases of Taylor's original theory are observed. For short time delay, τ , the particle velocity is perfectly correlated with itself; that is, as $\tau \rightarrow 0$ then $R_L(\tau) \rightarrow 1$. When the diffusion time t is larger, the particle velocity becomes uncorrelated, $R_L(\tau) \rightarrow 0$, and the dispersion develops linearly in time. The slope of the curve according to equation (13) is defined to be the fluid particle diffusivity D_{fy} , as follows.

$$D_{fy} = \frac{1}{2} \frac{d}{dt} \overline{y^2(t)} \quad (17)$$

Equation (17) defined for a fluid particle can be generalized to the description of the dispersion of bubbles or particles in shear flows subject to availability of the measurement of their mean squared displacement. Such measurement for the bubbles in the mixing layer can be achieved in the simulation as described below.

As the bubbles are transported by the large eddies, the mean transport times for bubbles and fluid particles to arrive at a given downstream station are obtained by ensemble averaging the time each bubble or fluid particle takes to reach that sampling station. Such information is easily available since we are tracking each bubble and fluid particle by integrating the generalised force law (Thomas *et al.* 1983). The mean transport time measurements are shown in figure 30 and the mean square displacement of the bubbles is depicted on figure 31.

With the transport time for each bubble and fluid particle available we can present truly Lagrangian statistics for bubble dispersion. This is achieved by combining the data of figure 30 and figure 31 as shown in figure 32. Inspection of figure 32 reveals that for $\Pi=0$ the lateral dispersion for bubbles is nearly commensurate with that for fluid particles. However, for $\Pi=0.5$, the lateral dispersion of bubbles is obviously less than those of fluid particles due to the confinement of the bubbles in the large eddies. With the mean square displacement available, the bubble diffusivity can be estimated according to equation (14), which is shown in figure 33. We notice that the curve of the bubble diffusivity D_{by} is not much different to that of fluid particles for $\Pi=0$, as expected.

4 DISCUSSION

Having presented the results of bubble dispersion and bubble trajectories in turbulent shear flows, we now generalise our findings to make inferences on bubble transport in such shear flows.

4.1 Suitability of The Use of The Stokes Number For Bubble Transport in Shear Flows

We have addressed generality of the use of three parameters Π , Γ and γ rather than the use of the Stokes number S_t for dispersive transport in section 2. It is now widely accepted that the Stokes number can be used to characterize particle transport in shear flows (e.g. Crowe *et al.* 1993). However, when the Stokes number is employed for the description of bubble transport in large eddies, the Stokes number S_t is always far less than 1 because the bubbles have a very short response time to the flow. For example, the response time for even the largest bubbles is on the order of milliseconds, as pointed out by Stewart and Crowe (1993). The conceptual model proposed for particle dispersion by Crowe *et al.* (1985) has indicated that particles with $S_t \ll 1$ tend to remain in dynamic equilibrium with the fluid and are strongly dispersed by turbulence. It is obviously contradictory here that the conceptual model of Crowe *et al.* (1985) is used to describe bubble transport, supposing that the Stokes number is adopted. As has been observed, bubbles are indeed trapped by the large eddies and their motion is strongly influenced by the fluid motion. The key point here is that the aerodynamic response time measures how soon the bubbles attain the transiently dynamic equilibrium rather than how rapidly particles accelerate to match the surrounding flow. It is clear that the traditional S_t criterion developed for solid particles is inappropriate to describe bubble motion in shear flows. To meet this point, we have presented suitability of three key dimensionless parameters Π , Γ and γ in description of dispersive transport in shear flows. We will further investigate this aspect in chapter 4.

4.2 The Effect of Forces Acting On Bubbles in Shear Flows

We have shown in section 3 that bubble motion in a solid vortices is very sensitive to the pressure gradient which drives bubbles towards the vortex centre. When the effect of both

forces is excluded, the bubble motion is defined by a circular orbit located horizontally off-centre from the vortex centre as demonstrated by Tooby *et al.* (1977) and Sene *et al.* (1994). For $\Gamma \ll 1$, the bubble orbits are nearly symmetric to the centre of the vortex. If both the pressure gradient and shear lift forces are taken into account, then the bubbles converge to an equilibrium location on the downflowing side (Sene *et al.* 1994). These results suggest that when bubbles move inside a turbulent mixing layer excluding the effect of the pressure gradient and lift forces, the bubble trajectories are roughly symmetric to the axis of the mixing layer as has shown in figure 14b. However, this effect is obvious when the pressure gradient and lift forces are included (shown in figure 14a). The important implication drawn from these realisations is that if the flow field is time-averaged the bubble trajectory calculation based on the averaged field will be incorrect. Moreover, introduction of a Gaussian perturbation for fluctuation velocities and superposition on a mean field, as was widely adopted in calculations combined with engineering turbulence models (Shuen *et al.* 1983; Gosman and Ioannides 1981), will not compensate this effect. We will return this account in Chapter 4.

4.3 Gradient Diffusion Model For Bubbles in Shear Flows

As we have shown in section 3.4, the bubble dispersion is as competitive as the fluid particle dispersion when $\Pi \ll 1$. In this case, it is known that gradient diffusion models can be used to give reasonable estimates of bubble concentration distributions in such flows. However, the main difficulty in using these models is how to determine the bubble diffusion coefficient or alternatively an effective Schmidt number. The account of incorporating turbulent dispersion for bubbles in the shear layer has been considered by Sene *et al.* (1994). As they pointed out, the radial convergence of bubbles towards the centre of a coherent

structure is usually inhibited by the dispersive effects of small-scale turbulence in the large eddy in shear flow. They suggested that the effect of the turbulence in a coherent structure on bubble motion can be represented by introducing a diffusion coefficient D_{by} if the shear is weak. In the mixing layer, this diffusion coefficient with $\delta \propto X$ can be written

$$D_{by}/\Delta U = Xh(Y/X) \quad (18)$$

where h is some function of $\eta=Y/X$ and needs to be determined. The bubble concentration C_T inside the coherent structure is then given by

$$U_{by}C_T = D_{by}\frac{\partial C_T}{\partial y} \quad (19)$$

where U_{by} is the radial convergence velocity of bubbles towards the centre of the coherent structure. The concentration given by (19) can be directly related to the concentrations in an Eulerian frame of reference by using an intermittency function. More generally this idea can be applied to the shear layer for the mean bubble concentrations C as follows:

$$C\nabla \cdot \mathbf{U}_b + \mathbf{U}_b \cdot \nabla C = \nabla \cdot (D_{by} \nabla C) \quad (20)$$

where \mathbf{U}_b is the bubble velocity vector. On the condition that $\Gamma \ll 1$, bubble slip velocity due to lift, inertia and buoyancy can be neglected. Thus the above equation for two-dimensional mixing layer reduces to

$$U\frac{\partial C}{\partial x} + V\frac{\partial C}{\partial y} = \frac{\partial}{\partial y}(D_{by}\frac{\partial C}{\partial y}) \quad (21)$$

To determine the mean bubble concentration distribution in the shear layer from (21) requires knowledge of the bubble diffusion coefficient. Since a large number of bubble trajectories have been traced by the use of the Lagrangian measurements presented in section 3.4, a variance of bubble displacements of an arbitrary point and of an arbitrary time in the

mixing layer can be obtained, and their substitution into the variance into equation (17) gives the estimation for bubble diffusion coefficient. Calculated results for the bubble diffusion coefficient have been shown in figure 33. Examination of figure 33 reveals that the bubble diffusivity for $\Pi=0.0$ is larger than that for $\Pi=0.5$. As discussed in the previous section, bubble trapping is enhanced with the increase of the inertial force. This confinement depresses bubble dispersion in a shear layer. The dispersion for small Π is larger than that for large Π in line with expectations on capture and confinement within travelling eddies. Moreover, it appears that the dispersion for $\Pi=0$ approaches proportionality to T^2 , as would be expected for fluid particles in homogeneous turbulence (Hinze 1975). We take this as evidence that a primitive diffusion model may be only an adequate approximation for smaller Π . The plot of the turbulent Schmidt number, which was obtained by using the values of D_{by} and D_{fy} in figure 33, is shown in figure 34. It can be seen that the eddy Schmidt number of the bubbles is about 0.6 for $\Pi=0.0$ and about 1.0-1.5 for $\Pi=0.5$. These results again reinforce the earlier picture that bubble mixing layers spread less quickly than passive scalars, consistent with our earlier reinforcement of Sene's *et al.* (1994) findings that inertial confinement cannot be ignored.

4 CONCLUSIONS

Two-fluid models of bubble transport by turbulent flows introduce serious uncertainties in their closure assumptions. Predictions using Eulerian models of the flow and Lagrangian descriptions of the discrete phase transport introduce uncertainties in both the flow modelling and the assumed effective Lagrangian scales for the fluctuation transport. We argue here that discrete vortex modelling incorporating a Lagrangian approximation to both the continuum

eddy structure and the discrete phase transport can offer an adequate description of particle and bubble dispersion in two-dimensional turbulent free shear flows. In particular, the discrete phase trajectories are calculated by integrating a generalized equation of motion (Auton 1987; Thomas *et al.* 1983), following and extending the discrete vortex methods described in Sene *et al.* (1994). The trapping effect of large eddies in such free shear flows on bubble dispersion were assessed through the examination of bubble trajectories and introduction of a Lagrangian measurement. The main aspects of this work are summarised below.

Our discrete vortex simulations compared favourably with experimental results for mean velocity profiles, turbulence intensities and shear stress. Eddy patterns and eddy pairing behaviour were reasonably well reproduced, sufficiently for our investigation of their effects on bubble transport. The energy spectrum at the centre of the mixing layer is presented. The spectrum shows that the effect of values of random jitters mainly covers the corresponding range of mid frequencies.

We have briefly demonstrated that three non-dimensional parameters Π , Γ and γ , are the united groups to describe bubble motion in turbulent free shear flows. Γ plays a very important role in determining the bubble retention and Π does the role in determining bubble trapping by large eddies.

For the downflow mixing layer used here, our bubble trajectory simulations revealed that inertial forces discourage bubble dispersion. Inertial forces drive the bubbles towards the high speed side of the flow, resulting in skewness of the number flux profiles such that

classical diffusion modelling would not be adequate here. However, if $\Pi \rightarrow 0$ (negligible inertial confinement) then the bubble number flux profiles appear to be nearly symmetric and the gradient diffusion model may suffice. In this regard we have confirmed the findings reported in Sene *et al.* (1994) by introducing Lagrangian measurement statistics to evaluate the bubble diffusivity. As an extension of Sene's *et al.* (1994) work we also compared the dispersion coefficient for the bubbles with that for fluid elements, and have found the ratio indeed approaches 1.0 for a long time dispersion. Our findings have further reinforced the finding of Sene *et al.* (1994) that if a diffusivity representation is sought, an effective turbulent Schmidt number of about unity for bubbles in shear layer is demanded to reproduce the spread rate behaviour. Further clarification is needed in connection with the utilisation of our approach as an enhancement of engineering calculation methods for which the effective Schmidt number is presently an empirically assigned modelling parameter.

REFERENCES

- Ashurst, W. T. 1979 Numerical simulation of turbulent mixing layers via vortex dynamics. *In Turbulent Shear Flows I* (ed. F. Durst, B. E. Launder, F. W. Schmidt & J. H. Whitelaw) pp. 402-413. Springer.
- Auton, T. R. 1983 The dynamics of bubbles, drops and particles in motion in liquids. PhD thesis, University of Cambridge.
- Auton, T. R. 1987 The lift force on a spherical body in a rotational flow. *J. Fluid Mech.* **183**, 199.
- Batchelor, G. K. 1957 Diffusion on free turbulence shear flows. *J. Fluid Mech.* **98**, 67.
- Berlemont, A., Desjonqueres, P. and Gouesbet, G. 1991 Particle turbulent dispersion in 3D magnetic field by using a Lagrangian approach. *Part. Part. Syst. Charact.* **8**, 151-158.
- Berlemont, A., Desjonqueres, P. & Gouesbet, G. 1990 Particle Lagrangian simulation in turbulent flows. *Int. J. Multiphase Flow* **16**, 19-34.
- Brown, G. L. and Roshko, A. 1974 Density effects and large-scale structure in turbulent

- mixing layer. *J. Fluid Mech.* **64**, 775-816.
- Chein, R. and Chung, J. N. 1987 Effects of vortex pairing on particle dispersion in turbulent shear flows. *J. Multiphase Flow* **13**, 785-802.
- Chein, R. and Chung, J. N. 1988 Simulation of particle dispersion in a two-dimensional mixing layer. *J. AIChE.* **34**, 946-954.
- Chorin, A. J. 1973 Numerical study of slightly viscous flow. *J. Fluid Mech.* **57**, 85.
- Chung, J. N. and Troutt, T. R. 1988 Simulation of particle dispersion in an axisymmetric jet. *J. Fluid Mech.* **186**, 199-222.
- Clift, R., Grace, J. R. & Weber, M. E. 1978 *Bubbles, Drops and Particles*. Academic.
- Crowe, C. T., Gore, R. and Troutt, T. R. 1985 Particle dispersion by coherent structures in free shear flows. *Particulate Science and Tech.* **3**, 149-158.
- Crowe, C. T., Chung, J. N. & Troutt, T. R. 1988 Particle mixing in free shear flows. *Prog. Energy Combust. Sci.* **14**, 171-194.
- Crowe, C. T., Chung, J. N. & Troutt, T. R. 1993 Particle dispersion by organised turbulent structures. In *Particulate Two-Phase Flows* (Edited by Roco, M. C.), Butterworth-Heinemann, New York.
- Durst, F., Milojevic, D. & Schönung, B. 1984 Eulerian and Lagrangian predictions of particulate two-phase flows: a numerical study. *Appl. Math. Modelling* **8**, 101-115.
- Elghobashi, S. E. and Abor-Arab, T. W. 1983 A two equation turbulence model for two phase flows. *Phys. Fluids.* **17**, 19-25.
- Elghobashi, S. E., Abou Arab, T. W., Rizk, M. & Mostafa, A. 1984 Prediction of the particle laden jet with a two equation turbulence model. *Int. J. Multiphase Flow* **10**, 697-710.
- Faeth, G. M. 1987 Evaporation and combustion of sprays. *Prog. Energy Combust. Sci.* **9**, 1-76.
- Gosman, A. D. & Ioannides, E. 1981 Aspects of computer simulation of liquid-fueled combustors. *AIAA paper* 81-0323.
- Hinze, J. O. 1975 *Turbulence*. McGraw-Hill: New York.
- Hunt, J. C. R., Auton, T. R., Sene, K., Thomas, N. H. and Kowe, R. 1988 Bubble motions in large eddies and turbulent flows. *Transient Phenomena in Multiphase Flow*, (Edit by N. H. Afgan), Hemisphere.
- Hunt, J. C. R., Perkins, R. J. and Lunde, K. 1993 Modelling bubbly flows. *Bubble*

- Dynamics and Interface Phenomena*, 257-268. (Edit by J. R. Blake & N. H. Thomas), Kluwer Academic Publishers.
- Hussain, A. K. M. F. 1983 Coherent structures -reality and myth. *Phys. Fluids* **26**, 2816.
- Inoue, O. 1985 Vortex simulation of a turbulent mixing layer. *J. AIAA*. **23**, 367-373.
- Kowe, R., Hunt, J. C. R., Hunt, A., Couet, B. & Bradbury, L. J. S. 1988 The effects of bubbles on the volume fluxes and the pressure gradients in unsteady and non-uniform flow of liquids. *Int. J. Multiphase Flow* **14**, 587-606.
- Laitone, J. A. 1981 A numerical solution for gas-particle flow at high Reynolds numbers. *J. Applied Mech.* **48**, 465-471.
- Launder, B. E. & Spalding, D. B. 1974 The numerical computation of turbulent flows. *Comput. Mech. Appl. Mech. Engng* **3**, 269.
- Leonard, A. 1980 Vortex methods for flow simulation. *J. Computational Phys.* **37**, 289-335.
- Levich, V. G. 1962 *Physico-Chemical Hydrodynamics*. Prentice-Hall.
- Magnaudet, J., Rivero, M. & Fabre, J. 1995 Accelerated flows past a rigid sphere or a spherical bubble. part 1. Steady straining flow. *J. Fluid Mech.* **284**, 97-135.
- Maxey, M. R. & Riley, J. J. 1983 Equation of motion for a small-rigid sphere in a nonuniform flow. *Phys. Fluids* **26**, 883-889.
- Maxey, M. R., Chang, E. J. & Wang, L-P. 1994 Simulation of interactions between microbubbles and turbulent flows. *Appl. Mech. Rev.* **47(6)**, s70-s74.
- Mostafa, A. A. & Elghobashi, S. E. 1985 A two-equation turbulence model for jet flows laden with vaporizing droplets. *Int. J. Multiphase Flow* **11**, 515.
- Nir, A. & Pismen, L. M. 1979 The effect of a steady drift on the dispersion of a particle in turbulent fluid. *J. Fluid Mech.* **94**, 364-381.
- Onslow, R. J. & Thomas, N. H. 1994 *Vorticity and Sandwaves: The dynamics of ripples and dunes*. In *Turbulence: Perspectives on Flow and Sediment Transport*. (Ed. N. J. Clifford, J. R. French & J. Hardisty) Wiley.
- Picart, A., Berlemont, A. & Gouesbet, G. 1986 Modelling and predicting turbulence fields and the dispersion of discrete particles transported by turbulent flows. *Int. J. Multiphase Flow* **12**, 237-261.
- Pui, N. K. & Gartshore, I. S. 1979 Measurement of the growth rate and structure in plane turbulent mixing layers. *J. Fluid Mech.* **91**, 111.
- Reeks, M. W. 1977 On the dispersion of small particle suspended in an isotropic turbulent

- fluid. *J. Fluid Mech.* **83**, 529-546.
- Rivero, M., Maganudet, J. & Fabre, J. 1991 Quelques résultats nouveaux concernant les forces exercées sur une inclusion sphérique par unécoulement accéléré. *C.R. Acad. Sci. Paris*, t. **312**, Série II, 1499-1506.
- Roshko, A. 1976 Structures of turbulent flows, A new look. *AIAA J.* **14**, 1349.
- Ruetsch, G. R. & Meiburg, E. 1993 On the motion of small spherical bubbles in two-dimensional vortical flows. *Phys. Fluids A* **5**(10), 2326-2341.
- Sarpkaya, T. 1989 Computational methods with vortices- The 1988 free scholar lecture. *Trans. ASME. J. Fluids Engineering* **111**, 5-52.
- Schlichting, H. 1968 Boundary Layer theory. Pergamon Press: London.
- Sene, K. 1985 Aspects of bubbly two phase flow, Ph.D. Thesis, University of Cambridge.
- Sene, K., Hunt, J. C. R. and Thomas, N. H. 1994 The role of coherent structures in bubble transport by turbulent shear flows. *J. Fluid Mech.* **259**, 219-240.
- Shuen, J. S., Chen, L. D. & Faeth, G. M. 1983 Evaluation of a stochastic model of particle dispersion in a turbulent round jet. *AIChE J.* **29**(1), 167.
- Shuen, J. S., Solomon, A. S. P., Zhang, Q. F. & Faeth, G. E. 1985 Structure of particle-laden jets: Measurements and predictions. *AIAA J.* **23**, 396.
- Simonin, O. 1991 Eulerian formulation for particle dispersion in turbulent two phase flows. Proceedings 5th Workshop on Two Phase Flows Predictions (Eds. Sommerfeld and Wennerberg) Erlangen 1990.
- Snyder, W. H. & Lumley, J. L. 1971 Some measurements of particle velocity autocorrelation functions in a turbulent flow. *J. Fluid Mech.* **48**, 41-71.
- Spalart, P. R. & Leonard, A. 1981 Computation of separated flows by a vortex tracing algorithm. *AIAA 14th Fluid and Plasma Dynamics Conf.*, Palo Alto, California.
- Squires, K. D. & Eaton, J. K. 1990 Measurements of particle dispersion obtained from direct numerical simulations of isotropic turbulence. *J. Fluid Mech.* **226**, 1-35.
- Squires, K. D. & Eaton, J. K. 1994 Effect of selective modification of turbulence on two-equation model for particle-laden turbulent flows. *J. Fluids Engng.* **116**.
- Sridhar, G. & Katz, J. 1995 Drag and lift forces on microscopic bubbles entrained by a vortex. *Phys. Fluids* **7**(2), 389-399.
- Stewart, C. W. & Crowe, C. T. 1993 Bubble dispersion in free shear flows. *Int. J. Multiphase Flow* **19**, 501-507.

- Taylor, G. I. 1921 Diffusion by continuous movements. *Proc. Lond. Math. Soc.* **20**, 196.
- Thomas, N. H., Auton, T.R., Sene, K. and Hunt, J.C.R. 1983 Entrapment and transport of bubbles by transient large eddies in multiphase turbulent shear flow. *Int. Conf. on the Physical Modelling of Multiphase Flow*, Coventry, England, Paper E1.
- Thomas, N. H. 1982 Air demand distortion in hydraulic models. *Proc. Intl Conf. on Hydraulic Modelling of Civil Engineering Structures*, Coventry, UK. BHRA.
- Tooby, P. F., Wicks, G. L. & Isaacs, J. D. 1977 The motion of a small sphere in a rotating velocity field: a possible mechanism for suspending particles in turbulence. *J. Geophys. Res.* **82**, 2096.
- Townsend, A. A. 1976 The structure of turbulent shear flows, 2nd edn. Cambridge University Press.
- Wells, M. R. & Stock, D. E. 1983 The effects of crossing trajectories on the dispersion of particles in a turbulent flow. *J. Fluid Mech.* **136**, 31-62.
- Wen, F., Kamalu, N., Chung, J. N., Crowe, C. T. & Troutt, T. R. 1992 Particle dispersion by vortex structure in plane mixing layers. *Trans. ASME. J. Fluids Engineering* **114**, 657-666.
- Winant, C. D. & Browand, F. K. 1974 Vortex pairing, the mechanics of turbulent mixing layer growth at moderate Reynolds numbers. *J. Fluid Mech.* **63**, 237.
- Wood, D. H. & Bradshaw, P. 1982 A turbulent mixing layer constrained by a solid surface. Part 1. Measurements before reaching the surface. *J. Fluid Mech.* **122**, 57.
- Wynanski, I. & Weisbrot, I. 1988 On the pairing process in an excited plane turbulent mixing layer. *J. Fluid Mech.* **195**, 161.
- Yang, X. & Thomas, N. H. 1994 Simulation of particle and bubble dispersion in turbulent free shear flows. *Numerical Methods in Multiphase Flows*, ASME-FED **185**, 259-268.

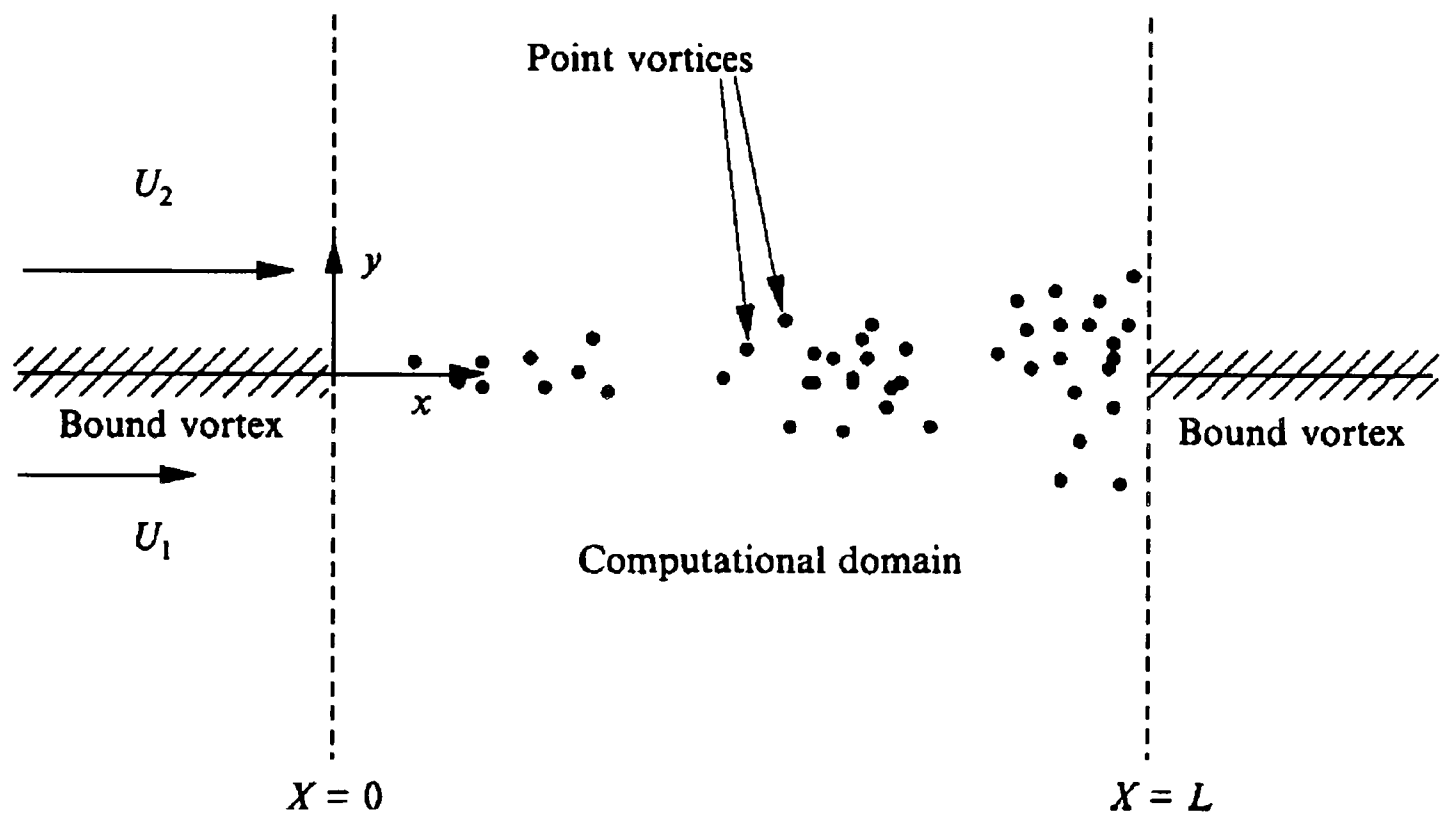


Figure 1. Definition sketch for discrete vortex simulation of a two-stream planar turbulent mixing layer. Taken from Sene *et al.* (1994).

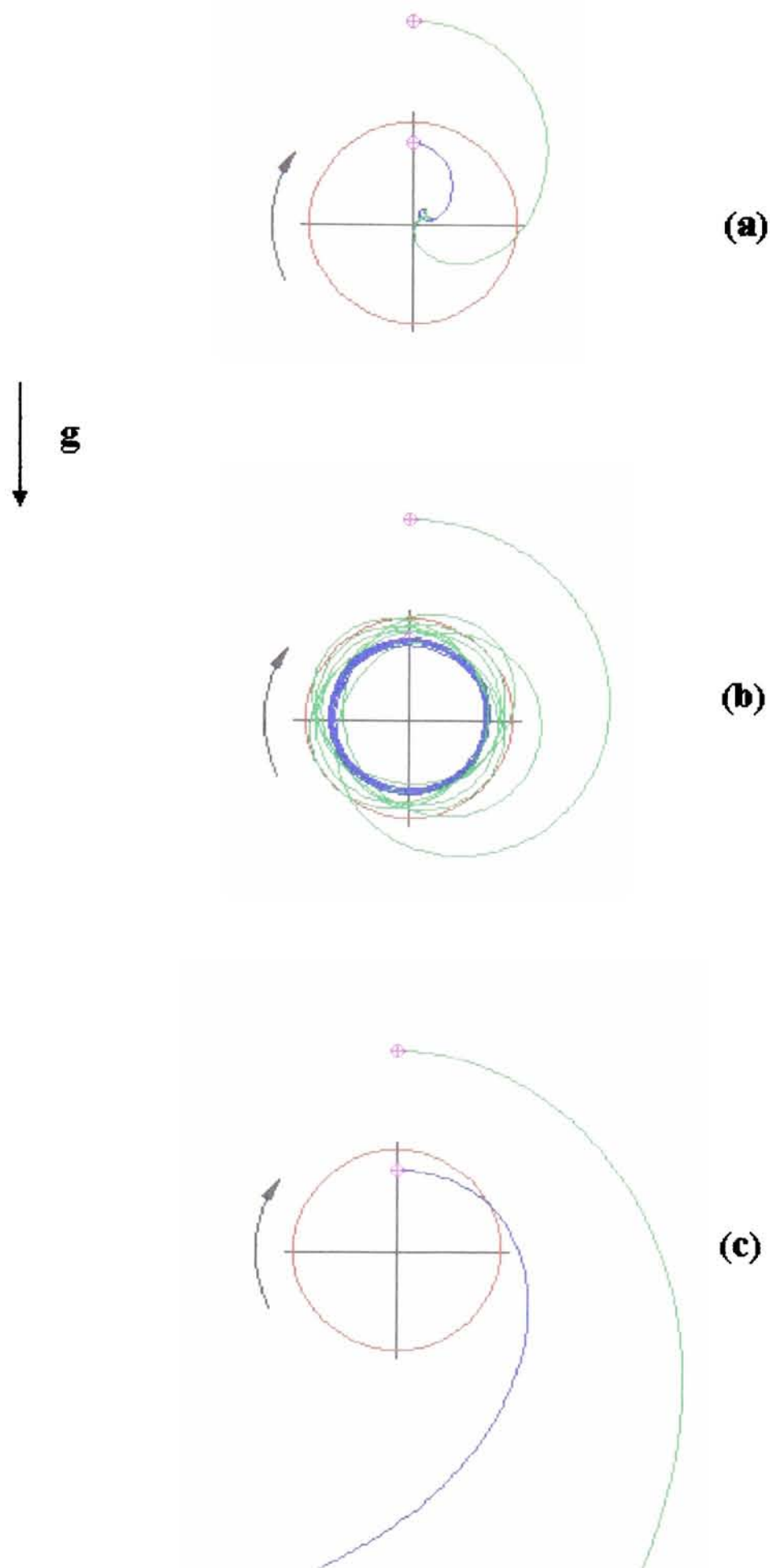


Figure 2. The effect of varying the mass ratios on bubble, droplet and particle trajectories. The terminal velocity is 0.2 m/s and the initial velocity is set to equal to local velocity of the flow field for all three cases. For all three cases $\Pi_{Ran}=10.0$ and $\Gamma_{Ran}=5.0$. Release locations are $(0.0,0.8R)$ inside the vortex and $(0.0,2.0R)$ outside the vortex. (a) $\gamma=0.0$ for bubbles; (b) $\gamma=0.9$ for droplets; (c) $\gamma=2.5$ for particles.

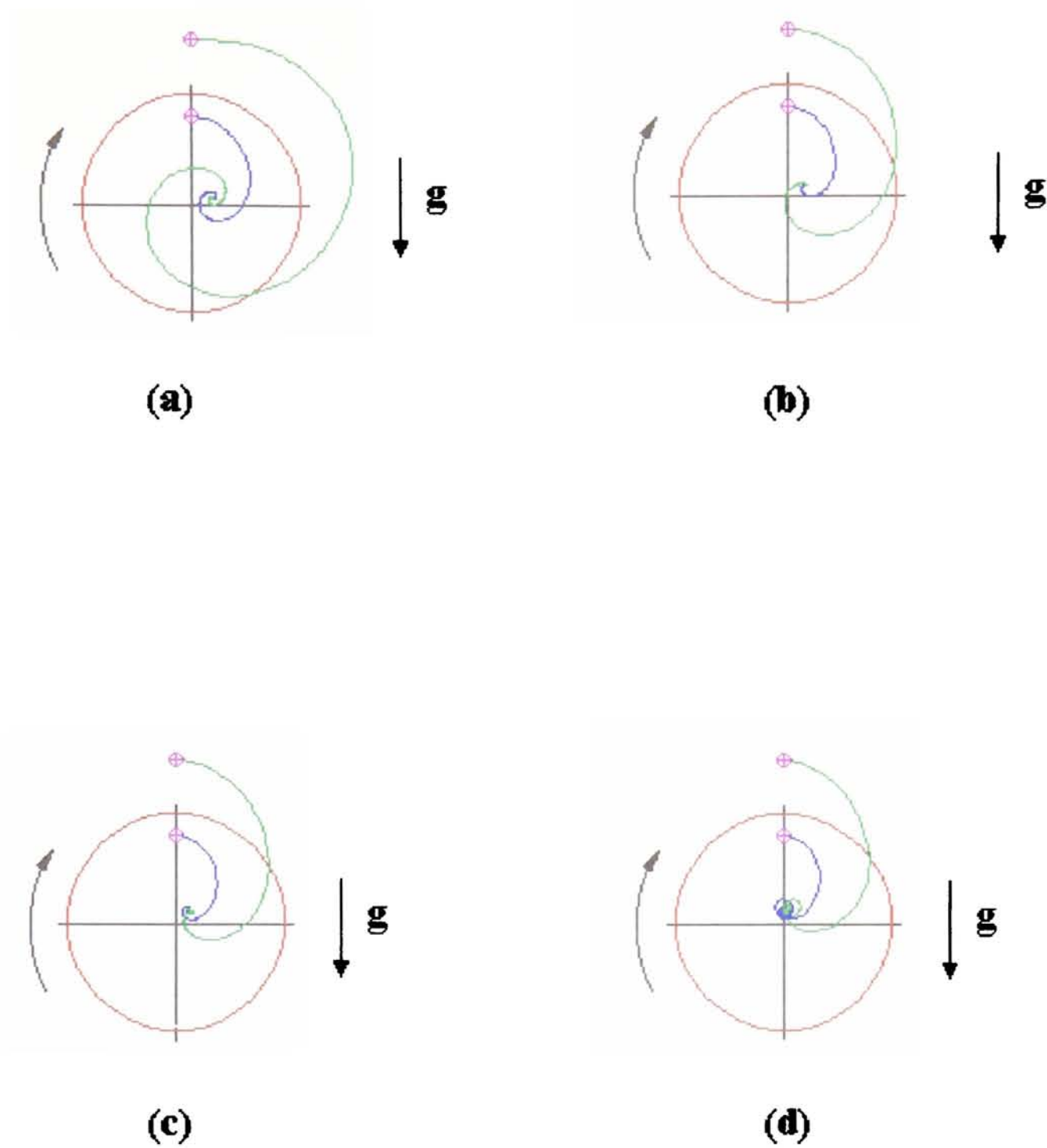


Figure 3. The effect of varying Π_{Ran} on bubble trajectories. The terminal velocity is 0.2 m/s and the initial velocity is set to equal to local velocity of the flow field for all four cases. For all four cases $\Gamma_{Ran}=5.0$. Bubbles were released from $(0.0,0.8R)$ inside the vortex and $(0.0,1.5R)$ outside the vortex. (a) $\Pi_{Ran}=2.5$; (b) $\Pi_{Ran}=5.0$; (c) $\Pi_{Ran}=10.0$; (d) $\Pi_{Ran}=20.0$.

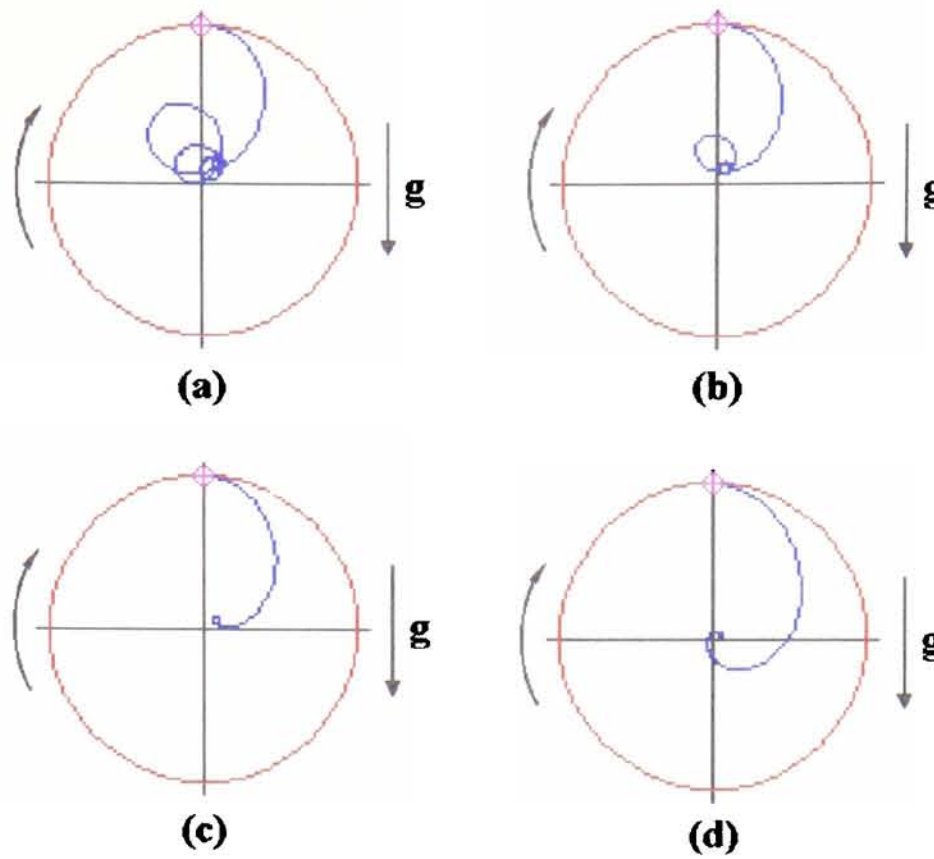


Figure 4a. The effect of varying Γ_{Ran} on bubble trajectories. The terminal velocity is 0.2 m/s and the initial velocity is set to equal to local velocity of the flow field for all four cases. For all four cases $\Pi_{Ran}=10.0$. Bubbles were released from $(0.0,1.0R)$ of the vortex. (a) $\Gamma_{Ran}=2.5$; (b) $\Gamma_{Ran}=5.0$; (c) $\Gamma_{Ran}=10.0$; (d) $\Gamma_{Ran}=20.0$.

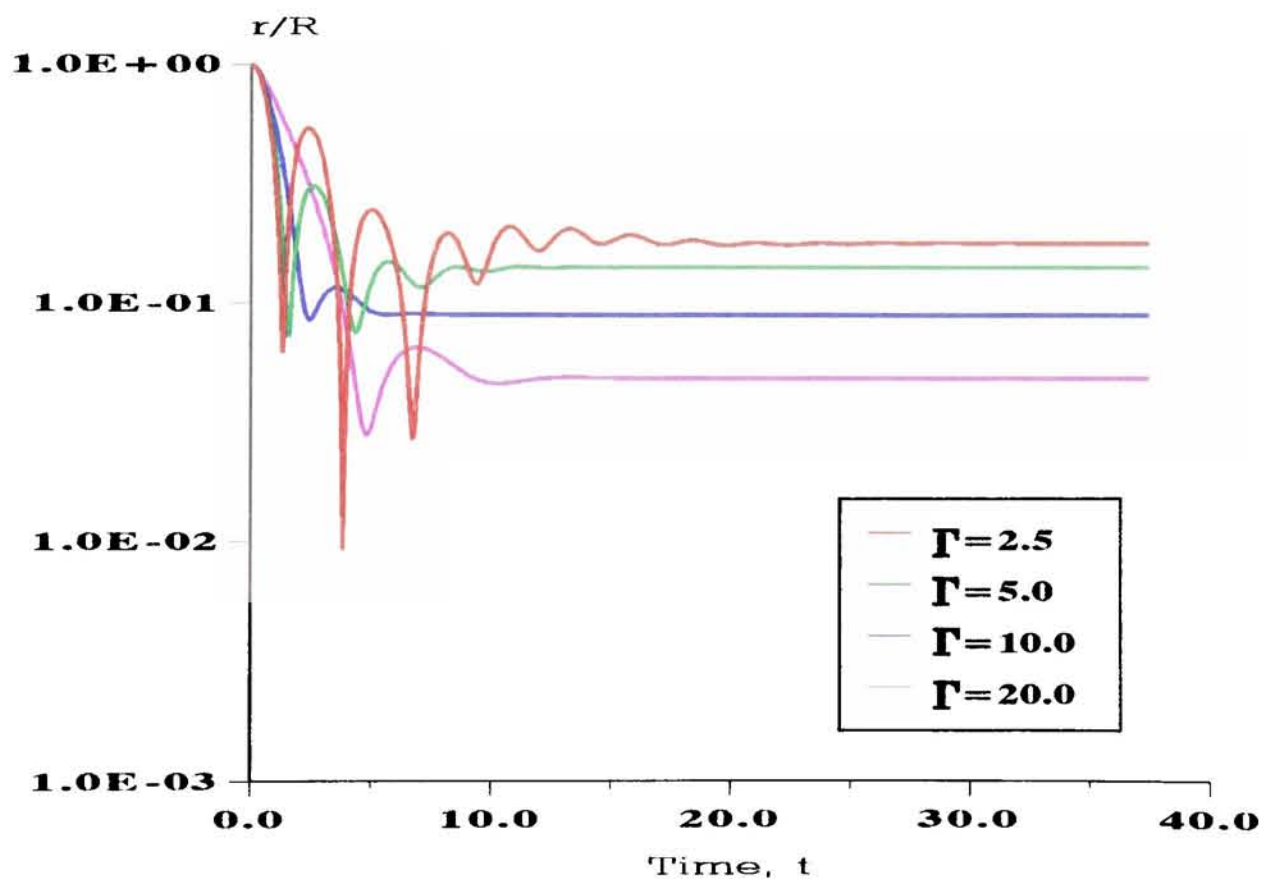


Figure 4b. The effect of varying Γ_{Ran} on bubble radius time series with $\Pi_{Ran}=10.0$ and $\gamma=0.0$.

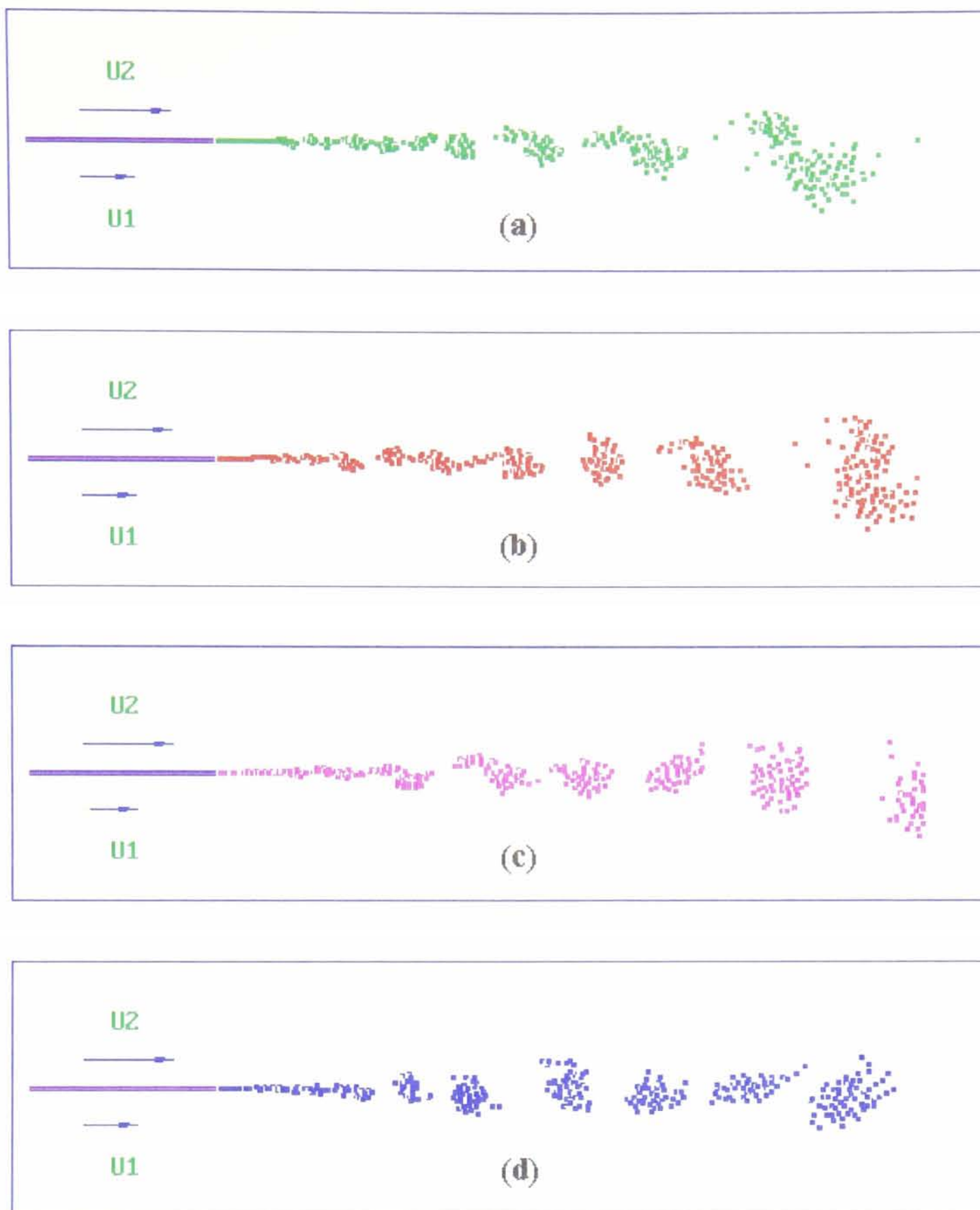


Figure 5. Instantaneous discrete vortex patterns in a two-stream mixing layer:
(a) $T=1.0L/\Delta U$; (b) $T=1.1L/\Delta U$; (c) $T=1.2L/\Delta U$; (d) $T=1.3L/\Delta U$.

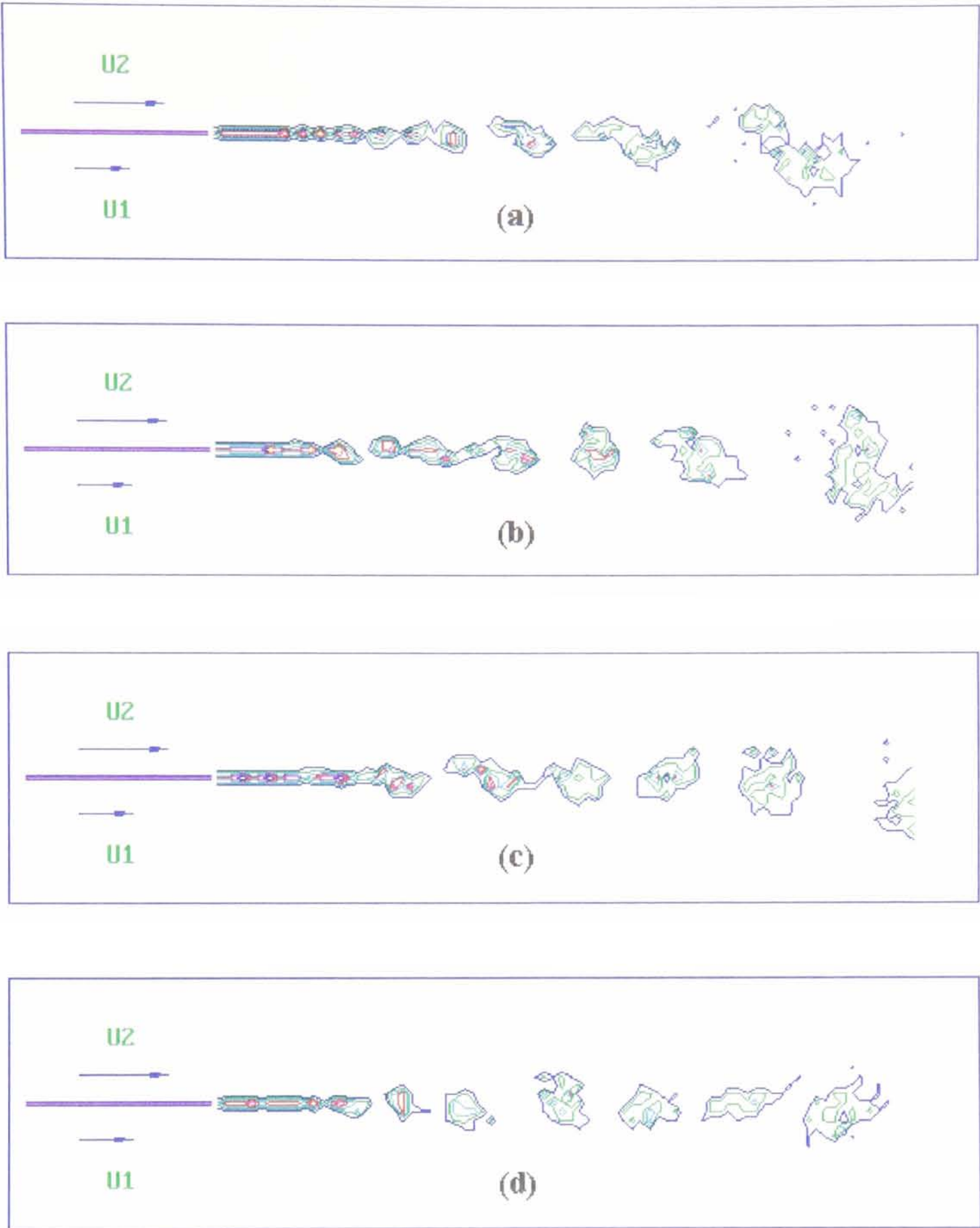


Figure 6. Vorticity contours in the discrete vortex simulation at different times, corresponding to figure 5. (a) $T=1.0L/\Delta U$; (b) $T=1.1L/\Delta U$; (c) $T=1.2L/\Delta U$; (d) $T=1.3L/\Delta U$.

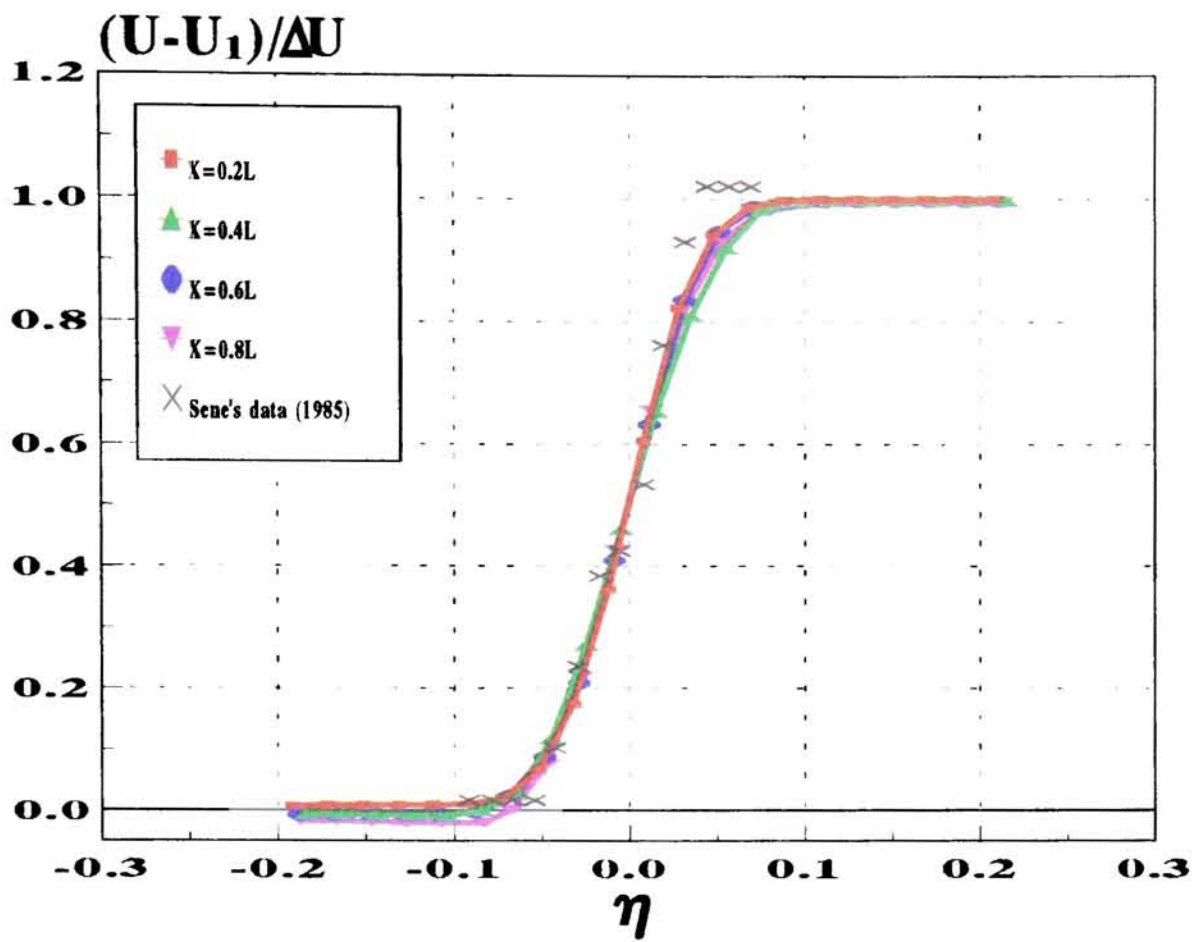


Figure 7. Time-averaged mean velocity profiles from numerical simulations and the experimental results (Sene 1985).

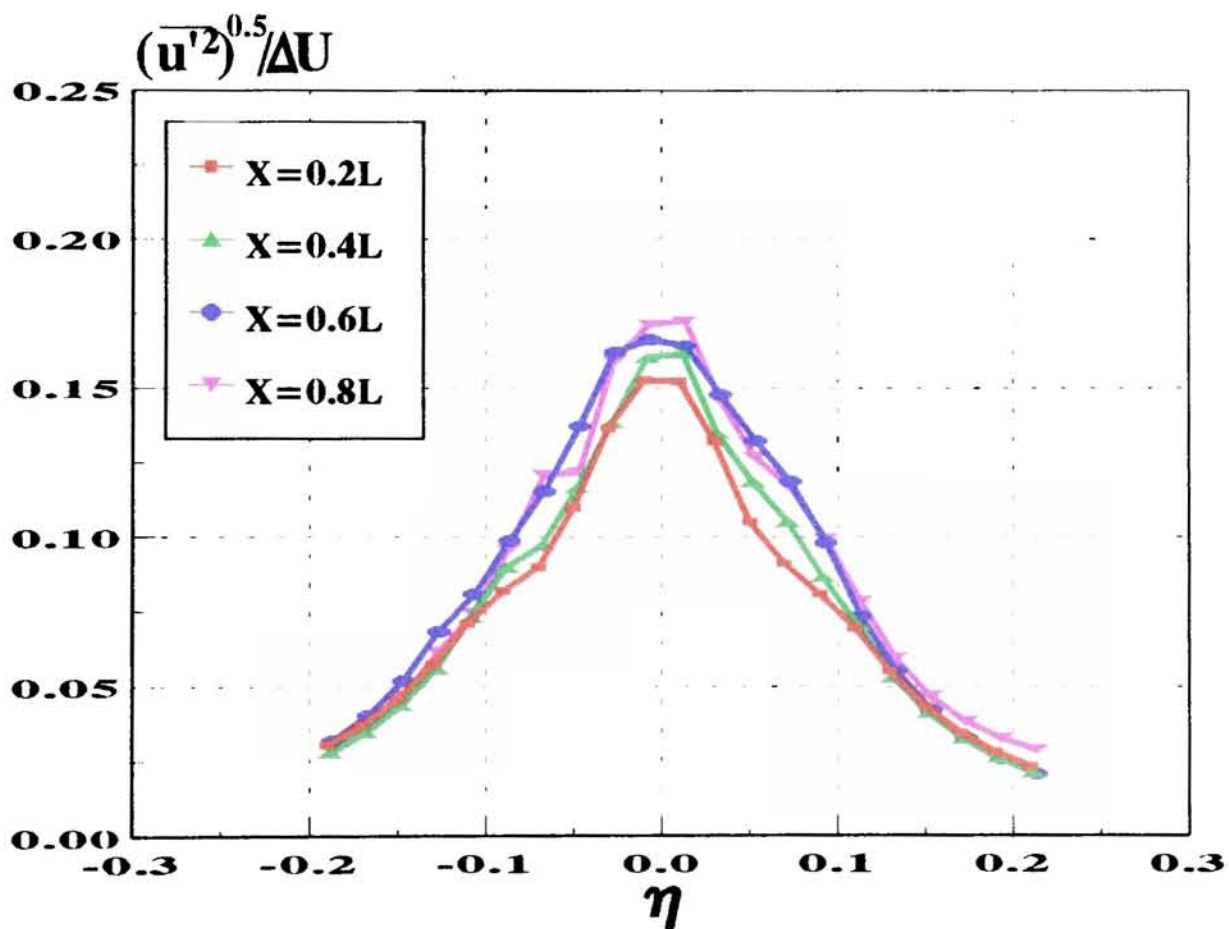


Figure 8. Longitudinal turbulence intensities at different downstream cross-sections of the mixing layer.

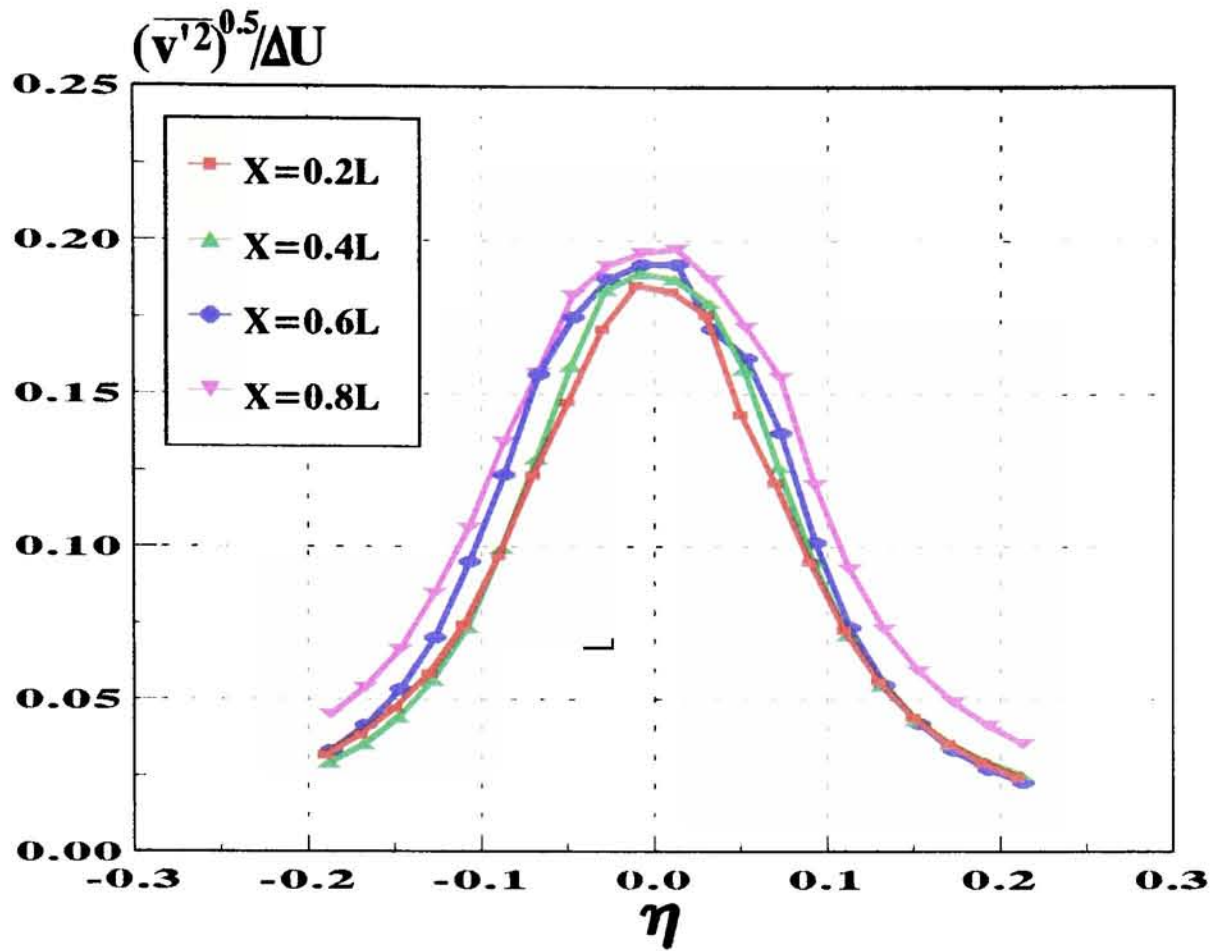


Figure 9. Cross-stream turbulence intensities at different downstream cross-sections of the mixing layer.

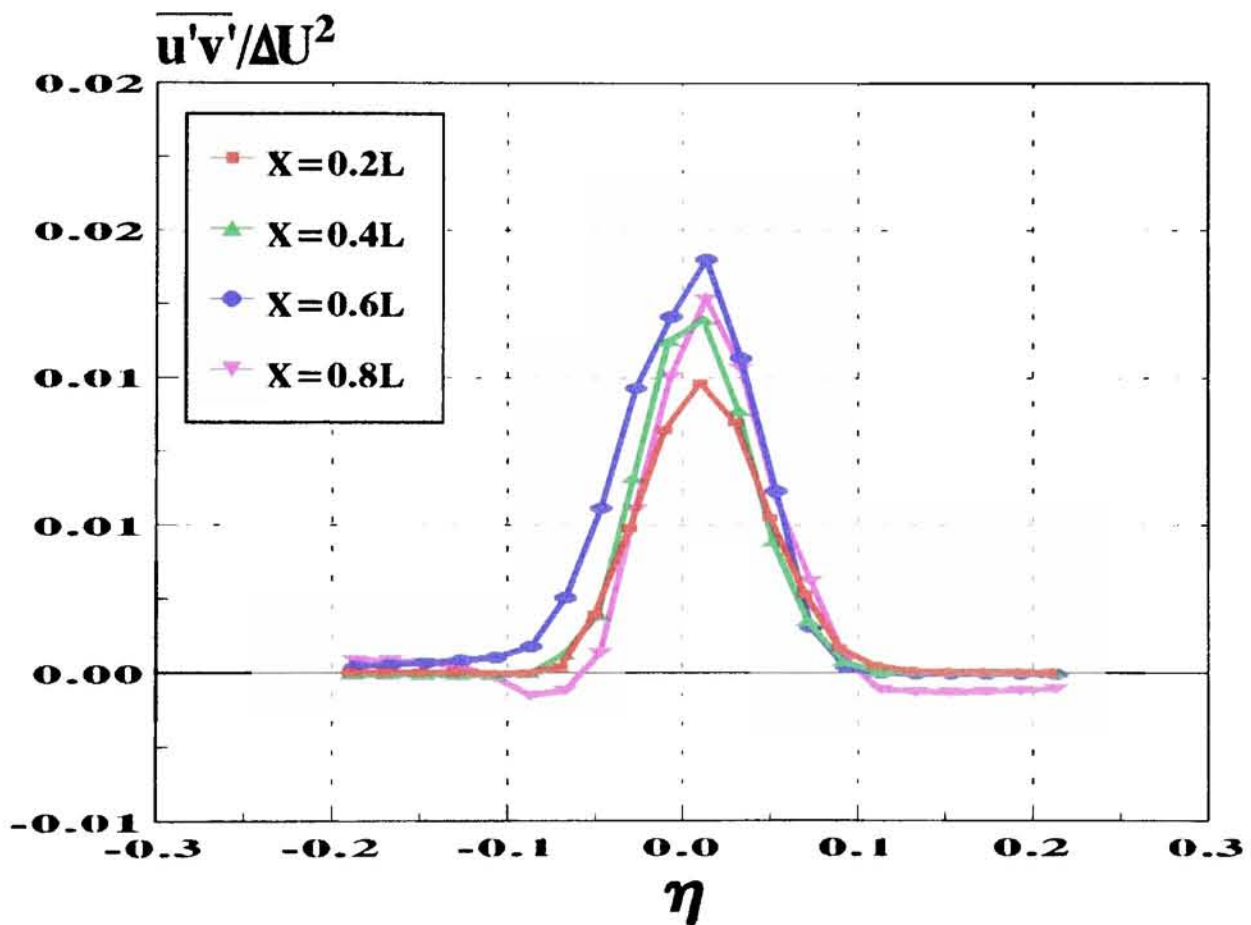


Figure 10. Shear stress distribution at different downstream cross-sections of the mixing layer.

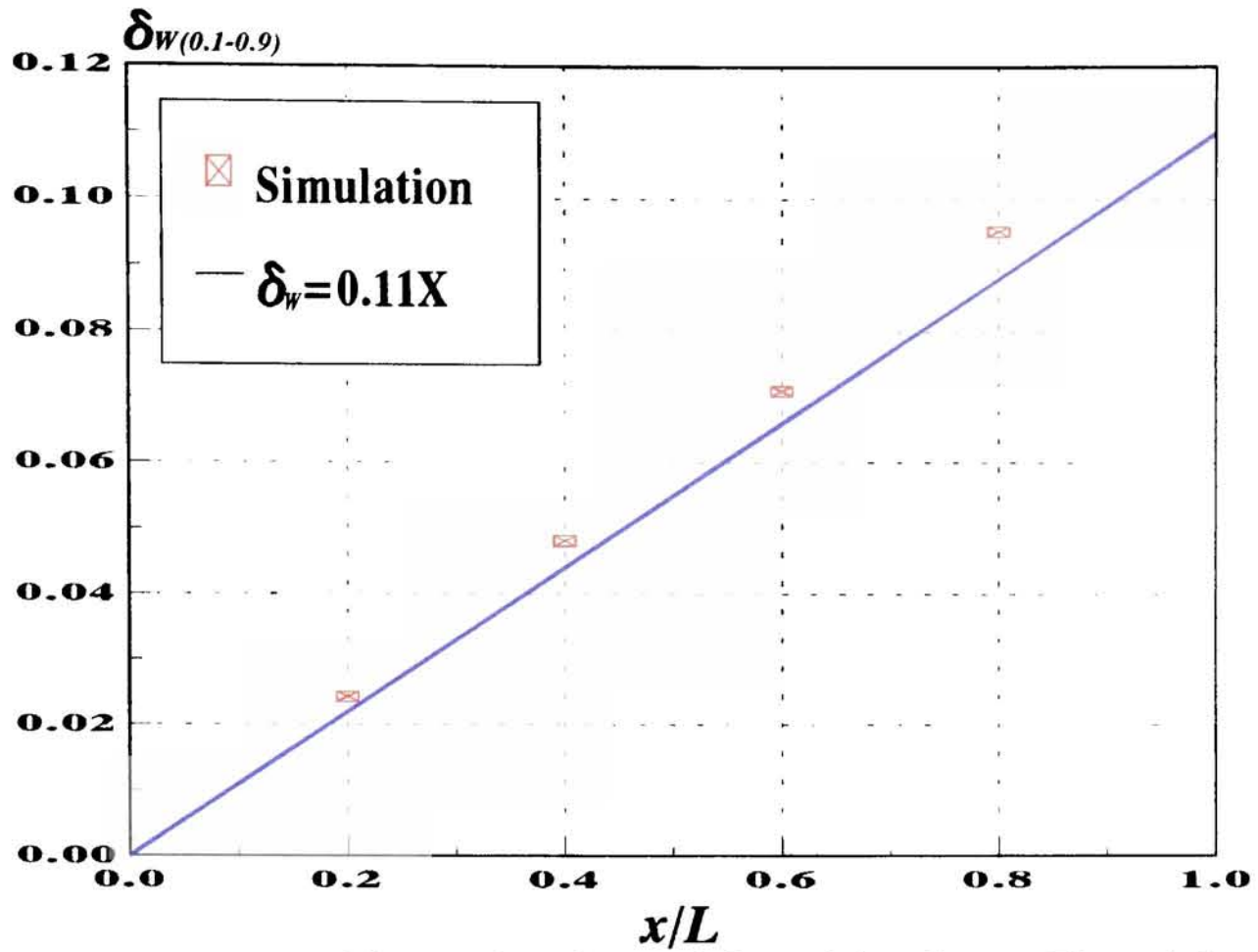


Figure 11. Spread rate at different locations of the mixing layer. The mixing layer width is defined as the distance between the points at which the velocity differs 10% from the stream value.

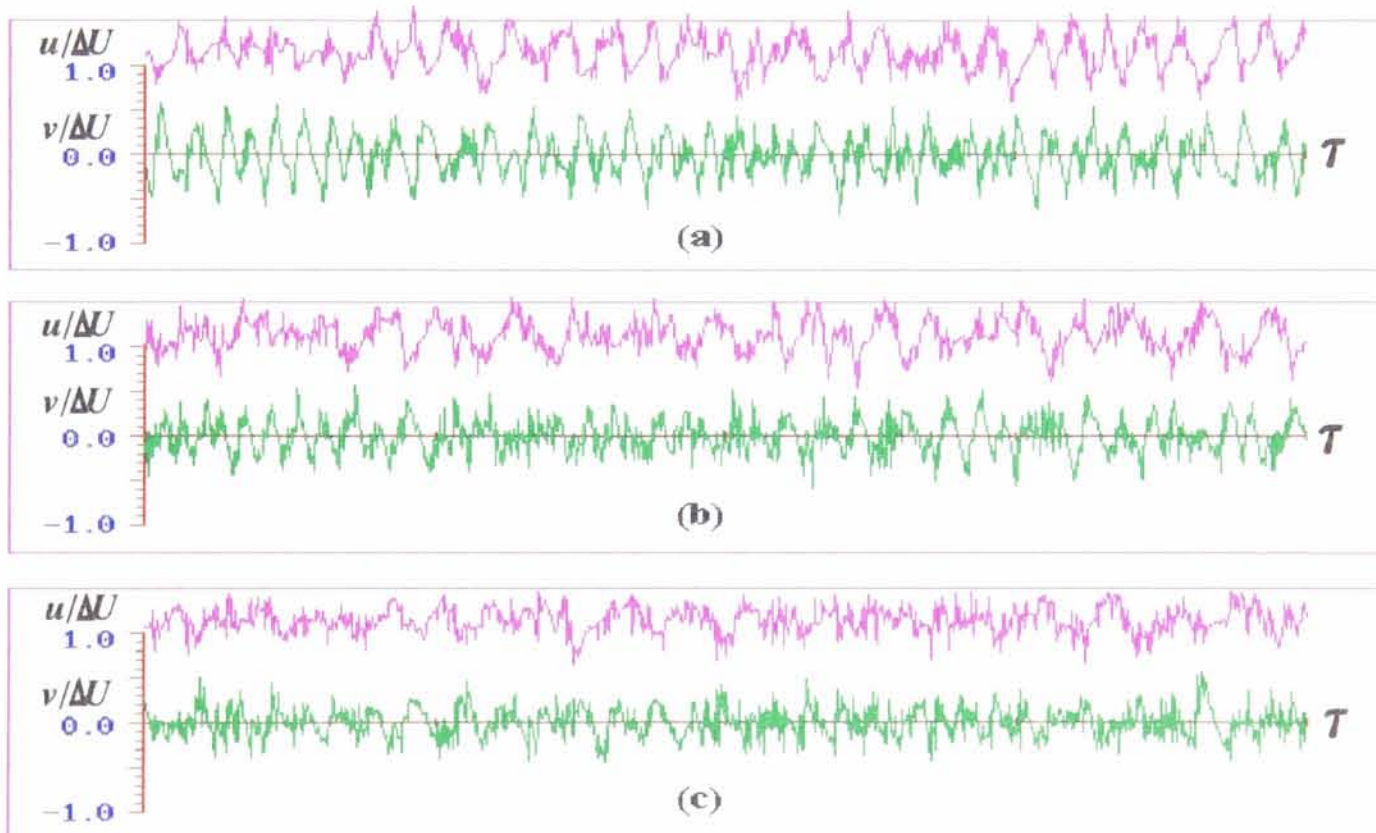


Figure 12. Fluctuation velocity time records for 2000 time steps, with three different random jitters, sampled at the centre of the mixing layer. (a) $\zeta=0.0$; (b) $\zeta=0.2U_m\Delta t$; (c) $\zeta=0.4U_m\Delta t$.

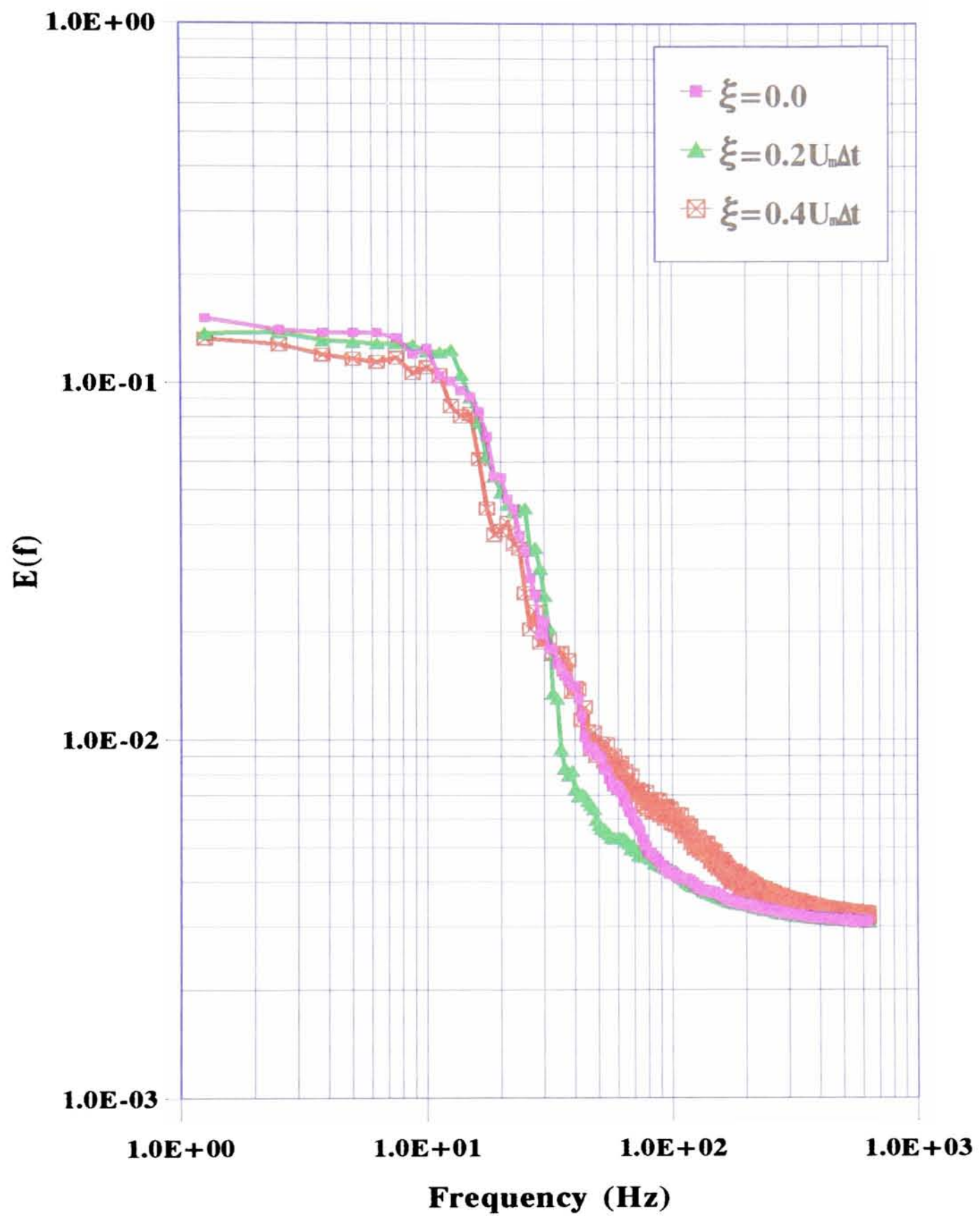


Figure 13. Power spectra of axial velocity fluctuation u' , sampled at the centre of the mixing layer with $U_2/U_1=3.0$.

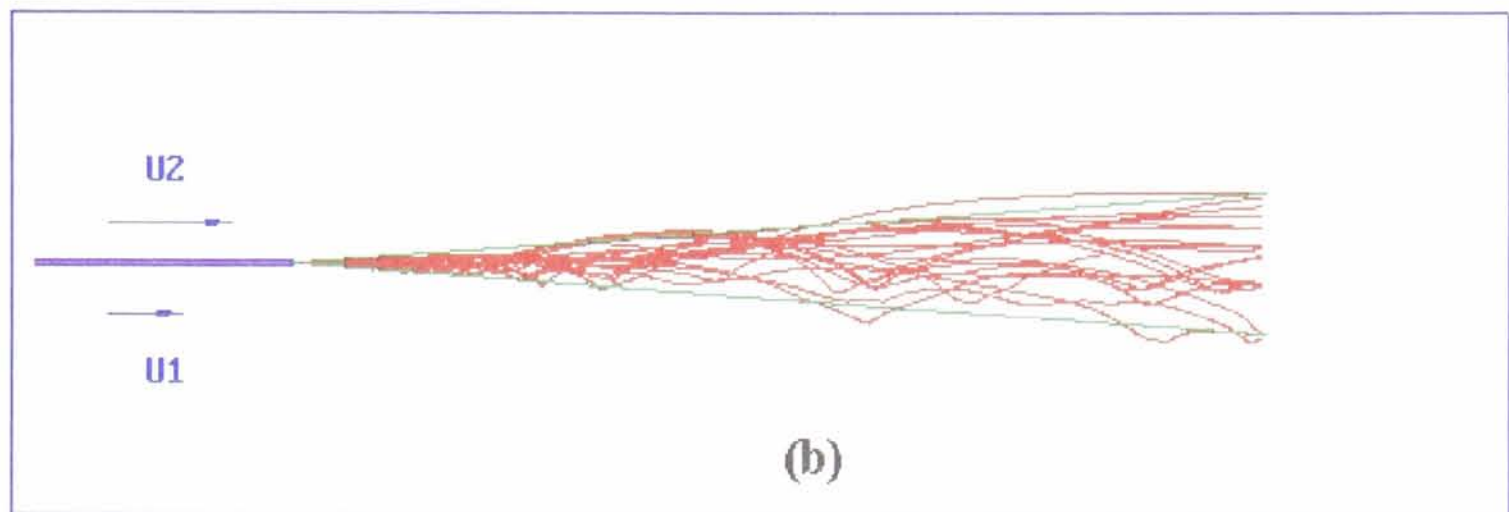
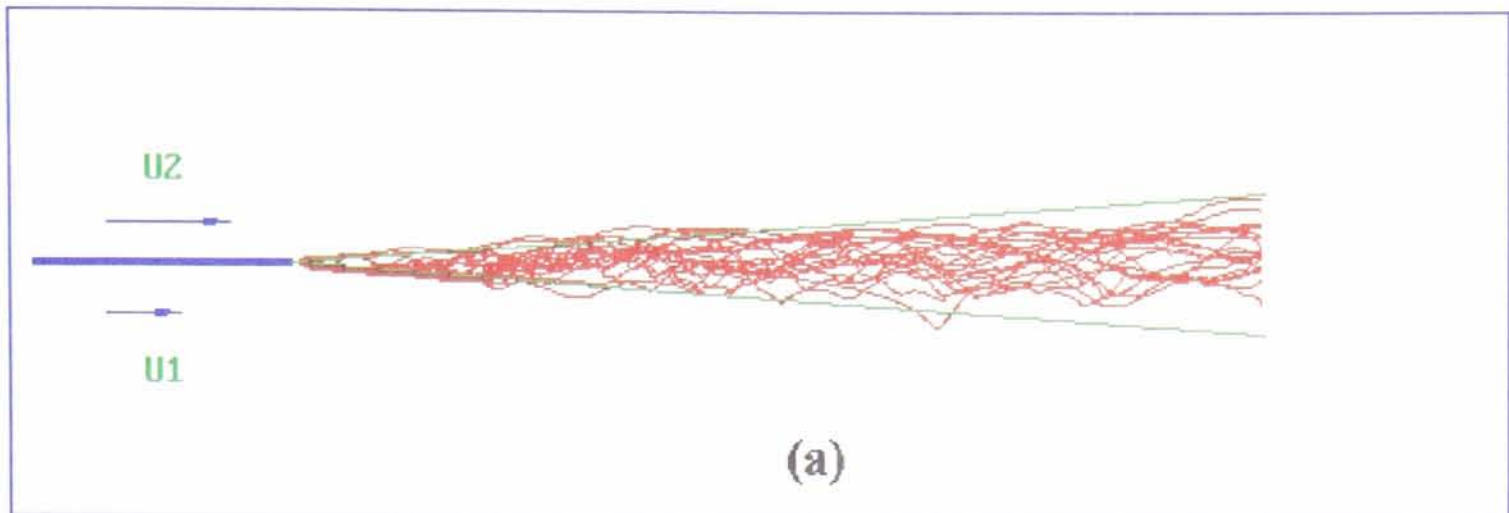


Figure 14. Computer simulations of bubble trajectories in a vertical, downflowing, two stream mixing layer. Bubbles (400 bubbles in total) were released every Δt from the location close to the mixing layer. (a) $\Pi=0.5$, $\Gamma=10.0$; (b) $\Pi=0.0$, $\Gamma=10.0$. (Note: Only 20 trajectory realisations were displayed.)

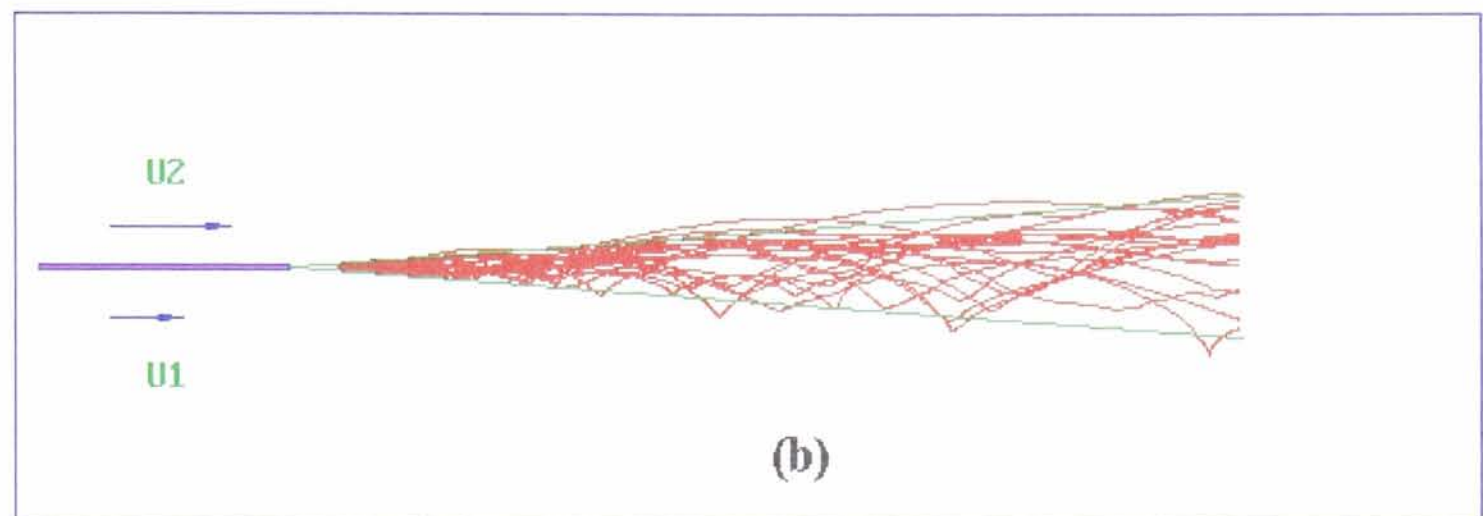
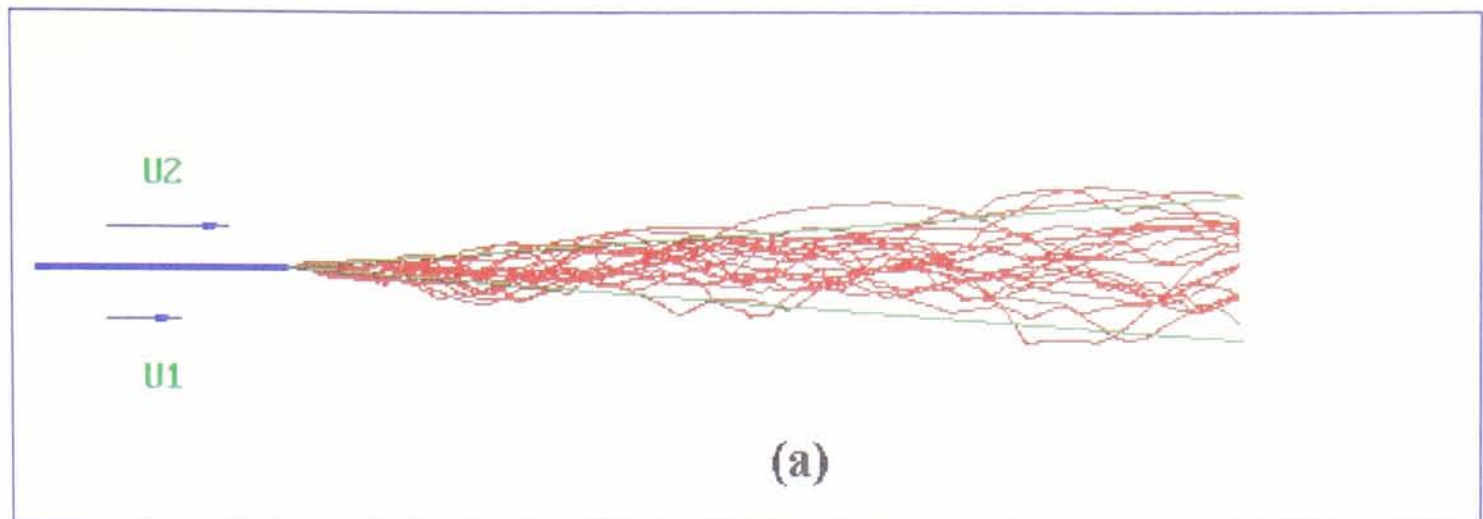


Figure 15. Computer simulations of bubble trajectories in a vertical, downflowing, two stream mixing layer. Bubbles (400 bubbles in total) were released every $10\Delta t$ from the location close to the mixing layer. (a) $\Pi=0.5$, $\Gamma=10.0$; (b) $\Pi=0.0$, $\Gamma=10.0$. (Note: Only 20 trajectory realisations were displayed.)

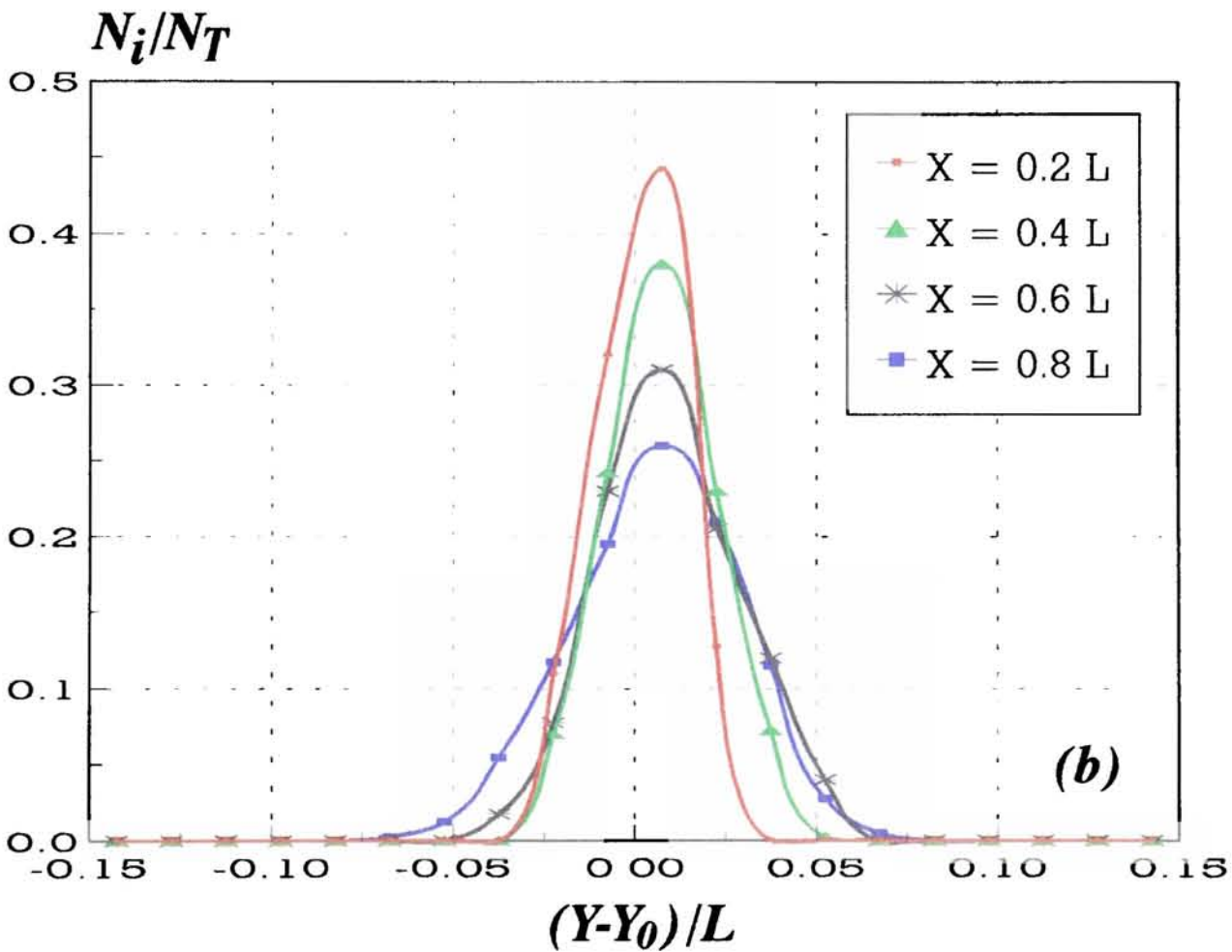
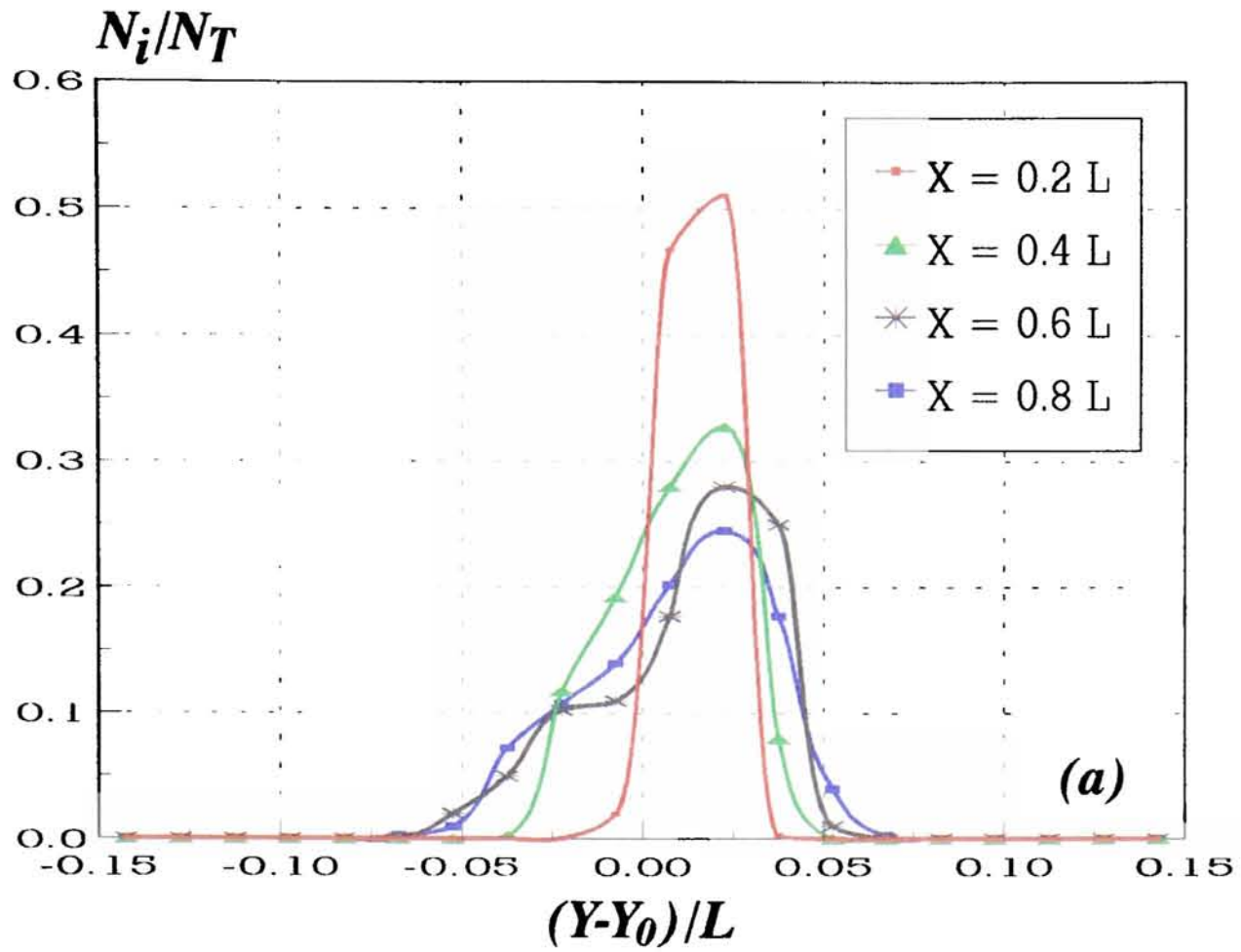


Figure 16. Bubble number fluxes in a vertical, downflowing, two stream mixing layer, calculated from the bubble trajectories shown in figure 14 : (a) $\Pi=0.5$, $\Gamma=10.0$; (b) $\Pi=0.0$, $\Gamma=10.0$. Bubbles were released every Δt . (Note: $N_T=400$. N_i is the bubble number sampled at i th sampling box in a downstream cross-section of the mixing layer and Y_0 is the axis of the mixing layer.)

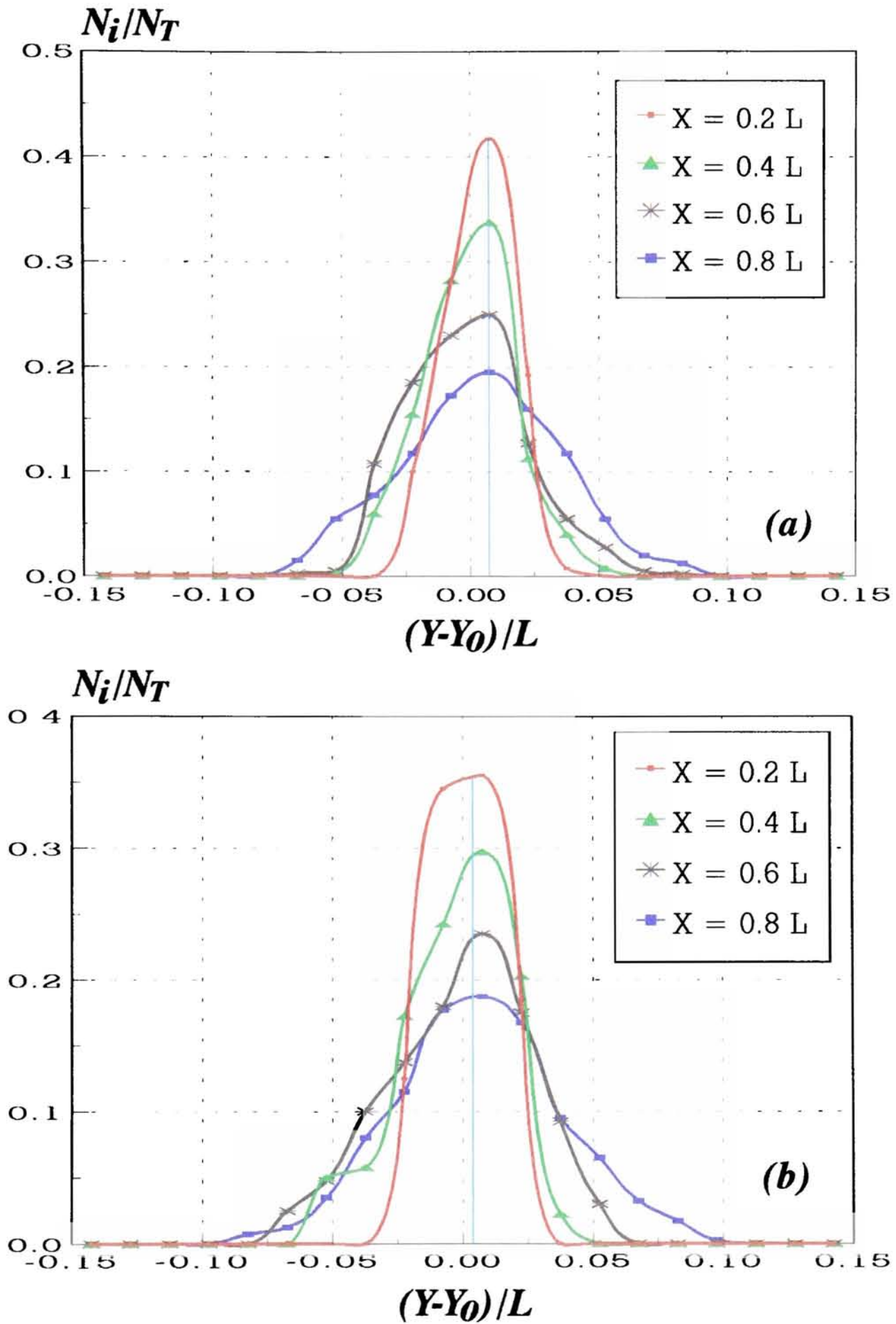


Figure 17. Bubble number fluxes in a vertical, downflowing, two stream mixing layer, calculated from the bubble trajectories shown in figure 15 : (a) $\Pi=0.5$, $\Gamma=10.0$; (b) $\Pi=0.0$, $\Gamma=10.0$. Bubbles were released every $10\Delta t$. (Note: $N_T=400$. N_i is the bubble number sampled at i th sampling box in a downstream cross-section of the mixing layer and Y_0 is the axis of the mixing layer.)

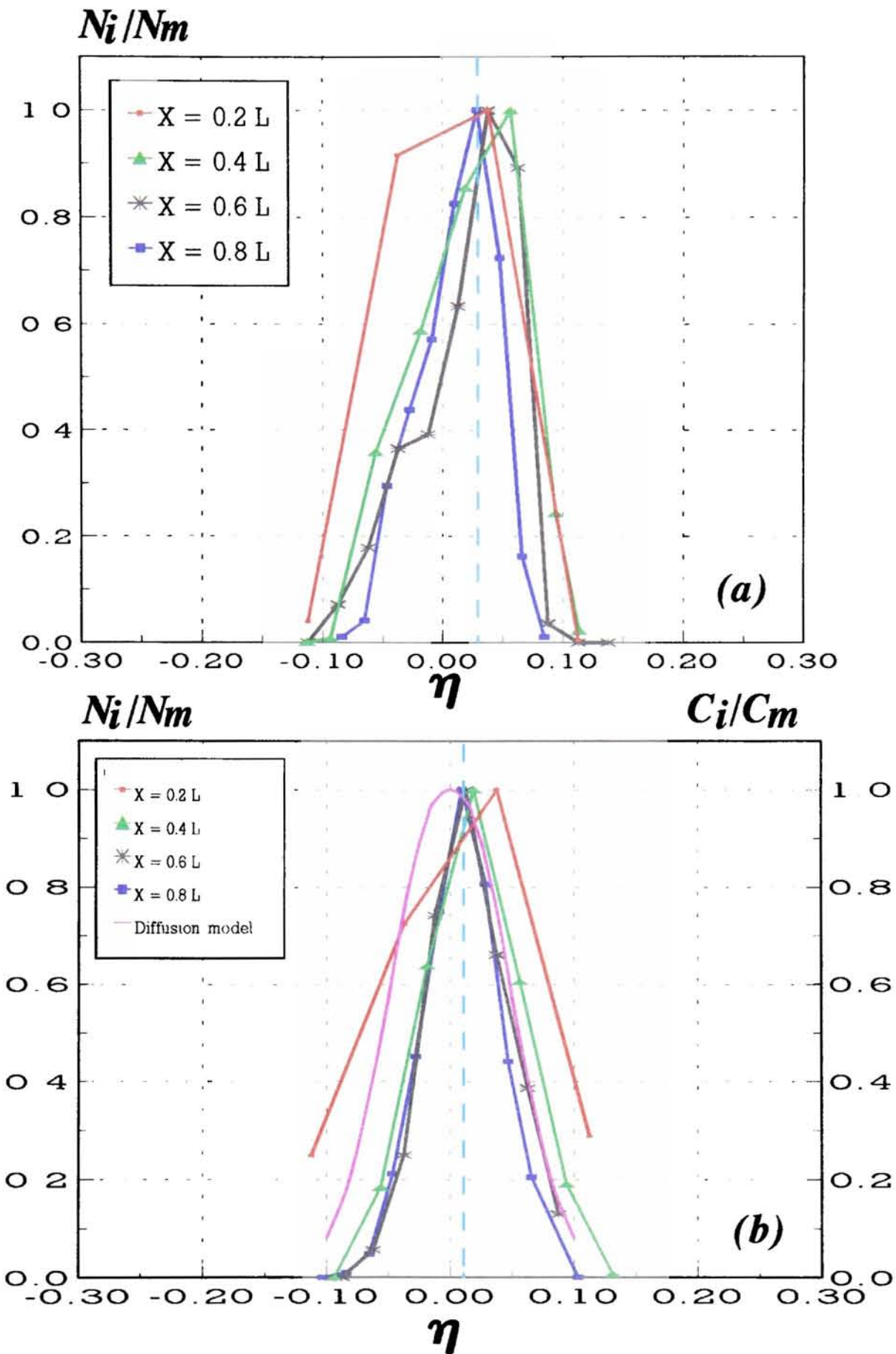


Figure 18. Bubble concentration fluxes in a vertical, downflowing, two stream mixing layer, calculated from the bubble trajectories shown in figure 14: (a) $\Pi=0.5, \Gamma=10.0$; (b) $\Pi=0.0, \Gamma=10.0$. Bubbles were released every Δt . (Note: N_i and N_m are respectively the bubble number sampled at i th sampling box in a downstream cross-section of the mixing layer and the maximum bubble number sampled.)

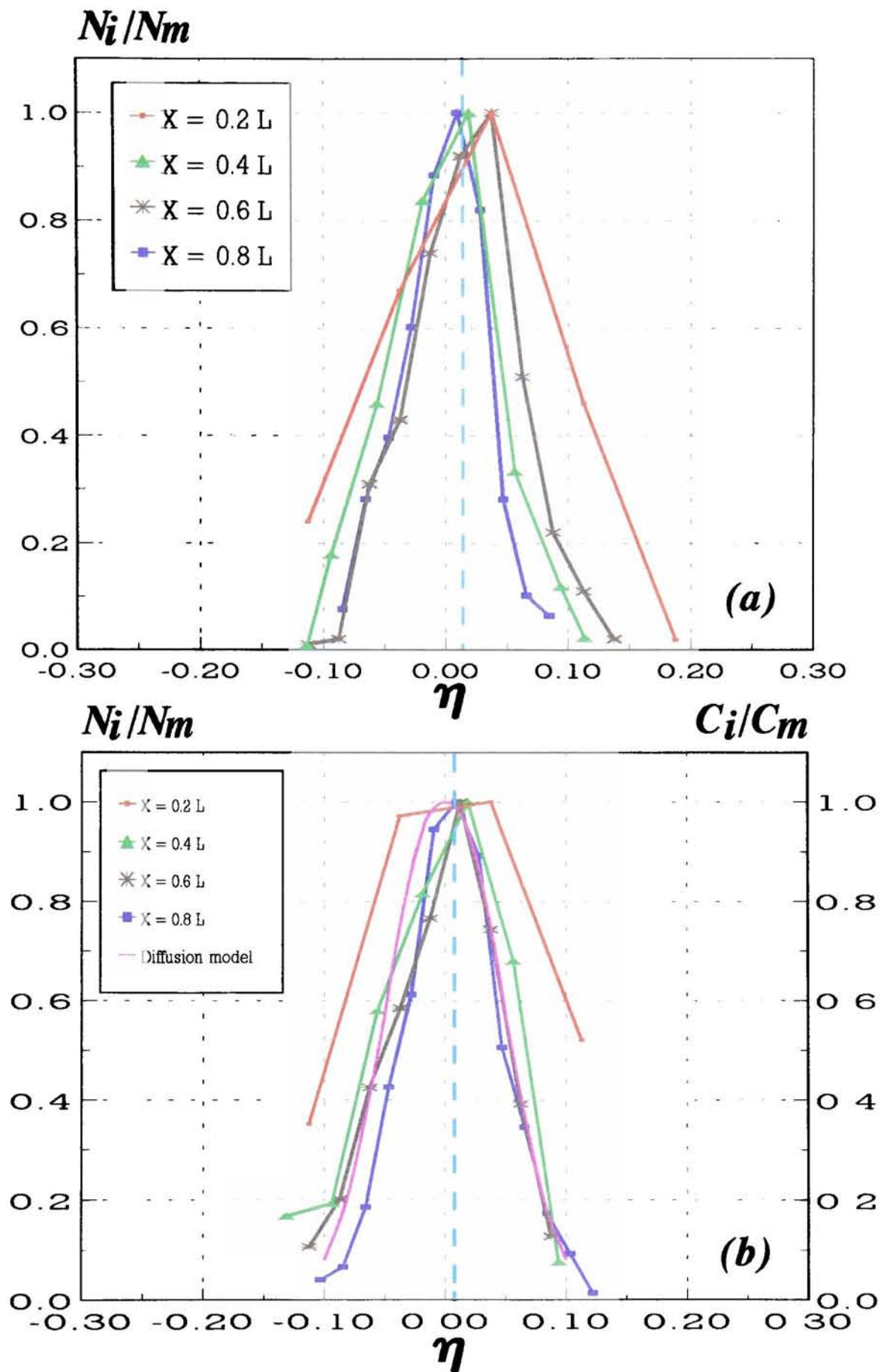


Figure 19. Bubble concentration fluxes in a vertical, downflowing, two stream mixing layer, calculated from the bubble trajectories shown in figure 15 : (a) $\Pi=0.5, \Gamma=10.0$; (b) $\Pi=0.0, \Gamma=10.0$. Bubbles were released every $10\Delta t$. (Note: N_i and N_m are respectively the bubble number sampled at i th sampling box in a downstream cross-section of the mixing layer and the maximum bubble number sampled.)

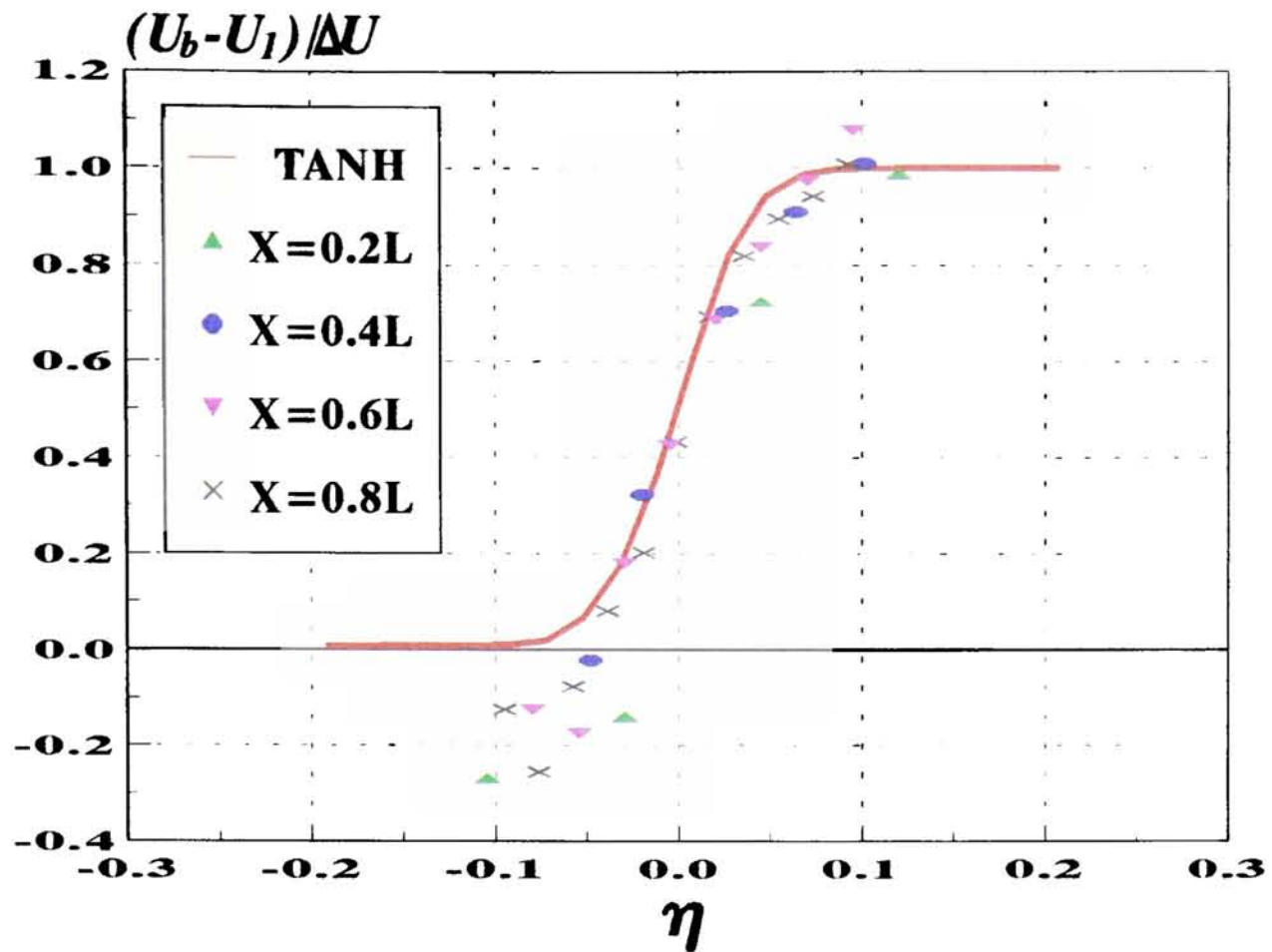


Figure 20. Time-averaged mean velocity profiles for bubbles at different locations of the mixing layer, based on 400 trajectory realisations. $\Pi=0.0$, $\Gamma=10.0$, $N_T=400$.

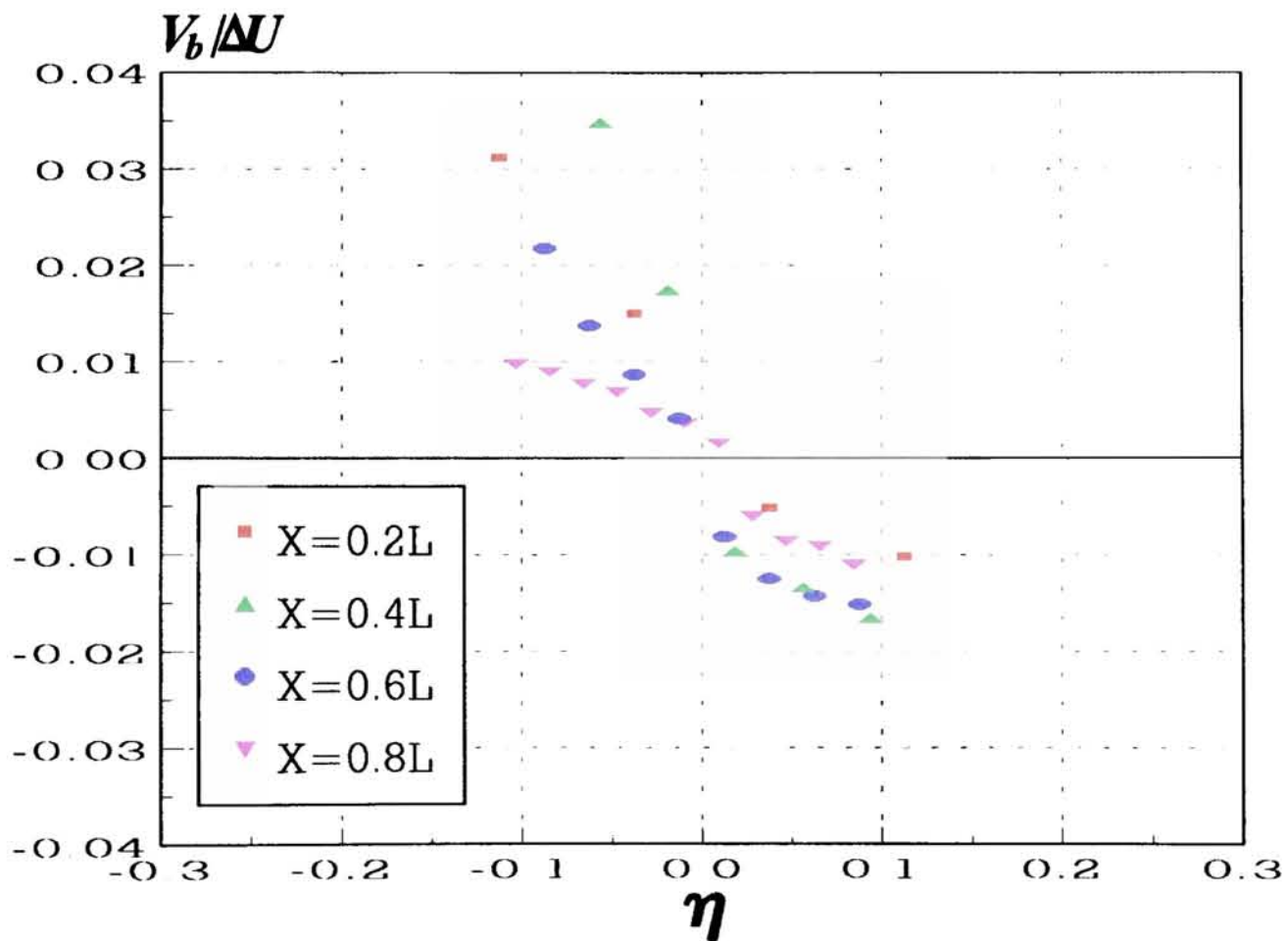


Figure 21. Time-averaged cross-stream velocity profiles for bubbles at different locations of the mixing layer, based on 400 trajectory realisations. $\Pi=0.0$, $\Gamma=10.0$, $N_T=400$.

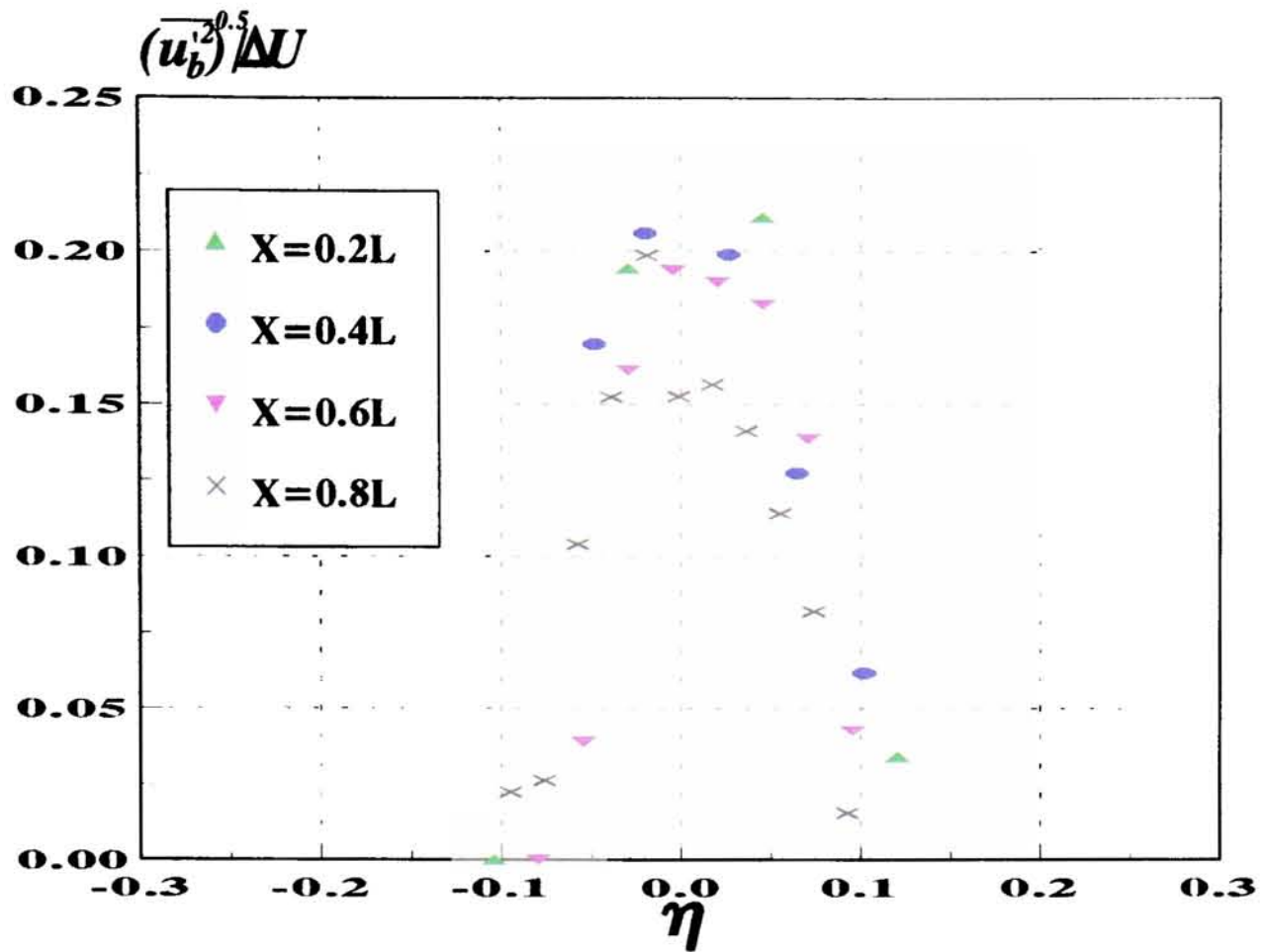


Figure 22. Longitudinal velocity fluctuations for bubbles at different downstream locations of the mixing layer, based on 400 bubble trajectory realisations. $\Pi=0.0$, $\Gamma=10.0$, $N_T=400$.

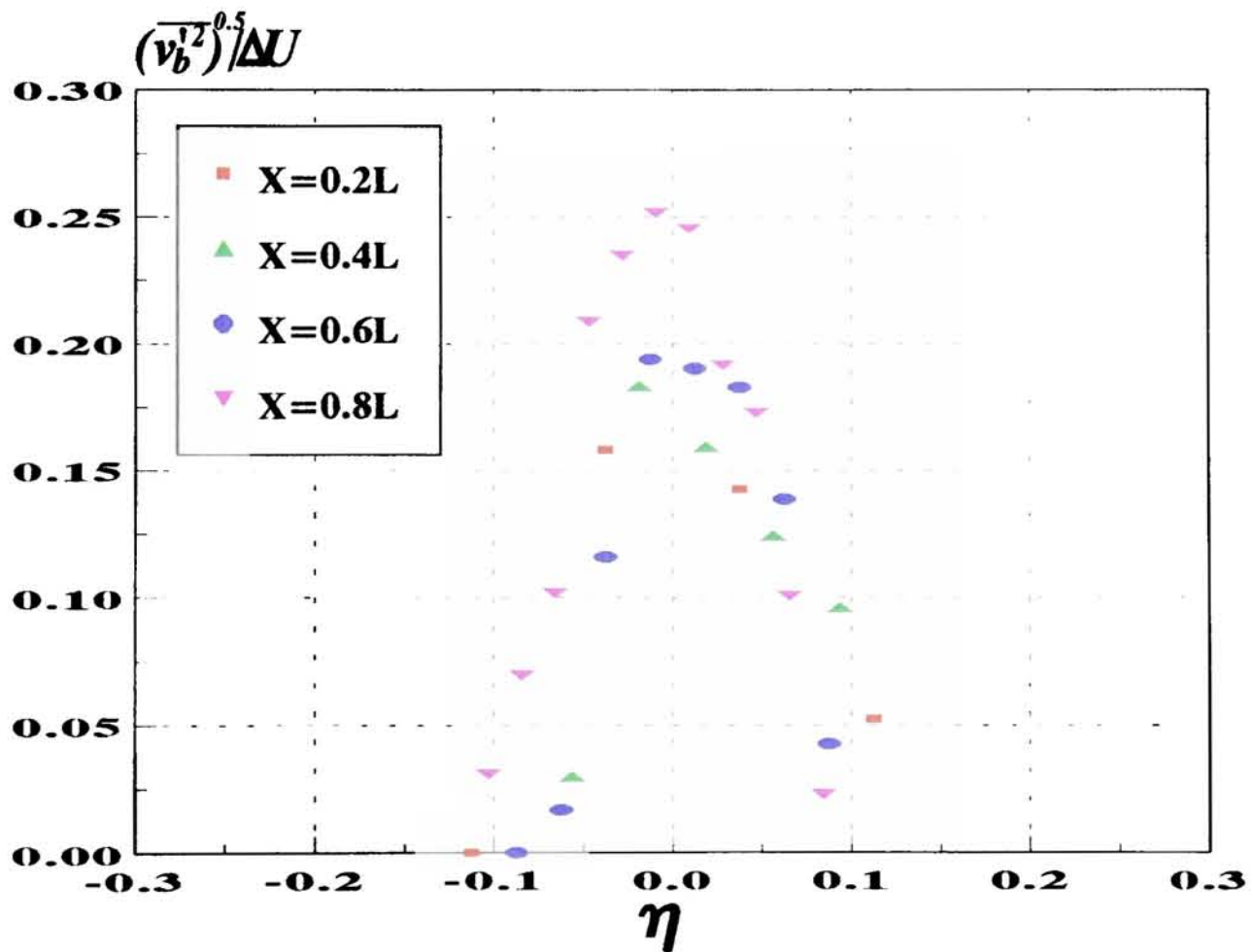


Figure 23. Cross-stream velocity fluctuations for bubbles at different downstream locations of the mixing layer, based on 400 bubble trajectory realisations. $\Pi=0.0$, $\Gamma=10.0$, $N_T=400$.

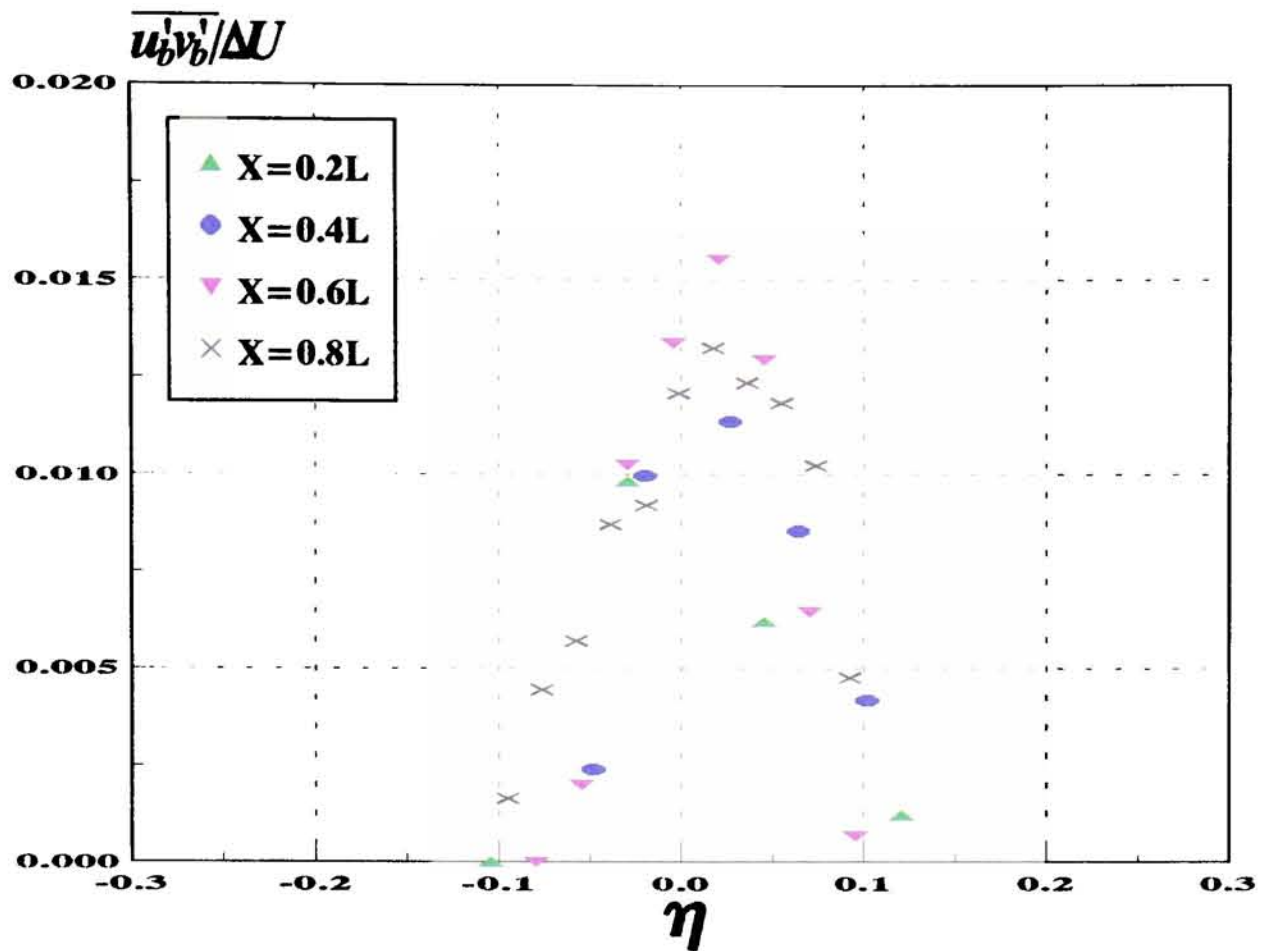


Figure 24. Correlations of bubble velocity fluctuation at different downstream locations of the mixing layer, based on 400 bubble trajectory realisations. $\Pi=0.0$, $\Gamma=10.0$, $N_T=400$.

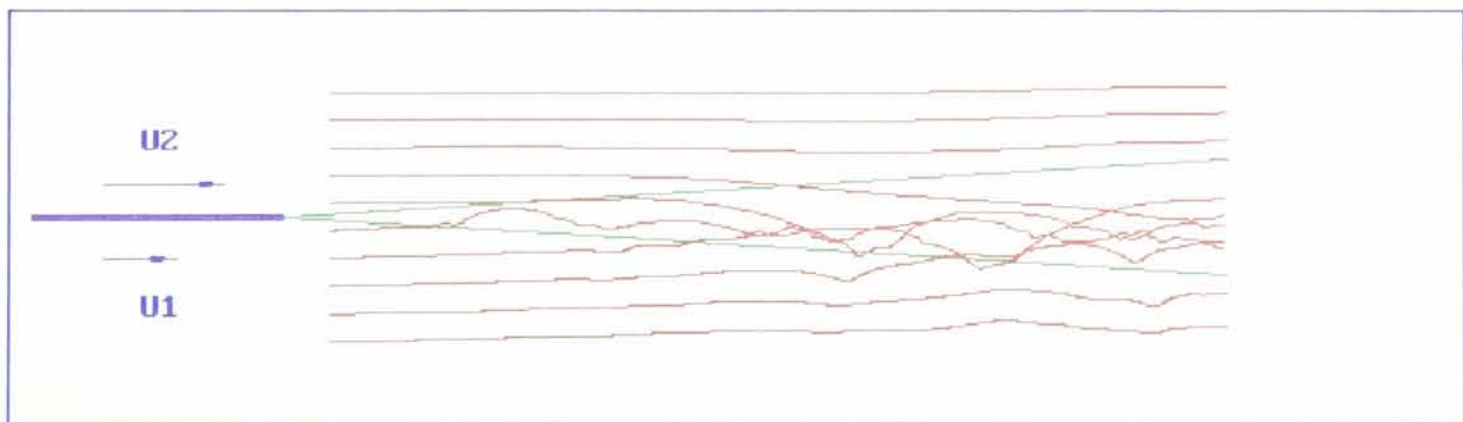


Figure 25. 10 bubble trajectories. Bubbles were released from both the high and low speed sides of a vertical, downflowing, two-stream mixing layer for $\Pi=0.0667$, $\Gamma=5.0$.

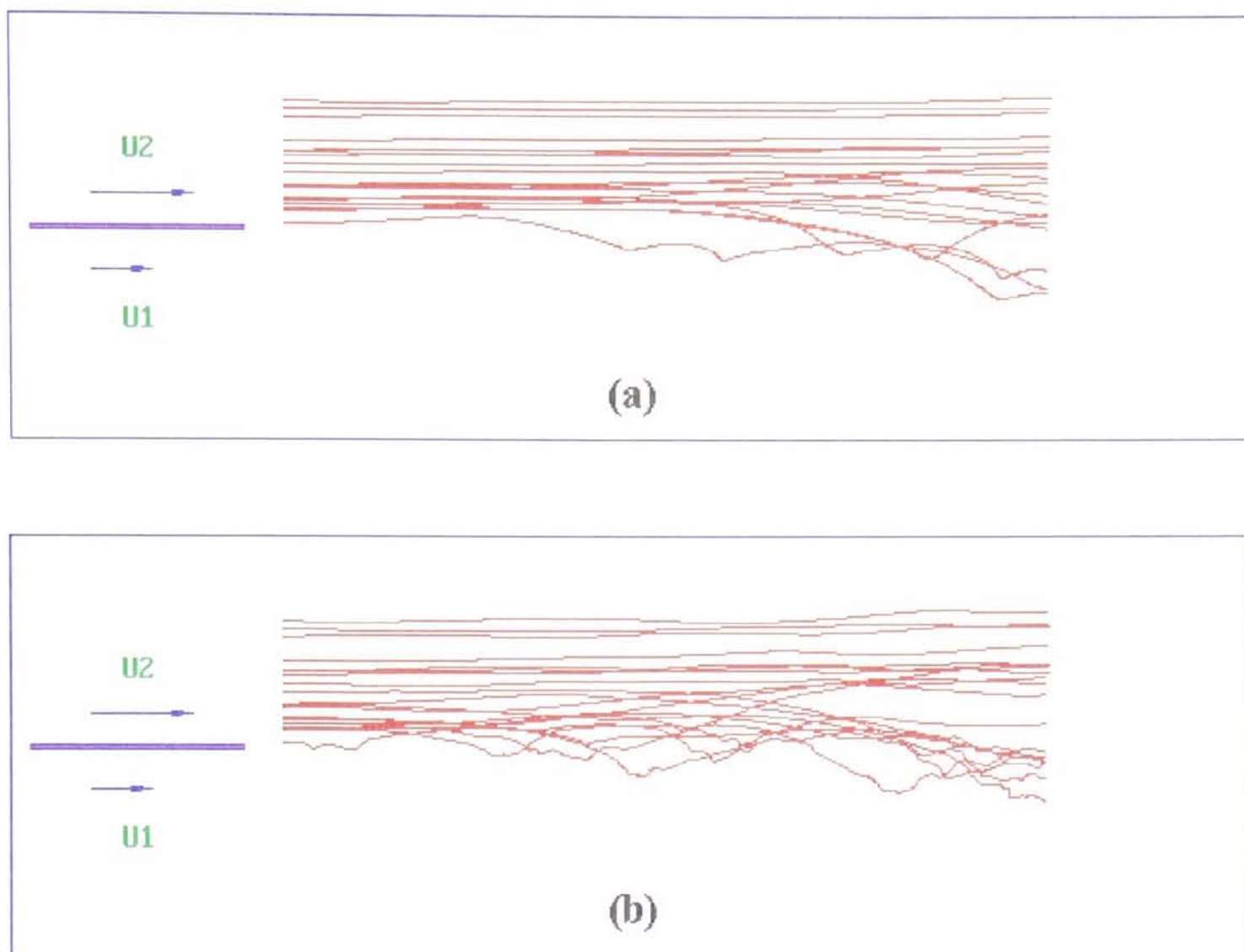


Figure 26. Computer simulations of bubble trajectories in a vertical, downflowing, two stream mixing layer. 400 bubbles were released from the high speed side of the mixing layer. (a) $\Pi=0.0$, $\Gamma=5.0$; (b) $\Pi=0.0667$, $\Gamma=5.0$. (Note: Only 20 trajectory realisations were displayed)

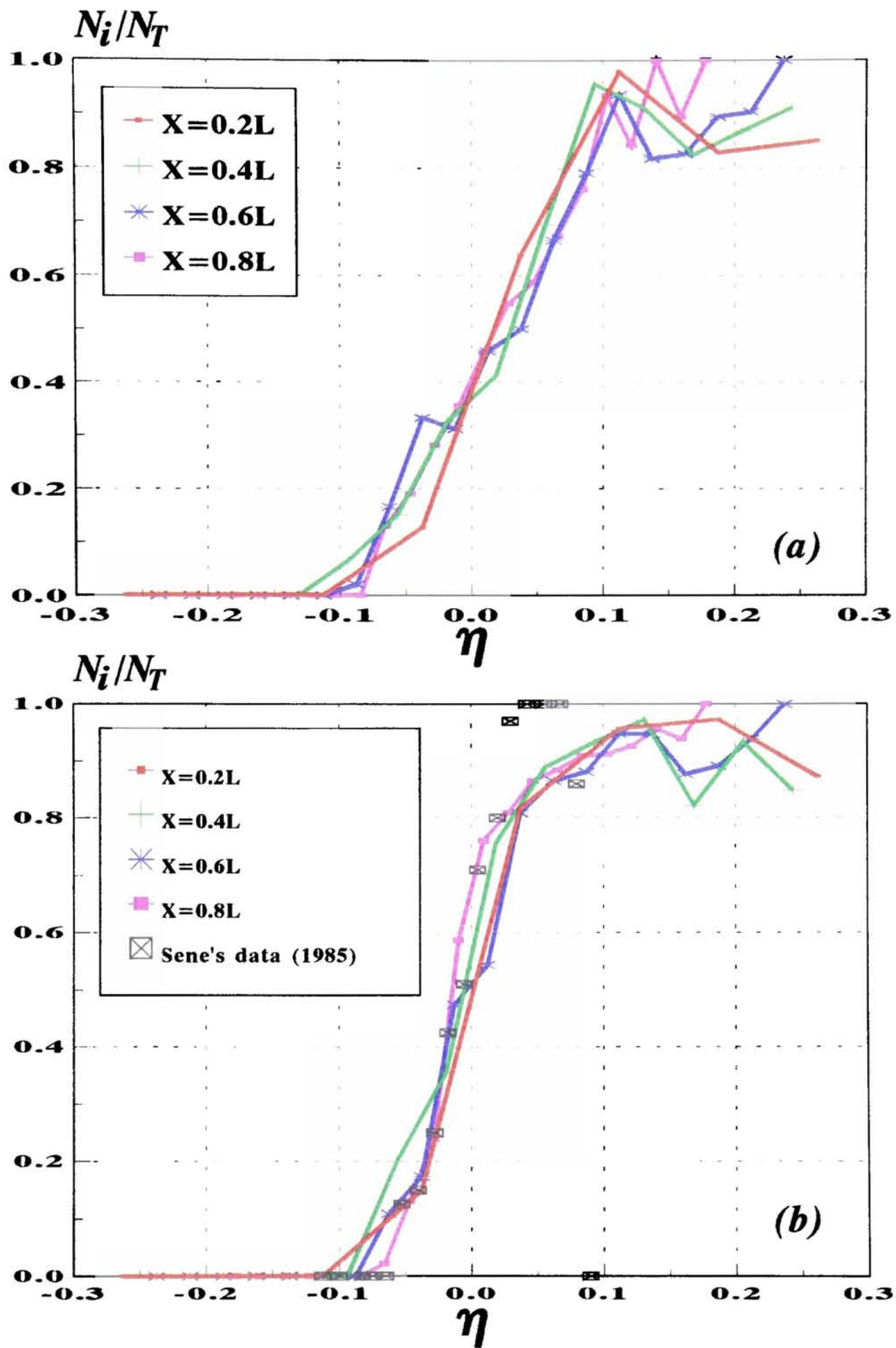


Figure 27. Calculations of bubble number fluxes in a vertical, downflowing, two stream mixing layer. N_T (=400) bubbles were released into the high speed side ($0 < y < 0.15L$) of the mixing layer: (a) $\Pi=0.0$, $\Gamma=5.0$; (b) $\Pi=0.0667$, $\Gamma=5.0$.

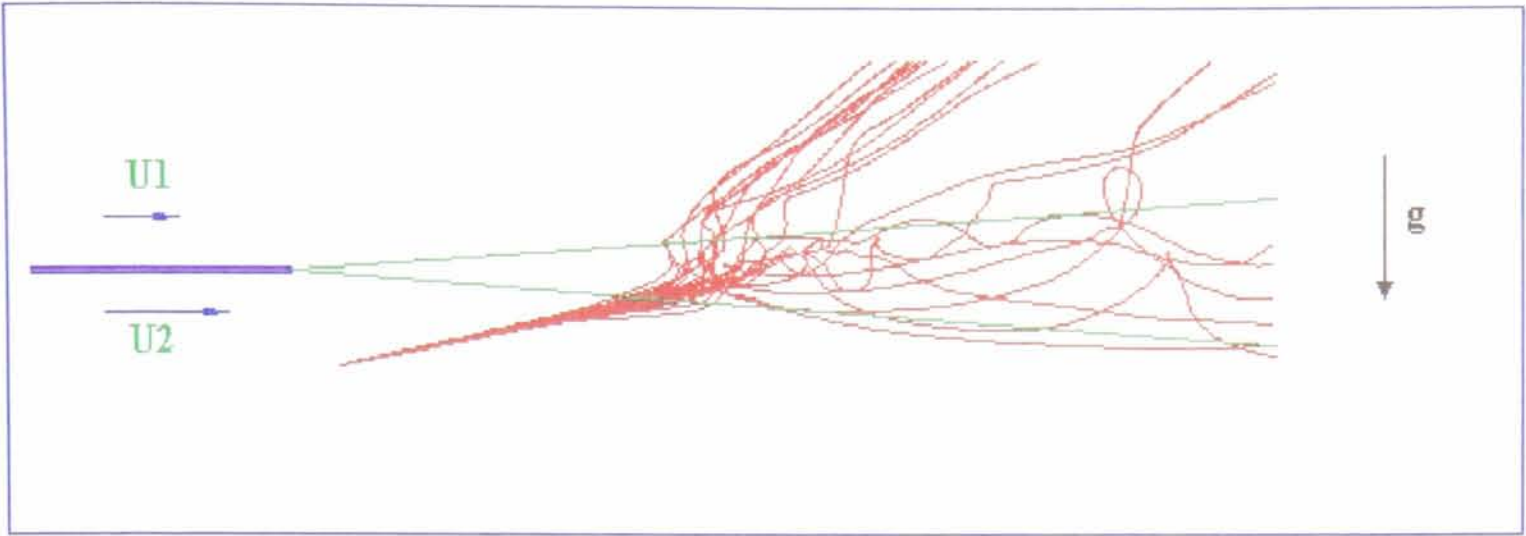


Figure 28. Simulation of 20 bubble trajectories in a horizontal mixing layer. $\Pi=0.05$, $\Gamma=2.0$.

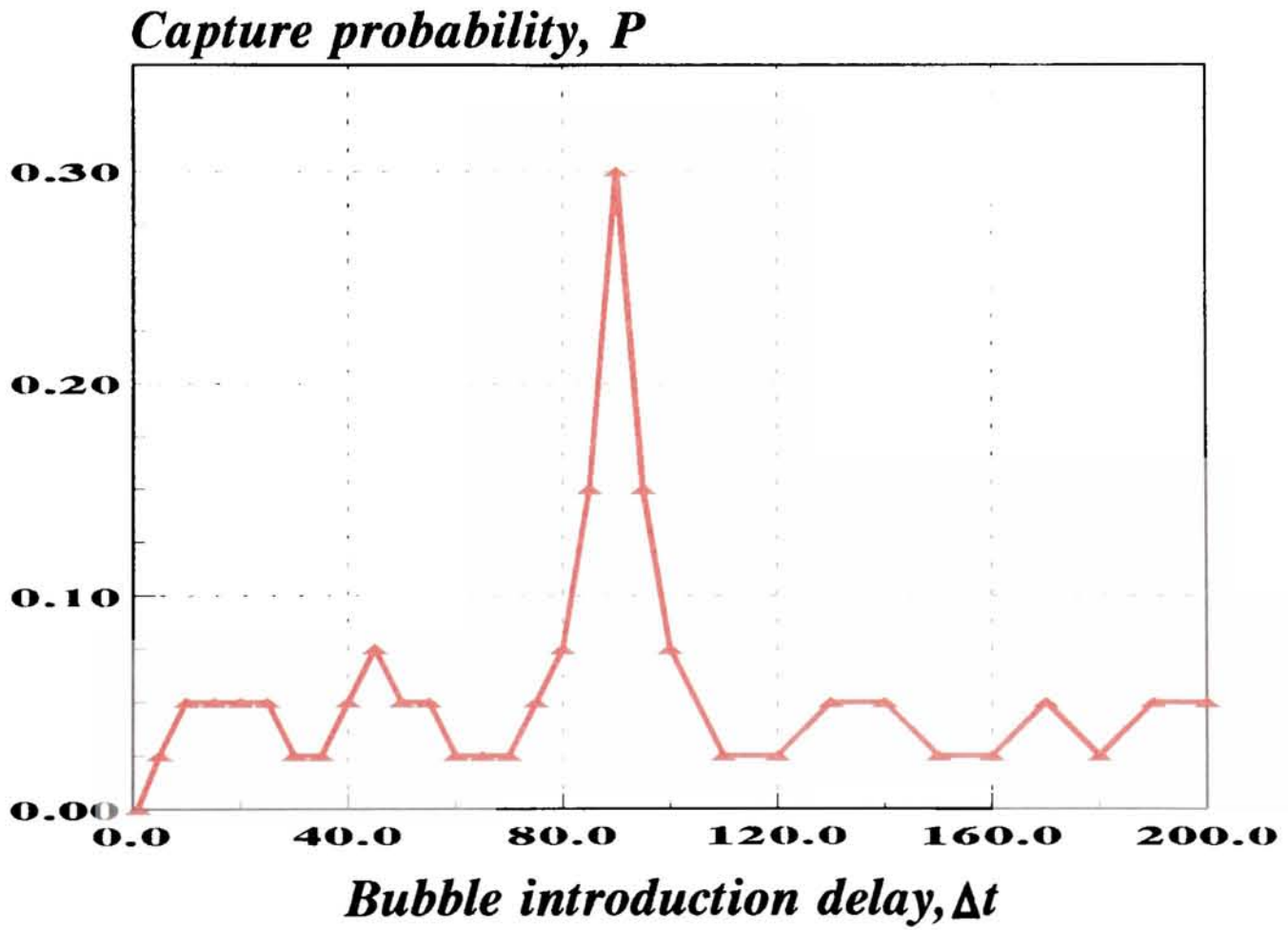


Figure 29. Calculations of the probability of bubble capture by the large eddies in a horizontal mixing layer: $\Pi=0.05$, $\Gamma=2.0$.

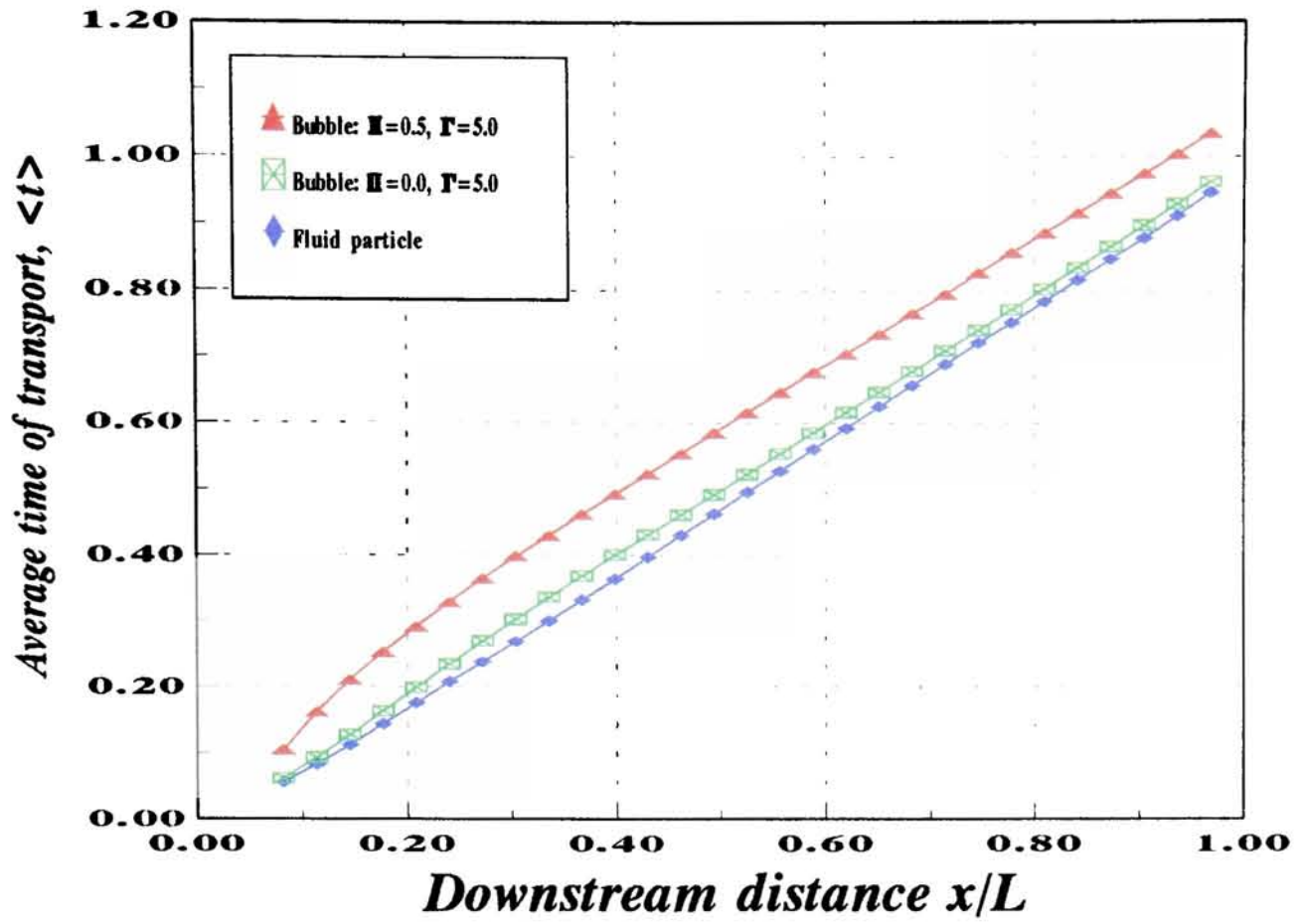


Figure 30. Ensemble-averaged time-of-transport measurement of bubble dispersion in a vertical, downflowing, two stream mixing layer.

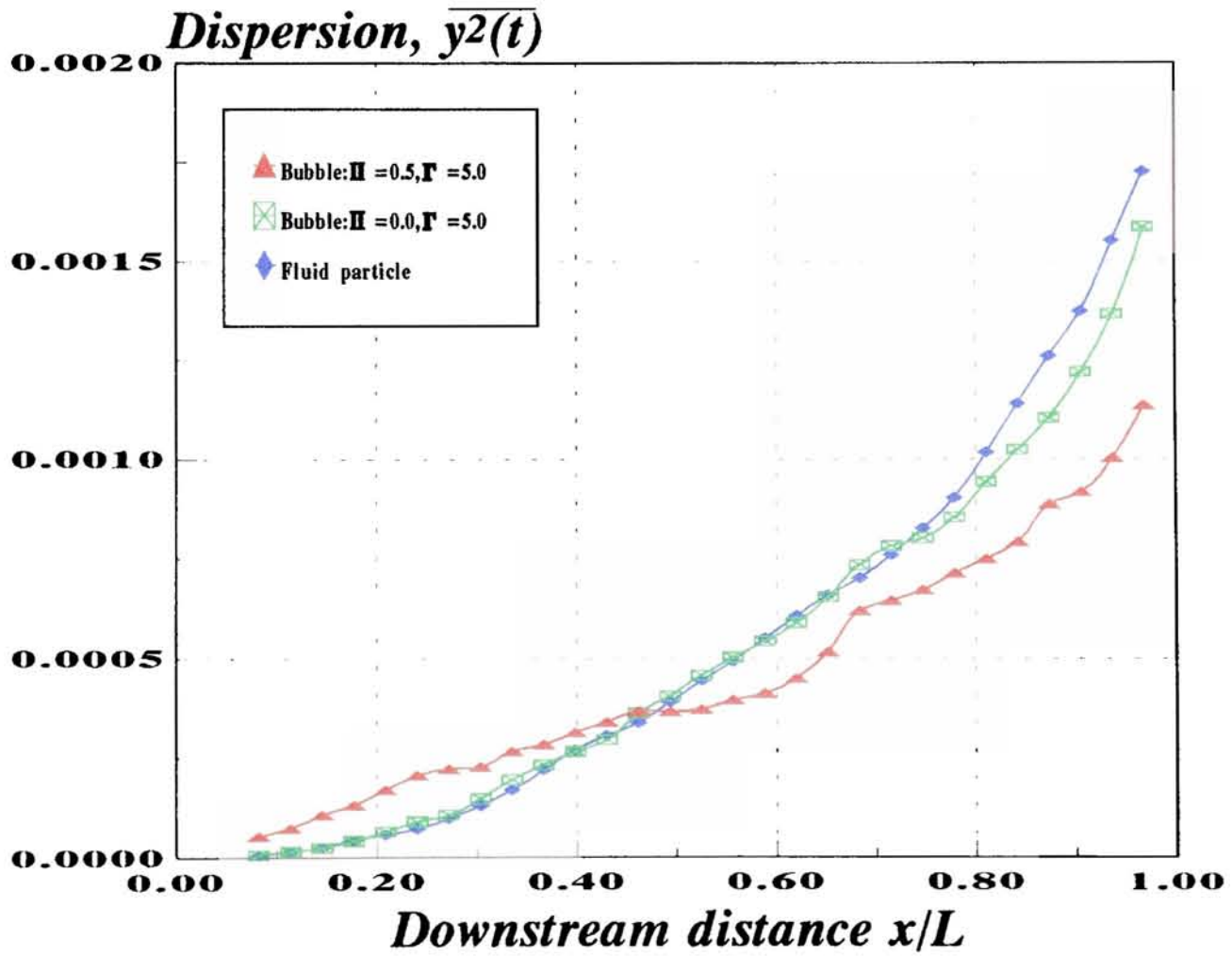


Figure 31. Eulerian bubble dispersion measurements as a function of downstream distance in a vertical, downflowing, two stream mixing layer.

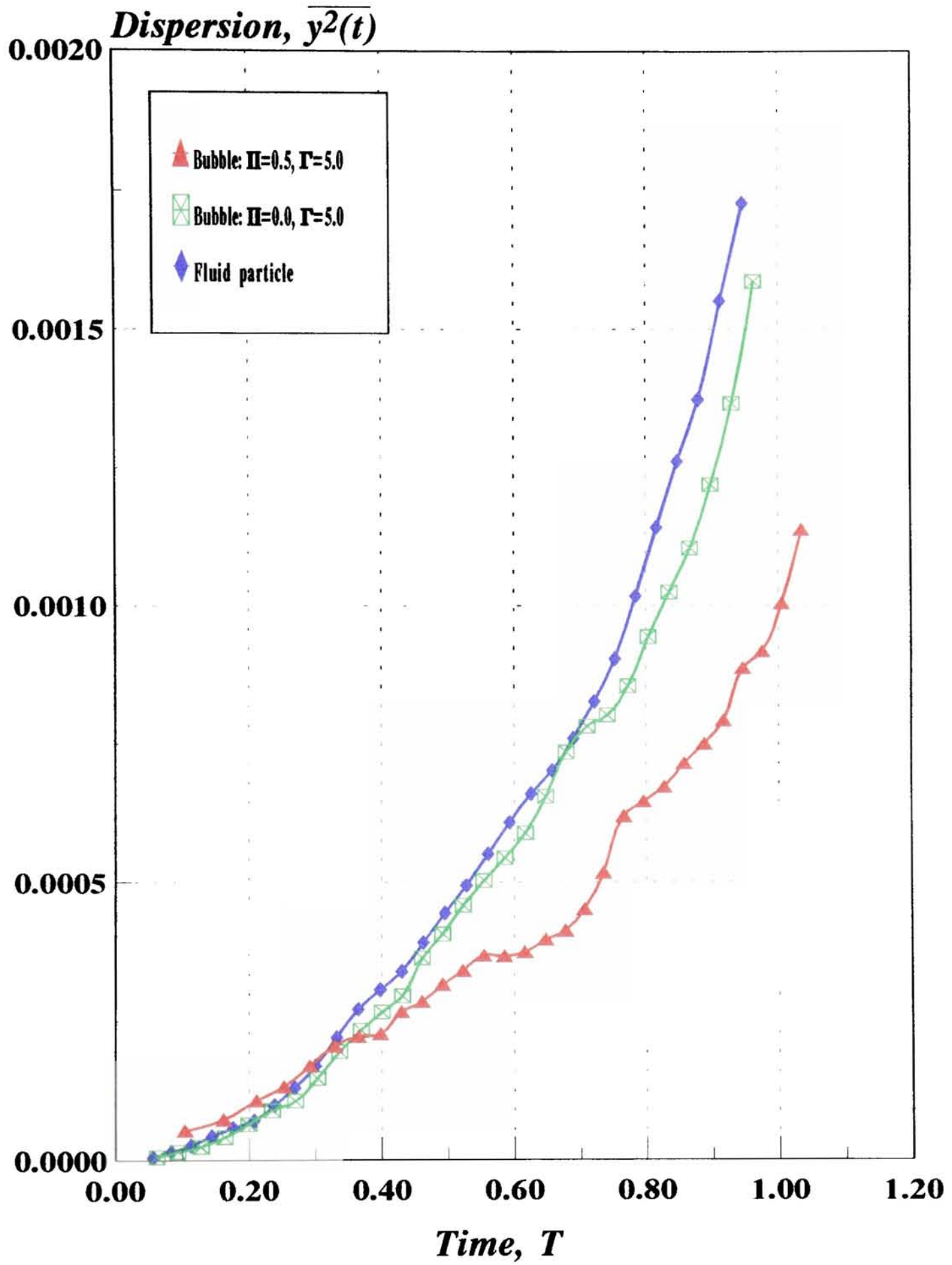


Figure 32. Ensemble-averaged Lagrangian predictions of bubble transverse dispersion in a vertical, downflowing, two stream mixing layer.

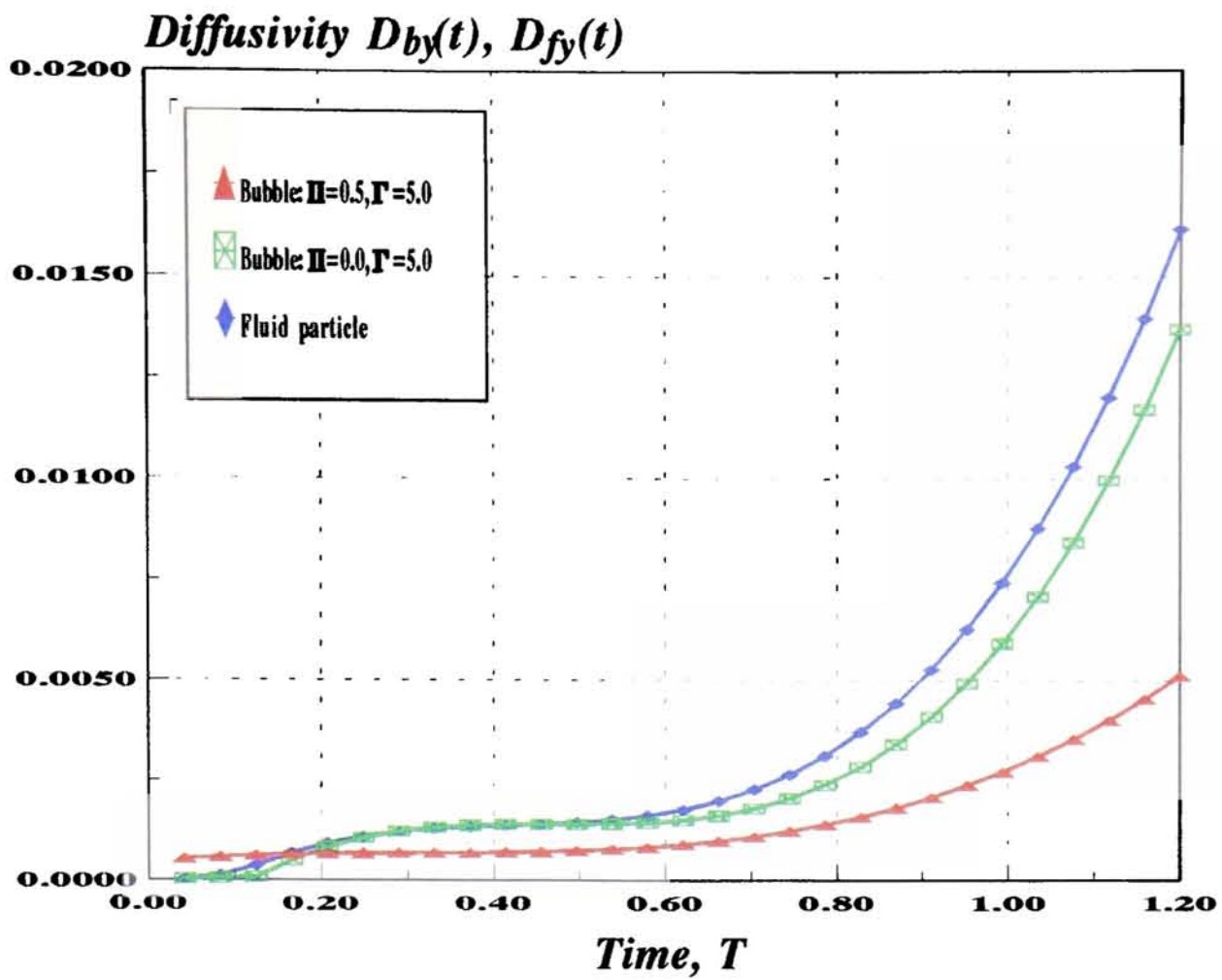


Figure 33. Bubble diffusivity and fluid diffusivity in a vertical, downflowing, two stream mixing layer.

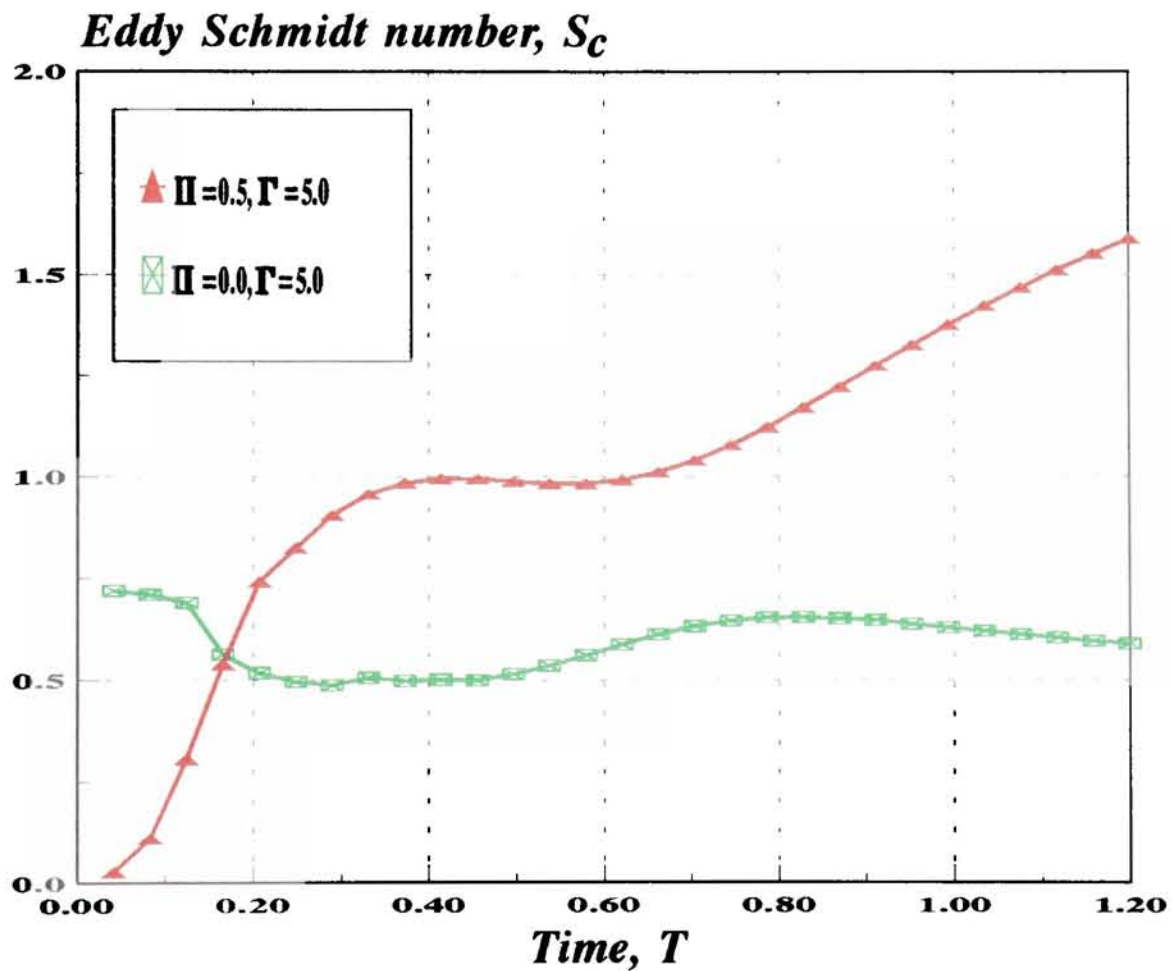


Figure 34. Eddy schmidt number of the bubbles in a vertical, downflowing, two stream mixing layer.

CHAPTER 4: PARTICLE DISPERSION BY ORGANIZED VORTEX STRUCTURES IN TURBULENT FREE SHEAR FLOWS.

SUMMARY

A discrete vortex model is used to simulate large eddy turbulent free shear flows and investigate the effects on Lagrangian particle trajectories of eddy structure patterns. We present detailed results for the dispersion of small, spherical non-interacting particles in two-dimensional large scale turbulent free shear flows. Our results confirm earlier experimental observations and numerical simulations (Wen *et al.* 1992; Crowe *et al.* 1993) that heavy particles entrained into large scale organised structures are centrifuged from the vortex cores and tend to concentrate around their the peripheries. We further demonstrate that two key independent scaling groups, the ratio of inertia to buoyancy forces; $\Pi = \Delta U^2 / g\delta$ and a retention parameter; $\Gamma = \Delta U / V_T$, together with the mass ratio parameter γ , play a comparably important role in determining the dispersion for particles as they do for bubbles in free shear flows. We show that their ratio, Π/Γ , is equivalent to the Stokes number. The predictions are not sensitive to details of the drag law formulations.

The particle dispersion patterns with different Π/Γ in the vicinity of the stagnation point flow, which can be regarded as an approximation of the local flow field between two successive large eddies in the mixing layer, are presented. We also compare the discrete vortex modelling simulation with the trajectories computed using a time-averaged modelling method. We highlight the importance of local instantaneous pressure gradient and the added mass force experienced by the particles with the density being of the same order of the carrier fluid, clearly demonstrating shortcomings in earlier models of stochastic dispersion

(e.g. Gosman and Ioannides 1981) where the continuous phase flow is treated as a mean field on which is superposed random perturbation for modelling the discrete phase transport.

1 INTRODUCTION

Particle-laden flows are widely encountered in nature and in engineering applications, and particle transport in turbulent shear flows is now recognised to play a key role in the performance of a wide variety of industrial and energy processes, such as combustors and chemical reactors (Eaton & Fessler 1994). Such flows invariably involve to greater or lesser extent large scale vortical structure (recall chapter 3). Unlike recent advances in particle-laden gas flows, the local dynamics of particle-laden flows with the particle density being of the same order of the carrier fluid has received little attention. The main purpose of the present study is to address particle transport by transient large eddies in such free shear flows.

Much of the established knowledge about the dispersion of particles in turbulent flows is due to classical considerations. Treatments usually regard such transport as a Fickian diffusion process (Hinze 1975). The closure problem thus centres on assigning an appropriate dispersion coefficient and many studies (e.g. Faeth 1987) have been concerned with selection of these parameters. Early works identified the ratio of the particle response time to turbulence time scale as crucial, with associated reduced diffusivity, often referred to as the crossing trajectories effect (e.g. Wells & Stock 1983). However, Reeks (1977) showed that the diffusion coefficient of heavy particles can exceed that of the turbulence in homogeneous isotropic fields.

Most numerical approaches utilise the Monte Carlo method (e.g. Faeth 1987), in which the flow velocity fluctuation is selected randomly at each time step. The velocity response of the particle is decomposed into mean and the fluctuation values, and the fluctuation value is assumed to be unchanged either over the eddy life time or for the time taken by the particles to traverse the eddy (crossing trajectory effect). Various applications of this method have been reported by, for example, Gosman and Ioannides (1981), Shuen *et al.* (1983, 1985) and Kallio and Reeks (1989). More sophisticated models which have included velocity fluctuation correlations have been also reported. Zhou and Leschziner (1991) proposed a particle dispersion model in which turbulent fluctuations are correlated temporally and spatially between two successive time steps. Legg (1983) presented the time-correlated random-walk model in which the fluctuation correlations along the particle trajectory are found based on a Langevin equation. Zhuang *et al.* (1989) made a distinction between the starred fluid element and the driving fluid element during the particle-eddy interaction, and proposed that the driving fluid velocity remains correlated by the Markov-chain along the particle trajectory. The attraction of these approaches is their easy implementation, often in conjunction with an engineering calculation scheme (e.g k - ϵ model) for the mean flow and turbulence. However, there is a major omission insofar as the formulation does not utilise instantaneous velocity fields capturing extended structural features of large scale eddies, and this omits important couplings between the particle dynamics and such flow features, irrespective of any other limitations associated with the force law adopted for particle motions.

In order to capture such effects, Thomas *et al.* (1983) introduced vorticity simulation for bubble transport, later adopted by Crowe *et al.* (1985) for particle dispersion (recall Chapter

1). Following established practice for modelling of particle dispersion, Crowe *et al.* (1985) adopted a coupling parameter, the Stokes number $S_t = \tau_p / \tau_f$, where τ_p is aerodynamic response time and τ_f is the transit time for large eddies. Thus, when $S_t \ll 1$, it corresponds to a particle aerodynamic response time much less than eddy transit time and the particles essentially follow all details of the fluid motion. When $S_t \sim 1$, the particles tend to be centrifuged to the outer edges of the eddy structures, thereby attaining enhanced dispersion. For $S_t \gg 1$, the particles are essentially insensitive to fluctuations in fluid velocity. Crowe's *et al.* (1985) numerical studies have been corroborated by extensive experimental evidence of the role played by Stokes number as a key parameter for particle dispersion in large scale structure. However, for bubble dispersion, as an extension of the ideas in Thomas *et al.* (1983), Hunt *et al.* (1988) introduced dimensionless parameters, Π and Γ , which physically represent the ratio of inertial to buoyancy forces and the trapping potential of the large eddies. Extensive numerical and experimental studies (e.g. Sene *et al.* 1994, Yang & Thomas 1994) have substantiated this formulations, which was also recently adopted by Stewart & Crowe (1993).

Numerical simulations of particle dispersion in Stuart's vortex street as a model of free shear layers were reported by Crowe *et al.* (1985), and they noted the tendency of particles to attain a large spread for Stokes numbers near unity. Since then many numerical models have appeared utilising the discrete vortex method, following Thomas *et al.* (1983) pursuing calculations on bubbles in mixing layer turbulence. Chein and Chung (1987, 1988) applied their method to particle dispersion in mixing layers and showed that particle dispersion can exceed that of the fluid dispersion, especially for $S_t \sim 1$. They also reproduced the observed tendency of particles to accumulate around the edges of the vortices. Similar results were reported by Wen *et al.* (1992) using a modified discrete vortex simulation, in which the

effect of the confining walls of wind tunnel has been taken into account in a numerical scheme (Ghoniem & Ng 1987). Their simulation results further indicated that particle dispersion could usefully be distinguished according to two mechanisms which they describe as 'stretching and folding', although satisfactory physical explanations were not documented. Further insight into the dynamics of particles in shear flows has been gained by numerically analysing the motions of individual particles in idealised representations of the flow field. For example, Ganán-Calvo and Lasheras (1991) investigated a periodic Stuart vortex flow with heavy, settling particles and found certain sized particles to be permanently suspended in the flow rather than sedimented. Tio *et al.* (1993) extended this work to buoyant particles, and reported that buoyant particles can become suspended at the stable equilibrium points within the vortices while heavy particles are trapped in a thin layer above the vortices. Perkins and Hunt (1986) adopted a Rankine vortex to model large scale structure and show how dense particles can be either trapped or dispersed.

Like numerical studies on particle dispersion, experimental studies of particle dispersion in large eddies have also been reported by many researchers. Kamalu *et al.* (1988) and Wen *et al.* (1992) reported flow visualisation and point measurements of particles released into a plane mixing layer. Their flow visualisation results clearly showed that particles with $S_r \sim 1$ are centrifuged to the peripheries of vortex structures, leaving the centres nearly devoid of particles. Using Laser Doppler measurements of particle velocity, they also showed that the time-averaged cross-stream particle velocities were outwards from the cores, thereby demonstrating long term centrifugation. Other experiments by Lázaro and Lasheras (1989) using a light scattering technique also indicated that the eddy structures play a dominant role in particle dispersion.

Here we describe the dynamics of small, rigid, spherical particles in two-dimensional shear flow, in particular the two-stream turbulent mixing layer. Our purpose is to further elucidate the underlying mechanisms, and demonstrate the shortcomings of simplified stochastic models. We caution that the analysis relates to dilute suspension, such that the particles do not introduce any dynamical feedback to the flow. The governing equations of motion and modelling assumptions are discussed in section 2. Section 3 presents our detailed numerical results. Our findings will be discussed in section 4 and the main conclusions are drawn in section 5.

2 PARTICLE DYNAMICS

2.1 Equation of Particle Motion

Particle transport, like bubble transport, in free shear flows is strongly influenced by the large eddy structures and reliable prediction of trajectory statistics really demands detailed calculation according to the Lagrangian force law. Whilst there remain serious uncertainties about the force law formulation, broadly speaking the force laws of Auton (1987) and Maxey and Riley (1983) have been shown to be applicable under defined asymptotic idealisations for simple shear flows. To focus attention on the restrictions that should strictly apply, we briefly recapitulate the picture as follows.

Foremost we must recognise that our work is confined to passive particles whose motions are driven entirely by flow forces independently of other particles in the flow. This means that the coupling between particles and the fluid motion is ignored. Other main restrictions and assumptions include that (1) the particle is spherical, with drag coefficient given by

standard drag curve (Clift et al. 1978); (2) the viscous drag force can be simply added to the inviscid forces on the particle; (3) the radius of the particle is small compared to the scale over which the shear velocity gradient varies; (4) the change in the ambient velocity field over the scale of the particle is small compared to the slip velocity and (5) the effect of turbulence is negligible and deterministic trajectories may be calculated. On this basis, then, the following equation of motion was derived by Auton (1983) as first reported in Thomas *et al.* (1983):

$$\left(\frac{\rho_b}{\rho_f} + C_m\right) \frac{d\mathbf{v}}{dt} = (1 + C_m) \frac{D\mathbf{u}}{Dt} - g \frac{\mathbf{w}}{V_T} f\left(\frac{|\mathbf{w}|}{V_T}\right) - \left(\frac{\rho_b}{\rho_f} - 1\right) \mathbf{g} - C_L \mathbf{w} \times (\nabla \times \mathbf{u}) \quad (1)$$

where \mathbf{v} is the velocity of the particle, \mathbf{u} is the velocity of the carrier fluid, $\mathbf{w} = \mathbf{v} - \mathbf{u}$ is the slip velocity, V_T is the terminal velocity of the particle, C_m ($=1/2$) is the added mass coefficient and C_L ($=1/2$) is the vorticity-lift coefficient of the particle. On the other hand, for small solid particles (slip speed Reynolds number about unity), Maxey and Riley (1983) derived the following equation:

$$m_p \frac{d\mathbf{v}}{dt} = (m_p - m_f) \mathbf{g} + m_f \frac{D\mathbf{u}}{Dt} + \frac{1}{2} m_f \left(\frac{D\mathbf{u}}{Dt} - \frac{d\mathbf{v}}{dt} \right) + 3\pi d_p \mu \mathbf{w} + \frac{3}{2} \pi d_p^2 \mu \int_0^t \frac{d\mathbf{w}/d\tau}{\sqrt{\pi \nu (t - \tau)}} d\tau \quad (2)$$

where m_p and m_f are the mass of the particle and the mass of the fluid displaced by the particle, d_p is the particle radius and other symbols are as given above. Comparing the two equations, we may note the main differences between them are as follows. A lift force due to the shear vorticity is included in equation (1), but not in equation (2). We note that vorticity-lift force is not always negligible especially for the particle in a strong shear vorticity (e.g. Sridhar & Katz 1994). On the other hand, no Basset history term appears in equation (1) whereas it does in equation (2). Recent investigations (e.g. Mei *et al.* 1991;

Rivero *et al.* 1991) have indicated that the Basset term as given in equation (2) overpredicts the time contribution which in the far-field decays as $(t-\tau)^{-2}$ rather than $(t-\tau)^{-1/2}$. Whilst the drag force expression appears to be different, in fact the formulation in equation (1) encompass the Stokes' drag description in equation (2) within the presumption for the *Reynolds* number dependent factor f to be assigned independently as the force law asymptote for steady slip balancing drag and weight of the particle. Finally, we note that, with reservations, the force law may be applicable to particles with sufficiently small departures from sphericity (Auton *et al.* 1988; Hunt *et al.* 1993).

Our analysis here utilises equation (1), more particularly with reference to particle transport in free shear layers for which the reference velocity scale is ΔU measuring the strength of vorticity in the shear turbulence together with δ as length scale measured in terms of the thickness for the mixing layer, hence reflecting the size of individual large eddies.

$$(\gamma + C_m) \frac{d\bar{v}}{d\bar{t}} = (1 + C_m) \frac{D\bar{u}}{D\bar{t}} - \frac{\Gamma \bar{w}}{\Pi} f\left(\frac{|\bar{w}|}{\Gamma}\right) - (\gamma - 1) \frac{\mathbf{g}}{g\Pi} - C_L \bar{w} \times (\nabla \times \bar{u}) \quad (3)$$

where $v = v/\Delta U$, $\bar{u} = u/\Delta U$ and $\bar{t} = t\Delta U/\delta$ and we have introduced two nondimensional groups, $\Gamma = V_T/\Delta U$, $\Pi = \Delta U^2/g\delta$ with $\gamma = \rho_p/\rho_f$ as discussed by Hunt *et al.* (1993). As used by many practitioners in work on particle transport dynamics, the particle response time is expressed in terms of the terminal velocity for weight-drag equilibrium; namely:

$$\tau_p = \frac{V_T}{g} \left[\frac{4d_p(\rho_p - \rho_f)}{3C_D\rho_f g} \right]^{1/2} \quad (4)$$

where the drag coefficient C_D (particle Reynolds numbers less than 1000) is often assigned

on the basis of the semi-empirical relationship reported in Clift *et al.* (1978).

$$C_D = \frac{24}{Re_p} [1 + 0.15 Re_p^{0.687}] \quad (5)$$

Here Re_p is the particle Reynolds number based on the particle diameter d_p , its relative velocity $|\mathbf{v}-\mathbf{u}|$ and the fluid viscosity ν . We note that the ratio Π/Γ is in effect a Stokes number for particles, that is, a non-dimensional measure of the relaxation time τ_p (i.e. as $\tau_p \Delta U/\delta$). However, unlike most formulations for particle transport, including equation (2), the retention of Π and Γ as independent parameters here provides for a more complete description insofar as vorticity-lift couplings are retained. On the other hand, for gas-solid shear flows, the mass ratio γ is of the order of 10^3 so that the drag and buoyancy forces are often dominant in comparison to the other forces and the equation can be simplified accordingly. However, for small solid particles moving in liquids with comparable density, all terms in the force law are then of the same order (Onslow & Thomas 1994). Despite this strict request that vorticity-lift be retained, the fact is that most practical schemes still disregard this term (e.g. Maxey *et al.* 1994).

2.2 Effect of Drag Force on Particle Dispersion

As a preliminary to calculations involving the complexity of unsteady travelling eddy structure, we briefly turn to considerations of Reynolds number effect as characterised via factor f in the drag law formulation of equation (1). Also, in the interest of simplicity we restrict our demonstration to large γ ($\approx 10^3$) representative of particles in gas where the added mass and the lift force can be neglected. In the spirit of previous demonstration exercises (Thomas *et al.* 1983; Onslow & Thomas 1994), we adopt Rankine vortex flow as a simple model flow field. With these restrictions, thus, figure 1 compares the trajectories

obtained with a low- R_e linear drag law and a high- R_e quadratic drag law, both for $\gamma=10^3$ and for $\gamma=0$; i.e. bubbles as benchmark (chapter 3). Figure 2 presents this information as radial distance versus time. Clearly for each assigned value of γ there is not much difference although there is (of course) a striking difference between the behaviour of particles and bubbles. However, care should be exercised in supposing that C_D selection is never important - in particular, consider that the approach to equilibrium may not always be monotonic as in this example. Conceivably, other combinations of parameters and initial conditions could even result in such striking differences as trajectories for which one terminates at equilibrium and the other escapes entirely.

2.3 Particle Entrainment in a Time-decayed Lamb-Oseen Vortex

The representation of particle transport in the coherent structures of free shear flows can be assessed by modelling the flow as a succession of travelling vortices with rotational cores (Sene *et al.* 1994). More realistically, the rotational cores spread and decay with time corresponding to the effects of entrainment by the external irrotational fluid, and we seek to incorporate this behaviour here. Moreover, coherent structure investigations (Hussain 1986) have shown that the vorticity distributions inside coherent structures are roughly bell-shaped, for which representation as a Lamb-Oseen vortex (Milne-Thompson 1968) is closer than a Rankine vortex. In pursuing this idealisation, we use an eddy diffusivity ν , to simulate turbulent diffusive spreading, as suggested by Squire (Govindaraju & Saffman 1971) for a description of turbulent trailing vortices. With this picture in mind, then, we adopt the vorticity and velocity distributions as:

$$v_{\theta}(r,t) = \frac{\Gamma_0}{2\pi r} (1 - e^{-r^2/4\nu t}) \quad (6)$$

$$\omega(r,t) = \frac{\Gamma_0}{4\pi\nu t} e^{-\frac{r^2}{4\nu t}} \quad (7)$$

where v_θ is the tangential velocity and Γ_0 is the circulation around the core. As a representative scale for the core radius we take the radius r_0 , corresponding to a maximum tangential velocity as given by the derivative of equation (6). The paths of two particles, released from the same point, one following a Lamb-Oseen vortex with a initial radius r_0 and one following a Rankine vortex with cut-off radius r_0 , are shown in figure 3a, with corresponding radius-time plots in figure 3b. Both particles follow an outwards spiral, but the L-O particle escapes more slowly than the R-particle. This is due to vorticity decay with time in the L-O vortex so that the velocity decreases, resulting in the radial outwards motion of the L-O particle being opposed by the pressure gradient.

3 TRANSPORT IN FREE SHEAR LAYERS

The discrete vortex method is used here as previously described (chapter 3), the main points of which are as follows. The planar mixing layer was chosen as one of the simplest and experimentally best documented examples of a turbulent shear flow. For statistical validation of this base flow, we tuned our simulation algorithm (details in chapter 3) for the best overall matching of time averaged velocity and shear stress profiles with the experimental data. The mean velocity and shear stress obtained agreed with the experimental data. The peak rms u was also in reasonable agreement, but peak rms v was overestimated by about 30%, a persistent discrepancy related to the algorithm or a consequence of excluding spanwise turbulence fluctuations. As noted in chapter 3, we do not regard this as a major

restraint on simulation of particle transport.

As direct extensions of the transport modelling with bubbles, we explore the effects of parameters Π and Γ as well as sensitivity of the trajectories to release conditions. Values of $\gamma=1920$ were adopted here, being key representative of practical situations with particle transport in gas (particle density about 2400 kg/m^3 and gas density about 1.25 kg/m^3). Of special concerns in conducting these simulations are the following points: (a) particle dispersion patterns; (b) Eulerian and Lagrangian measurements of particle dispersion; (c) Distribution of particle velocity field; (d) Effect of pairing on particle dispersion; and (e) Comparisons between using a stochastic model and using the discrete vortex model, and the effect of the instantaneous pressure gradient or the added mass force. Again, all trajectory realisations for various particle release conditions are confined to a vertical mixing layer since vertical orientation eliminates the cross-stream buoyancy influence, but still includes the mainstream buoyancy influence. In addition, for the simulation results presented in this section the initial particle velocity when it was introduced is set to be equal to the local fluid velocity. This assumption - that particles are in dynamic equilibrium with the flow - has been widely accepted (Crowe *et al.* 1993).

3.1 Particle Dispersion Patterns

(a) Effect of variations of Π/Γ on particle dispersion patterns

Different, uniform size particles ($d_p=0, 10, 20$ and $40 \mu\text{m}$), corresponding to $\Pi/\Gamma=0, 0.002, 0.032$ and 0.155 (corresponding Stokes numbers are $0, 0.1, 1.0, 10.0$), were released at a constant rate (every time step) into the simulated flow field from different cross-stream positions at the exit of the both sides of the mixing layer, assessing the effect of different

combinations of Π/Γ on the particle dispersion patterns by coherent eddy structures. Instantaneous particle distribution patterns corresponding to the above different combinations of Π/Γ , are shown in figure 4. It can be seen that the fluid tracer dispersion pattern mimics the experimental smoke visualisation pictures (e.g. Brown and Roshco 1974; Wen *et al.* 1992). The particles with size $10 \mu m$ ($\Pi/\Gamma=0.002$) disperse very similarly to those of fluid tracers, with little difference in dispersion pattern. However, particles with $\Pi/\Gamma=0.032$ are clearly seen to be centrifuged to the edges of the vortex structures, leaving the centre of the vortex structure devoid of particles. In this case, the particles acquire the largest spread. Further increase in Π/Γ leads to a decrease in the spread rate and dispersion. The particle dispersion patterns described in our simulations are broadly visually consistent with earlier experimental and numerical results (Crowe *et al.* 1993). It is interesting to note here that for the case of $\Pi/\Gamma=0.155$ some particles are overshooting from the saddle regions between two successive vortex structures. This behaviour should be attributed to the larger inertia of the particle, so that the particles are less influenced by the large scale structures.

(b) Particle dispersion patterns under different release conditions

Individual realisations are obviously highly dependent on the phase relationship between particle release and the passage of large eddies. To illustrate this point, we examine the transport patterns for two different particle release conditions; from the low speed and from the high speed side of the mixing layer. Figures 5a and 5b show the particle dispersion patterns for particles introduced from the low speed side and from the high speed side. It can be seen from figure 5a that a defined band of particles emerging from the region between two successive large eddies surrounds the lower perimeters of the vortex structures for particle release from the high speed side. In contrast, the particles released from the low

speed side form not only a thin band around the upper perimeters but an apparent band around the lower perimeters of the vortex structures. It is believed that this is strongly associated with the pressure experienced by the particle. On the high speed side, the effect of the force due to the pressure gradient on the particle is less than that due to the centrifugal force so that the particles are kept away the core until they achieve the force balance. On the low speed side, the force due to the pressure gradient pushes the particle toward the core first, but the effect of the force on the particle is balanced by the centrifugal force in the neighbourhood of the perimeter of the vortex structure, resulting in the particle accumulation around the lower perimeters. We also noticed that for both particle release conditions, particle distributions in the region between two successive large scale vortex structures are aligned in a sheet, where a high shear gradient exists. We conjecture that the flow field associated with the high shear gradient may play a crucial role in the formation of the particle streaks. Streaks of particles in the region with high shear gradient which form tongue-shaped structures have been observed in experiments and in earlier numerical simulations (e.g. Lázaro and Lasheras 1989; Wen *et al.* 1992; Martin and Meiburg 1994). The physical insight into this behaviour needs further exploration. We will further discuss this in the next section.

(c) Dispersion pattern difference between particles and bubbles

Unlike the particles, the motion of the bubbles is strongly influenced by the local acceleration of the fluid and the added mass force is always dominant. This force is acting towards the core of the vortex so that the bubbles are driven to move toward the core centre rather than to be centrifuged outward as the solid particles. Figures 6a and 6b show respectively the dispersion patterns of particles and bubbles in the mixing layer. The value

of Π/Γ for both cases is 0.05. It can be seen clearly from figure 6b that the bubble dispersion pattern exhibits a thoroughly different picture in comparison to the particle dispersion pattern (figure 6a). Bubbles were trapped to travel in clusters, which is similar to the experimental observations reported by Thomas (1982). As we have seen from this demonstration, particle dispersion and bubble dispersion present different dynamic behaviour because of their different mass ratio γ . It is this difference in the mass ratio that results in a radical change in the role played by the added mass force acting on the particle or the bubble. A common feature of the transport dynamics in either particle or bubble motion in shear flows, however, can be recognised that local concentration excursions are highly correlated with vorticity excursions as indicated by Thomas (1994). We will further highlight this crucial point in chapter 6.

3.2 Eulerian and Lagrangian Measurements of Particle Dispersion

For Eulerian measurements of particle dispersion, we can evaluate the particle dispersion from the particle number flux profiles at different downstream cross-sections of the mixing layer. The particle mean square displacement $y_p^2(x)$ can be obtained as

$$\overline{y_p^2(x)} = \frac{\sum_{i=1}^N N_i y_i \Delta y_i}{\sum_{i=1}^N N_i \Delta y_i} \quad (8)$$

where N_i is the number of particles that pass through i th bin. We divide the cross-stream distance at different downstream locations of the mixing layer into bins so that we can count the number of particles entering and leaving a particular bin. Δy_i is the height of a bin. The particle number fluxes for different particle sizes are shown in figure 7. The corresponding

mean square displacements of particles are displayed in figure 8. It is clearly seen from this quantitative measurement that the particles with $\Pi/\Gamma=0.002$ spread nearly the same as fluid tracers. The particles with $\Pi/\Gamma=0.032$ disperse more than fluid tracers, but the particles with $\Pi/\Gamma=0.155$ disperse less than fluid tracers. These quantitative results are consistent with the experimental observations and the numerical simulation results (Chein and Chung 1988). In figure 9, $y_p^2(x)/y_f^2(x)$, where $y_f(x)$ is defined for fluid tracers, is plotted for four different downstream locations. Again, a larger particle dispersion is found for the case of $\Pi/\Gamma=0.032$.

To evaluate particle dispersion in the mixing layer more physically, Lagrangian tracking of the particle transverse displacement are needed. As the particles are transported downstream by the large eddies, the flight times and the displacements for individual particles and fluid tracers can be recorded. We then define different time intervals and find the mean square displacements of the particles in the flow for that particular instant to evaluate the particle dispersion and dispersion coefficient in such flows (Snyder and Lumley 1971) according to the following formulation.

$$D_p(x,t) = \frac{1}{2} \frac{d}{dt} \overline{y_p^2(x,t)} \quad (9)$$

The particle dispersion profiles for different combinations Π/Γ , together with those for fluid tracers are shown in figure 10. Again, the prediction results are consistent with those obtained by Eulerian measurements, i.e. the particles with $\Pi/\Gamma=0.032$ achieve a larger dispersion than the other cases. The dispersion coefficients and corresponding Schmidt numbers for these cases are shown in figure 11 and 12. It can be seen from figure 12 that the Schmidt number for $\Pi/\Gamma=0.032$ attains a minimum value, again confirming our findings.

3.3 Distributions of Particle Velocity Field and Correlations

The time-averaged particle velocity field, and the particle velocity fluctuation structures and their correlations, are crucial for assessing the quality of two phase closure models (Simonin 1992). The time-averaged particle velocity, velocity fluctuations over the cross-section at different locations are shown in figures 13-17. The shape of the profiles is in general similar to that of the flow profiles. An important result is obtained for the time-averaged cross-stream velocity component as can be seen in figure 14. The cross-stream particle velocities tend to be positive on the high speed side of the flow and negative on the low speed side of the flow within the shear region, displaying the opposite trend to that of the fluid. This result indicates that the particles are prevalently pushed outward from the centre of the mixing layer which is consistent with the experimental results (Wen *et al.* 1992).

As know from turbulence theory, the joint probability density for u' and v' in two dimensional turbulence can be used to characterise some important flow features. In analogy to this, the joint probability densities for particle velocity fluctuations, u_p' and v_p' , and for fluid tracer velocity fluctuations, u' and v' , sampled at the centre of the mixing layer, are presented in figure 18.

3.4 Effect of Pairing on Particle Dispersion

We expected that the particle dispersion during the pairing events would be enhanced in line with Chein and Chung (1987) who concluded that particle dispersion increases during such events more than before and afterwards. A simulation was run to look at this aspect, displaying the relevant vorticity contours. $\Pi/\Gamma=0.032$ was chosen for exercise since for this case a large dispersion is acquired. The results are displayed in figure 19, where particle

dispersion patterns are shown at times related to the vortex pairing process. It can be seen clearly from the figure that the particle spread after pairing is obviously larger than that before the pairing for the same observation plane.

3.5 Particle Dispersion in The Vicinity of The Stagnation Point

As we have seen, the particle dispersion pattern around the region between two successive large eddies in the mixing layer is strongly influenced by the local flow field. A group of particles gathers in the region and then becomes stretched, evolving into a thin band (recall figure 5). In this region, the velocity field is very similar to that described by the well-known stagnation point flow (Milne-Thompson 1968) in a coordinate system whose axes are aligned with the direction of extensional and compressive strain. To illustrate this point, a trajectory computation was done based on the flow field associated with a series of Rankine vortices of equal separation representative of the mixing layer simulations, and more particularly the region just upstream of the first pairing. The velocity field is then given by

$$\left. \begin{aligned}
 u(x,y) &= \sum_{k=1}^N \frac{\Gamma_0}{2\lambda} \frac{\sinh\left(\frac{2\pi(y-y_k)}{\lambda}\right)}{\left[\cosh\left(\frac{2\pi(y-y_k)}{\lambda}\right) - \cos\left(\frac{2\pi(x-x_k)}{\lambda}\right)\right]} \\
 v(x,y) &= \sum_{k=1}^N \frac{\Gamma_0}{2\lambda} \frac{\sin\left(\frac{2\pi(x-x_k)}{\lambda}\right)}{\left[\cosh\left(\frac{2\pi(y-y_k)}{\lambda}\right) - \cos\left(\frac{2\pi(x-x_k)}{\lambda}\right)\right]}
 \end{aligned} \right\} \text{for } r = \sqrt{x^2 + y^2} > r_0 \quad (10)$$

and

$$\left. \begin{aligned}
u(x,y) &= \frac{\Gamma_0}{2\pi} \frac{y}{r_0^2} \sum_{k=1}^N \frac{\Gamma_0}{2\lambda} \frac{\sinh\left(\frac{2\pi(y-y_k)}{\lambda}\right)}{\left[\cosh\left(\frac{2\pi(y-y_k)}{\lambda}\right) - \cos\left(\frac{2\pi(x-x_k)}{\lambda}\right)\right]} \\
v(x,y) &= -\frac{\Gamma_0}{2\pi} \frac{x}{r_0^2} + \sum_{k=1}^N \frac{\Gamma_0}{2\lambda} \frac{\sin\left(\frac{2\pi(x-x_k)}{\lambda}\right)}{\left[\cosh\left(\frac{2\pi(y-y_k)}{\lambda}\right) - \cos\left(\frac{2\pi(x-x_k)}{\lambda}\right)\right]}
\end{aligned} \right\} \text{for } r = \sqrt{x^2 + y^2} \leq r_0 \quad (11)$$

where Γ_0 and (x_k, y_k) are the strength and position of the k th Rankine vortex, respectively. N is the total number of the Rankine vortices. For $\lambda=2r_0$ (here r_0 is the radius of the Rankine vortices), we plot particle dispersion patterns for $\Pi/\Gamma=0.01, 0.1$ and 1.0 in figure 20, here with $\Pi=r_0^2\omega^2/2gr_0$ and $\Gamma=r_0\omega/V_T$ for this demonstration. It is noted here that we display relative particle dispersion because a Lagrangian coordinate which is assumed to move with the convection velocity U_m , was chosen. The particles were uniformly released into the flow field at 10 transverse locations each with initial velocity equal to the local fluid velocity. For $\Pi/\Gamma=0.01$, the particle dispersion resembles that of the fluid as shown in figure 20(a). For $\Pi/\Gamma=0.1$ ($S_r=O(1.0)$), however, there is an enhanced focusing of particles towards the stagnation streamlines. The particle dispersion pattern is strongly coupled with the dividing streamline resulting in a build-up of particles corresponding to the streamlines, seen in figure 4 for the mixing layer, also as discussed by Eaton and Fessler (1994) for a converging stagnation flow characterised by high strain rate and low vorticity. They pointed out that a high concentration of particles in the central region of the flow would be expected.

Figure 20(c) shows the particle dispersion pattern for $\Pi/\Gamma=1.0$, when inertia carries particles across the stagnation streamline, but they then travel back in the counter flow. Accumulation here is, thus, even more focused than we saw in the mixing layer calculation with $\Pi/\Gamma=0.032$

(shown in figure 4), where a single band arises. Similar findings were reported very recently by Raju and Meiburg (1995).

3.6 The Effect of Using a Time-Averaged Modelling Method on Particle Dispersion

We have shown that the dominant forces on particle transport in free shear flows for the density ratio of the order of 10^3 are drag and buoyancy. When the density ratio is about unity, the added mass force becomes comparable with that of drag and buoyancy. To highlight its importance, we compare the present simulation with those trajectories computed using a time-averaged modelling method to show how time-averaging distorts the time effects of the pressure gradient and fluid inertia, and the consequences for estimates of particle dispersion. As conducted here, our time-averaged modelling represents as mixed Eulerian-Lagrangian calculation comparable to those employed in engineering methods where the time-averaged turbulence is delivered by a one-point closure model (e.g. k - ϵ ; Rodi 1980). Here we use the discrete vortex method to obtain the time-averaged and rms velocity field (turbulence kinetic energy). For particle tracking, the instantaneous local velocity is assigned to be the time-averaged velocity field plus a random Gaussian fluctuation with appropriate variance. Thus, the fluctuating velocities are

$$\left\{ \begin{array}{l} u' = \sqrt{\frac{2}{3}k} \xi_u \\ v' = \sqrt{\frac{2}{3}k} \xi_v \end{array} \right. \quad (12)$$

where k is the turbulent kinetic energy and ξ_u, ξ_v are Gaussian jitters. Sample trajectories computed using these two methods (note that the same force law is adopted) are compared in figure 21, showing 10 realisations out of 1000 computed, with the total set utilised to calculate the flux profiles shown in figure 22. Derived measures of the dispersion and

dispersion coefficients, together with the ratio between the dispersion coefficient of fluid tracers and the dispersion coefficient of the particles, appear in figures 23 to 25. Apparently, there is a significant effect due to the instantaneous pressure gradient associated with large eddy structure since the difference between the two calculation methods is quite striking. In particular, the trajectories estimated from the time-averaged + jittered flows exhibit greater dispersion, consistent with expectations when the transient attraction focusing of eddy pressure field is omitted. In other words, although this effect is perhaps not significant for density ratio $\rho_p/\rho_f \gg 1$, for $\rho_p/\rho_f \sim 1$ and especially for $\rho_p/\rho_f \ll 1$ (bubbles), the disperse phase responds selectively to force law terms that are effectively switched off when the velocity field is merely time-averaged + isotropic jitter (no structure). Thus it seems fair to say that Eulerian-Lagrangian engineering calculation methods using $k-\varepsilon$ turbulence models, plus Gaussian jitter must necessarily fail to collect the role of transverse pressure gradient, indeed mean as well as fluctuation values if the calculation is formulated as parabolic under the thin shear layer approximations. A modified calculation has been performed (Zhou and Leschziner 1991), which sought to introduce space-time correlation (memory) of successive particle-eddy encounters, but this adjustment does not compensate for the extended correlations intervals implied by the instantaneous couplings described by the time-dependent simulations.

4 BROADER DISCUSSION

As we have seen, dispersion of particles in mixing layers is often dominated by the presence of the large-scale eddy structures in such flows. From the evidence presented here it seems that the ratio Π/Γ represents the key parameter for characterising the motion of the particles,

akin to the Stokes number used by Crowe *et al.* (1985). For $0.02 < \Pi/\Gamma < 0.05$, particle dispersion exceeds fluid dispersion, as was also found experimentally and numerically by other researchers (e.g. Crowe *et al.* 1993). More specifically, particles get entrained into the large-scale structure and are then subsequently centrifuged, tending to accumulate around the edges of the eddies and especially in the local stagnation point regions between consecutive eddies. Whilst it seems Π , Γ and γ suffice as scaling set to characterize dispersive phase transport from bubbles to particles, we emphasise that bubble dispersion is distinctly different from particle dispersion. However, both are highly correlated with vorticity excursions (figure 6) and the latter are outlined in time-averaged calculation schemes. However, different drag laws do not significantly affect the results. Importantly, particle dispersion is enhanced during vortex pairing events as also found by Chein and Chung (1988).

The time-averaged particle concentration profiles exhibit bimodal development which would not readily be accommodated by a classical diffusion model, even with prescribed diffusivity calculated to account for the effects of Π/Γ as noted above. Indeed, even eschewing diffusion modelling in favour of stochastic Monte Carlo calculation may not suffice if the scheme does not simulate the effects of transiently coherent eddy structure.

It is necessary to note here that the dispersion coefficient has little significance in modelling the dispersion of particles in organised turbulent structures. An adoption of the dispersion coefficient implies that the particle dispersion is caused by a concentration gradient. However, many studies (e.g. Thomas *et al.* 1983; Sene *et al.* 1994; Crowe *et al.* 1993) together with the present study have revealed that particle dispersion in organised turbulent

structure is mainly controlled by the eddy structure so that the use of the diffusion model with introduction of a dispersion coefficient for closure to describe these types of flows is not appropriate and provides no insight into the governing mechanisms. Moreover, the transient behaviours of particle and bubble dispersion in such large eddy structure are not exposed correctly using this numerical description.

CONCLUSIONS

We have employed discrete vortex modelling to simulate large eddy turbulent free shear flows and investigated the effects on Lagrangian particle trajectories of eddy structure patterns. We also present detailed results for the dispersion of small, spherical non-interacting particles in two-dimensional large scale turbulent free shear flows. Several important conclusions are drawn as follows.

First, our results confirm earlier experimental observations and numerical simulations (e.g. Wen *et al.* 1992; Crowe *et al.* 1993) that heavy particles entrained into large scale organised structures are centrifuged from the vortex cores and tend to concentrate around their peripheries. We further demonstrate that two key independent scaling groups, the ratio of inertia to buoyancy forces; $\Pi = \Delta U^2 / g\delta$ and a retention parameter; $\Gamma = \Delta U / V_T$, together with the density ratio parameter γ , play a comparably important role in determining the dispersion for particles as they do for bubbles in free shear flows. In particular, we show that their ratio, Π/Γ , is equivalent to the Stokes number. We also found the predictions are not sensitive to details of the drag laws adopted.

Secondly, the comparison of tracking particle trajectories between the use of a time-averaged model and the use of the discrete vortex model highlights the importance of the local instantaneous pressure gradient and the added mass force experienced by the particles with comparable density to the carrier fluid, clearly demonstrating shortcomings in earlier models of stochastic dispersion (e.g. Gosman and Ioannides 1981) where the continuous phase flow is treated as a mean field on which is superposed random perturbation for modelling the discrete phase transport.

REFERENCES

- Auton, T. R. 1983 The dynamics of bubbles, drops and particles in motion in liquids. PhD thesis, University of Cambridge.
- Auton, T. R. 1987 The lift force on a spherical body in a rotational flow. *J. Fluid Mech.* **183**, 199.
- Brown, G. L. and Roshko, A. 1974 Density effects and large-scale structure in turbulent mixing layer. *J. Fluid Mech.* **64**, 775-816.
- Chein, R. and Chung, J. N. 1987 Effects of vortex pairing on particle dispersion in turbulent shear flows. *J. Multiphase Flow* **13**, 785-802.
- Chein, R. and Chung, J. N. 1988 Simulation of particle dispersion in a two-dimensional mixing layer. *J. AIChE.* **34**, 946-954.
- Chung, J. N. and Troutt, T. R. 1988 Simulation of particle dispersion in an axisymmetric jet. *J. Fluid Mech.* **186**, 199-222.
- Clift, R., Grace, J. R. & Weber, M. E. 1978 *Bubbles, Drops and Particles*. Academic.
- Crowe, C. T., Gore, R. & Troutt, T. R. 1985 Particle dispersion by coherent structures in free shear flows. *Particulate Science and Tech.* **3**, 149-158.
- Crowe, C. T., Chung, J. N. & Troutt, T. R. 1993 Particle dispersion by organized turbulent structures. *Particulate Two-Phase Flow* (ed. M. C. Roco), Butterworth-Heinemann, Stoneham, MA.
- Eaton, J. K. & Fessler, J. R. 1994 Preferential concentration of particles by turbulence. *Int.*

- J. Multiphase Flow* **20**, 169.
- Faeth, G. M. 1987 Mixing, transport and combustion in sprays. *Prog. Energy Comb. Sci.* **13** 293-346.
- Ganán-Calvo, A. M. & Lasheras, J. C. 1991 The dynamics and mixing of small spherical particles in a plane, free shear layer. *Phys. Fluids A* **3**, 1207.
- Ghoniem, & Ng, 1987
- Gosman, A. D. & Ioannides, E. 1981 Aspects of computer simulation of liquid-fuelled combustors. *AIAA paper* 81-0323.
- Govindaraju, S. P. & Saffman, P. G. 1971 Flow in a turbulent Trailing Vortex. *The Physics of Fluids* **14**(10), 2074-2080.
- Hinze, J. O. 1975 *Turbulence*, McGraw-Hill, N.Y.
- Hunt, J. C. R., Auton, T. R., Sene, K., Thomas, N. H. and Kowe, R. 1988 Bubble motions in large eddies and turbulent flows. *Transient Phenomena in Multiphase Flow*, (Edit by N. H. Afgan), Hemisphere.
- Hunt, J. C. R., Perkins, R. J., Lunde, K. & Thomas, N. H. 1993 Modelling bubbly flows. *Bubble Dynamics and Interface Phenomena*, 257-268. (ed. J. R. Blake & Thomas, N. H.), Kluwer Academic Publishers.
- Hussain, A. K. M. F. 1986 Coherent structures and turbulence. *J. Fluid Mech.* **173**, 303-356.
- Kallio, G. A. & Reeks, M. W. 1989 A numerical simulation of particle deposition in turbulent boundary layers. *Int. J. Multiphase Flow* **15**, 433-446.
- Kamalu, N., Wen, F., Troutt, T. R. & Crowe, C. T. 1988 Particle dispersion by ordered motion in turbulent mixing layers. *ASME Cavitation and Multiphase Flow Forum*, *FED* **64**, 150-154.
- Lázaro, B. J. & Lasheras, J. C. 1989 Particle dispersion in a turbulent, plane, free shear layer. *Phys. Fluids A* **1**, 1035.
- Legg, B. J. 1983 Movement of plane pathogens in the crop canopy. *Phil. Trans. R. Soc. Lond. B* **302**, 559-574.
- Martin, J. E. and Meiburg, E. 1994 The accumulation and dispersion of heavy particles in forced two-dimensional mixing layers. I. The fundamental and subharmonic cases. *Phys. Fluids* **6**(3), 1116-1132.
- Maxey, M. R. & Riley, J. J. 1983 Equation of motion for a small-rigid sphere in a nonuniform flow. *Phys. Fluids* **26**, 883-889.

- Maxey, M. R., Chang, E. J. & Wang, L-P. 1994 Simulation of interactions between microbubbles and turbulent flows. *Appl. Mech. Rev.* **47**(6), s70-s74.
- Mei, R., Lawrence, C. J. & Adrian, R. J. 1991 Unsteady drag on a sphere at finite Reynolds number with small fluctuations in the free-stream velocity. *J. Fluid Mech.* **233**, 613-631.
- Milne-Thompson, L. M. 1968 *Theoretical Hydrodynamics*, MacMillan, London.
- Onslow, R. J. & Thomas, N. H. 1993 Vorticity and sandwaves: the dynamics of ripples and dunes. *Turbulence Perspectives on Flow and Transport* (ed. N. J. Clifford). Wiley.
- Perkins, R. J. & Hunt, J. C. R. 1986 Particle transport in turbulent shear flows. *Final Report to the SERC*.
- Raju, N. and Meiburg, E. 1995 The accumulation and dispersion of heavy particles in forced two-dimensional mixing layers. Part 2: The effect of gravity. *Phys. Fluids* **6**(3), 1241-1264.
- Reeks, M. W. 1977 On the dispersion of small particle suspended in an isotropic turbulent fluid. *J. Fluid Mech.* **83**, 529-546.
- Rivero, M., Maganudet, J. & Fabre, J. 1991 Quelques résultats nouveaux concernant les forces exercées sur une inclusion sphérique par unécoulement accéléré. *C.R. Acad. Sci. Paris*, t. **312**, Série II, 1499-1506.
- Rodi, W. 1980 *Turbulence Models and Their Application in Hydraulics*. IAHR state-of-the-art paper presented by the section on Fundamentals of Division II: Experimental and Mathematical Fluid Dynamics.
- Ruetsch, G. R. & Meiburg, E. 1993 On the motion of small spherical bubbles in two-dimensional vortical flows. *Phys. Fluids A* **5**(10), 2326-2341.
- Schlichting, H. 1968 *Boundary Layer theory*. Pergamon Press: London.
- Sene, K. 1985 Aspects of bubbly two phase flow, Ph.D. Thesis, University of Cambridge.
- Sene, K., Hunt, J. C. R. and Thomas, N. H. 1994 The role of coherent structures in bubble transport by turbulent shear flows. *J. Fluid Mech.* **259**, 219-240.
- Shuen, J. S., Chen, L. D. & Faeth, G. M. 1983 Evaluation of a stochastic model of particle dispersion in a turbulent round jet. *AIChE J.* **29**(1), 167.
- Shuen, J. S., Solomon, A. S. P., Zhang, Q. F. & Faeth, G. E. 1985 Structure of particle-laden jets: Measurements and predictions. *AIAA J.* **23**, 396.
- Simonin 1992

- Snyder, W. H. & Lumley, J. L. 1971 Some measurements of particle velocity autocorrelation functions in a turbulent flow. *J. Fluid Mech.* **48**, 41-71.
- Sridhar, G. & Katz, J. 1994 Drag and lift forces on microscopic bubbles entrained by a vortex. *Phys. Fluids* **7**(2),389-399.
- Stewart, C. W. & Crowe, C. T. 1993 Bubble dispersion in free shear flows. *Int. J. Multiphase Flow* **19**, 501-507.
- Thomas, N. H. 1982 Air demand distortion in hydraulic models. *Proc. Intl Conf. on Hydraulic Modelling of Civil Engineering Structures, Coventry, UK*. BHRA.
- Thomas, N. H., Auton, T.R., Sene, K. and Hunt, J.C.R. 1983 Entrapment and transport of bubbles by transient large eddies in multiphase turbulent shear flow. *Int. Conf. on the Physical Modelling of Multiphase Flow*, Coventry, England, Paper E1.
- Thomas, N. H. 1994 Plunging flow aeration: some fundamental and functional factors. FED-Vol. 184.
- Tio, K. -K., Ganán-Calvo, A. M. & Lasheras, J. C. 1993 The dynamics of small, heavy, rigid spherical particles in a periodic Stuart vortex flow. *Phys. Fluids A* **5**(7), 1679-1693.
- Wells, M. R. & Stock, D. E. 1983 The effects of crossing trajectories on the dispersion of particles in turbulent flow. *J. Fluid Mech.* **136**, 31-62.
- Wen, F., Kamalu, N., Chung, J. N., Crowe, C. T. & Troutt, T. R. 1992 Particle dispersion by vortex structure in plane mixing layers. *Trans. ASME. J. Fluids Engineering* **114**, 657-666.
- Wynanski, I. & Weisbrot, I. 1988 On the pairing process in an excited plane turbulent mixing layer. *J. Fluid Mech.* **195**, 161.
- Yang, X & Thomas, N. H. 1994 Simulation of particle and bubble dispersion in turbulent free shear flows. *Numerical Methods in Multiphase Flows*, FED-Vol. 185, 259-268.
- Zhou, Q. & Leschziner, M. A. 1991 A time-correlated stochastic model for particle dispersion in anisotropic turbulence. 8th Turbulent Shear Flows Symposium, Munich.
- Zhuang, Y., Wilson, J. D. & Lozowski, E. P. 1989 A trajectory-simulation model for heavy particle motion in turbulent flow. *J. Fluids Engng.* **111**, 492-494.

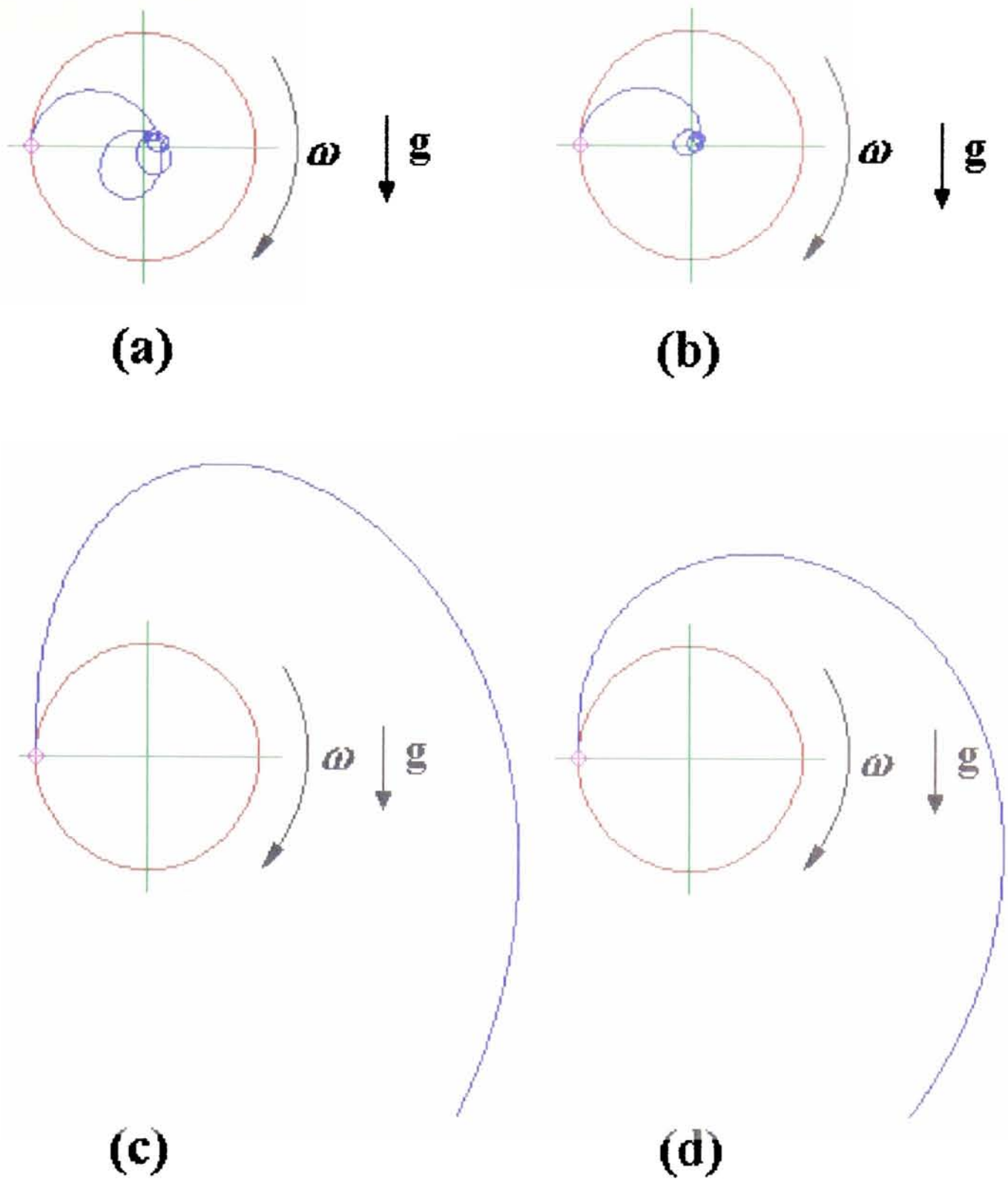


Figure 1. The effect of choice of drag law on particle and bubble trajectories within a Rankine vortex. For both cases particle was released from the same location at $(-r_0, 0)$. Here r_0 is a core radius for the Rankine vortex. r_0 is equal to 0.005 m and the angular velocity of the vortex is 200.0 s^{-1} . The density of the bubble and the density of the fluid for cases (a) and (b) are respectively 0.0 kg/m^3 and 1000.0 kg/m^3 . The density of particle and the density of the fluid for cases (c) and (d) are respectively 2400.0 kg/m^3 and 1.25 kg/m^3 . (a) and (c): Linear drag law (i.e. $f=1$); (b) and (d): Non-linear drag law (i.e. $f=(|\mathbf{v}-\mathbf{u}|/V_T)$).

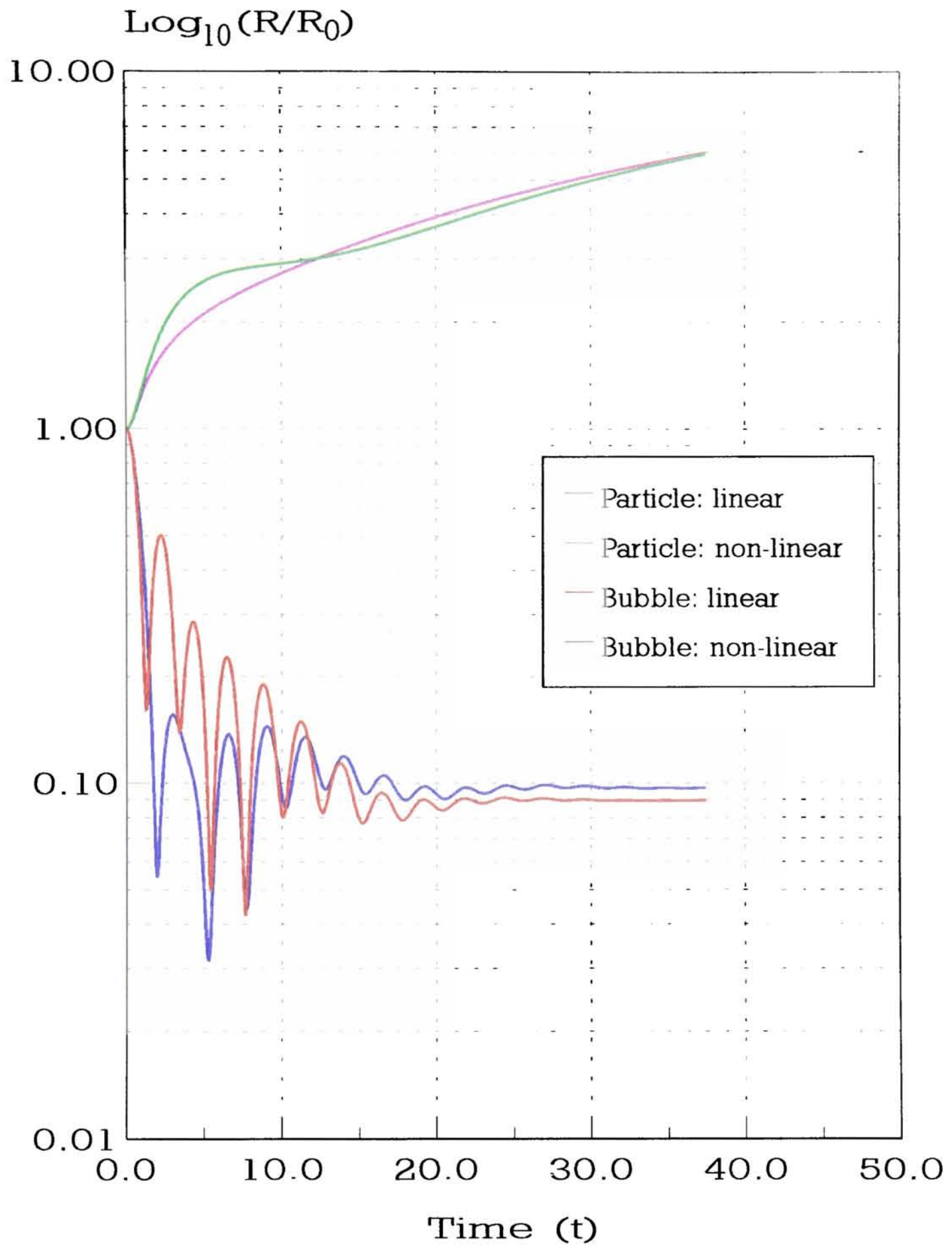


Figure 2. Particle and bubble radius time histories, using linear drag law and non-linear drag law. The long term growth rate of particle and the long term decay rate of bubble are little affected by using different drag modifications.

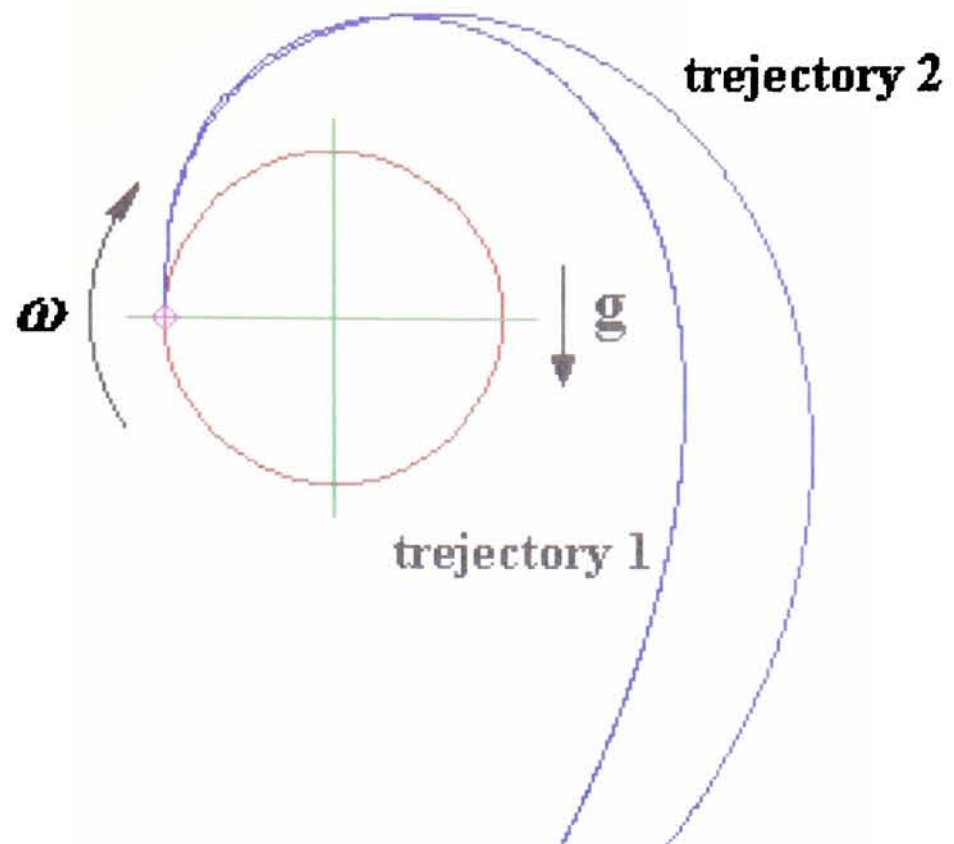


Figure 3a. Particle trajectories within a turbulent Lamb-Oseen vortex and a Rankine vortex. For both cases particle was released from the same location at $(-r_0, 0)$. Here r_0 is an initial radius specified for the Lamb-Oseen vortex and a core radius for the Rankine vortex. r_0 is equal to 0.005 m and the initial angular velocity of the vortex is 200.0 s^{-1} . The density of particle and the density of fluid are respectively 2400.0 kg/m^3 and 1.25 kg/m^3 . Trajectory 1 corresponds to the particle released in the Lamb-Oseen vortex. Trajectory 2 corresponds to the particle released in the Rankine vortex.

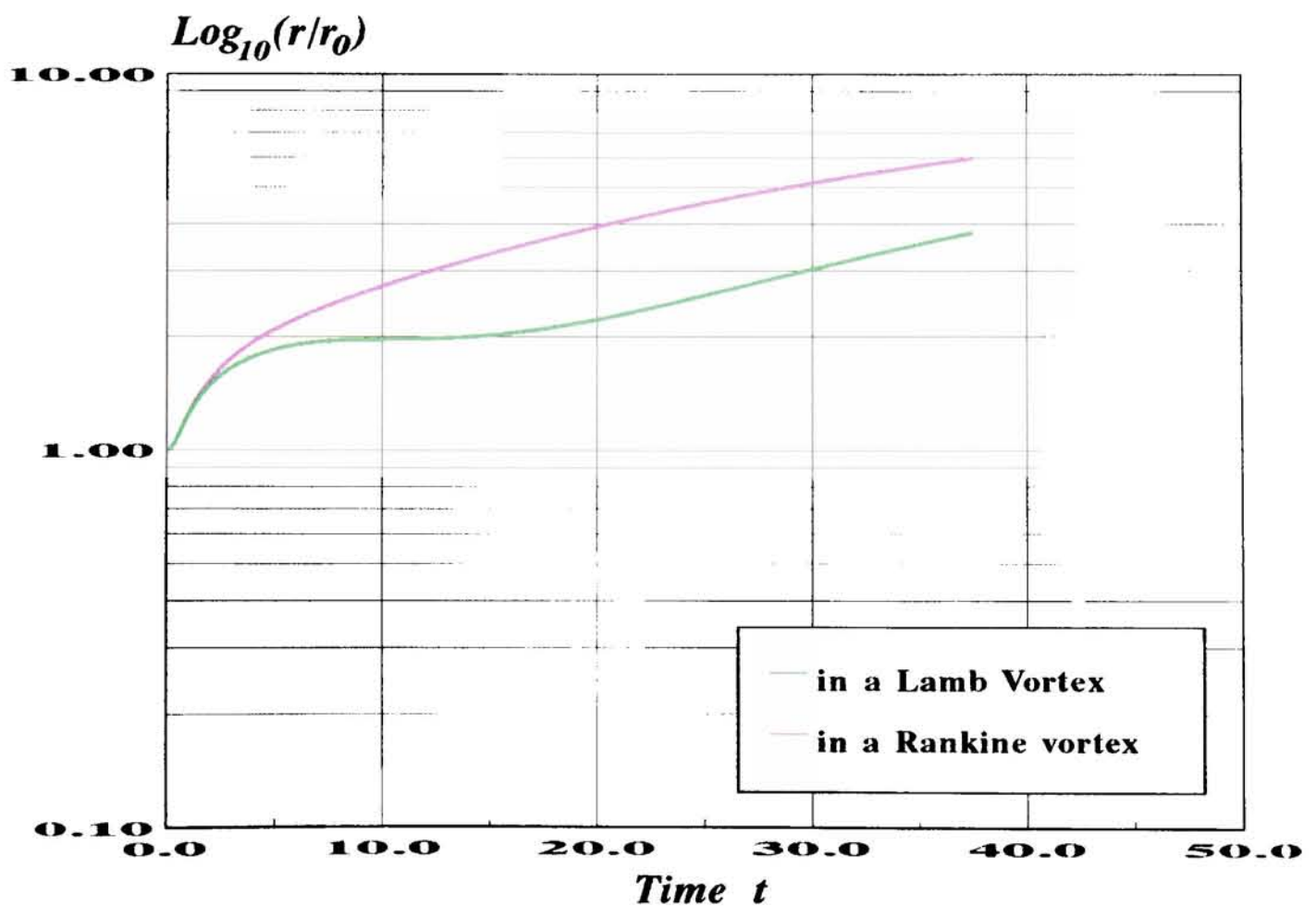


Figure 3b. Particle radius time histories with a Lamb-Oseen vortex and a Rankine vortex. The initial radius is set to equal to 0.005 m and the initial angular velocity is 200 s^{-1} . Particles were released at $(-r_0, 0)$.

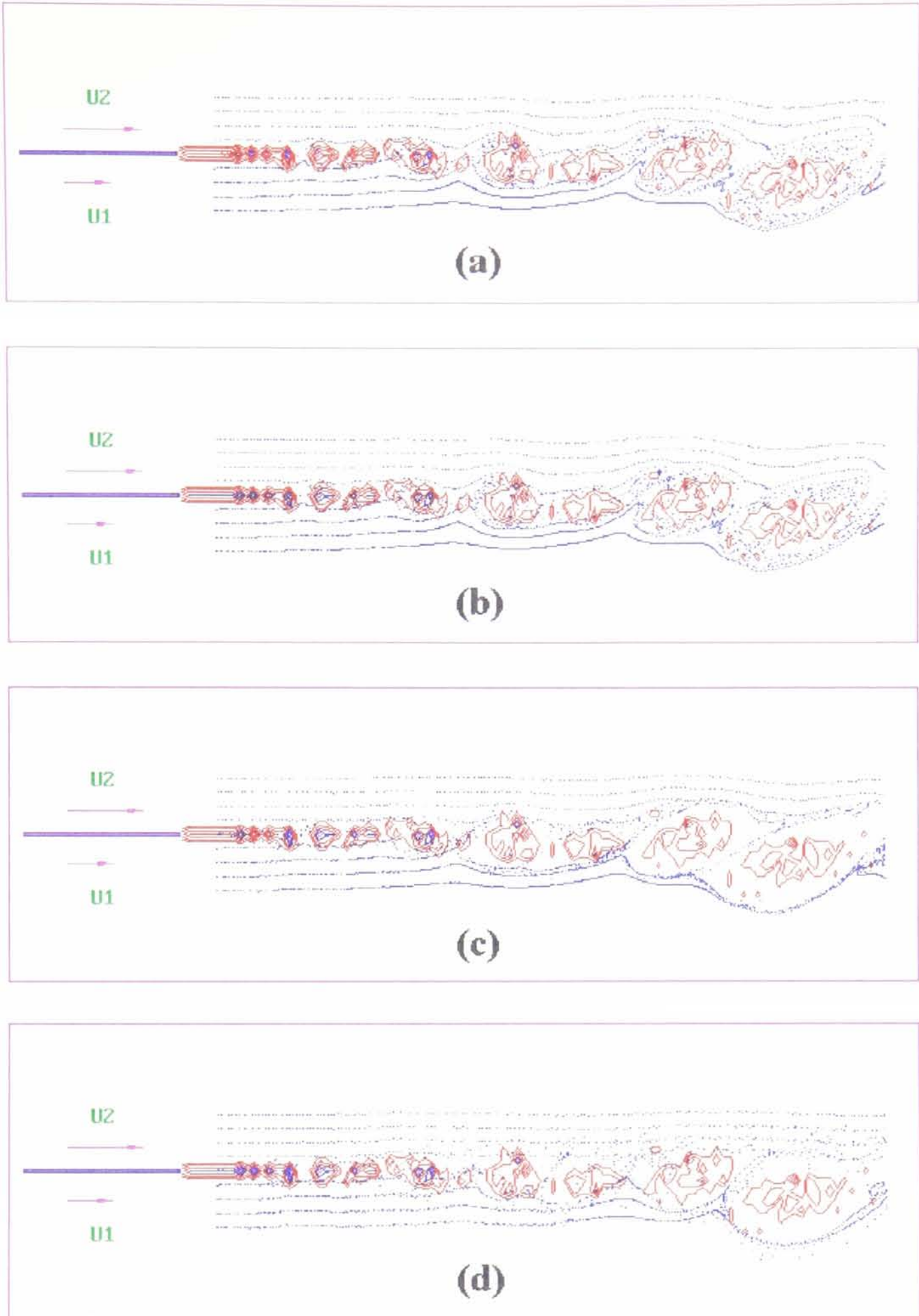


Figure 4. Instantaneous particle dispersion patterns for fluid tracers and particles with different Π/Γ . (a) $\Pi/\Gamma=0.0$, $\gamma=1.0$; (b) $\Pi/\Gamma=0.002$, $\gamma=1920.0$; (c) $\Pi/\Gamma=0.032$, $\gamma=1920.0$; (d) $\Pi/\Gamma=0.155$, $\gamma=1920.0$. The corresponding Stokes numbers for (a), (b), (c) and (d) are 0, $O(0.1)$, $O(1.0)$, $O(10.0)$. The vorticity contours are displayed by red colour and blue dots represent fluid tracers or particles.

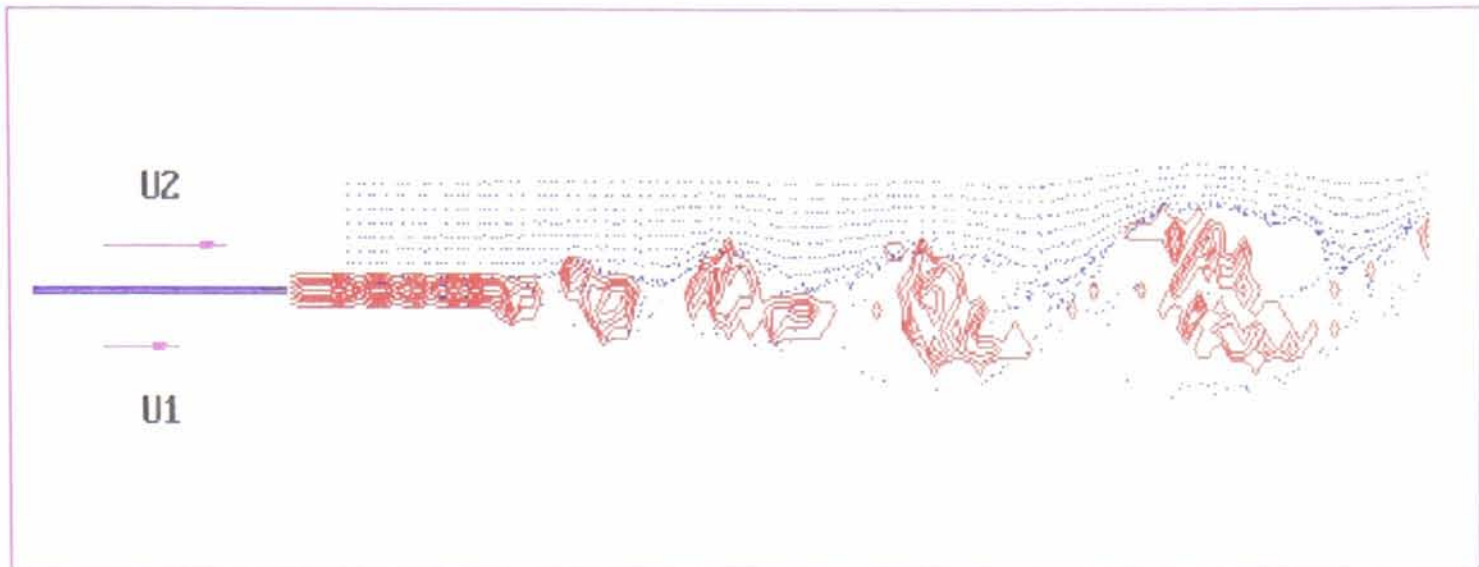


Figure 5a. Instantaneous vorticity contours and particle streaklines with $\Pi/\Gamma=0.032$ for particles released from the high speed side of the mixing layer. A thin band of particles emerges from the region between two successive large eddies and surrounds the lower perimeters. (Note: gravity acts from left to right here.)

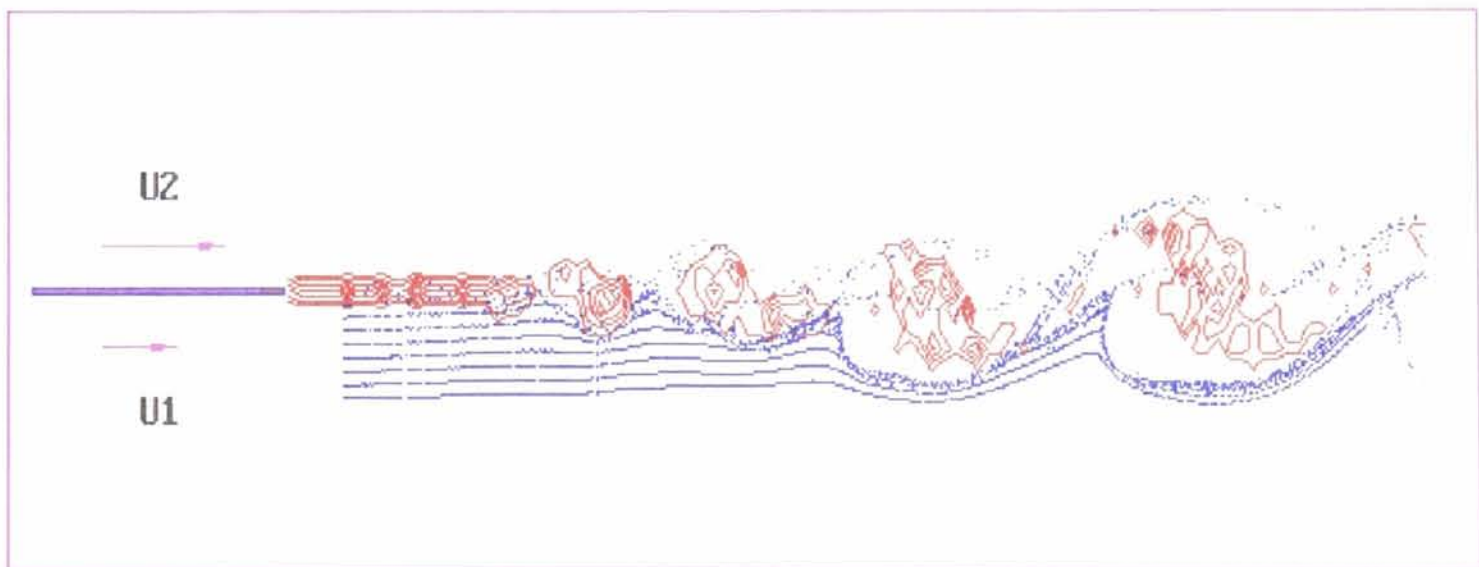


Figure 5b. Instantaneous vorticity contours and particle streaklines with $\Pi/\Gamma=0.032$ for particles released from the low speed side of the mixing layer. A thin band of particles emerges from the saddle point of two successive large eddies, surrounding the higher peripheries and a roll-over wave like band surrounds the lower perimeters. (Note: gravity acts from left to right here.)

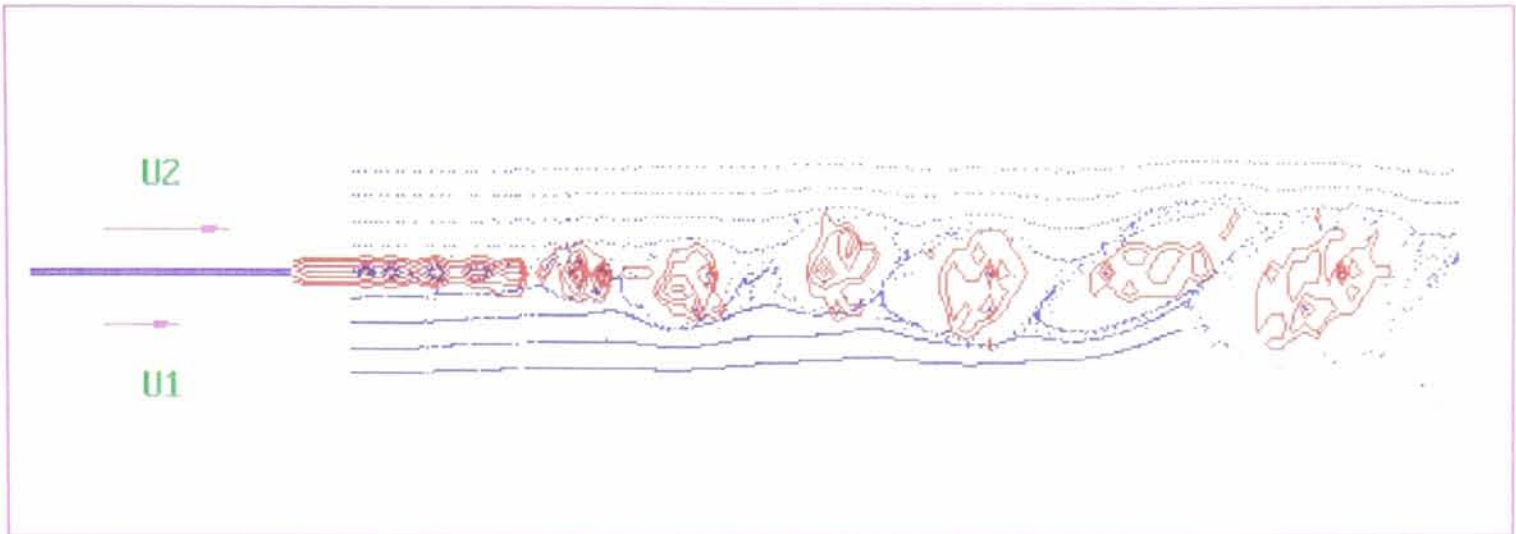


Figure 6a. Instantaneous vorticity contours and particle streaklines with $\Pi/\Gamma=0.05$ and $\gamma=1920.0$ at time $t=1.5625$. Particles are centrifuged from the large-scale vortex cores and surround the peripheries of the vortices, indicating an enhanced dispersion. (Note: gravity acts from left to right here.)

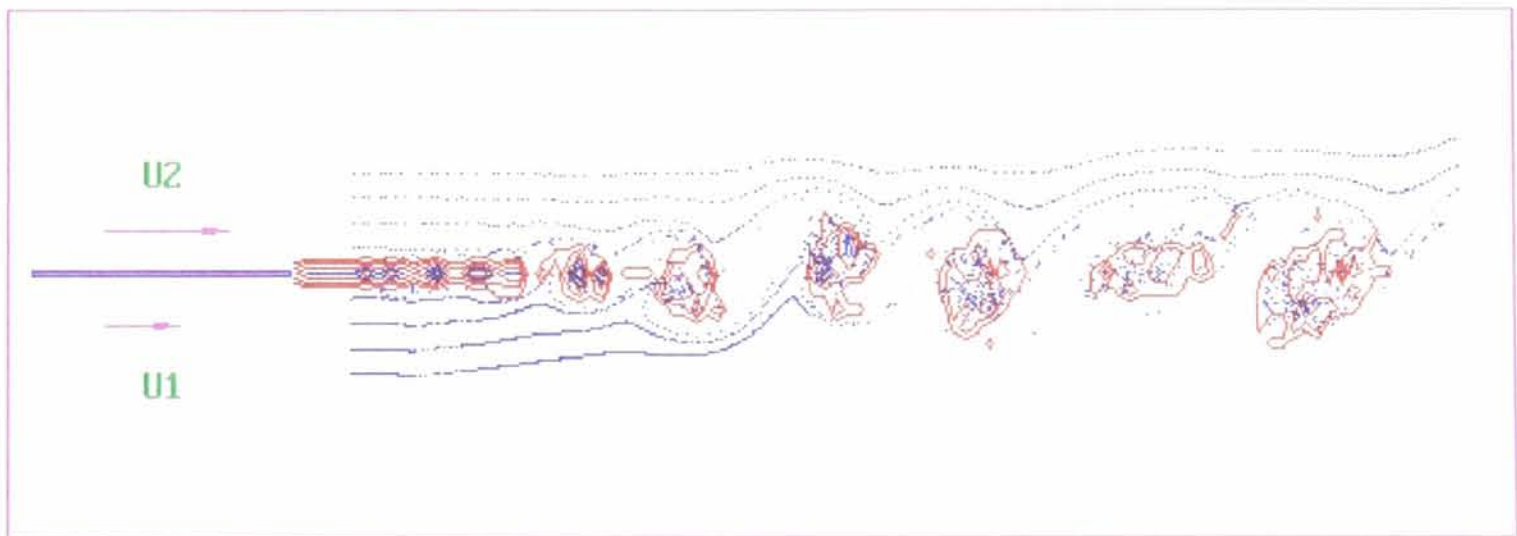


Figure 6b. Instantaneous vorticity contours and bubble streaklines with $\Pi/\Gamma=0.05$ and $\gamma=0.0$ at time $t=1.5625$. Bubbles are trapped by the large-scale vortex cores and obviously group in clusters, which is similar to the experimental observations (Thomas 1982). (Note: gravity acts from left to right here.)

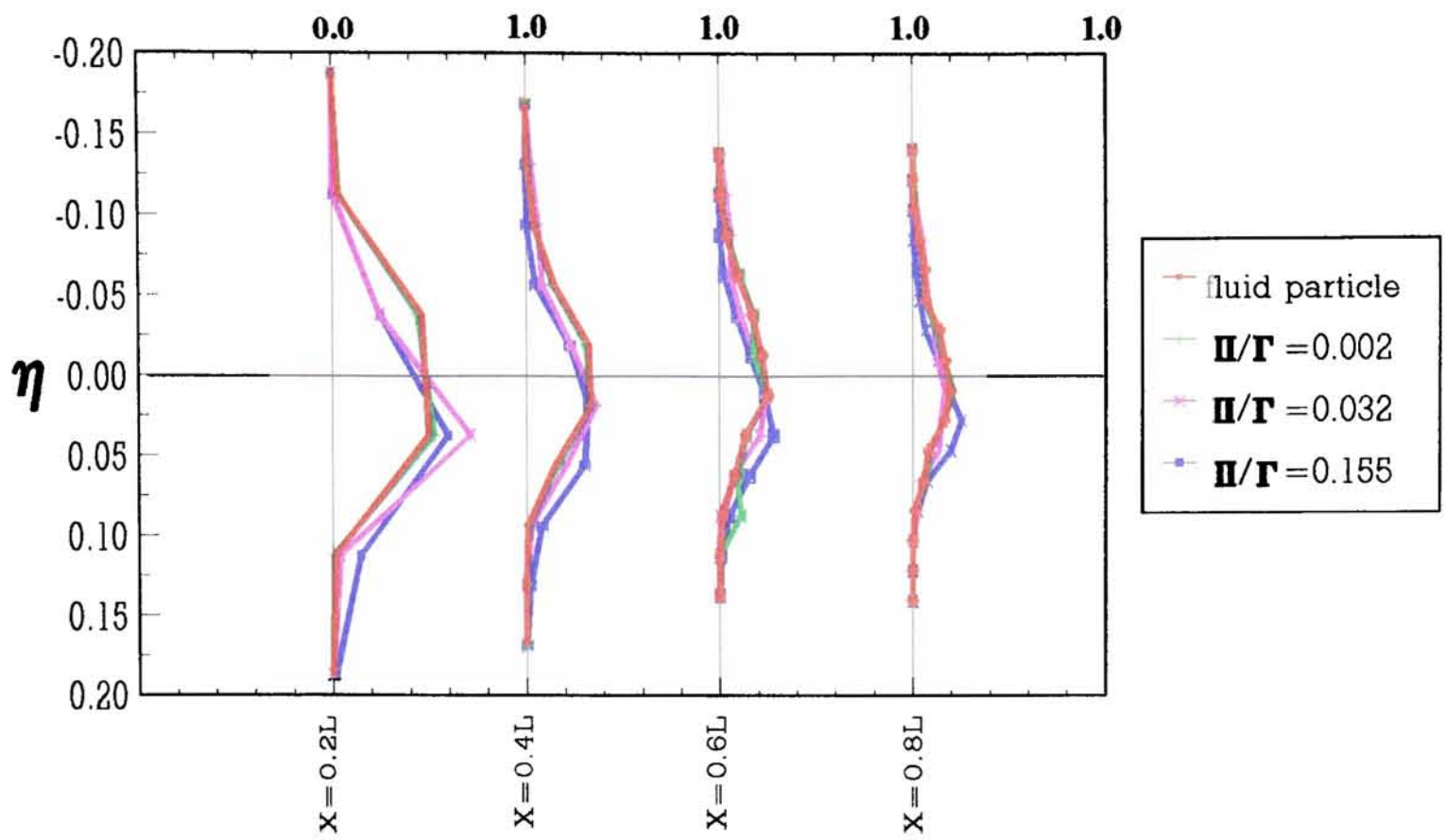


Figure 7. Particle number flux distribution at various downstream locations of the mixing layer from numerical simulations with different values of Π/Γ .

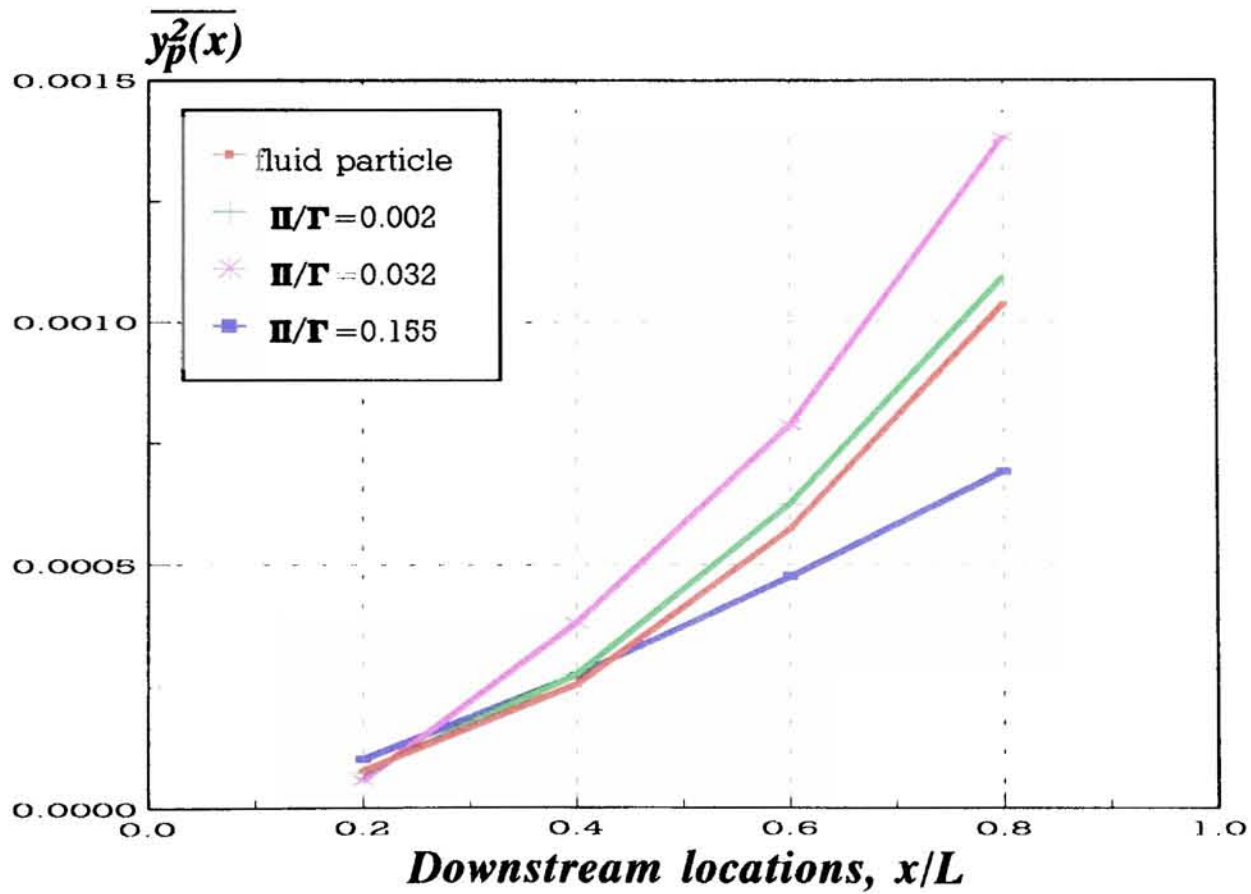


Figure 8. Variations of particle mean square displacement, calculated from the particle number flux profiles shown in figure 7.

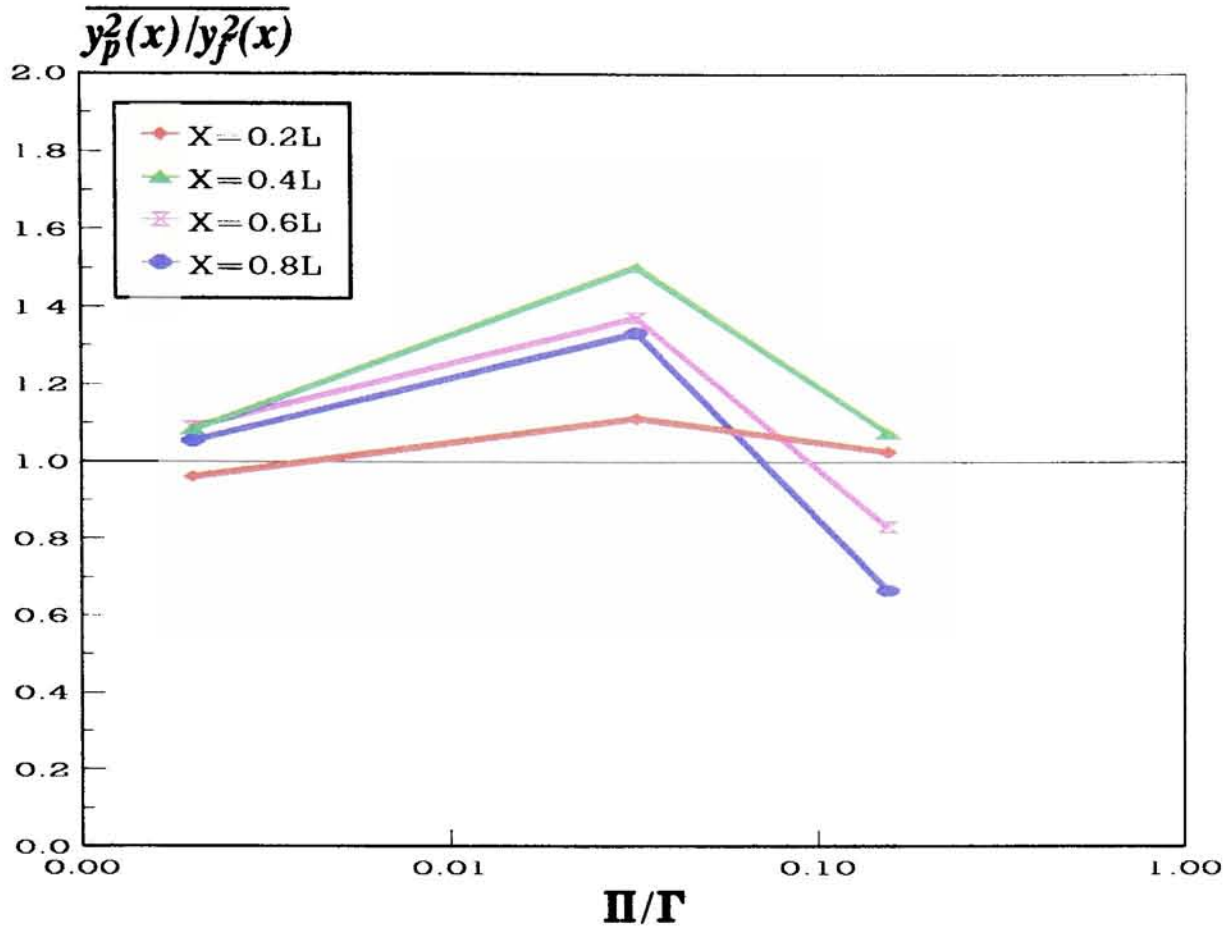


Figure 9. The ratio of dispersion as a function of Π/Γ (or the corresponding Stokes number S) for different downstream distances, calculated from the results as shown in figure 8.

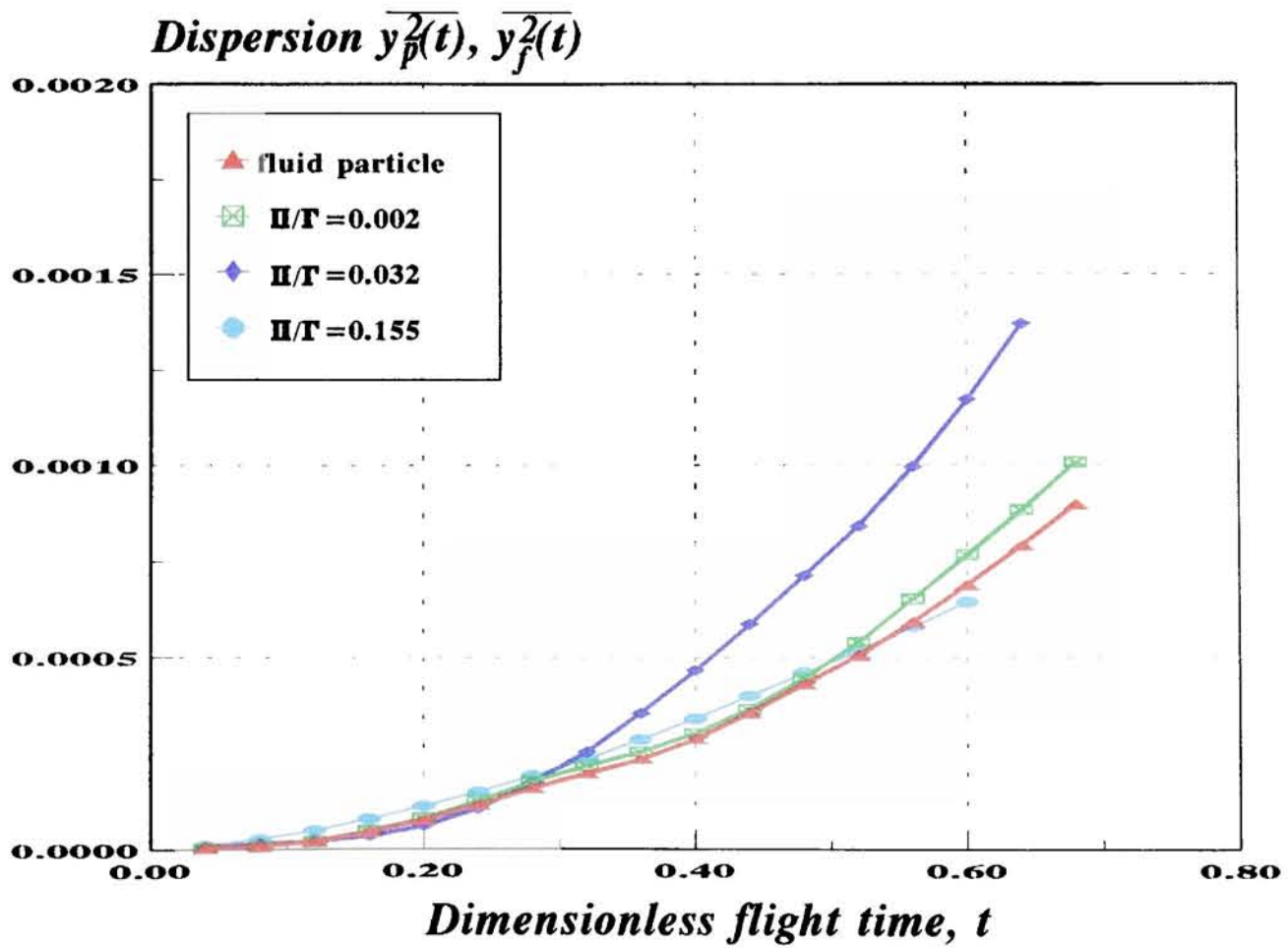


Figure 10. Lagrangian measurements of particle dispersion in a vertical, downflowing mixing layer.

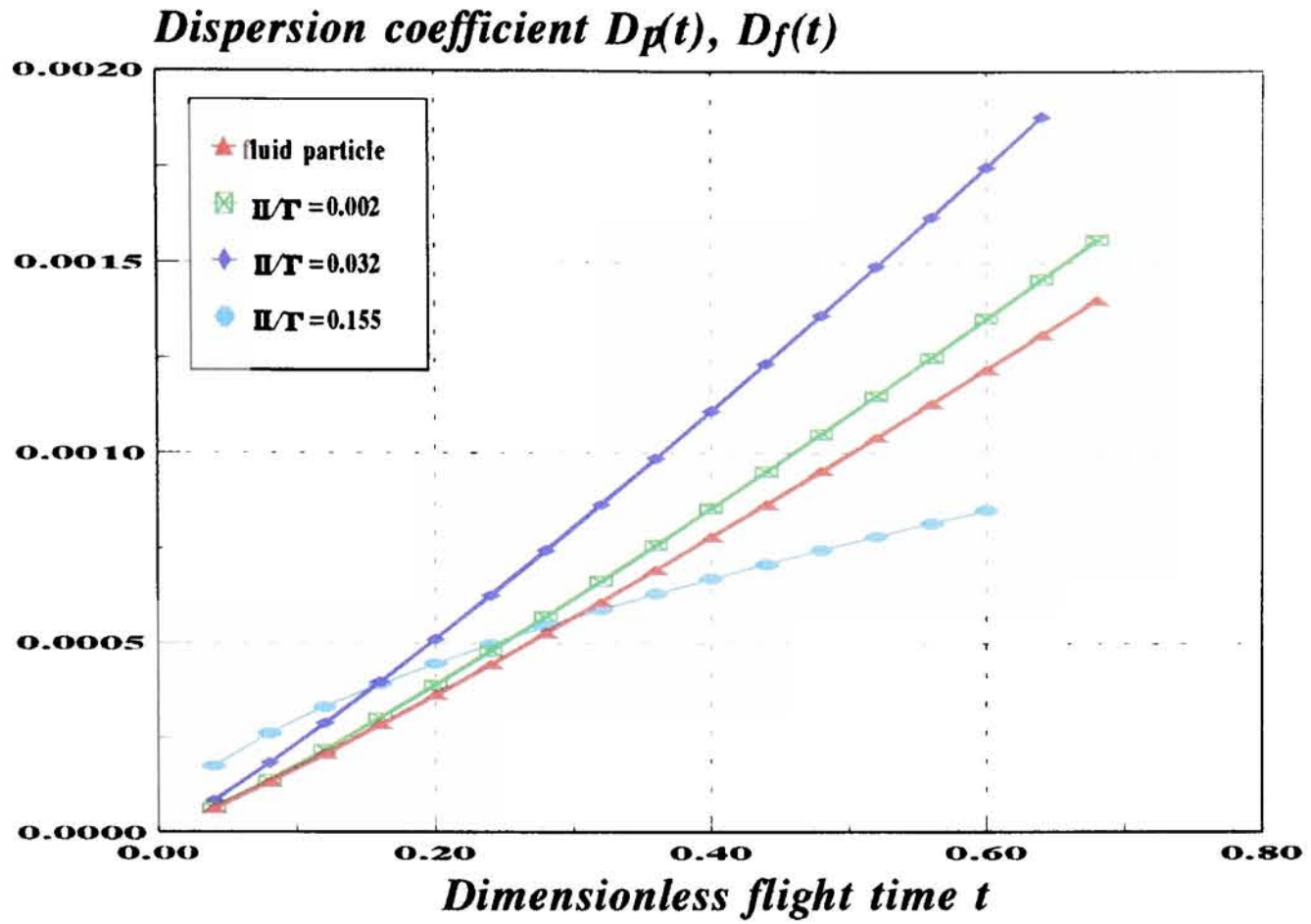


Figure 11. Particle dispersion coefficients versus time in a vertical, downflowing mixing layer, calculated from the data shown in figure 10.

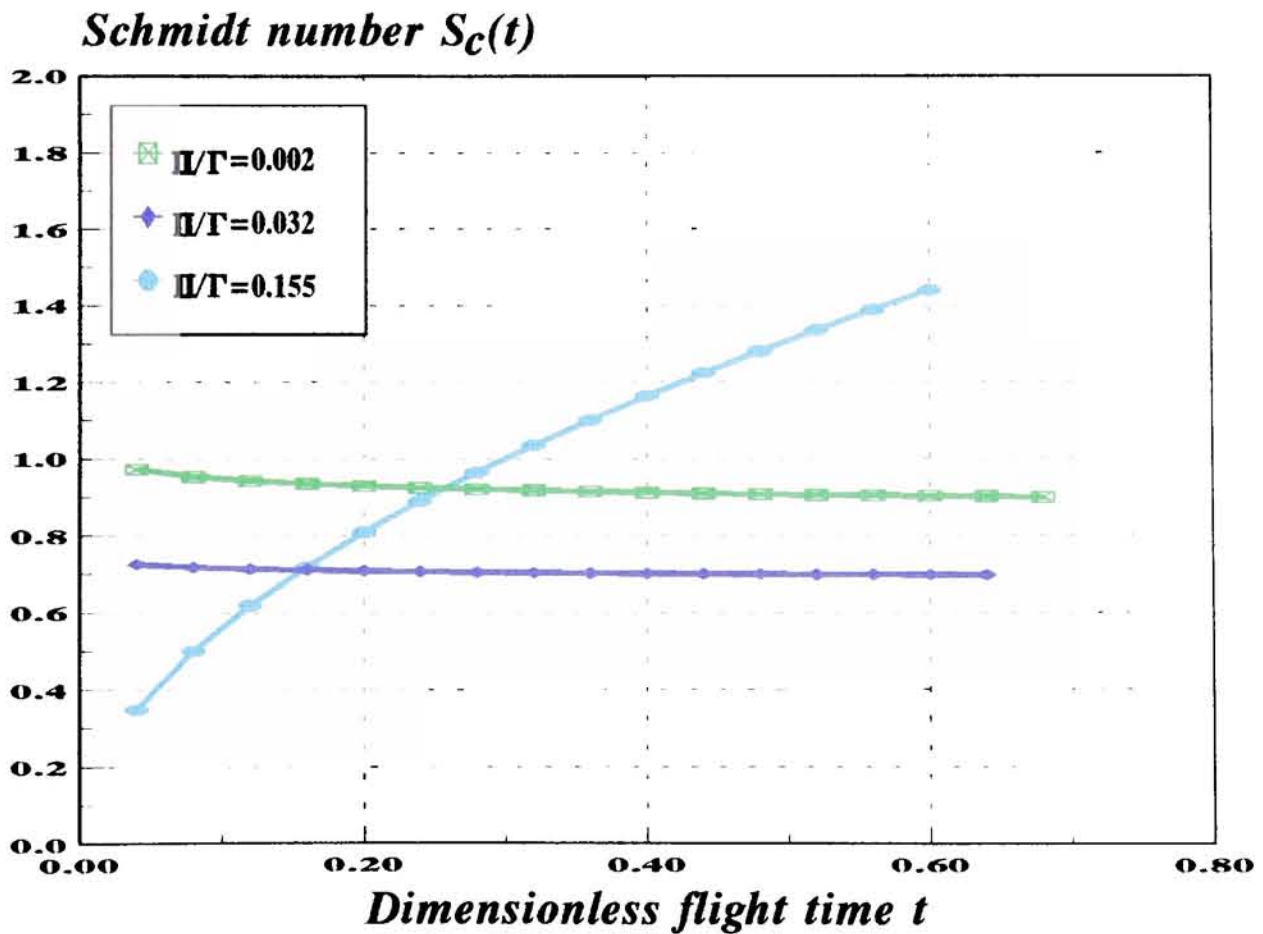


Figure 12. Eddy turbulent Schmidt number of particles versus time in a vertical, downflowing mixing layer, calculated from the data shown in figure 11.

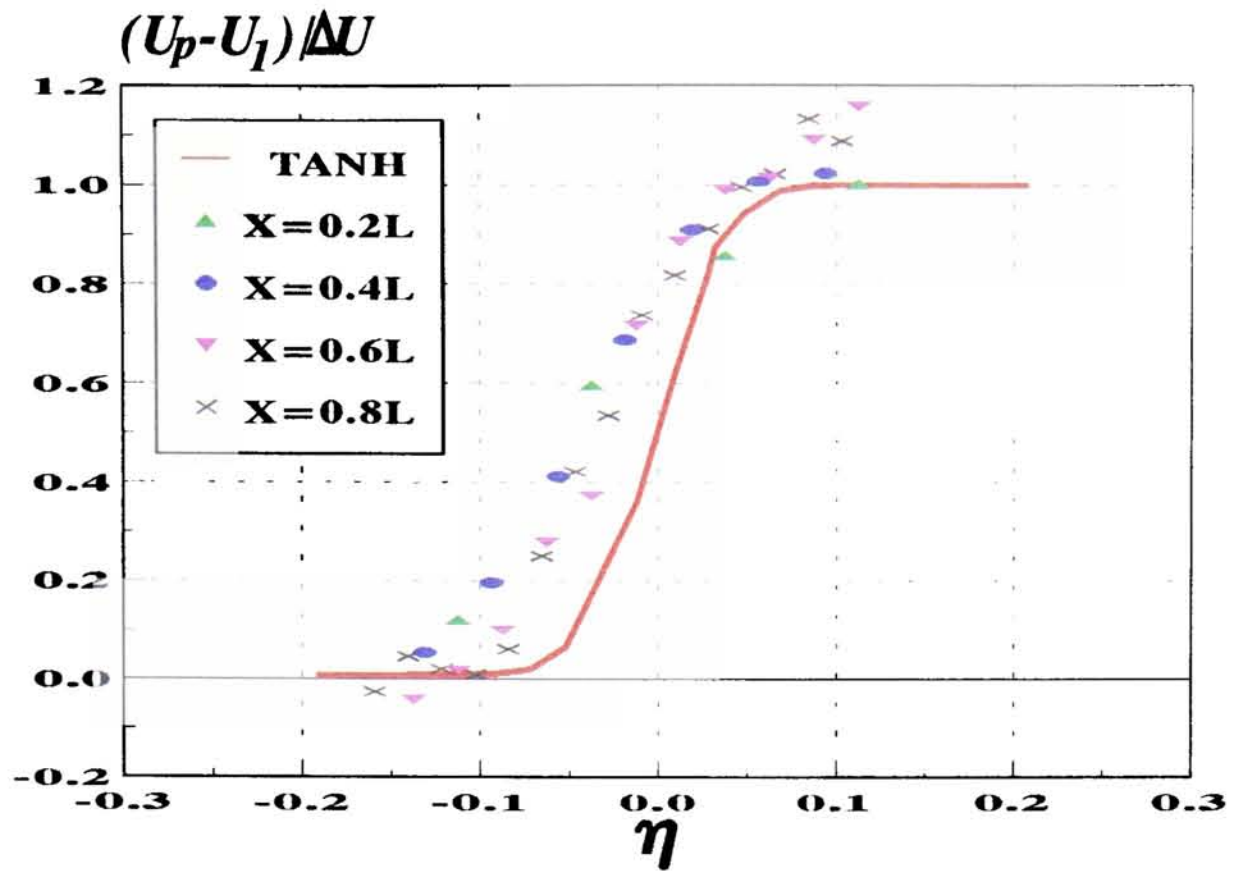


Figure 13. Time-averaged downstream mean velocity profiles of particles at various downstream locations of a vertical, downflowing mixing layer from numerical simulations. ($\Pi/\Gamma=0.032$, $\gamma=1920.0$).

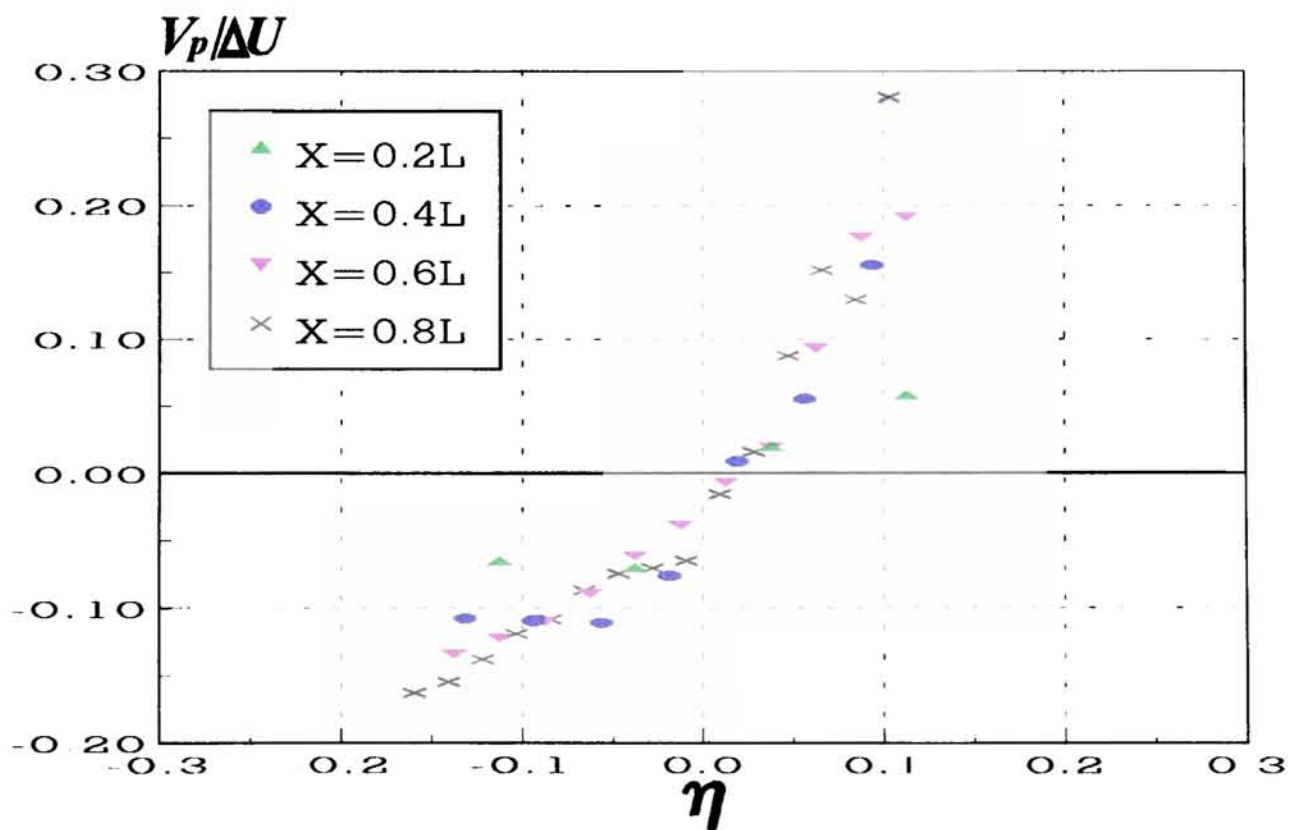


Figure 14. Time-averaged cross-stream velocities of particles at various downstream locations of a vertical, downflowing mixing layer from numerical simulations. ($\Pi/\Gamma=0.032$, $\gamma=1920.0$).

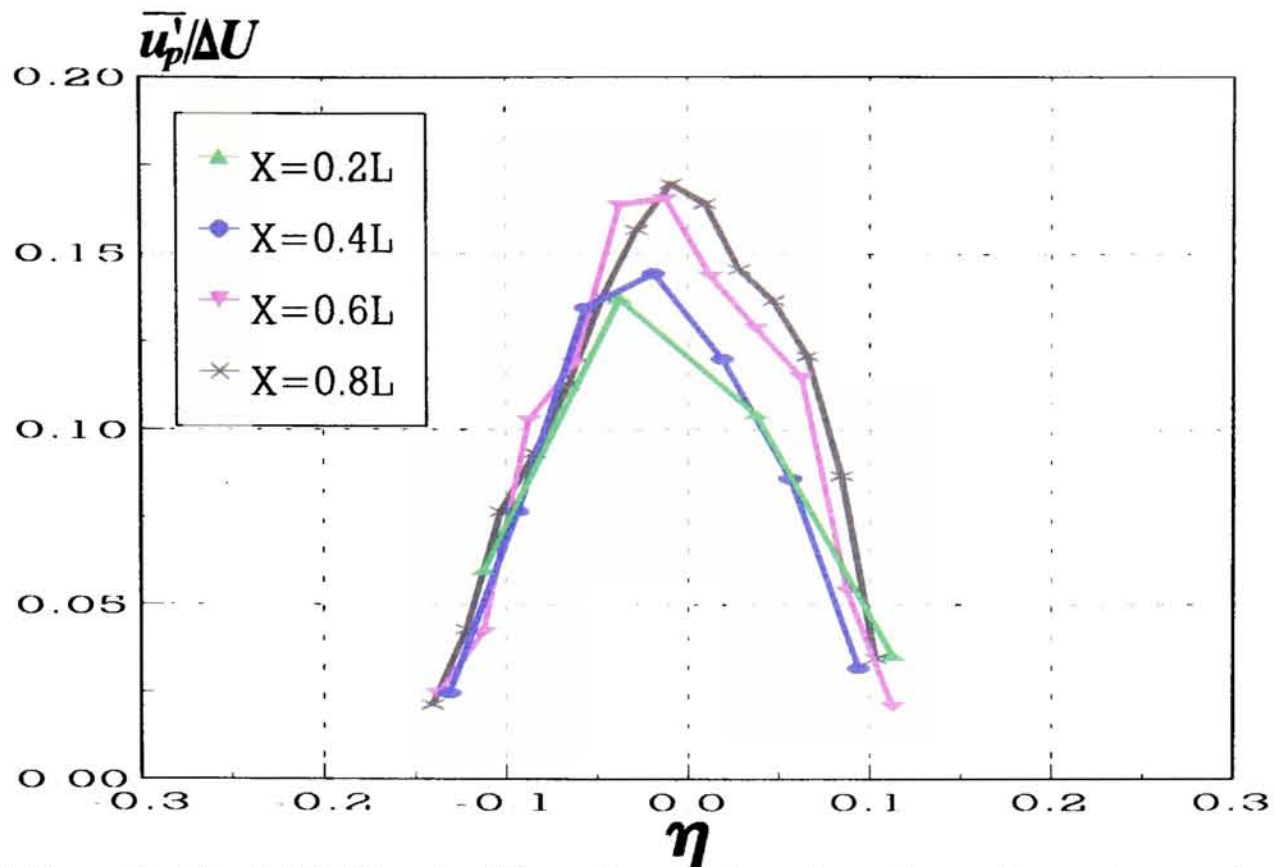


Figure 15. Longitudinal RMS velocities of particles at various downstream locations of a vertical, downflowing mixing layer from numerical simulations. η is defined as $\eta=y/x$. ($\Pi/\Gamma=0.032$, $\gamma=1920.0$).

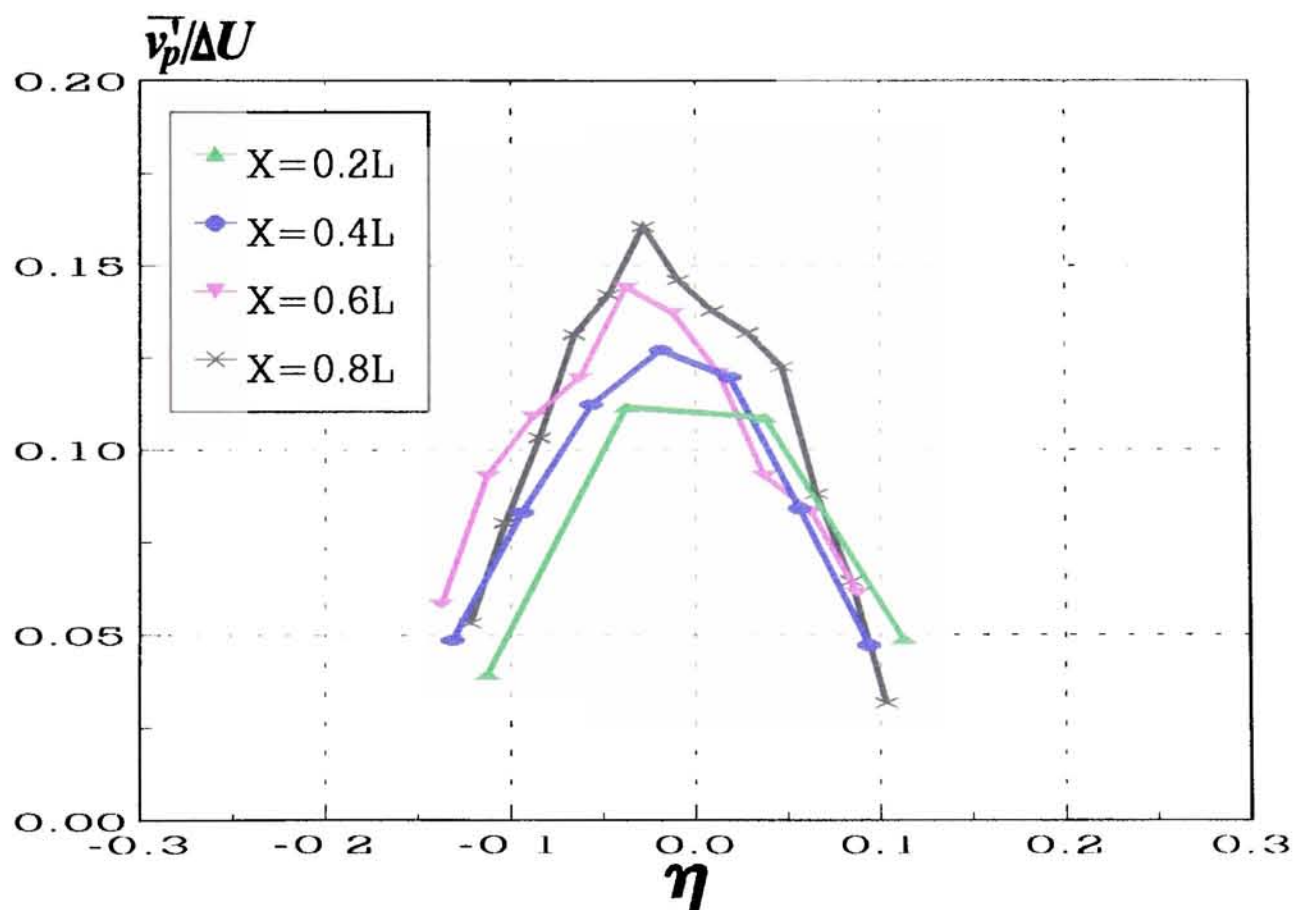


Figure 16. Cross-stream RMS velocities of particles at various downstream locations of a vertical, downflowing mixing layer from numerical simulations. η is defined as $\eta=y/x$. ($\Pi/\Gamma=0.032$, $\gamma=1920.0$).

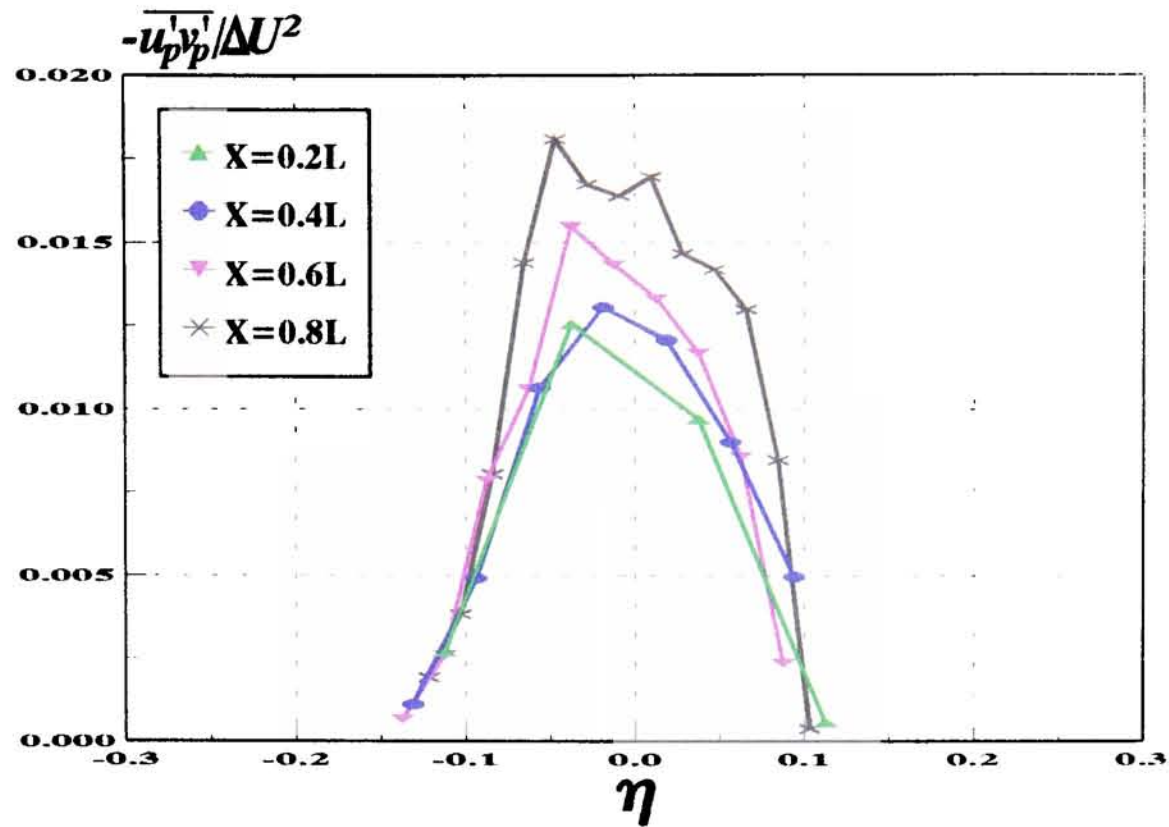


Figure 17. Shear stress of particles, $\overline{u'_p v'_p}$, at various downstream locations of a vertical, downflowing mixing layer from numerical simulations. ($\Pi/\Gamma=0.032$, $\gamma=1920.0$).

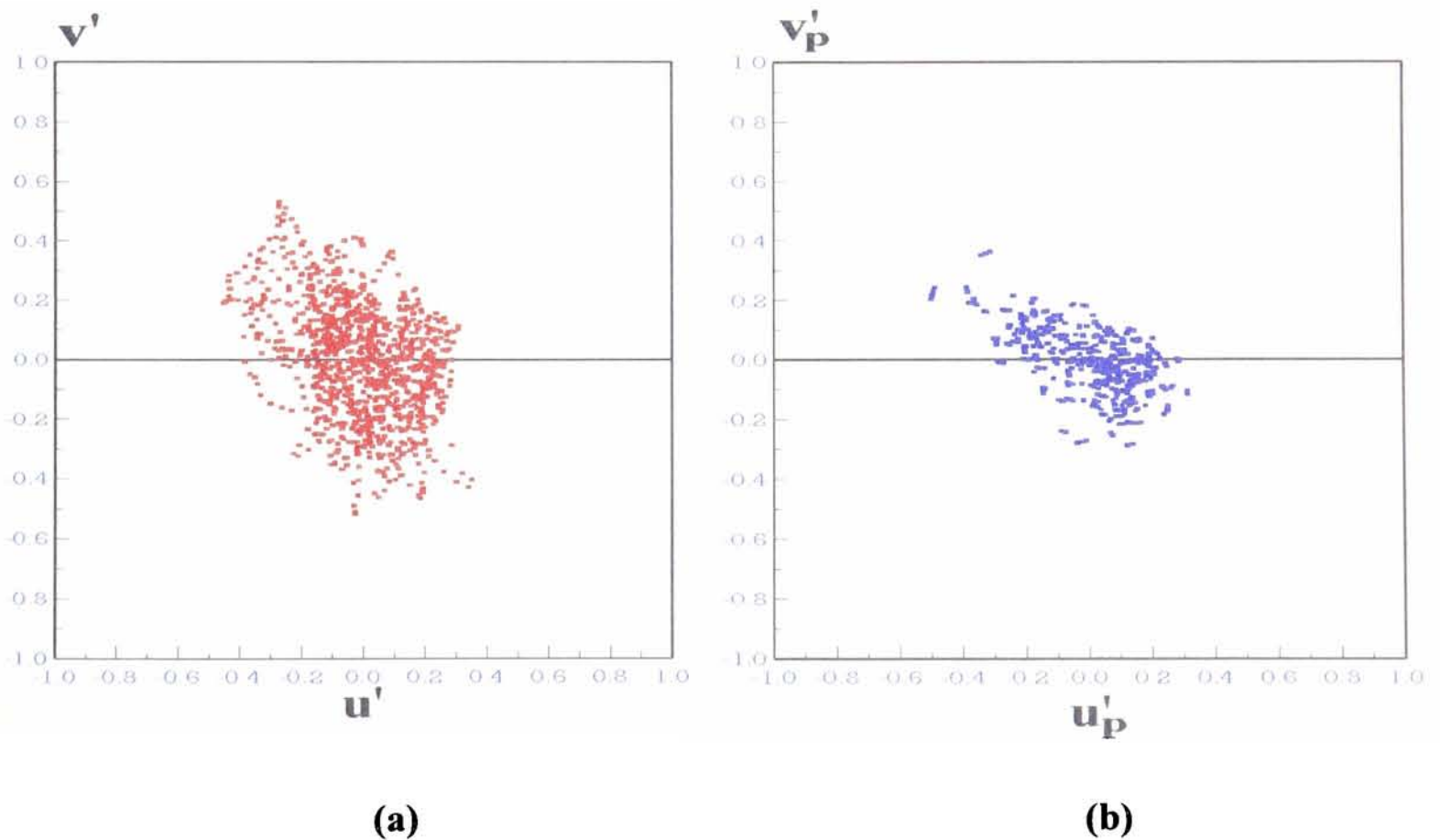


Figure 18. Joint probabilities of u and v fluctuations for fluid tracers and particles, sampled from the centre of the mixing layer. Total 1000 particles and 1000 fluid tracers were released from the location close to the origin of the mixing layer. (a) fluid tracers; (b) particles with $\Pi/\Gamma=0.032$.

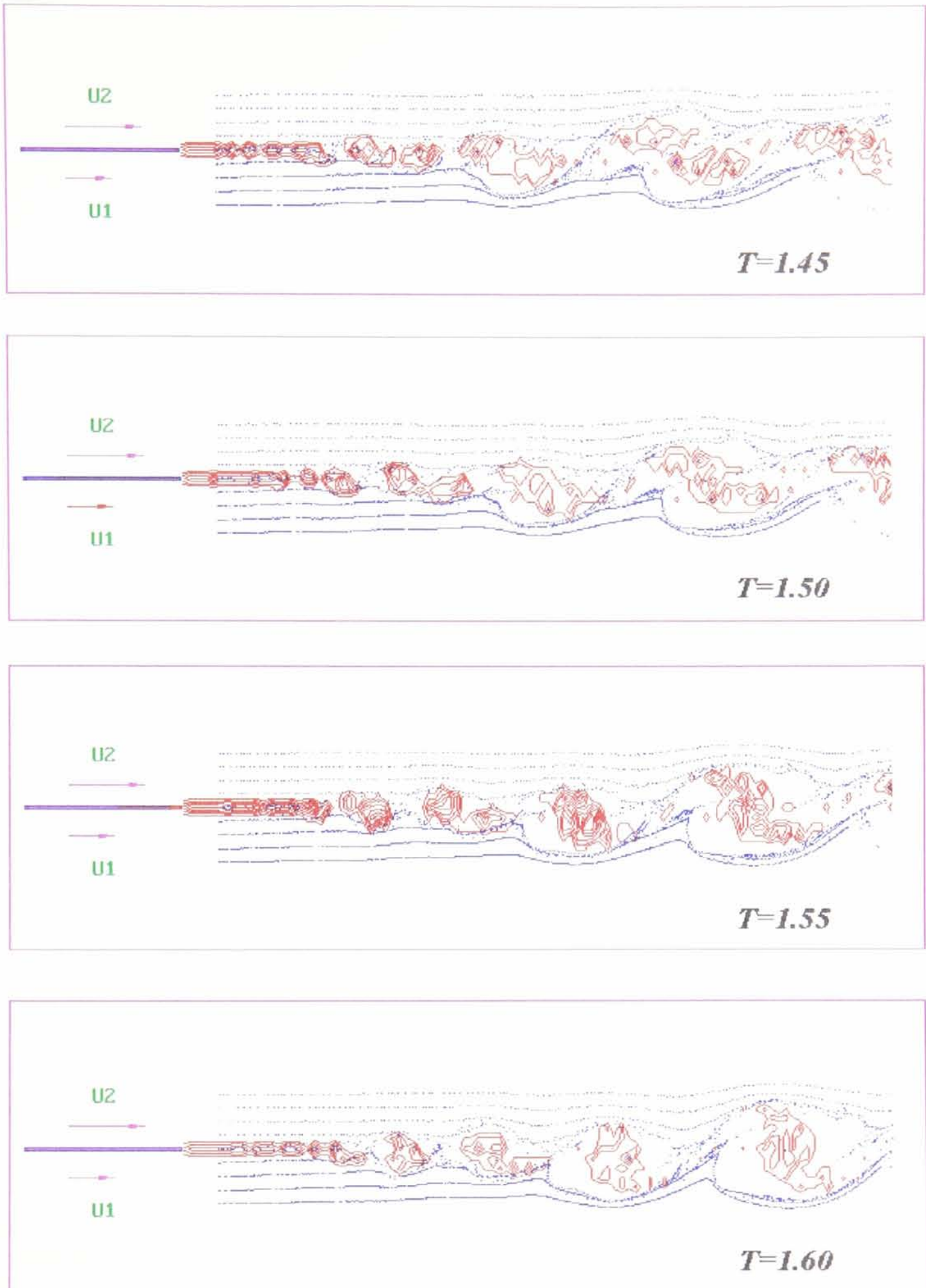


Figure 19. Particle positions with vorticity contours superimposed for $\Pi/\Gamma=0.032$ at four different time instants for the coherent structures undergoing a pairing event. During the pairing, particle streaks between pairing vortices become depleted. An enhanced dispersion can be obviously observed.

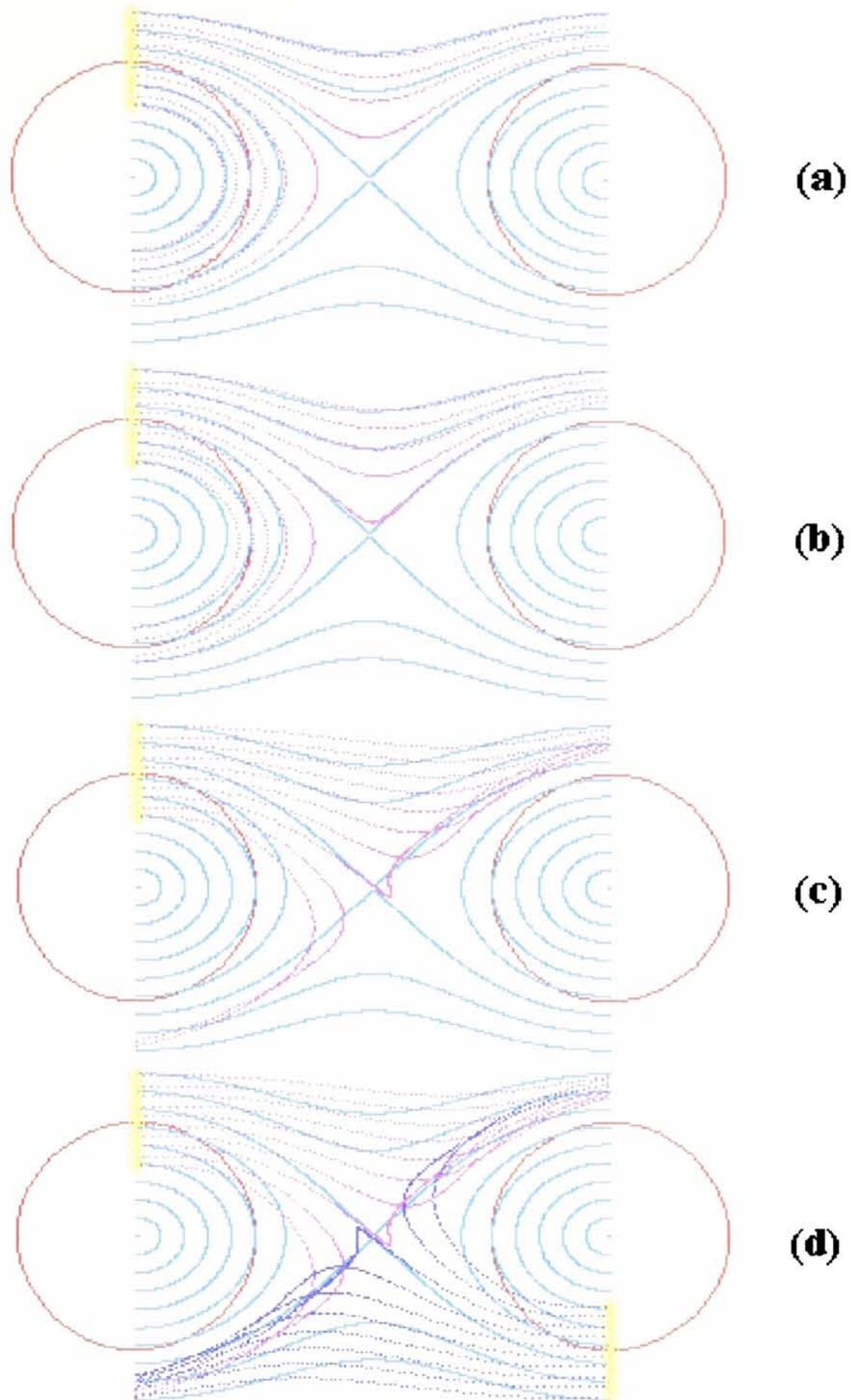


Figure 20. Particle dispersion patterns (particle positions are represented by purple and blue dots, and the cyan lines indicate the streamlines.) in a series of Rankine vortices for different values of Π/Γ (Note: $\Pi=r_0^2\omega^2/2gr_0$ and $\Gamma=r_0\omega/V_T$ are defined here.). Particles were released from different radial positions at the same location at $-r_0$. Here r_0 is a core radius for the Rankine vortex and the coordinate origin is located at the stagnation point as shown in the figure. r_0 is equal to 0.005 m and the angular velocity of the vortex is 200.0 s^{-1} . The density of the particles and the density of the carrier fluid are respectively 2400.0 kg/m^3 and 1.25 kg/m^3 . (a) $\Pi/\Gamma=0.01$; (b) $\Pi/\Gamma=0.1$; (c) $\Pi/\Gamma=1.0$ and (d) the value of Π/Γ is the same as (c). A thick band of particle accumulation occurs.

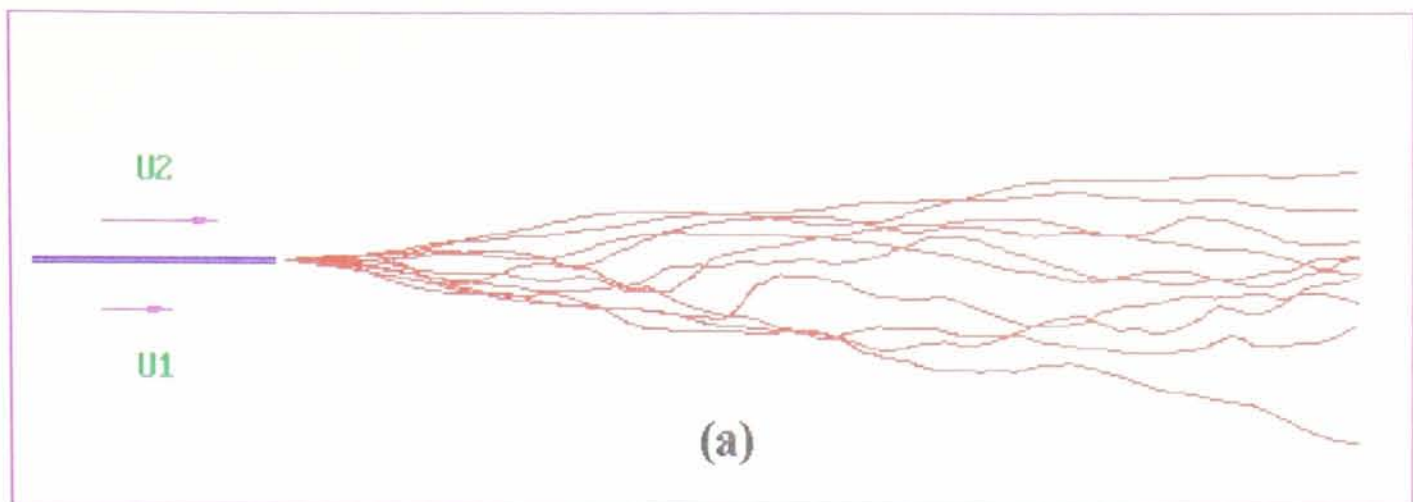


Figure 21a. Particle trajectories with $\Pi/\Gamma=0.059$, computed by using a time-averaged modelling method (The mean flow properties were calculated by time-averaging the instantaneous flow field. 1000 time steps were chosen here). Particles were released from a location very close to the origin of the mixing layer. 1000 particles were released for this demonstration. For clarity, only 10 realisations amongst all particle trajectories are displayed. The density of particles is set to 2850.0 kg/m^3 and the density of carrier fluid is 1000.0 kg/m^3 . (Note: gravity acts from left to right here.)

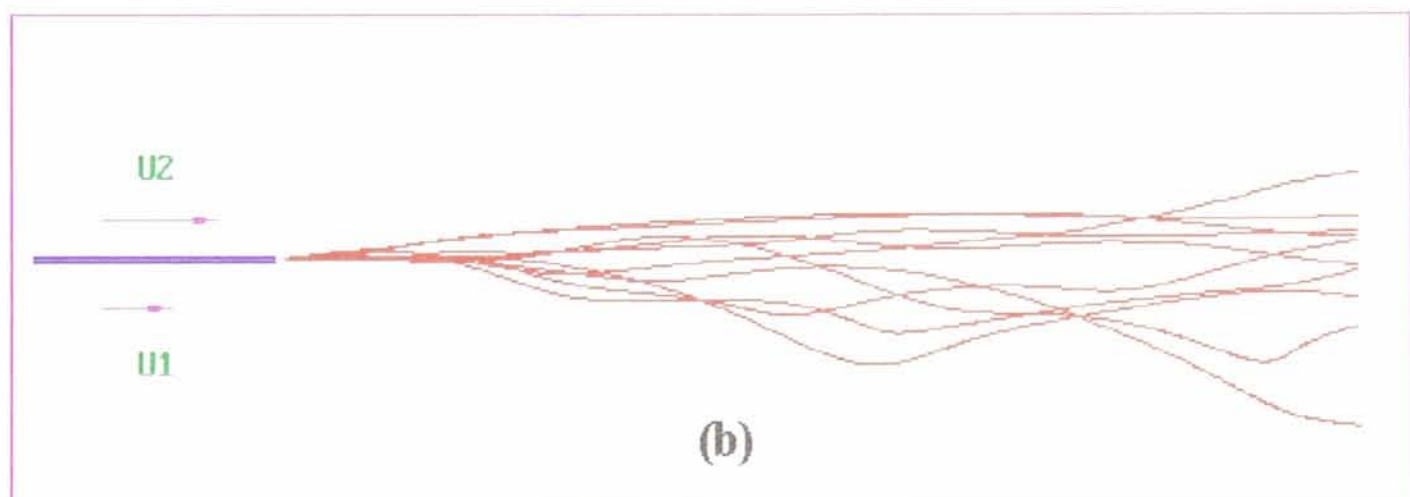


Figure 21b. Particle trajectories with $\Pi/\Gamma=0.059$, computed by using a time-dependent modelling method (discrete vortex method). Particles were released from a location very close to the origin of the mixing layer. 1000 particles were released for this demonstration. For clarity, only 10 realisations amongst all particle trajectories are displayed. The density of particles is set to 2850.0 kg/m^3 and the density of carrier fluid is 1000.0 kg/m^3 . (Note: gravity acts from left to right here.)

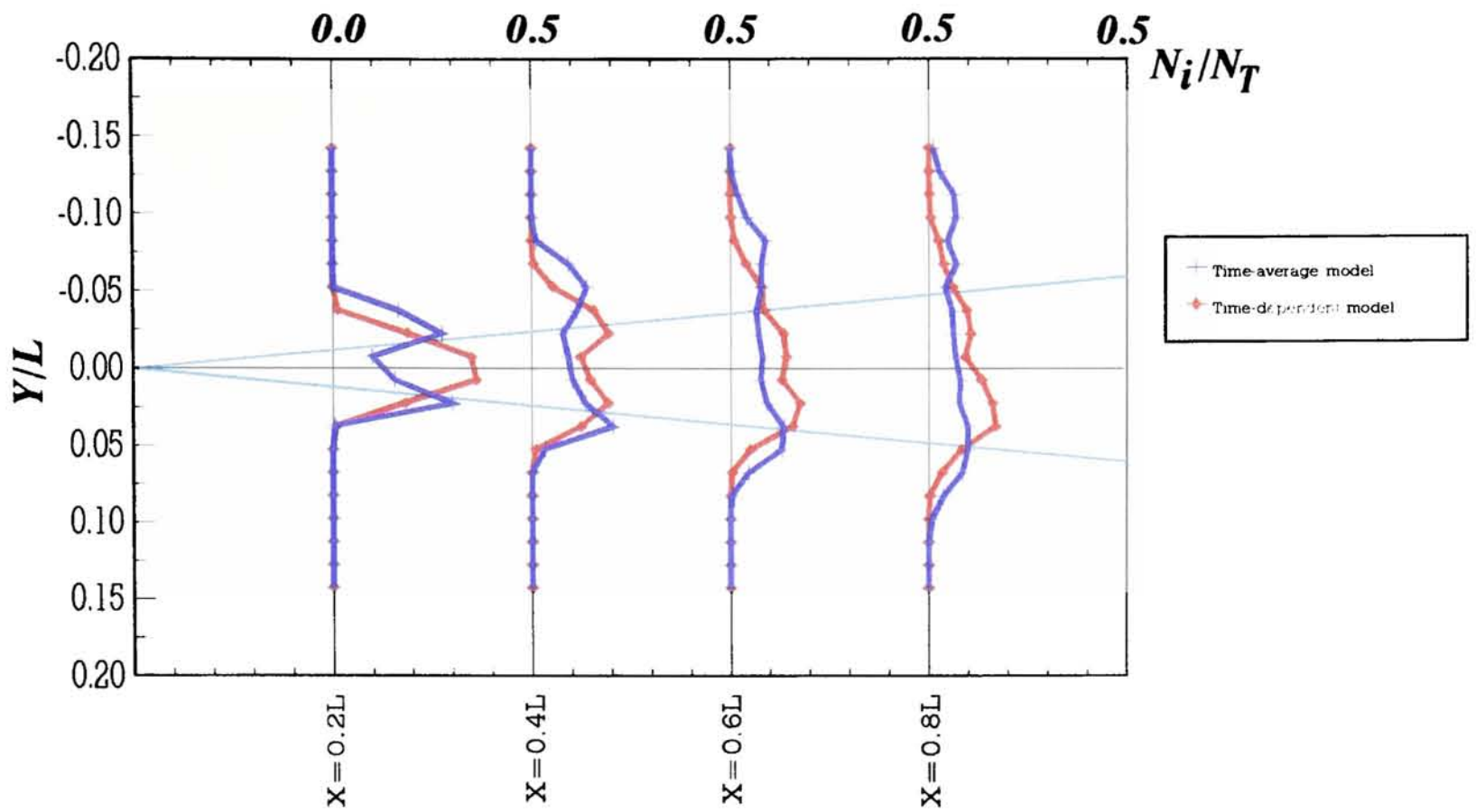


Figure 22. Comparisons of particle number flux distributions at various downstream locations of a vertical, downflowing mixing layer, calculated by using both the time-averaged model and the time-dependent model.

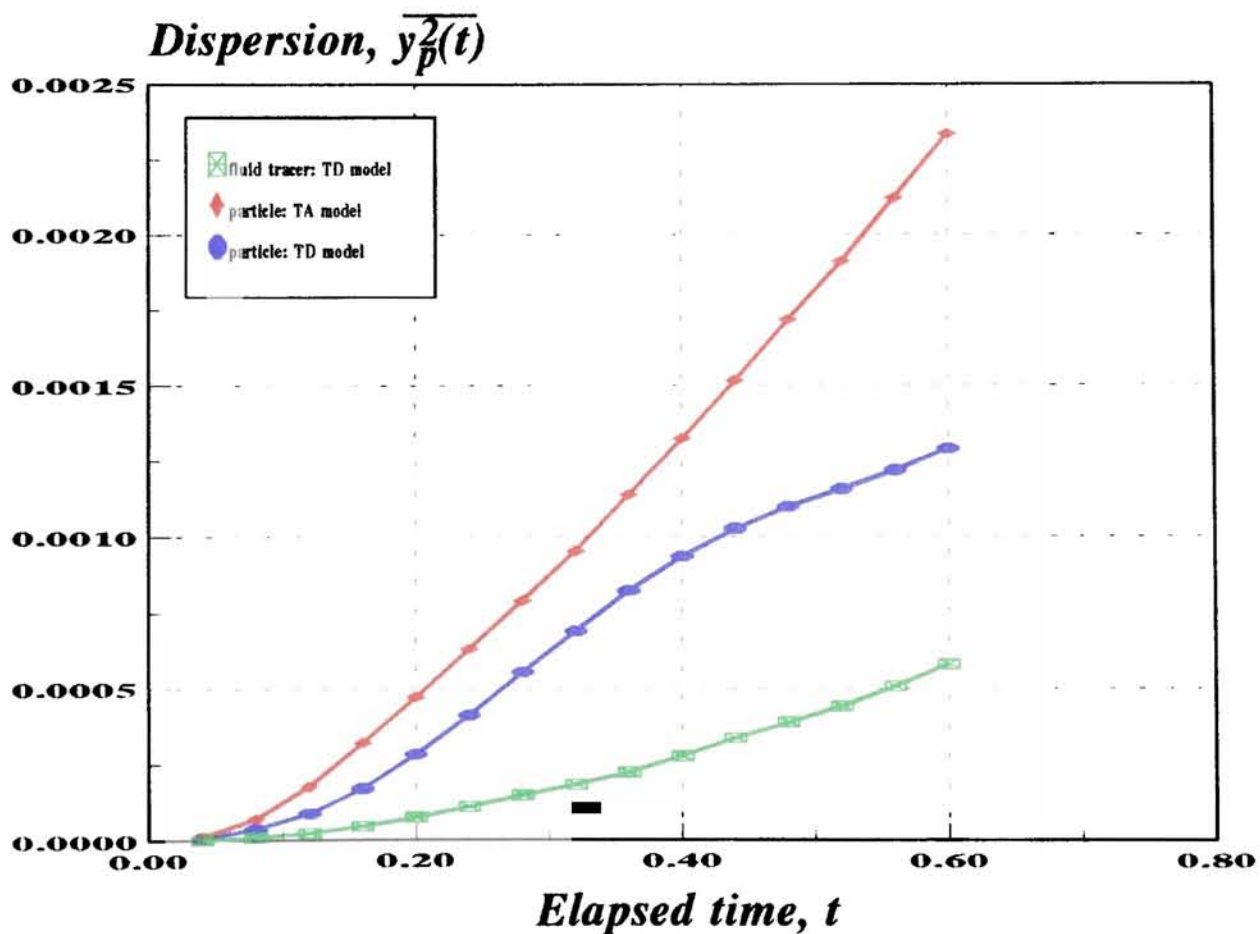


Figure 23. Lagrangian measurements of particle dispersion in a vertical, downflowing mixing layer, calculated by using the time-averaged model and the time-dependent model.

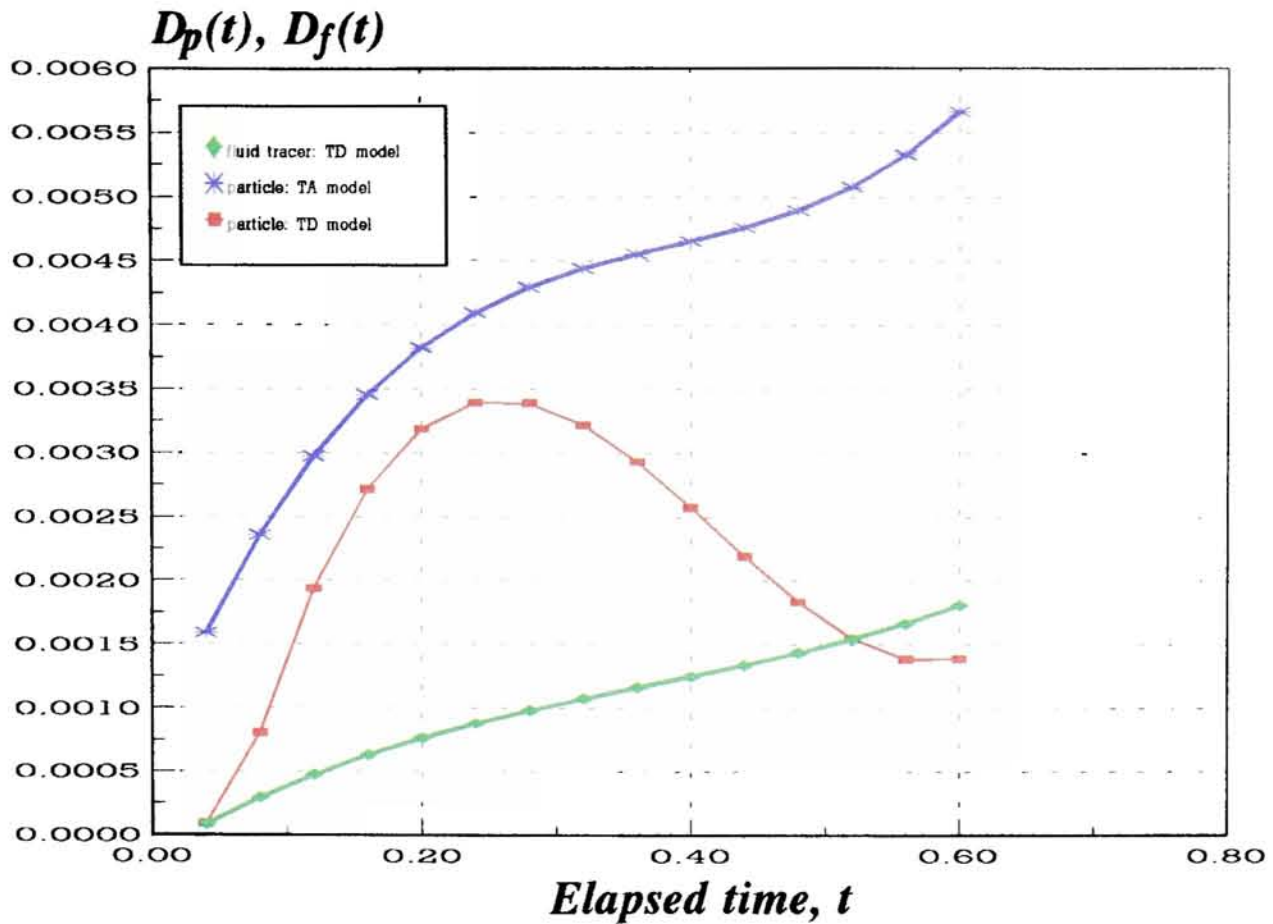


Figure 24. Particle and fluid dispersion coefficients versus time in a vertical, downflowing mixing layer. (TD model: Time-dependent model, TA model: Time-averaged model)

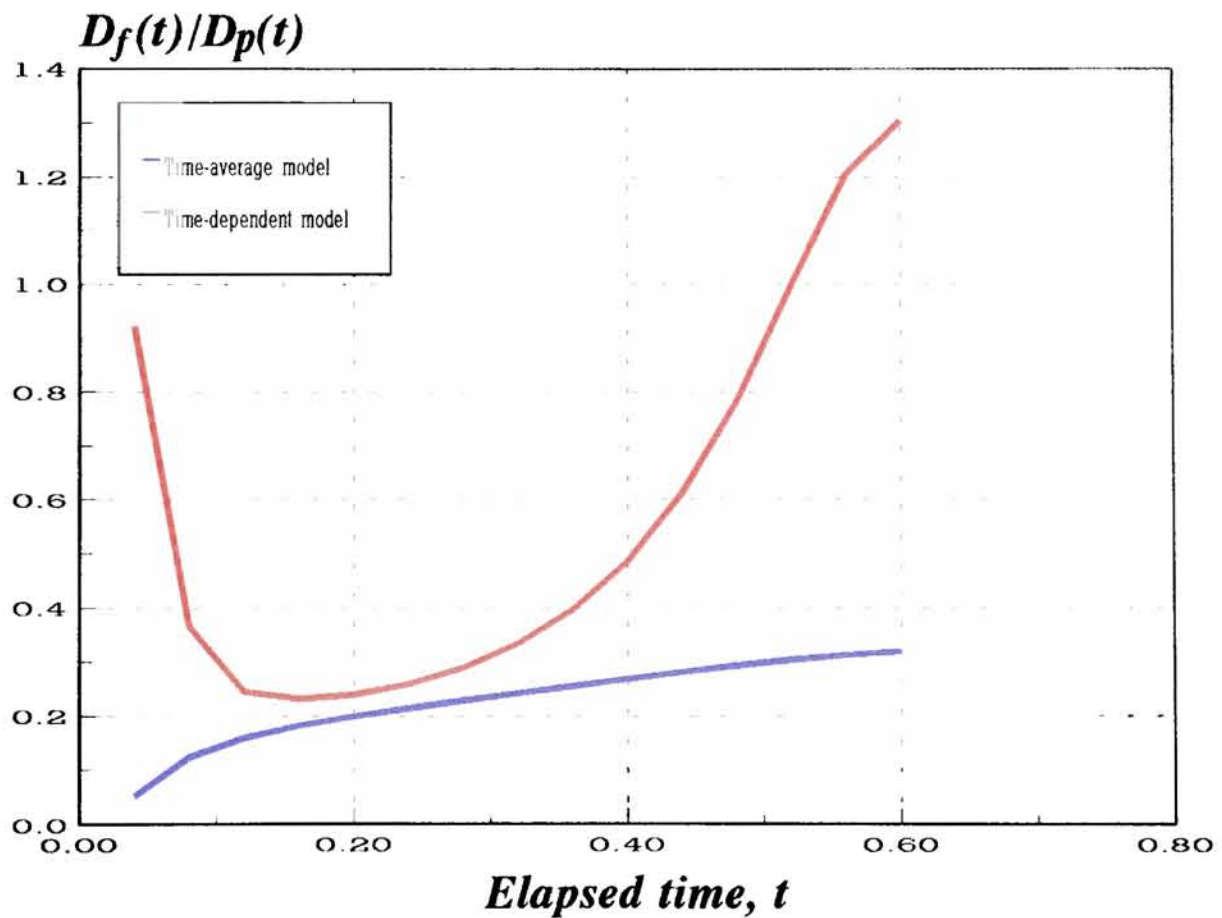


Figure 25. Eddy turbulent Schmidt number of particles versus time in a vertical, downflowing mixing layer, calculated from the data shown in figure 24.

CHAPTER 5: EFFECT OF EDDY STRUCTURE ON BUBBLE DISPERSION IN PLANE TURBULENT JETS

SUMMARY

Recognition of the influence of the large-scale structure in turbulent free shear flows such as turbulent mixing layers on bubble and particle dispersion has been addressed in chapters 3 and 4. We now examine the dynamic behaviour of bubble transport in another type of turbulent shear flow; the turbulent plane jet. Bubble dispersion in such a turbulent shear flow is found to be very important dynamical process, and many industrial applications are very closely associated with this type of dispersion, for example, bubbly plume and jet (e.g. Iguchi *et al.* 1995). Hence, fundamental improvement in the understanding of bubble dispersion in a turbulent jet lends itself to practical applications. As an important initial step, properly conducted numerical predictions of bubble dispersion in turbulent jet flows are necessary.

Two-dimensional plane turbulent jet transport of bubbles is investigated numerically by following bubble trajectories using a discrete vortex model. Both average and local flow features reported in the experimental measurements (e.g. Bradbury 1965) are reasonably simulated. The simulation shows how the bubble dispersion is strongly influenced by large-scale shear vortices. In particular, for vertical upflow we found that off-centre peaks appear in the bubble flux concentration profiles; a phenomenon that is more obvious with increasing shear rate. We take this finding as evidence that inertial forces and vorticity-induced lift forces play an important role in the transport, such as reported for mixing layers. Gaussian profiles and/or diffusion formulations, as have been adopted in previous investigations (e.g.

Iguchi *et al.* 1995), cannot adequately describe this behaviour.

1 INTRODUCTION

Developments in the understanding of turbulent shear flows (Brown & Roshko 1974; Winant & Browand 1974; Ho & Huerre 1984; Browand & Troutt 1985; Hussain 1986) have clearly illustrated the presence of large, essentially two-dimensional roller vortices with the axis perpendicular to the plane mean shear. These investigations have important implications concerning the motion of bubble and particle dispersion in such flows. Experimental and numerical results (e.g. Oler & Goldschmidt 1982; Goldschmidt *et al.* 1983) have indicated that coherent structure also exists in plane jets, and that this structure plays a role similar to that in mixing layers. However, a different manifestation of structure in two-dimensional plane jet flows is the 'flapping' phenomenon (e.g. Antonia *et al.* 1983) which Oler and Goldschmidt (1982) argued was caused by a variant on the Kármán vortex street, and has subsequently been verified in experimental observations (e.g. Antonia *et al.* 1983, 1986). Generally, for bubble transport the key feature is the presence of trains of large eddies with opposite circulations on each sides of the jet. The coupling between bubble trajectories and large vortices is proposed and, as pointed out by Sene *et al.* (1994) (Chapter 3), bubbles converge in the vortex downflow at a location which is dependent on the ratio of inertial to lift forces. Not surprisingly then, we anticipate a tendency for voidage profiles to exhibit bimodal profiles corresponding to the capture and retention of the bubbles in these trains of counterrotating eddies.

Predictions of solid particle dispersion in shear flows using the discrete vortex model (as

adopted here) have been made by Chein & Chung (1987, 1988) for a plane mixing layer and by Chung & Troutt (1988) for an axisymmetric jet, as well as by Laitone (1981) for gas-particle flow over a circular cylinder. Wen *et al.* (1992) investigated the dispersion of particles in a plane mixing layer using both experimental and numerical techniques and they proposed a two-part model involving 'stretching and folding' to describe particle dispersion. The stretching is associated with the high velocity gradient regions near the high and low speed boundaries of the adjoining large eddies and the folding appears to be associated with the pairing interactions of the adjoining large eddies. All of these contributions emphasised that particle dispersion is strongly coupled with the large eddy structure, just as Thomas *et al.* (1983) had identified for bubble transport, advocating numerical simulations using the discrete vortex method as adopted and extended in Hunt *et al.* (1988).

The particle dispersion mechanisms can be quantified using different approaches. Batchelor (1956) analyzed passive fluid particles in a self-developing turbulent shear flow and suggested the use of a lateral dispersion function, defined by

$$D_y^2(T) = \frac{1}{N(T)} \sum_{i=1}^{N(T)} [Y_i(T) - Y_m(T)]^2 \quad (1)$$

and

$$Y_m(T) = \frac{1}{N(T)} \sum_{i=1}^{N(T)} Y_i(T) \quad (2)$$

where $N(T)$ is the total number of particles in the flow at time T . $Y_i(T)$ is the lateral location of the i th particle at time T . $Y_m(T)$ denotes the mean value of particle lateral displacement position at time T . The lateral particle dispersion functions for a particle varies in time. This analysing approach has been adopted in Chein and Chung (1988), Chung and Troutt (1988)

in their numerical studies for particle dispersion in a mixing layer and in an axisymmetric jet as mentioned. Using relation (1), they found that the dispersion function was proportional to time for high Stokes numbers, and the results were similar to those given by Hinze (1975) for dispersion in a homogeneous turbulent flow. Using this measure of dispersion, they further observed that the particle dispersion at intermediate Stokes number exceeded that of the surrounding carrier fluid.

As described in Sene *et al.* (1994), and also in Yang and Thomas (1994) and in Chapter 3, the turbulent Schmidt number for gradient diffusion modelling of bubble dispersion in turbulent mixing layers is around unity, a finding which indicates that bubbles are confined with the shear layer, as opposed to neutral tracers (about 0.7) and particles.

Engineering calculations of particle-laden jets using Eulerian turbulence transport models have been widely documented (e.g. Viollet & Simonin 1994), even though the coupling between the phases is not well understood and their treatment of the discrete phase as an effective continuum lacks fundamental justification. Hybrid schemes using mixed Eulerian-pseudo Lagrangian models for turbulent particle-laden jets have been described by Crowe (1982), Shuen *et al.* (1983, 1985) and Berlemont *et al.* (1990). Here, an instantaneous velocity field is synthesised as a random velocity fluctuation (usually Gaussian) superposed on the computed mean flow, with coupling between the fluid phase and discrete phase incorporated via source/sink terms in the governing equations. However, because turbulent free shear flows comprise much energy associated with assemblages of travelling eddies, neither of these engineering schemes can really capture essential aspects of the transport since the transient inertia effects on particle dispersion are statistically averaged. On the

other hand, the discrete vortex method (Chapter 3) can be used to mimic the main structural features of the turbulence travelling structure, even retaining quantitative estimates by judicious tuning of the procedures. The most restrictive assumption in the model is its imposition of two-dimensionality; an assumption which may be reasonable for a few exit widths of the jet downstream of the exit, but is questionable thereafter. Nevertheless, for purpose of calculating bubble transport and especially its coupling with large eddy structure in an understandable way, the approach is substantially more justified than the cruder engineering methods mentioned above.

While we here use the method only as a vehicle to deliver structural simulation, other workers have argued the merits of discrete vortex modelling for the dynamics themselves: e.g. Davies & Hardin (1973); Edwards & Morfey (1981) and Acton (1980). Acton's (1980) time averaged results were found to be in reasonable qualitative agreement with experimental observations, indicating that an ample portion of the large scale structure of jets can be treated as axisymmetric. For the turbulent plane jet, vortex growth has been simply modelled by Beavers & Wilson (1970) using two vortex sheets, and the flow features of the laboratory flows were reproduced qualitatively in their calculations. However, their simulation gave no prediction about the flow properties of the jet.

The present study uses these methods, and more particularly adopts our earlier modelling of the plane mixing layer as a basis for describing structured plane jet flow and hence simulating the trajectories of bubbles using the generalised force law (Auton 1987; Thomas *et al.* 1983). The statistics of these trajectories are then used to determine the bubble number flux profile, the mean bubble velocities and the turbulent Schmidt number. Our account is

presented in the following sections describing the modelling formulation, bubble trajectories in two separately staggered Rankine vortices, plane jet characterisation and bubble dispersion in such plane jet.

2 MODELLING FORMULATION

2.1 Discrete Vortex Model For A Plane Turbulent Jet

Before proceeding to develop a model of the plane jet, it is instructive to examine briefly simpler ideal flows which resemble plane jet flow. For simplicity, the discussion is confined to two dimensions to accommodate our simulations. Let us first consider the case of two infinite vortex sheets with circulation $\Gamma=U_0$ per unit length, but with the opposite sign, surrounded by ambient fluid at rest (as shown in figure 1). Each sheet will travel with a velocity $U_0/2$ induced on it by the other. The uniform velocity U_0 found inside the strip is induced by both sheets acting together. However, for the case of two half infinite vortex sheets, only a flow rate $U_0/2$ for the injection of fluid across the exit plane can be found. Hence, one can place a uniform source of strength U_0 across the exit plane in order to keep the correct boundary conditions. However, if a pair of sheets with finite length are placed downstream of the exit of the jet, the exit velocity condition is still approximately met. Bearing this in mind, we now consider the plane jet model.

More realistically as shown in figure 2, the flow comprises uniform axial exit velocity U_0 over the jet exit plane of width D . If the surroundings are at rest, then the jet delivery (internal flow) can be modelled by two semi infinite vortex sheets with the strength U_0 per unit length. The strength of any vortex filament exiting the nozzle in a short time interval

Δt is then as follows,

$$\Delta \Gamma = \frac{1}{2} U_0^2 \Delta t \quad (3)$$

Downstream of the exit, the free shear layers are then approximated in discrete form by two semi-infinite series of point vortex filaments, sequentially shed from the nozzle edge in $x=0$, joining the free vorticity in the downstream shear layers. Once in the shear layers, these point vortices move under the influence of the convection velocity field $U_m = U_0/2$, the velocity field induced by the two vortex sheets upstream of the jet and the velocities induced by all other vortex filaments shed into the flow. Those point vortex filaments exiting downstream of the simulation domain are removed in order to limit the total number of the vortices and so reduce the computing effort, assuming that its upstream influence is negligible - as supposed in Leonard's (1980) simulation (recall chapter 3). Downstream of the computation domain, the effect of the removed vortex filaments is represented by two semi-infinite sheets, as adopted in chapter 3. The velocity of the n th vortex filament at the location (X_n, Y_n) is thus given by

$$U_n = U_m + \frac{U_0}{2\pi} \left[\tan^{-1} \left(\frac{Y_n - \frac{D}{2}}{X_n} \right) - \tan^{-1} \left(\frac{Y_n + \frac{D}{2}}{X_n} \right) \right] + \sum_{\substack{j=1 \\ j \neq n}}^{N_T} \frac{\Delta \Gamma_j |\Delta \Gamma_j|}{2\pi R_n^2 \Delta \Gamma_j} (X_n - X_j) \quad (4)$$

$$V_n = V_m + \frac{U_0}{2\pi} \ln \frac{\sqrt{[X_n^2 + (Y_n - \frac{D}{2})^2]}}{\sqrt{[X_n^2 + (Y_n + \frac{D}{2})^2]}} - \sum_{\substack{j=1 \\ j \neq n}}^{N_T} \frac{\Delta \Gamma_j |\Delta \Gamma_j|}{2\pi R_n^2 \Delta \Gamma_j} (X_n - X_j) \quad (5)$$

where $R_n^2 = (X_n - X_j)^2 + (Y_n - Y_j)^2$ and N_T is the total number of point vortex filaments in the computation domain. In each equation, the first term on the right hand side corresponds to

the mean field convective velocity, the second term is due to the contribution from the upstream bound sheets and the third term represents the field effects of free vortices. The movement of vortices in the flow is described by the kinetic relations

$$\frac{dX_n}{dt} = U_n, \quad \frac{dY_n}{dt} = V_n \quad (6)$$

and the simulation is time step progressing using a first-order Euler predictive scheme

$$X_n^{j+1} = X_n^j + U_n(X_n^j, Y_n^j) \Delta t, \quad Y_n^{j+1} = Y_n^j + V_n(X_n^j, Y_n^j) \Delta t \quad (7)$$

Remember our purpose here is to employ the model for bubble dynamic studies, having demonstrated it provides a adequate description of the flow field, but not in any sense regarded as a rigorously justified prediction scheme for the flow dynamics. Shortcomings in the primitive scheme (as noted in chapter 3) include the high induced velocities when two point vortices approach each other, suppressed here (as previously Chorin 1973) by introducing a core to the vortices, defined according to:

$$u_\theta = \begin{cases} \frac{1}{2\pi r} \Gamma & (r \geq \sigma) \\ \frac{r}{2\pi \sigma^2} \Gamma & (r < \sigma) \end{cases} \quad (8)$$

where r is the distance measured from the centre of the point vortex and core radius σ was here set to be equal to $\sigma = 2.24\sqrt{\nu t}$, not in any sense with severe fundamental justification but simply to optimise the comparisons with experimental results on the flow field and structures. Here, ν is the kinematic viscosity and t is the elapsed time since the vortex is shed from the exit of the jet.

2.2 Bubble Motion

Bubble motions are again supposed to follow the equation of motion given by Auton *et al.* (1988), because of the assumptions of which were described in chapter 3. Specifically, then,

$$(\gamma + C_m) \frac{dv}{dt} = (1 + C_m) \frac{Du}{Dt} - |\gamma - 1| \frac{\Gamma w}{\Pi} f\left(\frac{w}{\Gamma}\right) + (\gamma - 1) \frac{g}{g\Pi} - C_L w \times (\nabla \times u) \quad (9)$$

where ΔU is taken as velocity scale and $b_u/\Delta U$ as time scale again with $\Gamma = \Delta U/V_T$ and $\Pi = \Delta U^2/gb_u$ (Hunt *et al.* 1988), also $\gamma = \rho_b/\rho_f$ as density ratio parameter. b_u is the half width of the jet. In the calculation, we define Π as $\Pi = \Delta U^2/Gl$, since b_u is proportional to the exit width downstream (or the distance downstream from the exit). For V_T , measurements have shown that $V_T = 0.2-0.25$ m/s for water bubbles with diameters of 1-5 mm (Clift *et al.* 1978) and a value of $V_T = 0.2$ m/s was adopted throughout this study.

Contributions to bubble motion from each term of equation (9) have been also addressed in chapter 1. In order to generalise the flow computation, all length scales, velocities and times were nondimensionalized. For a turbulent jet, the velocity difference between the jet exit core and the ambient, where $\Delta U = U_0$, can be taken as a velocity scale and the downstream distance X , measured from the nominal origin of the jet, as a convenient length scale. In this calculation, the time step for integration of equation (9) was chosen to accommodate both the flow field and the bubble motion calculations. The method adopted here was the same as that for the mixing layer simulations.

The importance of lift forces on the bubble motion noted in chapter 3 for the mixing layer studies, will again be demonstrated here for bubble flux profiles in the jet.

2.3 Bubble Trajectories in Two Separately Staggered Rankine Vortices

Before addressing the calculation of the bubble motions in the turbulent plane jet, it is very useful to examine four special cases; bubble release beneath either of two separately allocated Rankine vortices or beneath two separately staggered Rankine vortices, with or without overlapping. These cases could be thought of as corresponding to two different dominant modes observed in plane jets, symmetric and anti-symmetric modes, as indicated by Husain *et al.* (1987). They showed that close to the exit of the jet, the usual mode is symmetrical or varicose mode and the two shear layers retain their distinct identities even after the breakdown of the structures (figure 3). However, the dominant mode in the downstream self-preserving region of the plane jet is anti-symmetric or sinuous mode (Antonia *et al.* 1983; Husain *et al.* 1987) (figure 3). For these cases one hundred bubbles were released from the location upstream of the first Rankine vortex, $X=2R$, where R is the Rankine vortex core radius. The core radius R and vortex strength ω can be specified respectively according to Oler and Goldschmidt (1982):

$$R=1.3b_u \quad (10)$$

$$\omega = \frac{0.5U_m}{b_u} \quad (11)$$

where b_u and U_m can be approximately given by (Oler & Goldschmidt 1982)

$$b_u = \beta x \quad (12)$$

$$U_m = C_m x^{-\frac{1}{2}} \quad (13)$$

Here $\beta=0.1$ and $C_m=2.36$. The bubble trajectories for different cases are shown in figures 4 and 5, respectively. It is obvious that for all the cases bubbles are trapped by the vortices. These examples have implications on bubble motion in turbulent plane jets. The transient

locally high void fraction can be found in the jet since the bubble are trapped by the large-scale eddies and cluster with the motion of the large-scale eddies in the jet. In the fully developed flow region of the jet, the large eddies on both sides of the jet are gradually overlapped. Figure 5 shows that the bubble trajectories for these latter cases. It is interesting to note that although the interaction between two Rankine vortices with the opposite circulation for these latter cases has become stronger, the performance of bubble trapping still does not change fundamentally. These demonstrations imply that bubble dispersion patterns in turbulent plane jets may present a bimodal behaviour, i.e. a Gaussian-like distribution assumption for bubble concentration profile in the jet may be not a good representation. For both the modes observed in plane jets, we expect that either the symmetrically arranged or alternatively arranged vortices may result in time-averaged saddle-like concentration distributions with the highest concentrations occurring on both sides of the centerline. This argument will be further reinforced in next section.

3 RESULTS AND DISCUSSION

3.1 The Plane Jet Flow Characterization

The simulated starting flow of the plane jet into an ambient environment at rest is shown in figure 6; plots of instantaneous vortex patterns at different dimensionless times from $T=0.5$ to $T=2.0$ are displayed. It is clearly seen from this figure that two series of large vortices cluster alternatively and travel downstream, consistent with the experimental observations. It should be noted that an initial perturbation for the first 100 point vortex shedding at one side has to be introduced in order to excite an asymmetric instability.

Instantaneous axial velocity traces computed at the centerline for $X/D=30$ from $T=1.0$ to $T=3.6$ are shown in figure 7. Mean velocity profiles in both axial and transverse directions calculated from the numerical results after time-averaging at different downstream positions $X/D=20, 30, 40$ are shown respectively in figures 8 and 9. It can be seen from figure 8 that the axial mean velocity profiles are self-preserved based on the scale b_u , which denotes half-width, where the velocity value is half the axial velocity on the centerline of the jet, and are in reasonable good agreement with experimental data for a plane jet (Bradbury 1965). The turbulent intensities and the Reynolds stress profiles (figures 10-12) predicted are also in reasonably agreement with the experimental data. As has been discussed by Bradbury (1965), fully developed status is attained when $X/D \geq 30$ for most plane jet experiments. It seems that this status has achieved in our simulations, as can be seen from figures 8 to 12. However, we noted that the longitudinal turbulent fluctuations are larger in magnitude than the experiment data when b_u is larger than 2.0. This discrepancy may be attributed to the perturbation due to removal of vortex filaments exited from the computation domain, or it may be related to the unreasonable representation of the model. Even so, the discrete vortex numerical simulation still reasonably models the plane jet flow and serve as a platform for bubble transport calculation.

3.2 Bubble Dispersion

Model bubbles were introduced into the flow at locations near the nozzle and following a period of flow establishment. Initial velocity on release was set to be equal to the sum of the local velocity and the bubble slip velocity ($V_T=0.2$ m/s), corresponding to the approaching condition at rest for upstream of the (vertical) upjet. Their dispersion was analyzed by sampling across the flow at several streamwise stations.

(a) Effect of large-scale structure of the jet on bubble dispersion

A total of 400 bubbles were released from the exit plane of the nozzle with one bubble every time step. Their trajectories for the cases $\Pi=0.02$, $\Gamma=1.5$ and $\Pi=0.05$, $\Gamma=2.5$ are shown in figures 13 and 14, showing how for both cases the bubbles were engaged by the large eddy structure and incline towards both low speed sides. However, case $\Pi=0.05$, $\Gamma=2.5$ is more skewed than that $\Pi=0.02$, $\Gamma=1.5$ and it can be expected that this behaviour will become more apparent with increasing shear rate, resulting in a locally high concentration of bubbles. In Chapter 3, bubbles converged in the vortex downflow at a location offset from the vortex centre. This offset depends on the ratio of inertia to lift forces. We conjecture that the same argument can be applied to the case of an upflowing plane jet. This has the implication that bubble motion in an upflowing jet will tend to form two alternative clusters provided that the bubbles are trapped by the eddies, since the plane jet can be envisioned to be two arrays of moving Rankine vortices which are superimposed by a mean convection and whose sizes increase with time. Furthermore, in an upflowing jet, the time-averaged effect of lift forces is to promote bubbles movement towards both the low speed sides. Hence, it is anticipated that time-averaged bubble concentration profiles will present two peaks. However, we caution here that the effect of turbulent diffusion on bubble motion in such a flow has not been accommodated in the simulation.

The bubble number flux profiles obtained through counting the bubbles in the flows for both these two cases are shown in figures 15 and 16 for the downstream locations $X/D=20$, 30, 40. The bubble number flux profiles for both these cases are not self-preserved like those in turbulent mixing layers (Sene *et al.* 1994). However, self-preservation should be obtained if the simulation permits the tracing of bubbles further downstream. It is seen that double

peaks are found in bubble number flux profiles. As mentioned before, this is mainly due to the condition that bubbles are trapped into the centres of those large-scale eddies aligning alternatively at the centerline of the jet. Our simulation results indicate that at least for the transit region of the jet the conventional assumption of Gaussian distribution on the concentration profile of a jet fails to represent real situations. We caution that this argument is only derived from the simulations and needs further experiment support.

(b) Effect of lift force acting on bubbles on bubble dispersion

As mentioned in the second section, the effect of the lift force acting on bubbles increases with increasing of shear rate. Figures 17 and 18 show respectively the bubble trajectories and the bubble concentration flux profiles obtained by including and excluding the lift forces. It is obvious that the results with inclusion of the lift forces are different from those obtained with exclusion of the lift forces. The simulation results displayed are for the case $\Pi=0.02$, $\Gamma=1.5$. The simulations clearly demonstrate that the lift force acting on bubbles in turbulent shear flows plays an important role in the determination of bubble motion. The results of figures 17 and 18 indicate that this lift force cannot be ignored, especially when the shear becomes stronger. However, we caution that since the force law we are applying is accommodated to the inviscid non-uniform shear flow (Thomas *et al.* 1983), the vorticity-induced lift force may be overestimated (Maxey *et al.* 1994).

(c) Quantification of bubble dispersion in the plane jet

In these studies, quantification of particle dispersion was in accordance with tracer particles initially released from certain points. We also adopt equation (1) to quantify the bubble dispersion. Fluid tracer trajectories and bubble trajectories for case $\Pi=0.02$, $\Gamma=1.5$ are

displayed in figure 19. Bubble dispersion as a function of time for bubbles released from the exit of the jet for $\Pi=0.02$, $\Gamma=1.5$ and $\Pi=0.05$, $\Gamma=2.5$ are shown in figure 20. It is interesting to note that more dispersions for the case $\Pi=0.05$ are seen than those for the case $\Pi=0.02$, as expected. This can be explained by the fact that because the increasing shear rate increases both the inertial forces and the vorticity-induced lift forces acting on the bubbles, the effect of time-averaging both forces is to encourage the entrapment of bubbles into the large scale structures on both sides of the jet. The stronger the shear rate, the larger the dispersion that is attained. It is of interest to note that the lateral dispersion of bubbles is larger than that of tagged fluid particles, as can be seen from figure 20 (note: These tagged fluid particles were released into the flow at the same positions as the bubbles). This behaviour is related to the fact that bubble motions in the jet are affected by the presence of the large scale structures, but the tagged fluid particles are less affected by these large-scale structures since the tagged fluid particles are passive scalars. The spreading of the tagged fluid particles is certainly less than that of the bubbles. It is also noted that the dispersion functions for tagged fluid particles can be described as nearly proportional to T^2 , as addressed by Hinze (1975) for particle dispersion in homogeneous turbulent flows. For bubble dispersion function versus time, this deduction holds within a smaller time range, as can be seen from figure 20. However, for a larger time range, the bubble dispersion function displays a different behaviour due to the confinement of bubbles by the large eddies on both sides of the jet.

In order to further quantitatively examine the dispersion of bubbles, we consider the comparison of bubble dispersions with that of the fluid in the jet by using the ratio between both the dispersion functions. The dispersion function for fluid tracers in the jet is defined

as the same for those of bubbles, i.e. $D_{fy}^2(T)$. This ratio can be thought of as being approximately the turbulent Schmidt number, as adopted in chapter 3.

$$\gamma(T) = \frac{D_{fy}^2(T)}{D_y^2(T)} \quad (14)$$

The ratios as a function of time for both cases of bubbles released from the exit of the jet are shown in figure 21. It can be seen from figure 21 that the ratios decrease rapidly with time, and then approach a nearly fixed value. The magnitude of the ratios for both the cases is far smaller than 1.0, unlike those addressed for the bubbly mixing layer. However, this does not indicate that bubbles in the upflowing plane jet spread more than passive scalars in the jet. We should be careful to assess this result because the bubble number flux profiles are bimodal. Their variance is larger than that of the fluid. A more relevant approach would be to consider the situation as two overlapping Gaussian profiles centred on the edges of the shear layers.

4 CONCLUSIONS

Numerical simulation results of the bubble dispersion in a plane free jet are presented. The jet flow is modelled using a discrete vortex model. The predicted mean velocities and instantaneous velocity fluctuations are compared with the experimental results (Bradbury 1965) and are found to be in reasonable agreement.

This study has shown that by neglecting the lift force transverse dispersion of bubbles will be underestimated while the bubbles are trapped by the jet. It is clearly demonstrated that in a shear flow, the vorticity-induced lift force acting on the bubbles (or particles less dense

than the carrier fluid) cannot be ignored when employing the Lagrangian force law for the trajectory calculation.

For an upflowing jet the bubble dispersion simulations have revealed that two peaks appear in bubble flux concentration profiles, and that this phenomena becomes more obvious with increasing shear rate. This indicates that for an upflowing jet the time averaged composite effects of the inertial forces and lift forces acting on the bubbles in the flow cause bubbles to drift away from the centerline of the jet, and result in a larger dispersion than those characterising a passive scalar. This result implies that the assumption of a Gaussian distribution for the bubble void fraction in either a bubbly plume or a bubbly jet, previously adopted in many engineering calculations, may be not valid. Indeed, this phenomena has been observed in an unpublished experimental observation of a bubbly turbulent jet, carried out by the *FAST* Team. We caution here that we have not found any published literature that experimentally supports this finding. We hope to further confirm this point by more detailed experimental studies.

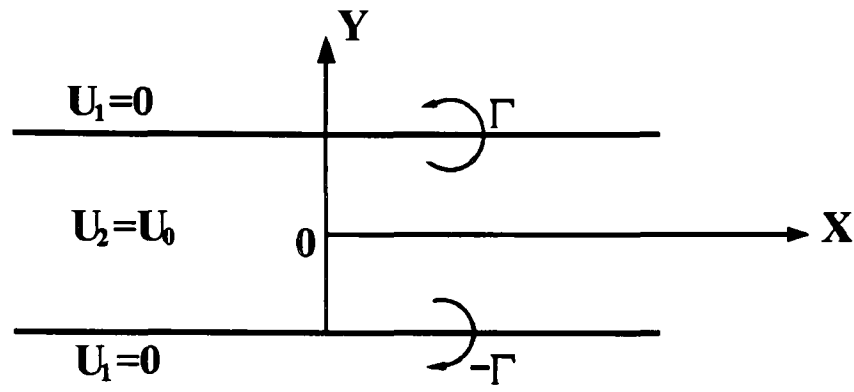
REFERENCES

- Acton, E. 1980 A modelling of large eddies in an axisymmetric jet. *J. Fluid Mech.* **98**, 131.
- Antonia, R. A., Browne, L. W. B., Rajagopalan, S., & Chambers, A. J. 1983 On the organised motion of a turbulent plane jet. *J. Fluid Mech.* **134**, 49-66.
- Antonia, R. A., Chambers, A. J., Britz, D. & Browne, L. W. B. 1986 Organized structures in a turbulent plane jet: Topology and contributions to momentum and heat transport. *J. Fluid Mech.* **172**, 211-229.
- Auton, T. R., Hunt, J. C. R. & Prud'homme, M. 1988 The force exerted on a body inviscid unsteady nonuniform rotational flow. *J. Fluid Mech.* **197**, 241.

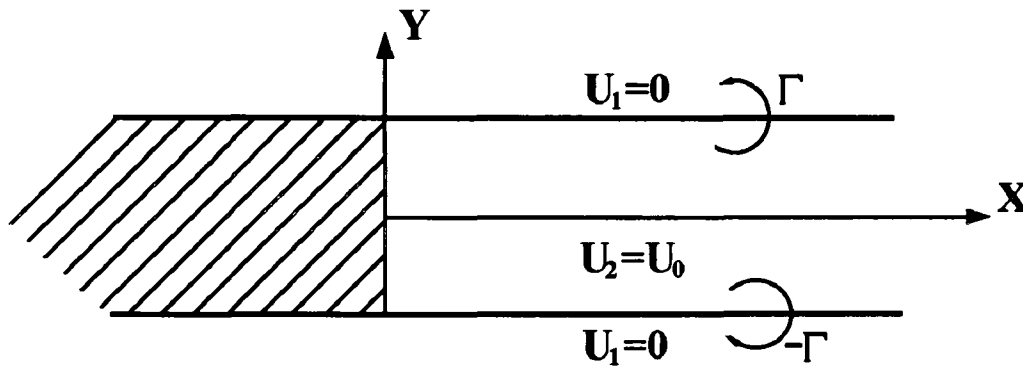
- Batchelor, G. K. 1956 Diffusion on free turbulence shear flows. *J. Fluid Mech.* **98**, 67.
- Beavers, G. S. & Wilson, T. A. 1970 Vortex growth in jets. *J. Fluid Mech.* **44**, 97-112.
- Berlemont, A., Desjonqueres, P. & Gouesbet, G. 1990 Particle Lagrangian Simulation in turbulent flows. *Int J. Multiphase Flow* **16**(1), 19-34
- Bradbury, L. J. S. 1965 The structure of a self-preserving turbulent plane jet. *J. Fluid Mech.* **23**, 31-64.
- Brown, G. L. and Roshko, A. 1974 Density effects and large-scale structure in turbulent mixing layer. *J. Fluid Mech.* **64**, 775-816.
- Browand, F. K. & Trout, T. R. 1985 The turbulent mixing layer: Geometry of large vortices. *J. Fluid Mech.* **158**, 489-509.
- Chein, R. and Chung, J. N. 1987 Effects of vortex pairing on particle dispersion in turbulent shear flows. *J. Multiphase Flow* **13**, 785-802.
- Chein, R. and Chung, J. N. 1988 Simulation of particle dispersion in a two-dimensional mixing layer. *J. AIChE.* **34**, 946-954.
- Chorin, A. J. 1973 Numerical study of slightly viscous flow. *J. Fluid Mech.* **57**, 85.
- Chung, J. N. and Trout, T. R. 1988 Simulation of particle dispersion in an axisymmetric jet. *J. Fluid Mech.* **186**, 199-222.
- Clift, R., Grace, J. R. & Weber, M. E. 1978 Bubbles, Drops and Particles. Academic Press, New York.
- Crowe, C. T. 1982 Review - Numerical models for dilute gas particle flows. *Trans. ASME I: J. Fluids Engng.* **104**, 297-303.
- Crowe, C. T., Gore, R. and Trout, T. R. 1985 Particle dispersion by coherent structures in free shear flows. *Particulate Science and Tech.* **3**, 149-158.
- Davies, P. O. A. L. & Hardin, J. C. 1973 Potential flow modelling of unsteady flow. *Int. Conf. on Numerical Methods in Fluid Dynamics*, Dept. of Civil Engng, University of Southampton.
- Edwards, A. V. J. & Morfey, C. L. 1981 A computer simulation of turbulent jet flow. *Computers and Fluids* **9**, 205-221.
- Elghobashi, S. E., Abou Arab, T. W., Rizk, M. & Mostafa, A. 1984 Prediction of the particle laden jet with a two equation turbulence model. *Int. J. Multiphase Flow* **10**, 697-710.
- Goldschmidt, V. W., Moallemi, M. K. & Oler, J. W. 1983 Structures and flow reversal in

- turbulent plane jets. *Phys. Fluids* **26**(2), 426-432.
- Hinze, J. O. 1975 *Turbulence*. 2nd ed. McGraw-Hill, New York.
- Ho, C. M. and Huerre, P. 1984 Perturbed free shear layers. *Ann. Rev. Fluid Mech.* **16**, 365-424.
- Hunt, J. C. R., Auton, T. R., Sene, K., Thomas, N. H. and Kowe, R. 1988 Bubble motions in large eddies and turbulent flows. *Transient Phenomena in Multiphase Flow*, (Edit by N. H. Afgan), Hemisphere.
- Husain, H., Bridges, J. E. & Hussain, A. K. M. F. 1987 Turbulence management in free shear flows by control of coherent structures. *Transport Phenomena in Turbulent Flows: Theory, Experiment, and Numerical Simulation*. (ed. M. Hirate and N. Kasagi) Hemisphere Publishing Corporation, 111-130.
- Hussain, A. K. M. F. 1986 Coherent structures and turbulence. *J. Fluid Mech.* **173**, 303-356.
- Iguchi, M., Ueda, H. & Uemura, T. 1995 Bubble and liquid flow characteristics in a vertical bubbling jet. *Int. J. Multiphase Flow* **21**, 861-873.
- Leonard, A. 1980 Vortex methods for flow simulation. *J. Computational Phys.* **37**, 289-335.
- Maxey, M. R., Chang, E. J. & Wang, L-P. 1994 Simulation of interactions between microbubbles and turbulent flows. *Appl. Mech. Rev.* **47**(6), s70-s74.
- Oler, J. W. & Goldschmidt, V. W. 1982 A vortex-street model of the flow in the similarity region of a two-dimensional free turbulent jet. *J. Fluid Mech.* **123**, 523-535.
- Sene, K. 1985 Aspects of bubbly two phase flow, Ph.D. Thesis, University of Cambridge.
- Sene, K., Hunt, J. C. R. and Thomas, N. H. 1994 The role of coherent structures in bubble transport by turbulent shear flows. *J. Fluid Mech.* **259**, 219-240.
- Sheun, J. S., Chen, L. D. & Faeth, G. M. 1983 Evaluation of a stochastic model of particle dispersion in a turbulent round jet. *AIChE J.* **29**(1), 167.
- Sheun, J. S., Solomon, A. S. P., Zhang, Q. F. & Faeth, G. E. 1985 Structure of particle-laden jets: Measurements and predictions. *AIAA J.* **23**, 396.
- Thomas, N. H., Auton, T.R., Sene, K. and Hunt, J.C.R. 1983 Entrapment and transport of bubbles by transient large eddies in multiphase turbulent shear flow. *Int. Conf. on the Physical Modelling of Multiphase Flow*, Coventry, England, Paper E1.
- Viollet, P. L. & Simonin, O. 1994 Modelling dispersed two-phase flows: Closure, validation and software development. *Appl. Mech. Rev.* **47**(6), s80-s84.
- Wen, F., Kamalu, N., Chung, J. N., Crowe, C. T. and Troutt, T. R. 1992 Particle dispersion

- by vortex structures in plane mixing layers. *J. Fluids Engng.* **114**, 657-666.
- Winant, C. D. & Browand, F. K. 1974 Vortex pairing, the mechanics of turbulent mixing layer growth at moderate Reynolds numbers. *J. Fluid Mech.* **63**, 237.
- Yang, X & Thomas, N. H. 1994 Simulation of particle and bubble dispersion in turbulent free shear flows. *Numerical Methods in Multiphase Flows*, ASME-FED 185, 259-268.



(a) Two infinite vortex sheets



(b) Two semi-infinite vortex sheets

Figure 1. Simply ideal flows induced by two infinite vortex sheets.

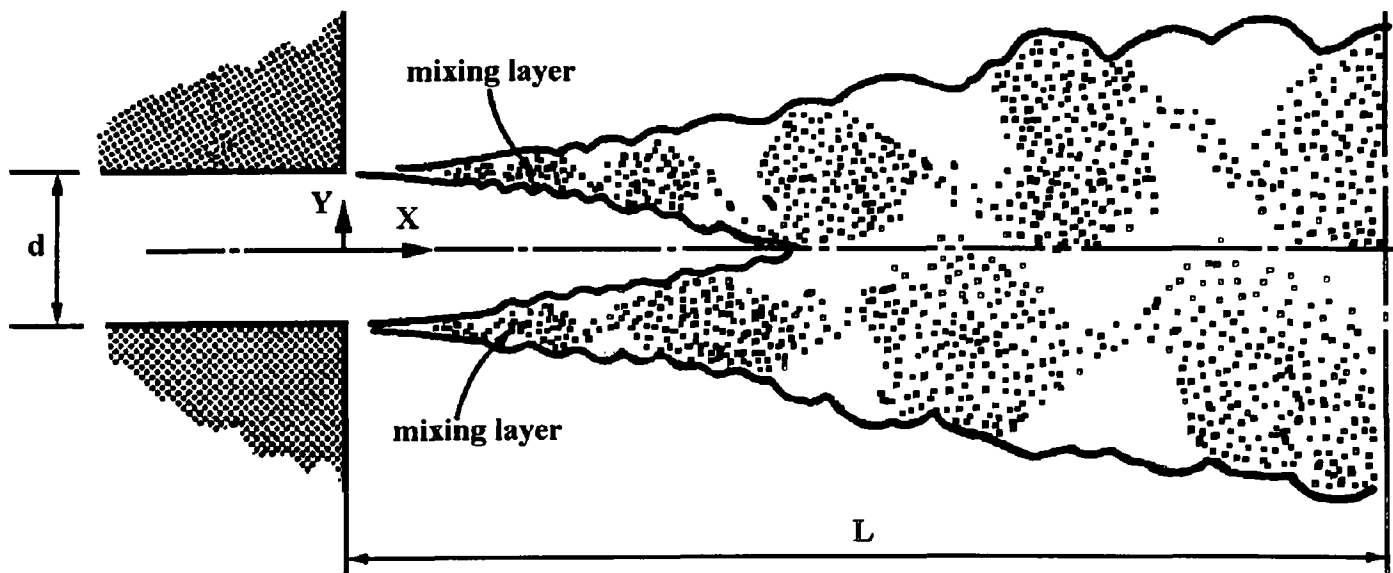


Figure 2. Sketch of discrete vortex simulation of a plane turbulent jet.

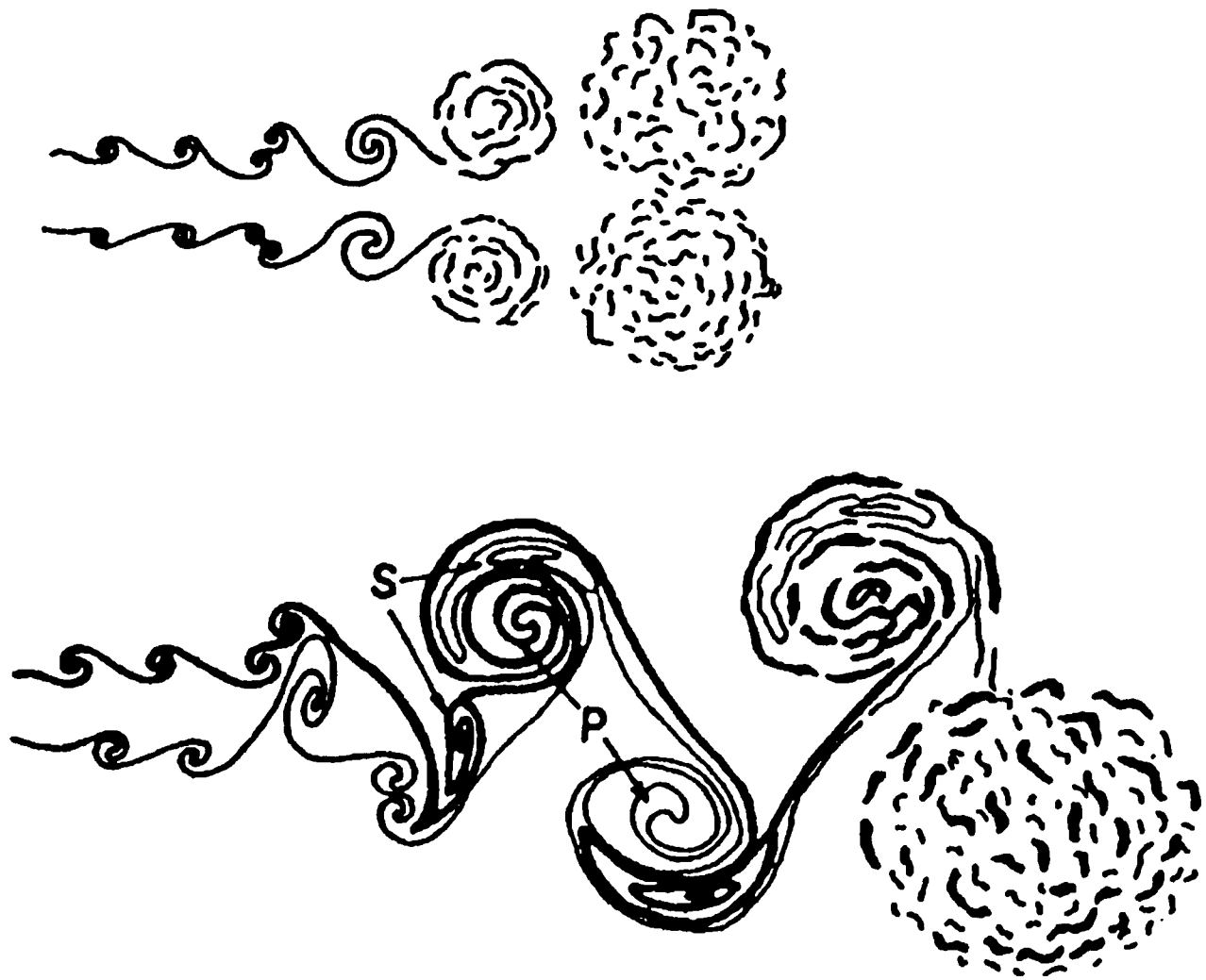
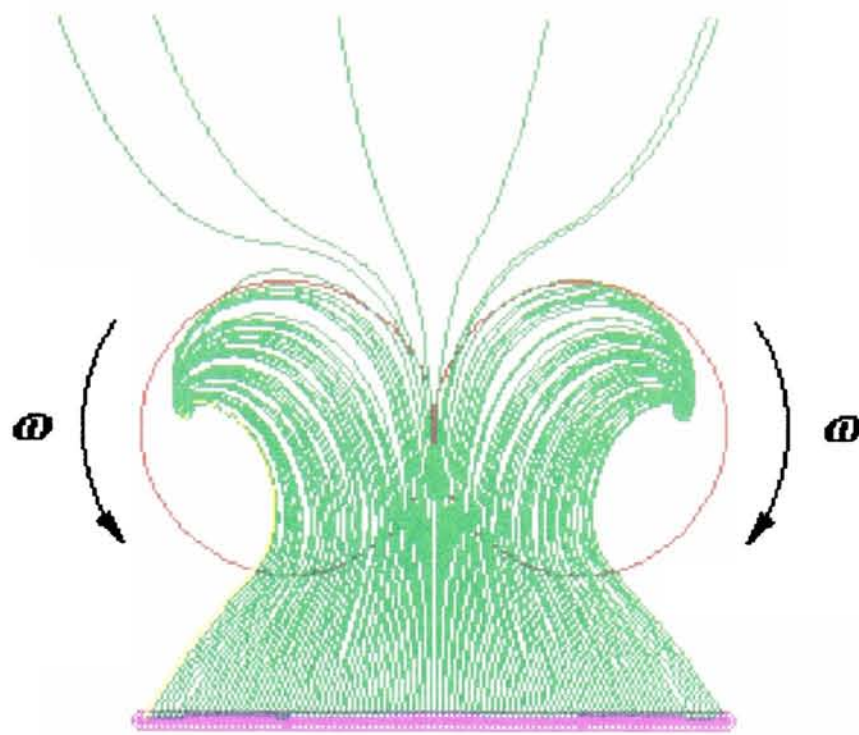
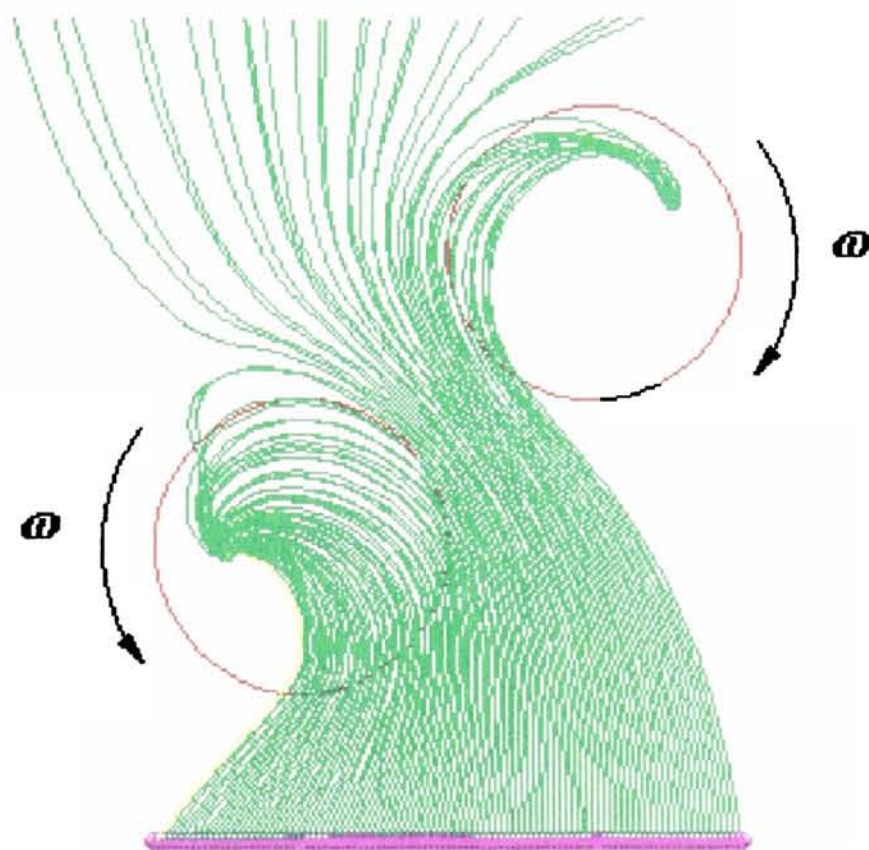


Figure 3. Coherent structure interaction in the near field of a plane jet; (a) top-hat velocity profile; (b) fully developed initial velocity profile. Two distinct modes of vortex formation can be clearly seen from the figure. Taken from Husain *et al.* (1987).

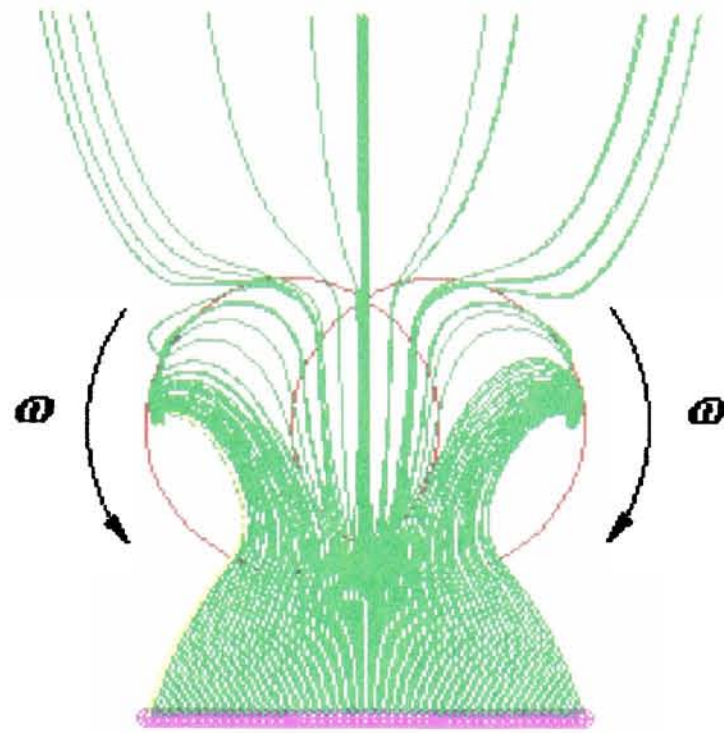


(a)

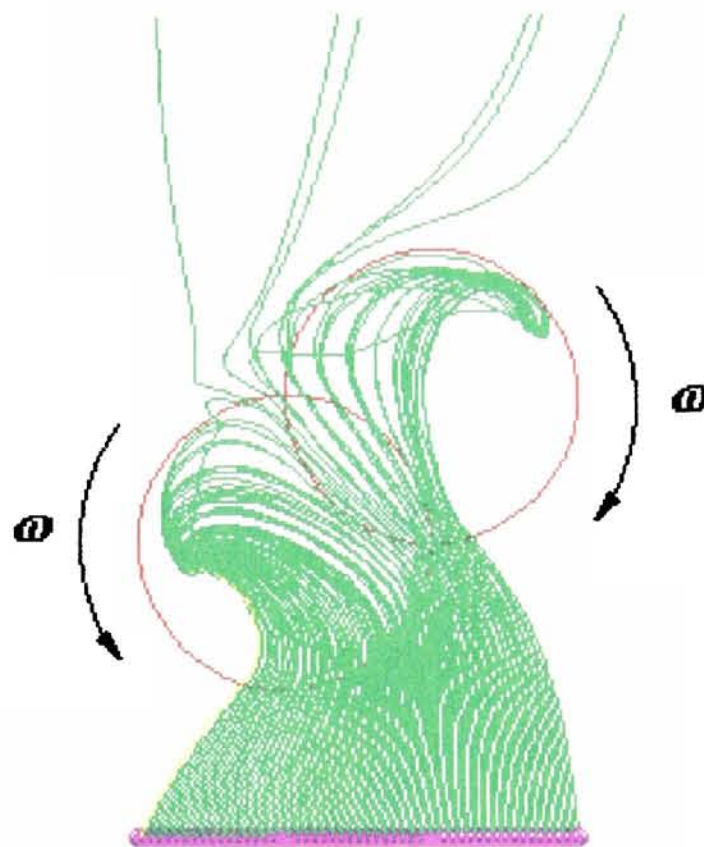


(b)

Figure 4. The trajectories of bubbles trapped by two allocated Rankine vortices. Bubbles were released from 2 radii below the first Rankine vortex. (a) Rankine vortices allocated horizontally; (b) Rankine vortices staggered.



(a)



(b)

Figure 5. The trajectories of bubbles trapped by two allocated Rankine vortices. The two vortices have been partially overlapped. Bubbles were released from 2 radii below the first Rankine vortex. (a) Rankine vortices allocated horizontally; (b) Rankine vortices staggered.

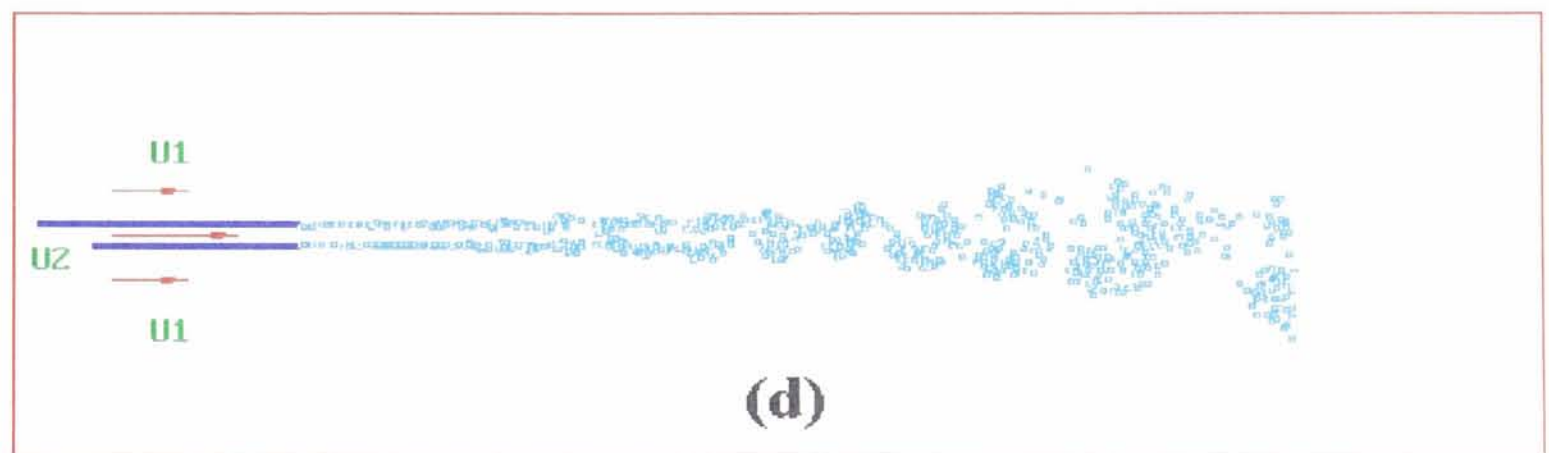
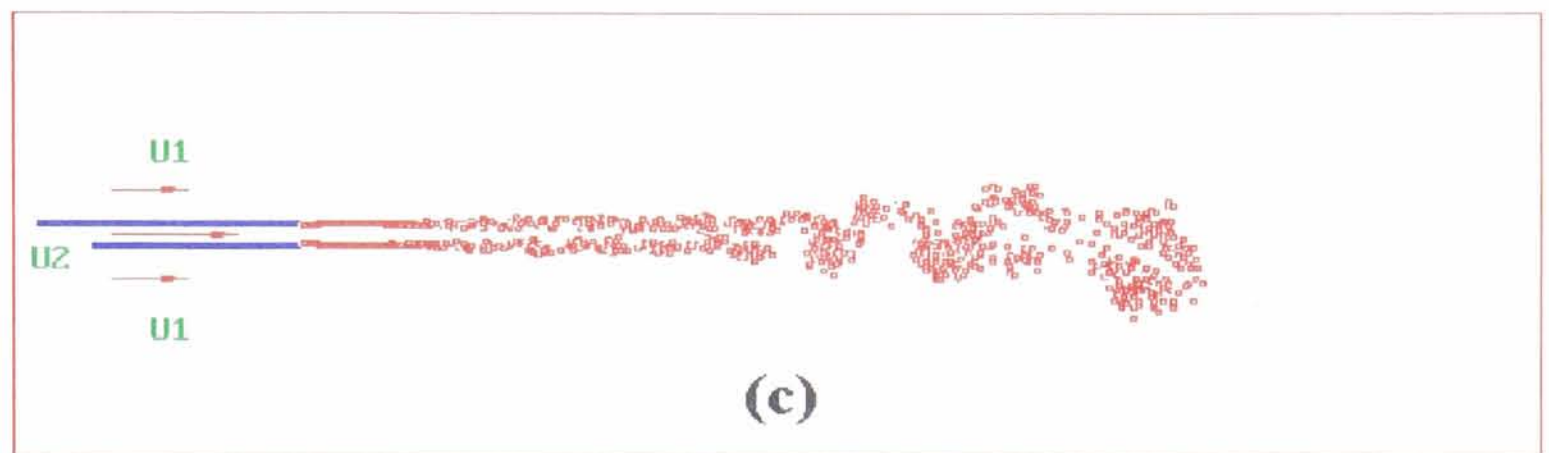
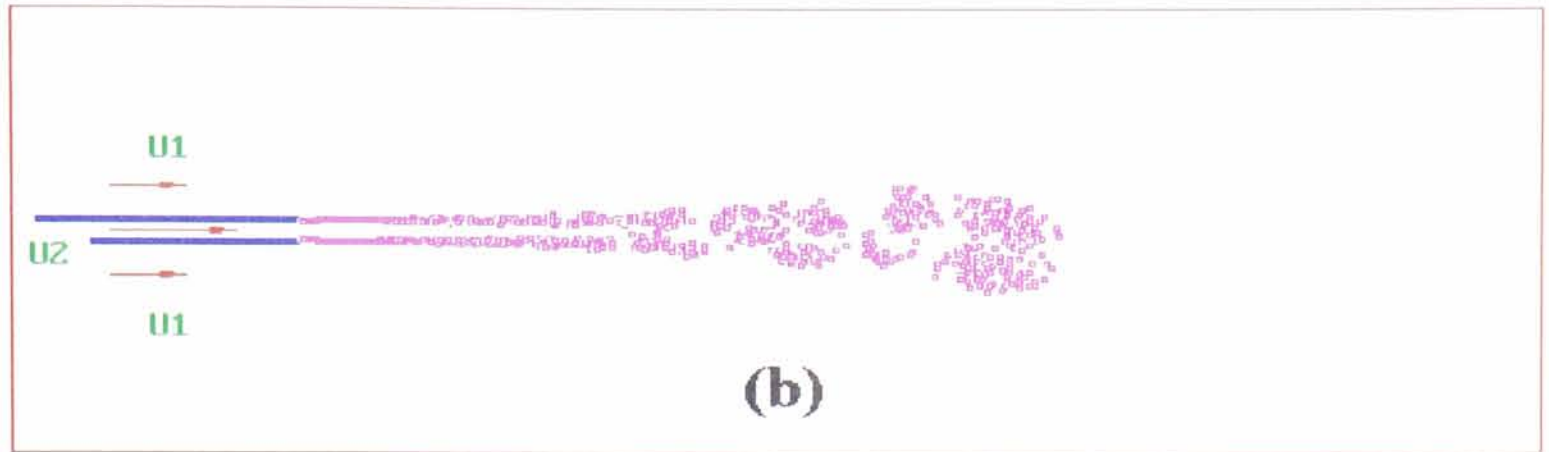
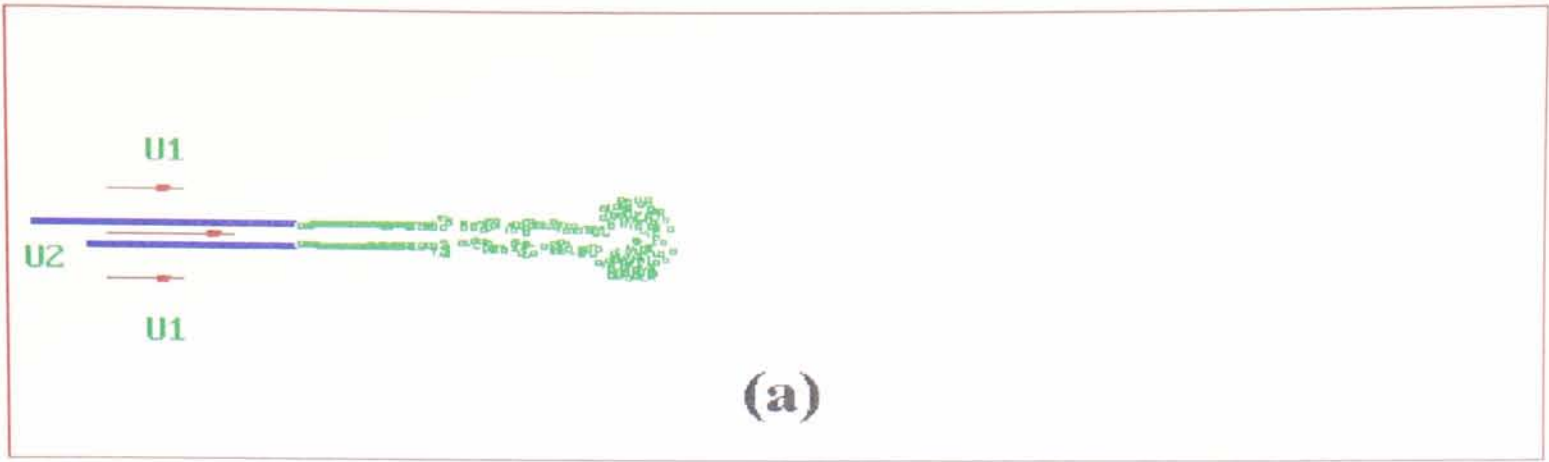


Figure 6. For caption see next page.

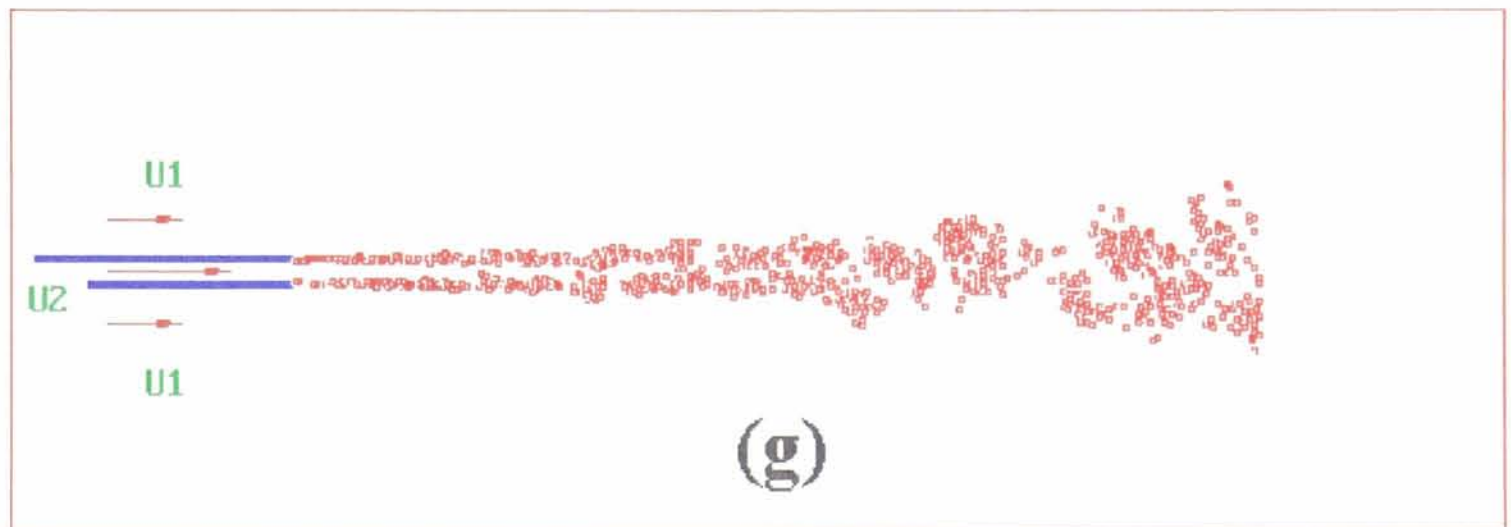
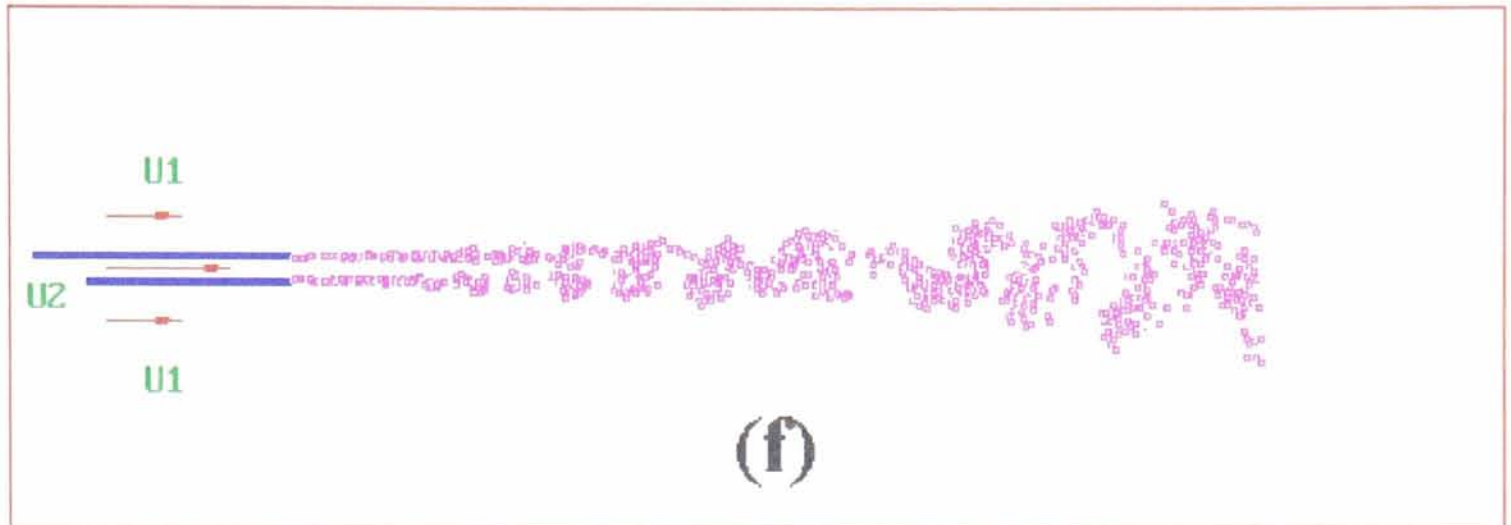
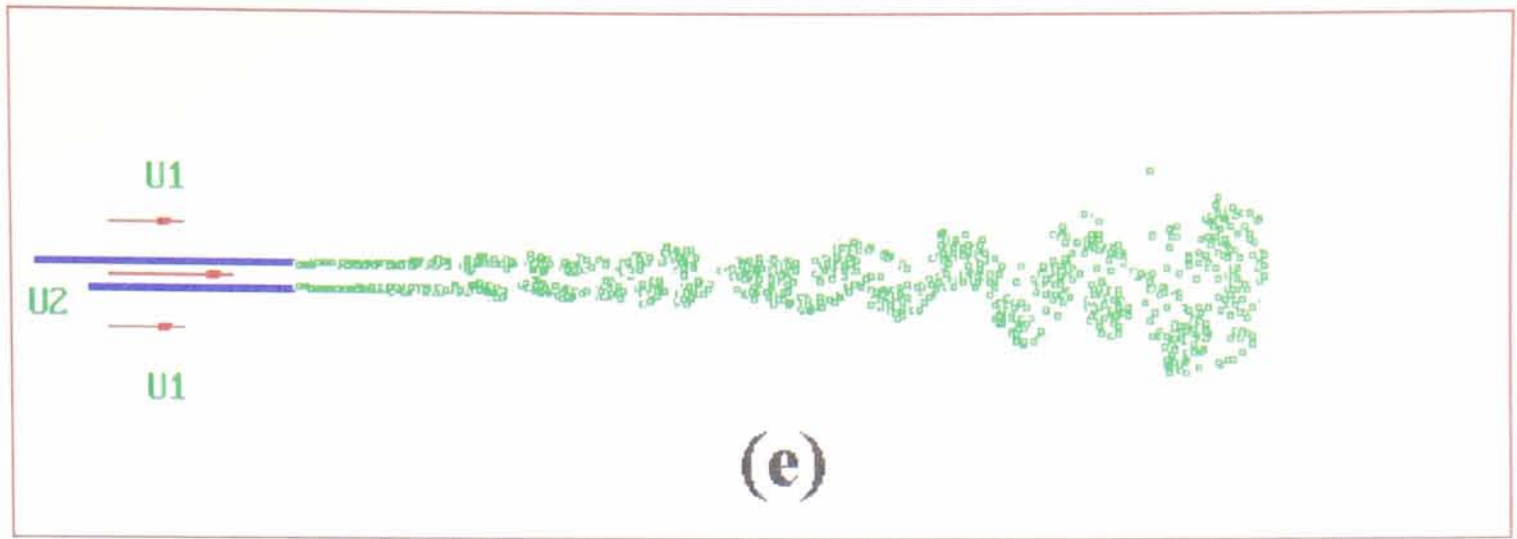


Figure 6. Plane jet development represented by two arrays of discrete vortex filaments: (a) $T=0.5$; (b) $T=1.0$; (c) $T=1.2$; (d) $T=1.4$; (e) $T=1.6$; (f) $T=1.8$; (g) $T=2.0$.

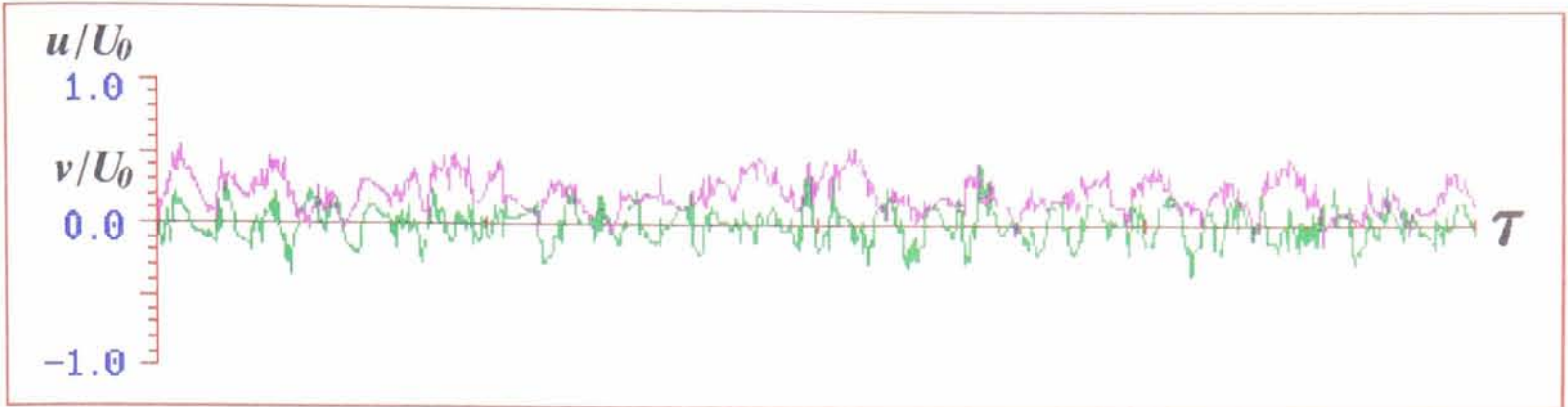


Figure 7. Instantaneous axial and transverse velocity time histories at $X/D=80$ on the centerline of the plane jet. The exit velocity: $U_0=0.3$ m/s. Carrier fluid: water.

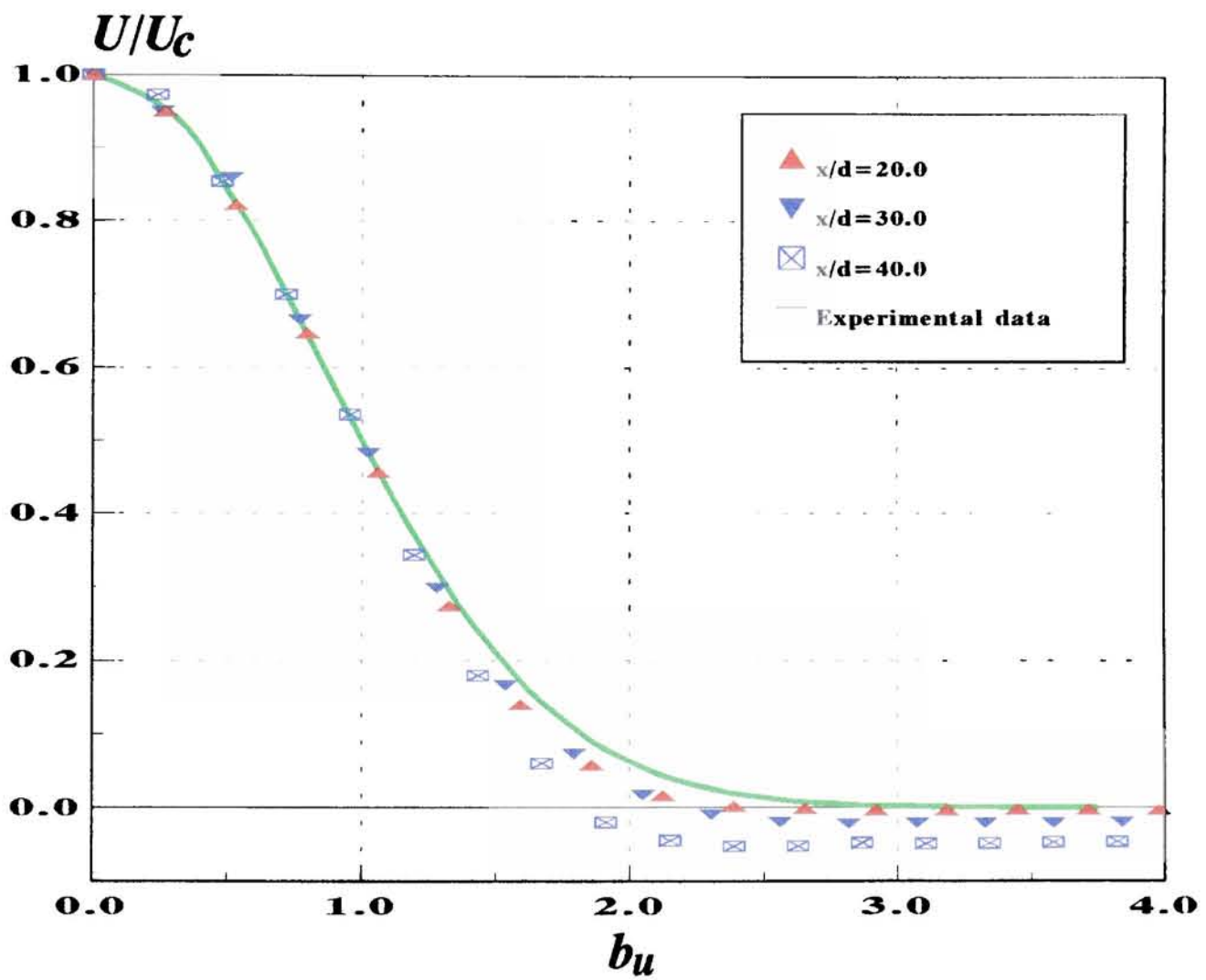


Figure 8. Time-averaged mean axial velocity components and the experimental data fit (Bradbury 1965).

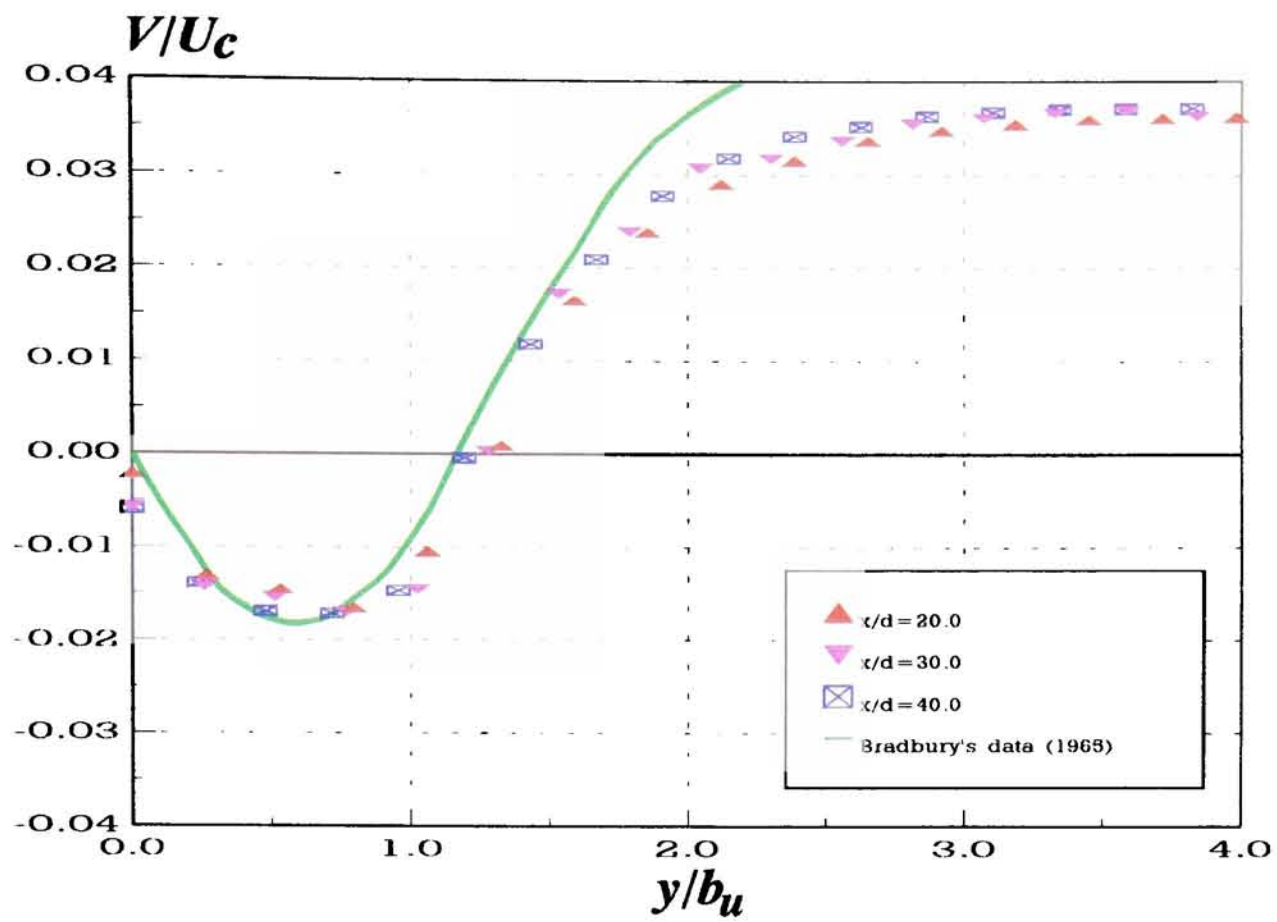


Figure 9. Time-averaged mean cross-stream velocity profiles from numerical simulations and the experimental data fit (Bradbury 1965).

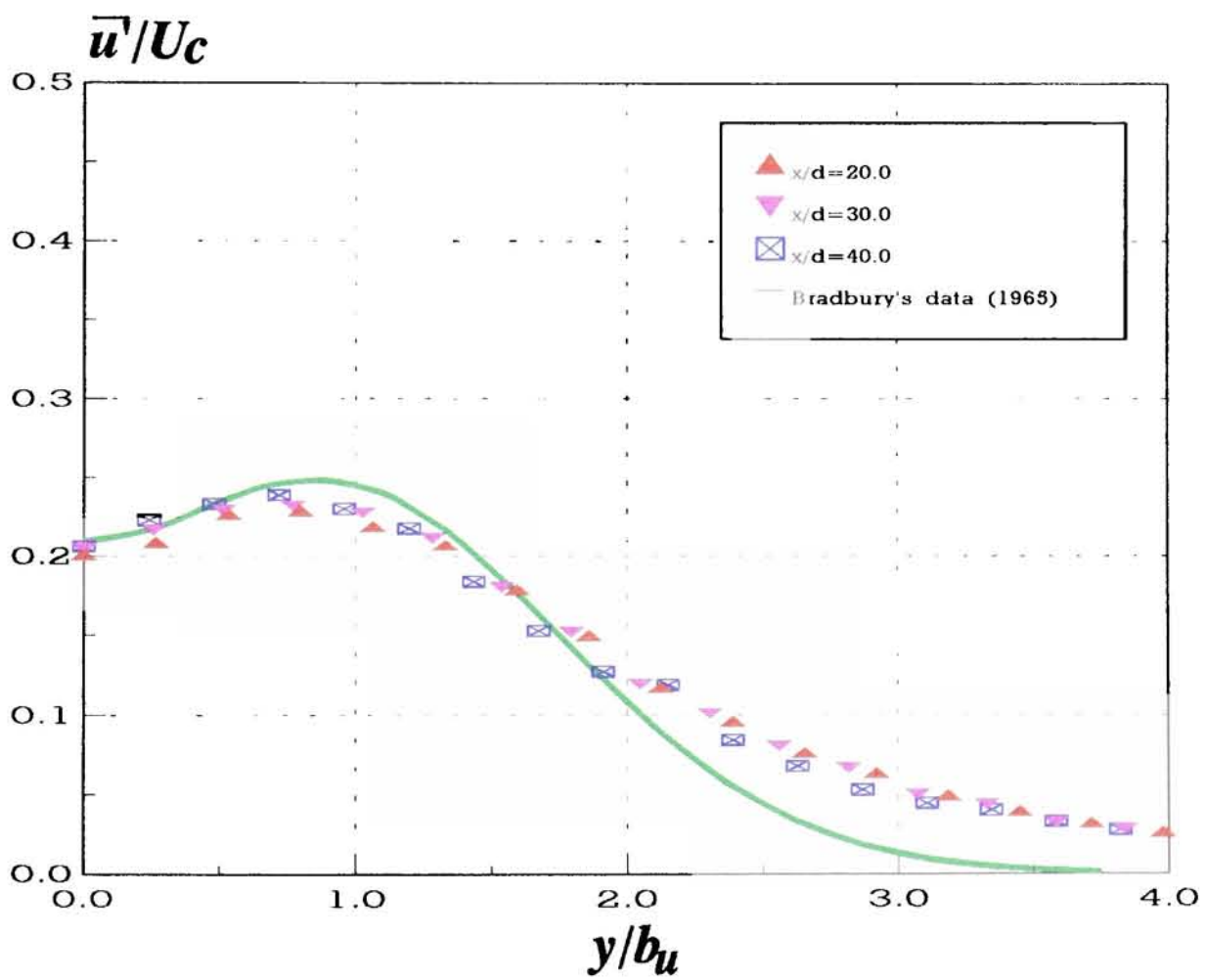


Figure 10. Longitudinal turbulence intensities at different downstream cross-sections and the experimental data fit (Bradbury 1965).

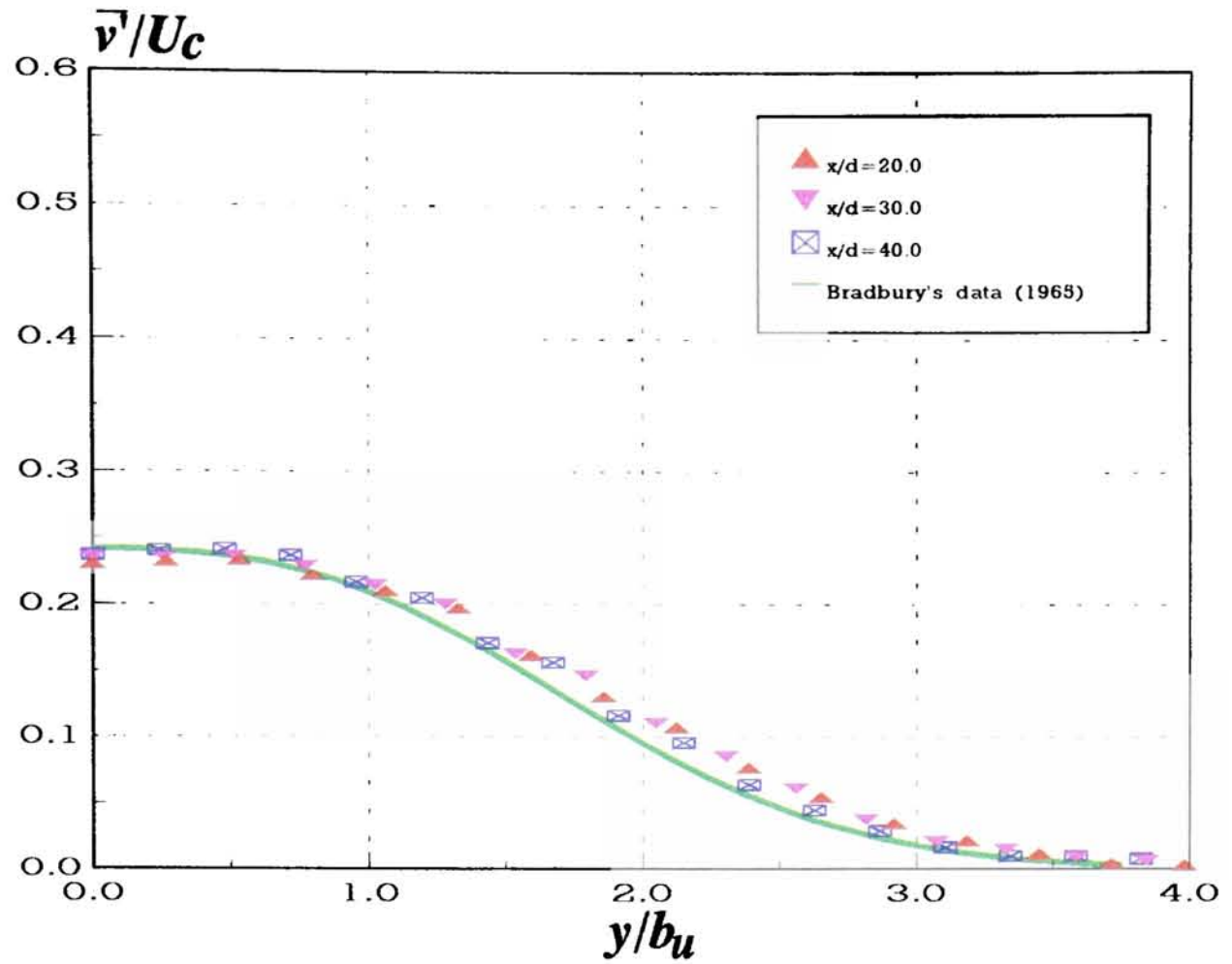


Figure 11. Cross-stream turbulence intensities calculated and the experimental data (Bradbury 1965).

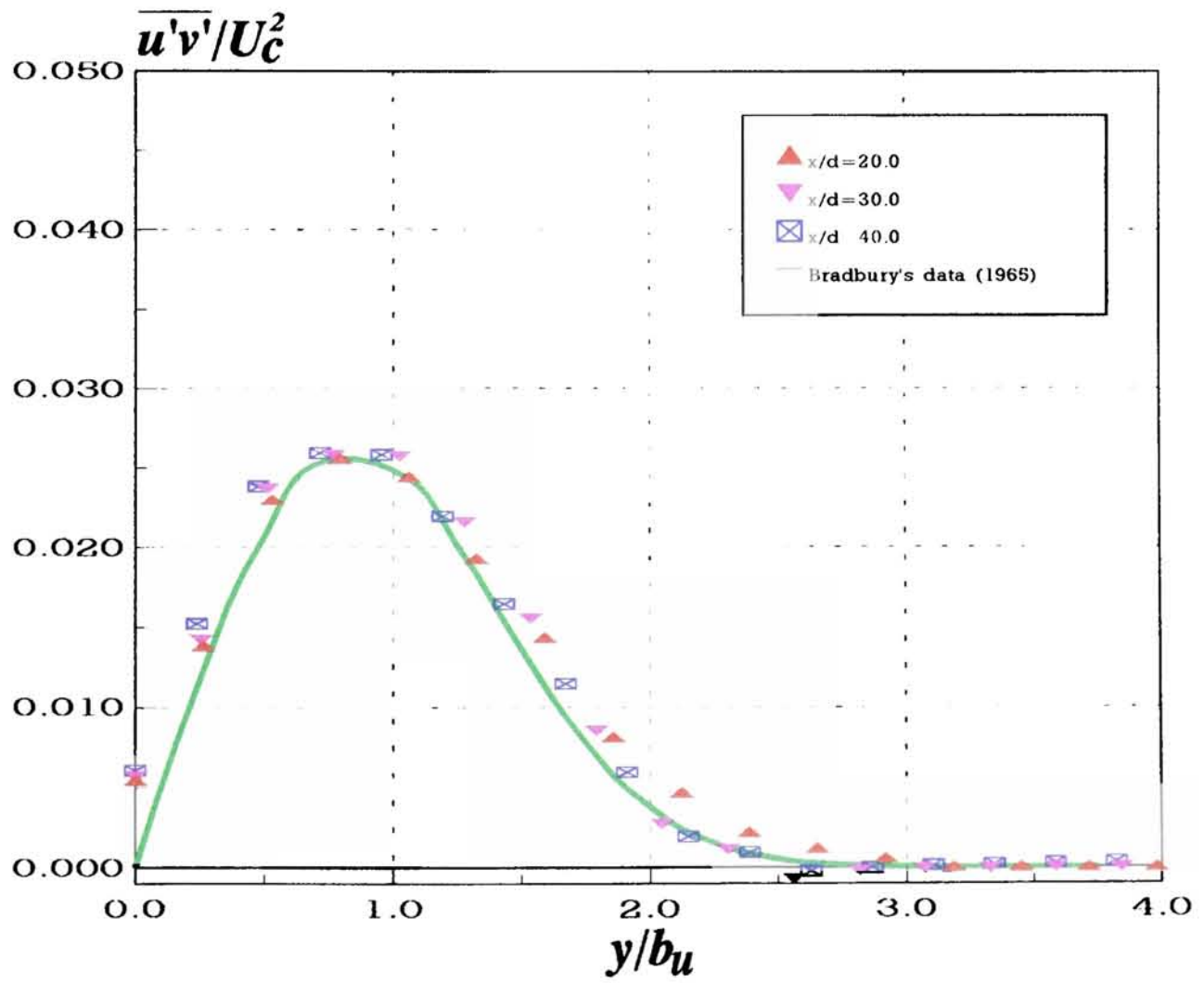


Figure 12. Shear stress profiles at different downstream cross-sections and the experimental data (Bradbury 1965).

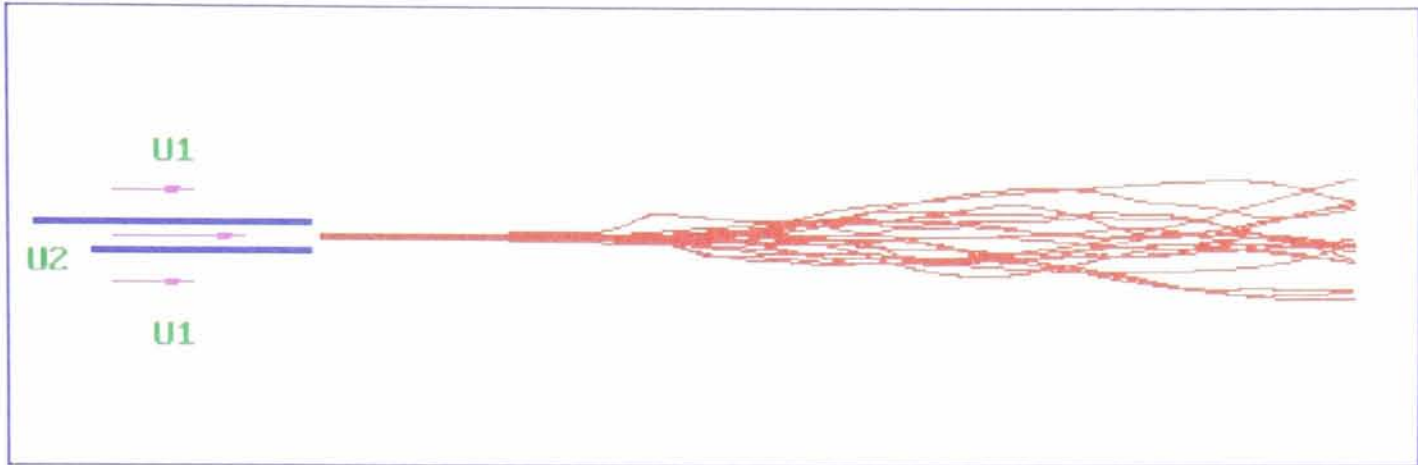


Figure 13. Computer simulation of bubble trajectories in an upflowing turbulent plane jet. Bubbles were released from the centerline of the jet exit for the condition $\Pi=0.02$, $\Gamma=1.5$. Total 400 bubbles were released. For clarity only 20 bubble trajectories were displayed in the figure.

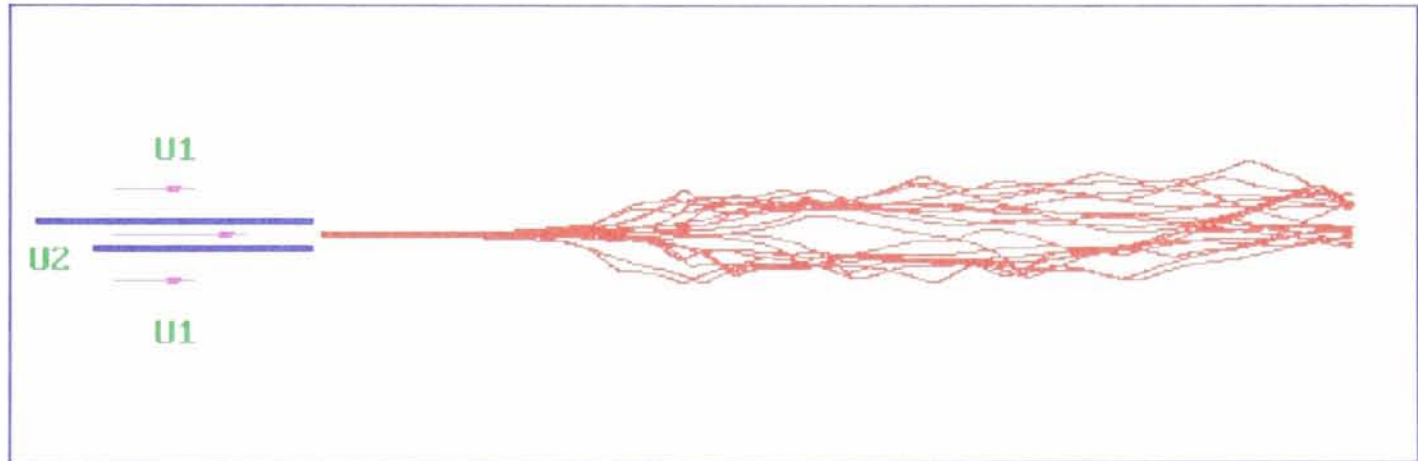


Figure 14. Computer simulation of bubble trajectories in an upflowing turbulent plane jet. Bubbles were released from the centerline of the jet exit for the condition $\Pi=0.05$, $\Gamma=2.5$. Total 400 bubbles were released. For clarity only 20 bubble trajectories were displayed in the figure.

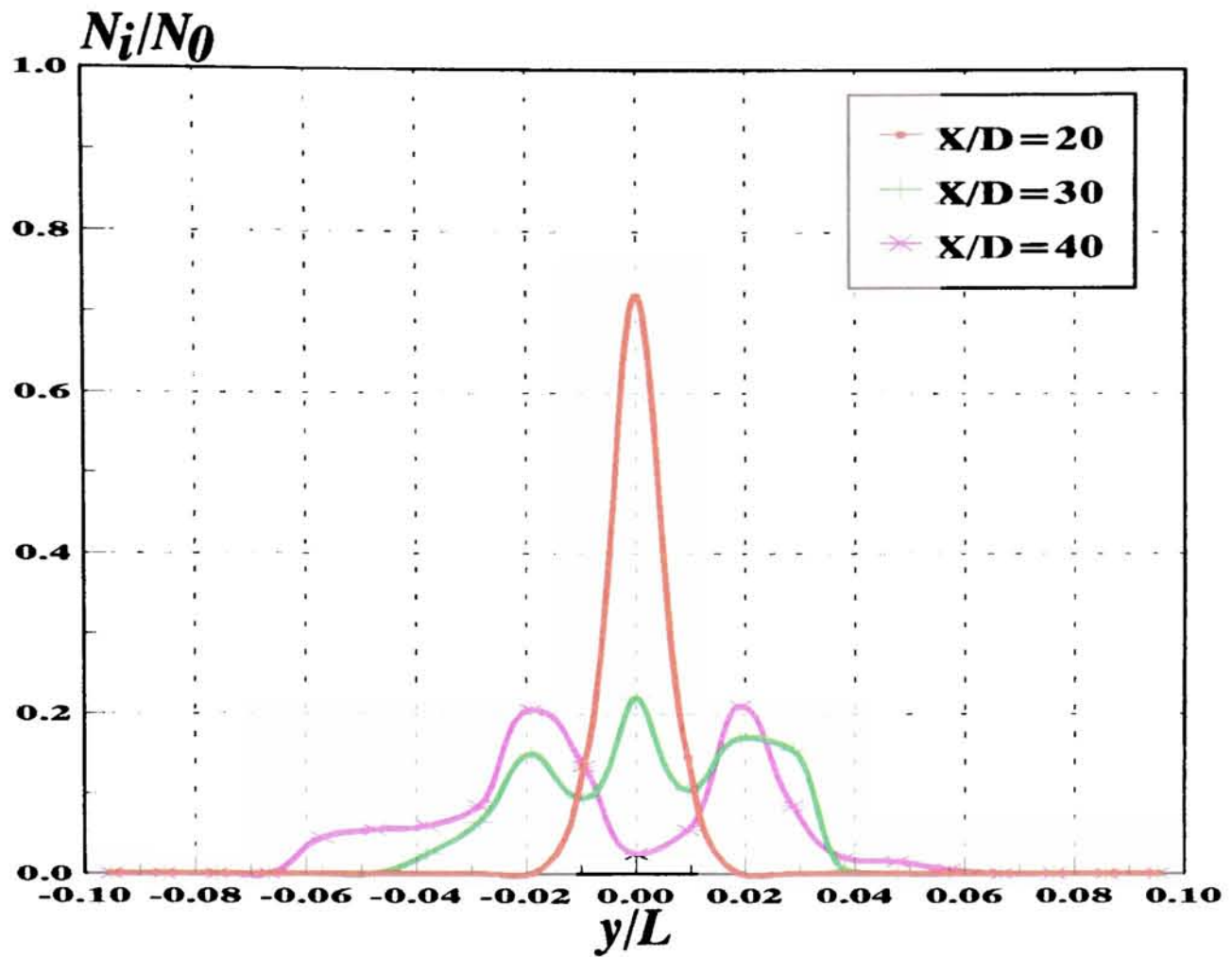


Figure 15. Bubble number fluxes in a vertical, upflowing plane jet, calculated from the bubble trajectory statistics shown in figure 13. ($\Pi=0.02$, $\Gamma=1.5$, $N_0=400$.)

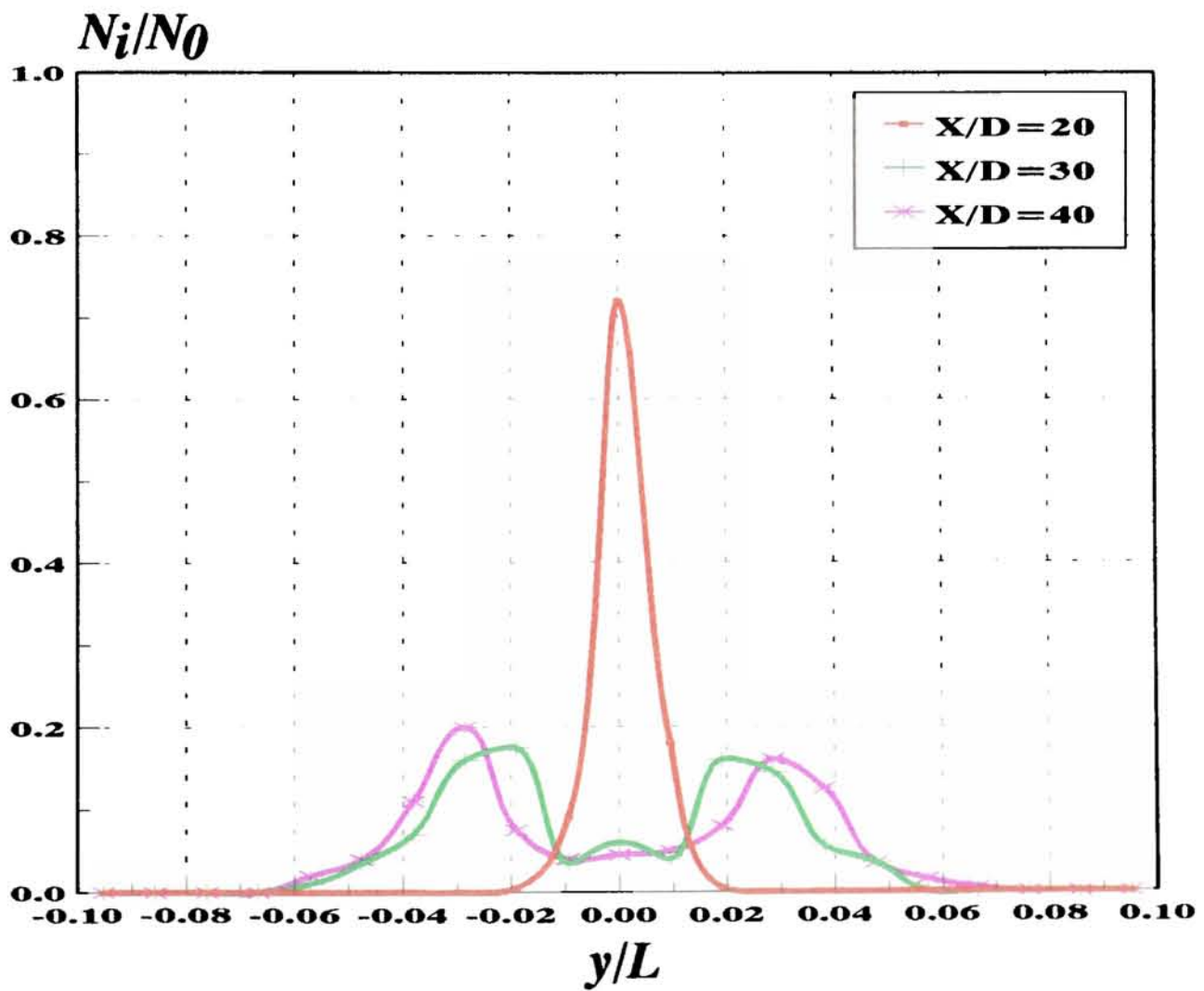


Figure 16. Bubble number fluxes in a vertical, upflowing plane jet, calculated from the bubble trajectory statistics shown in figure 14. ($\Pi=0.05$, $\Gamma=2.5$, $N_0=400$.)

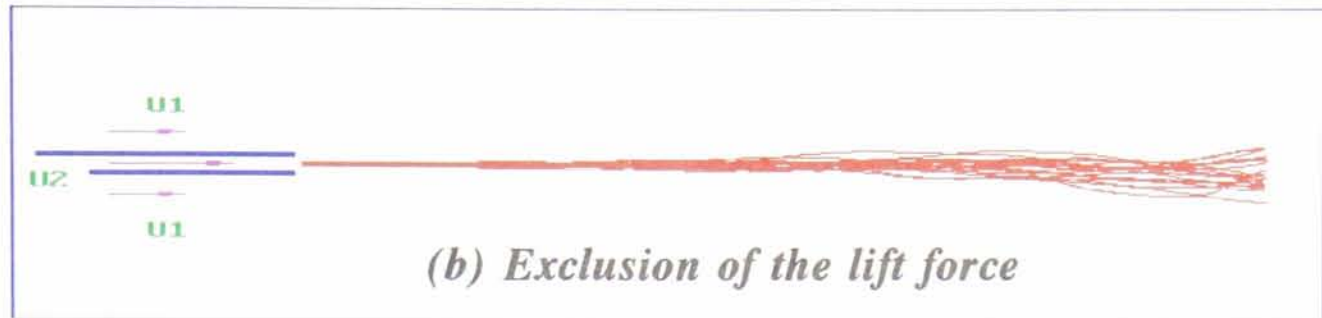
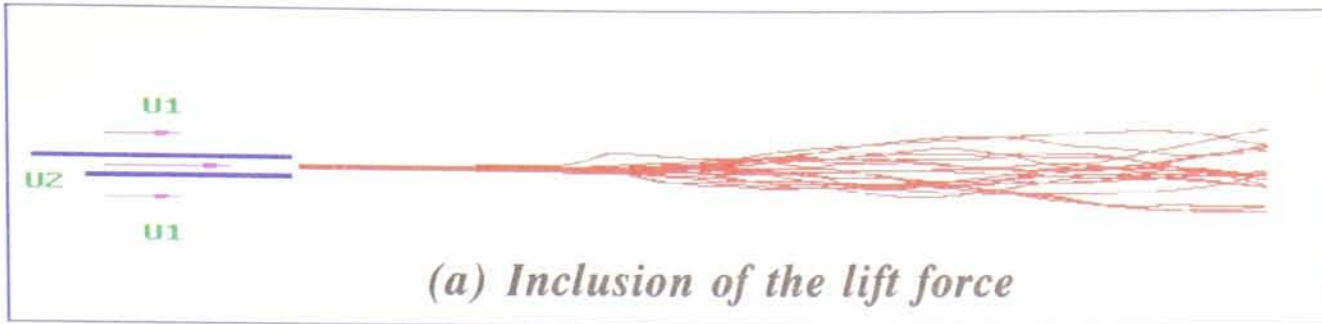


Figure 17. Comparisons of two bubble trajectory calculations with and without inclusion of the lift force. ($\Pi=0.02$, $\Gamma=1.5$, $N_0=400$.)

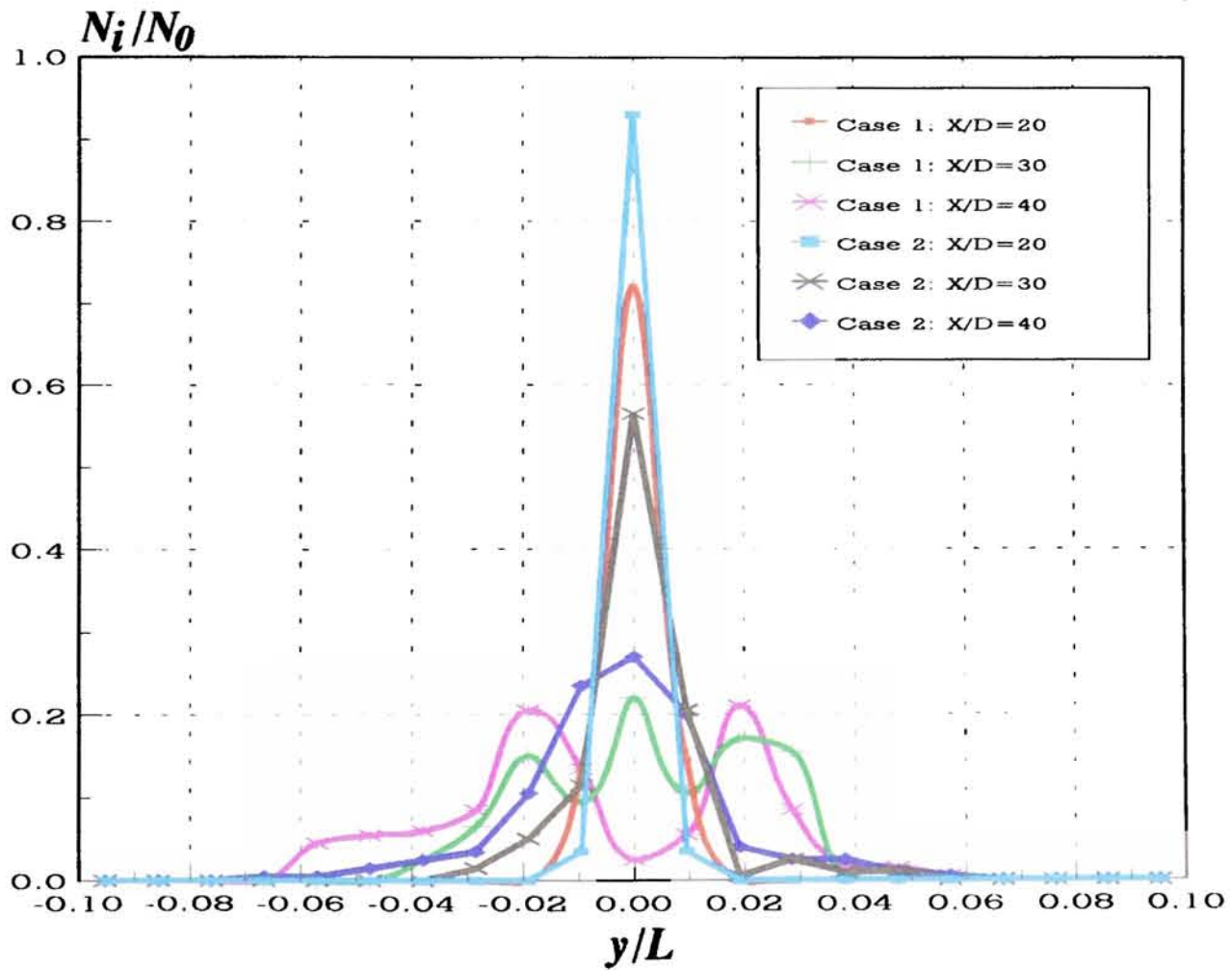


Figure 18. Comparisons of bubble number fluxes in vertical, upflowing plane jets, with and without inclusion of the lift force ($\Pi=0.02$, $\Gamma=1.5$, $N_0=400$). Case 1: Inclusion of the lift force; Case 2: Exclusion of the lift force.

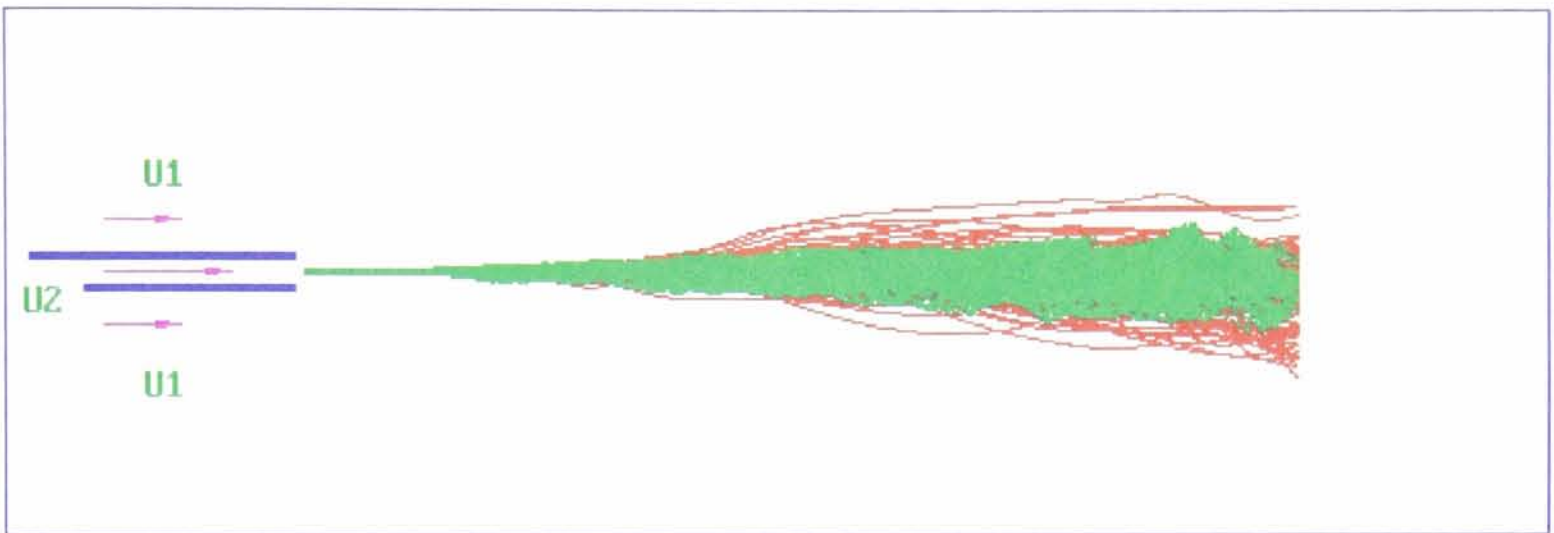


Figure 19. Computer simulation of bubble and tagged fluid particle trajectories in a vertical, upflowing plane jet. Both bubbles and tagged fluid particles (total 400 for both) were released from the same location at the centerline of the jet exit for the condition $\Pi=0.02$, $\Gamma=1.5$.

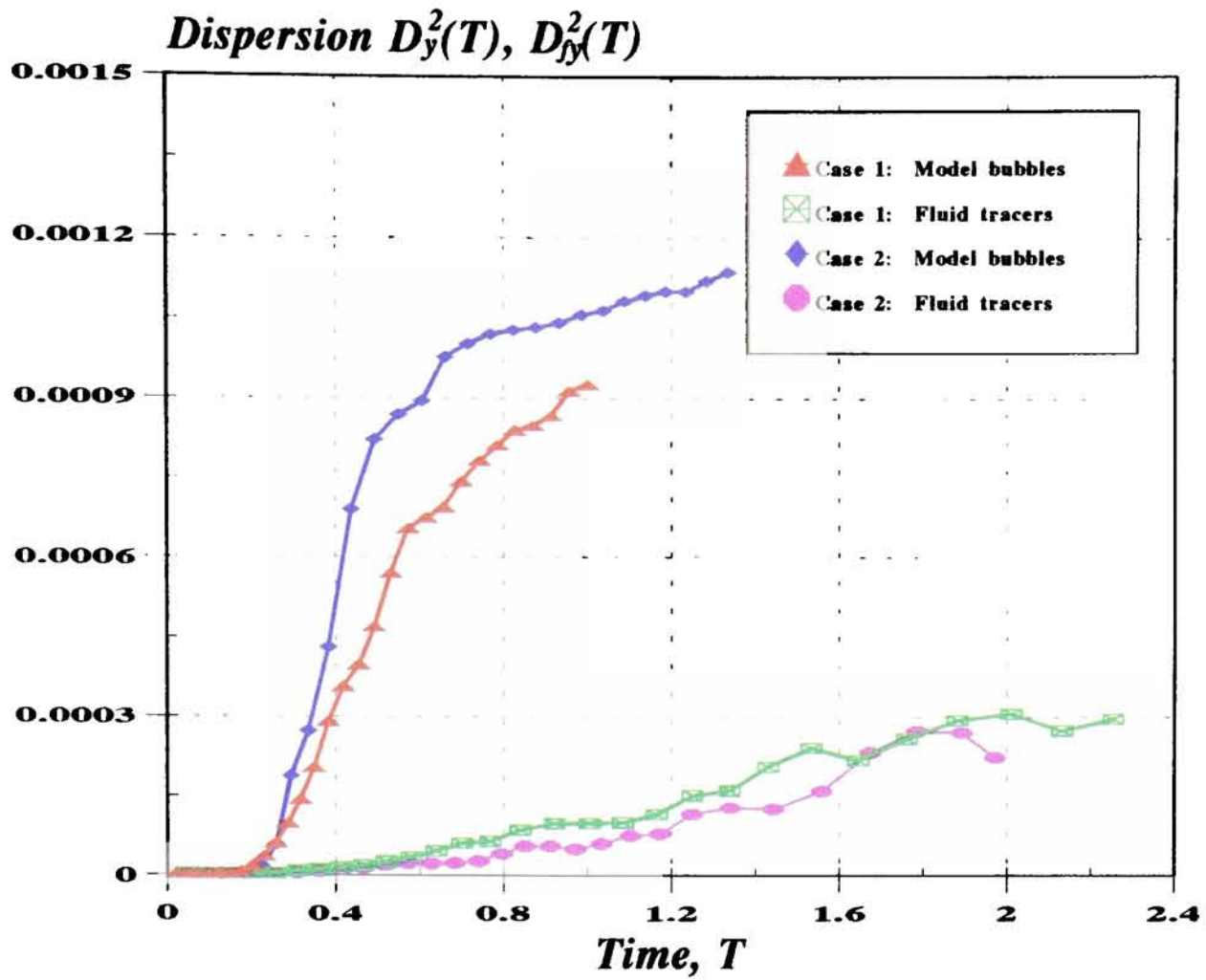


Figure 20. Ensemble-averaged Lagrangian prediction of bubble transverse dispersion in a vertical, upflowing plane jet. (Case 1: $\Pi=0.02$, $\Gamma=1.5$; Case 2: $\Pi=0.05$, $\Gamma=2.5$.)

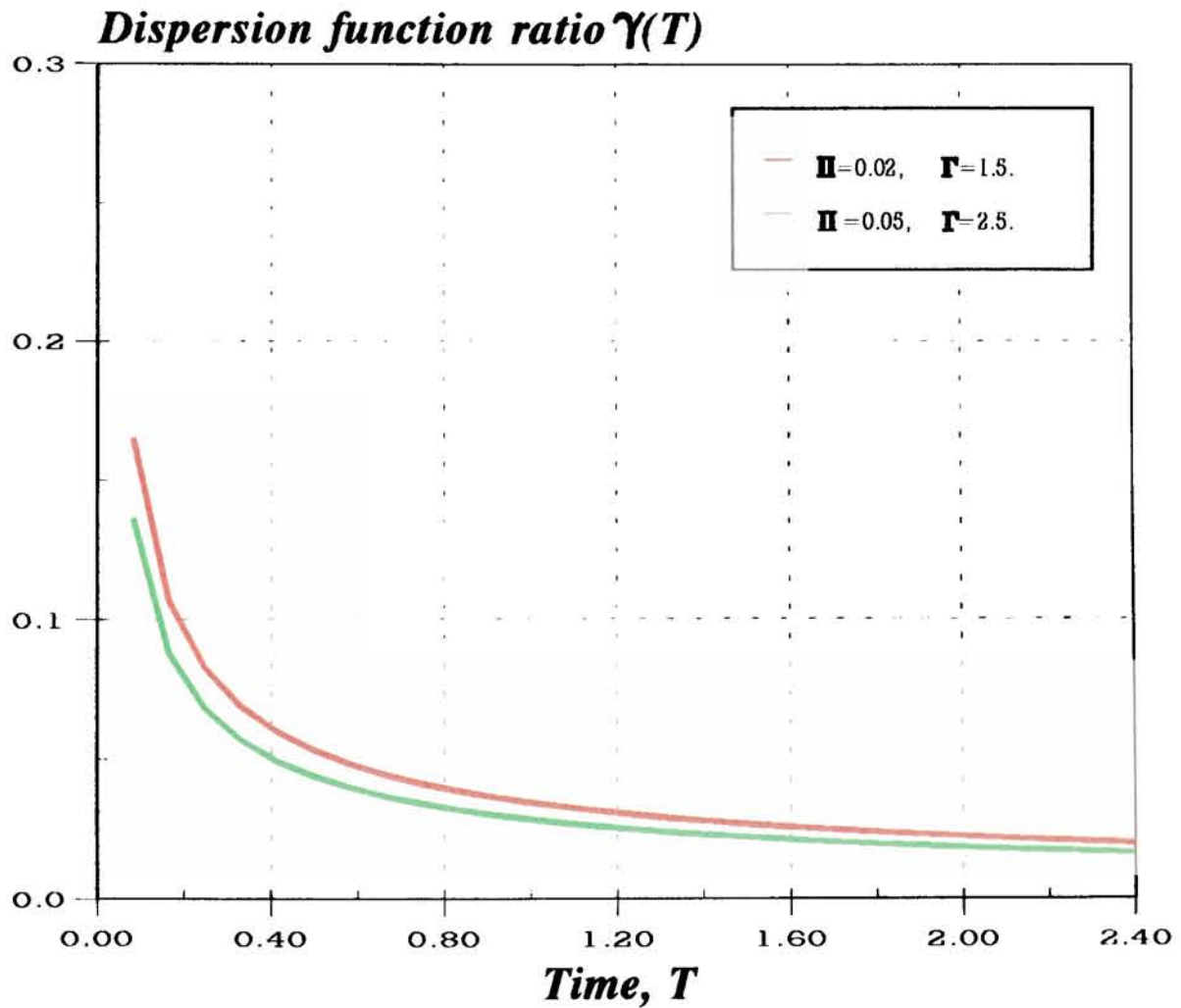


Figure 21. The ratio between the dispersion functions (bubbles and tagged fluid particles) with time in a vertical, upflowing plane jet. Results were obtained from the least-square fitting for the data shown in figure 20.

CHAPTER 6: COUPLING OF FLUCTUATING VORTICITY AND VOIDAGE FLUXES

SUMMARY

The central role played by large scale eddies in turbulent free shear dispersion of particles and bubbles is now well documented, and our earlier demonstrations have shown that local dispersed phase (voidage) transport is highly correlated with transient vorticity. Here we seek to quantify the couplings between the fluxes of fluctuating vorticity and bubbles or particles, utilising the simulations described earlier and following the methods of Sene *et al.* (1994), that is by sampling the Lagrangian trajectories at different positions within an Eulerian frame. Our results show that the correlation between the fluctuation fluxes is higher in the core region of the mixing layer for bubbles, but lower for particles, as compared with the correlation along the edges of the mixing layer for particles. This finding is both consistent with and quantifies previous results (Sene *et al.* 1994; Martin & Meiburg 1994) on trapping confinement of bubbles and centrifuged expulsion of particles, the latter hovering around the edges of the mixing layer.

1 INTRODUCTION

Observations of the motions of bubbles in air-entraining flows (Thomas *et al.* 1983; Chapter 1, figure 15) and in bluff-body wake flows (Hulin *et al.* 1982) first revealed the phenomenon of bubbles clustering within large eddies in free shear layers. Simulations and analysis (Sene *et al.* 1994) have provided a good understanding of the basic phenomena shown here (e.g. figure 1, taken from the present simulations). Particles denser than the carrier fluid in such free shear layers preferentially accumulate around the eddies (Crowe *et al.* 1993; Eaton & Fessler 1994), but do not enter their cores.

The physical cause of scavenging and retention of bubbles by coherent structures is the radial pressure gradient which they induce in their external irrotational flows (Sene *et al.* 1994). Once a bubble has been trapped within an eddy, its motion undergoes large scale inertial drag, buoyancy and vorticity forces and is also subject to dispersion by small-scale interior turbulence (Hussain 1986; Sene *et al.* 1994). Because such coherent structures are invariably manifested as individual travelling eddies with significant spacing, their passage and associated transport of trapped bubbles/particles displays considerable Eulerian intermittency.

To some extent, this behaviour is modulated by outwards dispersion due to turbulence within the large eddies. Sene *et al.* (1994) used a diffusion coefficient K_{pr} , distributed symmetrically within each eddy (each eddy taken as being circular cross-section for simplicity). As eddy size can be roughly equated to vorticity thickness δ of the mixing layer, and the latter is proportional to the downstream distance x , this dispersion coefficient can be written as

$K_{pr}/\Delta U = xh(r/x)$, where h is an unprescribed function of r/x . Bubble concentration C_T inside the coherent structure is then given by $U_{pr}C_T = K_{pr}\partial C_T/\partial r$, where U_{pr} is radial migration flux velocity. Clearly this approach spells out the significance of local travelling vorticity and Sene *et al.* (1994) further introduced an intermittency function of fractional time associated with eddy passage to relate this Lagrangian concentration to the Eulerian concentration measured with a fixed probe. Lázaro & Lasheras (1989, 1992) measured particle statistics using laser attenuation to estimate the correlation between the turbulent velocity field and the particle dispersion expressed as $\overline{\xi u}$ (ξ is the fluctuation attenuation). They found that $\overline{\xi u}$ can be related to the particle turbulent transport $\overline{\alpha_p u_p}$. Here α_p is the local particle volume fraction and u_p is the particle velocity.

A useful way of thinking about this behaviour is in terms of the correlation dimension defined as $D_{cor} = \lim_{l \rightarrow 0} (1/\log l) \log \sum p_i^2$, where l is a spacing parameter and p_i is the probability that the spacing between two particles is less than l . The correlation dimension can then be recovered by graphing the correlation integral ($\sum p_i^2$) as a function of the length scale l on a log-log plot and taking the slope of the resulting curve. It was introduced by Grassberger & Procaccia (1983) and applied to particle dispersion in mixing layers and later extended to a bluff body wake by Tang *et al.* (1992). The "correlation dimension" measures the extent to which particle "focusing" arises and Tang *et al.* (1992) argued it provides a quantitative characterisation of this behaviour. They provided some typical examples of the correlation integral as a function of distance along a plane mixing layer and a wake at different Stokes numbers (figure 2). The minimum correlation dimension was found to occur for a Stokes number of the order of unity, in contrast to larger values for other values. Physically this means that dispersion patterns are maximally organised for particle time scales close to the

Lagrangian time scale of large-scale eddies, such that for larger and shorter particle time scale, the correlation dimension increases, representing more disorganised dispersion patterns.

In seeking to clarify and extend these existing pictures of the correlation between bubble or particle number flux fluctuations and vortex number flux fluctuations, we have in mind eventually to consider vorticity transport formulation for Eulerian transport modelling of two-phase shear flows. In the next section, we present the detailed numerical results, showing how the local vorticity fluctuation influences bubble and particle distribution in the flow. A brief discussion about the physical implication of such correlations is presented in section 3, followed by a summary of the main findings and the conclusions which appears in section 4.

2 VOIDAGE-VORTICITY CORRELATION FOR DISPERSIVE TRANSPORT

As pointed out by Hussain (1986), turbulent free shear flows are characterized by high levels of vorticity fluctuation. We wish to evaluate the extent to what concentration correlates with vorticity, i.e. $\overline{c\omega}$, extracting this information from the statistics of our simulation for the plane mixing layer. Briefly then, the flow configuration is two-dimensional streamwise in the x direction with gravity acting in the same direction, and the flow is represented using the discrete vortex model described in chapters 3 and 4. The shear velocity scale ΔU is the velocity difference across the mixing layer with δ denoting the vorticity thickness which is proportional to x (Townsend 1976), so we choose x as the reference length parameter. Numerically, all velocities are scaled on the shear velocity ΔU and all lengths on L , the length of the computational domain. The equation of motion for the discrete phase possesses

two key parameters Π and Γ , the former representing the ratio of inertia to buoyancy, the latter inertia to drag, together with the mass ratio γ .

Bubbles were introduced into the flow at a location close to the origin of the mixing layer ($\Delta t=0.003125$ between each insertion). Figure 3 shows their subsequent locations and progressively we see how they are trapped in the eddies (the instantaneous vorticity field) at increasing time (for $\Pi=0.5$ and $\Gamma=10.0$). Shown in figure 4 are details of the bubble locations and the vorticity contours corresponding to a particular eddy located at $0.55L < x < 0.85L$ ($t=3.525$). In contrast to this picture, figures 5 and 6 show the same sequence (same Π and Γ), but with particles of mass ratio $\gamma=1920.0$. Notice that we have employed the same terminal velocity V_T as the bubble for particle trajectory calculation. The particles clearly accumulate around the edges of the eddy, preferentially displaying braid streaks on the high speed side of the mixing layer, consistent with results reported by other workers (e.g. Wen *et al.* 1992; Lázaro & Lasheras 1989). To more clearly illustrate the contrast between bubble trapping and particle centrifuging, figure 7a and 7b show local concentration contours and vorticity contours for both bubbles and particles. The bubble or particle numbers falling within a sampling bin are normalised by the total number of bubbles or particles falling within a specified range $0.55L < x < 0.85L$. Contour levels are drawn on the plot, corresponding to normalised bubble or particle number densities. These contour plots show that the regions of the highest bubble concentration lie at the centre of the vortex structure, as can be seen from figure 7a, while the highest particle concentrations lie along the edge of the high speed side of the vortex structure (figure 7b).

3 CORRELATIONS BETWEEN BUBBLE OR PARTICLE NUMBER FLUX AND VORTICITY

In order to assess the correlation between concentration transport and vorticity as instantaneous fluxes, five sampling stations ($x=0.5L, 0.6L, 0.7L, 0.8L$ and $0.9L$) were selected; each with N rectangular bins, counting the number $n_{b_{i,j}}(t)$ of bubbles or $n_{p_{i,j}}(t)$ of particles and the number $n_{v_{i,j}}(t)$ of point vortices falling the bin for $i=1, M$, and $j=1, N$. Here M is the number of sampling stations. Care has to be taken in selecting appropriate size insofar as the bins must be small enough to resolve the structure yet large enough to achieve convergence with a reasonable time. Taking both constraints into account, the number of bins was taken as 6. The layout of sampling bins is shown in figure 8.

Figure 9 shows the time record of the number of local bubble and point vortices in the sampling bin located at $x=0.8L$ and $y=0.0147L$. It clearly demonstrates that the transport of bubbles is phase-locked with that of the vorticity such that the dynamics of the latter suffices to characterise that of the bubbles. Contrast figure 10 showing particle counting, where there is essentially an inverse, anti-phase locking - as indeed was portrayed in the snapshot picture of figure 6.

The ensemble-averaged number of bubbles $\bar{n}_{b_{i,j}}$ or particles $\bar{n}_{p_{i,j}}$ passing through the bin around $y_{i,j}$ is given by

$$\bar{n}_{bij} = \frac{1}{N_T} \sum_{k=1}^{N_T} n_{bij} \quad \text{or} \quad \bar{n}_{pij} = \frac{1}{N_T} \sum_{k=1}^{N_T} n_{pij} \quad (1)$$

where N_T is the total number of sampling time steps during the whole sampling time. The correlation between the local bubble or particle number flux and the local point vortex number flux fluctuations at this y location is then given by

$$\overline{n_{bij}n_{vij}} = \frac{1}{N_T} \sum_{k=1}^{N_T} n_{bij}n_{vij} \quad \text{or} \quad \overline{n_{pij}n_{vij}} = \frac{1}{N_T} \sum_{k=1}^{N_T} n_{pij}n_{vij} \quad (2)$$

With the available data, this quantity can give insight into the relation between the vorticity field and the dispersive transport response, which is related to the dispersive transport by the coherent vorticity $\overline{\alpha \omega}$. We can thus introduce a temporal cross-correlation coefficient

$\rho_{n_{bij}n_{vij}}$, defined as

$$\rho_{n_{bij}n_{vij}}(\tau) = \frac{\overline{n_{bij}(t)n_{vij}(t+\tau)}}{\overline{n_{bij}(t)}^2 \overline{n_{vij}(t)}^2} \quad \text{or} \quad \rho_{n_{pij}n_{vij}}(\tau) = \frac{\overline{n_{pij}(t)n_{vij}(t+\tau)}}{\overline{n_{pij}(t)}^2 \overline{n_{vij}(t)}^2} \quad (3)$$

The correlations $\overline{n_{bij}n_{vij}}$ and the autocorrelations $\overline{n_{vij}n_{vij}}$ with time delay $\tau=0$ for bubbles along the cross-stream coordinate are shown in figures 11a and 11b while the correlations $\overline{n_{pij}n_{vij}}$ with time delay $\tau=0$ for particles are shown in figures 12. We notice from figures 11a and 11b that the cross-correlation achieves a maximum inside the mixing layer though offsetting from the coordinate $\eta=0$ whereas the autocorrelation for local vorticity flux with time delay $\tau=0$ presents the same trend. It can be seen from these figures that both correlations are very similar. For particles, figure 12 shows that the correlation attains larger values at the edge of the high speed side of the mixing layer, but smaller values around the centre of the mixing layer, consistent with the earlier snapshot picture of figure 6.

4 DISCUSSION

4.1 Effect of Inertial Force on Bubble and Particle Crossing Trajectories

Clearly, the local bubble flux is highly correlated with local fluctuating vorticity flux and this preferential component as compared with the fluid elements is due to the bubbles' low effective mass so that they have greater response to the sub-pressures associated with the vortex motions, resulting in the 'crossing trajectories' effect, shown in figures 13 and 14.

In order to more clearly illustrate the difference mentioned above, we also perform the cross-correlation statistics calculation for fluid particles. As for the bubbles, fluid particles were introduced at the location close to the origin of the mixing layer and local fluid particle number flux $n_{f,j}(t)$ is recorded as well. The correlation coefficients defined by relation (3) for both bubbles and fluid particles with time delay are shown in figure 15. It seems that there exist approximately repetitive patterns to characterize these correlations. Notice from figure 15 that the time delay characterizing the behaviour of repetitive bubble accumulation within two consecutive eddies is given by the difference $\Delta\tau$ between the values corresponding to two consecutive maxima or minima. An estimated $\Delta\tau$ from the curve shown in figure 15 gives a non-dimensionalized time $\Delta\tau=0.20$, corresponding to a Strouhal number $S_h=5$ (Here $S_h=Fl/\Delta U$). Because local bubble number flux is highly correlated with local vorticity flux, it can be expected that this value should be roughly the same as the Lagrangian time scale of two consecutive large eddies. Hussian (1986) has indicated that the large eddies are transported at a mean convection velocity about $0.7U_m$. Our simulation results have shown that this mean convection velocity is about $0.5U_m$ and the thickness of the mixing layer is about $0.12x$ (roughly estimated from the mean velocity profiles) under

the conditions specified; i.e. $U_2/U_1=3.0$. Thus, the thickness of the mixing layer when $x=0.8L$ should be about $\delta=0.096L$. If the downstream large eddy structure of the mixing layer is approximated by this scale, then estimation of passage frequency according to $f=0.5U_m/\delta$ would correspond to a Strouhal number $S_h \approx 5.2$. The same estimation from the curve of the correlation between fluid particle number flux and local vorticity flux shows the value $\Delta\tau=0.22$. This result indicates that both fluid particles and bubbles have a similar length scale response to the large eddies, but the length scale for fluid particles is slightly larger than that of bubbles. In contrast to figure 15, figure 16 shows the correlation coefficients for particles and fluid particles. The correlation coefficient for particles achieves the largest value with a finite time delay rather than with time delay $\tau=0$. Again, this finding is consistent with the simulation results shown in figure 5, particles preferentially accumulating along the edge of the high speed side of the mixing layer, but penetrating between two consecutive eddies.

4.2 Implications For Practical Modelling of Voidage-Vorticity Transport Equation

An Eulerian vorticity transport model would clearly hold much more prospect of reliable prediction of bubble dispersion than the present generation of momentum transport closure model. As a first-cut conduction for a two-dimensional field the concentration and vorticity correlation equations are given by

$$\frac{\partial c}{\partial t} + u_j \frac{\partial c}{\partial x_j} = -u_{dj} \frac{\partial c}{\partial x_j} \quad (4)$$

$$\frac{\partial \omega}{\partial t} + u_j \frac{\partial \omega}{\partial x_j} = 0 \quad (5)$$

where u_{dj} is the drift velocity, here taken to include both buoyancy and pressure induced.

Combining equations (4) and (5), we obtain

$$\frac{\partial(c\omega)}{\partial t} + u_j \frac{\partial(c\omega)}{\partial x_j} = -\omega u_{dj} \frac{\partial c}{\partial x_j} \quad (6)$$

It can be seen from equation (6) that the transport term $c\omega$, directly corresponding to $\overline{c\omega}$, is affected by the drift velocity. As indicated by Sene (1985), inertial forces cause a net lateral drift of bubbles in vertical shear flows. The drift velocity due to buoyancy forces is of the order of the terminal velocity of the bubble, V_T , in still liquid. The drift velocity due to the shear lift acts along the direction of the mean shear (Sene *et al.* 1994) and the drift velocity due to inertia acts towards the downgoing side of the coherent structures. When bubbles are trapped by large eddies, the drift velocity is directed into the centre of the eddy structure. Thus, the transport $c\omega$ is enhanced as can be seen from equation (6). In contrast to this, the particle transport within the eddy structure is decreased because the drift velocity for particles is directed out of the eddy structure. It seems that a correct determination of the drift velocity can result in a proper description of dispersive transport in shear flows. However, the determination of the drift velocity is strongly dependent on a correct Lagrangian force law. Of course, following the usually adopted Reynolds averaging, we can decompose the instantaneous values of the vorticity ω and concentration c into their mean and fluctuation values, respectively, $\Omega + \omega'$ and $C + c'$, and use some algebra and averaging to obtain the vorticity/voidage fluctuation transport equations. However, we notice that the solution of such equations is needed to introduce the closure models for those terms such as $\overline{c'\omega'}$.

5 CONCLUSIONS

The statistical results, obtained numerically by tracking bubbles and particles in turbulent mixing layers, have compared and quantified the correlation between local concentration fluctuations of disperse phase and local vorticity excursions. The correlations achieve their largest values within the core of the mixing layer for bubbles, and on the high speed edge for heavy particles. Clearly, the main implication here is that an Eulerian vorticity transport model may be more appropriate for modelling purposes than the momentum transport models employed in current two-fluid schemes where one major problem is the prescription of closure for pressure coupling of the vortices. The need now is to bridge the gap between this understanding and the formulation of such transport models for practical engineering purposes.

REFERENCES

- Crowe, C. T., Chung, J. N. & Troutt, T. R. 1993 Particle dispersion by organized turbulent structures. In *Particulate Two-Phase Flows* (Edited by Roco, M. C.), Butterworth-Heinemann, New York.
- Eaton, J. K. & Fessler, J. R. 1994 Preferential concentration of particles by turbulence. *Int. J. Multiphase Flow* **20**, 169-209.
- Grassberger, P. & Procaccia, I. 1983 Measuring the strangeness of strange attractors. *Physica D* **9**, 189.
- Hulin, J. P., Fierfort, C. & Coudol, R. 1982 Experimental study of vortex emission behind bluff obstacles in a gas liquid vertical two-phase flow. *Int. J. Multiphase Flow* **6**, 475-490.
- Hussain, A. K. M. F. 1986 Coherent structures and turbulence. *J. Fluid Mech.* **173**, 303-356.
- Lázaro, B. J. & Lasheras. J. C. 1989 Particle dispersion in a turbulent, plane shear layer

- Phys. Fluids* **A1(6)**, 1035-1044.
- Lázaro, B. J. & Lasheras 1992 Particle dispersion in the developing free shear layer. Part 1. Unforced flow *J. Fluid Mech.* **235**, 143-178.
- Martin, J. E. & Meiburg, E. 1994 The accumulation and dispersion of heavy particles in forced two-dimensional mixing layers. I. The fundamental and subharmonic cases. *Phys. Fluids* **6(3)**, 1116-1132.
- Sene, K. 1985 Aspects of bubbly two phase flow, Ph.D. Thesis, University of Cambridge.
- Sene, K., Hunt, J. C. R. and Thomas, N. H. 1994 The role of coherent structures in bubble transport by turbulent shear flows. *J. Fluid Mech.* **259**, 219-240.
- Tang, L., Wen, F., Yang, Y., Crowe, C. T., Chung, J. N. & Troutt, T. R. 1992 Self-organized particle dispersion mechanism in a plane wake. *Phys. Fluids* **A4(10)**, 2244-2251.
- Thomas, N. H., Auton, T. R., Sene, K. & Hunt, J. C. R. 1983 Entrainment and transport of bubbles by transient large eddies in multiphase turbulent shear flows. In *Proc. Intl Conf. on Physical Modelling of Multiphase Flows*, Coventry, UK. BHRA.
- Thomas, N. H. 1994 Plunging flow aeration: some fundamental and functional factors. *Aeration Technology* ASME FED-Vol. **184**.
- Townsend, A. A. 1976 The structure of turbulent shear flow. 2nd Ed. Cambridge University Press.
- Wells, M. R. & Stock, D. E. 1983 The effects of crossing trajectories on the dispersion of particles in a turbulent flow. *J. Fluid Mech.* **136**, 31-62.
- Wen, F., Kamalu, N., Chung, J. N., Crowe, C. T. and Troutt, T. R. 1992 Particle dispersion by vortex structures in plane mixing layers. *J. Fluids Engng.* **114**, 657-666.

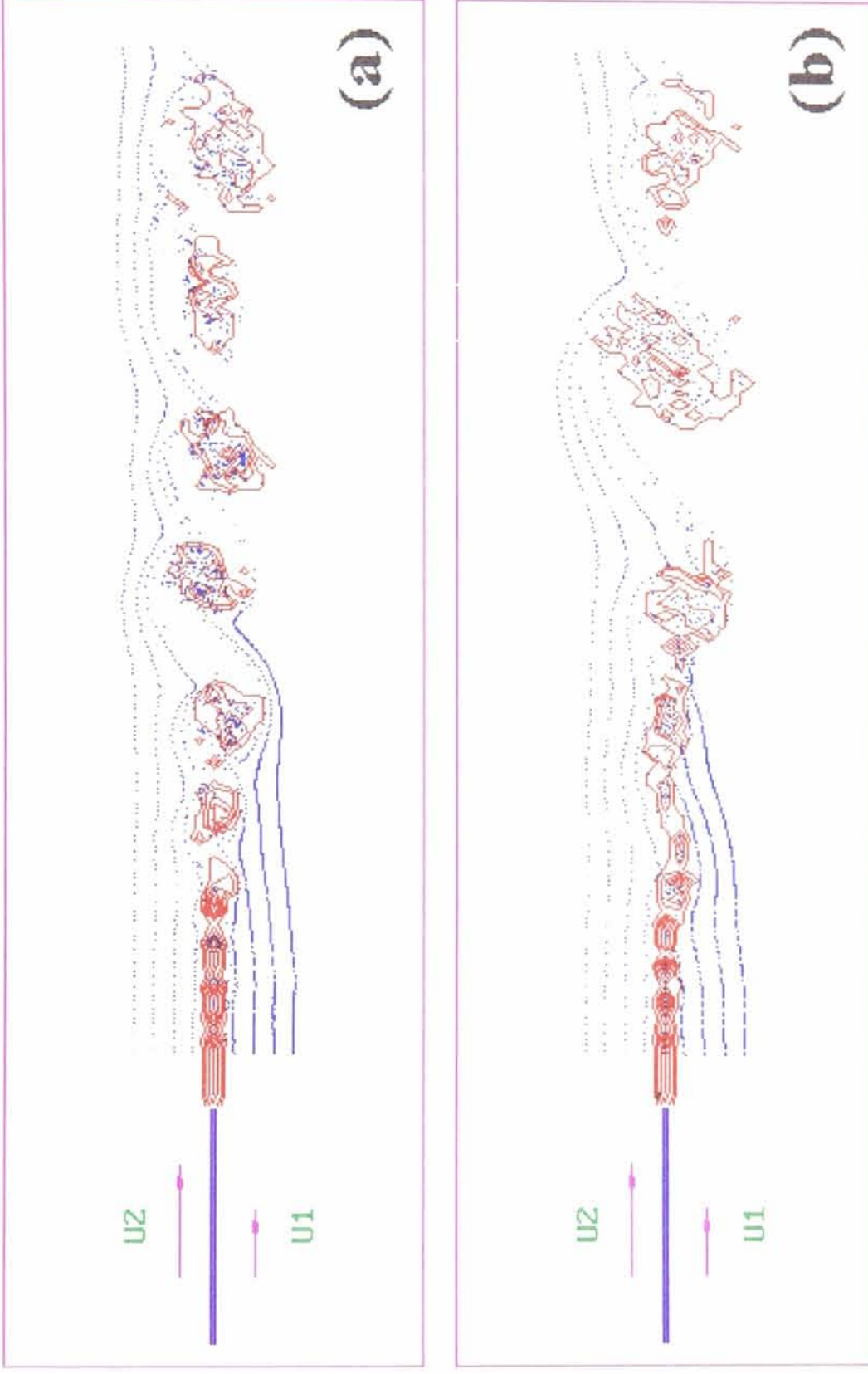


Figure 1. Instantaneous vorticity contours (red) and bubble streaklines (blue). Bubbles are trapped by the large-scale eddies and group in clusters. (a) $\Pi=0.5$, $\Gamma=10.0$ at time $t=1.5625$; (b) $\Pi=0.5$, $\Gamma=20.0$ at time $t=1.5625$.

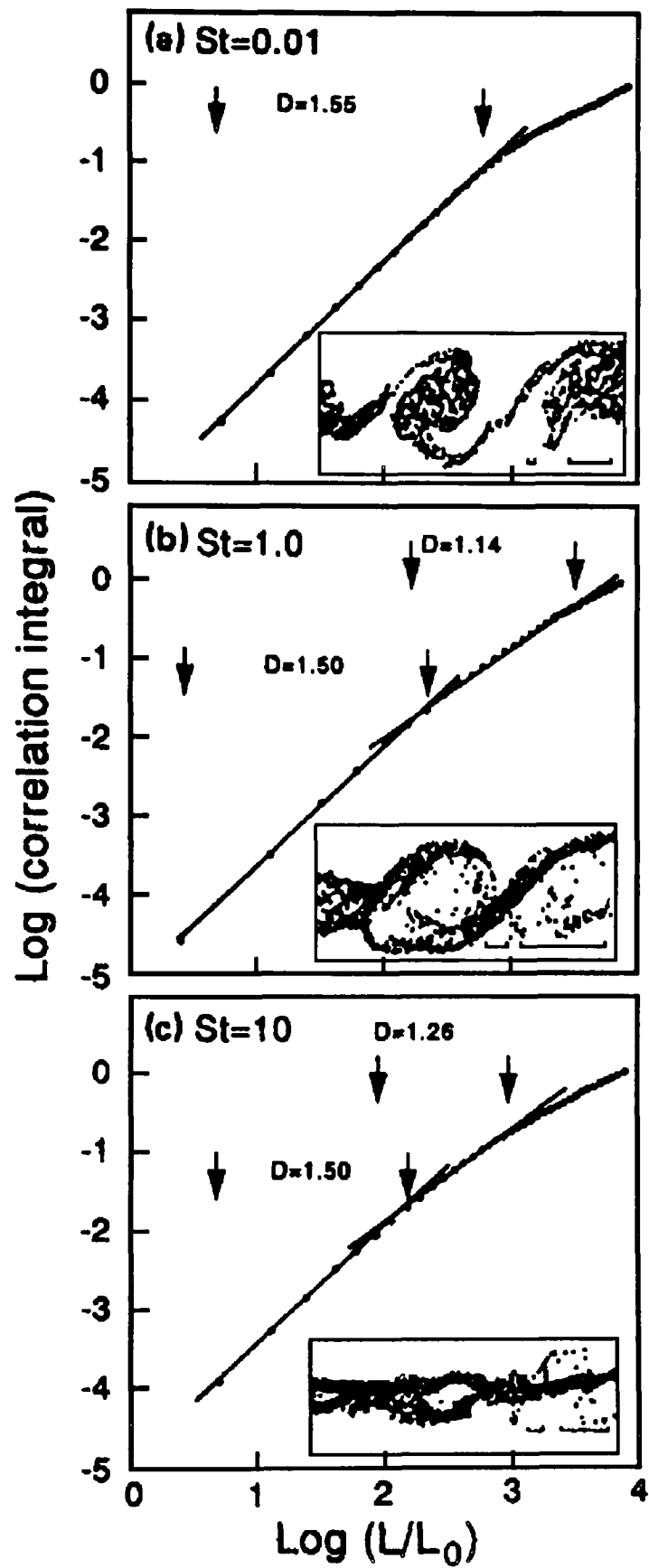


Figure 2. Typical logarithmic correlation integral plots for particles from mixing layer simulations. (a) $S_i=0.01$; (b) $S_i=1.0$; (c) $S_i=10.0$. (Here S_i is the Stokes number, defined as $S_i=\rho_p d^2 \Delta U / 18 \mu \delta$). Taken from Tang *et al.* (1992).

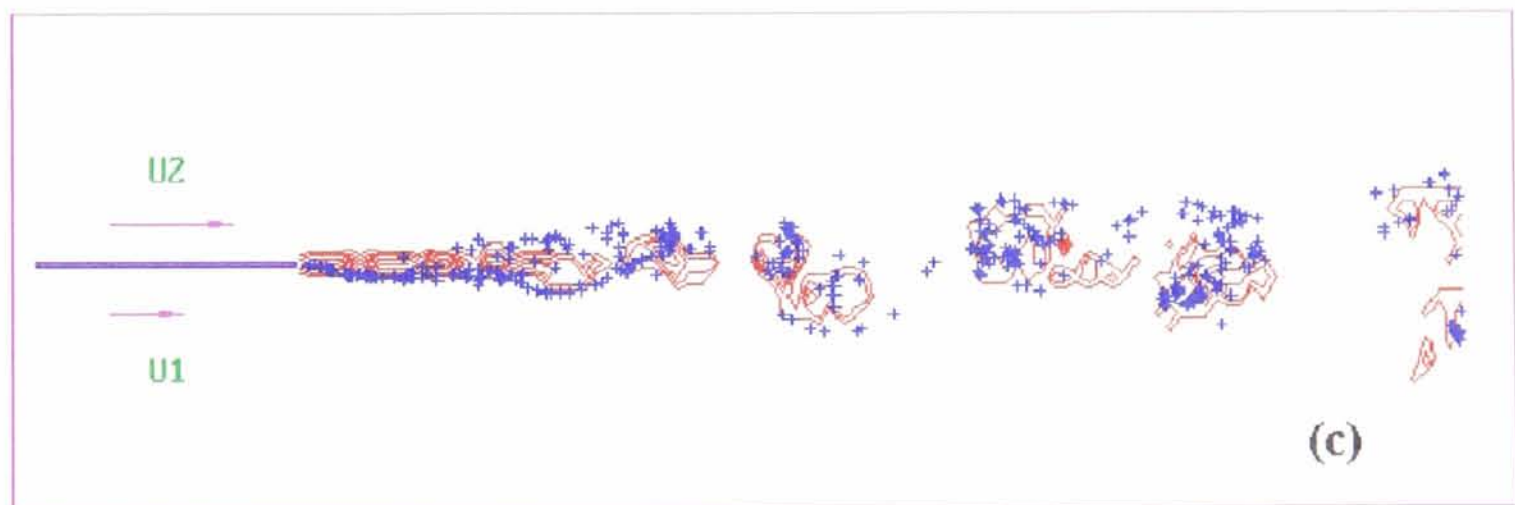
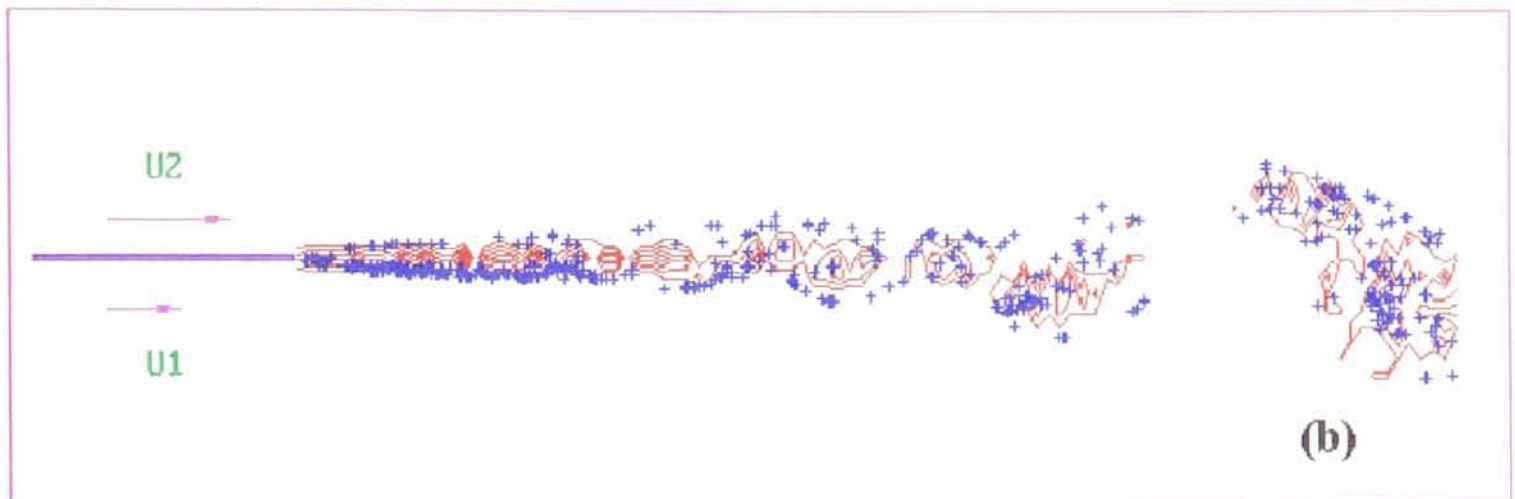
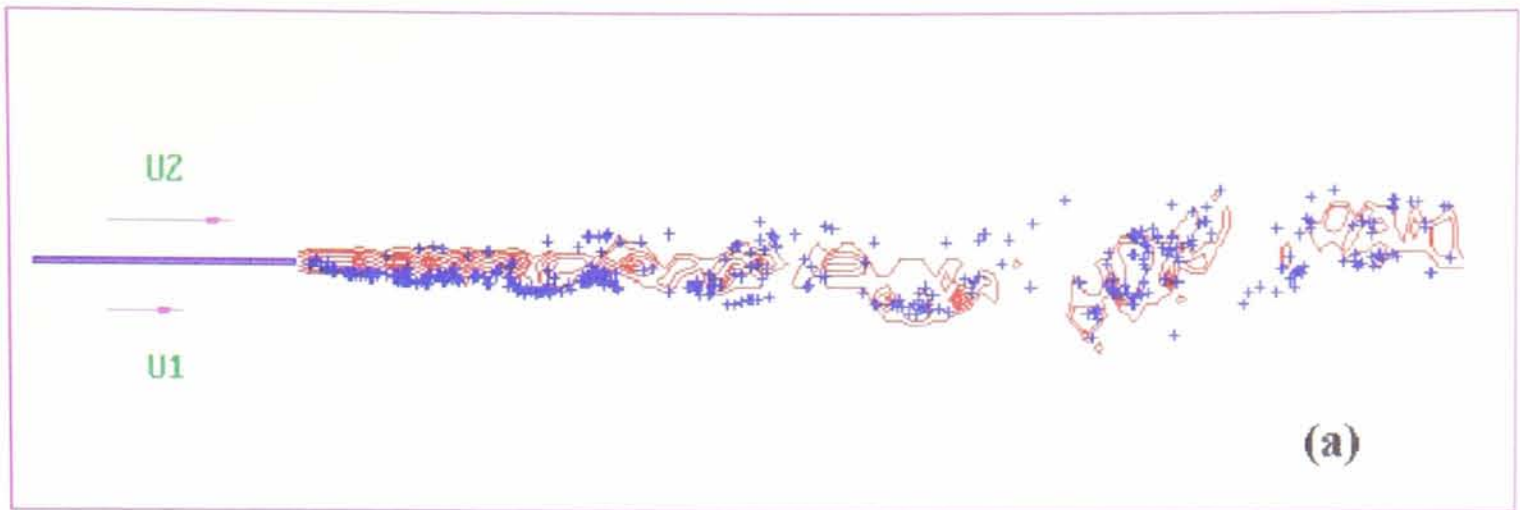


Figure 3. Instantaneous vorticity contours (red) and bubble locations (blue) at three different time instants with $\Pi=0.5$, $\Gamma=10.0$ and $\gamma=0.0$. (a) $T=2.525$; (b) $T=3.025$; (c) $T=3.525$.

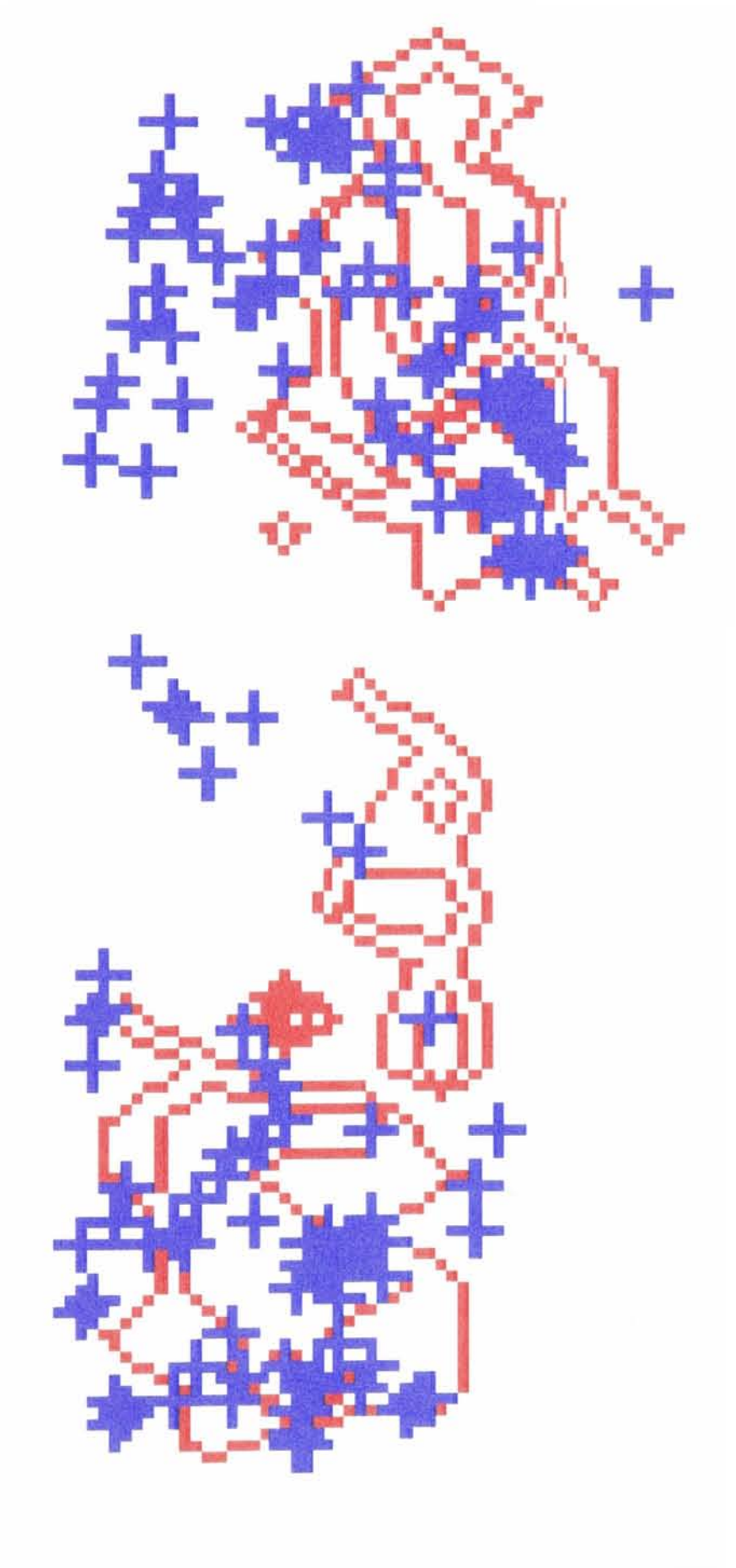


Figure 4. Instantaneous vorticity contours (red) and bubble locations (blue) at $0.55L < x < 0.85L$ at $T=3.525$ with $\Pi=0.5$, $\Gamma=10.0$ and $\gamma=0.0$.

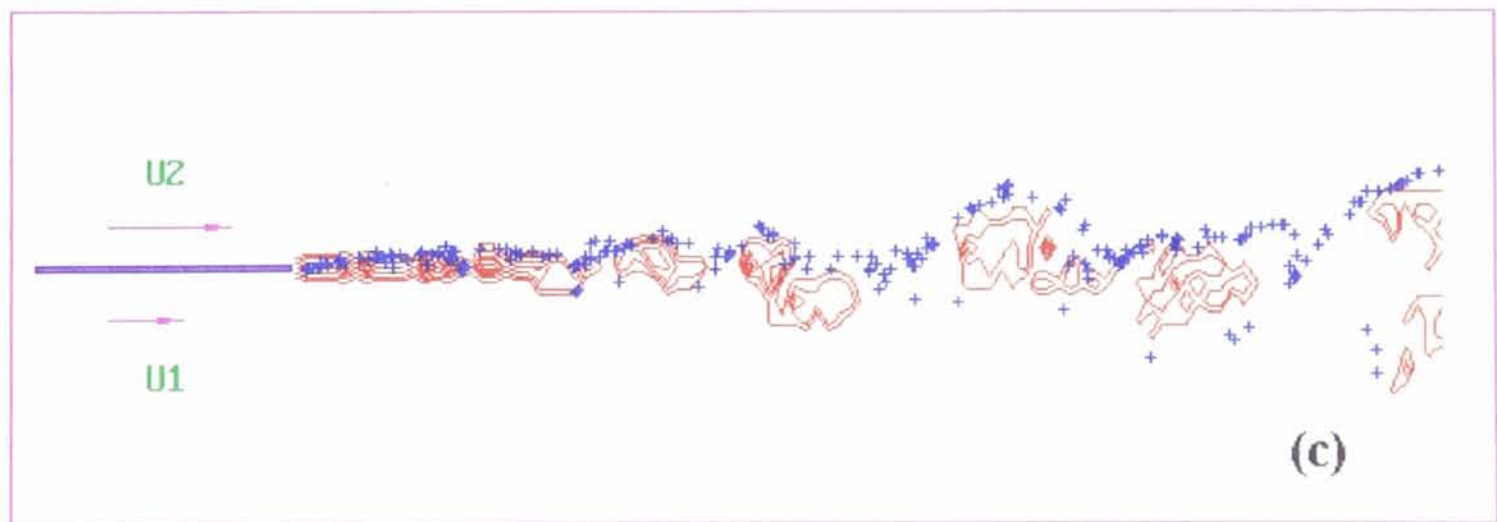
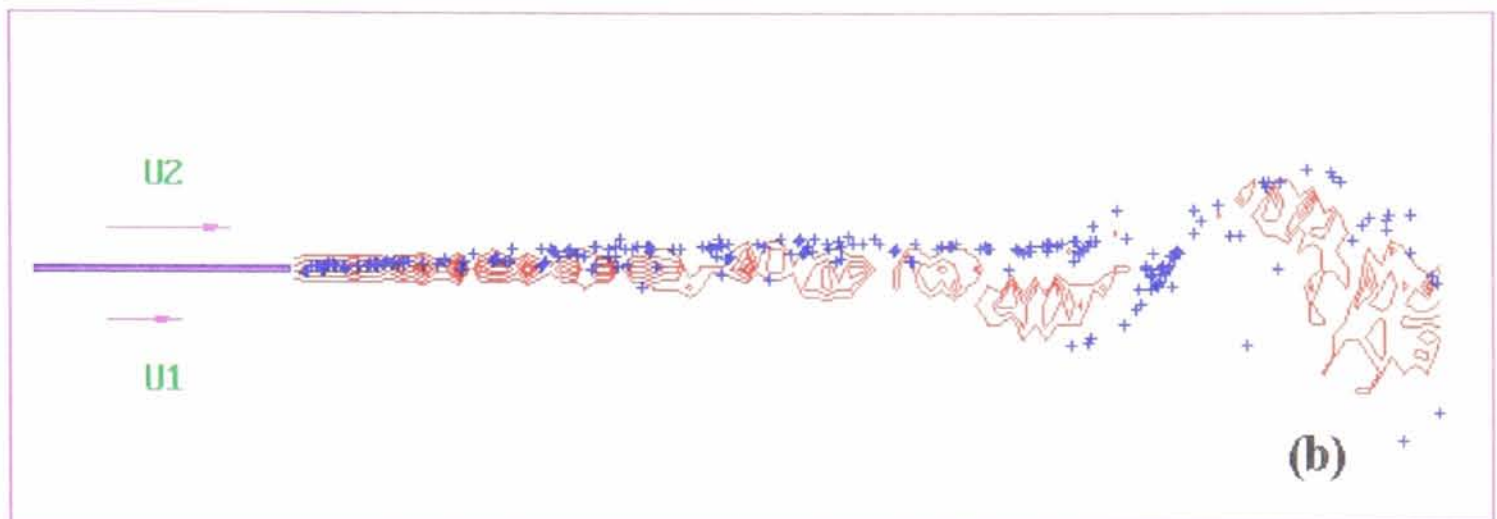
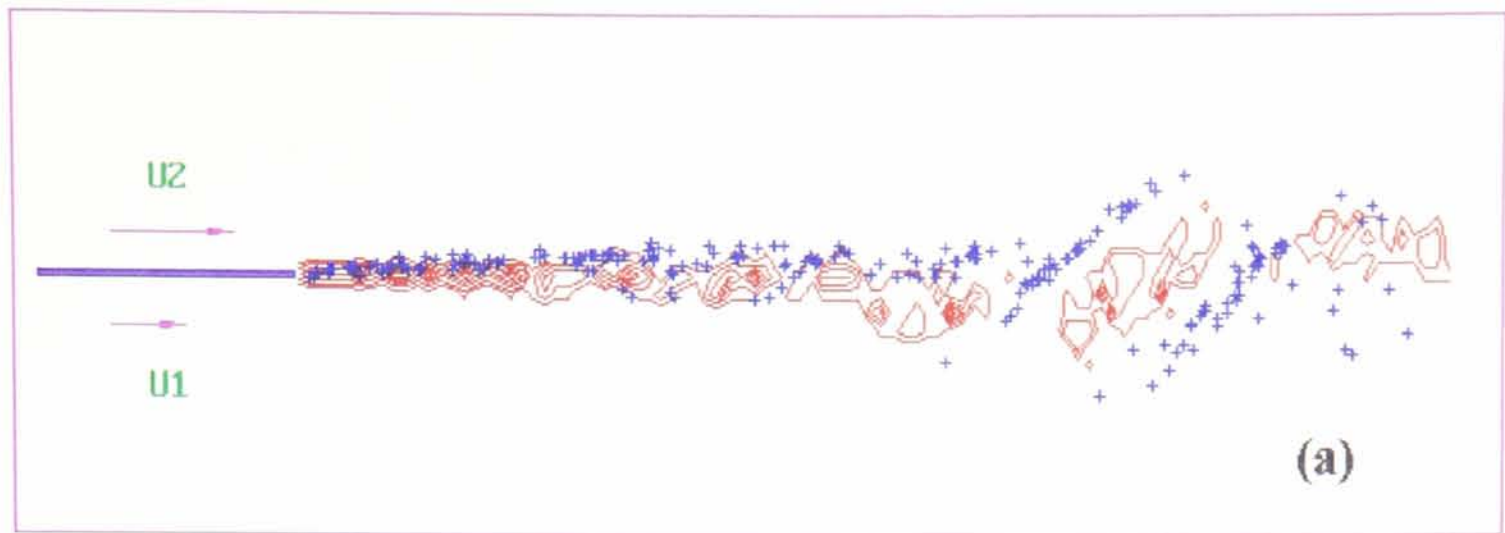


Figure 5. Instantaneous vorticity contours (red) and particle locations (blue) at three different time instants with $\Pi=0.5$, $\Gamma=10.0$ and $\gamma=1920.0$. (a) $T=2.525$; (b) $T=3.025$; (c) $T=3.525$.

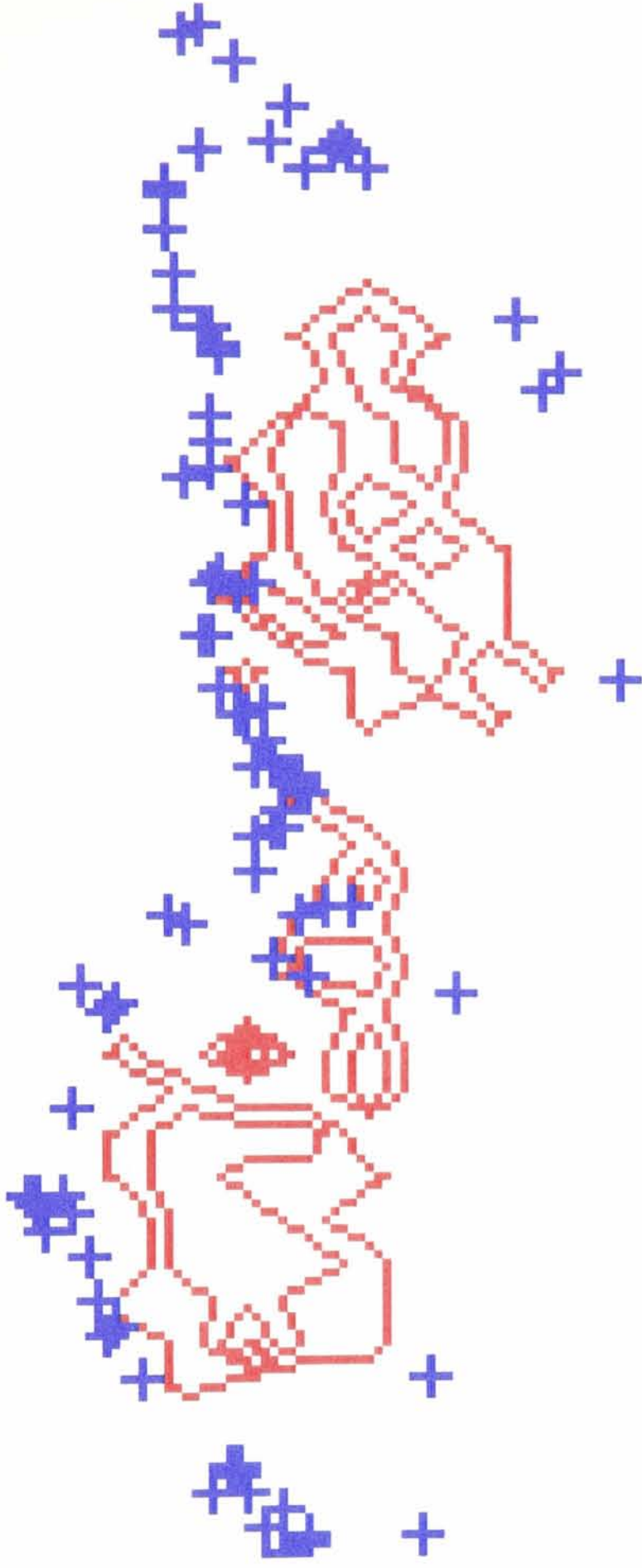


Figure 6. Instantaneous vorticity contours (red) and particle locations (blue) at $0.55L < x < 0.85L$ at $T=3.525$ with $\Pi=0.5$, $\Gamma=10.0$ and $\gamma=1920.0$.



— vorticity — — bubble or particle number density

Figure 7. The contour plots of instantaneous vorticity, and bubble or particle number density at $0.55L < x < 0.85L$. (a) $\Pi=0.5$, $\Gamma=10.0$ and $\gamma=0.0$ at $T=1.425$; (b) $\Pi=0.5$, $\Gamma=10.0$ and $\gamma=1920.0$ at $T=0.725$.

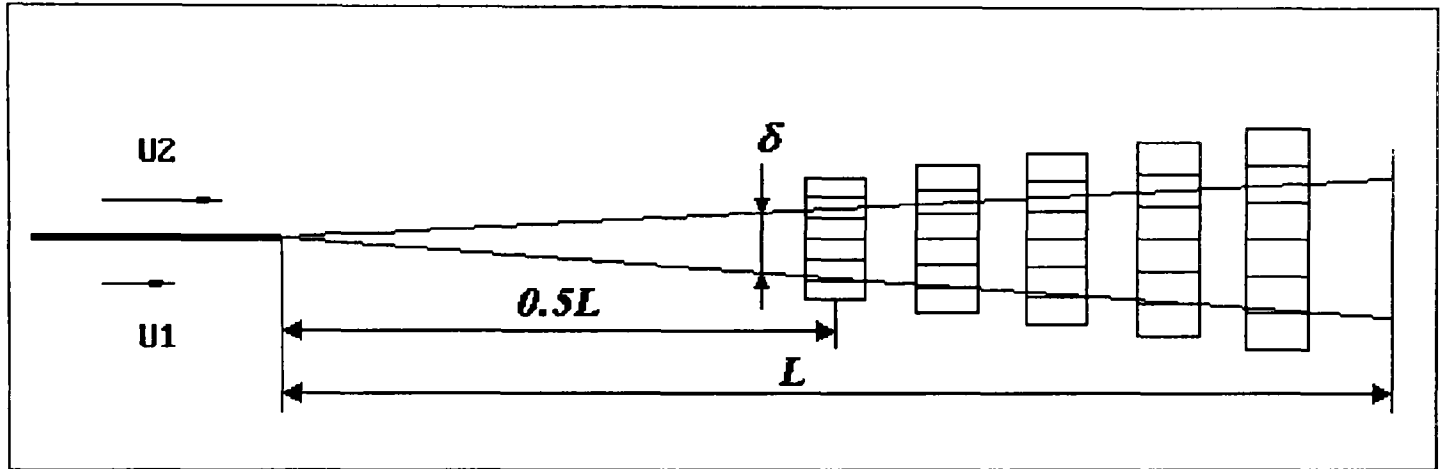


Figure 8. A schematic layout of the bins for sampling the numbers of bubbles or particles and the numbers of point vortices.

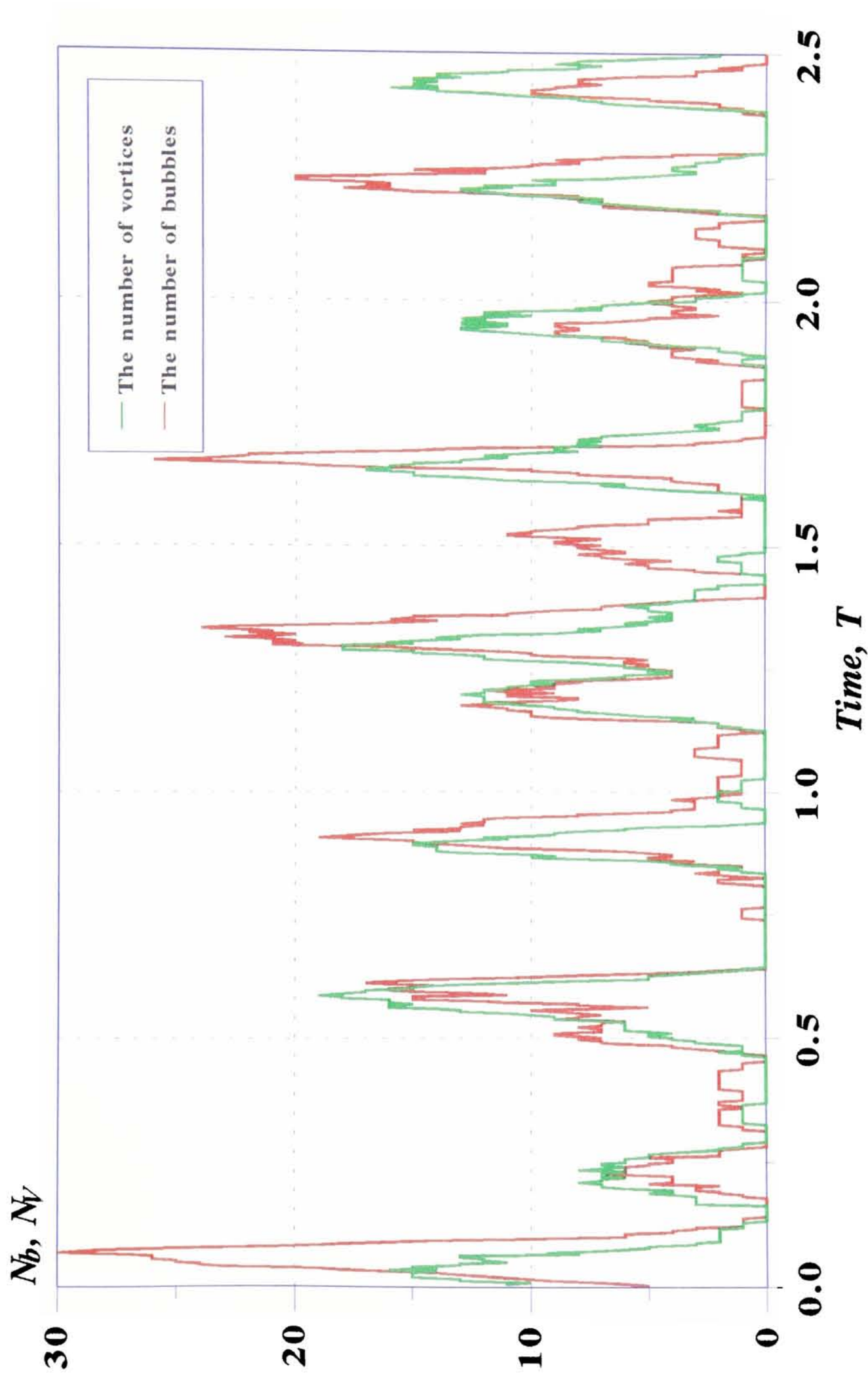


Figure 9. Time-history records of local bubble number flux and local point vortex number flux under the conditions $\Pi=0.5$, $\Gamma=10.0$ and $\gamma=0$, sampled at $x=0.8L$ and $y=0.0147L$. Bubbles were released from the location close to the origin of the mixing layer. Sampling records were started when bubbles were fully engaged in the eddies in the computation domain.

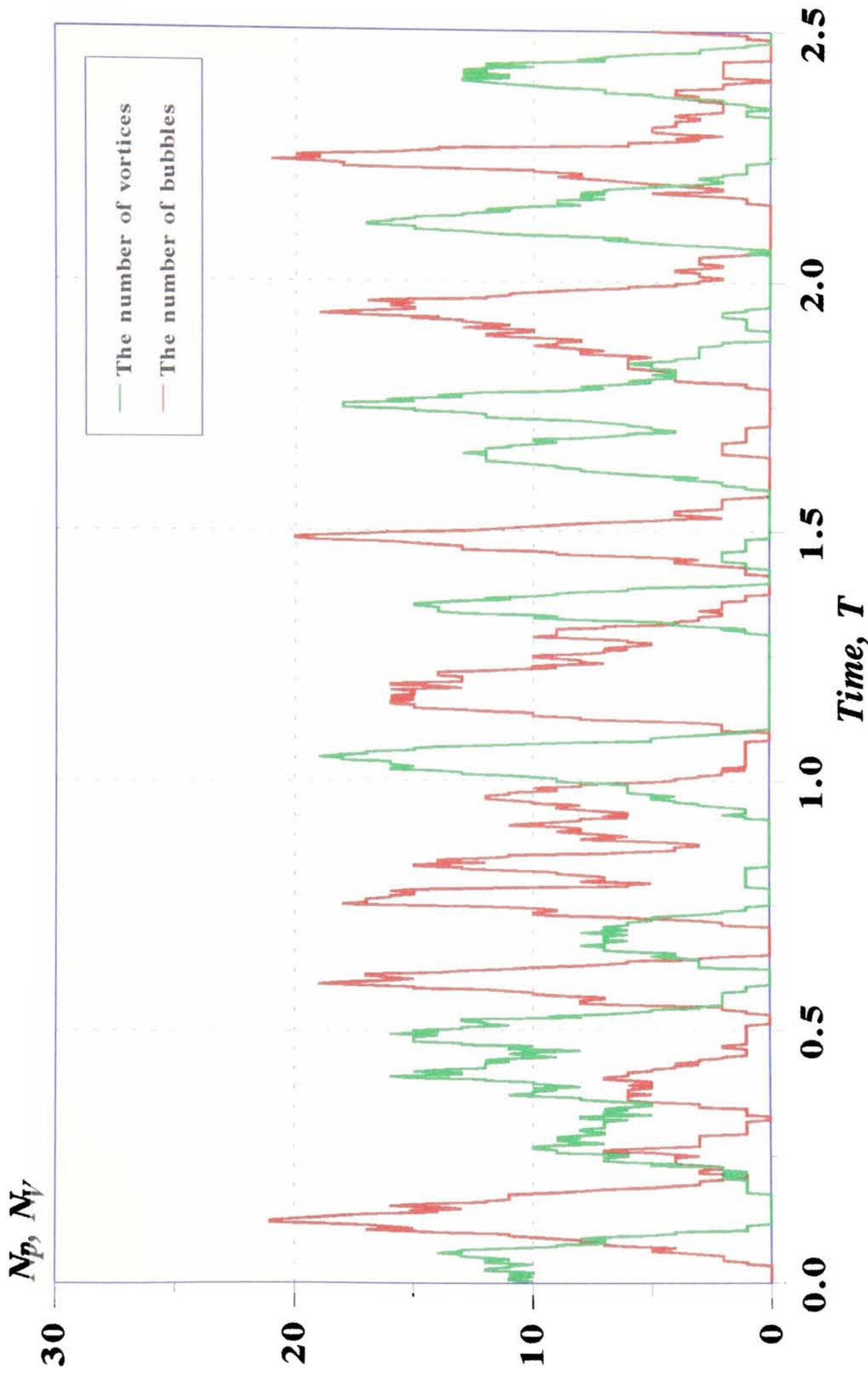


Figure 10. Time-history records of local particle number flux and local point vortex number flux under the conditions $\Pi=0.5$, $\Gamma=10.0$ and $\gamma=0.0147L$. Bubbles were released from the location close to the origin of the mixing layer. Sampling records were started when particles were fully engaged in the eddies in the computation domain.

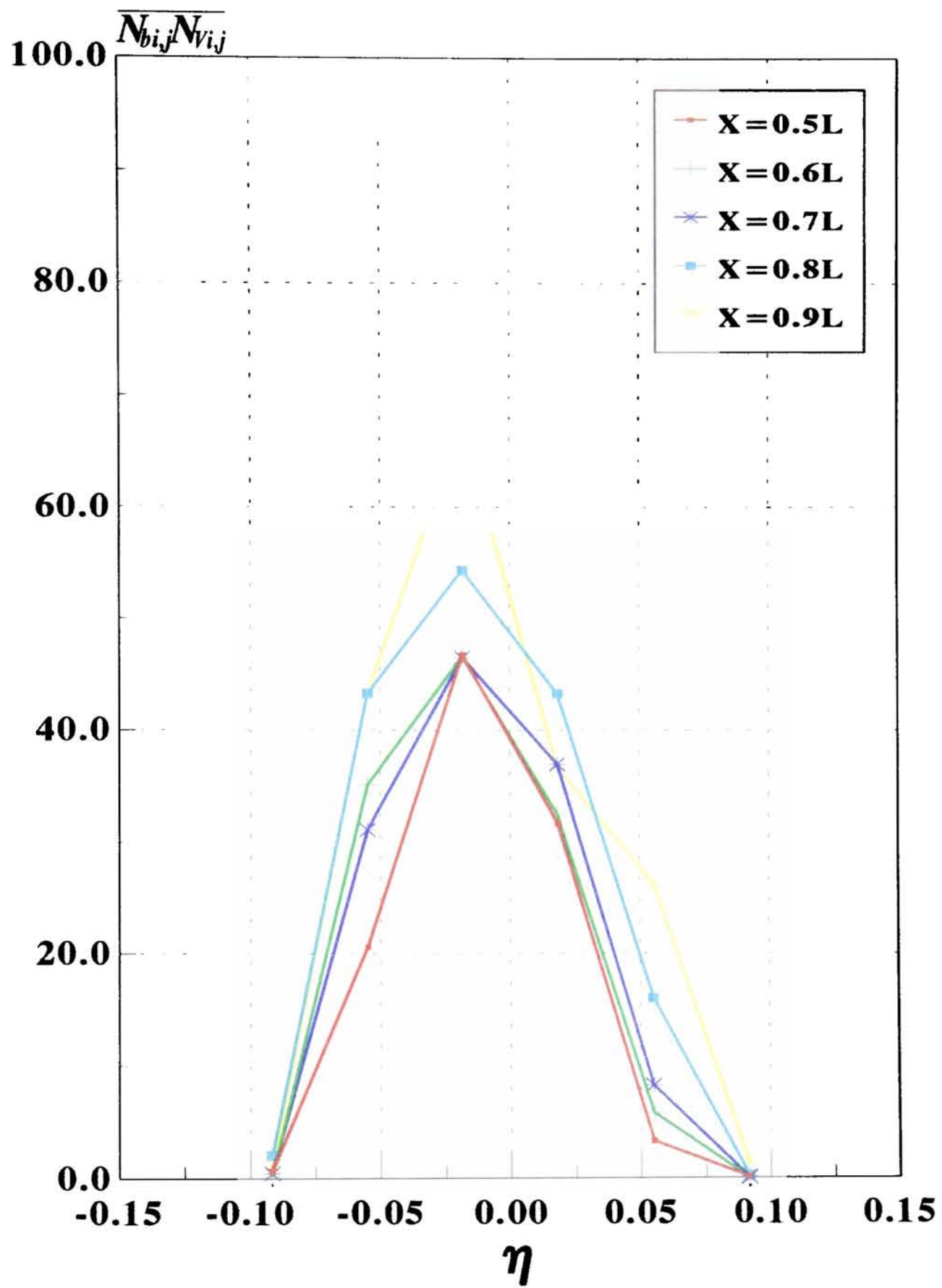


Figure 11a. Cross-correlations between local bubble number flux $n_b(t)$ and local point vortex number flux $n_v(t)$ at different downstream cross-sections ($\eta=y/x$) of the mixing layer, with time delay $\tau=0$.

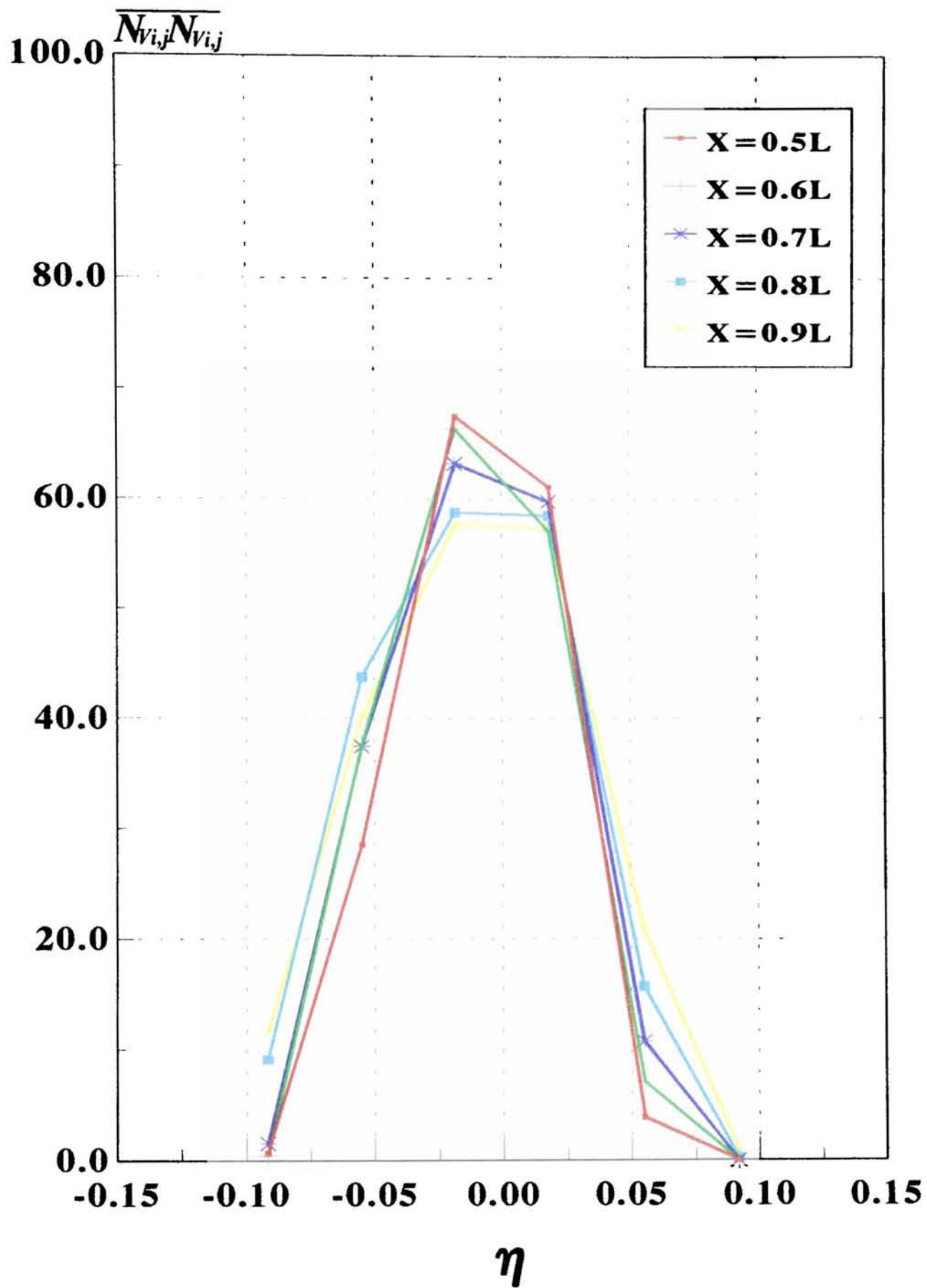


Figure 11b. Autocorrelations of local point vortex number flux $n_v(t)$ at different downstream cross-sections ($\eta=y/x$) of the mixing layer, with time delay $\tau=0$.

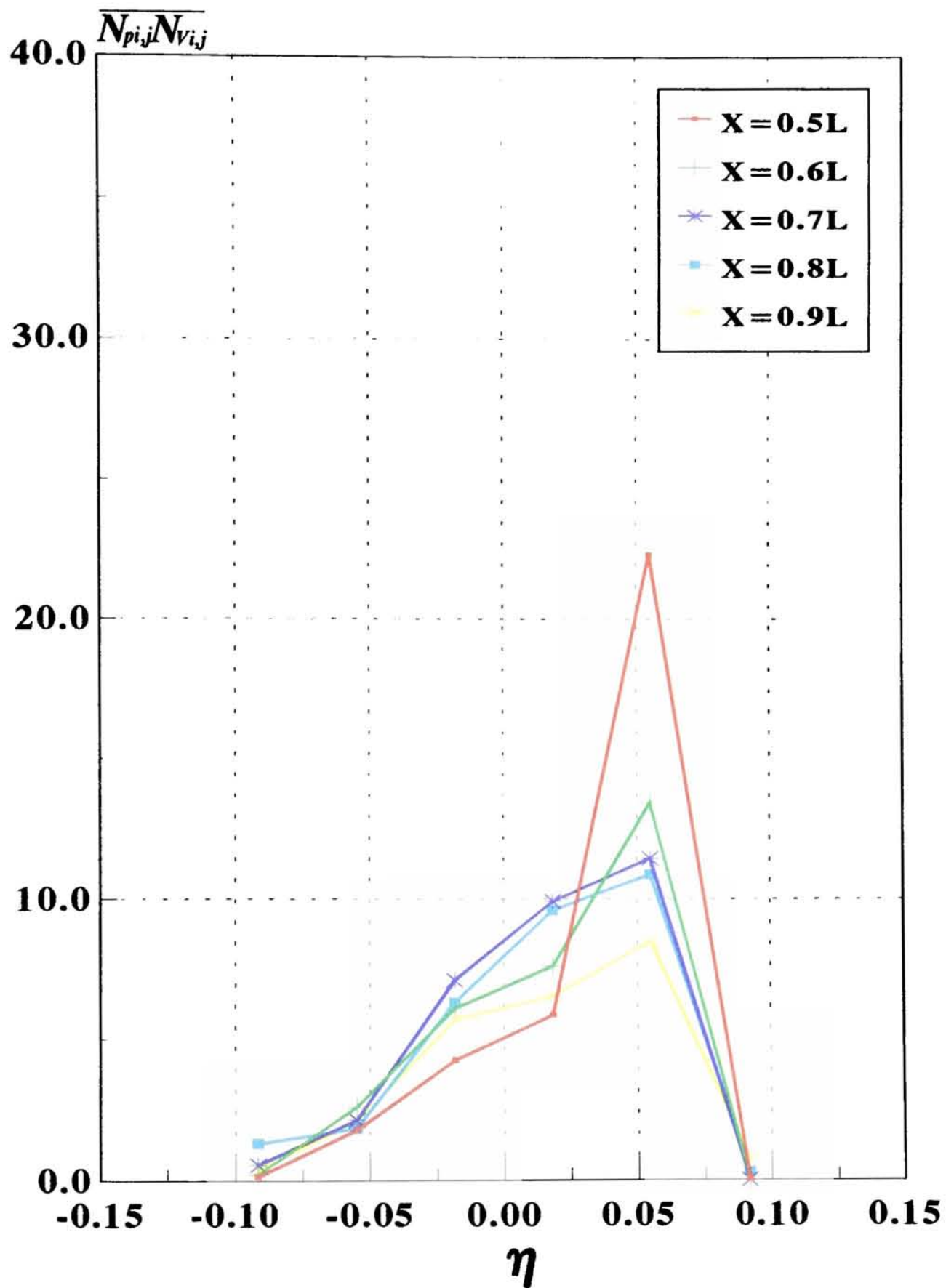


Figure 12. Cross-correlations between local particle number flux $n_p(t)$ and local point vortex number flux $n_v(t)$ at different downstream cross-sections ($\eta=y/x$) of the mixing layer, with time delay $\tau=0$.

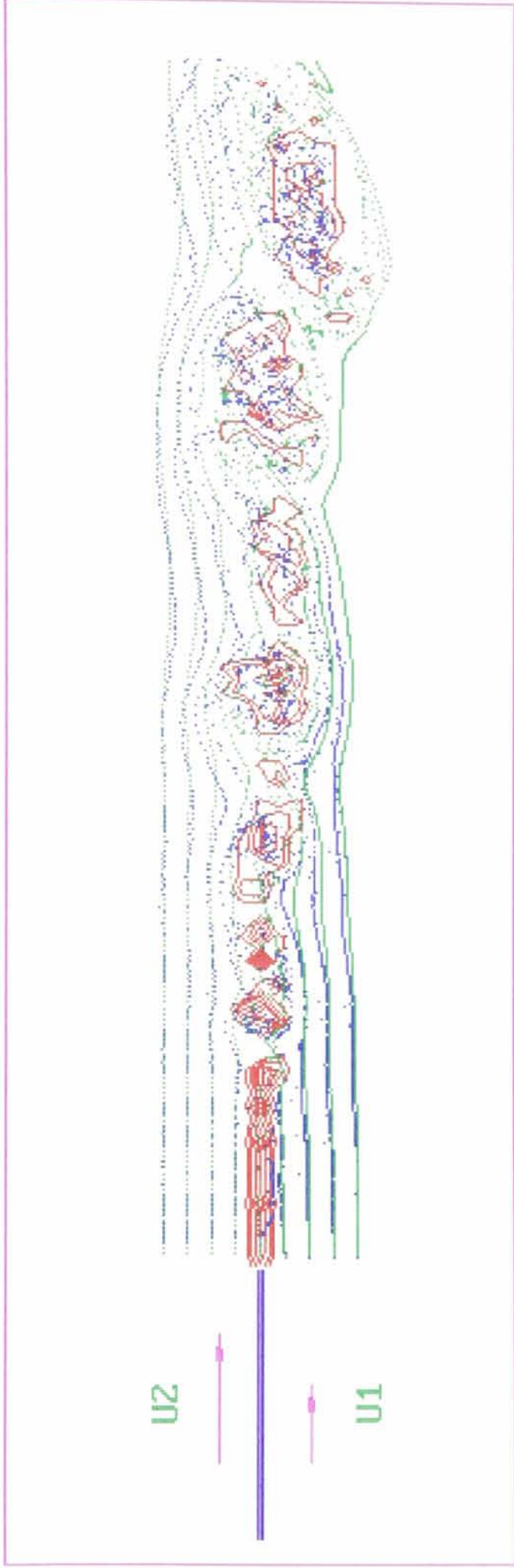


Figure 13. Instantaneous vorticity contours, bubble streaklines and fluid particle streaklines at $t=2.575$. Both bubbles and fluid particles were released from the same locations with $\Pi=0.5$, $\Gamma=10.0$. Blue dots and green dots represent bubbles and fluid particles respectively.



Figure 14. Instantaneous vorticity contours, bubble streaklines and fluid particle streaklines at $t=2.575$. Both bubbles and fluid particles were released from the same locations with $\Pi=0.5$, $\Gamma=20.0$. Blue dots and green dots represent bubbles and fluid particles respectively.

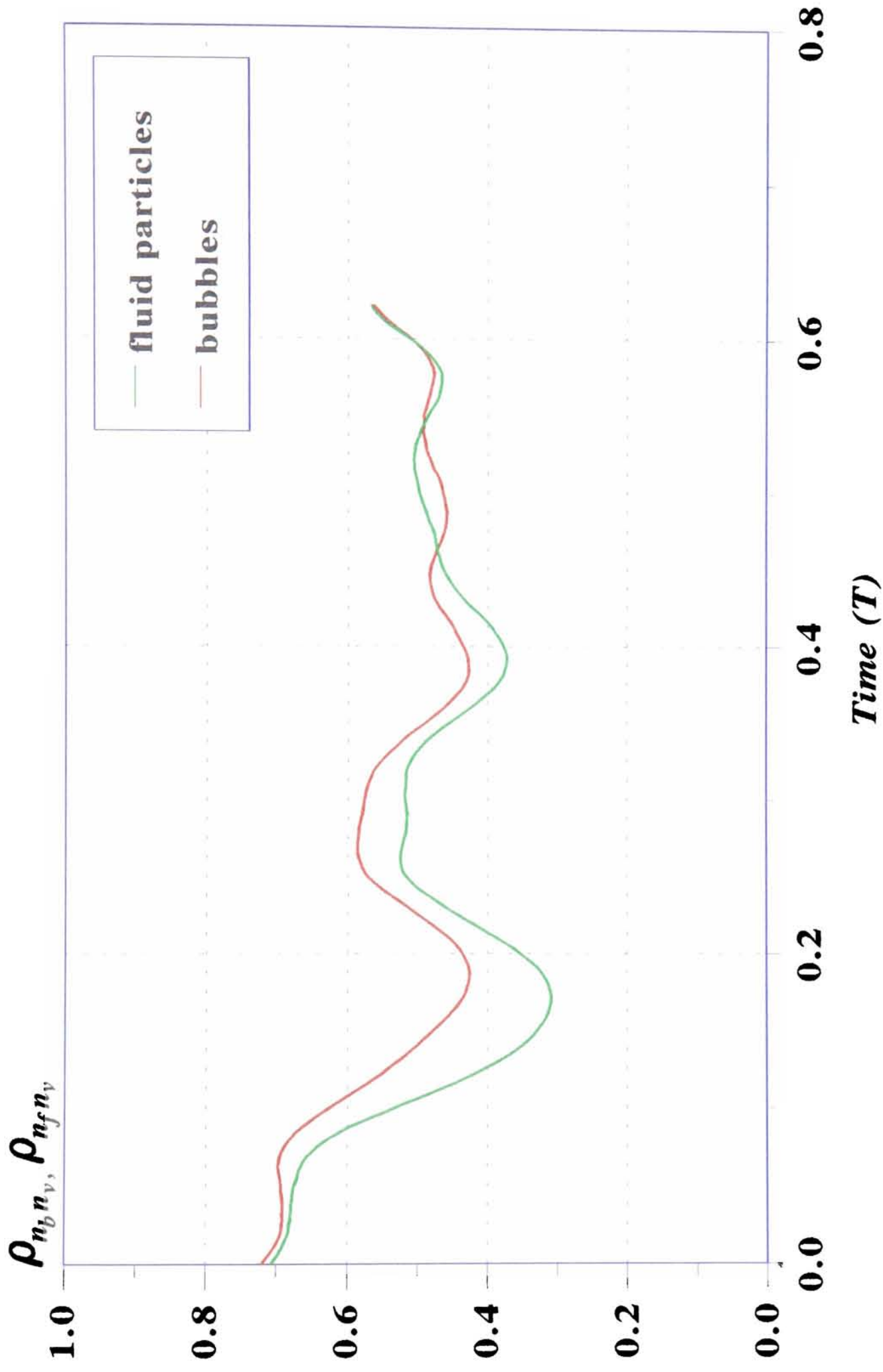


Figure 15. Variation over time of cross-correlations between local bubble number flux /local point vortex number flux and local fluid particle number flux /local point vortex number flux under conditions $\Pi=0.5$, $\Gamma=10.0$ and $\gamma=0$, sampled at $x=0.8L$ and $y=0.0147L$. Bubbles and fluid particles were released from the location close to the origin of the mixing layer. Sampling records were started when bubbles and fluid particles were fully engaged in the eddies in the computation domain.

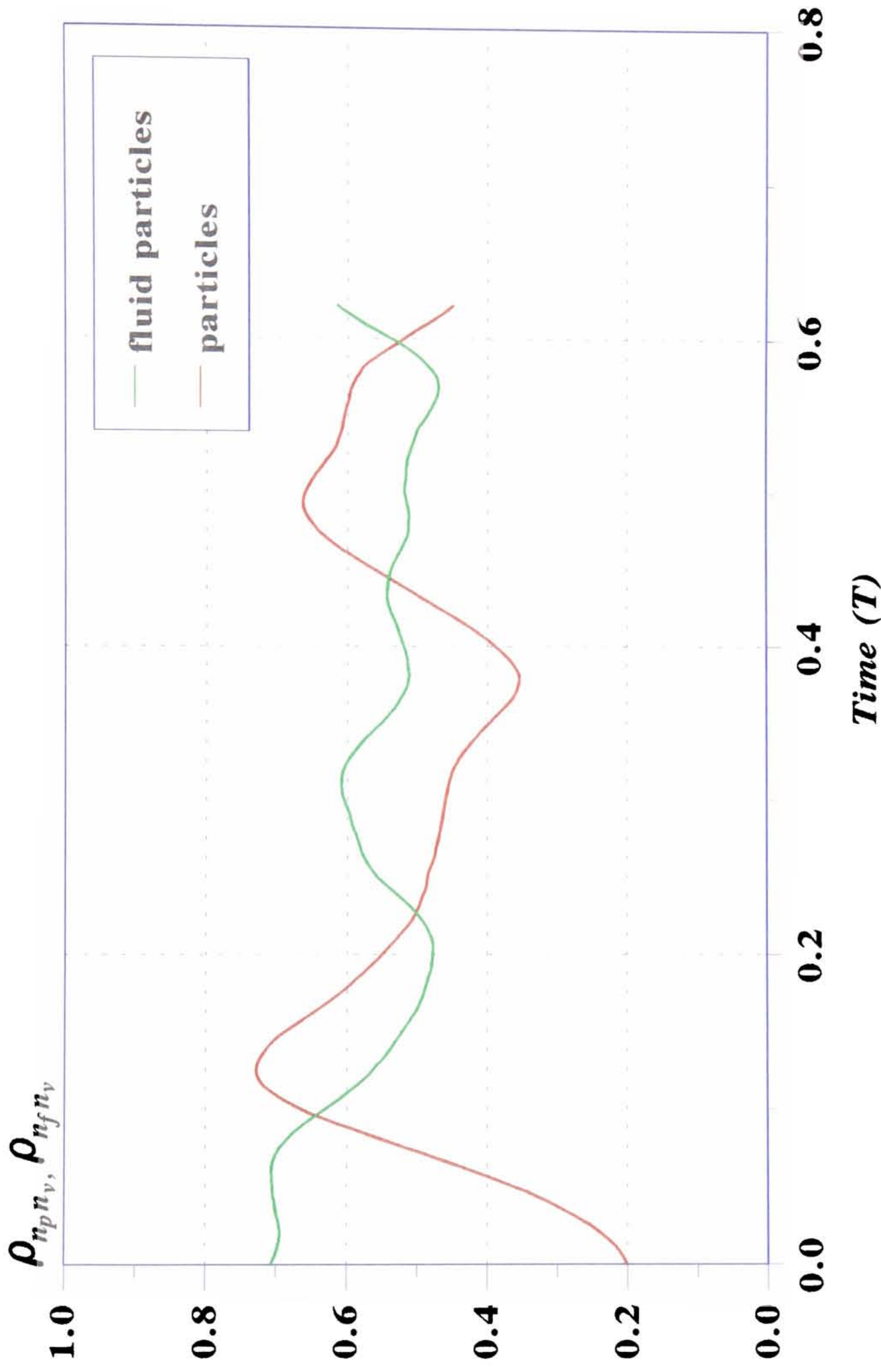


Figure 16. Variation over time of cross-correlations between local particle number flux /local point vortex number flux and local fluid particle number flux /local point vortex number flux under conditions $\Pi=0.5$, $\Gamma=10.0$ and $\gamma=1920$, sampled at $x=0.8L$ and $y=0.0147L$. Particles and fluid particles were released from the location close to the origin of the mixing layer. Sampling records were started when particles and fluid particles were fully engaged in the eddies in the computation domain.

CHAPTER 7: RECAPITULATION AND RECOMMENDATIONS

1 TWO-PHASE FLOW NUMERICAL MODELLING

Recent literature on existing models was reviewed in chapter 1. There are several fundamentally different formulations couched in terms of macroscopic equations. The two-fluid model (e.g. Drew 1983) describes each phase in terms of conservation equations governing the balances of mass, momentum and energy. The interaction terms coupling interphase exchanges of these quantities remain uncertain, and their inadequate modelling can give rise to errors exceeding those arising from semi-empirical gradient diffusion representations describing concentration distributions. Existing turbulence closure models are still mainly based on *ad hoc* modifications of single-phase turbulence models (e.g. widely used K - ϵ models) (e.g. Violette & Simonin 1994). Nevertheless, such schemes can provide useful first-cut representations for engineering calculations in design and applications.

Attractive conceptual models for bubble and particle dispersion in free shear flows proposed by Thomas *et al.* (1983) and Crowe *et al.* (1985) provide Lagrangian representation of bubble and particle dispersion in turbulent shear flows characterised by the large eddies.

The most obvious distinction between these approaches is in terms of their formulations as Eulerian-Eulerian, Eulerian-Lagrangian or Lagrangian-Lagrangian and we have summarised the main advantages and disadvantages of these approaches. Eulerian-Eulerian models like two-fluid scheme regard the phases as "interpenetrating continua" and involve Reynolds averaged equations coupled by interphase exchanges, the latter expressed as semi-empirical force law closures. The resulting description can only convey a statistically smeared picture

of two phases. Eulerian-pseudo Lagrangian approaches adopt Reynolds averaged equations to represent the carrier fluid phase flow and turbulence, and the discrete phase is then simulated using a Lagrangian force law model. However, the fluctuating flows are invariably introduced as a Gaussian perturbation superimposed on the mean flows, an approximation which essentially eliminates important features of structure dependent discrete phase engagement and entrapment (Thomas *et al.* 1983). Lagrangian-Lagrangian methods incorporate representations of the travelling structure, and also have transient localised capture of discrete phase (Crowe *et al.* 1993; Hunt *et al.* 1993).

Whilst Lagrangian-Lagrangian approaches incorporate important eddy structural effects on transport, reliable estimations of the discrete phase trajectories still rely on independent formulation of the Lagrangian force law. Although many uncertainties remain (chapter 1), there is now a broad consensus that the formulation given by Auton *et al.* (1988) and Thomas *et al.* (1983) is correct in the asymptotic limits of the assumptions on which it was derived (Thomas 1994). On the other hand, the force law derived by Maxey and Riley (1983) for low Reynolds numbers discrete phase has been widely cited by the workers on particle-laden shear flows. It is noted that the force law of Maxey and Riley (1983) contains a Basset term. Recently, the validity of the Basset term, which results from diffusion of the vorticity generated at the particle-fluid interface, has been brought into question. Reeks and Mckee (1984) has pointed out that the Basset term is applicable only in the Stokes regime, in which it is not even uniformly valid over the entire time domain; the kernel $(t-\tau)^{1/2}$ is correct for short times, but decays much faster for long times.

Little has been done on exploitation of Lagrangian-Lagrangian approaches for practical

numerical simulations of two-phase flows. General purpose and now widely used turbulence modelling package (**PHOENICS, FLUENT, FLOW3D, FIDAP**, etc.), all employ Eulerian two-fluid models for the flow field. Even advanced diagnostic codes (like **Mélodif** and **ESTET-ASTRID**) retain the Eulerian approach. Despite their success in many industrial problems, there remain many fundamental uncertainties that probably can only be surely addressed via conduction of Lagrangian field descriptions, which are crucial to the capture of the instantaneous flow features of the flow field so as to correctly address the dispersive transport in such flows.

2 SPECIFIC REALISATIONS

2.1 Bubbly Pipe Flows

In chapter 2 we addressed the behaviour of voidage profiles as reported by Serizawa *et al.* (1975a,b) and Wang *et al.* (1987) for vertical pipe flow, with notable near-wall voidage 'peaking' for upward flow and 'coring' on the centerline for downward flow. Using a simple transport model expressing the balance between lift force and wall attraction by transverse pressure gradient and an independent the bubble dispersion, the results showed how the lift force dominates the pressure gradient associated with the gradient of Reynolds averaged normal stresses. However, there remain reservation about estimation of the Reynolds normal stresses (they have been underestimated in our predictions) from the turbulence kinetic energy equations.

For upflows, then, the net effect is to drive the bubbles to accumulate near the wall and voidage peaking occurs because both the lift force and the radial pressure gradient are

directed towards the wall. In downflow, however, the lift force is directed toward the axis of the pipe, opposed to the radial pressure gradient, and the net effect there is that voidage peaking near the wall is suppressed. A primitive representation of bubble-induced turbulence (after Sato *et al.* 1981; Lance & Battaile 1991) was employed and this typically was large compared with the shear turbulence diffusivity. An overall best fit to the data was delivered by assuming a Prandtl-Schmidt number of unity in line with the conclusions by Sene *et al.* (1994) for bubble dispersion in mixing layers.

2.2 Bubbly Free Shear Flows

A Lagrangian-Lagrangian scheme first reported in Thomas *et al.* (1983) has been applied to survey the behaviour of bubble dispersion in two-dimensional turbulent free shear layer flows, adopting the generalized equation of motion (Auton *et al.* 1988) and extending the calculations reported in Sene *et al.* (1994). Particular attention was paid to the trapping effect of large eddies and the evaluations in terms of bubble trajectories and Lagrangian statistical measures. Like Sene *et al.* (1994), we adopted the discrete vortex method because it provides adequate description for important flow quantities (mean velocity profiles, turbulence intensities and shear stress) as well as providing plausible representation of eddy patterns and pairing behaviour. As an extension of previous studies, we looked at the energy spectra inside the mixing layer, demonstrating that Gaussian jitter introduced as numerical artefact (perhaps a representation of fine scale turbulence) mainly contributes to the low frequency spectra. Of the three dynamical parameters Π , Γ and γ , giving discrete phase motion in the force law, γ (mass density ratio) is irrelevant for bubbles but Π plays a key role in attracting the bubbles into the large eddies and Γ in their retention and locations within the eddies.

More especially, when $\Pi \rightarrow 0$ (negligible inertial attraction) the dispersion is nearly neutral and the use of the gradient diffusion model may well suffice. Following the approach of Sene *et al.* (1994), we estimated the dispersion coefficients through Lagrangian statistics, and compared the values for the bubbles and for the fluid, showing their ratio is about 1.0 for a long term dispersion, and thus reinforcing the findings of Sene *et al.* (1994). The implied effective Prandtl-Schmidt number of unity means the bubbles (in their limit) fill width of the mean shear layer, but do not extend outside.

The modelling approach (chapter 5) was also applied to bubble dispersion in a plane free jet, using the simulation to show that inertial and shear-induced lift forces are responsible for bubble trapping by large eddies along the edges of the jet. For an upflowing jet, the calculations delivered bimodal voidage profiles consistent with expectations for the mixing layer studies. Such a finding is clearly at odds with assumed Gaussian profiles adopted in previous studies of bubbly plumes and jets, although conclusive experimental evidence remains to be established.

An important genuine conclusion from the calculations (Chapter 6) is that discrete phase dispersion (particles and bubbles) is highly correlated with vorticity excursions. The need now is to formulate Eulerian statistical modelling that specifically incorporate this behaviour, thereby reducing the uncertainties of interphase pressure closure encountered with existing two-fluid couched in terms of momentum transport.

2.3 Particle Free Shear Flows

The dispersion calculations for particles in mixing layers (Chapter 4) indicate that the ratio of inertial to shear force (Π/Γ) represent a parameter scaling which plays a similar role to the Stokes number used in the specialist literature on this topic (e.g. Crowe *et al.* 1985), and that particle dispersion exceeds that of the fluid as reported experimentally and numerically by the other researchers (e.g. Crowe *et al.* 1993). This behaviour is particularly pronounced for values of Π/Γ around 0.02-0.05. Physically our simulations here show that particles entrained into the large-scale structure are subsequently centrifuged to the outer edges of the eddies where they accumulate at, and preferentially migrate towards, the stagnant zone between adjoining large eddies. Supplemented by mass density ratio γ , Π and Γ comprise essential dimensionless groups characterizing discrete phase transport.

The importance of transient pressure gradient in the external irrotational flows induced by travelling eddies is also crucial to adequate reproduction of the transport dynamics. Comparing the results of our discrete vortex simulation with a simple Gaussian stochastic model has clearly demonstrated the importance of the structure in the instantaneous velocity field. Eulerian-pseudo Lagrangian models (e.g. Gosman & Ioannides 1981) fail to capture these features and hence cannot reproduce the intermittency manifested in Lagrangian-Lagrangian simulations.

3 RECOMMENDATIONS FOR FUTURE WORK

More consideration is needed on the formulation of physically sound diffusivity for voidage, especially recognising the eddy scavenging effect addressed here which represents a counter gradient contribution. Existing one-point formulations crudely express diffusivity as the sum

of contributions from the flow turbulence and from the pseudo turbulence associated with the bubbles. However, experimental measurements of turbulence in bubbly flows show evidence of amplification and diminution, especially in terms of spectral composition (e.g. Serizawa *et al.* 1975a,b; Wang *et al.* 1987; Moursali *et al.* 1995). The shear-induced lift force acting on the bubbles also needs further consideration since the assigned value of lift coefficient significantly affects the accuracy of prediction, as shown here and by others (e.g. Antal *et al.* 1991). In the vicinity of walls, bubbles experience not only strong shear, but also wall blockage effects and it is known that bubble size is an important factor in the near wall behaviour. Bubble shape also affects the near wall behaviour (e.g. Serizawa & Kataoka 1989).

Even though large-scale structure in a mixing layer may sometimes be basically two-dimensional (as supposed here), there are spanwise structure (Hussain 1986) which can seldom be ignored in reality. Recent developments using three-dimensional Lagrangian approaches (e.g. Squires and Eaton 1990; Wang and Maxey 1993) have broadly supported the main physical features of vorticity coupling with discrete phase, further confirming how important it is to capture the instantaneous structure of the flow field. To what extent 2-D methods, like the discrete vortex method used here, can be extended to 3-D fields is not entirely clear (e.g. Eaton & Fessler 1994).

We have only considered fluxes in which the bubbles and particles are present in such low concentration as not to affect the flow (or interact between themselves). The effect of two-way coupling may well often be important for practical calculations, especially with bubbles accumulating in shear layer eddies. Only a few preliminary considerations have been given

to this aspect (e.g. Elghobashi & Truesdell 1993; Tang *et al.* 1990) and more effort is required. The incorporation of coupling effects into the discrete vortex method simulation, which uses only simple kinematic simulation of vortex dynamics at present, would be desirable.

REFERENCES

- Antal, S. P., Lahey, R. T. & Flaherty, J. E. 1991 Analysis of phase distribution in fully developed laminar bubbly two-phase flow. *Int. J. Multiphase Flow* **17**, 635-652.
- Auton, T. R., Hunt, J. C. R. & Prud'homme, M. 1988 The force exerted on a body in inviscid unsteady nonuniform rotational flow. *J. Fluid Mech.* **197**, 241.
- Crowe, C. T., Gore, R. A. & Troutt, T. R. 1985 Particle dispersion by coherent structures in free shear flows. *Part. Science Technology* **3**, 149.
- Crowe, C. T., Chung, J. N. & Troutt, T. R. 1993 Particle dispersion by organized turbulent structures. *Particulate Two-Phase Flow*, edited by M. C. Roco (Butterworths, New York, 1993).
- Drew, D. A. 1983 Mathematical modeling of two-phase flow. *Ann. Rev. Fluid Mech.* **15**, 261-291.
- Eaton, J. K. & Fessler, J. R. 1994 Preferential concentration of particles by turbulence. *Int. J. Multiphase Flow* **20**, 169-209.
- Elghobashi, S. E. & Truesdell, G. C. 1993 On the two-way interaction between homogeneous turbulence and dispersed solid particles I: Turbulence modification. *Phys. Fluids A* **5**, 1790-1801.
- Gosman, A. D. & Ioannides, E. 1981 Aspects of computer simulation of liquid-fuelled combustors. AIAA paper 81-0323, 19th Aerospace Sciences Meeting, St. Louis.
- Hunt, J. C. R., Perkins, R. J., Lunde, K. & Thomas, N. H. 1993 Modelling bubbly flows. *Proc. IUTAM Sympos. (Birmingham) on "Bubble Dynamics and Interface Phenomena"* (eds. J. R. Blake & N. H. Thomas), Kluwer.
- Hussain, A. K. M. F. 1986 Coherent structures and turbulence. *J. Fluid Mech.* **173**, 303-356.
- Lance, M. & Battaile, J. 1991 Turbulence in the liquid phase of a uniform bubbly air-water flow. *J. Fluid Mech.* **22**, 95-118.

- Maxey, M. R. & Riley, J. J. 1983 Equation of motion for a small-rigid sphere in a nonuniform flow. *Phys. Fluids* **26**, 883-889.
- Moursali, E., Marié, J. L. & Bataille, J. 1995 An upward turbulent bubbly boundary layer along a vertical flat plate. *Int. J. Multiphase Flow* **21**, 107-117.
- Reeks, M. W. & Mckee, S. 1984 The dispersive effects of Basset history forces on particle motion in a turbulent flow. *Phys. Fluids* **27**, 1573.
- Sato, Y., Sadatomi, M. & Sekoguchi, K. 1981 Momentum and heat transfer in two-phase bubbly flow -I. *Int. J. Multiphase Flow* **7**, 167-177.
- Sene, K. J., Hunt, J. C. R. & Thomas, N. H. 1994 The role coherent structures in bubble transport by turbulent shear flows. *J. Fluid Mech.* **259**, 219-240.
- Serizawa, A. & Kataoka I. 1989 Phase distribution in two-phase flow. *ICHMT International Seminar on Transient Phenomena in Multiphase Flow*, Dubrovnik, Yugoslavia, 179-224.
- Serizawa, A., Kataoka, I. & Michiyoshi, I. 1975 Turbulence structure of air-water bubbly flow II. Local properties. *Int. J. Multiphase Flow* **2**, 235-246.
- Serizawa, A., Kataoka, I. & Michiyoshi, I. 1975 Turbulence structure of air-water bubbly flow III. Transport properties. *Int. J. Multiphase Flow* **24**, 247-259.
- Squires, K. D. & Eaton, J. K. 1990 Particle response and turbulence modification in isotropic turbulence. *Phys. Fluids* **A2**, 1191-1203.
- Tang, L., Crowe, C. T., Chung, J. N. & Troutt, T. R. 1990 A numerical model for droplets dispersing in a developing plane shear layer including coupling effects. *Numerical Methods for Multiphase Flows*, ASME FED-Vol. **91**, 27-33.
- Thomas, N. H., Auton, T. R., Sene, K. & Hunt, J. C. R. 1983 Entrapment and transport of bubbles by transient large eddies in multiphase turbulent shear flows. *Proc. Intl Conf (Coventry, England) on Physical Modelling of Multiphase Flows*. BHRA (Cranfield) Paper E1.
- Viollet, P. L. & Simonin, O. 1994 Modelling dispersed two-phase flows: Closure, validation and software development. *Appl. Mech. Rev.* **47**(6), s80-s84.
- Wang, L. P. & Maxey, M. R. 1993 Settling velocity and concentration distribution of heavy particles in homogeneous isotropic turbulence. *J. Fluid Mech.* **256**, 27-68.
- Wang, S. K., Lee, S. J., Jones Jr, O. C. & Lahey Jr, R. T. 1987 3-D turbulence structure and phase distribution measurements in bubbly two-phase flows. *Int. J.*

